Available online at www.sciencedirect.com

ScienceDirect

Nuclear Data Sheets 148 (2018) 1–142

Nuclear Data Sheets

www.elsevier.com/locate/nds

ENDF/B-VIII.0: The 8th Major Release of the Nuclear Reaction Data Library with CIELO-project Cross Sections, New Standards and Thermal Scattering Data

D. A. Brown,[1] M. B. Chadwick,[2,*] R. Capote,[3] A. C. Kahler,[2] A. Trkov,[3] M. W. Herman,[1] A. A. Sonzogni,[1] Y. Danon,[4] A. D. Carlson,[5] M. Dunn,[6] D. L. Smith,[7] G. M. Hale,[2] G. Arbanas,[8] R. Arcilla,[1] C.R. Bates,[2] B. Beck,[9] B. Becker,[10] F. Brown,[2] R. J. Casperson,[9] J. Conlin,[2] D. E. Cullen,[9] M.-A. Descalle,[9] R. Firestone,[11] T. Gaines,[12] K. H. Guber,[8] A. I. Hawari,[13] J. Holmes,[14] T. D. Johnson,[1] T. Kawano,[2] B. C. Kiedrowski,[15] A. J. Koning,[3] S. Kopecky,[16] L. Leal,[17] J. P. Lestone,[2] C. Lubitz,[18] J. I. Márquez Damián,[19] C. M. Mattoon,[9] E. A. McCutchan,[1] S. Mughabghab,[1] P. Navratil,[20] D. Neudecker,[2] G. P. A. Nobre,[1] G. Noguere,[21] M. Paris,[2] M. T. Pigni,[8] A. J. Plompen,[16] B. Pritychenko,[1] V. G. Pronyaev,[22] D. Roubtsov,[23] D. Rochman,[24] P. Romano,[7] P. Schillebeeckx,[16] S. Simakov,[25] M. Sin,[26] I. Sirakov,[27] B. Sleaford,[9] V. Sobes,[8] E. S. Soukhovitskii,[28] I. Stetcu,[2] P. Talou,[2] I. Thompson,[9] S. van der Marck,[29] L. Welser-Sherrill,[2] D. Wiarda,[8] M. White,[2] J. L. Wormald,[13] R. Q. Wright,[8] M. Zerkle,[14] G. Žerovnik,[16] and Y. Zhu[13]

[1] *Brookhaven National Laboratory, Upton, NY 11973-5000, USA*
[2] *Los Alamos National Laboratory, Los Alamos, NM 87545, USA*
[3] *International Atomic Energy Agency, PO Box 100, A-1400 Vienna, Austria*
[4] *Rensselaer Polytechnic Institute, Troy, NY 12180, USA*
[5] *National Institute of Standards and Technology, Gaithersburg, MD 20899-8463, USA*
[6] *Spectra Tech, Inc., Oak Ridge, TN 37830, USA*
[7] *Argonne National Laboratory, Argonne, IL 60439-4842, USA*
[8] *Oak Ridge National Laboratory, Oak Ridge, TN 37831-6171, USA*
[9] *Lawrence Livermore National Laboratory, Livermore, CA 94551-0808, USA*
[10] *Gesellschaft für Anlagen und Reaktorsicherheit, Schwertnergasse 1, D-50667 Köln, Germany*
[11] *Lawrence Berkeley National Laboratory, Berkeley, CA 94720, USA*
[12] *AWE plc, Reading RG7 4PR, United Kingdom*
[13] *North Carolina State University, Raleigh, NC 27695, USA*
[14] *Naval Nuclear Laboratory, West Mifflin, PA 15122, USA*
[15] *University of Michigan, Ann Arbor, MI 48109, USA*
[16] *EC-JRC, B-2440 Geel, Belgium*
[17] *Institut de Radioprotection et de Sûreté Nucléaire, 92262 Fontenay aux Roses, Cedex, France*
[18] *Naval Nuclear Laboratory, Niskayuna, NY 12309, USA*
[19] *Centro Atómico Bariloche, S. C. de Bariloche, Argentina*
[20] *TRIUMF, Vancouver, BC V6T 2A3, Canada*
[21] *CEA, DEN, DER, SPRC, Cadarache, 13108 Saint-Paul-lèz-Durance, France*
[22] *PI Atomstandart at SC Rosatom, Moscow, Russian Federation*
[23] *Canadian Nuclear Laboratories, Chalk River, Ontario, Canada*
[24] *Paul Scherrer Institut, 5232 Villigen, Switzerland*
[25] *Karlsruhe Institute of Technology, Hermann-von-Helmholtz-Platz, 1 76344 Eggenstein-Leopoldshafen, Germany*
[26] *University of Bucharest, Bucharest-Magurele, RO-077125, Romania*
[27] *Institute for Nuclear Research and Nuclear Energy, BAS, BG-1784 Sofia, Bulgaria*
[28] *Joint Institute for Energy and Nuclear Research, Minsk, Belarus*
[29] *NRG, Westerduinweg 3, 1755 LE Petten, The Netherlands*

(Received 18 September 2017; revised received 21 November 2017; accepted 14 December 2017)

We describe the new ENDF/B-VIII.0 evaluated nuclear reaction data library. ENDF/B-VIII.0 fully incorporates the new IAEA standards, includes improved thermal neutron scattering data and uses new evaluated data from the CIELO project for neutron reactions on ^{1}H, ^{16}O, ^{56}Fe, ^{235}U, ^{238}U and ^{239}Pu described in companion papers in the present issue of *Nuclear Data Sheets*. The evaluations benefit from recent experimental data obtained in the U.S. and Europe, and improvements in theory and simulation. Notable advances include updated evaluated data for light nuclei, structural materials, actinides, fission energy release, prompt fission neutron and γ-ray spectra, thermal neutron scattering data, and charged-particle reactions. Integral validation testing is shown for a wide range of criticality, reaction rate, and neutron transmission benchmarks. In general, integral validation performance of the library is improved relative to the previous ENDF/B-VII.1 library.

https://doi.org/10.1016/j.nds.2018.02.001
0090-3752/© 2018 Published by Elsevier Inc.

CONTENTS

---

* Corresponding author: mbchadwick@lanl.gov

I. INTRODUCTION

The ENDF library project is coordinated by the Cross Section Evaluation Working Group (CSEWG) and CSEWG is releasing the new ENDF/B-VIII.0 library, incorporating work from across the US and the international nuclear science community over the last six years. The library is being issued in the traditional ENDF-6 format, as well as in an alternative new Generalized Nuclear Database Structure (GNDS) format.

As was the case for previous ENDF releases [1, 2], the ENDF/B-VIII.0 library has not been developed in isolation, but rather, it continues to evolve through close interactions with parallel organizations around the world, most notably with Europe (JEFF) [3], Japan (JENDL) [4, 5], and with South Korea. Collaborations with the International Atomic Energy Agency (IAEA) have had numerous impacts, most notably on Collaborative International Evaluation Library Organization (CIELO) nuclides [6–8], the standards [9, 10], prompt fission neutron spectra (PFNS) evaluations [11], and dosimetry cross sections [12, 13]. A number of collaborations via the Nuclear Energy Agency (NEA) Working Party on Evaluation Cooperation (WPEC) provided valuable contributions, especially CIELO (Subgroup 40) [6, 7], a plutonium resonance analysis (Subgroup 34) [14], a new GNDS format option (Subgroup 38) [15], data adjustment studies (Subgroup 39) [15], and thermal scattering data (Subgroup 42) [16].

The new ENDF/B-VIII.0 library, in contrast to ENDF/B-VII.1, has major changes for neutron reactions on the major actinides and other nuclides that impact simulations of nuclear criticality. The important isotopes ^{1}H, ^{16}O, ^{56}Fe, ^{235,238}U, and ^{239}Pu have been the focus of the international CIELO collaboration, and the resulting advances have been incorporated into ENDF/B-VIII.0. Additional information on the CIELO collaboration findings is given in companion articles in the present edition of *Nuclear Data Sheets*: a CIELO overview [8], uranium [17], plutonium capture [18], iron [19], and prompt fission neutron spectra (PFNS) [20]. Additionally a major update to the standards has been made by a group of researchers under the auspices of the IAEA, and these new standards have been mostly incorporated into ENDF/B-VIII.0 (and are also documented in a companion article [10]). Other notable advances in ENDF/B-VIII.0, described further in this article, include updates to neutron reactions on minor actinides, structural materials, light nuclei, dosimetry cross sections, fission energy release, decay data, charged-particle reactions, and thermal neutron scattering data for modeling neutron reactions on molecules at low energies.

The previous ENDF/B-VII.1 library was built upon the earlier ENDF/B-VII.0 library in various ways: extensive nuclear reaction data on uncertainties (covariance data evaluations) were provided; minor actinide cross section evaluations were improved; structural material evaluations were advanced through use of recent resolved and unresolved resonance analyses of new measured data; new light nucleus *R*-matrix evaluations were developed

TABLE I. Overview of the ENDF/B library releases and the 15 sublibraries in ENDF/B-VIII.0. Shown in the columns are the number of materials present in each sublibrary in each release. Here Spontaneous Fission Yields is abbreviated as SFY and Neutron-induced Fission Yields as NFY.

Sublibrary	VIII.0	VII.1	VII.0	VI.8
Neutron	557	423	393	328
Thermal n-scattering	33	21	20	15
Proton	49	48	48	35
Deuteron	5	5	5	2
Triton	5	3	3	1
Helium3	3	2	2	1
Alpha	1	n/a	n/a	n/a
Photonuclear	163	163	163	n/a
Atomic relaxation	100	100	100	100
Electron	100	100	100	100
Photoatomic	100	100	100	100
Decay data	3821	3817	3838	979
SFY	9	9	9	9
NFY	31	31	31	31
Standards	10	8	8	8

for the nuclides ^{3}He, ^{9}Be, and ^{6}Li; fission product data for fast and 14 MeV neutrons incident on plutonium were re-evaluated, including details of the neutron energy dependence over the fast neutron range from 0.5–2.0 MeV; new data for fission energy release were provided; and a new decay data library was developed. But for all these upgrades, the previous ENDF/B-VII.1 preserved much of the ENDF/B-VII.0 library capabilities, and most notably the major actinides were not changed, and there was the intent that VII.1 should generally preserve, and improve upon, the good integral criticality performance testing seen in ENDF/B-VII.0 [1, 21]. Indeed ENDF/B-VII.1 did generally perform well in such integral validation tests, as described by Kahler *et al.* [22]. But it has taken this present ENDF/B-VIII.0 effort - including related CIELO project work - to accomplish the many upgrades made to important nuclides such as the actinides, and those in the new standards.

II. OVERVIEW OF ENDF/B-VIII.0 LIBRARY

ENDF/B-VIII.0 represents the biggest change to the ENDF library in many years, including CIELO evaluations (^{1}H, ^{16}O, ^{56}Fe, ^{235}U, ^{238}U, ^{239}Pu), revised neutron standards and a vastly expanded thermal scattering law sublibrary along with numerous other significant changes. Indeed, the CIELO and thermal scattering law sublibrary improvements are primarily responsible for the improved performance in integral benchmarks documented in Section XII. The library is also much larger: the neutron sublibrary has expanded 32% to contain 557 evaluations (see Table I).

Highlighted changes in the neutron sublibrary include

- **CIELO evaluations**: New ^{1}H, ^{16}O, ^{56}Fe, ^{235}U, ^{238}U, ^{239}Pu, including prompt fission neutron spectra (PFNS) and prompt fission gamma spectra (PFGS)
- **Light elements**: New n, ^{2}H, ^{3}He, ^{6}Li, ^{9}Be, ^{10}B, C (^{12,13}C, tuned to match $^{\mathrm{nat}}$C standards), and ^{35,37}Cl; adopted ^{18}O from ROSFOND [23, 24]
- **Structural materials**: New ^{40}Ca, constituents of steel (^{54,56,57,58}Fe, $^{58-62,64}$Ni), ^{59}Co, ^{63,65}Cu, $^{174-182}$Hf, $^{182-186}$W and revised ^{105}Rh, ^{132}Te
- **Rare earths**: Adopted Dy and Yb from JENDL-4.0
- **Noble gases**: Revised ^{40}Ar, ^{78}Kr, ^{124}Xe; $^{20-22}$Ne from TENDL-2015
- **Minor actinides**: New ^{236m}Np, ^{240}Pu, new nubars and revised ^{241,243}Am
- **Misc. materials**: New $^{73-75}$As and ^{197}Au; $^{190-198}$Pt adopted from TENDL-2015
- **Unstable isotopes**: Added all isotopes with $T_{1/2} \geq 1$ year and all the intermediate nuclei needed to produce these isotopes through neutron-induced reactions using a combination of TENDL-2015 evaluations and EMPIRE calculations
- **Primary gammas**: Added to ^{6,7}Li, ^{11}B, ^{19}F, ^{23}Na, ^{27}Al, ^{28}Si and ^{35,37}Cl to support nondestructive assay applications

These changes, especially to CIELO isotopes, carbon and gold, are rooted in the revised neutron standards. In this sublibrary we have:

- Added the integral of the ^{235}U(n,f) cross section from 7.8–11 eV as a standard
- Added the Au(n,γ) 30 keV Maxwellian-averaged cross section as a standard
- Added high energy fission reference cross sections ^{235}U(n,f), ^{238}U(n,f) from 200 MeV up to 1 GeV; ^{209}Bi(n,f) and ^{nat}Pb(n,f) from about 20 MeV up to to 1 GeV
- Revised thermal neutron constants

The changes to the thermal scattering law (TSL) sublibrary are significant since every evaluation except benzene was either revised dramatically or (re)evaluated. In addition, all evaluations except benzene have the model inputs provided (in the form of NJOY/LEAPR files) so that more detailed checking and peer review is possible. Together we have:

- **Fuels**: New UO$_2$ and UN
- **Moderators**: New heavy and light water, graphite (reactor grade and crystalline), polyethylene, lucite, and yttrium hydride

- **Reflectors**: Revised Be and BeO
- **Natural materials**: New ice and SiO_2
- **Cladding**: New SiC

There were also many updates to other libraries:

- **Light Charged Particles**: New alpha sublibrary, p,d,t on ^{7}Li and ^{3}He on ^{3}He
- **Decay sublibrary**: Improved beta intensities for some fission products; modified K X-ray energies for selected actinides
- **Atomic sublibraries**: Minor fixes and reformatting resulting in a update of all three atomic sublibraries

All these changes were performed in an environment of dramatically improved quality assurance enabled by computational advances. Much of the ENDF/B workflow has been automated now. This process started with the introduction of the GForge collaboration environment installed at the National Nuclear Data Center which includes both revision control, library release management and bug tracking. GForge has now been connected to the ADVANCE continuous integration system [25]. ADVANCE runs a battery of physics and format checks on every changed evaluation of every commit. This checking with ADVANCE completely automates the traditional ENDF/B Phase I testing. ADVANCE also benefits from the code modernization push that led to both the development of the FUDGE and NJOY2016 processing codes. These processing improvements in turn led to new tests and identification of issues in various evaluations. The processing code modernization efforts in the US, Europe and Asia are in large part a result of the roll out of the new GNDS formatting option discussed in Section XIII.

III. NEUTRON CROSS SECTION SUBLIBRARY

A. Z=0-20

1. *n, the Neutron*

A new evaluation of the $n-n$ scattering cross section is available at energies up to 50 MeV in ENDF/B VIII.0. It uses essentially the same R-matrix parameters as the $N-N$ analysis[1] described in the next section. That is, the isospin-1 parameters used to describe $p-p$ scattering are also used to predict values of the $n-n$ scattering cross section. This charge-symmetric model is modified by allowing a single energy shift of all the $p-p$ ($T=1$) energy levels to account for the Coulomb difference between the di-neutron and di-proton systems. The value of this energy shift is determined by fitting the experimental value of the singlet $n-n$ scattering length, a_0 =-18.5 fm [26]. The $n-n$ scattering cross section resulting from this calculation is shown in Fig. 1, compared to the $n-p$ scattering cross section from the same analysis. They are similar below about 600 keV, but above that energy the contributions from the $T=0$ states make the $n-p$ cross section cross over and become larger than the $n-n$ cross section. Note that the $n-n$ scattering cross section shown in Fig. 1 is half the integrated differential elastic scattering cross section, as is appropriate for identical particles, whereas the $n-p$ scattering cross section is equal to the angle-integrated differential elastic scattering cross section.

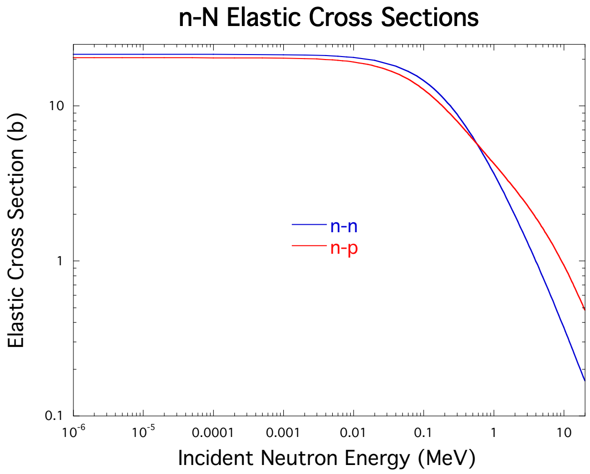

FIG. 1. (Color online) The elastic cross sections for $n-n$ (blue curve) and $n-p$ (red curve) scattering calculated at energies below 20 MeV from the charge-independent $N-N$ R-matrix analysis. They are similar below about 600 keV, with the differences above that energy coming from the $T=0$ contributions to $n-p$ scattering.

2. ^1H

The $n-p$ scattering cross sections used in this new version (VIII.0) of the ENDF/B file came from a charge-independent (CI) analysis of the $N-N$ system at energies up to 50 MeV, part of the IAEA standards. The channels, reactions, and data included in the analysis are summarized in Table II. The CI R matrix has the form

$$R(E) = \sum_{\lambda,T} \frac{\gamma_\lambda^{(T)} \tilde{\gamma}_\lambda^{(T)}}{E_\lambda^{(T)} - E}, \tag{1}$$

where $T=1$ for $\ell+s$ even, and $T=0$ for $\ell+s$ odd. The relativistic energy is given in terms of the total 4-momentum squared, Mandelstam's s-variable, and the total $p+p$ channel mass M, by $E=(s-M^2)/2M$. The same isospin-1 reduced widths $\gamma_\lambda^{(1)}$ are used to describe $p-p$ and $n-n$ scattering, as well as the $T=1$ part of $n-p$ scattering (making it a CI model), but the corresponding $p-p$

---

[1] In subsections III A 1 and III A 2, 'N' refers to 'nucleon' and *not* to 'nitrogen' as is used elsewhere in this paper.

TABLE II. Channel configuration (top) and data summary (bottom) for the charge-independent $N-N$ analysis up to 50 MeV. Since the number of free parameters is 43 resonance parameters + 83 normalizations, the chi-squared per degree of freedom for the analysis is 0.90.

Channel	a_c (fm)	$l_{\max}$
$p+p$	3.26	3
$n+p$	3.26	3
$\gamma+d$	84.6	1
$n+n$	3.26	3

Reaction	# Pts.	χ^2	Observable Types
$p(p,p)p$	675	951	$\sigma(\theta), A_y(p), C_{x,x'}, C_{y,y'}, K_x^{x'}, K_y^{y'}, K_z^{x'}$
$p(n,n)p$	4815	3764	$\sigma_{\mathrm{T}}, \sigma(\theta), A_y(n), C_{y,y'}, K_y^{y'}$
$p(n,\gamma)d$	86	179	$\sigma_{\mathrm{int}}, \sigma(\theta), A_y(n)$
$d(\gamma,n)p$	88	77	$\sigma_{\mathrm{int}}, \sigma(\theta), \Sigma(\gamma), P_y(n)$
$n(n,n)n$	1	0	a_0
Norms.	80	86	
Total:	5745	5057	20

eigenenergies $E_\lambda^{(1)}$ are shifted by a Coulomb energy difference, Δ_Z, that depends only on the total charge of the system ($Z=0$ for $n-n$, and $Z=1$ for $n-p$).

This simple, Coulomb-corrected, CI model appears to work well for describing all the $N-N$ data up to 50 MeV, obtaining a chi-square per degree of freedom of 0.90. Figure 2 shows the fit to selected $n-p$ total cross section measurements. The fits to some of the $n-p$ differential cross sections and polarizations are shown in Figs. 3 and 4, respectively. It should be remembered that many other measurements not shown, for example, for $p-p$ scattering, and for $n-p$ capture, are also fit quite well by this analysis, and they further constrain the results for $n-p$ scattering.

The new analysis preserves the values of the low-energy $n-p$ scattering lengths, $a_0=-23.719(5)$ fm and $a_1=5.414(1)$ fm obtained in an earlier analysis that went up to 30 MeV, which formed the basis for the ENDF/B VII.1 hydrogen evaluation. The changes from that earlier analysis remain small at higher energies, as shown in Fig. 5 [10], which plots the ratios of ENDF/B-VIII.0 to ENDF/B-VII.1 for the total cross section and for the zero-degree proton laboratory differential cross section. A small change in the thermal capture cross section, from 332.00 mb to 332.58 mb, now agrees better with one of the most precise experimental values [27].

Although the analysis goes to 50 MeV, we provided cross sections for ENDF/B-VIII.0 only up to 20 MeV. This is because the analysis will eventually be extended to 200 MeV (a preliminary version already exists for energies up to 100 MeV).

3. ^2H

During post-release testing of the final version of ENDF/B-VI (ENDF/B-VI.8), it was discovered [55] that calculated eigenvalues (k_{eff}) for a set of D_2O solution benchmarks from the ICSBEP project [56] had decreased substantially (by about 1000 pcm) relative to an earlier version, ENDF/B-VI.4. The cause was traced to modifications made to the deuterium cross sections in ENDF/B-VI.5 and retained through ENDF/B-VII.0 and VII.1. In the ENDF/B-VI.5 evaluation, $\sigma_s(E)$ and $P_s(E,\mu)$ below $E\simeq 4$ MeV were compared to results of a coupled-channels R-matrix analysis [57]. The $\sigma_s(E)$ from ENDF/B-VI.4 was found to be consistent with this R-matrix analysis and was retained. However, the $P_s(E,\mu)$ data below $E=3.2$ MeV were replaced with new tabulated distributions from the R-matrix analysis [57], and a sparse energy grid E_i was chosen for the tabular data $P_s(E_i,\mu_j)$ at 0.01 - 0.1 MeV $< E <$ 1 - 10 MeV.

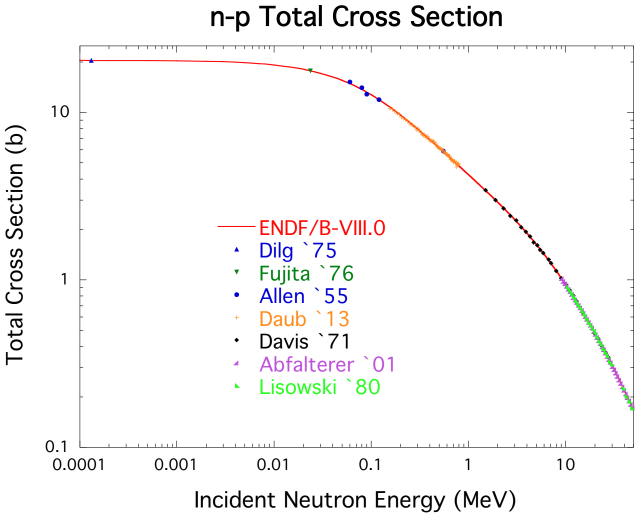

FIG. 2. (Color online) The $n-p$ total cross section between 100 eV and 50 MeV. The red curve is ENDF/B-VIII.0, and the colored symbols are from various measurements [28–35].

It was also noticed [58] that the existing experimental data on the angular distributions of out-scattered neutrons in the ^{2}H(n,n) reaction were old, sparse, and even inconsistent, and it was recommended [58] that new measurements and theoretical study [59, 60] to be undertaken. Although the ENDF/B-VII.1 evaluation of ^{2}H performs reasonably well in comparison with the new neutron scattering measurements at $E<2$ MeV [61] and in modelling heavy water reactor benchmarks [62, 63], the recent experimental results [64] on backward-to-forward ratio in the neutron angular distributions at 0.2 MeV $<E<$ 2 MeV favour the evaluations of $P_s(E,\mu)$ based on the three-body theory (Faddeev [65] or Alt-Grassberger-Sandhas (AGS) [66] equations) and the modern nucleon-nucleon (NN) potentials [67] rather than the evaluations based on R-matrix analysis.

In the nuclear data releases world-wide, some evaluations of MF = 4, MT = 2 data for ^{2}H(n,n) are based on the three-body theory, such as, in CENDL-3.1, JENDL-3.3 and -4.0, and in JEFF-3.2. The JEFF-3.2 evaluation of both $\sigma_s(E)$ and $P_s(E,\mu)$ of the ^{2}H(n,n) reaction is based on the solution of the three-body Faddeev equations with the INOY03 NN potentials [68]. The trial evaluations of neutron scattering data based on different choices for the

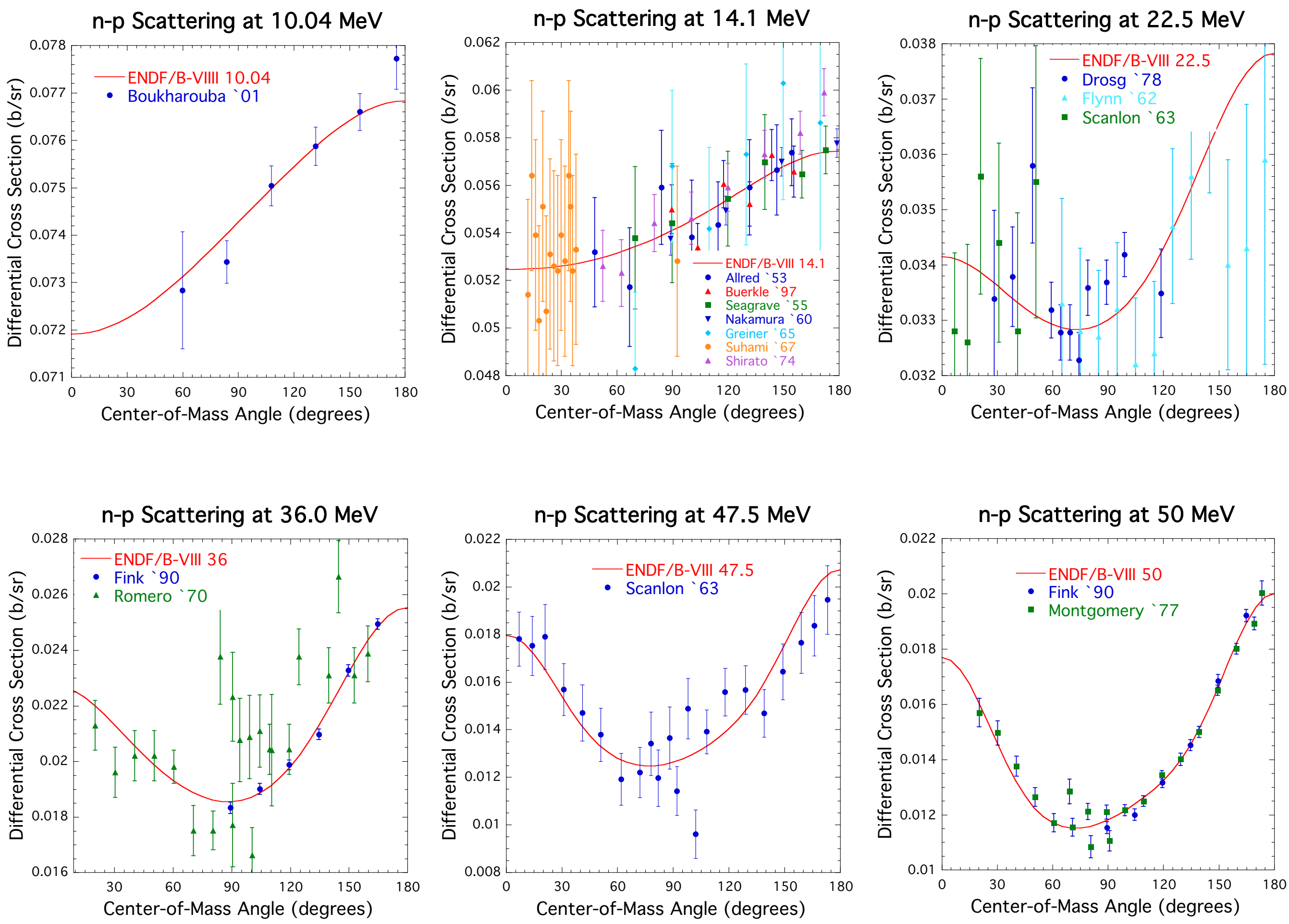

FIG. 3. (Color online) The differential cross section for $n-p$ scattering at energies between 10 and 50 MeV. The red curve is ENDF/B-VIII.0, and the points are from various measurements [36–48].

NN potentials [69] show good performance in the estimates of criticality (k_{eff}) of the heavy water benchmarks (critical assemblies and nuclear reactors) [56], including the notorious HEU-SOL-THERM-004 (HST-4) [55, 70].

Therefore, to improve the performance of deuterium nuclear data, the evaluation of deuterium (^{2}H) is modified in the final release of ENDF/B-VIII.0 in comparison with the ENDF/B-VII.1 version (retained up to ENDF/B-VIII.0β4). The evaluation of the angular distributions of neutrons in the elastic scattering reaction (MF = 4, MT = 2) is modified by using data from the JEFF-3.2 evaluation of ^{2}H, for the incident neutron energies 10^{-5} eV $\leq E \leq$ 28.0 MeV. At higher neutron energies, the ENDF/B-VII.1 data is retained. As a result, the combined data block of MF = 4, MT = 2 makes use of the dual representation, namely, LTT = 3, or Legendre moment expansion, at $E \leq$ 28.0 MeV taken from JEFF-3.2 data file and using JEFF grid for E_i and the tabular form at 28.0 MeV $< E <$ 150.0 MeV from the original ENDF/B-VII.1 file. In Fig. 6, we show differential cross sections $\sigma_s(E,\mu) = (\sigma_s(E)/2\pi)P_s(E,\mu)$ of ^{2}H(n,n) in the center-of-mass reference frame at 1.0 MeV $< E <$ 2.4 MeV. One can notice that, in ENDF/B-VIII.0, the backward scattering weight (contributions of μ near $\mu = \cos 180^\circ = -1$ into $\int P_s(E,\mu)\,\mathrm{d}\mu$) is increased at $E \simeq 1$ MeV in comparison with ENDF/B-VII.1 (Fig. 6) in the center-of-mass frame. On the other hand, the agreement of the evaluated data with the experimental results of Vedrenne [71] for the angular distributions of out-scattered neutrons needs an improvement at low incident neutron energies $E \lesssim 1$-5 MeV, from both the experimental and theoretical standpoints.

Cross sections (MF = 3 data) for n+^{2}H are the same in ENDF/B-VIII.0 and B-VII.1. For example, in ENDF/B-VIII.0, the thermal cross sections of deuterium are

$$\sigma_{s,\mathrm{th}} = 3.395 \pm 0.051\,(\pm 1.5\%)\ \mathrm{b},$$
$$\sigma_{\mathrm{th}}(n,\gamma) = 0.506 \pm 0.015\,(\pm 3\%)\ \mathrm{mb}.$$

The value of $\sigma_{\mathrm{th}}(n,\gamma)$ lies higher, but within $\pm 2\sigma$ of the evaluated cross-section uncertainty (MF = 33), than the result of recent measurements by Firestone and Revay [72] (measured value of 0.489 ± 0.006 mb).

For E = 14 MeV, MF = 3, 33 of ^{2}H, ENDF/B-VIII.0

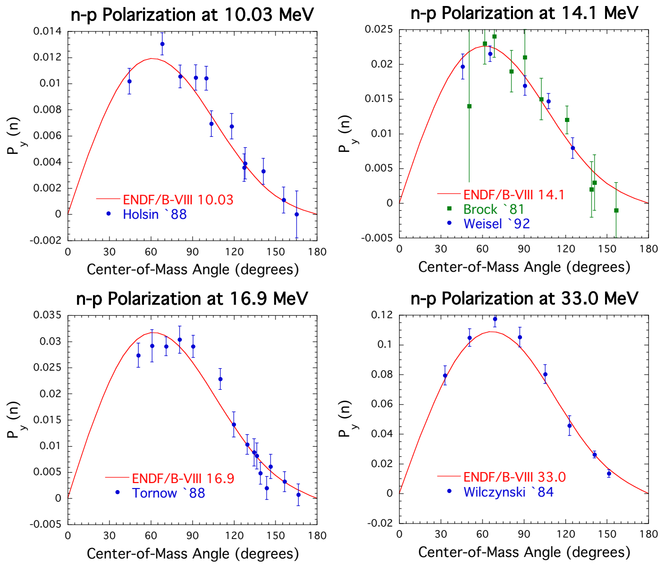

FIG. 4. (Color online) The neutron polarization for $n-p$ scattering at energies between 10 and 33 MeV. The red curve is ENDF/B-VIII.0, and the points are from various measurements [49–53].

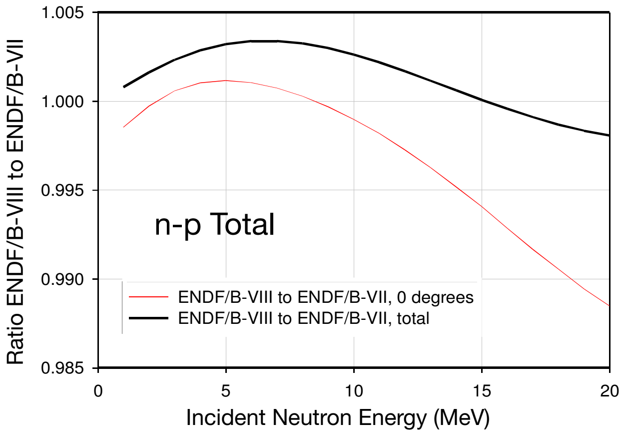

FIG. 5. (Color online) The cross-section ratios of VIII.0/VII.1 for the $n-p$ total cross section (black curve) and the differential cross section for detecting protons at zero degrees in the laboratory system (red curve) at energies below 20 MeV. Figure taken from Fig. 1 of Ref. [54].

give the following estimates:

$$\sigma_{s,14\,\mathrm{MeV}} = 0.644 \pm 0.032\,(\pm 5\%)\ \mathrm{b},$$
$$\sigma_{14\,\mathrm{MeV}}(n,2n) = 0.166 \pm 0.036\,(\pm 21.5\%)\ \mathrm{b},$$
$$\sigma_{14\,\mathrm{MeV}}(n,\gamma) = 9.5 \pm 7.6\,(\pm 80\%)\ \mu\mathrm{b}.$$

4. ^{3}*He*

No new work was done on the n+^{3}He cross sections for ENDF/B VIII.0. A newer R-matrix analysis of the reactions in the ^{4}He system exists that could form the basis of an updated evaluation, and we are considering using it in a future update to ENDF/B-VIII.0.

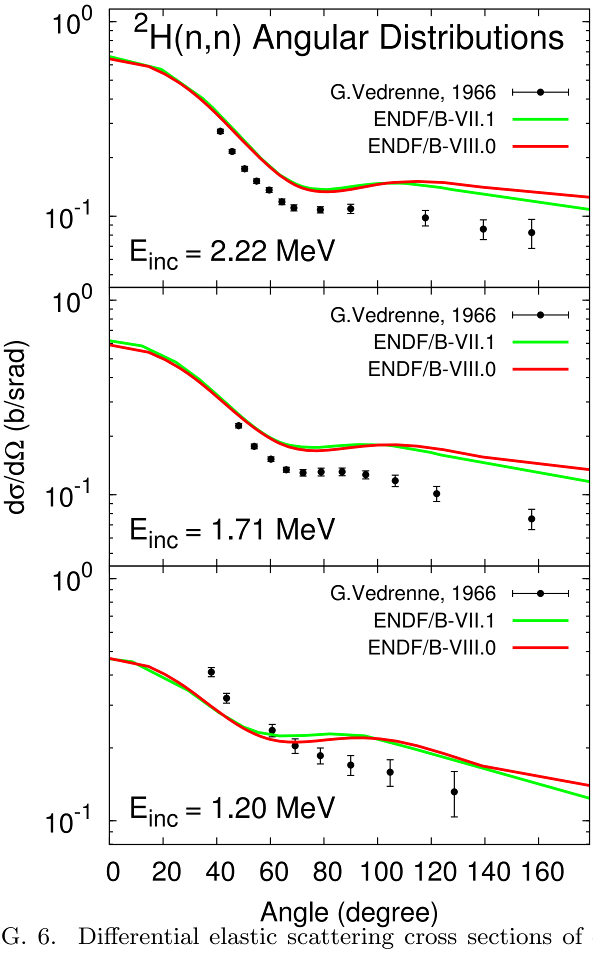

FIG. 6. Differential elastic scattering cross sections of deuterium $\sigma_s(E,\mu)$ at 1.0 MeV $< E <$ 2.4 MeV; comparison of the ENDF/B-VII.0 (= VII.1) evaluation, the ENDF/B-VIII.0 evaluation and available experimental data from Vedrenne [71] (EXFOR 21148014).

5. ^{6}*Li*

The R-matrix analysis informing the n+^{6}Li evaluation used the `EDA` code and included data for all reactions open in the ^{7}Li system at energies up to $E_n = 4$ MeV (E_x=10.7 MeV). The data set initially included more than 3900 experimental points for the reactions listed in Table III. The fit to these data was quite good overall, with a χ^2 per degree of freedom of 1.36. The differential cross sections and analyzing powers for t+^{4}He elastic scattering were especially well represented. The parameters of this fit were then used to provide the n+^{6}Li cross sections and covariances input to the least-squares fitting code `GMA` for the 2017 standard cross section analysis, described in Sec. VIII. The `GMA` analysis included calculations from another R-matrix fit, as well as experimental data for ratio measurements involving the ^{6}Li$(n,t)^{4}$He cross section.

For the general-purpose ENDF/B-VIII.0 file, however, it was decided to re-fit the ^{7}Li system data set with the experimental cross sections for the ^{6}Li$(n,t)^{4}$He reaction replaced with the (unsmoothed) standard cross sections and uncertainties from the `GMA` analysis. This procedure

TABLE III. Channel configuration (top) and data summary (bottom) for the ^{7}Li system analysis. Chi-squared per degree of freedom for the analysis is 1.36.

Channel	a_c (fm)	$l_{\max}$
t+^{4}He	4.02	5
n+^{6}Li	5.0	3
n+^{6}Li*	5.5	1
d+^{5}He	6.0	0

Reaction	Energy Range (MeV)	# Data Points	Observables
^{4}He$(t,t)^4$He	E_t=0–14	1661	$\sigma(\theta), A_y(\theta)$
^{4}He$(t,n)^6$Li	E_t=8.75–14.4	37	$\sigma_{\rm int}, \sigma(\theta)$
^{4}He$(t,n)^6$Li*	E_t=12.9	4	$\sigma(\theta)$
^{6}Li$(n,t)^4$He	E_n=0–4	1406	$\sigma_{\rm int}, \sigma(\theta)$
^{6}Li$(n,n)^6$Li	E_n=0–4	800	$\sigma_{\rm T}, \sigma_{\rm int}, \sigma(\theta), P_y(\theta)$
^{6}Li$(n,n')^6$Li*	E_n=3.35–4	8	$\sigma_{\rm int}$
^{6}Li$(n,d)^5$He	E_n=3.35–4	2	$\sigma_{\rm int}$
	Total:	3918	13

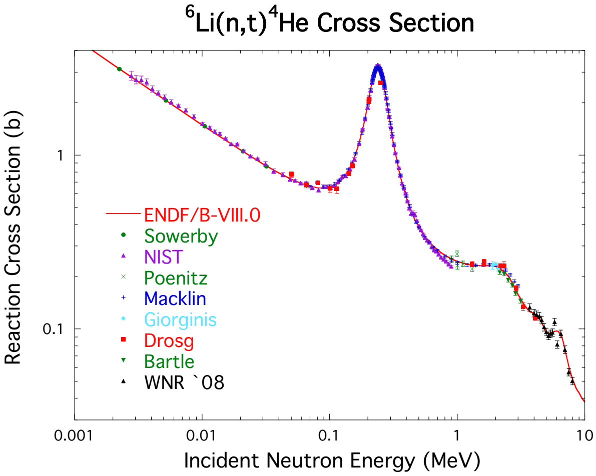

FIG. 7. (Color online) The cross section for the ^{6}Li$(n,t)^4$He reaction. The red curve is ENDF/B-VIII.0, and the points are from various measurements [73–81] (listed in the order cited in the figure). The evaluated thermal cross section is 938 b.

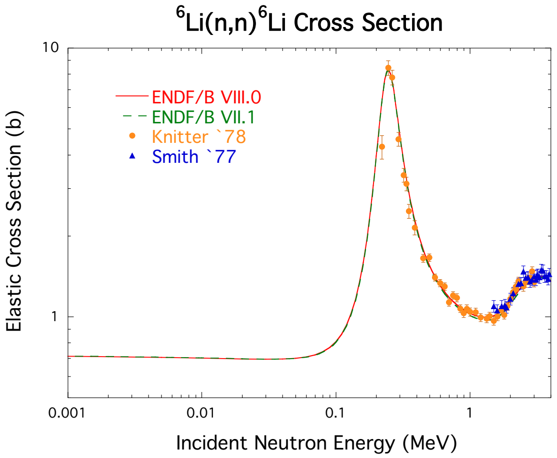

FIG. 8. (Color online) The cross section for n+ ^{6}Li elastic scattering. The red solid curve is ENDF/B-VIII.0, the green dashed curve is ENDF/B-VII.1. The data are from Knitter [82] and Smith [83].

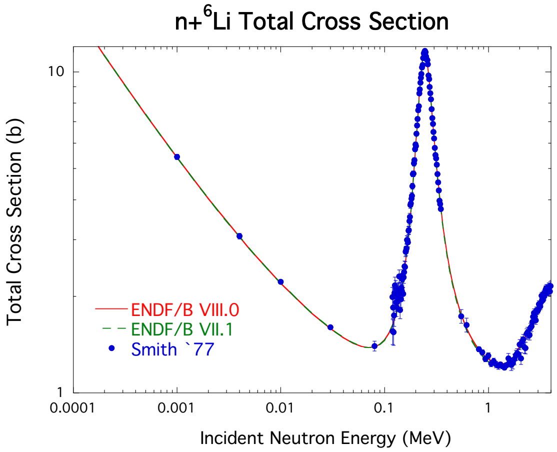

FIG. 9. (Color online) The total cross section for neutrons on ^{6}Li. The red solid curve is ENDF/B-VIII.0, the green dashed curve is ENDF/B-VII.1. Data points are from Ref. [83].

allowed the standards cross section to influence the fit, while imposing the smoothing and unitary constraints on all the n+^{6}Li cross sections that result from a multi-channel R-matrix analysis. The resulting ^{6}Li(n,t) cross section changed very little from the `GMA` analysis, and mostly within its uncertainties. It also still gives a very good representation of the direct measurements of the reaction cross section, as shown in Fig. 7. The elastic and total cross sections are shown in Figs. 8 and 9, respectively. The differences with ENDF/B VII.1 are generally small, and good agreement with the experimental data was maintained. The version VIII.0 cross sections were matched to those of version VII.1 at around 3.8 MeV, and they are identical to VII.1 above that energy.

6. ^{9}*Be*

ENDF/B-VIII.0 adopts the previous ENDF/B-VII.1 cross section evaluation, but replaces the elastic angular distribution and the $(n,2n)$ angular and energy distributions from the JENDL-4.0 evaluation, see Fig. 10. This was motivated by the fact that the JENDL-4.0 evaluation by Shibata was more recent. Additionally, using these JENDL-4.0 angular distributions tended to reduce calculated criticality in fast plutonium and HEU assemblies, as described in the integral data testing section of this paper (Section XII), leading to generally-improved comparisons with measured criticality (although a large spread in C/E values remains).

The $(n,2n)$ cross section is unchanged relative to VII.1 and shown in Fig. 11. The total cross section is shown in Fig. 12; again, this is unchanged compared to VII.1, and includes the changes made after ENDF/B-VII.0 to reproduce the measurement of Danon *et al.*

The small ^{9}Be(n,γ) cross section is shown in Fig. 13.

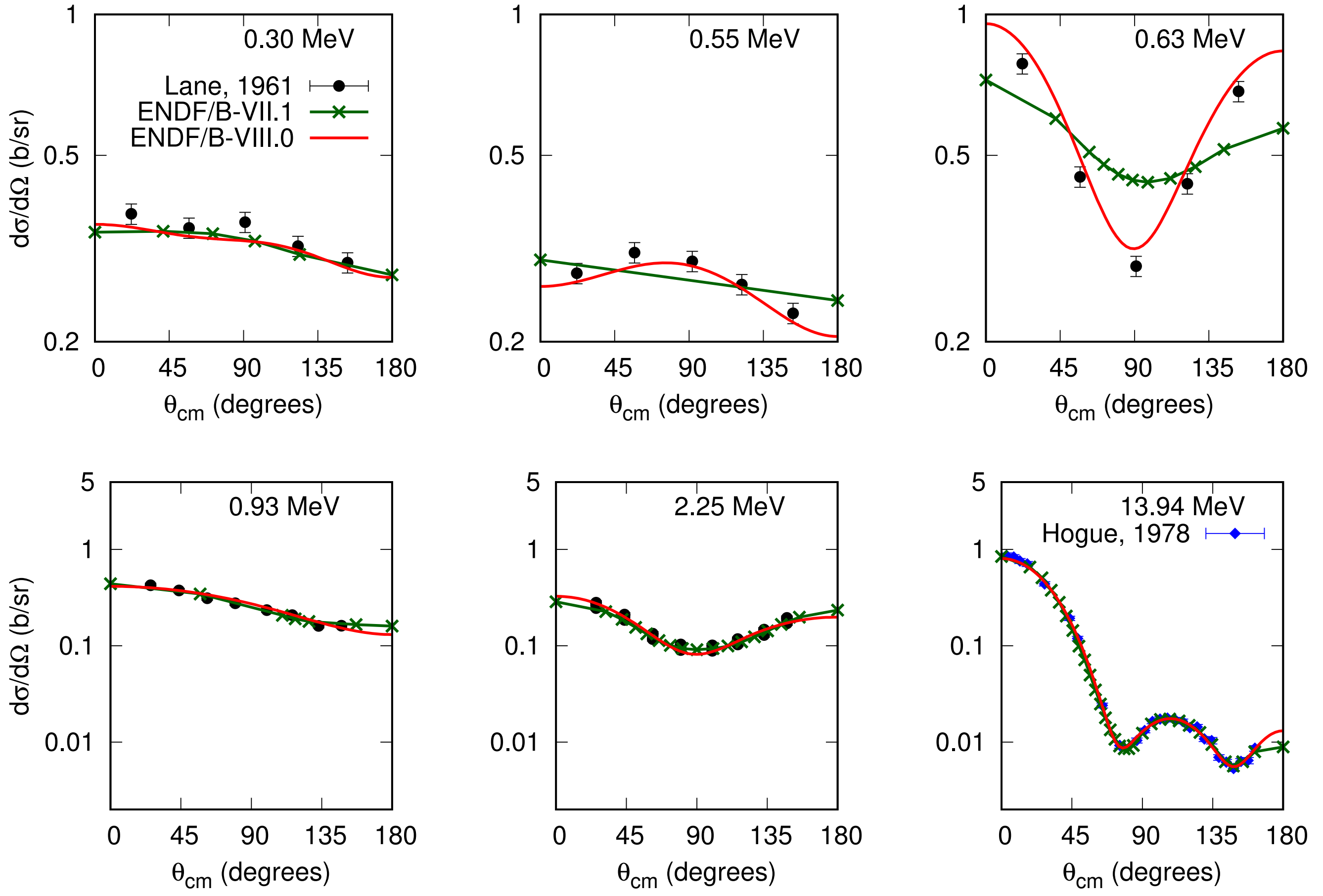

FIG. 10. (Color online) ^{9}Be angular distributions $d\sigma/d\Omega$ as a function of center-of-mass angle. Each panel gives, in the upper-right corner the incident neutron energy (MeV). The red curves are the new ENDF/B-VIII.0 evaluation; the line-connected data points in green are the ENDF/B-VII.1 evaluation; data are shown in black as taken from Lane [84] and Hogue [85].

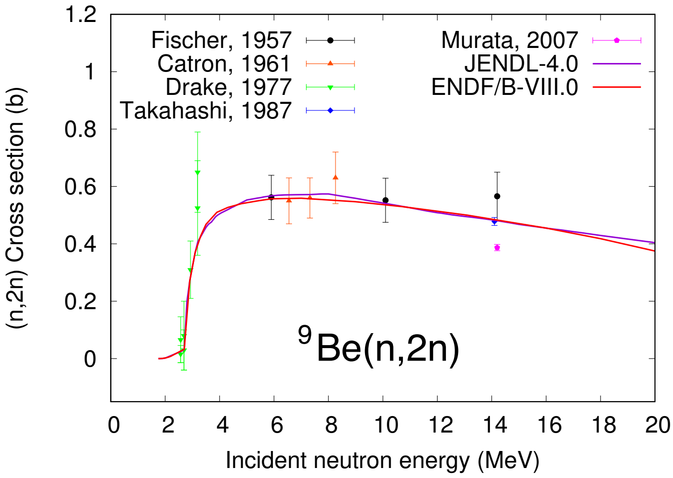

FIG. 11. (Color online) ^{9}Be$(n,2n)$ cross section as a function of incident neutron energy (MeV). The red curve is the new ENDF/B-VIII.0 evaluation (unchanged from ENDF/B-VII.1). Data are from Refs. [86–90].

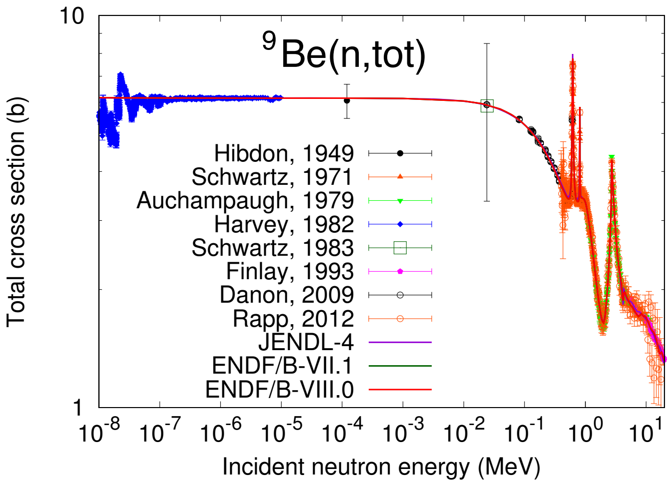

FIG. 12. (Color online) Total cross section for neutrons on ^{9}Be. The red curve is the new ENDF/B-VIII.0 evaluation (=VII.1) compared to JENDL-4.0. Data are from Refs. [91–97].

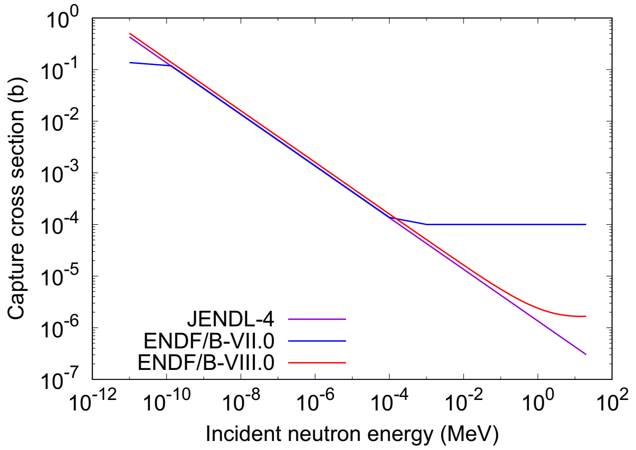

FIG. 13. (Color online) Capture cross section for neutrons on ^{9}Be. The red curve is the ENDF/B-VIII.0, which is identical to the ENDF/B-VII.1 evaluation. It is compared to JENDL-4.0 and ENDF/B-VII.0.

7. ^{10}B

The ENDF/B-VIII.0 evaluation is based at low energies on an R-matrix analysis of reactions in the ^{11}B system. The data set initially included more than 6600 experimental points for the reactions listed in Table IV. The new evaluation gives much better agreement with measurements than before, as can be seen in Figs. 14–18. The (n, α_1) cross section (Fig. 16) was changed in the 1.5–6 MeV region to agree better with the Schrack data. The total (n, α) cross section (Fig. 17) was changed in that region to agree better with the Giorginis data. The changes in the (n, α_0) cross section (Fig. 15) resulted from subtracting the (n, α_1) cross section from the total (n, α) cross section. The total neutron cross section shown in Fig. 18 was changed at energies above 8 MeV to agree better with the data of Abfalterer and the 200 m data of Wasson, and the difference was put into the elastic cross section. An increase in the elastic cross section was not inconsistent with some of the measurements in that energy region.

TABLE IV. Channel configuration (top) and data summary (bottom) for the ^{11}B system analysis. Chi-squared per degree of freedom for the analysis is 1.14.

Channel	a_c (fm)	l_{max}
n+^{10}B	4.05	1
α+^{7}Li	4.00	3
α+^{7}Li*	6.17	3
t+^{8}Be	6.00	2

Reaction	Energy Range (MeV)	# Data Points	Observables
^{10}B$(n,n)^{10}$B	$E_n = 0 - 1.04$	385	$\sigma_{\rm T}, \sigma_{\rm int}, \sigma(\theta)$
^{10}B$(n,\alpha_0)^{7}$Li	$E_n = 0 - 0.98$	2815	$\sigma_{\rm int}, \sigma(\theta)$
^{10}B$(n,\alpha_1)^{7}$Li*	$E_n = 0 - 1.01$	2875	$\sigma_{\rm int}, \sigma(\theta)$
^{10}B$(n,t)^{8}$Be	E_n=0-0.42	3	$\sigma_{\rm int}$
^{7}Li$(\alpha,n)^{10}$B	E_α=4.45-5.49	588	$\sigma_{\rm int}, \sigma(\theta)$
	Total:	6666	10

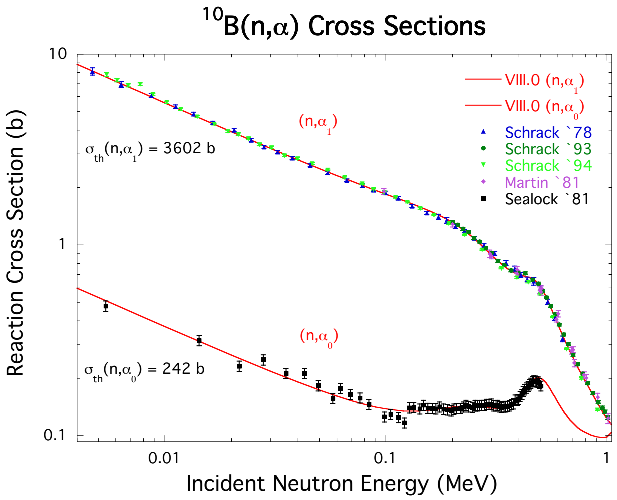

FIG. 14. (Color online) A comparison of the evaluated ^{10}B(n, α) cross sections in ENDF/B-VIII.0 (red curve) with various measurements [74, 98–100] in the standards energy region below 1 MeV.

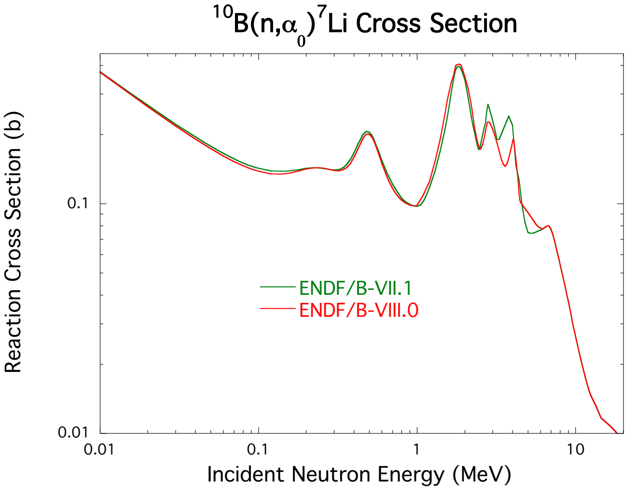

FIG. 15. (Color online) A comparison of the evaluated cross sections in ENDF/B-VIII.0 (red curve) and -VII.1 (green curve) for the ^{10}B$(n, \alpha_0)^{7}$Li reaction. The differences are large in the region from about 2.5 MeV to 6.5 MeV, in order to agree better with new data for the (n, α_1) and (n, α) reactions in that region.

8. ^{12}C

The ENDF/B-VIII.0 release is the first ENDF/B release to include ^{12}C (98.9%) and ^{13}C (1.1%) isotopic evaluations in lieu of a natural carbon evaluation. The cross sections for n+^{12}C were taken at energies below 6.5 MeV from an R-matrix analysis of the ^{13}C system that included reactions among the channels n+^{12}C, n+^{12}C*, and γ+^{13}C. A summary of the channel configuration and data for the reactions included is given in Table V. Although particular attention was paid to the data in the standards region (E_n < 2 MeV) for the carbon isotopes, the analyses extend to energies well above that for both the ^{13,14}C systems. The types of data used are mostly

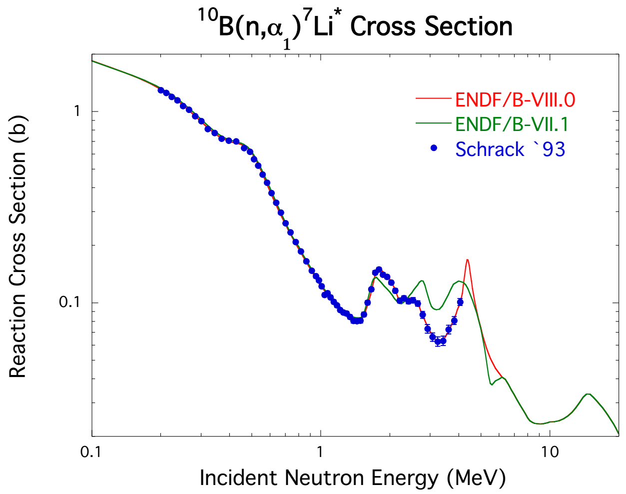

FIG. 16. (Color online) The evaluated cross sections in ENDF/B-VIII.0 (red curve) and -VII.1 (green curve) for the ^{10}B$(n,\alpha_1)^7$Li* reaction. The differences are large in the region from about 1.5 MeV to 6 MeV, in order to agree better with the data of Schrack *et al.* [98].

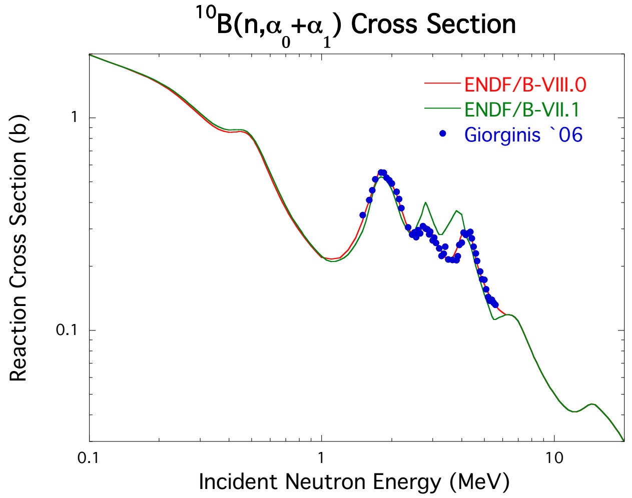

FIG. 17. (Color online) The evaluated cross sections in ENDF/B-VIII.0 (red curve) and -VII.1 (green curve) for the summed ^{10}B$(n,\alpha_0+\alpha_1)$ reactions. The differences are large in the region from about 2.3 MeV to 6 MeV, in order to agree better with the data of Giorginis *et al.* [101].

differential and integrated (total) cross sections, but some analyzing-power measurements are also included.

The fits to the data are generally quite good, as can be seen in Figs. 19 and 20. Some of the cross sections were allowed to renormalize, as given in Table VI. Most of the normalization factors for the total cross section are near unity, although the ones at 2 % may be significant, in view of the discussion below. Much larger renormalizations (+11 to -13 %) are required to make the Geel and Wender data consistent with the calculations and with each other. Some changes were also made in the n+^{12}C capture cross section, as can be seen in Fig. 21. The flat region between 0.2 and 7 MeV in ENDF/B-VII.1 has been replaced with a more physically reasonable behavior when joined to the higher-energy data above 10 MeV.

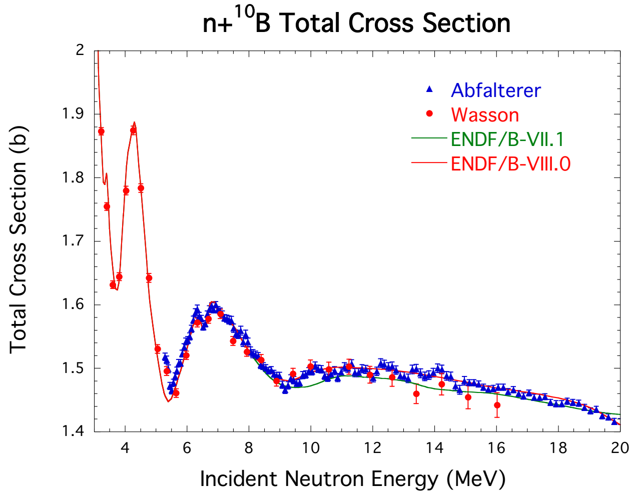

FIG. 18. (Color online) The evaluated total cross section for n+^{10}B in ENDF/B-VIII.0 (red curve) and -VII.1 (green curve) compared with the data of Abfalterer [102] (blue triangles) and of Wasson [103] (red points). The evaluated cross section was changed in the region above about 8 MeV in order to agree better with these data.

TABLE V. Channel configuration (top) and data summary (bottom) for the ^{13}C system analysis. Chi-squared per degree of freedom for the analysis is 1.54.

Channel	a_c (fm)	l_{max}
n+^{12}C(0^+)	4.6	4
n+^{12}C*(2^+)	5.0	1
γ+^{13}C	50.0	1

Reaction	Energy Range (MeV)	# Data Points	Observables
^{12}C$(n,n)^{12}$C	$E_n = 0-6.45$	6940	$\sigma_{\rm T}, \sigma(\theta), A_n(\theta)$
^{12}C$(n,n')^{12}$C*	$E_n = 5.3-6.45$	443	$\sigma_{\rm int}, \sigma(\theta)$
^{12}C$(n,\gamma)^{13}$C	$E_n = 0-0.2$	7	$\sigma_{\rm int}$
	Total:	7390	5

The elastic cross section in the new evaluation gradually becomes larger than ENDF/B-VII.1, until the difference approaches 2 % at energies in the minimum below the first resonance. This is at the upper end of the standards cross section range (1.8 MeV), and is of concern because the difference lies outside the uncertainty of both evaluations. There appear to be no consequential effects of the difference on critical benchmarks, however. At energies above about 6.5 MeV, the cross sections were matched smoothly onto the existing (VII.1) natural carbon evaluation, so that the two evaluations are the same above that energy.

9. ^{13}*C*

The n+^{13}C (^{14}C system) analysis fits solely the total cross section data of Cohn (1961), Auchampaugh (1979), and Abfalterer (2001) as shown in Fig. 22. Despite the relatively poor description of the data at ener-

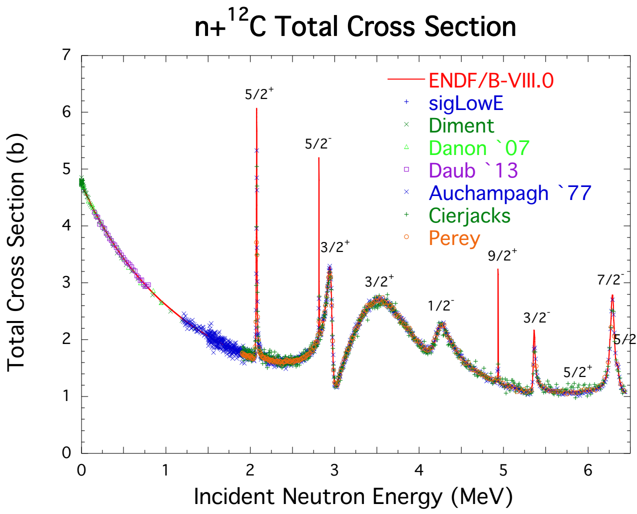

FIG. 19. (Color online) Total cross section for n+^{12}C compared to experimental data [93, 104–108]. The J^{π} values of the resonances are indicated above the peaks. Figure adapted from Fig. 4 of Ref. [109].

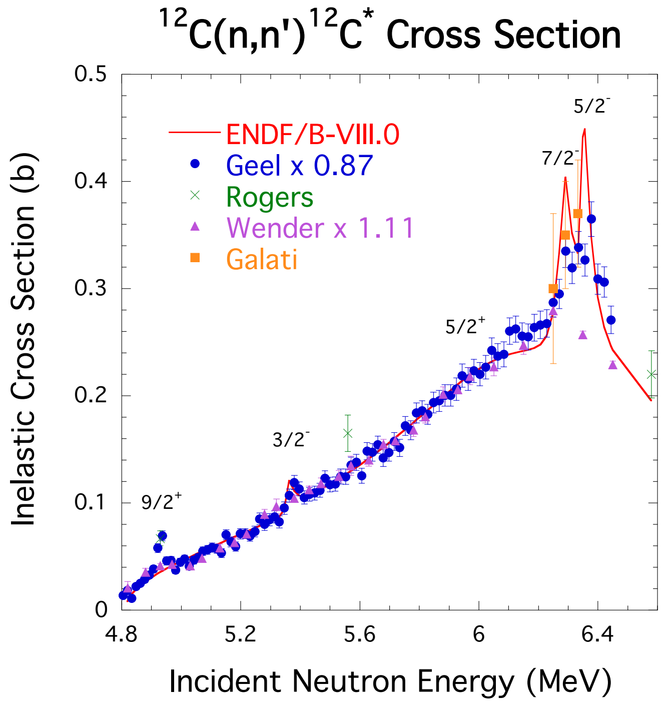

FIG. 20. (Color online) Cross section for n+^{12}C inelastic scattering to the first level compared to experimental data [110–113]. The J^{π} values of the resonances are indicated above the peaks. Figure adapted from Fig. 5 of Ref. [109].

gies $E_n \lesssim 0.7$ MeV with an overall χ^2/datum of 2.24 over region $0 \leq E_n \leq 20$ MeV, the present analysis is notable as it is an R-matrix description of the data through the entire region and it is the largest such analysis to date, incorporating six two-particle partitions (n+^{13}C$_0$, n+^{13}C$_1^*$, n+^{13}C$_2^*$, α+^{10}Be, n+^{13}C$_3^*$, and n+^{12}C) encompassing 90 channels in the channel-spin basis with $\ell_{\max} = 3$.

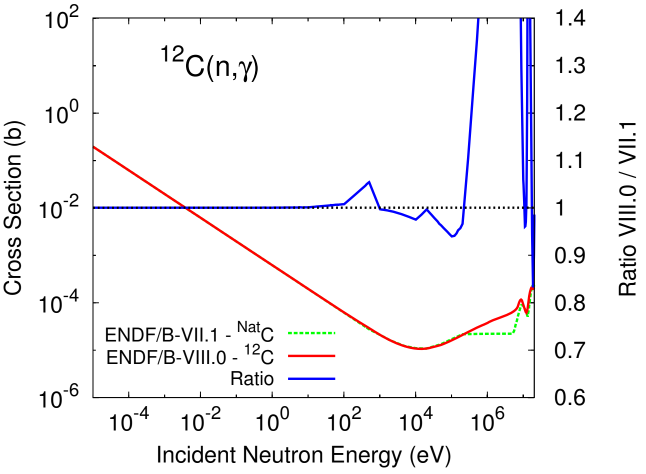

FIG. 21. (Color online) Cross sections for n+^{12}C capture. The dotted black curve is ENDF/B-VII.1 and the new cross section is the red curve. The green curve gives the ratio to ENDF/B-VII.1.

TABLE VI. Normalizations and energy shifts (ΔE) for the ^{13}C-system cross-section data analyzed.

Authors (n, n) :	Energy Range	Norm.	ΔE
Diment	74 – 1341900 eV	1.006	0
Danon	24 – 948 keV	1.004	0
Daub	0.8 – 935 keV	1.013	0
Auchampaugh	1.20 – 6.45 MeV	1.020	0
Cierjacks	1.90 – 6.45 MeV	1.020	0
Perey	1.91 – 6.44 MeV	1.008	0
Authors (n, n') :			
Geel *et al.*	4.82 – 6.44 MeV	0.868	-58 keV
Wender *et al.*	4.82 – 6.45 MeV	1.112	0
Rogers *et al.*	4.93 – 6.58 MeV	1.0 (fixed)	0
Galati *et al.*	6.24 – 6.33 MeV	1.0 (fixed)	0

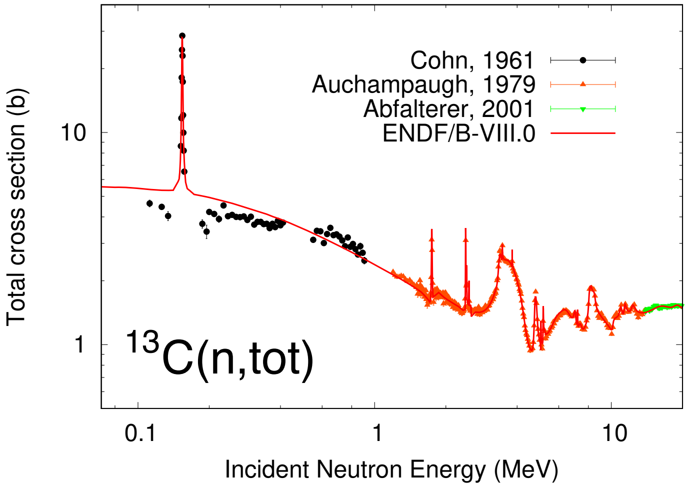

FIG. 22. (Color online) ^{13}C total cross section (in barn) as a function of the incident neutron energy (MeV) compared with data [93, 102, 114].

TABLE VII. Channel configuration (top) and data summary (bottom) for the ^{17}O analysis. Chi-squared per degree of freedom for the analysis is 1.75.

Channel	a_c (fm)	$l_{\max}$
$n+^{16}$O	4.4	4
$\alpha+^{13}$C	5.4	5
$\gamma+^{17}$O	10.	1

Reaction	Energy Range (MeV)	# Data Points	Observables
$^{16}O(n,n)^{16}O$	$E_n = 0-7$	2540	$\sigma_T, \sigma(\theta), P_n(\theta)$
$^{16}O(n,\alpha)^{13}C$	$E_n = 2.35-5$	672	$\sigma_{\rm int}, \sigma(\theta), P_n(\theta)$
$^{16}O(n,\gamma)^{17}O$	$E_n = 0.02-0.56$	12	$\sigma_{\rm int}$
$^{13}C(\alpha,n)^{16}O$	$E_\alpha = 0-5.4$	870	$\sigma_{\rm int}$
$^{13}C(\alpha,\alpha)^{13}C$	$E_\alpha = 2-5.7$	1168	$\sigma(\theta)$
$^{17}O(\gamma,n_0)^{16}O$	$E_\gamma = 4.4-6.7$	186	$\sigma(90^\circ)$
	Total:	5448	10

10. ^{16}O

The new evaluation of $n+^{16}$O cross sections for neutron energies up to 7 MeV is based on an *R*-matrix analysis of all possible reactions between the channels $n+^{16}$O, $\alpha+^{13}$C, and $\gamma+^{17}$O in the ^{17}O system.

This is summarized in Table VII. Particular attention was paid to the data in the low-energy region for $n+^{16}$O elastic scattering, shown in Fig. 23. The thermal cross section is lower than before, but still at the upper end of the range of recommended values, in excellent agreement with a high-precision measurement by Schneider [115].

TABLE VIII. Normalizations and energy shifts (ΔE) for the ^{17}O-system cross-section data analyzed.

Authors (n,n) :	Energy Range	Norm.	ΔE
Schneider	0.0253 eV	1.0 (fixed)	0
Dilg, Koester, Block	0.13 – 23.5 keV	1.0 (fixed)	0
Ohkubo (corr. for H)	0.8 – 935 keV	0.9989	0
Johnson & Fowler (including LOX)	49 – 3139 keV	0.9799	0
Cierjacks *et al.*	3.143 – 7.0 MeV	1.0378	0
Authors (α,n) :			
Drotleff *et al.*	346 – 1389 keV	1.0 (fixed)	0
Heil *et al.*	416 – 899 keV	1.0 (fixed)	0
Kellog	445 – 1045 keV	1.506	0
Bair & Haas	0.997 – 5.402 MeV	0.941	-4 keV

At higher energies, as shown in Fig. 24, the ^{17}O analysis follows in great detail the total cross section measurements of Ohkubo [116], Johnson [117], Fowler [118], and Cierjacks [119] with reasonable normalization factors (see Table VIII). It also agrees quite well with the $^{13}C(\alpha$,n$)^{16}$O cross section measurement of Bair and Haas [120] at roughly their original normalization scale (0.94), a consequence of the unitarity imposed by an *R*-matrix description. The resulting $^{16}O(n,\alpha)^{13}C$ cross sections are shown in Fig. 25. They agree with the measurements and evaluation done at JRC-Geel by Giorginis [121], which are 30 – 50% higher than the ENDF/B VII.1 cross sections, and with the normalization (0.95) of the Bair and Haas [120] data determined independently by Giorginis.

A post-analysis check of the evaluated total cross section was provided by measurements of Danon *et al.* [122] at RPI. This is shown at energies below 9 MeV in Fig. 26. The resolution and scatter of the measurement are not as good as those of the other data we fit, but the normalization was determined in a novel way, by using a water target and normalizing to the total cross section for hydrogen scattering in the oxygen window at 2.35 MeV. When the evaluated total cross section and the RPI measurement are binned in the same way (2-3 MeV widths), the C/E ratios in those bins deviate from unity by 1 % or less at energies up to 9 MeV, confirming that the average normalization and shape of the evaluation is correct.

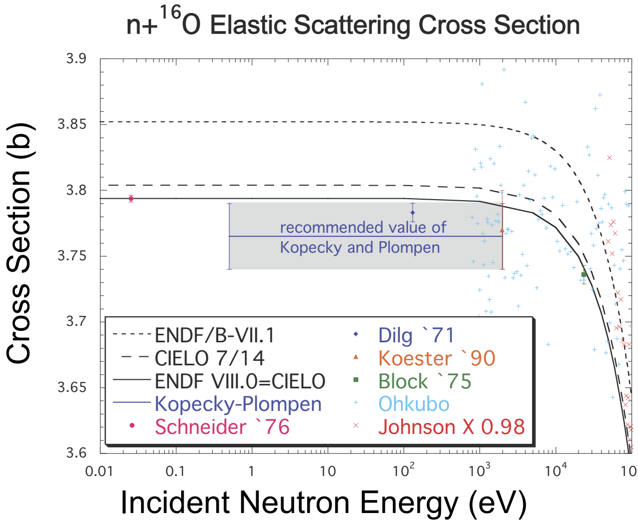

FIG. 23. (Color online) The neutron elastic cross section on ^{16}O at low energies as a function of the incident neutron energy (MeV) for the current ENDF/B-VIII.0 analysis is compared with data and previous evaluations of ENDF/B-VII.1 (green curve) and data [115, 123–128]. Figure taken from Fig. 1 of Ref. [109].

Another goal of the analysis was to obtain more reasonable capture cross sections for ^{16}O. This was done by including the 90-degree excitation function for the $^{17}O(\gamma,n_0)^{16}O$ reaction measured by Holt *et al.* [129], as well as the low-energy measurements of the $n+^{16}$O total capture cross section by Firestone [72] and by the Japanese groups [130, 131]. The value of the Holt data is that they cover a wide enough energy range to reveal the resonant structure of the photo-disintegration cross section over the first 6–7 resonances above the neutron threshold in ^{17}O. Therefore, we were able to extend the energy range in which resonance effects on the capture cross section are taken into account (typically this has been done only over the first resonance). The fits to these data are shown in Figs. 27 and 28. At energies above 2 MeV, the *R*-matrix calculation was joined to a direct-capture calculation by Kawano.

Above the range of the *R*-matrix analysis (7 MeV),

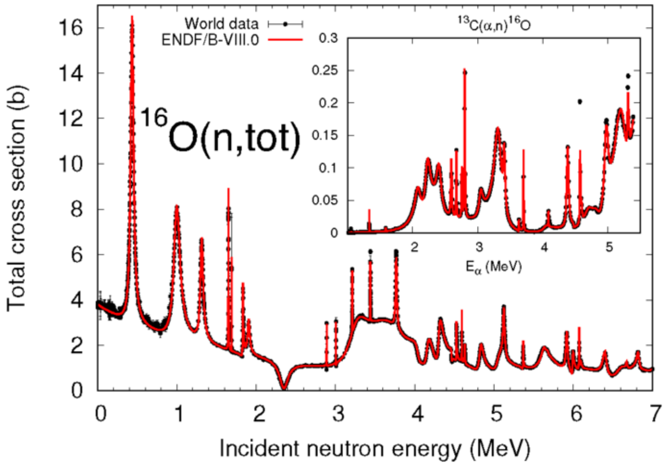

FIG. 24. (Color online) The total neutron cross section (barn) on ^{16}O as a function of the incident neutron energy (MeV) for the current ENDF/B-VIII.0 analysis is compared with data. The inset shows the fit to the ^{13}C(α, n) data of Bair and Haas [120], normalized by 0.94. Figure adapted from Fig. 2 of Ref. [109].

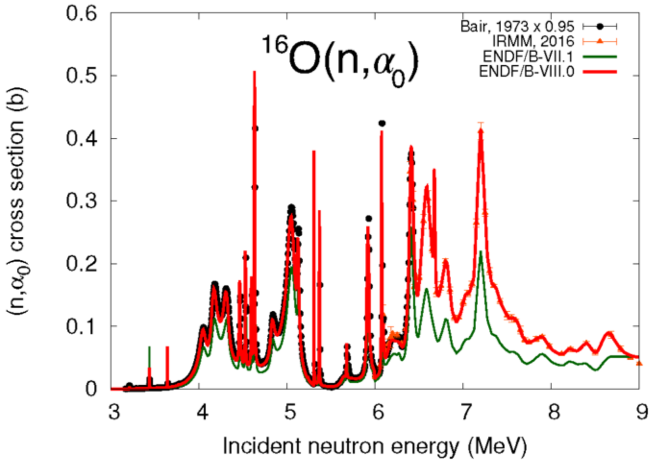

FIG. 25. (Color online) ^{16}O(n, α_0) reaction cross section (in barn) as a function of the incident neutron energy (MeV). The ENDF/B-VII.1 evaluation (green curve) is compared to the data of Bair and Haas and the current ENDF/B-VIII.0 (red curve). Also displayed is the reevaluation of the JRC-Geel data (green triangles; JRC-Geel) [121]. Figure adapted from Fig. 3 of Ref. [109].

the cross sections were matched smoothly to the existing evaluation, taking into account the experimental data, so that, except for capture (`MT=102`), VIII.0 is identical to VII.1 at energies above 9 MeV.

11. ^{18}O

The 2005 evaluation of ^{18}O from M.N. Nikolaev was adopted from ROSFOND [23, 24] in part because it was the only ^{18}O evaluation available. This evaluation uses resonances from the Atlas of Neutron resonances [132] below 5 MeV. Above 5 MeV, the evaluation is mostly taken from the J. Kopecky and D. Nierop evaluation in EAF-3. To supplement these cross sections, the inelastic scattering cross section is taken from ^{16}O and the elastic cross section is the difference of the total and reaction cross sections. Elastic angular distributions were taken from ^{17}O and other secondary angular distributions were assumed to be isotropic in the center of mass system. Evaporation spectra were used to describe the secondary neutron energy distributions.

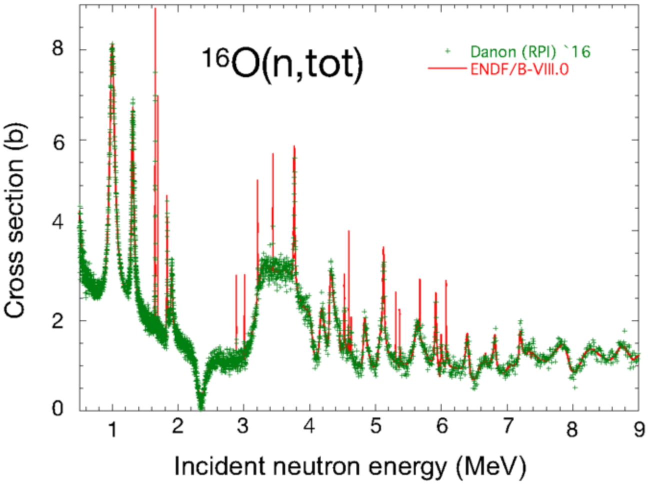

FIG. 26. (Color online) The total neutron cross section for ^{16}O as a function of the incident neutron energy (MeV) for the current ENDF/B-VIII.0 analysis is compared with data from Danon *et al.* [122].

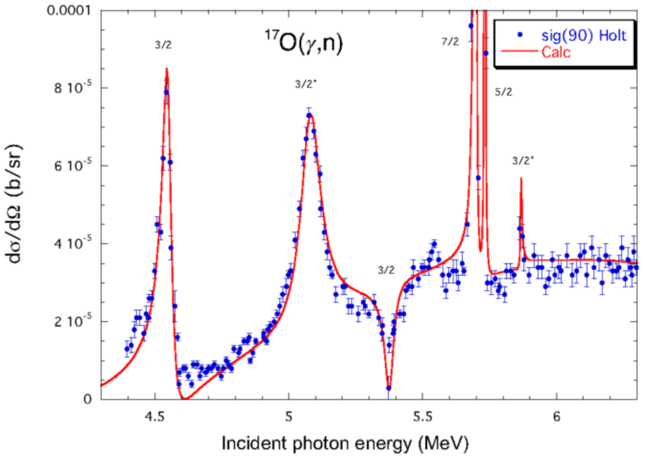

FIG. 27. (Color online) The differential cross section for the ^{17}O$(\gamma, n_0)^{16}$O reaction at 90° (lab). The measurements (blue points) are from Holt *et al.* [129], and the solid red curve is the R-matrix calculation, with the indicated J^π values of the resonances.

12. ^{40}Ar

The ^{40}Ar evaluation in ENDF/B-VII.1 was taken from JENDL-3.3 [133], and one of the issues in this file is that

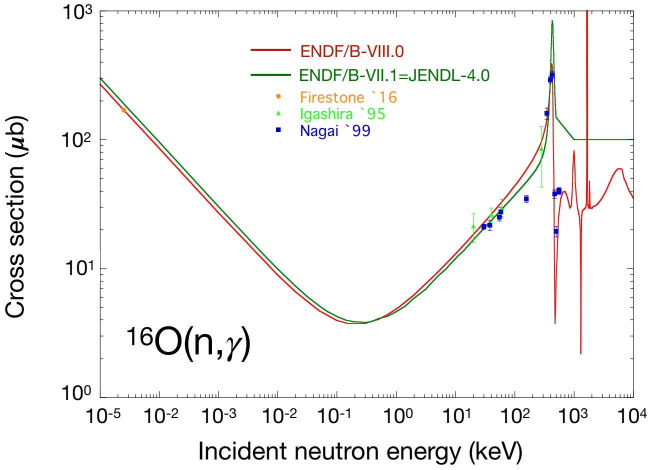

FIG. 28. (Color online) The total neutron capture cross section for ^{16}O as a function of the incident neutron energy (keV) compared with experimental data [72, 130, 131]. The red line is the ENDF/B-VIII.0 evaluation, and the green line is ENDF/B VII.1 = JENDL 4.0.

the particle energy spectra and the angular distributions are given in the MF4 and MF5 sections. In the current evaluation, they are now in MF6. The evaluation is based on the partial γ-ray production cross section measurement with the GErmanium Array for Neutron Induced Excitations (GEANIE) detector [134]. The γ-ray production cross section calculation was performed with the CoH$_3$ code [135]. The statistical model calculations in the relatively light mass region, such as for argon, require careful selection of discrete levels included, because the nuclear structure and the γ-ray decay scheme significantly impact the calculated γ-ray production cross sections. The discrete states up to 4.43 MeV are included in the calculation, and the continuum state is assumed above that energy. At higher energies the direct (non-compound) population of collective levels is very important for the γ-ray production cross section calculation. The discrete levels of 2.52, 3.21, 3.92, 3.68, 4.08, and 4.32 MeV were included as collective states and the DWBA calculation was performed. Finally the (n,p) cross section was slightly adjusted to reproduce available experimental data near 14 MeV.

13. ^{40}Ca

Background

A resonance parameter evaluation of ^{40}Ca in the neutron energy range of thermal up to 1.5 MeV was performed with support from the US Nuclear Criticality Safety Program (NCSP) in an effort to provide improved calcium cross section and covariance data for the Hanford Plutonium Finishing plant and Hanford Tank Farms in the DOE complex. Calcium is present in structural materials such as concrete and admixed materials in waste streams, but it is also a neutron-absorbing element that can influence the reactivity of systems with fissionable material.

The evaluation methodology used the Reich-Moore approximation of the R-matrix formalism to fit high-resolution transmission and capture measurements performed between 2012 and 2014 at the GEel LINear Accelerator facility (GELINA) [136], as well as other experimental data sets on natural and isotopic calcium available in the EXFOR library [137–140]. Table IX presents an overview of the experimental data sets used in the fitting procedure, as well as some of their features, such as sample thickness and average uncertainty.

TABLE IX. n+^{40}Ca experimental data overview.

Sample	Author Facility/Year	Energy range Thick.(at/b)	Type	$\overline{\Delta\sigma}$(%)
^{nat}Ca	Cierjacks [137] KIT/1968	0.5–31 MeV 0.21326	Total[a]	1.5
^{nat}Ca	Perey [138] ORNL/1972	0.2–29 MeV 0.7028	Total[a]	16.4
^{40}Ca	Johnson [139] ORNL/1973	40 keV–6 MeV 0.0656	Total[a]	3.8
^{nat}Ca	Singh [140] NSC/1974	1.6 keV–0.5 MeV 0.029762	Total[a]	10.0[b]
^{nat}Ca	Guber [136] GEEL/2014	20 eV–1 MeV 0.10971	Trans.	2.6
^{nat}Ca	Guber [136] GEEL/2014	10 eV–0.6 MeV 0.01674	Capture	14.8
^{nat}Ca	Guber [136] GEEL/2015	10 eV–0.6 MeV 0.10971	Capture	17.2

[a] Fitted as transmission data.
[b] Assumed uncertainty since no error analysis was reported.

Along with the elastic and capture channels, there are two additional energetically possible channels for the n+^{40}Ca reaction system in the neutron range up to 1.5 MeV. Table X shows that the (n,α) reaction channel, having a positive Q-value, is defined over the whole neutron energy range, and the (n,p) reaction channel has an energy threshold at about 0.5 MeV. Even though, in the analyzed energy range, these channels can be of a small magnitude ($\lesssim 10^{-4}$–10^{-3} b), it is important to include them within the R-matrix formalism. By using built-in capabilities of the SAMMY code [142, 143] for fitting resonant cross sections in the ingoing and outgoing charged particle channels, the present ENDF/B-VIII.0 set of evaluated resonance parameters considered not only the neutron and gamma exit channels, but also α-particle and proton exit channels for three incident neutron

TABLE X. Reaction Q-values and thresholds for n+^{40}Ca.

Reaction products	Q-value[a] (keV)	Threshold[a] (keV)
^{41}Ca+γ	8362.82	0
^{37}Ar+α	1747.66	0
^{40}K+p	-528.55	541.89

[a] Calculated by mass values from the 2012 Atomic Mass Evaluation [141].

partial waves. The level energies E_λ, the probability amplitudes (γ_c^λ), and the related partial widths (Γ_c^λ) were defined within a comprehensive set of reaction channels c. Thanks to the $I = 0^+$ ground state spin of ^{40}Ca, the total spin J^π of a given resonance implicitly defines the l-value of that resonance. The analysis of the experimental data used the SAMMY code that performed a multi-level multi-channel R-matrix fit to neutron data using experimental conditions such as resolution function, finite size of the sample, and nonuniform thickness. Nuclide abundances of the samples, multiple scattering, self-shielding, normalization, background, and Doppler broadening were also taken into account.

Previous Evaluations

In both previous ENDF/B-VII.0 and -VII.1 libraries, the evaluated set of neutron resonance parameters was reported over the energy range from thermal up to 0.5 MeV and adopted from JEFF-3.1 (released in 2005), which in turn adopted the resonance evaluation from JENDL-3.3 (released in 2002). The original set of resonance parameters was based on the analysis of Mughabghab [132] and defined in terms of the Multi Level Breit Wigner formula. In the libraries mentioned above, no covariance information was available.

Results

The results of the evaluated cross sections and related uncertainties at thermal energy are displayed for three reaction channels in Table XI. No significant discrepancies between the evaluated values and the values reported in the ATLAS are present. The conservatively large uncertainty for the (n,α) reaction channel is justified by the lack of recent experimental data and by the difficulty in accurately measuring these reaction cross sections partly due to their modest magnitudes. In this regard, the only (n,α) measurement found in the EXFOR library was performed by Münnich in the late fifties [144].

TABLE XI. ^{40}Ca thermal cross sections (in barn) calculated at T=293.6 K compared to the values found in the *Atlas of Neutron Resonances.*

^{40}Ca	(n,el)	(n,γ)	(n,α)
ENDF/B-VIII.0	2.66±2.6%	0.41±4.6%	$2.48{\cdot}10^{-3}$±83%
ATLAS	2.73±2.2%	0.41±4.8%	$2.50{\cdot}10^{-3}$±44%

In Fig. 29, the total (solid black line) and capture (solid red line) cross sections calculated from the ENDF/B-VIII.0 R-matrix resonance parameters in the Reich-Moore approximation are compared with the experimental data [136]. They are also compared to the cross sections reconstructed from ENDF/B-VII.1 R-matrix resonance parameters (dashed lines) in the Multi Level Breit Wigner formula. As shown in the figure, the improved set of transmission and capture experimental data made it possible to obtain reasonable values of the neutron and capture widths in the specified energy range.

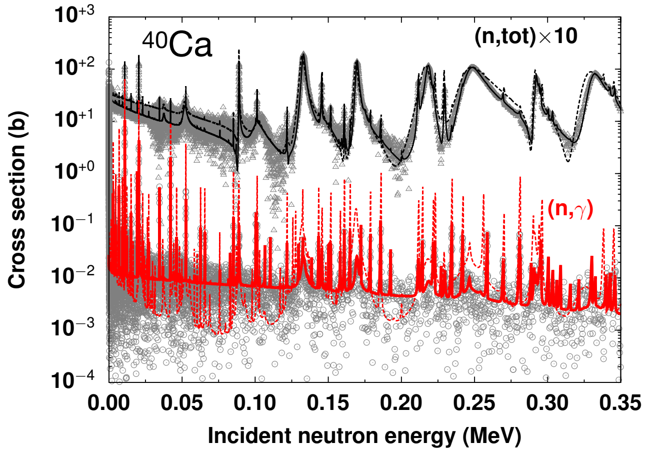

FIG. 29. (Color online) ^{40}Ca(n,γ) and total cross sections in the energy range up to 0.35 MeV calculated from the ENDF/B-VIII.0 (solid lines) and ENDF/B-VII.1 (dashed lines) resonance parameters are compared with the experimental data [136].

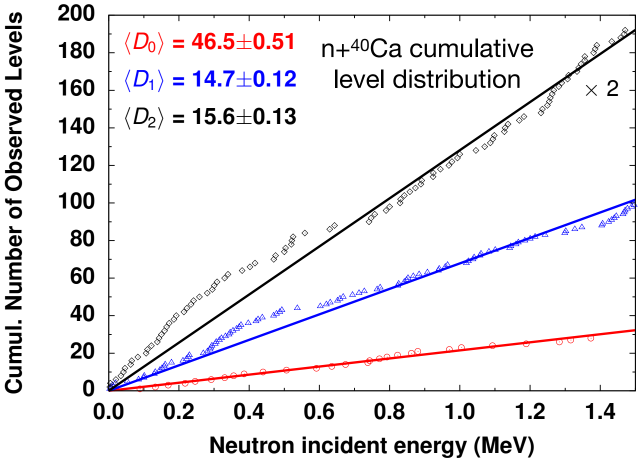

FIG. 30. (Color online) Plot of the ENDF/B-VIII.0 cumulative number of observed s- (red dots), p- (blue triangles) and d-levels (black diamonds) vs energy for n+^{40}Ca. The values of average s-level spacings $\langle D_0\rangle$, p-level spacings $\langle D_1\rangle$, and d-level spacings $\langle D_2\rangle$ shown in the plot represent the inverse of the slope of a straight line fitted to the data (red, blue, black lines) for the given channel radius a_c.

In Figs. 30–31, the average level spacings $\langle D_0\rangle$, $\langle D_1\rangle$, $\langle D_2\rangle$ and the strength functions S_0, S_1, S_2 (in units of 10^{+4}) for the observed s- (red dots), p- (blue triangle) and d-levels (black diamonds) are displayed with the fitted curves (solid lines). Except for s-wave, the level spacings and the strength functions are displayed for two mixed populations of levels for which the weak dependence of the total spin J^π was neglected. In the neutron energy region up to 0.6 MeV, the average level spacing $\langle D_2\rangle$ seems to grow more rapidly than the average level spacings for s- and p-wave for which their behavior is close to linear. The departure from linearity of $\langle D_2\rangle$ and partly $\langle D_1\rangle$, might be attributed to the tendency of the level densities to

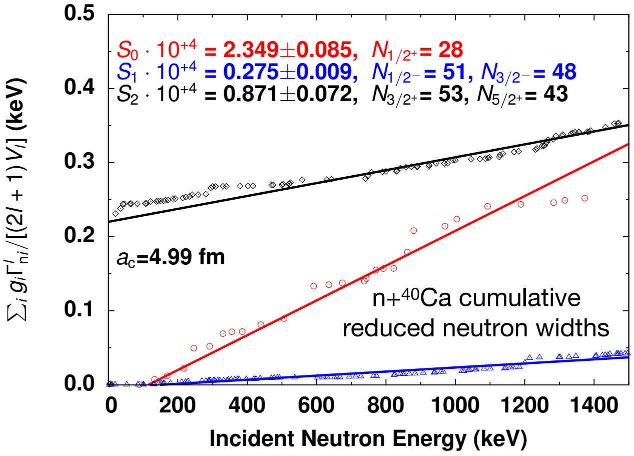

FIG. 31. (Color online) Plot of cumulative reduced neutron-widths $\sum_i g_i \Gamma_i^0$ vs energy for n+^{40}Ca for three partial waves l. The slopes of the straight lines give the strength functions S_0, S_1, S_2 (in 10^{+4} unit) for the given channel radius a_c. For partial waves $l \geq 1$ the reduced neutron-widths are defined in terms of the square well potential V_l.

grow exponentially. This can be more evident for populations with high fractional density due to their total spin according to the $2J+1$ rule.

Figure 31 shows results of the strength functions up to 1.5 MeV, which is a small slice of excitation energy in the compound nucleus ^{41}Ca. To some extent, the impact of levels outside this energy region are seen, as in the low value of the p-wave strength function S_1. This can be attributed to a hierarchy of more complicated configurations such as centroids of single-particle states [145] for p-levels above 2 MeV. This is also consistent with the large negative value found for the R^{∞}_{1J} parameter indicating centroids of the $2p_{1/2}$ and $2p_{3/2}$ levels.

B. Z=21-60

1. ^{56}Fe

Background

Iron is an extremely common structural material, leading to its inclusion in the CIELO project. ^{56}Fe is the dominant isotope with a natural abundance of 91.8%. This isotope is therefore the main focus of the CIELO iron project and is the main subject of the iron evaluation summary paper also included in this volume [19]. We summarize this ^{56}Fe evaluation here.

Resolved Resonance Region

After careful performance studies, it was decided to adopt for the resolved resonance range (up to the incident energy of 850 keV) the evaluated resonances from JENDL-4.0 [4], which originates from the Froehner evaluation [146] for JEF-2.2 [147] with corrections. A resonance energy was changed from 767.240 keV to 766.724 keV and the spurious resonance at 59.9 keV was deleted in this new file. The background near 800 keV was reduced by 40 percent. An artificial "background" was added to capture around 24.5 keV, since previous estimates of capture in the region where a dip in the elastic cross section is observed seemed to be low and certain critical assembly benchmarks are sensitive to this quantity. It was thought that the previous ENDF/B-VII.1's broad minimum in capture in this energy region was caused by inappropriately-placed bound states. The adjusted capture cross section now nearly follows the $1/v$ behavior. More details on such corrections and reasoning of the choices made can be found in Ref. [19]. Fig. 32 shows the ^{56}Fe neutron capture cross section compared with ENDF/B-VII.1 and experimental data, where the impact of the increased background can be clearly seen.

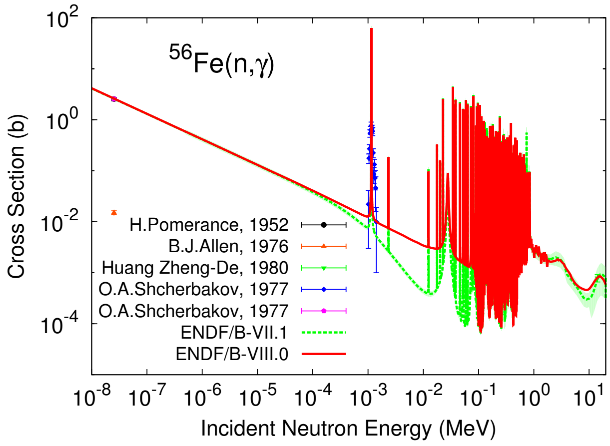

FIG. 32. (Color online) Evaluated ^{56}Fe(n,γ) cross section compared with data retrieved from EXFOR and with the previous evaluation.

The choice, based on validation, for capture cross sections above 860 keV was the one from the RPI data presented by Y. Danon in Ref. [148].

The elastic angular distributions in the resolved resonance range are chosen from resolution-broadened Perey data [149]. Sample plots of angular distributions are shown in Fig. 33 for two different incident energies. It was found that the data from Kinney *et al.* [150] present noticeable anisotropy relative to forward and backward data, as can be clearly seen in Fig. 33, upper panel. Such anisotropic behavior of the elastic angular distribution data from Kinney fades as neutron incident energy progresses to higher values, as can be seen in Fig. 33, bottom panel.

While Froehner's evaluation for the ^{56}Fe resonances was effectively adopted, the covariance on these parameters have since been lost. Rather than re-evaluating the resonance region, a more pragmatic approach was adopted. Resonances from the Atlas of Neutron Resonances [132] were matched with those in the ENDF file and, after matching, both the parameters and their uncertainties were used to generate covariances with the resonance module of the EMPIRE code. For missing resonance uncertainties, an educated guess based on average parameter uncertainties was used. The uncertainties of the negative resonance parameters were chosen to reproduce uncertainties of the thermal constants and the uncertainty of the scattering radius was taken into account. With this input, the EMPIRE resonance module produced a MF=32 file with covariances for the resonance parameters.

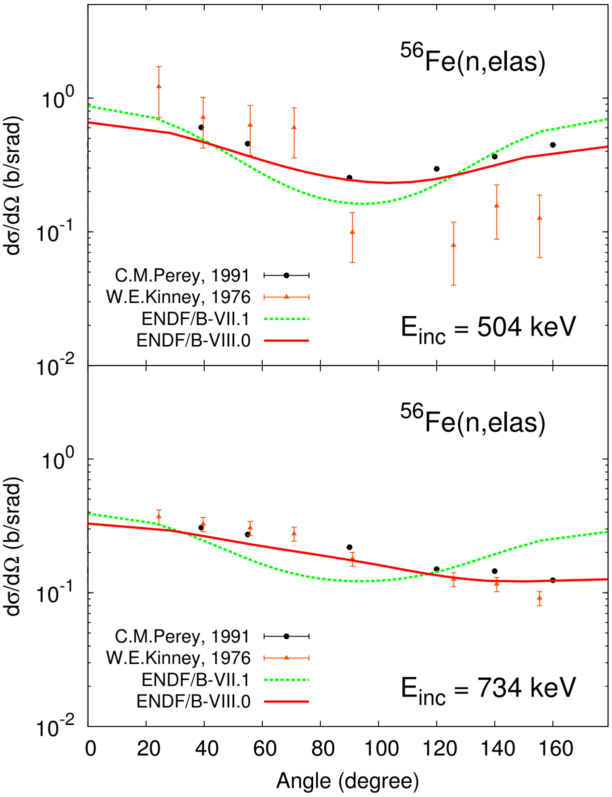

FIG. 33. (Color online) Elastic angular distributions for neutron incident energies of 504 and 734 keV, compared to ENDF/B-VII.1. By comparing the different datasets of both panels one can observe the anisotropic behavior of Kinney data at lower incident energies.

Fast Region

The JEFF-3.2 [151] evaluation contains inelastic cross sections measured by Dupont *et al.* [152], even though the authors have discovered normalization concerns and the results were not published. New measurements were performed by Negret *et al.* [153], but with a lower resolution. The Dupont and Negret data were binned over a suitable energy mesh and a piecewise linear scaling parameter was constructed to adjust Dupont data such that they agree on average with the Negret data. It was also found that the energy calibration of the Negret data did not match the resonances of the total cross section. For this reason, a correction was made to the energy scale which amounted to 2.5 keV at 1.8 MeV. The adopted inelastic cross sections between 850 keV and 3.5 MeV are the ones from JEFF-3.2 [151]. In addition, the inelastic cross section below 1 MeV was reduced by 15% to approximately agree with Perey data [149]. The total inelastic cross section is shown in Fig. 34.

Level-density parameters for compound, target and the different residual nuclides were fitted to achieve a reasonably good agreement with the IRDFF evaluation [12, 13] for the (n,p) reaction. Even though this reaction was eventually replaced by IRDFF in the final file (with the difference put into the elastic channel), the fit allowed consistency between all other reactions. The (n,p) partial cross sections are re-scaled to match the total (n,p) cross section in the IRDFF-v1.05 file.

Considering the reasoning detailed in Ref. [19], the total cross sections adopted above the resonance range were from JEFF-3.2 [151], which originates from the Vonach-Tagesen evaluation [154] with superimposed fluctuations that correspond to the Berthold measurements [155] on $^{\mathrm{nat}}$Fe. The contribution of the minor isotopes was taken into account.

The elastic cross section is defined as the difference between the total and the remaining partial cross sections. To test the consistency, the cross section was resolution-broadened to 0.3 percent, achieving good agreement with Kinney data.

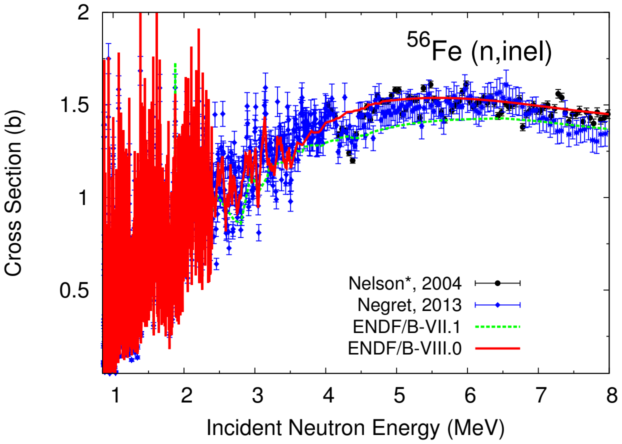

FIG. 34. (Color online) Evaluated ^{56}Fe(n,n') neutron inelastic cross section compared with data retrieved from EXFOR and with the previous evaluation. The asterisk on the Nelson data indicates that they are renormalized as described in Ref. [19].

Above the resonance range and up to 2.5 MeV the angular distributions correspond to re-fitted Kinney data [150] with some adjustments based on the comparison with Perey data [149] in the overlapping region. In the range 2.5-4.0 MeV the angular distributions are taken from Smith [156] while above said incident-energy region the EMPIRE [157] calculations are adopted.

For the ^{56}Fe fast region, covariances were computed for the major reaction channels represented in the evaluations i.e., total, elastic, inelastic, capture, $(n,2n)$, and (n,p). Inelastic scattering to individual discrete levels (MT=51,...,90) and to the continuum (MT=91) were combined together into MT=4. Additionally, covariances for the sum of all the remaining channels (MT=5) were provided as well as cross-correlations among all reactions mentioned above. These covariances were determined using Kalman filter-inspired Bayesian update procedure originally coded by Kawano and Shibata in the KALMAN code and included in EMPIRE [157]. The KALMAN methodology combines experimental uncertainties with the model constraints imposed through the sensitivity profiles provided by the EMPIRE code. With it, EMPIRE model parameters are sequentially adjusted to each experiment considered and cross section covariances are obtained by propagating covariances of the model parameters. Therefore, all physical constraints and correlations are included in the cross section covariances by construction in addition to the correlations imposed by the experimental covariance.

IRDFF recommendations [12, 13] were given special treatment in the ^{56}Fe evaluation. As discussed above, IRDFF cross sections were used in the evaluation procedure in place of the experimental datasets and, after fitting, EMPIRE calculated cross sections were replaced with the IRDFF values. Therefore, it was desirable to also retain IRDFF covariances. This was achieved by adjusting the weights of the IRDFF cross sections to reproduce original IRDFF uncertainties. The resulting off-diagonal part of the covariance matrix necessarily differs from the IRDFF since the IRDFF covariance is purely based on ^{56}Fe(n,p) experimental data while the CIELO ^{56}Fe includes also physics constraints and the correlations with other reactions. The CIELO ^{56}Fe(n,p) uncertainties are shown in Fig. 35.

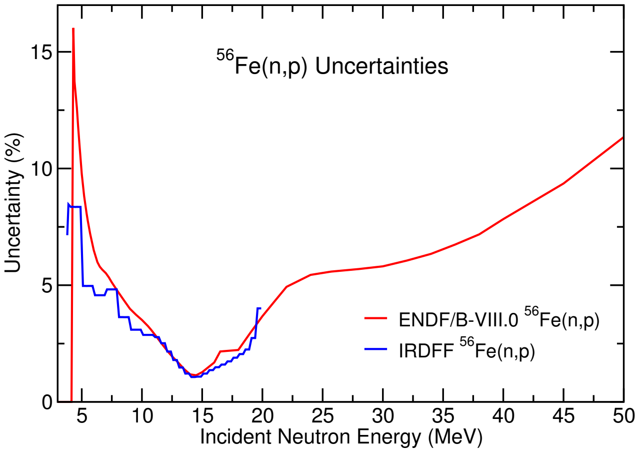

FIG. 35. (Color online) Evaluated ^{56}Fe(n,p) neutron cross section uncertainty, compared with IRDFF.

2. ^{54}Fe, ^{57}Fe and ^{58}Fe

Although ^{56}Fe is the dominant iron isotope, there is a significant contribution from the minor isotopes in any naturally occurring iron sample. Therefore, as part of the CIELO iron project, ^{54}Fe, ^{57}Fe and ^{58}Fe were also evaluated. As their evaluations are covered in detail in the iron evaluation summary paper also included in this issue of *Nuclear Data Sheets* [19], we do not discuss them here.

3. ^{59}Co, $^{58-62,64}$Ni

LANL updated the reaction cross sections (above the resonance range) of several isotopes in the structural material region, ^{59}Co and ^{58,59,60,61,62,64}Ni based on the CoH$_3$ calculations. The MF6 representation is consistently used for the continuum energy and angular distributions for emitted particles as well as the γ-ray production, since MF6 is suitable for radiation shielding and γ heating calculations. This was especially important for ^{59}Co, because isotropic angular distributions were given to many reactions in the previous evaluation and no proton and α-particle angular distributions were given.

In the evaluation procedure, particular attention was paid to the radiative capture, (n,p), (n,α), and (n,2n) cross sections by comparing with available experimental data. When experimental data from different laboratories were inconsistent with each other, we revisited the nuclear data used in the data analysis, and looked for a possible systematic bias prior to performing the model calculations. Although the evaluation includes the ^{2}H, ^{3}H, ^{3}He emission channels too, they tend to be purely theoretical predictions since few experimental data exit.

The α-particle production cross section for these nuclei was calculated with an improved Iwamoto-Harada model [158], which reproduces the measured data at LANSCE.

4. ^{63,65}Cu

Background & Previous Evaluations

Over the past decade, discrepancies between the computed and measured $k_{\rm eff}$ of criticality safety benchmark experiments containing copper were noticed by the nuclear data and criticality safety community [159]. The most notable of these benchmarks is the set of highly enriched uranium metal fuel systems with copper reflectors from the International Criticality Safety Benchmark Evaluation Project's (ICSBEP's) Zeus experiment [160]. The US Department of Energy (DOE) Nuclear Data Advisory Group, which maintains and constantly updates lists of materials that are considered important for applications in nuclear criticality safety, identified ^{63}Cu and ^{65}Cu as "important for measurement and evaluation in the next five years." Over 25 other ICSBEP benchmark evaluations contain significant amounts of copper, so the new evaluation results in statistically significant changes in the calculated $k_{\rm eff}$. Therefore, improving the copper evaluation will not only allow for more accurate criticality safety calculations involving copper as a material, but it will also result in better agreement between calculated and measured integral benchmark results.

Copper is also commonly used as a minor structural material in many fission power facilities, and it is an important structural component in Scandinavian spent fuel final disposal canisters. Copper is also an important heat sink material for fusion power reactors and is used for diagnostics, microwave waveguides, and mirrors in the International Thermonuclear Experimental Reactor (ITER). Consistent and correct nuclear data evaluations for the isotopes of copper are a high priority for applications to the International Fusion Materials Irradiation Facility (IFMIF), where the equipment must withstand high-energy particle irradiation. The neutron cross section of the copper isotopes is also important to the astrophysics community. The two stable copper isotopes lie along the beta-decay valley of stable isobars involved in the slow-neutron-capture-process (s-process). The s-process occurs in stars, is responsible for the creation of approximately half of the stable isotopes heavier than iron, and plays an important role in the galactic chemical evolution.

The copper resolved resonance region evaluations in the ENDF/B-VII.1 library are based on the resonance parameters from Mughabghab [161]. The authors of the previous copper evaluations contained in the ENDF/B-VII.1 library used these resonance parameters to fit the 1977 transmission data of Pandey *et al.* [162]. The authors noted the fit of the experimental data was improved when an additional constant background was added. However, this yielded a total average cross section that was too large. In addition, the original authors indicated the need to include a capture background from 60 keV to 99.5 keV. The original evaluation for both isotopes of copper did not include evaluation of experimental capture data. In the ENDF/B-VII.1 evaluation, the angular distribution of neutrons from elastic scattering was originally generated with the GENOA code [163]. The angular distributions are represented as coefficients of Legendre polynomials. There are only four energy points across the ENDF/B-VII.1 resolved resonance region (RRR) for the representation of the angular distribution. They are 10^{-5} eV, 0.0253 eV, 10 keV, and 100 keV.

Resonance Region

To address the nuclear criticality safety community's concerns about the performance of the copper isotopes in integral benchmarks, the resolved resonance region of the two copper isotopes was reevaluated based on the experimental data sets shown in Table XII. Furthermore, experimental capture cross section measurements were analyzed for the first time in the resonance evaluation of copper. Analyzing both the capture and transmission experimental data sets allows for the capture-to-scattering ratio to be set correctly for the entire RRR.

TABLE XII. Experimental data used in the RRR evaluation. Both stable copper isotopes were studied in each experiment. Table taken from Table 1 of Ref. [164].

Reference	Energy Range (eV)	Facility	Measurement
Pandey *et al.* [162]	32–185,000	ORELA	Trans. at 78 m
Pandey *et al.* [162]	1,000–1,400,000	ORELA	Trans. at 78 m
Guber *et al.* [165]	100–300,000	GELINA	Cap at 58 m
Guber *et al.* [165]	100–90,000	GELINA	Cap at 58 m
Sobes *et al.* [166]	0.01–0.1	MITR	Trans. at 1.2 m

As shown in Table XII, the new resonance evaluation is based on two sets of transmission data from the Oak Ridge Electron Linear Accelerator (ORELA) [162] and one data set from the MIT Nuclear Reactor (MITR) [166], plus two ^{63,65}Cu(n,γ) high-resolution measurements performed by Guber *et al.* [165] at GELINA in 2011. The first ORELA data set ranges from 32 eV to 185 keV, and the second data set is from 1 keV to 1.4 MeV. The first data set has better energy resolution than the second set in the energy region below 10 keV. The second data set has significantly better energy resolution at energies above approximately 60 keV. Finally, the third new experimental data set spans the thermal region of 0.01–0.1 eV and was measured to determine the low energy shape of the cross section and approximate the negative-energy resonances.

The new evaluation was done based on the Reich-Moore approximation of the R-matrix theory of nuclear resonance reactions. The evaluation method used the generalized least squares (GLS) method implemented in the SAMMY evaluation code to find the optimum value of the resonance parameters.

All sets of experimental data in Table XII were analyzed simultaneously.

The external resonances were determined from fitting the experimental data above 100 keV. The negative-energy external resonances received additional treatment in this evaluation because of the availability of cross section data spanning the thermal energy region (0.01–0.1 eV). The negative-energy external resonances were adjusted to fit the shape of the total thermal cross section instead of the typical practice of fitting a single value at thermal energy.

The angular distributions of elastic scattering are based on averaging of angular distributions reconstructed from resonance parameters following the Blatt and Biedenharn formalism [167]. This technique results in angular distributions that are more consistent with the evaluated elastic scattering cross section.

A statistical search using the GLS methodology was performed for the value of the scattering radius for both isotopes based on the analyzed experimental data. No evidence was found to support a change from the 6.7 fm value reported for both isotopes in Ref. [161]. The Wescott integral calculated from the evaluated resonance parameters is unity, indicating a $1/v$ neutron capture cross section in the thermal energy region.

The Maxwellian-averaged capture cross sections (MACS) for ^{63}Cu and ^{65}Cu are presented in Figs. 36 and 37, respectively. The MACS for both isotopes were calculated from the resonance parameters evaluated based on the differential experimental data in Table XII and the high-energy evaluated cross sections described in the section below. The systematically larger MACS value for ^{63}Cu is corroborated by a new measurement from Weigand *et al.* at the Los Alamos Neutron Science Center (LANSCE) Experimental Facility [168].

Further, feedback from integral experiments also suggests that the capture cross section of ^{63}Cu may be too large to fit the KADoNiS data [169, 170].

Resonance parameter covariance matrices were generated through the GLS methodology in SAMMY. It is well known that the GLS methodology results in unre-

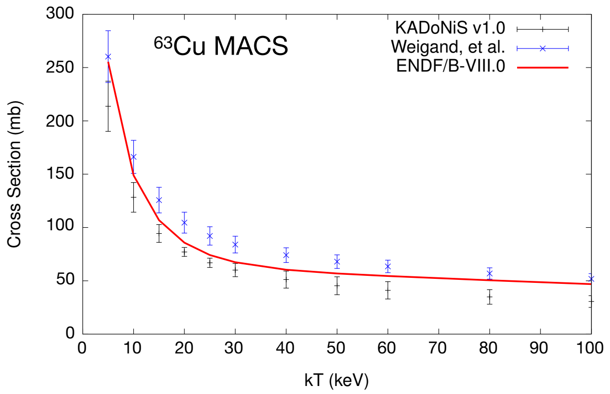

FIG. 36. (Color online) ^{63}Cu Maxwellian-averaged capture cross section calculated from the ENDF/B-VIII.0 evaluation and compared with data from the Karlsruhe Astrophysical Database of Nucleosynthesis in Stars [169, 170].

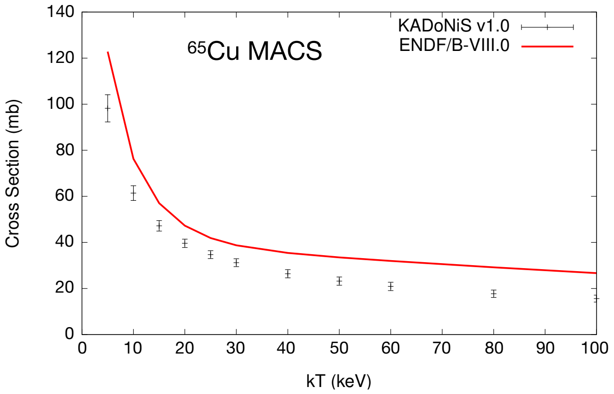

FIG. 37. (Color online) ^{65}Cu Maxwellian-averaged capture cross section calculated from the ENDF/B-VIII.0 evaluation and compared with data from the Karlsruhe Astrophysical Database of Nucleosynthesis in Stars [169, 170].

alistically small variances on the resonance parameters, particularly for the resonance energies. Therefore, the variances on the resonance parameters were artificially increased so the calculated cross section uncertainties would be on the order of the uncertainty in the differential measurements when calculated for a 44 group cross section covariance matrix using a constant flux. On the other hand, the correlation matrix for the resonance parameters is considered to be reliable and consequently is useful for the calculation of multigroup cross section correlation matrices, such as the group-to-group correlations between capture and elastic scattering in the RRR.

(n,tot) Total Cross Section
Figures 38 and 39 show the calculated transmission from the ENDF/B-VII.1 and ENDF/B-VIII.0 evaluations compared with one of the experimental data sets from Pandey *et al.* [162]. The plots show a good fit of the experimental data for both isotopes up to incident neutron energies of 100 keV. Figures 40 and 41 show the details of two select energy regions, 44–51 keV and 59–66 keV, respectively. In these two regions, the improvements in resonance analysis in the ENDF/B-VIII.0 library are evident compared with the ENDF/B-VII.1 library.

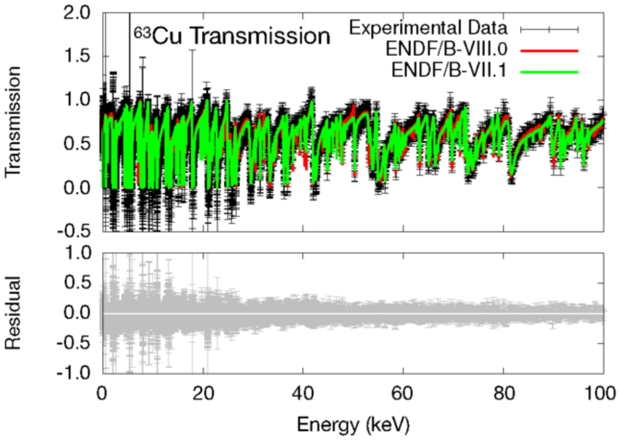

FIG. 38. (Color online) ^{63}Cu calculated transmission from the ENDF/B-VII.1 library and the ENDF/B-VIII.0 evaluation are compared with experimental data from Pandey *et al.* [162] and plotted with one standard deviation uncertainty. The residual fit of the ENDF/B-VIII.0 experimental data is plotted at the bottom with one standard deviation uncertainty.

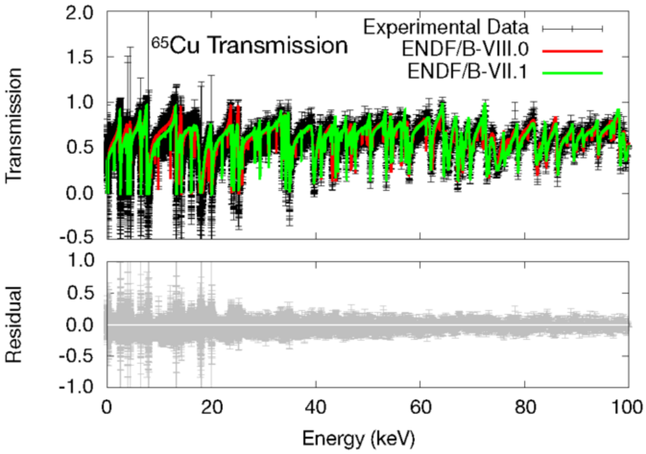

FIG. 39. (Color online) ^{65}Cu calculated transmission from the ENDF/B-VII.1 library and the ENDF/B-VIII.0 evaluation are compared with experimental data from Pandey *et al.* [162] and plotted with one standard deviation uncertainty. The residual fit of the ENDF/B-VIII.0 experimental data is plotted at the bottom with one standard deviation uncertainty.

(n,γ) Capture
Figures 42 and 43 show neutron capture cross sections calculated from the ENDF/B-VII.1 library and the ENDF/B-VIII.0 evaluation compared with one of the experimental data sets from Guber *et al.* [165]. The ENDF/B-VIII.0 resonance evaluation fits the Guber *et al.* experimental data well up to 100 keV. Drastic improvements in the evaluated capture cross section in the resolved resonance region are evident in the energy range of 50–100 keV in Figs. 42 and 43. Figures 44 and 45 show the details of two select energy regions, 14–20 keV and 54–61 keV.

High Energy Region
The incident neutron cross sections for energies above

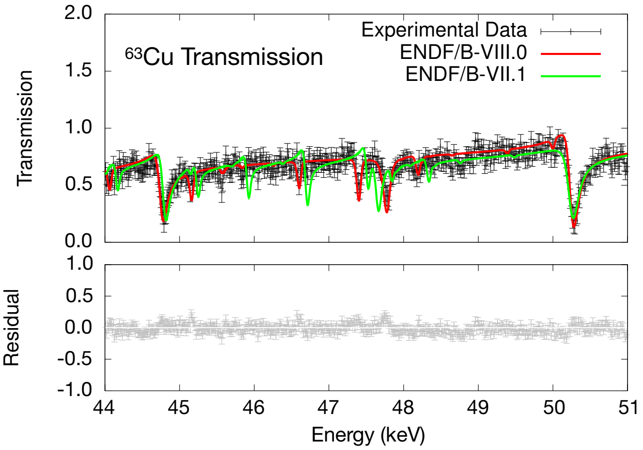

FIG. 40. (Color online) Zoomed in energy scale of earlier figure: ^{63}Cu calculated transmission from the ENDF/B-VII.1 library and the ENDF/B-VIII.0 evaluation are compared with experimental data from Pandey *et al.* [162] and plotted with one standard deviation uncertainty. The residual fit of the ENDF/B-VIII.0 experimental data is plotted at the bottom with one standard deviation uncertainty.

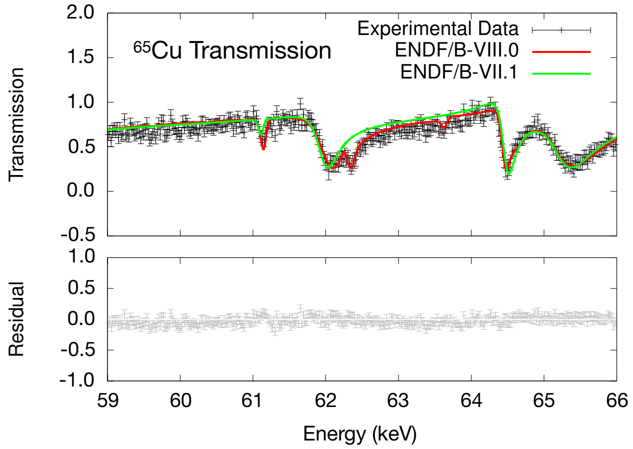

FIG. 41. (Color online) Zoomed in energy scale of earlier figure: ^{65}Cu calculated transmission from the ENDF/B-VII.1 library and the ENDF/B-VIII.0 evaluation are compared with experimental data from Pandey *et al.* [162] plotted with one standard deviation uncertainty. The residual fit of the ENDF/B-VIII.0 experimental data is plotted at the bottom with one standard deviation uncertainty.

100 keV (high energy region) were calculated using the CoH$_3$ code. As in the Ni and Co evaluations, the MF6 representation is consistently used for the continuum energy and angular distributions for emitted particles as well as the γ-ray production, since MF6 is suitable for radiation shielding and γ heating calculations. Particular attention was paid to the radiative capture, (n,p), (n,α), and (n,2n) cross sections by comparing with available experimental data. Differential elastic scattering, reaction, and total cross sections were calculated up to 150 MeV and were connected to the resonance region evaluation at 100 keV where the angle-integrated cross sections were seen to connect smoothly.

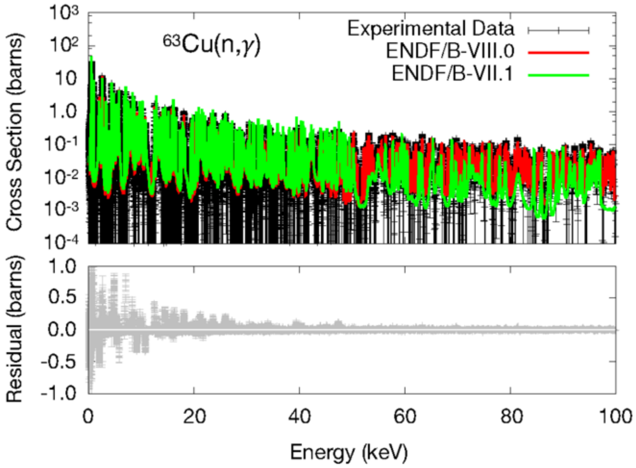

FIG. 42. (Color online) ^{63}Cu neutron capture cross sections calculated from the ENDF/B-VII.1 library and the ENDF/B-VIII.0 evaluation are compared with experimental data from Guber *et al.* [165] plotted with one standard deviation uncertainty. The residual fit of the ENDF/B-VIII.0 experimental data is plotted at the bottom with one standard deviation uncertainty.

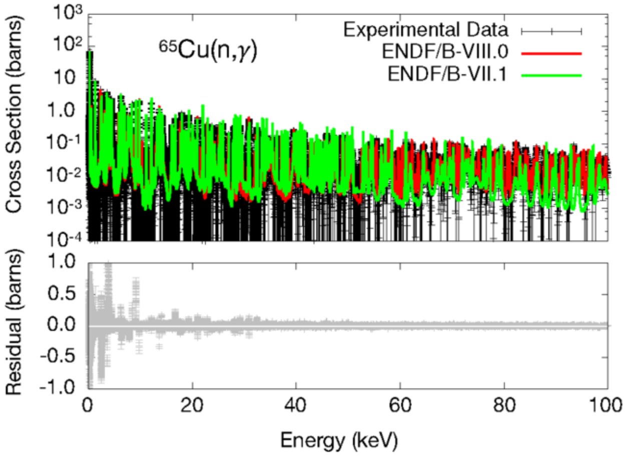

FIG. 43. (Color online) ^{65}Cu neutron capture cross sections calculated from the ENDF/B-VII.1 library and the ENDF/B-VIII.0 evaluation are compared with experimental data from Guber *et al.* [165] plotted with one standard deviation uncertainty. The residual fit of the ENDF/B-VIII.0 the experimental data is plotted at the bottom with one standard deviation uncertainty.

Future Work

A set of resonance parameters with varied radiations widths that fit the five data sets in Table XII up to 300 keV is available by request from one of the authors of this paper (V. Sobes, ORNL). This set of resonance parameters extended the resolved resonance region to higher energies, where certain ICSBEP intermediate neutron spectrum benchmarks have significant amounts of sensitivity to copper. However, this set of evaluated resonance parameters did not show as good of a level of agreement in integral benchmark calculations when compared to the CoH$_3$ calculated cross sections in the fast neutron range adopted in ENDF/B-VIII.0 above 100 keV.

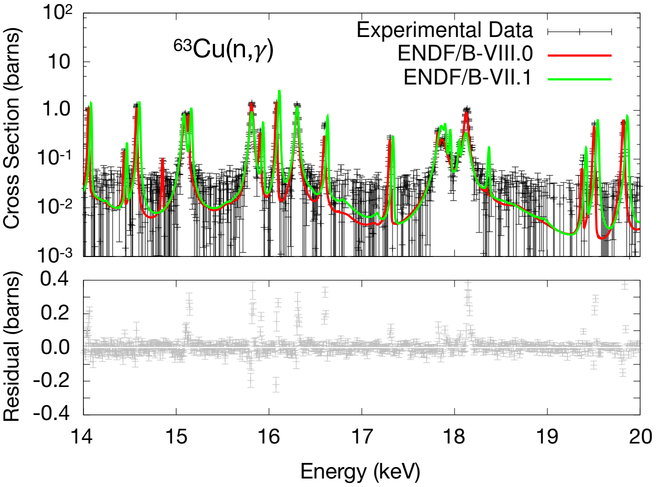

FIG. 44. (Color online) Zoomed in energy scale of earlier figure: ^{63}Cu neutron capture cross sections calculated from the ENDF/B-VII.1 library and the ENDF/B-VIII.0 evaluation are compared with experimental data from Guber *et al.* [165] plotted with one standard deviation uncertainty. The residual fit of the ENDF/B-VIII.0 of the experimental data is plotted at the bottom with one standard deviation uncertainty.

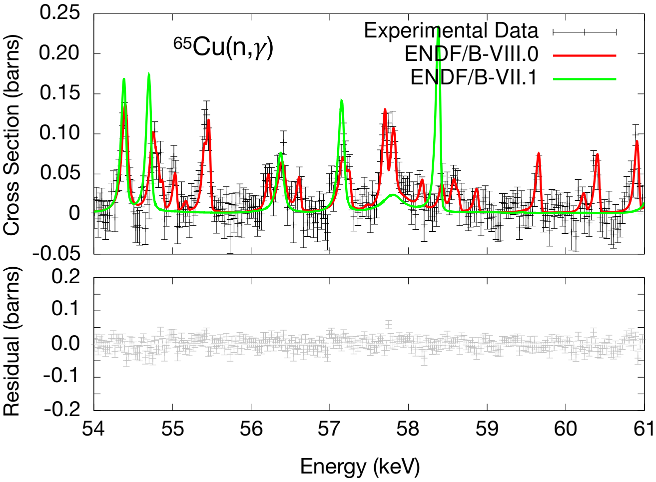

FIG. 45. (Color online) Zoomed in energy scale of earlier figure: ^{65}Cu neutron capture cross sections calculated from the ENDF/B-VII.1 library and the ENDF/B-VIII.0 evaluation are compared with experimental data from Guber *et al.* [165] plotted with one standard deviation uncertainty. The residual fit of the ENDF/B-VIII.0 of the experimental data is plotted at the bottom with one standard deviation uncertainty.

5. ^{73,74,75}*As*

The cross sections for ^{73,74,75}As above the resonance range were calculated with CoH$_3$ and the γ-ray, neutron, proton, and α-particle emission channels were included. The total cross section was calculated with the coupled-channels method implemented in CoH$_3$, considering a strong oblate deformation for the arsenic isotopes, typically $\beta_2 = -0.25$. Because the coupling scheme of arsenic is not very clear, only the ground state and the first possible rotational band member are coupled. Starting with the Koning-Delaroche spherical global optical potential [171], an imaginary part was reduced, which effectively accounts for the channel coupling. The calculated total cross sections show better reproduction of the experimental total cross section data in the 4–8 MeV region. This optical potential was used for all arsenic isotopes, with the isospin correction term in the Koning-Delaroche potential.

In the statistical Hauser-Feshbach calculation, the proton optical potential by Koning and Delaroche [171] and the α-particle potential by Avrigeanu *et al.* [172] were adopted. For the capture reaction, the Γ_γ/D_0 value was derived by comparing with available ^{75}As experimental data, and the same Γ_γ value was applied to ^{73,74}As. The calculated (n,p), (n,np), (n,α), (n,nα), and (n,2n) cross sections were tuned by adjusting the model parameters to the ^{75}As experimental data, and the same parameters were used for the calculations of ^{73}As and ^{74}As. The (n,2n) and (n,α) cross sections were obtained by almost no parameter adjustment. However, a relatively strong modification to the proton emission channel was needed in order to reproduce the experimental (n,p) cross sections.

6. ^{78}*Kr*, ^{132}*Te*, *and* ^{124}*Xe*

There was a long-standing issue of energy balance reported for quite a few nuclei in the fission products region. Above the resonance region, they were often evaluated by a statistical model calculation since experimental data are very scarce or not available. The coupled-channels Hauser-Feshbach technique to calculate the cross sections was adopted, and the optical potential of Kunieda *et al.* [173] is used. In addition to the energy balance problem, some old evaluations use the combination of MF4 and MF5. This should be replaced by the MF6 representation. These files were upgraded through the use of new CoH$_3$ calculations, because this code is designed to conserve the total energy carefully. The updated nuclei include ^{78}Kr, ^{124}Xe, ^{132}Te, and six hafnium isotopes. Although the evaluation largely relies on the model code prediction, the calculations are tuned to the measured cross sections whenever available.

7. ^{105}*Rh*

The ^{105}Rh evaluation from ENDF/B-VII.1 was taken from JENDL-3.3. The resonances were modified in 2016 by N. Iwamoto, correcting a long standing error with the target spin assignment. The revised resonance region consists of one Single Level Breit-Wigner resonance which was converted to the Multi-Level Breit-Wigner approximation.

C. Z=61-88

1. ^{169}Tm

The ^{169}Tm evaluation in ENDF/B-VIII.0 was carried over from the previous ENDF/B-VII.1 evaluation, where the (n,2n) cross section was taken from the IAEA dosimetry IRDFF file [12, 13]. Since that work, the cross section has been measured at TUNL by Champine *et al.* [174] and is in very good agreement with the evaluation, see Fig. 46.

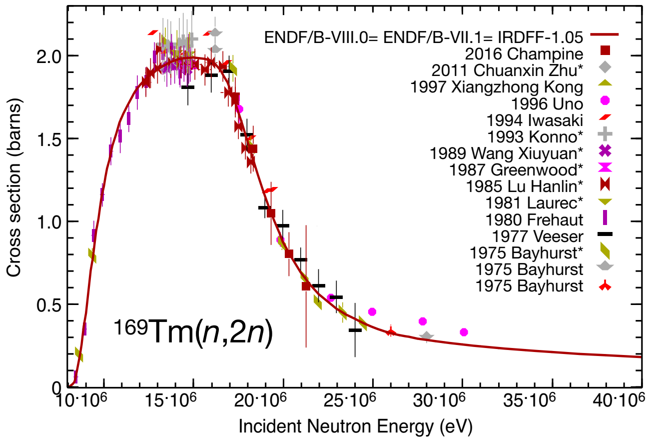

FIG. 46. (Color online) The ENDF/B-VIII.0 ^{169}Tm$(n,2n)$ cross section compared with all available data in EXFOR. The asterisk on some of the experimental data indicates that they are automatically renormalized by the EXFOR project upon retrieval of the data [175].

2. Dy, Yb, Os

The isotopes ^{154,159}Dy, $^{168,170-174,176}$Yb and $^{184,186-190,192}$Os from JENDL-4.0 were judged to be high quality and therefore were adopted for ENDF/B-VIII.0.

3. $^{174,176,177,178,179,180,181,182}Hf$

JENDL-4.0 evaluations we judged to be of high quality for ^{181,182}Hf and were adopted for ENDF/B-VIII.0. The other six hafnium isotopes were re-evaluated for ENDF/B-VIII.0. The resonances for these six hafnium isotopes are taken from ENDF/B-VII.1. The fast region was updated using the same methodology as in subsection III B 6. This resolved the same long-standing energy balance problem discussed in subsection III B 6.

4. ^{197}Au

The resolved resonance parameters were re-evaluated up to 2 keV [176, 177] using the new measurements performed at JRC-Geel and n_TOF [178]. At the thermal energy the constants reflect the recommendations from the new standards [10]. Above the resolved resonance range the recommended capture cross sections (which are strictly not standards but were evaluated with the standards) are given as bin-average values up to 20 keV. Fine tuning was done to the original JRC-Geel evaluation to force consistency with bin-average values of the recommended cross sections. Above 20 keV the pointwise values from standards were adopted, except for smoothing some fluctuations, which are not expected at higher energies due to physical considerations. File assembly was done with the LSSF flag set to one, implying that the cross sections in the unresolved resonance region, which extends to 100 keV, are given in pointwise form; the unresolved resonance parameters are only used for the self-shielding calculations. The remaining cross sections were adopted from the ENDF/B-VII.1 library.

The covariance matrix block for the capture reaction that corresponds to the region evaluated with standards is also updated.

5. $^{182,183,184,186}W$

Background

Tungsten is a structural material of interest in many high-temperature nuclear applications including fusion systems. In ENDF/B-VII.1 [2], ^{180,182,183,184,186}W were extensively updated as part of an IAEA Data Development Project [179, 180]. The focus of this evaluation was the fast region and relatively minor adjustments were made to ^{182,183,184,186}W resonances. New experimental data allowed reevaluations of the resonance parameters of four tungsten isotopes (^{182,183,184,186}W) in the neutron energy range of thermal up to several keV [143, 181–183]. This nuclear data work was performed with support from the US Nuclear Criticality Safety Program (NCSP) in an effort to provide improved tungsten cross section and covariance data for criticality safety analyses.

The evaluation methodology used the Reich-Moore approximation of the R-matrix formalism of the code SAMMY to fit high-resolution measurements performed in 2010 and 2012 at the Geel linear accelerator facility (GELINA) [184], as well as other experimental data sets on natural tungsten available in the EXFOR library [185]. An overview of the RRR is shown in Table XIII. This work nearly doubles the resolved resonance region (RRR) present in the previous US nuclear data library ENDF/B-VII.1.

The ENDF/B-VIII.0 evaluated set of neutron resonance parameters documented in three published papers [181–183], considered the neutron and gamma exit channel, c, for incident neutron partial s- and p-wave to define the level energies E_λ, the probability amplitudes (γ_c^λ) and the related partial widths (Γ_c^λ). The analysis of the experimental data used the SAMMY code [142], which performed a multi-level, multi-channel R-matrix

TABLE XIII. Neutron energy range for the ENDF/B-VIII.0 tungsten evaluations. The number of fitted levels is also shown. All resonances are given in the Reich-Moore approximation.

Nucleus (I^π)	$E_{\max}$	Levels	s-wave	p-wave
^{182}W (0^+)	10 keV	306	171	135
^{183}W ($1/2^-$)	5 keV	387	346	21
^{184}W (0^+)	10 keV	178	94	84
^{186}W (0^+)	10 keV	169	95	74

fit to neutron data using the Reich-Moore approximation. Experimental conditions such as resolution function, finite size of the sample, nonuniform thickness, as well as nuclide abundances of sample, multiple scattering, self-shielding, normalization, background, and Doppler broadening were also taken into account. In addition to the previous publications, a recent paper [143] was devoted to present the validation analysis of the set of tungsten evaluations and to show the improved agreement with the experimental response of the Grenoble Lead-Slowing-Down benchmarks when this set was included in the ENDF/B-VII.1 library.

Previous Resonance Evaluations

In the ENDF/B-VII.0 library released in December 2006, the tungsten evaluations of the neutron-resonance parameters were performed in the 1970s for the ENDF/B-V library and successively adopted by the different releases of ENDF. The evaluated resonance parameters were based on the analysis performed by Goldberg [186], along with the results of capture and transmission measurements performed by Bartolome [187] over the energy range from thermal up to 760 eV (^{183}W), and for the even-A isotopes up to 4.5 keV (^{182}W), 2.6 keV (^{184}W), and 3.2 keV (^{186}W). Due to the poor energy resolution of those measurements and their higher level detection sensitivity included in the resonance analysis, spurious levels might have led to unrealistic s-wave data.

In the ENDF/B-VII.1 library released in December 2011, the tungsten evaluations in the resolved resonance region were extended to 2.2 keV (^{183}W), 4.5 keV (^{182}W), 4 keV (^{184}W), and 8.5 keV (^{186}W). In defining the resonance parameters, these evaluations adopted the Reich-Moore formalism, and based on the JENDL-3.3 library with small adjustments to the parameters by Leal [180]. The evaluations used the results of neutron time-of-flight resonance measurements performed by Camarda [188] and Ohkubo [189] in the early 1970s, and by Macklin [190] in the 1980s, along with the values of resonance parameters taken from the work of Mughabghab [191].

New Resonance Evaluations

The results of the evaluated cross sections at thermal energy and other geometrical quantities such as scattering radius and (in)coherent scattering lengths are displayed for ^{182,183,184,186}W isotopes in Table XIV. There is a significant discrepancy between the evaluated value and the value reported in the ATLAS for the elastic thermal cross section of ^{183}W. This was found to be significantly underestimated as well as in other major libraries. The origin of the underestimated value of the scattering cross section is thought to be derived from the measurement of Alexandrov [192], who reported a value of the coherent scattering length of b_{coher}=4.3±0.5 fm more than 2 fm smaller than the precise coherent scattering length measurement of Knopf [193], b_{coher}=6.59±0.04 fm.

For the ^{186}W isotope the value of the thermal capture cross section is based on the experimental data measured by Friesenhahn [194] that revealed to be consistent with the experimental capture and transmission data used in the evaluation. In fact, dominated by the the 18.8 eV level, the capture cross section at thermal energy depends on the product $\Gamma_n\Gamma_\gamma$ of the neutron and capture widths. In addition, correlation between the energy bound levels and the resonance at 18.8 eV provided the grounds for an excellent representation of the coherent scattering length. On the contrary, the present set of resonance parameters was found incompatible with a recent measurement performed by Hurst [195] who reported a reduction of about 14% (≈4.6 barns) in the ^{186}W(n_{th},γ) cross section.

TABLE XIV. Thermal cross sections (in barn), scattering radius and (in)coherent scattering lengths (in femtometers) compared to the values found in the *Atlas of Neutron Resonances*.

		Total	Capture	Elastic	R'	b_{coh}	b_{incoh}
^{182}W	This work	29.18	20.31	8.87	7.6	7.11	—
	ATLAS	—	19.90	8.84	8.1	7.04	—
^{183}W	This work	15.56	9.87	5.69	7.9	6.47	−0.43
	ATLAS	—	10.40	2.40	8.1	6.59	—
^{184}W	This work	8.98	1.63	7.35	7.6	7.41	—
	ATLAS	—	1.70	7.35	8.0	7.55	—
^{186}W	This work	37.97	37.88	0.09	7.7	−0.76	—
	ATLAS	—	38.10	0.07	7.6	−0.73	—

For the odd-A isotope ^{183}W the set of resonance parameters was obtained in the energy range between thermal up to 5 keV, while for the even-A isotopes, the upper energy limit was set up to 10 keV.

As an example, in Figs. 48 and 47 the total (in black) and capture (in red) cross sections calculated from the ENDF/B-VIII.0 resonance parameters are compared with the experimental data [184] and the cross sections reconstructed from ENDF/B-VII.1 resonance parameters (dashed lines) for two major isotopes ^{182,183}W.

As shown in the figure, the improved set of experimental data made it possible to obtain meaningful values of the neutron and capture widths in the specified energy range.

Contrary to the even-A tungsten isotopes, ^{183}W having $I^\pi = 1/2^-$, couples to make two compound-nuclear states $J^\pi = 0^-$ and $J^\pi = 1^-$ for s-wave. As suggested by comparing Fig. 48 and Fig. 47 and clearly seen in Fig. 49, the average level spacing $\langle D_0\rangle$ of ^{183}W tends to be

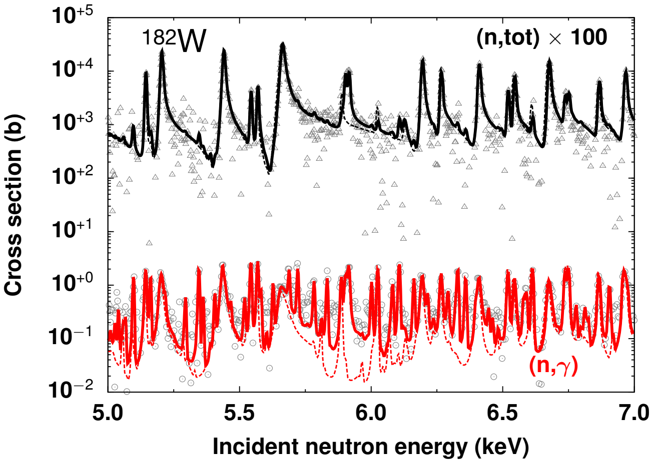

FIG. 47. (Color online) ^{182}W(n,γ) and total cross-sections in the energy range of 5–7 keV calculated from the ENDF/B-VIII.0 (solid lines) and ENDF/B-VII.1 (dashed lines) resonance parameters are compared with the experimental data [184].

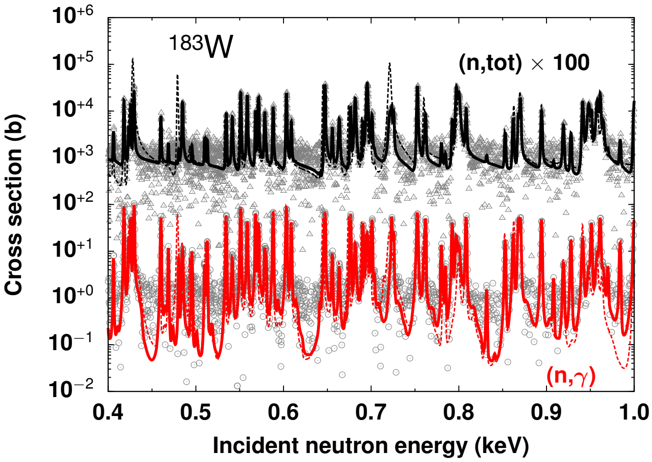

FIG. 48. (Color online) ^{183}W(n,γ) and total cross-sections in the energy range of 0.4–1 keV calculated from the ENDF/B-VIII.0 (solid lines) and ENDF/B-VII.1 (dashed lines) resonance parameters are compared with the experimental data [184].

much smaller than that of even-A isotopes since ^{183}W has two mixed independent populations with $J^{\pi} = 0^{-}$ and $J^{\pi} = 1^{-}$. This is also due to a higher separation energy, as the separation energy of ^{184}W is about 7.4 MeV rather than in the range 5.5–6.2 MeV for ^{183,185,187}W. This results in much stronger compound-nuclear effects. The differences in level spacing between even-A and odd-A, as reported in Table XIII, justify the choice of the different upper energy limit for RRR.

Figure 49 shows a nearly linear slope that extends to about 5 keV. This indicates that in the vast majority of our reported levels, there are no missed narrow weak s-levels contrary to the previous ENDF/B-VII.1 resonance evaluation (in gray full dots) whose slope starts to deviate from a linear behavior already at incident neutron energies above 1 keV.

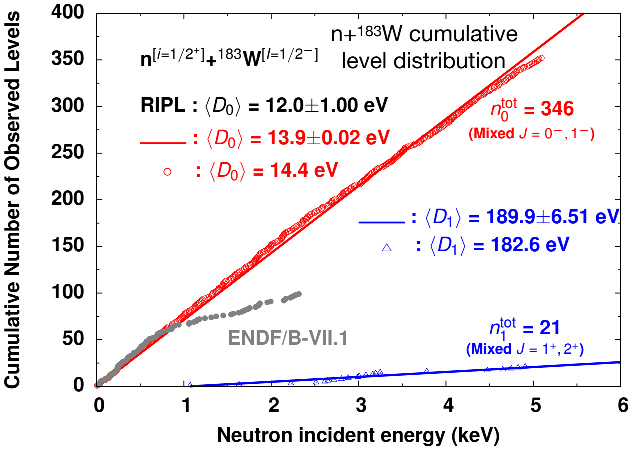

FIG. 49. (Color online) Plot of the ENDF/B-VIII.0 cumulative number of observed s- (red rots) and p-levels (blue triangle) vs energy for n+^{183}W. The values of average s-level spacings $\langle D_0 \rangle$ and p-level spacings $\langle D_1 \rangle$ shown in the plot represent the inverse of the slope of a straight line fitted to the data (red and blue lines). ENDF/B-VII.1 cumulative number of levels is also shown (gray full dots).

6. $^{190-198}$*Pt*

The isotopes of platinum were not present in previous versions of ENDF/B, and have therefore been adopted from the TENDL-2015 library. The platinum isotopes reside in the transitional range between the rare-earth, rotational deformed nuclides and the (near-spherical) Pb mass range. For these Pt evaluations, the spherical optical model of Koning-Delaroche [171] was used, with a vibrational description of the inelastic transitions. For this, only the most important 2+ and 3- levels were taken into account. As described in the evaluation procedure of Ref. [196], the level density parameters were tuned to the available experimental discrete level scheme and average neutron resonance spacing. Starting from a first global prediction of all reaction channels, the capture data in the fast range was fitted to the experimental data by adjusting the average radiative width, while for channels at higher energies, like (n,p) and $(n,2n)$, the pre-equilibrium partial state densities were slightly adjusted to get the best agreement with measurement. In the resonance range the available data from the Atlas of Mughabghab was used. This method was applied to all isotopes until a globally reasonable agreement with experimental data was obtained. Similar to all TENDL-2015 data files, the data extend to 200 MeV and come with full covariance matrices for cross sections, isomer production and angular distributions, obtained from the Bayesian Monte Carlo scheme [197].

D. Z=89-95

1. ^{233}U

The starter for this file was the JENDL-4.0 evaluation. The gamma and the fission widths of the bound level at -1.7565 eV were adjusted to reproduce the thermal constants from the new standards, as shown in Table XV. The resulting thermal constants are compared to different evaluated data in Table XVI.

TABLE XV. Adjustment of the capture and fission widths of the bound level at -1.7565 eV of ^{233}U.

	JENDL-4.0	ENDF/B-VIII.0
Γ_γ (eV)	0.03763	0.01263
Γ_f (eV)	2.166	2.191

TABLE XVI. ENDF/B-VIII.0 thermal constants of ^{233}U compared to ENDF/B-VII.1 values, and to the neutron standards 2017 and CONRAD values [198]. There are differences between the new B-VIII.0 values and the new 2017 standards, since the new standards work came too late to be adopted in B-VIII.0

	B-VII.1[a]	B-VIII.0[a]	standards 2017	CONRAD
σ_f (b)	531.3	534.1	533.0(2.2)	530.2(2.1)
σ_γ (b)	45.3	42.3	44.9(0.9)	45.1(9)
σ_el (b)	12.2	12.2	12.2(0.7)	12.3(7)
$\overline{\nu_{tot}}$	2.4968	2.4852	2.4870(50)	2.4927(50)

[a] T=0 K.

Thermal $\overline{\nu_p}$ was changed resulting in the change to $\overline{\nu_{tot}}$ shown in Table XVI and the values in the epithermal range up to 200 keV were increased up to 0.8% relative to JENDL-4 values, to improve the performance in the ICSBEP fast benchmarks (with different reflectors) containing ^{233}U. The adopted JENDL-4 multiplicity in the fast range below 3 MeV allow for a better reproduction of existing differential data as shown in Fig. 50.

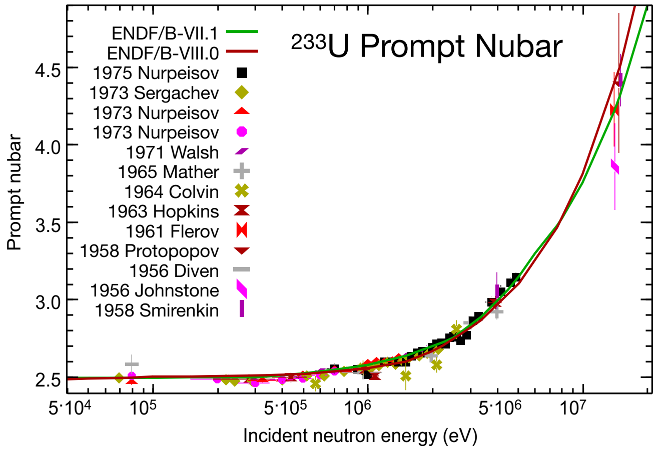

FIG. 50. (Color online) Neutron multiplicity measurements of $n+^{233}$U [175] are compared with ENDF/B-VIII.0 and ENDF/B-VII.1 evaluations.

2. ^{235}U

A focused international effort on ^{235}U in recent years has been coordinated by the IAEA within the CIELO project [199], and has been adopted for ENDF/B-VIII.0. A full description of this CIELO work for ^{235}U is given by Capote *et al.* in this issue of *Nuclear Data Sheets* [17]. Differences between this (CIELO-1) work and a related CEA (CIELO-2) evaluation, are described by Chadwick in the CIELO overview paper [8].

Background & Previous Evaluations
Earlier ENDF evaluations of ^{235}U neutron-induced reactions used resonance analyses by Leal, Derrien, Larson, and Wright, while higher energy cross sections came from evaluation work by Young, Chadwick, Talou, Kawano, MacFarlane, and Madland for prompt fission neutron spectrum (PFNS). This work was documented in the ENDF-B/VII big papers [1, 2] as well in the detailed summary on actinides by Young *et al.* [200].

A new PFNS has been derived for thermal neutrons incident on ^{235}U within the IAEA neutron standards by Trkov, Pronyaev and Capote [11, 201, 202] resulting in a reduction of the average energy of fission neutrons by 30 keV at thermal. Such a large change required a reevaluation of the resonance region cross sections and neutron multiplicities to reestablish the good integral performance of the ENDF/B-VII library for thermal HEU solution and thermal water lattices. This is described below.

A new resonance region analysis has been led by Pigni at ORNL in collaboration with Capote and Trkov at the IAEA [203]. The starting file was a modification of the original ENDF/B-VII.1 evaluation fitted to reduce capture by 30% near 1 keV by Leal [204] using new experimental data by Jandel *et al.* [205] and Danon *et al.* [206]. Such a reduction was initially suggested by Japanese researchers [207, 208].

The new evaluation in the fast region was by Capote, Trkov, Sin, and Herman [209], together with contributions by Neudecker, Talou, Chadwick, Stetcu, and Kahler for prompt fission neutron and gamma spectra. The new IAEA standard fission cross section was adopted above 150 keV; lower energy `GMA` fitted fission cross sections (from 20 to 150 keV) are reproduced on average by the new evaluation.

The previous ENDF/B-VII.1 evaluation performed very well for HEU thermal solution and thermal water lattices; such performance is maintained by the current VIII.0 file despite the extensive changes in PFNS, cross section and neutron multiplicities. In the fast region the previous ENDF/B-VII.1 uranium evaluation performed relatively well in integral validation simulation comparisons with bare and reflected critical assembly data, while simulations of intermediate energy assemblies showed varied levels of agreement, as documented in Refs. [2, 22], and this is also continued in ENDF/B-VIII.0.

However, it has been recognized that compensating errors in the individual reaction channel data play

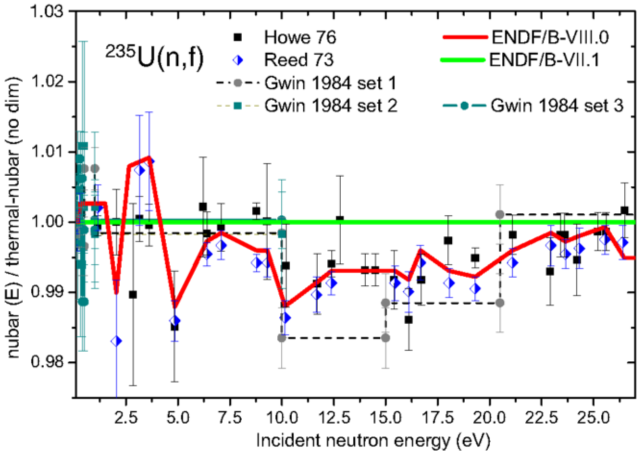

FIG. 51. (Color online) Neutron multiplicity measurements [210–213] are compared with ENDF/B-VIII.0 and ENDF/B-VII.1 evaluations below 27 eV.

a significant role in criticality predictions [214, 215], which ultimately involve small nuclear data calibration adjustments to match integral data such as the criticality of the Godiva assembly. This led to CIELO-project efforts in experiment, theory, and evaluation to better determine the ^{235}U fission, PFNS, and neutron capture, scattering and emission cross sections as described below.

Resonance region

The ^{235}U resolved resonance evaluation was developed on the basis of newly evaluated Thermal Neutron Constants [198], new prompt fission neutron spectra for thermal neutron-induced fission of ^{235}U [11, 201, 202], and a reevaluated neutron multiplicity below 30 eV to include fluctuations as shown in Fig. 51. Integral data were used as a validation tool to ensure that the benchmark performance of the ^{235}U HEU solutions is comparable to the previous ENDF/B-VII.1 evaluation. Within the Reich-Moore approximation of the *R*-matrix formalism of the code SAMMY [142], this task was achieved by maintaining reasonably good agreement with the experimental data with particular emphasis on restoring the important constraint of the standard fission integral in the neutron incident range between 7.8–11 eV. The average fission cross sections from 100 eV to 2 keV in 100 eV intervals were also recommended by neutron standards and this additional constraint was taken into account in the ENDF/B-VIII.0 file.

As in the resonance evaluation in the ENDF/B-VII.1 library, the present evaluation extends to neutron incident energies up to 2.25 keV, and the *s*-wave resonances have spin and parity, 3^- and 4^-, as displayed in Table XVII.

TABLE XVII. Neutron energy range for the ^{235}U evaluation and the number of fitted resonances for the two channel spins related to *s*-wave neutrons. All resonances are given in the Reich-Moore approximation.

Nucleus (I^π)	$E_{\max}$ (keV)	J_{3-}	J_{4-}
^{235}U ($7/2^-$)	2.25	1433	1731

In the thermal energy range, this work relies on values of the fission and capture cross sections obtained in the standard evaluation (Thermal neutron constants) and reported in Table XVIII, along with the values of the evaluated cross sections reconstructed for T=0 K.

TABLE XVIII. ENDF/B-VIII.0 thermal constants are compared to ENDF/B-VII.1 values, to the neutron standards 2017, and to CONRAD values [198]. Derived quantity α is also reported.

	B-VII.1[a]	B-VIII.0[a]	standards 2017	CONRAD
$\sigma_{\rm f}$ (b)	584.99	586.8	587.2(1.4)	586.4(1.5)
σ_γ (b)	98.69	99.4	99.3(2.0)	99.1(2.1)
$\sigma_{\rm el}$ (b)	15.11	14.11	14.09(22)	14.05(22)
$\overline{\nu_{tot}}$	2.4367	2.4298	2.4250(50)	2.4257(57)
α[b]	0.1687	0.1694	0.1690	0.1689

[a] T=0 K.

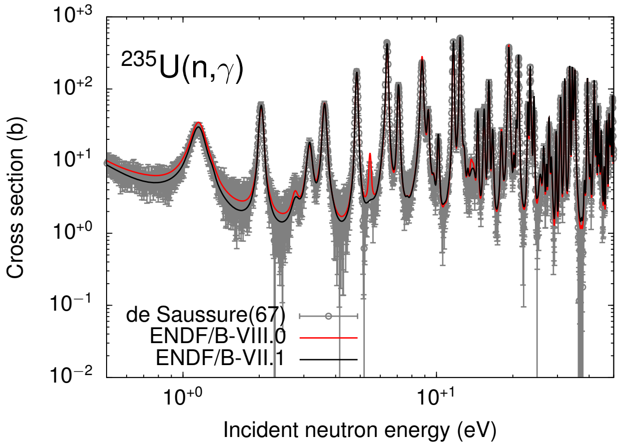

FIG. 52. (Color online) n+^{235}U de Saussure's capture measurement [216] compared to ENDF/B-VII.1 [2] (in black) and ENDF/B-VIII.0 values (in red).

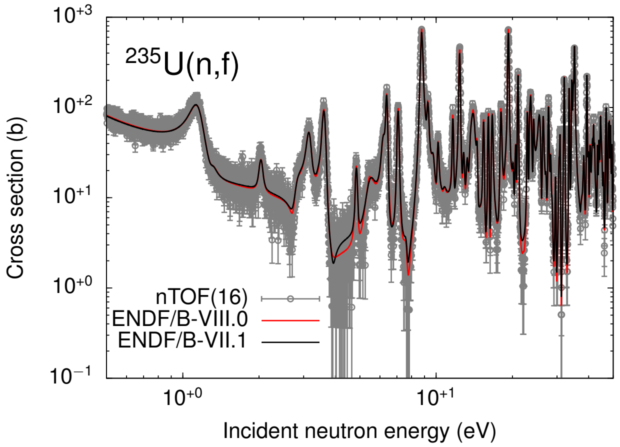

FIG. 53. (Color online) n+^{235}U n_TOF fission measurement [217] compared to ENDF/B-VII.1 [2] (in black) and ENDF/B-VIII.0 values (in red).

As a brief presentation of the results, Figs. 52 and 53 show two examples of high-resolution capture [216] and fission [217] cross section measurements along with ENDF/B-VII.1 (in black) and ENDF/B-VIII.0 (in red) reconstructed from resonance parameters capture and fission cross sections. As noticeable in both figures, a new resonance for the neutron energy at about 5.5 eV was included in the resonance evaluation.

Fast neutron region

Rigid-rotor structure has been shown to be an excellent approximation for odd-mass actinides [218]. Therefore, a dispersive coupled-channel optical model potential of Capote *et al.* [219, 220] (RIPL 2408 [221]) with the coupling of seven levels of the ground state rotational band was a key component in this IAEA evaluation, allowing an excellent description of available experimental data for total cross sections and elastic angular distributions.

Statistical reaction models including both an exciton model PCROSS [222] and a full featured Hauser-Feshbach [223] model have been used to calculate the observables for neutron induced reactions on ^{235}U with the `EMPIRE` nuclear reaction code system as discussed in Refs. [209, 224] using the optical model for fission [225, 226].

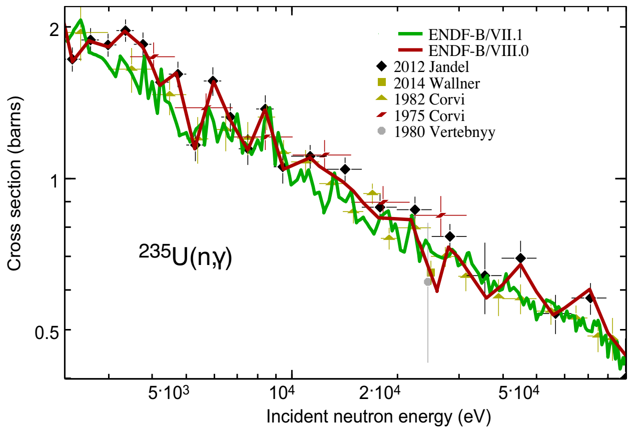

FIG. 54. (Color online) Selected ^{235}U(n,γ) experimental data from EXFOR [175] are compared with ENDF/B-VIII.0 and ENDF/B-VII.1 evaluations. Figure adapted from Fig. 3 of Ref. [7].

(n,γ) Capture Cross Section

The evaluated capture cross sections have changed significantly compared to ENDF/B-VII.1. They are shown in Figs. 54 and 55. The capture to fission ratio, alpha, is shown in Fig. 56. As noted earlier, the new evaluation is much reduced versus VII.1 in the 0.5-2 keV region, following the measurements of Jandel at Los Alamos, and Danon at RPI (see the Fig. 3 in Ref. [8]). For energies up to 80 keV the evaluation continues to follow Jandel's data, which now lies above the previous VII.1 evaluation. A priority was also given to matching Wallner's AMS data [227], as is shown in the integral data testing section of this paper (Section XII).

(n,f) Fission Cross Section

The ^{235}U fission cross section has been recently reeval-

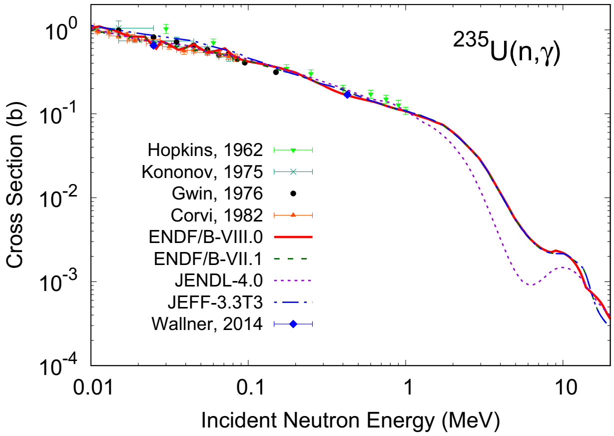

FIG. 55. (Color online) Selected ^{235}U(n,γ) neutron capture cross section experimental data from EXFOR [175] are compared with ENDF/B-VIII.0 and ENDF/B-VII.1 evaluations.

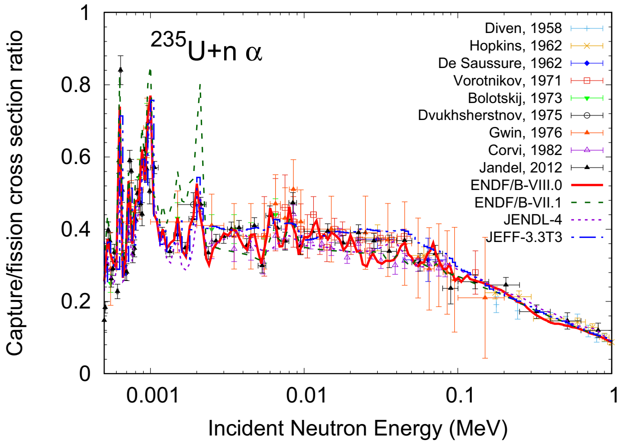

FIG. 56. (Color online) Capture to fission ratio data from EXFOR [175] are compared with ENDF/B-VIII.0 and ENDF/B-VII.1 evaluations.

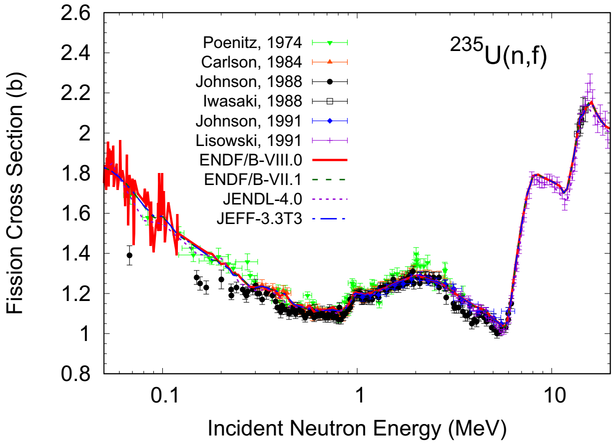

FIG. 57. (Color online) Selected ^{235}U(n,f) experimental data from EXFOR [175] are compared with ENDF/B-VIII.0 and ENDF/B-VII.1 evaluations.

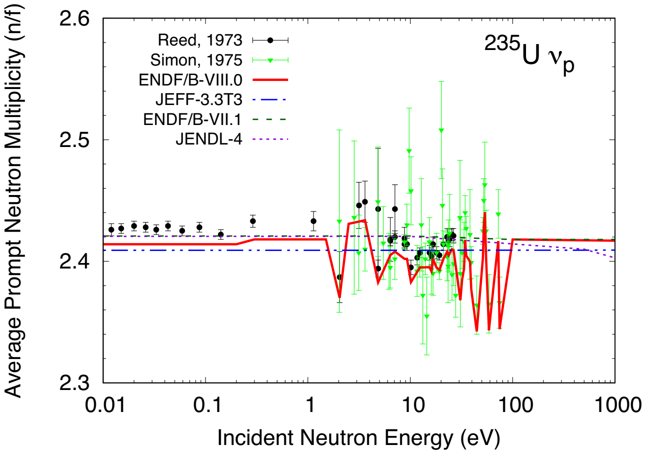

FIG. 58. (Color online) Selected ^{235}U(n,f) nubar experimental data from EXFOR [175] are compared with ENDF/B-VIII.0 and ENDF/B-VII.1 evaluations.

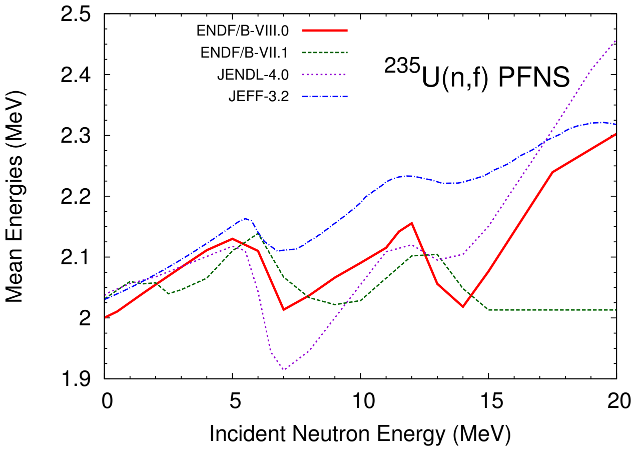

FIG. 59. (Color online) Mean energies calculated from the ENDF/B-VIII.0 evaluated ^{235}U PFNS are compared with those calculated from previous evaluations.

uated by the IAEA standards group, and the results are documented in a companion paper in this edition of *Nuclear Data Sheets* [10]. This cross section has been adopted without change by CIELO and by ENDF/B-VIII.0, for the fast region above 150 keV. The evaluated fission cross section is shown in Fig. 57. From 2.25 keV up to 150 keV the `GMA` fitted cross sections from the IAEA standard project are reproduced on average using a denser energy grid to capture some of observed fluctuations in the data. The new evaluation agrees within quoted uncertainties with ENDF/B-VII.1, being about 0.4% higher for incident energies below about 15 MeV. The standards paper [10] describes a recent decision to increase the standards fission uncertainties due to unrecognized systematic uncertainties.

(n,f) Fission $\overline{\nu}$

The new evaluations for prompt $\overline{\nu}$ are shown in Fig. 58 from .01 eV up to 1 keV and in Fig. 10 of Ref. [17] from 1 keV up to 5 MeV. In the lower incident energy region, resonance effects are now included in the evaluation. The $\overline{\nu}$ evaluations were adjusted to optimize predicted k_{eff} criticality. The ENDF/B-VIII.0 data also include evaluations of multiplicity-dependent ν data, P(ν).

(n,f) Prompt Fission Neutron Spectrum (PFNS)

The ENDF/B-VIII.0 ^{235}U PFNS consists of three different evaluations. At thermal energies, an evaluation by Capote *et al.* [11, 201, 202] was adopted. This evaluation was obtained as part of the IAEA standard effort by a least squares analysis of experimental data and their covariances and adjusting the high-energy tail above 10 MeV to reproduce the evaluated ^{90}Zr(n,2n) spectrum averaged cross section. Analytical functions are only used to extrapolate and smooth the PFNS. The mean energy calculated from PFNS in Fig. 59 is distinctly softer than the ENDF/B-VII.1 PFNS but corresponds well to experimental data there, as seen in Figs. 60, 61 and 62. At thermal energies the average emitted neutron energy is now 2.00 ± 0.01 MeV [11] versus the previous 2.03 MeV, and incidentally this value of 2.00 is identical to that published by Watt (Los Alamos) in 1952 in his seminal paper on the PFNS. The evaluated PFNS are shown in Fig. 60.

For E_{inc} > thermal, two generalized least squares evaluations by Neudecker *et al.* [20] were adopted. Both evaluations are based on an extended Los Alamos model [228, 229] and include all relevant physics processes and new experimental information [230–233] since ENDF/B-VII.1. One part of this new experimental information is related to uncovering possible biases in legacy ^{235}U and ^{239}Pu PFNS due to multiple scattering, incorrect background corrections and time-of-flight to energy deconvolution of the measured PFNS through `MCNP`® studies [231, 232]. The changes in the experimental databases due to those studies combined with the extended Los Alamos model resulted in an overall softer PFNS than the ENDF/B-VII.1 PFNS for $E_{\text{inc}} < 2$ MeV as seen in Fig. 60. This trend to a softer PFNS is well supported by the fact that the mean energies calculated from the new evaluations of Capote *et al.* and Neudecker *et al.* match well. In addition to that the ratio of ^{239}Pu to ^{235}U PFNS at $E_{\text{inc}} = 1.5$ MeV of ENDF/B-VIII.0 corresponds reasonably well to a ratio of Lestone NUEX PFNS data (Fig. 61) while the ENDF/B-VII.1 ratio describes Sugimoto *et al.* [234] better. Between E_{inc} =2–3 MeV, the previous ENDF/B-VII.1 mean energies drop distinctly—a trend which cannot be observed in any other evaluation and is related to the fact that the ENDF/B-VII.1 PFNS follows closely the data of Boikov *et al.* [235] for $E_{\text{inc}} = 3$ MeV, as seen in Fig. 62. A recent evaluation of Rising *et al.* [236] of consistent $^{229-238}$U PFNS indicate that these Boikov data might be questionable at high outgoing energies. In contrast, our new ENDF/B-VIII.0 evaluation has a mean energy that increases smoothly from 0–5 MeV, see Fig. 59.

The only difference between the input for the ENDF/B-VIII.0 evaluation at E_{inc} =0.5–5 and E_{inc} > 5 MeV is that recently-obtained Chi-Nu data [233] were only used for the latter. The Chi-Nu team readily provided preliminary, but close to final, data for the ENDF/B-VIII.0 evaluation shortly after the measurement. The resulting data set is

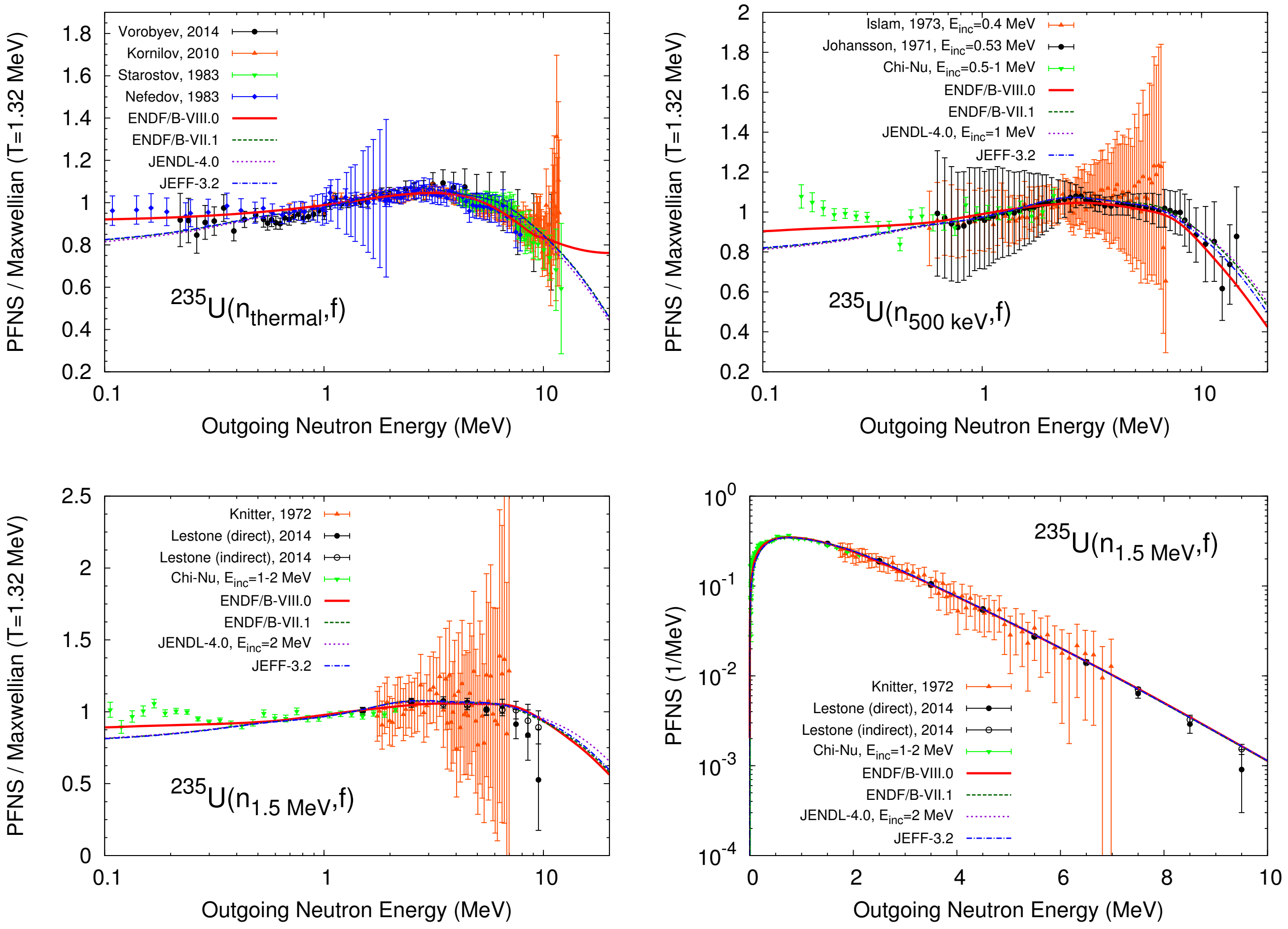

FIG. 60. (Color online) Evaluated ^{235}U PFNS for incident neutron energies $E_{\rm inc}$ =thermal–1.5 MeV are compared with experimental data used for evaluations and with previous evaluations. Top and bottom left panels show the PFNS in ratio to a Maxwellian spectrum while bottom right panel shows the PFNS itself in order to emphasize the high energy tail.

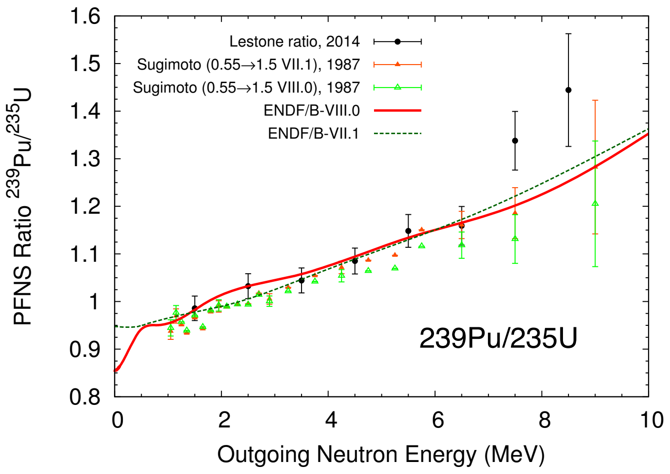

FIG. 61. (Color online) The ratios of ^{239}Pu and ^{235}U ENDF/B-VIII.0 and ENDF/B-VII.1 PFNS at an incident neutron energy of $E_{\rm inc}$ =1.5 MeV are compared to those of Lestone *et al.* [230] and Sugimoto *et al.* [234].

the first one providing ^{235}U PFNS up to $E_{\rm inc} = 20$ MeV and is thus of high interest for the evaluation. Given that the measured data were only analyzed with one out of their three envisioned analysis techniques and that their uncertainty quantification was still unfinished, it was decided to adopt evaluations with their data only for $E_{\rm inc} > 5$ MeV. The ENDF/B-VIII.0 and JENDL-4.0 evaluations are able to reproduce these data better than ENDF/B-VII.1 and JEFF-3.2 at $E_{\rm inc} = 6$ and 14 MeV. One reason for that is the pre-fission neutron modeling for ENDF/B-VIII.0 and JENDL-4.0 evaluations. Both PFNS evaluations correctly include only pre-fission neutrons emitted in compound nucleus formation and pre-equilibrium emission processes and neutrons emitted from the fission fragments, whereas for ENDF/B-VII.1 all neutrons evaporated from the initial and subsequent compound nuclei are counted. Therefore, a pre-equilibrium neutron peak can be observed around 8 MeV ($\approx E_{\rm inc} - B_f$ beig B_f the fission barrier) in the ENDF/B-VIII.0 and JENDL-4.0 PFNS at $E_{\rm inc} =$ 14 MeV which does not occur in ENDF/B-VII.1 and JEFF-3.2 data. The structure at low emitted energies

TABLE XIX. Evaluated ^{235}U PFNS and mean energy uncertainties are compared for ENDF/B-VIII.0 and ENDF/B-VII.1 for selected incident $\mathrm{E_{inc}}$ and outgoing E neutron energies. ENDF/B-VII.1 covariances are only provided for $E_{\mathrm{inc}} \leq 0.5$ MeV.

Quantity	B-VIII.0 Unc. (%)	B-VII.1 Unc. (%)
PFNS($\mathrm{E_{inc}}$=thermal, E=0.1 MeV)	4.3	8.5
PFNS($\mathrm{E_{inc}}$=thermal, E=0.5 MeV)	3.2	5.3
PFNS($\mathrm{E_{inc}}$=thermal, E=2 MeV)	1.9	1.6
PFNS($\mathrm{E_{inc}}$=thermal, E=5 MeV)	2.5	7.8
PFNS($\mathrm{E_{inc}}$=thermal, E=8 MeV)	3.7	17.9
PFNS($\mathrm{E_{inc}}$=0.5 MeV, E=0.1 MeV)	12.5	8.5
PFNS($\mathrm{E_{inc}}$=0.5 MeV, E=0.5 MeV)	5.1	5.3
PFNS($\mathrm{E_{inc}}$=0.5 MeV, E=2 MeV)	2.5	1.6
PFNS($\mathrm{E_{inc}}$=0.5 MeV, E=5 MeV)	4.1	7.8
PFNS($\mathrm{E_{inc}}$=0.5 MeV, E=8 MeV)	8.6	17.9
PFNS($\mathrm{E_{inc}}$=0.5–5 MeV, E=0.1 MeV)	12.5	-
PFNS($\mathrm{E_{inc}}$=0.5–5 MeV, E=0.5 MeV)	5.1	-
PFNS($\mathrm{E_{inc}}$=0.5–5 MeV, E=2 MeV)	2.5	-
PFNS($\mathrm{E_{inc}}$=0.5–5 MeV, E=5 MeV)	4.1	-
PFNS($\mathrm{E_{inc}}$=0.5–5 MeV, E=8 MeV)	8.6	-
PFNS($\mathrm{E_{inc}}$ 12–20 MeV, E=0.1 MeV)	6.4	-
PFNS($\mathrm{E_{inc}}$ 12–20 MeV, E=0.5 MeV)	4.0	-
PFNS($\mathrm{E_{inc}}$ 12–20 MeV, E=2 MeV)	3.3	-
PFNS($\mathrm{E_{inc}}$ 12–20 MeV, E=5 MeV)	6.9	-
PFNS($\mathrm{E_{inc}}$ 12–20 MeV, E=8 MeV)	17.4	-
Mean Energy(E_{inc}=thermal)	0.5 (10 keV)	3.7 (75 keV)
Mean Energy(E_{inc}=0.5 MeV)	1.6 (35 keV)	3.7 (75 keV)
Mean Energy(E_{inc}=1.5 MeV)	1.6 (35 keV)	-
Mean Energy(E_{inc}=14 MeV)	3.1 (64 keV)	-

in the ENDF/B-VIII.0 and JENDL-4.0 $E_{\mathrm{inc}} = 6$ MeV PFNS is caused by the treatment of pre-fission neutrons emitted in multiple chance fission processes and described in more detail in the subsection on ^{239}Pu PFNS.

The evaluated uncertainties of the new evaluations decreased compared to ENDF/B-VII.1 for most outgoing neutron energies provided in Table XIX given the new experimental information. For ENDF/B-VIII.0, five covariances are provided, namely for $E_{\mathrm{inc}} \leq 0.5$ MeV, 0.5–5 MeV, 5–7 MeV, 7–12 MeV and 12–20 MeV. Covariances for these specific incident energy bins were chosen to minimize the number of stored data while obtaining a sampled mean close to the original mean if sampled from these covariances. All these covariances were obtained out of the same evaluation as the mean values given in ENDF/B-VIII.0, *i.e.*, the covariances at $E_{\mathrm{inc}} \leq 0.5$ MeV were obtained from the evaluation of Capote *et al.*, while those at 0.5–5 MeV and above were obtained from the evaluation of Neudecker *et al.* without and with Chi-Nu data, respectively. The evaluated uncertainties above 0.5 MeV were rescaled with a factor of 4.914 ($\approx 5\%$) accounting for the unreasonable reduction of uncertainties when the Los Alamos model is used for the evaluation given the constraining model assumptions [229]. The rescaling factor was also chosen such that the 2-σ uncertainty bands enclose preliminary high outgoing neutron energy Chi-Nu experimental PFNS which were released right after ENDF/B-VIII.0β5.

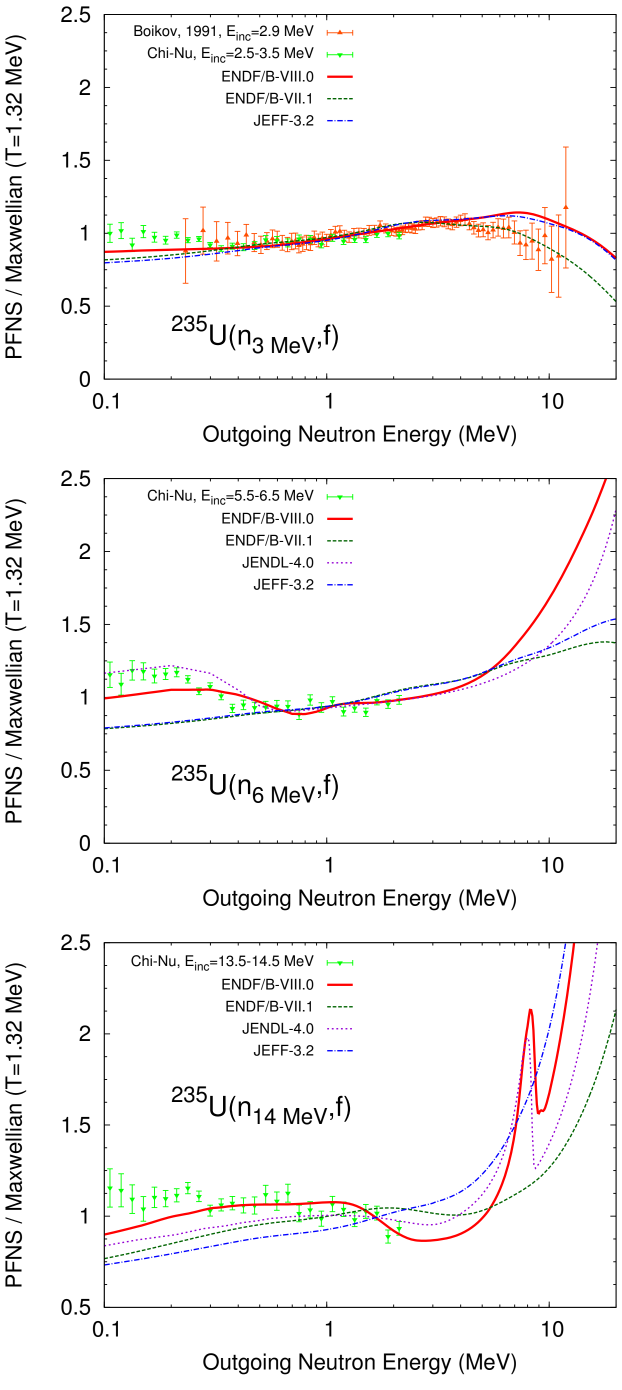

FIG. 62. (Color online) Evaluated ^{235}U PFNS for incident neutron energies E_{inc} =3–14 MeV are compared with experimental data used for evaluations and with previous evaluations.

(n,n'), (n,2n), (n,3n) and (n,xn) Cross Sections

The evaluated (n,n') inelastic, $(n,2n)$, and $(n,3n)$ cross sections are compared with measurements in Figs. 63 and 64. The total inelastic scattering cross section is slightly reduced compared to the earlier evaluation, Fig. 63. Differences in the $(n,2n)$ relative to the CEA JEFF-3.3T3 evaluation are described by Chadwick *et al.* in the CIELO overview paper [8]; that paper also shows the 14 MeV evaluated (n,xn) secondary neutron spectrum in ENDF/B-VIII.0, which compares favorably with Kammerdiener's data.

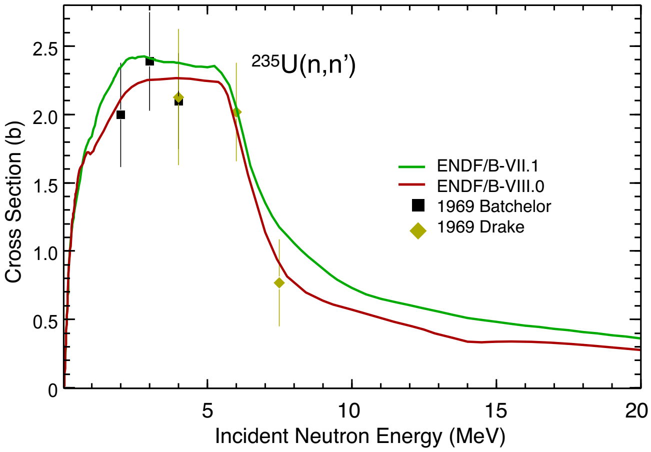

FIG. 63. (Color online) Selected ^{235}U(n,n') experimental data from EXFOR [175] are compared with ENDF/B-VIII.0 and ENDF/B-VII.1 evaluations.

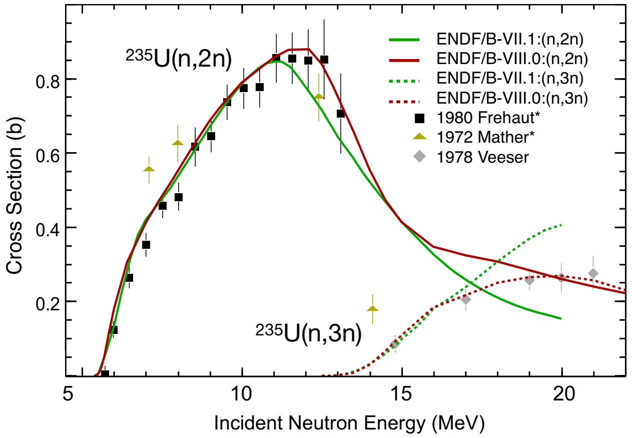

FIG. 64. (Color online) Selected ^{235}U(n,2n) and ^{235}U(n,3n) experimental data from EXFOR [175] are compared with ENDF/B-VIII.0 and ENDF/B-VII.1 evaluations. The asterisk on some of the experimental data indicates that they are automatically renormalized by the EXFOR project upon retrieval of the data [175].

3. ^{238}*U*

A focused international effort on ^{238}U has been coordinated by the IAEA within the CIELO project [199], and has been adopted for ENDF/B-VIII.0. A full description of this CIELO work for ^{238}U is given by Capote *et al.* [17]. Differences between this (CIELO-1) work and a related CEA (CIELO-2) evaluation, are described by Chadwick in the CIELO overview paper [8].

Previous Work
Earlier ENDF evaluations of ^{238}U neutron-induced reactions used resonance analyses by Derrien, Courcelle, Leal, and Larson, while higher energy cross sections came from evaluation work by Young, Arthur, Chadwick, Talou, Kawano, Wilson, and MacFarlane, and Madland for PFNS. This work was documented in the main ENDF big papers [1, 2] as well in the detailed summary on actinides by Young *et al.* [200].

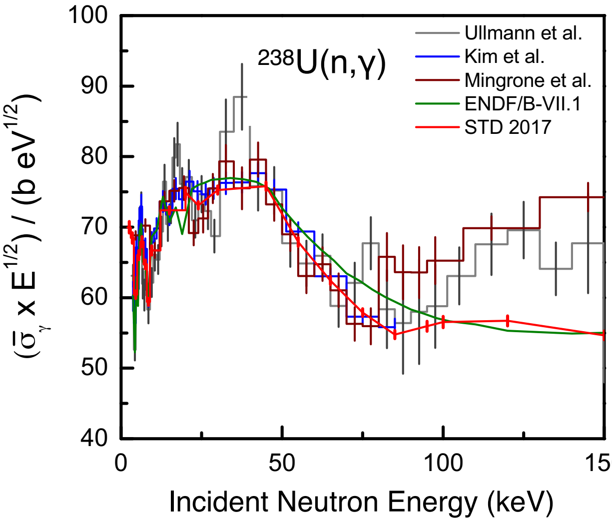

FIG. 65. (Color online) Average capture cross section $\overline{\sigma}_\gamma$ for ^{238}U(n,γ) as a function of neutron energy in the URR. The 2017 Standard evaluation (labeled STD2017 in the plot) is used in ENDF/B-VIII.0. The results of a least squares adjustment to experimental data (File 3) are compared with the data of Refs. [237–239] and the cross section recommended in ENDF/B-VII.1. The cross section based on a description in terms of average resonance parameters (File 2) is also shown.

Resonance region
The resonance parameter file in the resolved resonance region, including the covariance data, was constructed by replacing in the ENDF/B-VII.1 file the parameters for resonances below 1200 eV with those reported by Kim *et al.* [237]. The parameters in ENDF/B-VII.1 were based on the work of Derrien *et al.* [240]. The parameters obtained by Kim *et al.* [237] are derived from a least squares fit to the experimental capture yield of Kim *et al.* [237] and the transmission data of Olsen *et al.* [241, 242] using the resonance shape analysis code REFIT. The capture experiments of Kim *et al.* [237] were carried out at a 12.5 and 60 m measurement station of the GELINA. The total energy detection principle in combination with the pulse height weighting technique was applied using C_6D_6 liquid scintillators as prompt γ-ray detectors. The transmission data of Olsen *et al.* [241, 242] resulted from experiments at a 42 m and 150 m station using 7 samples of different areal density (from 0.0002 at/b to 0.175 at/b). Both the transmission and capture data were analyzed without applying any additional background correction. To fit the transmission data of Olsen *et al.* [241, 242] without applying a normalization factor, the contribution of the bound states had to be adjusted. The parameters of the bound states were adjusted to match the thermal capture cross section recommended by Trkov *et al.* [243].

The neutron widths in the region below 500 eV are in very good agreement with those reported by Derrien *et al.* [240]. They are on average ∼ 0.4 % higher with a standard deviation of ∼ 3%. For resonance energies above 500 eV a larger systematic difference is observed. The neutron widths are systematically lower with a difference that increases with increasing resonance energy. The average radiation width of 22.5 meV is ∼ 2.2 % lower compared to the one derived by Derrien *et al.* [240].

The evaluation of the cross sections in the unresolved resonance region resulted from a least squares adjustment to experimental data reported in the literature. The generalized least squares code `GMA` developed by Poenitz [244] was used. In the evaluation process the total cross section data of Refs. [245–250] were included in this evaluation process. The experimental capture cross section data that were used in the evaluation of Carlson *et al.* [9] were complemented with the capture data of Refs. [237–239]. The resulting average capture cross section (labeled STD 2017) is shown in Fig. 65 and compared with the data of Refs. [237–239] and the one recommended in ENDF/B-VII.1. The average total and capture cross sections were parameterized in terms of average resonance parameters maintaining consistency with results of optical model calculations using a dispersive coupled channel potential. The average partial cross sections have been expressed in terms of transmission coefficients by applying the Hauser-Feshbach statistical reaction theory including width-fluctuations. The generalized ENDF-6 model together with the standard boundary conditions has been used (see Sirakov *et al.* [177]). The coupled-channel OPTMAN code [251, 252] incorporated into the EMPIRE system [157] was used for the optical model calculations. The direct reaction contribution to the inelastic scattering was calculated by using the Dispersive Coupled-Channel Optical Model (DCCOM) potential of Quesada *et al.* [253]. Neutron strength functions have been obtained so as to reproduce the compound absorption cross sections of the optical model calculations. Hard-sphere potential scattering radius R' has been optimized on the results of the `GMA` total cross section. The resulting scattering radius R = 9.483 fm at zero energy is fully consistent with the effective scattering radius used for the analysis in the RRR. Capture parameters (capture transmission coefficients at zero energy and different parity) have been determined in a fit to the `GMA` capture cross section.

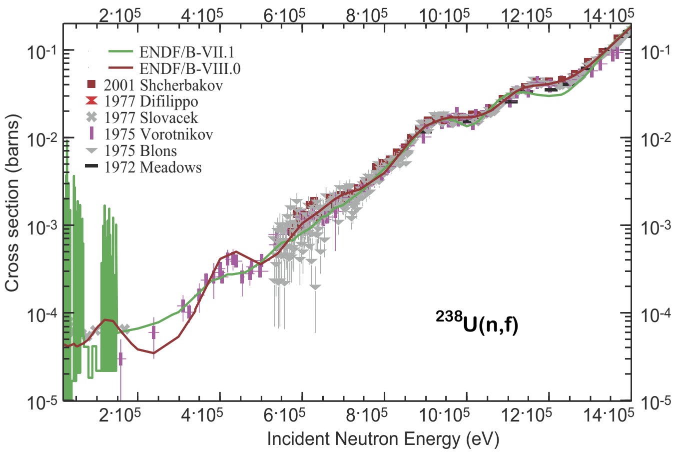

FIG. 66. (Color online) Selected experimental data from EXFOR [175] are compared with ENDF/B-VIII.0 and ENDF/B-VII.1 ^{238}U(n, f) cross section evaluations in the fast neutron region from 0.2–1.4 MeV.

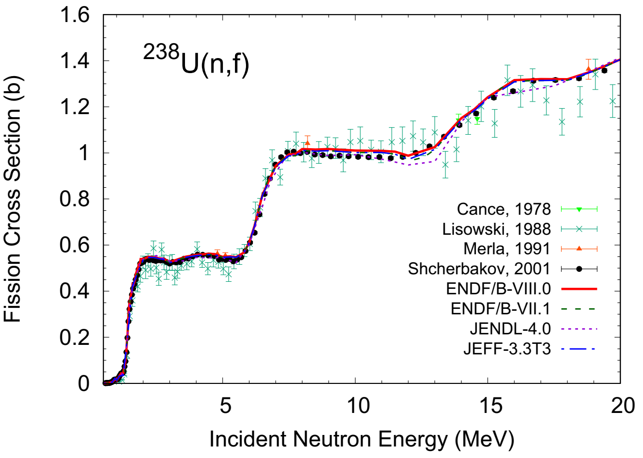

FIG. 67. (Color online) Selected experimental data from EXFOR [175] are compared with ENDF/B-VIII.0 and ENDF/B-VII.1 ^{238}U(n, f) evaluations in the fast neutron region from 1–20 MeV.

The total and capture unresolved cross sections resulting from a `GMA` analysis were adopted in File 3 with the LSSF=1 option as infinitely dilute total and capture cross sections respectively. The inelastic neutron scattering cross section data of Capote *et al.* [254], which include compound-direct interference effects, were also adopted for the present evaluation by modifying the calculated infinitely dilute inelastic cross section. The small average unresolved fission cross section of the order of 0.1 mb has been adopted from an estimation based on available fission cross section data. The estimation is very close to the JEFF fission evaluation, but shows a more reasonable trend at the URR boundaries. The cross section covariance File 33 for the whole resonance region was adopted from ENDF/B-VII.1.

(n,f) Fission Data in the Fast Range

The ^{238}U fission cross section has been recently reevaluated by the IAEA standards group, and the results are documented in a companion paper in this edition of Nuclear Data Sheets [10]. This cross section has been adopted without change by CIELO and by ENDF/B-VIII.0, for the fast region above 2 MeV. The evaluated fission cross section is shown in Figs. 66 and 67. From 0.5 MeV up to 2 MeV the `GMA` fitted cross sections from the IAEA standard project are reproduced on average using a denser energy grid to capture observed fluctuations in sub-threshold fission. The new evaluation agrees within quoted uncertainties with ENDF/B-VII.1 evaluation. The prompt fis-

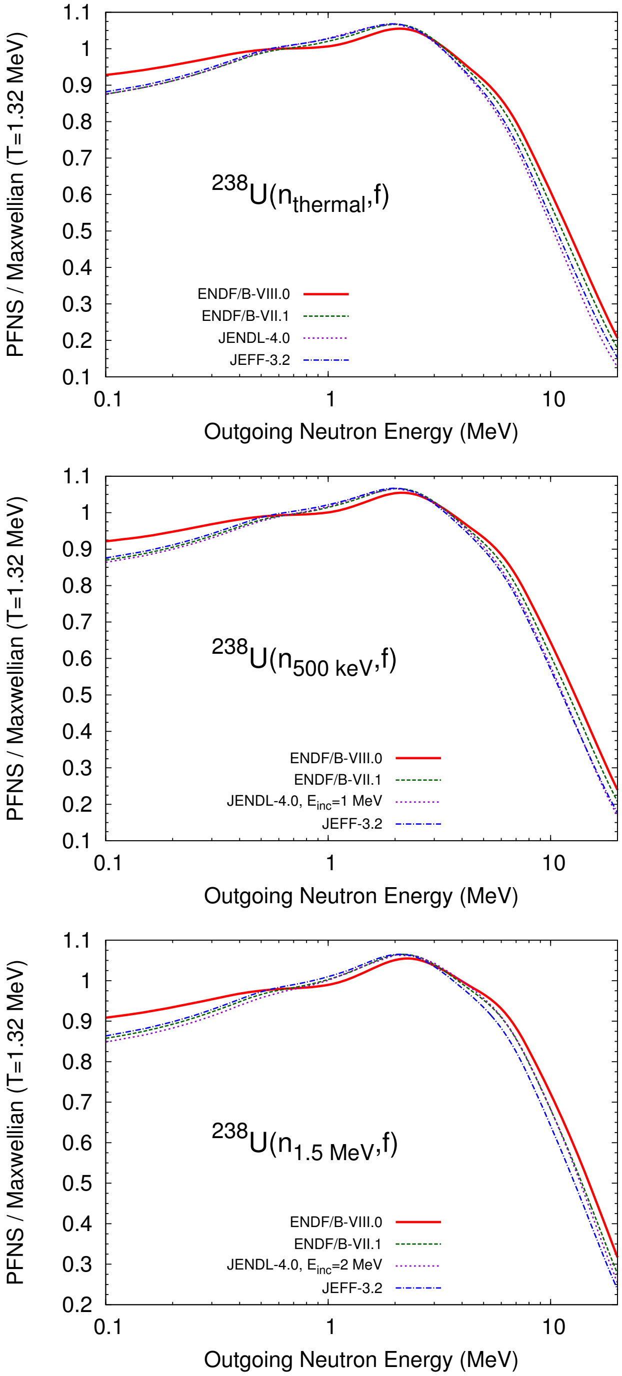

FIG. 68. (Color online) Evaluated ^{238}U PFNS for incident neutron energies $E_{\rm inc}$ =thermal–1.5 MeV are compared with previous evaluations.

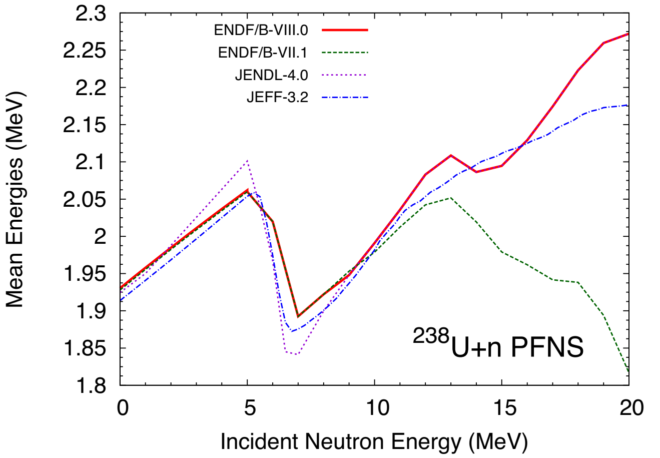

FIG. 69. (Color online) Mean energies calculated from evaluated ^{238}U PFNS are compared with those calculated from previous evaluations.

sion nubar evaluation is given in Fig. 21 of Ref. [17].

The ENDF/B-VII.1 ^{238}U PFNS was carried over unchanged for incident neutron energies $E_{\rm inc} > 5$–8 MeV, and the JENDL-4.0 PFNS was adopted above 8 MeV as the decrease of the average PFNS energy observed for ENDF-B/VII.1 is unphysical. For incident neutron energies below 5 MeV, the PFNS evaluation by Rising *et al.* [236] shown in Fig. 68 was adopted. Within this evaluation, $^{229-238}$U isotopes were simultaneously evaluated with a linear Kalman filter by exploiting mass and charge number-dependent systematics for the average total kinetic energy, the average energy release and the effective level density. This evaluation fits simultaneously to measured ^{233,235,238}U PFNS. The resulting PFNS differ distinctly in shape from ENDF/B-VII.1, JENDL-4.0 and JEFF-3.2 PFNS; they are larger at low and high outgoing neutron energies, but the mean energies in Fig. 69 calculated from ENDF/B-VIII.0 and ENDF/B-VII.1 spectra are very close to each other below 8 MeV incident energy.

(n,el) Elastic Scattering Angular Distributions

Examples of the elastic scattering angular distributions are given in Fig. 70 for 600 keV incident neutrons, and Fig. 71 for 14 MeV incident neutrons.

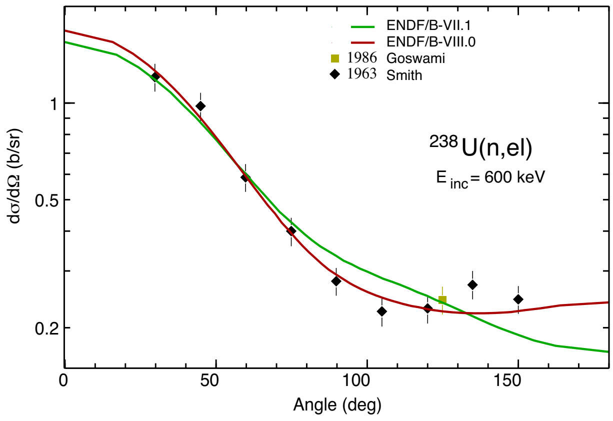

FIG. 70. (Color online) Measured elastic angular distribution on ^{238}U at 600 keV of neutron incident energy is compared with ENDF/B-VIII.0 and ENDF/B-VII.1 evaluations.

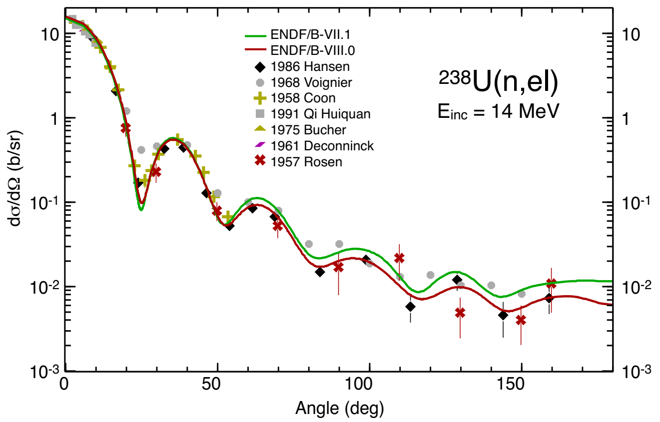

FIG. 71. (Color online) Measured elastic angular distribution on ^{238}U at 14 MeV of neutron incident energy is compared with ENDF/B-VIII.0 and ENDF/B-VII.1 evaluations.

(n,n'), (n,2n), and (n,3n) Cross Sections

The total inelastic scattering cross section is given in Fig. 72. The evaluated $(n, 2n)$ cross section is shown in Fig. 73. Its rise from threshold is seen to be very similar to that in ENDF/B-VII.1, having been confirmed by the recent TUNL measurements of Krishichayan. At 14 MeV the new evaluation is somewhat higher than the previous VII.1 evaluation.

Differences in the (n, n') and $(n, 2n)$ relative to the JEFF-3.3T3 (CIELO-2) evaluation are described by Chadwick *et al.* in the CIELO overview paper [8].

Capote *et al.* [17] shows the 14 MeV evaluated (n, xn) secondary neutron spectrum in ENDF/B-VIII.0, compared to measurements.

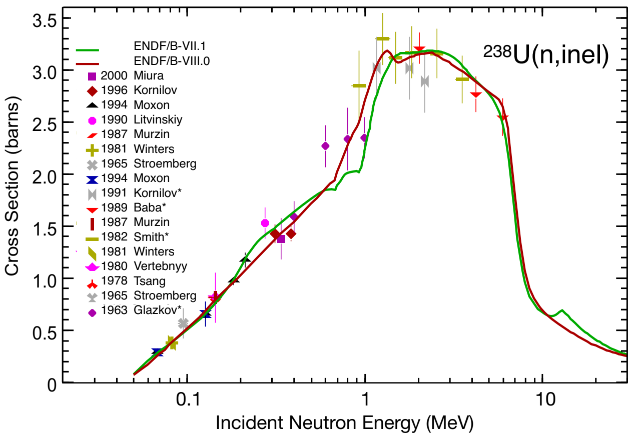

FIG. 72. (Color online) Selected ^{238}U(n, n') experimental data from EXFOR [175] are compared with ENDF/B-VIII.0 and ENDF/B-VII.1 evaluations. The asterisk on some of the experimental data indicates that they are automatically renormalized by the EXFOR project upon retrieval of the data [175].

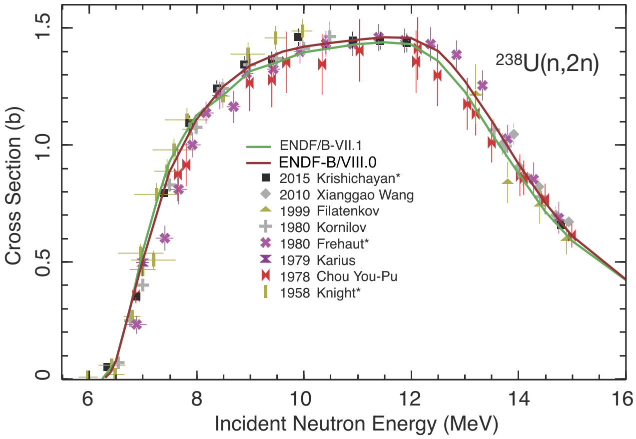

FIG. 73. (Color online) Selected ^{238}U$(n, 2n)$ experimental data from EXFOR [175] are compared with ENDF/B-VIII.0 and ENDF/B-VII.1 evaluations. The asterisk on some of the experimental data indicates that they are automatically renormalized by the EXFOR project upon retrieval of the data [175].

4. ^{239}*Pu*

Background & Previous Evaluations

A focused international effort on ^{239}Pu has been coordinated by Los Alamos for the CIELO project [199], and has been adopted for ENDF/B-VIII.0. Differences between this (CIELO-1) work and a related CEA (CIELO-2) evaluation, are described by Chadwick *et al.* in the CIELO overview paper [8].

Earlier ENDF evaluations of ^{239}Pu neutron reactions used resonance analyses by Derrien, Nakagawa, Leal, Larson, de Saussure, while higher energy cross sections came from evaluation work by Young, Arthur, Chadwick, Talou, and MacFarlane, and Madland for PFNS. This work was documented in the main ENDF big papers [1, 2] as well in the detailed summary on actinides by Young *et al.* [200].

Resonance region

The CIELO project [7, 8] adopted the earlier Nuclear Energy Agency WPEC Subgroup 34 collaboration work on plutonium resonances by de Saint Jean, Noguere, Peneliau, Bernard, Serot, Leal, Derrien, Kahler, and McKnight. To avoid ambiguities related to the reconstruction of the cross sections from the legacy unresolved resonance parameters, the starting values of the cross sections as reconstructed by the NJOY Processing System were inserted into File 3. Fission in the unresolved resonance region was modified so as to match the standards.

Earlier evaluations, such as ENDF/B-VII, JEFF-3.1, and JENDL-4.0 suffered from a longstanding deficiency: an overprediction of plutonium solution (thermal) criticality in transport simulations by approximately 500 pcm (0.5% in $k_{\rm eff}$) [14, 22]. The proposed resonance and prompt nubar updates by Subgroup 34 remove approximately half of this over-prediction. The further influence of our ^{16}O CIELO evaluation changes [8], and the new scattering kernels recommended by WPEC/Subgroup 42 (both adopted by ENDF/B-VIII.0) now lead to much-improved thermal plutonium solution criticality predictions as discussed below in Sec. XII.

Fast Region

In the fast region the previous ENDF/B-VII.1 plutonium evaluation performed relatively well in integral validation simulation comparisons with bare and reflected critical assembly data, while simulations of intermediate energy assemblies showed varied levels of agreement, as documented in Refs. [2, 22]. However, it has been recognized that compensating errors in the individual reaction channel data play a significant role in criticality predictions [215], which ultimately involve nuclear data calibration adjustments to match integral data such as the Jezebel critical assembly. Indeed, some of the underlying reaction cross sections in the fast 100s-keV and MeVs range were known to be poorly understood, and this led to CIELO-project efforts in experiment, theory, and evaluation to better determine the ^{239}Pu fission, prompt fission neutron spectrum (PFNS), and neutron capture cross sections described below (elastic and inelastic scattering cross sections have not been changed at this time).

(n,f) Fission Cross Section

The ^{239}Pu fission cross section has been recently reevaluated by the IAEA standards group, and the results are documented in a companion paper in this edition of Nuclear Data Sheets [10]. The standards fission cross section has increased by about 0.4 % below 1 MeV. This cross section has been adopted without change by CIELO and by ENDF/B-VIII.0, for the fast region above 30 keV. Below 30 keV the reference cross section is reproduced on average, but the energy grid is denser than in the standard file. The evaluated fission cross section is shown in Figs. 74 and 75.

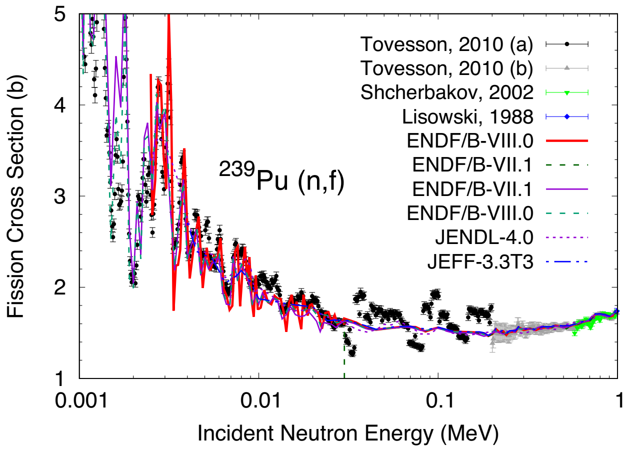

FIG. 74. (Color online) Evaluated ^{239}Pu(n,f) neutron induced fission cross section in the URR compared with data retrieved from EXFOR and with previous evaluations.

(n,f) Fission $\overline{\nu_p}$

The $\overline{\nu_p}$ above 40 keV used the ENDF/B-VII.1 values, but was increased by an average of 0.1 % in the range 0.3–1.0 MeV for better performance in integral benchmarks, see Figs. 76 and 77.

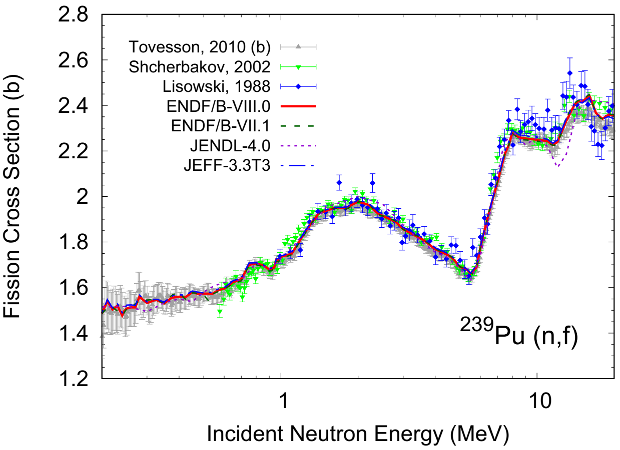

FIG. 75. (Color online) Evaluated ^{239}Pu(n,f) neutron induced fission cross section in the fast region compared with data retrieved from EXFOR and with previous evaluations.

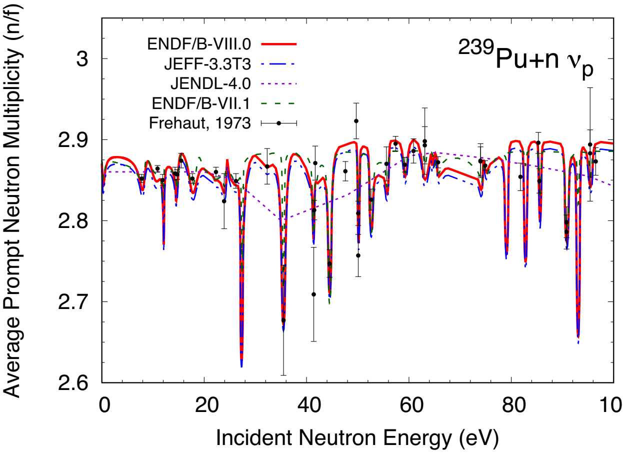

FIG. 76. (Color online) Evaluated ^{239}Pu(n,f) neutron induced fission prompt $\bar{\nu}_p$ in the resonance region compared with data retrieved from EXFOR and with previous evaluations.

(n,γ) Capture Cross Section

The neutron capture cross section on ^{239}Pu had been poorly known with uncertainty exceeding 10% in the fast range. This led to a new measurement at Los Alamos using the DANCE detector at LANSCE by Mosby *et al.* as described in a companion paper in this issue of *Nuclear Data Sheets* [18]. Their approach followed a recent high-accuracy measurement of the ^{235}U capture cross section by Jandel *et al.* at DANCE [205]. Limitations of the target led to a measured result that is less accurate than the ^{235}U capture measurement, but still an improvement on earlier measurements. As seen in Figs. 78 and 79, the new evaluation is influenced by these data and by a new CoH$_3$ code calculation, and results in a new capture evaluation that is higher than ENDF/B-VII.1 above 700 keV, is lower

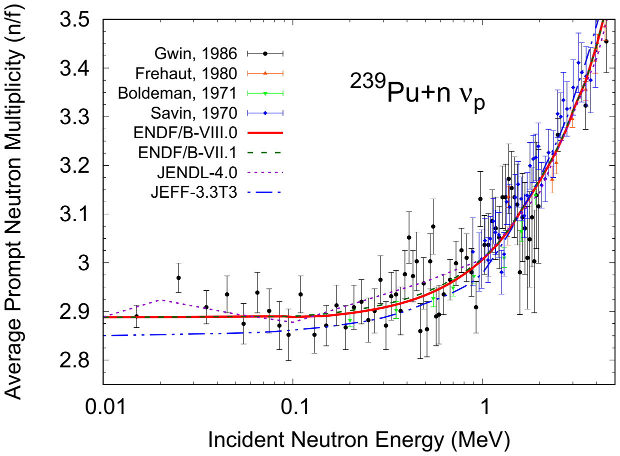

FIG. 77. (Color online) Evaluated ^{239}Pu(n,f) neutron induced fission prompt $\bar{\nu}_p$ in the fast region compared with data retrieved from EXFOR and with previous evaluations.

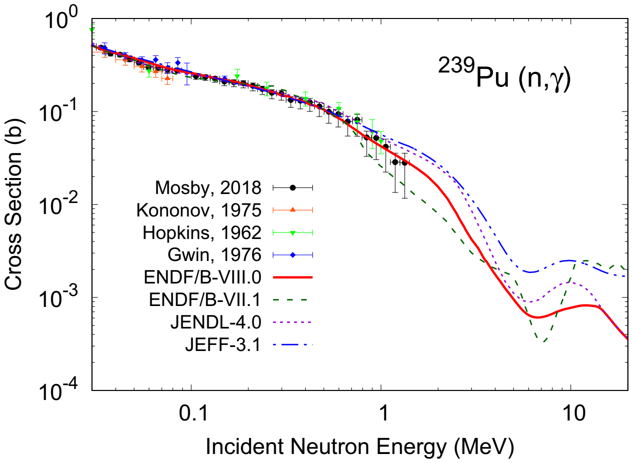

FIG. 78. (Color online) Evaluated ^{239}Pu(n,γ) neutron capture cross section compared with data retrieved from EXFOR and with previous evaluations and with the CoH$_3$ code calculation.

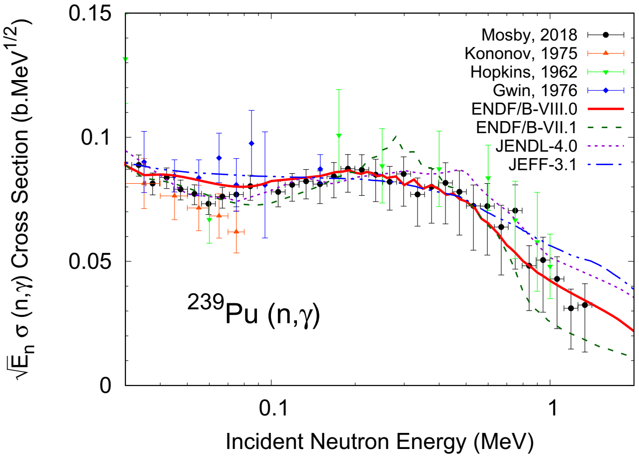

FIG. 79. (Color online) Evaluated ^{239}Pu(n,γ) neutron capture cross section (multiplied by the square root of the incident energy) compared with data retrieved from EXFOR and with previous evaluations and with the CoH$_3$ code calculation used in the ENDF/B-VIII.0 evaluation.

in the 200-300 keV region, and is higher in the 3-100 keV region (being also influenced by the older Gwin data here). The procedure used in Fig. 79 to multiply all data by the square root of the incident energy allows the data differences to be seen more clearly (since, if the capture cross section simply followed a "1/v" form, it would be flat on a plot).

It is impressive that the old 1962 Los Alamos data from Hopkins and Diven appear to be reasonably accurate; the new DANCE data are somewhat lower at the higher energies near an MeV, but in general are in fair agreement.

(n,f) Prompt Fission Neutron Spectrum (PFNS)
The ENDF/B-VIII.0 ^{239}Pu PFNS come from three different Los Alamos evaluations. At thermal the PFNS is a very slightly modified version of ENDF/B-VII.1 such that its shape (Fig. 80) remains very similar to the original ENDF/B-VII.1 PFNS but the thermal mean energy is 5.5 keV harder than the one calculated from the ENDF/B-VII.1. A trial evaluation had been made by Paul Romano [255] but the version adopted was an average between this and the original ENDF/B-VII.1 evaluation. This slight hardening of the PFNS contributed to improved modeling of Plutonium thermal solution benchmarks. Note however, other studies such as the IAEA CRP PFNS project have suggested that the thermal spectrum should be significantly softer (in analogy to the softening adopted for the ^{235}U thermal PFNS spectrum). Future data will help resolve this issue.

The ENDF/B-VII.1 ^{239}Pu PFNS was carried over unchanged for $E_{\rm inc}$ =0.5–5 MeV, while a new evaluation by Neudecker *et al.* [20] was adopted for $E_{\rm inc} >$ 5 MeV, as seen in Figs. 80 and 81. This new evaluation is based—similarly to ENDF/B-VII.1—on the Los Alamos model [228], but great care was taken to extend this model [229] following recent advances [256, 257], including all relevant physics processes for $E_{\rm inc} > 5$ MeV and new experimental information [230–232, 258, 259]. For instance, only pre-fission neutrons emitted in multiple chance fission processes and neutrons emitted from the fission fragments are considered, whereas for ENDF/B-VII.1 all neutrons evaporated from the initial and subsequent compound nuclei are counted. This difference leads to an increase in the ENDF/B-VIII.0 and JENDL-4.0 PFNS for $E_{\rm inc}$ = 6 MeV around a few hundred keV, whereas the ENDF/B-VII.1 PFNS is similar in shape to that at lower $E_{\rm inc}$. This increase is most prominent at $E_{\rm inc}$ = 6 MeV where the second-chance fission channel just opened up and thus pre-fission neutrons can be emitted only up to a threshold defined by the fission barriers. Therefore, the second-chance fission PFNS drops rapidly after this threshold and the combined first-and second-chance fission PFNS shows the structure around a few hundred keV. Also, pre-fission neutrons emitted in pre-equilibrium processes are considered in the ENDF/B-VIII.0 and JENDL-4.0 evaluations resulting in the sharp peak around 8 MeV

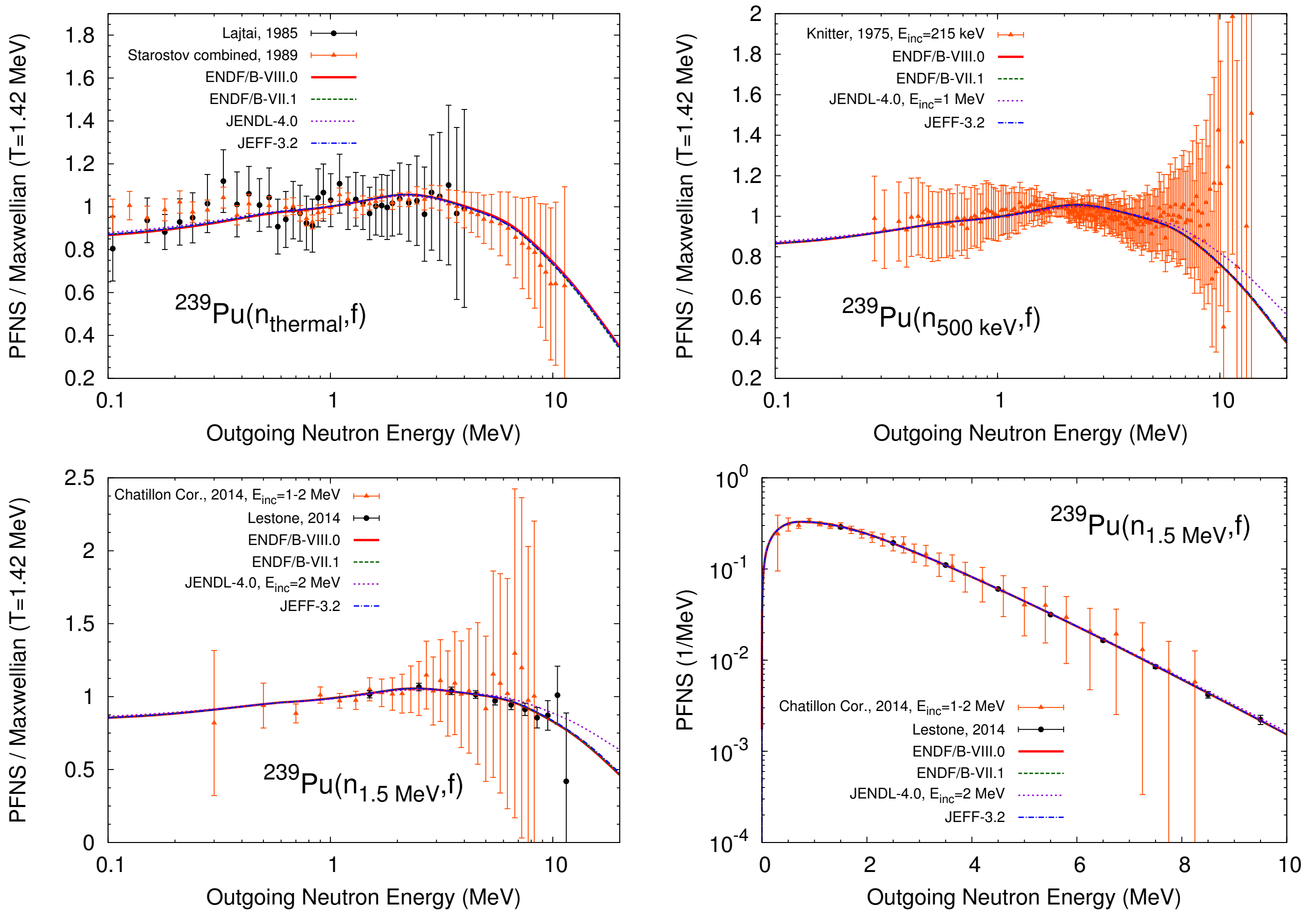

FIG. 80. (Color online) Evaluated ^{239}Pu PFNS for incident neutron energies $E_{\rm inc}$ =thermal–1.5 MeV are compared with experimental data used for evaluations and with previous evaluations. Panels (a)–(c) show the PFNS in ratio to a Maxwellian spectrum while panel (d) shows the PFNS itself in order to emphasize the high energy tail.

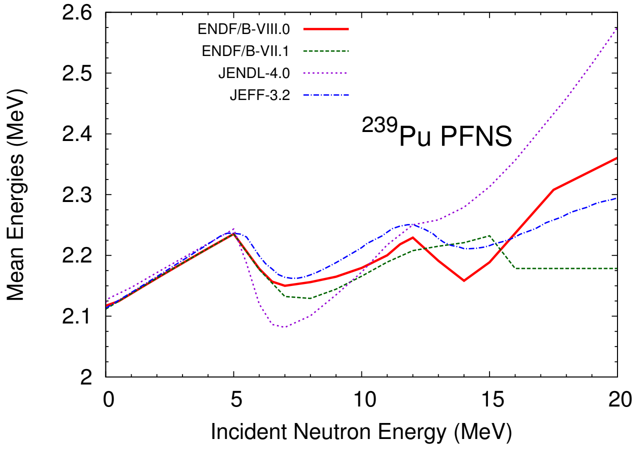

FIG. 81. (Color online) Mean energies calculated from evaluated ^{239}Pu PFNS are compared with those calculated from previous evaluations.

outgoing neutron energy in the $E_{\rm inc}$ = 14 MeV-PFNS, whereas this component was not included for ENDF/B-VII.1 and JEFF-3.2 evaluations, see Fig. 82.

In the new evaluation, recently published data covering a broad energy range by Chatillon *et al.* (with corrections suggested by Granier) [258, 259] and high-accuracy NUEX data of Lestone *et al.* [230], were taken into account. The evaluations agree reasonably well with these data. Also, recent information explaining the discrepancies between legacy ^{239}Pu PFNS measurements was included in the new evaluation by increasing uncertainties: the increased uncertainties account for possible biases due to multiple scattering, incorrect background correction and deconvolution of the measured PFNS.

As the evaluated mean values of ENDF/B-VII.1 were carried over for $E_{\rm inc}$ $\leq$ 0.5 MeV to ENDF/B-VIII.0, the corresponding covariances were carried over as well as can be observed in Table XX. These covariances were originally provided only up to 0.5 MeV but their range of applicability was extended up to 5 MeV given that the underlying physics processes (only first chance fission) and consequently the shape of evaluated PFNS changes only slightly in this incident neutron energy range as is, for instance, shown in Ref. [20]. Covariances are also supplied for ENDF/B-VIII.0 for $E_{\rm inc}$ = 5.5-6.5 MeV, 6.5-13 MeV and 13–20 MeV. Covariances for these specific incident energy bins were chosen to minimize the number of stored data while obtaining a sampled mean close to the original mean if sampled from these

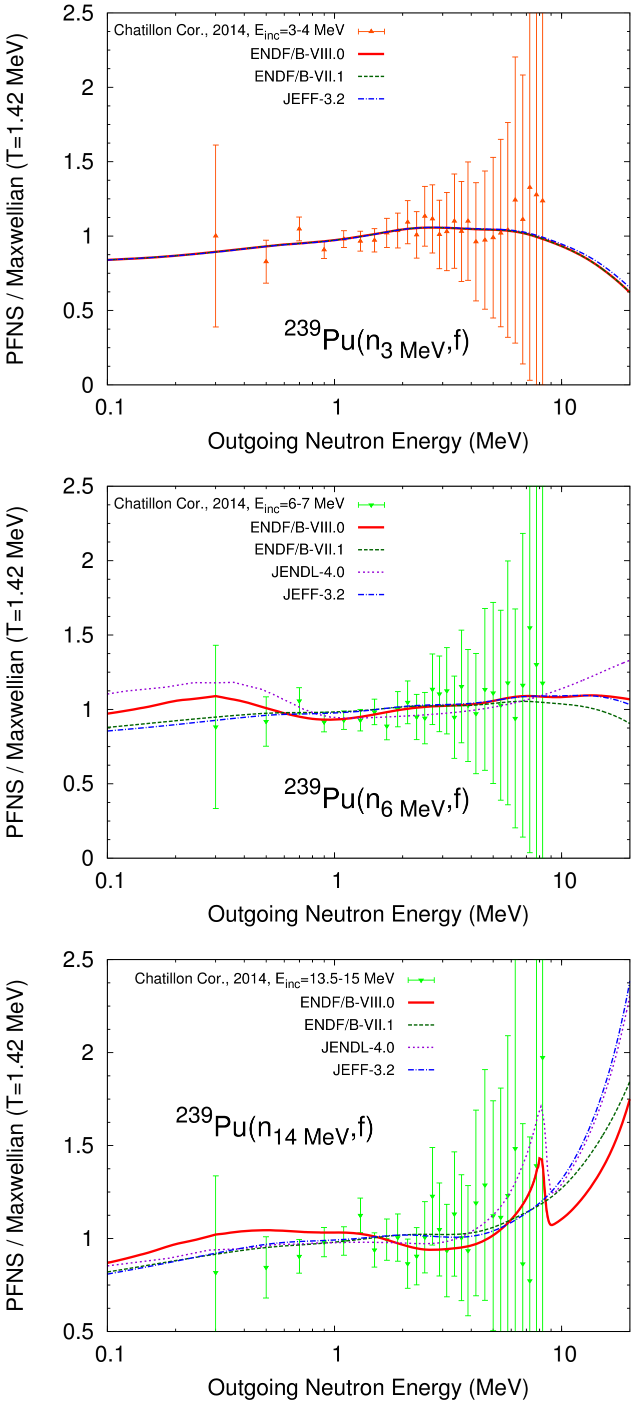

FIG. 82. (Color online) Evaluated ^{239}Pu PFNS for incident neutron energies $E_{\rm inc}$ =3–14 MeV are compared with experimental data used for evaluations and with previous evaluations.

covariances. These new covariances were obtained out of the same evaluation process as evaluated mean values in ENDF/B-VIII.0 at the same $E_{\rm inc}$. The evaluated uncertainties were rescaled with a factor of 2.2 to account for the unreasonable reduction of uncertainties when the Los Alamos model is used for the evaluation given the constraining model assumptions [229].

TABLE XX. Evaluated ^{239}Pu PFNS and mean energy uncertainties are compared for ENDF/B-VIII.0 and ENDF/B-VII.1 for selected energies. ENDF/B-VII.1 covariances are only provided for $E_{\rm inc} \leq 0.5$ MeV. For ENDF/B-VIII.0, these covariances were carried over and used for $E_{\rm inc} \leq 5$ MeV.

Quantity	B-VIII.0 Unc.(%)	B-VII.1 Unc.(%)
PFNS($E_{\rm inc} \leq 0.5$ MeV, E=0.1 MeV)	6.4	6.4
PFNS($E_{\rm inc} \leq 0.5$ MeV, E=0.5 MeV)	3.0	3.0
PFNS($E_{\rm inc} \leq 0.5$ MeV, E=2 MeV)	1.2	1.2
PFNS($E_{\rm inc} \leq 0.5$ MeV, E=5 MeV)	4.3	4.3
PFNS($E_{\rm inc} \leq 0.5$ MeV, E=8 MeV)	7.0	7.0
PFNS($E_{\rm inc}$ 0.5–5 MeV, E=0.1 MeV)	6.4	-
PFNS($E_{\rm inc}$ 0.5–5 MeV, E=0.5 MeV)	3.0	-
PFNS($E_{\rm inc}$ 0.5–5 MeV, E=2 MeV)	1.2	-
PFNS($E_{\rm inc}$ 0.5–5 MeV, E=5 MeV)	4.3	-
PFNS($E_{\rm inc}$ 0.5–5 MeV, E=8 MeV)	7.0	-
PFNS($E_{\rm inc}$ 13–20 MeV, E=0.1 MeV)	4.2	-
PFNS($E_{\rm inc}$ 13–20 MeV, E=0.5 MeV)	3.4	-
PFNS($E_{\rm inc}$ 13–20 MeV, E=2 MeV)	2.2	-
PFNS($E_{\rm inc}$ 13–20 MeV, E=5 MeV)	4.2	-
PFNS($E_{\rm inc}$ 13–20 MeV, E=8 MeV)	13.0	-
Mean Energy($E_{\rm inc}$=thermal)	1.8 (37 keV)	1.8 (37 keV)
Mean Energy($E_{\rm inc}$=0.5 MeV)	1.7 (37 keV)	1.7 (37 keV)
Mean Energy($E_{\rm inc}$=1.5 MeV)	1.7 (37 keV)	-
Mean Energy($E_{\rm inc}$=14 MeV)	2.2 (47 keV)	-

(n,2n) Cross Section

Only a modest change to the $(n,2n)$ cross section has been made for ENDF/B-VIII.0 – the rise from threshold has been increased, in the 6.5 to 8 MeV incident energy, after which the cross section follows ENDF/B-VII.1.

The previous ENDF/B-VII.1 evaluation came from the GEANIE-project evaluation by LLNL and LANL [260]. In the late 1990s and early 2000s, the GEANIE detector at Los Alamos measured gamma-ray decays contributing to the $(n,2n)$ reactions, and these data were augmented by GNASH model calculations for unmeasured components to infer the $(n,2n)$ cross section. The final evaluation, used

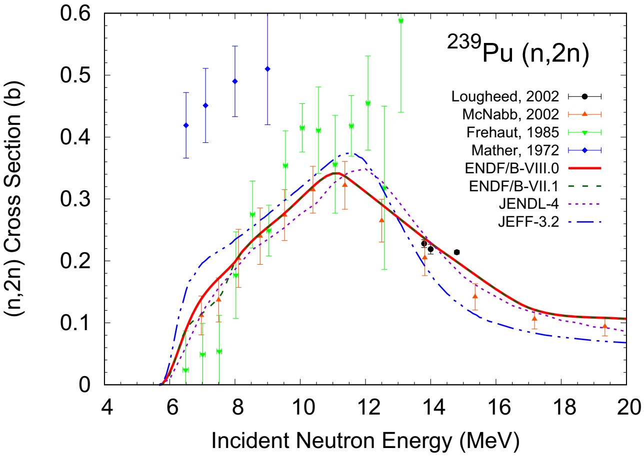

FIG. 83. (Color online) Evaluated ^{239}Pu(n,2n) cross section compared with data retrieved from EXFOR and with previous evaluations. The GEANIE project evaluation was previously adopted in ENDF/B-VII.1, based on the GEANIE and Lougheed data, as documented by McNabb [260].

in ENDF/B-VII, was based on a least-squares (covariance) analysis of these data together with the 1980s 14 MeV Lougheed [261] radiochemical data, as shown in Fig. 83. Other data, such as those from Fréhaut and from Mather, were not used in the analysis because it was felt that these sets had uncertainties that were too high.

Some integral feedback on the production of ^{238}Pu in a fission spectrum has suggested that this cross section should rise from its threshold somewhat faster. For example the PROFIL experiment suggested the need for a 25% higher cross section [22], in the threshold region, though internal LANL studies indicate the need for a much smaller increase. Therefore the evaluation has been modified in ENDF/B-VIII.0 to follow the upper uncertainty bars on the 7 – 7.5 MeV GEANIE data, as shown in Fig. 83.

The 14 MeV (n, xn) secondary neutron emission spectrum is shown in Fig. 84, compared with data. Of the many angles where data are available, just the results at 60 degrees are shown, which are representative of the ensemble of results. The new ENDF/B-VIII.0 results agree well with data, improving slightly over the previous VII.1 results owing to the influence of the slightly softer 14 MeV PFNS spectra in the new evaluation. (At the very lowest emission energies the data lie above the evaluation, but the data are thought to be suspect here since such large values would appear to be inconsistent with the value of nubar, and furthermore, there could be background scattering contamination in the experiment).

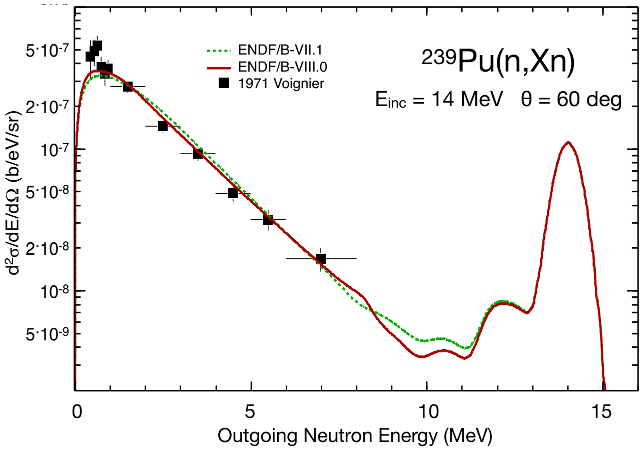

FIG. 84. (Color online) Evaluated 14 MeV ^{239}Pu(n,Xn) secondary neutron emission spectrum at 60 degrees.

Future Work
Neutron inelastic scattering [200] has not been changed in this latest revision of ENDF. More work will be done to assess the accuracy of the current evaluation; in particular, the semi-integral scattering technique pioneered by RPI, which has provided useful data for ^{238}U, C and Fe, will be applied to plutonium and uranium, at the LANSCE facility. Such future data should provide a useful validation check on the database, and point to improvements that may be needed in the magnitude and the angular distributions of inelastic and elastic scattering processes.

TABLE XXI. Thermal quantities for ^{240}Pu at 293.6 K = 0.0253 eV. Here σ_B is the total of the contributions of negative energy resonances and direct capture to the thermal cross section.

Quantity	Atlas	ENDF/B-VIII.0	ENDF/B-VII.1
σ_γ	289.5 ± 1.4 b	289.4 b	287.5 b
σ_s	1.73 ± 0.10 b	1.73 b	0.95 b
σ_f	0.056 ± 0.030 b	0.056 b	0.064 b
σ_B	18.8 b	17.96 b	3.02
Wescott's g-factor	1.0264	1.0259	1.0278

5. ^{240}Pu

Resonance Region
The negative (bound) levels of the Derrien *et al.* [262] RRR evaluation were adjusted with the evaluation code SAMMY to better match the thermal cross section values found in the *Atlas of Neutron Resonances* (Table XXI). The resonance parameter covariance matrix was adjusted accordingly to preserve the relative uncertainty of the cross section in the original evaluation of Derrien *et al.* [262].

Fast Region
The elastic cross section in the energy range 5.7-80 keV, the fission cross section in the energy range from 5.7 keV to 6 MeV and the capture cross section in the energy range from 5.7 keV to 20 MeV were replaced by the Weston evaluation from ENDF/B-VI.8. The capture cross section is about 5 % lower than ENDF/B-VII.1 in the unresolved resonance range. The capture cross section above the unresolved resonance range (above 42 keV) was further reduced by 2.5 % to improve the ^{240}Pu(n, γ) reaction rate measured in the PROFIL experiment, the reduction diminishing to zero at 1 MeV.

Additionally, in the unresolved resonance region that spans the energy range 5.7-40 keV the fission cross section was replaced by the Tovesson data, which exhibit considerable structure, although individual resonances are not resolved and hence self-shielding by the use of the unresolved resonance parameters is still valid. Above the unresolved resonance region the cross sections by Weston were adopted up to 190 keV. The chance-fission data were renormalised for consistency with the total fission cross sections.

6. ^{241}Am

The ^{241}Am evaluation for ENDF has been updated, based on CoH$_3$ model calculations that were calibrated to match data, notably recent measurements for the (n,2n) cross section. Figure 85 shows the (n,2n) cross section, which is seen to more rapidly rise from its threshold. This same analysis led to a slightly modified capture cross section (Fig. 86). The branching ratio to the ground state,

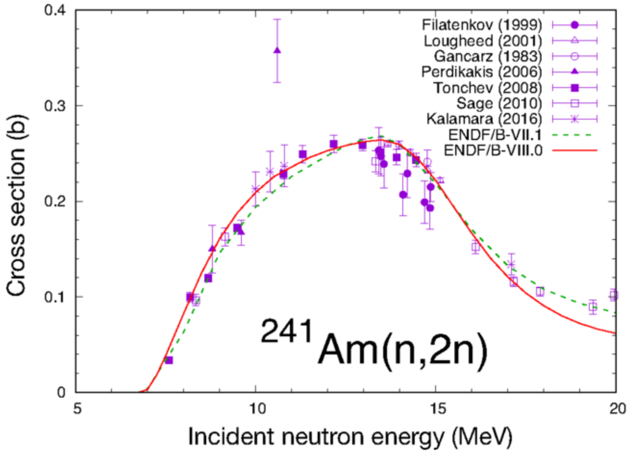

FIG. 85. (Color online) The ^{241}Am$(n, 2n)$ cross section in ENDF/B-VIII.0.

which beta decays to curium, is unchanged, see Fig. 87. However, this figure illustrates a possible need to update the branching ratio in future releases, where the fraction to the ground state is predicted to be higher above 1 MeV incident neutron energy by the CoH$_3$ code analysis.

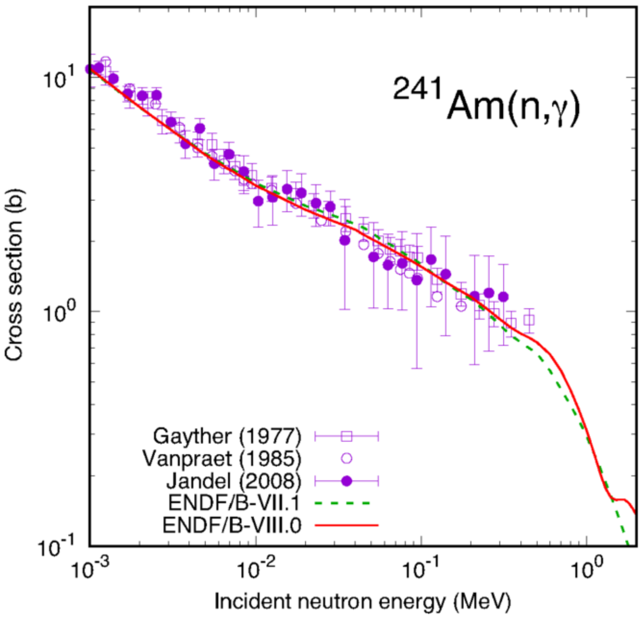

FIG. 86. (Color online) The ^{241}Am(n, γ) cross section in ENDF/B-VIII.0.

At this stage we have not modified the thermal capture cross section, which is 684 b. However, an ongoing study by the NEA's WPEC has studied the available data, and is concluding that the correct value is higher, perhaps in the 710–720 b range. Once this study has completed its work, the recommended value will be adopted in a future ENDF release.

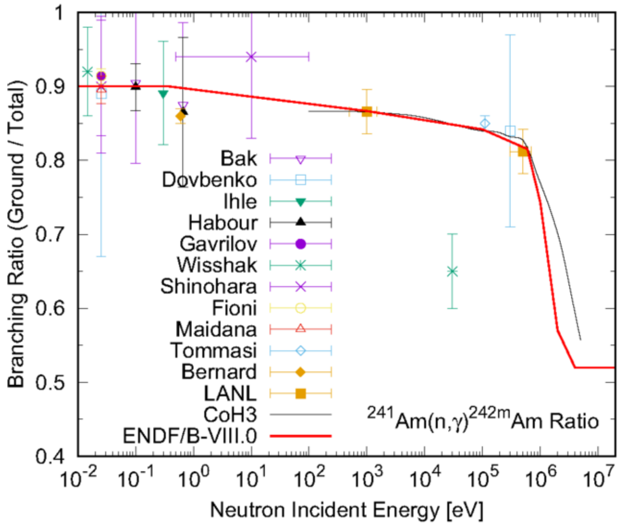

FIG. 87. (Color online) Ground state to total branching ratio for ^{241}Am capture. The ground state decays to curium.

E. TENDL+EMPIRE Isotopes

All isotopes with a half-life greater than 1 year have been added to ENDF/B-VIII.0 using a combination of EMPIRE and TALYS calculations [263], taken from the TENDL-2015 library. After consultation with the Nuclear Wallet Cards [264], it was found that the authors of Ref. [263] had overlooked several isotopes with a half-life ≥ 1 year. Furthermore, many of the isotopes considered for addition are more than one unit off stability, leaving gaps between isotopes. These gaps prevent modeling the creation of the added isotopes through say successive neutron capture. Given this, it was necessary to extend the number of isotopes under consideration. In the end, 52 isotopes from TENDL-2015 were adopted, including all stable neon and platinum and the major polonium isotopes. Also, 73 isotopes were adopted from EMPIRE calculations. The detailed list of evaluation sources are given in Appendix A.

All TALYS calculations for the present TENDL-2015 evaluations were performed up to 200 MeV, in default mode. The thermal (n,γ) cross sections were adjusted to match data (if available) or systematics. If no RRR measurements were available, a set of statistical resonances in the RRR were generated, consistent with the TALYS fast range calculation. Two problems with the TENDL-2015 formatting were noted and corrected:

- For the excited-target scattering TENDL-2015 normally cuts the "super inelastic" cross section off abruptly at lower energies, even though those correspond to zero-threshold processes.
- Sometimes the total inelastic has an unphysical sawtooth shape.

A default input was adopted for the EMPIRE calculations, consisting of EGSM level densities, MLO gamma strength functions and levels from RIPL-3, and the widthfluctuation correction up to 3 MeV. The direct-reaction mechanism was modeled using coupled channels, except for reactions with excited targets in the incident channel in which case a spherical model is assumed. In either case, the optical-model potential adopted was the one of Koning-Delaroche. For excited-target scattering, whenever there were levels of unknown spin between the ground and isomeric states, a random choice was made among the recommended values. Preequilibrium was calculated using PCROSS, with mean free path of 1.5 fm. Unknown fission barriers for even or odd number of neutrons were assumed to be the same as the ones for the next neighboring nucleus with known barriers and even or odd number of neutrons, respectively, with the same atomic mass. Since EMPIRE does not automatically create many resonances, the fast region calculations must be extended to very low incident energies in order to compute the average cross sections. In many cases, the lower cut-off needs to be adjusted.

There are several physics differences between the EMPIRE based evaluations and those in TENDL-2015. We summarize them here:

- Since EMPIRE uses a deformed optical model potential specifically designed for this mass range, it obtains better and more reliable cross sections for the well-deformed rare-earth nuclei.
- Both codes make different choices of levels to couple in coupled-channel calculations.
- The resonance treatment from TENDL-2015 leads to a more realistic-looking resonance region. However, the fact that these resonances are actually experimentally unknown may mislead the data user to believe the resonance region is well understood.
- The resonances from TENDL-2015 are extrapolated from the fast region and therefore can be 3 to 4 orders of magnitude too high.
- TENDL-2015 reproduces the 14 MeV canonical ∼ 1 mb capture cross section, while the EMPIRE preliminary calculations have not yet been tuned to reproduce this value.

F. Primary Gammas

High-resolution observation of gamma-rays produced in neutron-capture reactions provide an unambiguous fingerprint of the isotopes within an unknown sample. Nondestructive-assay applications exploit this phenomenon using passive interrogation if spontaneous-fission neutrons are present, or active interrogation where an external neutron source is used to probe the sample. The highest-energy gamma-ray transitions have $E_\gamma \sim$ 3-12 MeV and arise from thermal-neutron capture reactions to capture states just above the neutron separation energy. These states decay to the lowest lying levels giving the high energy gammas referred to as primaries. Primary gamma-rays are often easily seen in spectra from unknown assemblies as there are few competing reactions and clearly indicate the presence of Special Nuclear Materials (^{235,238}U and ^{239}Pu), fission products and an array of materials frequently associated with Special Nuclear Materials. However, nondestructive-assay applications are predicated on accurate data and there are well known data gaps in the neutron-capture gamma-ray line data in the ENDF libraries that limit these capabilities. The actinides, for example, have no high-energy capture lines at all. To address these data gaps, new gamma-ray spectroscopic data (high-resolution HPGe-quality data) has been added to ENDF/B-VIII.0 evaluations listed in Table XXII. The data is from an IAEA coordinated research project where the measurements were performed at the Budapest Reactor [265]. The Evaluated Gamma Ray Activation File (EGAF) assigned absolute cross sections and placed the lines in ENSDF-formatted decay schemes. Using EGAF, nine light isotopes in ENDF/B-VIII.0 have been updated in MF=12/MT=102. The EGAF-based evaluations also produce new total thermal capture cross sections. For these libraries, the total thermal cross sections from the decay spectra have been made consistent with the File 3 total thermal cross sections. Most of these light elements have complete decay schemes with all transitions experimentally resolved. When a quasi-continuum is present, File 15 data is scaled to maintain consistency with File 3.

TABLE XXII. List of ENDF/B-VIII.0 evaluations with updated thermal capture gamma data and number of lines included.

Isotope	% nat. abund.	σ(n,γ) (barns)	# lines
^{6}Li	7.589	0.0386	3
^{7}Li	92.411	0.0454	3
^{11}B	80.18	0.0055	13
^{19}F	100	0.0096	166
^{23}Na	100	0.53	244
^{27}Al	100	0.231	290
^{28}Si	92.2297	0.177	56
^{35}Cl	75.771	45.55	382
^{37}Cl	24.229	0.43	76

The LANL and LLNL validation and verification codes (*e.g.*, PREPRO [266], NJOY [267], and FUDGE [268]) are then used to check the integrity of the library. Table XXII lists the libraries upgraded and the number of capture gamma lines included.

Figure 88 shows and `MCNP`® predicted spectra comparing the new EGAF-based ENDF/B-VIII.0 library data with the ENDF/B-VII.1. In this case ∼100 gamma lines have been added to the library. While the added lines have generally lower cross sections, the primary lines above ∼6 MeV are very useful in applications. Figure 89 shows the same comparison with ^{19}F data and there is good agreement between the libraries.

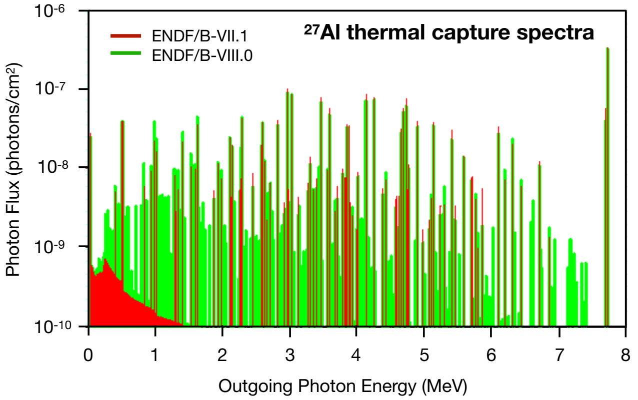

FIG. 88. (Color online) Comparison of new EGAF-based ENDF/B-VIII.0 ^{27}Al spectra to the previous ENDF/B-VII.1 library using `MCNP`®. The EGAF data had an additional ∼100 resolved lines significantly improving the utility of the library. In particular, lines above 6 MeV are very useful in applications.

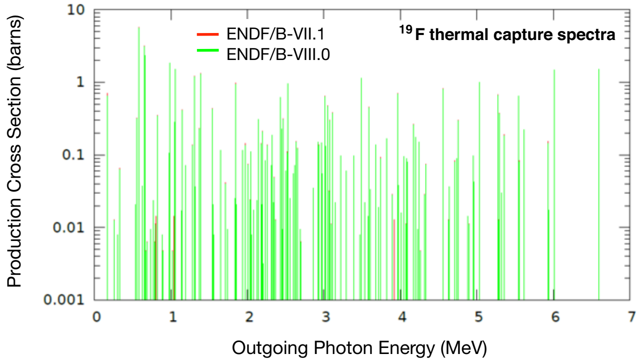

FIG. 89. (Color online) Comparison of EGAF-based ENDF/B-VIII.0 ^{19}F evaluation (green) the ENDF/B-VII.1 line spectra (red) showing good agreement between libraries. Clear improvements in thermal neutron capture spectroscopic data have been shown for some light isotopes and accordingly the transport modeling capabilities using these upgraded ENDF libraries is improved significantly. For medium and heavy isotopes, there are more gaps in the ENDF capture-gamma data.

G. Prompt Fission Neutrons, $\bar{\nu}_p$, for 53 Minor Actinides

To support various criticality safety and power generation applications, R.Q. Wright re-evaluated the prompt nubar of 53 actinides ranging from ^{235}U to ^{257}Fm at 0, 1, 2, 3, 4, 5, 9, 15, and 20 MeV [269]. Previously prompt-nubar calculations using the Madland-Nix method [228] were published by Brady *et al.* in 1991 [270] for ^{235,238}U, ^{237}Np, ^{238,239,240}Pu, ^{241,243}Am, and ^{243,244,245,246,247,248}Cm. A second report included calculated values of prompt-nubar for 13 additional actinides [271]. Revised input parameters from those used in Refs. [270, 271] were used in the present evaluation. These data were added to the ENDF/B-VIII.0 files and the affected files are noted in Appendix A.

The prompt-nubar values for thermal incident neutrons (0.0253 eV) were compared with the evaluated nuclear data file ENDF/B-VII.1 and the difference is less than 2% in 25 cases, 2-7% in 13 cases, and greater than 7% in 12 cases. Nubar uncertainty estimates as a function of energy were also determined. At thermal energy, these estimates vary from about 0.2-10%, depending on the particular nuclide. For a number of nuclides, good direct measurements are available (*e.g.*, ^{235}U and ^{239}Pu). For those two nuclides, the uncertainties for the direct measurements are on the order of 0.2%. For ^{235}U, ^{239}Pu, and several other nuclides, the uncertainties for the VII.1 evaluations are considerably smaller than the corresponding Madland-Nix calculation [228].

IV. PROMPT FISSION GAMMA OBSERVABLES

In recent years, new measurements of prompt fission gamma observables have become available. Concurrently, new theoretical capabilities have been developed that allow a detailed modeling of prompt neutron and gamma-ray emission from fission fragments, from which we can infer the average prompt fission gamma spectrum (PFGS), the average multiplicity and gamma-ray energy, correlations between emitted particles and so on. Thus, the latest progress in experiments and modeling have prompted an update by LANL and the IAEA of the following prompt fission gamma observables: the average PFGS, average multiplicity and average total gamma-ray energy released for ^{235}U(n,f), ^{238}U(n,f) and ^{239}Pu(n,f) reactions. Related work has been done recently by Serot *at al.* in the European work for JEFF3.3 and we are grateful to O. Serot for sharing these results with us [272].

Previous ENDF/B-VII.1 data only represented fission gamma data explicitly up to 1.09 MeV incident neutron energy for ^{235}U and ^{239}Pu. Above 1.09 MeV, all gammas were lumped into a production gamma-ray format. In the current ENDF/B-VIII evaluation, all channels are explicitly represented up to 20–30 MeV incident neutron energy.

CGMF (Cascade Gamma-Ray Multiplicity for Fission) is a code that models the de-excitation of fission fragments in the Hauser-Feshbach statistical decay model [223]. In CGMF, the fission fragment pairs are sampled from the fission yields in mass, charge, and TKE, parameterized based on available experimental data, and complemented by models for the initial spin distribution and energy sharing mechanism. The de-excitation of the sampled fission fragments can be run in a Monte Carlo mode, in which one samples the neutron and gamma-ray emission probabilities. In this case, one can obtain more detailed information, like the multiplicity probability or average multiplicity-dependent PFGS. However, at high outgoing gamma-ray energies, where the probability of emitting gammas is very small, the Monte Carlo mode requires the simulation of a large number of fission events. In this case, the deterministic mode of the decay is more appropriate, allowing calculation of gamma emission probabilities up to 20 − 30 MeV outgoing gamma ray energies. In the deterministic mode, only global average quantities can be obtained.

A good agreement between the results of CGMF and experiment and previous evaluations have been found for prompt gamma-ray observables in the case of thermal neutron induced fission of ^{235}U and ^{239}Pu and the spontaneous fission of ^{252}Cf [273–275]. Therefore, in the current evaluations, information provided by CGMF simulations were used together with measured data. In particular, CGMF results are used to extract the spectrum at outgoing gamma energies above 7-8 MeV where data are scarce.

In CGMF simulations, the PFGS depends only weakly on the incident neutron energy. This feature, observed for all the major actinides, was previously observed in experimental measurements by Kwan [276], as shown in Fig. 90, where the PFGS for fission induced by neutrons with different incident energies are compared with the evaluated PFGS obtained with experimental data and simulations of fission induced with thermal neutrons. Hence, one single average spectrum was used for all incident neutron energies. As a result, the average photon energy, $\langle\varepsilon_\gamma\rangle$, does not depend on the incident neutron energy in our evaluations. The existing data on the total gamma production also supports this assumption, and will be discussed below.

For the evaluations of the PFGS, in addition to guidance from recent experiments, CGMF calculations in a Monte Carlo framework up to 6-7 MeV outgoing gamma-ray energies were used. At low outgoing gamma-ray energies, for the ^{235,238}U($n_{\rm th}$,f) and ^{239}Pu($n_{\rm th}$,f) reactions, where recent measurements of the PFGS have been taken, the evaluation closely follows the experimental data. At energies above 6 MeV, the experimental data by Nishio [277] for ^{235}U(n,f), and CGMF simulations in deterministic mode for ^{238}U(n,f) and ^{239}Pu(n,f) were used.

For a meaningful comparison with the thermal experimental data, two issues have to be considered. First, the experimental energy threshold for the detection of gamma rays is between 100 keV and 400 keV depending on the experiment. Also, below 100 keV, a spurious contribution has been identified and removed from CGMF calculations. Tables XXIII–XXV present the comparison between evaluations and experimental data, as a function of the threshold energy characteristic to different experiments. Second, the results are fairly sensitive to the time coincidence window from fission that was used in measurements. As shown in Ref. [275], the average multiplicity depends quite strongly on the time window considered, as at longer times long-lived isomers start to contribute. In the current evaluation, a time coincidence window of 10 ns was used, which is typical for the experiments used in the evaluation.

The main experimental input used for determining the prompt fission gamma multiplicity above thermal energies was the total gamma production cross section from the Los Alamos measurements by Drake [287–289], from 1–14 MeV incident energy, for ^{235,238}U(n,f) and ^{239}Pu(n,f) reactions. The fission gamma-ray multiplicity, at selected incident neutron energies, was obtained by subtracting the calculated contributions of all the open channels, except fission, that produce gamma rays where total gamma production data are available from the Drake total gamma-ray production data. The uncertainties for the gamma production in those channels is sufficiently low so that the uncertainties in the inferred fission gamma multiplicity mainly comes from the uncertainties in the gamma-production experimental data. At thermal neutron energy, the latest measured multiplicities available were used.

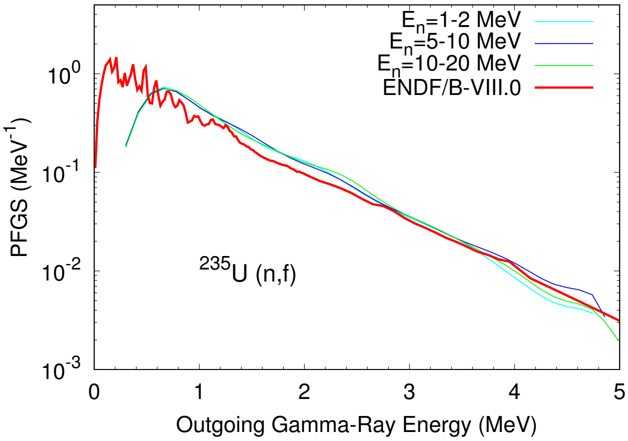

FIG. 90. (Color online) Comparison between the evaluated ENDF/B-VIII.0 PFGS, obtained from data and simulations at thermal incident neutron energy, and LLNL/LANL Kwan *et al.* experimental PFGS data [276] at higher incident energies for the ^{235}U(n,f) reaction. These data have an arbitrary normalization, but are seen to have very similar shapes for incident energies, contributing to our evaluation decision to use one PFGS spectra shape for all incident energies. (The red evaluated curve doesn't match the lines depicting the data very well since it was influenced by other higher-accuracy thermal data.)

The average total gamma-ray energy emitted E_γ^{tot} was obtained as the product of the average gamma multiplicity and the average photon energy, the latter remaining constant as a function of incident energy. Thus, the incident neutron dependence of the average total gamma energy comes entirely from the average gamma multiplicity dependence on the incident neutron energy. In Tables XXIII–XXV select properties are compared for the present evaluation against other existing evaluations and available experimental data.

A. ^{235}U(n,f) Prompt Fission γ-Ray Properties

The PFGS for the ^{235}U(n,f) reaction has been reevaluated using the output of the CGMF code in combination with experimental data. The current evaluation agrees well with existing experimental thermal spectra data, as shown in Fig. 91. The evaluation is thus closer to the 2013 Oberstedt data [279], than to a recent measurement of the PFGS by the same group [290].

The average multiplicity was also updated and is considerably different from ENDF/B-VII.1. The main reasons are that a decision was made to be most influenced by the

TABLE XXIII. Evaluation of prompt fission gamma-ray properties: comparison between the current evaluation, experimental data and CGMF for ^{235}U(n_{th},f). The low-energy emission threshold E_{thresh} is given in keV, while all the other energies are in MeV. We present the average gamma multiplicity, $\langle M_\gamma \rangle$, the average gamma-ray energy, $\langle \varepsilon_\gamma \rangle$, and the total prompt gamma energy released, E_γ^{tot}.

	E_{thresh}	$\langle M_\gamma \rangle$	$\langle \varepsilon_\gamma \rangle$	E_γ^{tot}
ENDF/B-VIII.0	0	8.58	0.85	7.28
ENDF/B-VII.1		7.04	0.94	6.60
JEFF 3.3		8.74	0.81	7.05
JENDL 4		7.43	0.94	6.96
CGMF		7.94	0.78	6.20
ENDF/B-VIII.0	100	8.19	0.89	7.25
ENDF/B-VII.1	100	6.87	0.96	6.59
Pleasonton [278]	90	6.51(30)	0.99(7)	6.43(30)
Oberstedt 2013 [279]	100	8.19(11)	0.84(2)	6.92(9)
Oberstedt 2017	100	7.22	0.87	6.27
CGMF	100	7.01	0.87	6.15
ENDF/B-VIII.0	140	7.78	0.93	7.21
ENDF/B-VII.1	140	6.72	0.98	6.57
Verbinski [280]	140	6.7(3)	0.97(5)	6.51(30)
Oberstedt 2017	140	7.01(18)	0.89(4)	6.24(20)
CGMF	140	6.68	0.91	6.10
Chyzh [281]	150	7.35		8.35
Peelle [282]	150	7.45(35)	0.99(7)	7.18(26)
ENDF/B-VIII.0	400	5.47	1.21	6.60
ENDF/B-VII.1	400	5.30	1.17	6.17
Jandel [283]	400	4.92	1.20	5.89
CGMF	400	4.87	1.19	5.78

TABLE XXIV. Evaluation of prompt fission gamma-ray properties: comparison between the current evaluation, experimental data and CGMF for ^{238}U(n_{th},f). For comparison with the Lebois data, we also show the CGMF calculation at 1.7 incident neutron energy, with the corresponding emission threshold energy $E_{\mathrm{thresh}} = 100$ keV. The low-energy emission threshold E_{thresh} is given in keV, while all the other energies are in MeV.

	E_{thresh}	$\langle M_\gamma \rangle$	$\langle \varepsilon_\gamma \rangle$	E_γ^{tot}
ENDF/B-VIII.0	0	7.61	0.74	5.61
ENDF/B-VII.1		7.53	0.89	6.68
JEFF 3.3		7.49	0.76	5.68
JENDL 4		6.45	0.97	6.22
ENDF/B-VIII.0 (1.7 MeV)	100	7.78	0.79	6.12
ENDF/B-VII.1 (1.7 MeV)	100	7.04	0.94	6.65
CGMF (1.7 MeV)	100	8.50	0.76	6.46
Lebois (1.7 MeV)	100	7.59	0.77(6)	

TABLE XXV. The same as in Table XXIII, but for the ^{239}Pu(n_{th},f) reaction.

	E_{thresh}	$\langle M_\gamma \rangle$	$\langle \varepsilon_\gamma \rangle$	E_γ^{tot}
ENDF/B-VIII.0	0	7.56	0.84	6.37
ENDF/B-VII.1		7.78	0.87	6.74
JEFF 3.3		7.89	0.80	6.34
JENDL 4		8.34	0.89	7.45
ENDF/B-VIII.0	100	7.33	0.87	6.35
ENDF/B-VII.1	100	7.38	0.91	6.72
Pleasonton [284]	90	6.88(35)	0.98(7)	6.73(35)
Gatera [285]	100	7.35(12)	0.85(2)	6.27(11)
CGMF	100	7.57	0.87	6.71
ENDF/B-VIII.0	140	7.07	0.89	6.32
ENDF/B-VII.1	140	7.14	0.94	6.69
Verbinski [280]	140	7.23(30)	0.94(5)	6.81
CGMF	140	7.12	0.94	6.66
Ullmann [286]	150	7.15(9)		7.46(6)
Chyzh [281]	150	7.93		6.94

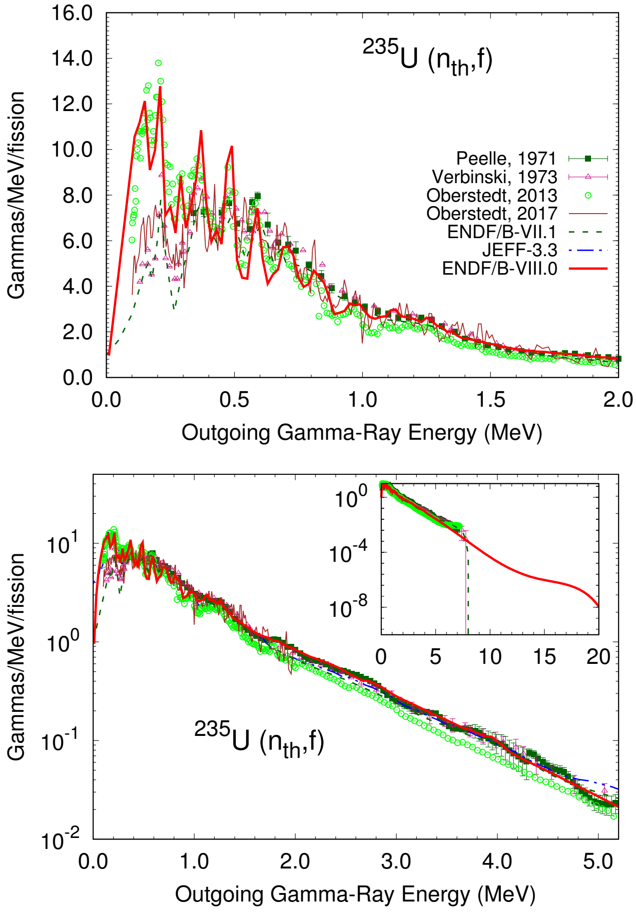

FIG. 91. (Color online) The PFGS for the ^{235}U(n_{th},f) reaction. The new evaluation is compared against previous libraries and data from Verbinski [280], Peelle [282], and Oberstedt [279]. Recent data by Nishio [277] was used in the evaluation of the high energy tail. The insert to the bottom panel shows the PFGS up to 20 MeV outgoing gamma-ray energy.

(higher) recent Oberstedt measurement at low energies, together with the fact that – in the old evaluation – the prompt fission gamma rays were lumped together with gamma rays from other emission channels above 1.09 MeV incident neutron energy, while the fission gamma multiplicity was set to zero above this value. The previous evaluations of the gamma-ray spectra were based on inclusive measurements [291]. In Fig. 92, the new evaluation is shown, as compared with the previous libraries and available experimental data. At thermal energies, the evaluation has been adjusted to reproduce the Oberstedt 2013 [279] reported value. The newest thermal multiplicity value reported by Oberstedt [290] is considerably lower than the previous measurement, but because this measurement has not been published yet, and the fact that the previous measurement is in very good agreement with CGMF below 300 keV, where the new measurement shows significantly lower gamma production, the previously measured Oberstedt 2013 [279] value of 8.19 photons per fission above the 100 keV threshold was used. Table XXIII demonstrates that the evaluated multiplicity is in good agreement with Oberstedt [279], Chyzh [292], Peele [282] and Jandel [283], and with the recently updated JEFF 3.3 evaluation, for various emission energy thresholds. The new evaluation is considerably higher than the values reported by Verbinski [280], and Pleasonton [278], because of an emphasis on matching the more recent Los Alamos, Livermore, and Geel/Budapest PFGS data. The reason for the higher ENDF/B-VIII.0 thermal gamma-ray multiplicity seen in Table XXIII, for all emission energies, is that the Oberstedt data for emission energies above 100 keV is augmented by an estimated contribution below 100 keV.

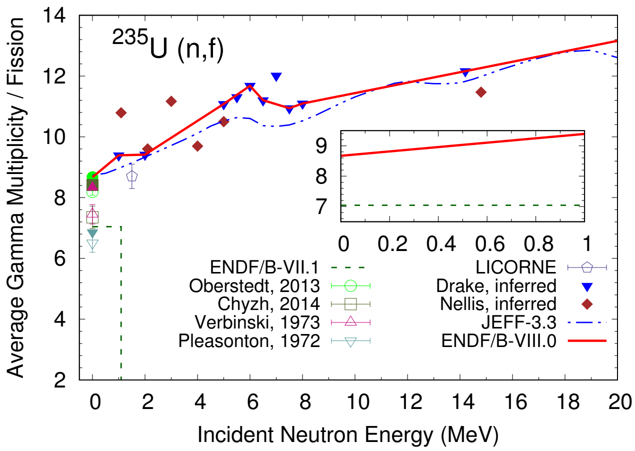

FIG. 92. (Color online) The average gamma-ray multiplicity as a function of incident neutron energy for the ^{235}U(n,f) reaction. The data provided by measurements, which includes only photons within a certain energy range, is shown with empty symbols, while the corresponding full symbols display the corrected data, based on ENDF/B-VIII.0 extrapolation. In the insert, we show the change in PFG multiplicity between thermal and 1 MeV incident neutron energy, the energy range relevant to many applications.

At higher incident energies, the evaluation is based on the total gamma production data measured by Drake [288, 289]. The inferred multiplicity in this case was obtained by removing from the experimental data the contribution from non-fission channels, and taking into account the experimental energy range in which the gamma production has been measured. The extracted average prompt fission gamma multiplicity dependence on the incident neutron energy is close to the latest JEFF-3.3 evaluation, as illustrated in Fig. 92.

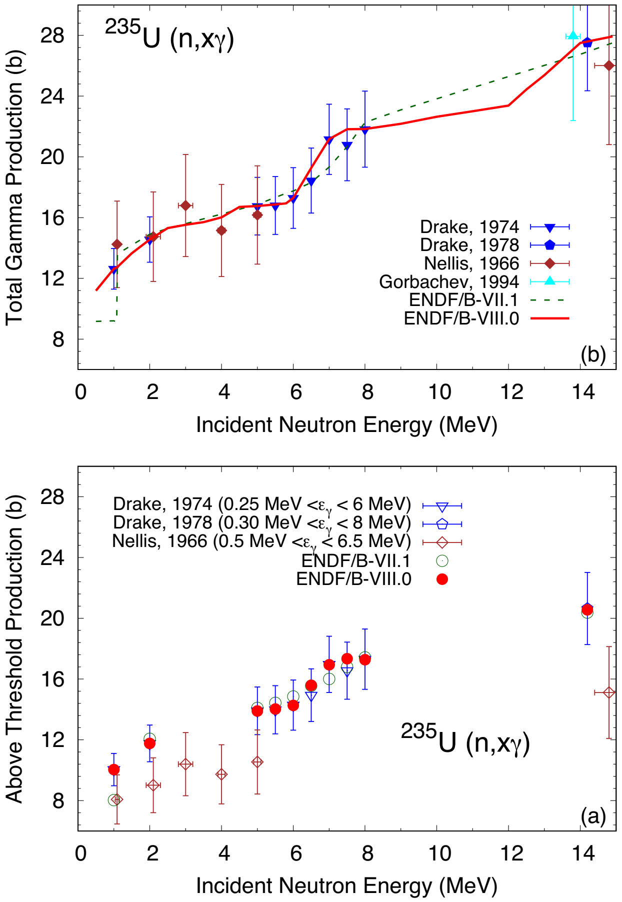

FIG. 93. (Color online) Total gamma production as a function of incident neutron energy for the ^{235}U(n,xγ) reaction. In the lower panel, the total gamma production has been calculated only at the neutron incident energies measured by Drake, and taking into account the outgoing photon energy range for each measurement. The Nellis data are systematically lower because it only includes photons with energies between 0.5 and 6 MeV, while the Drake measurement includes gammas between 0.25 and 6 MeV for incident neutron energies up to 8 MeV, and between 0.3 and 8 MeV for the 14.2 neutron incident energy measurement. In the upper panel, both the Nellis and Drake experimental data have been corrected for the excluded photon energy ranges, by performing an extrapolation from zero to 30 MeV outgoing photon energies based on the ENDF/B-VIII.0 evaluation.

For application purposes, the current ENDF/B-VIII.0 PFGS and multiplicity evaluation has been constructed with the goal of reproducing the available data on total gamma production (mainly by Drake). As noted above, the multiplicity has been adjusted to reproduce the Drake data on gamma production, a quantity in which the fission process dominates, and the comparison between ENDF/B-VII.1, the current evaluation and the experimental data are shown in Fig. 93. The Nellis data [293] shown in the lower panel is systematically lower than Drake simply because the low-energy detection threshold is higher at 0.5 MeV, and a significant number of gamma rays are produced below 0.5 MeV (see Fig. 91). When corrections are applied to account for the excluded gamma rays, the two experiments become consistent. In the upper panel, we compare the extrapolated data with the ENDF/B-VII.1 and ENDF/B-VIII.0 evaluations. As expected, ENDF/B-VII.1 exhibits a discontinuity at 1.09 MeV, due to the different representation of the gamma rays above and below this value. The consistent representation of all the open channels in ENDF/B-VIII.0 ensures a smooth dependence on the incident neutron energy over the entire range.

Even though no energy dependence is assumed for the prompt fission gamma spectrum as a function of incident neutron energy, a very good agreement with the available total gamma production spectra can be observed, as illustrated in Figs. 94 – 97. These log-log figures were constructed using IAEA computational tools that reconstruct the total spectra from all components (fission, capture, inelastic, n,2n *etc.*). An example of a lin-log representation is shown in Fig. 98 for the reconstructed spectra at 1 and 14.2 MeV incident energies, showing the dominance of the fission PFGS contribution to the total production.

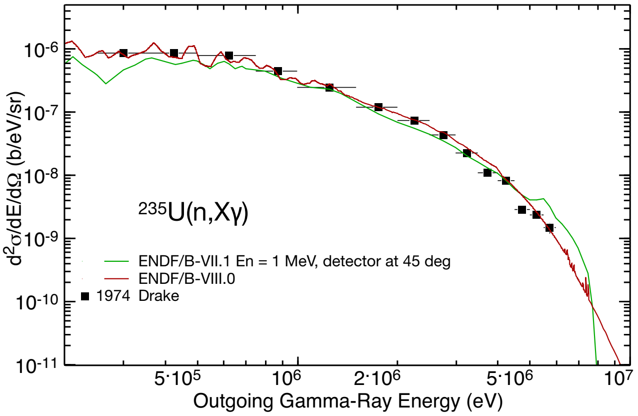

FIG. 94. (Color online) The double differential production cross section spectra of gamma-rays emitted in the bombardment of ^{235}U with 1 MeV incident neutrons.

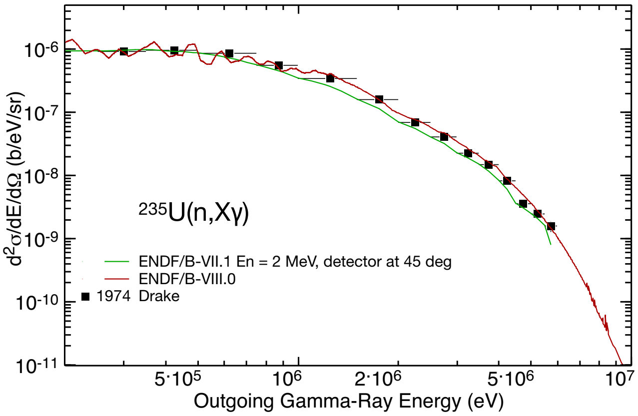

FIG. 95. (Color online) The same as in Fig. 94, but for 2 MeV incident neutrons.

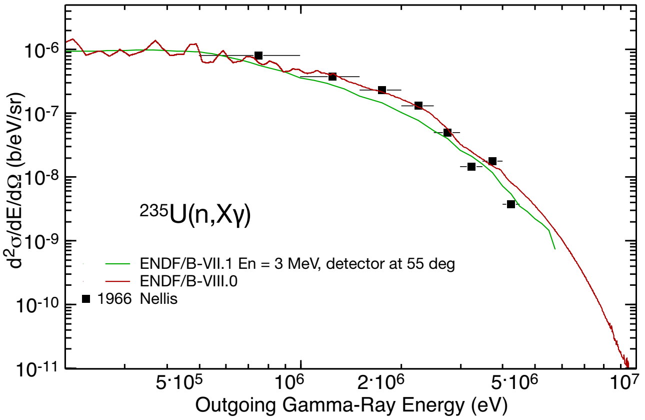

FIG. 96. (Color online) The same as in Fig. 94, but for 3 MeV incident neutrons.

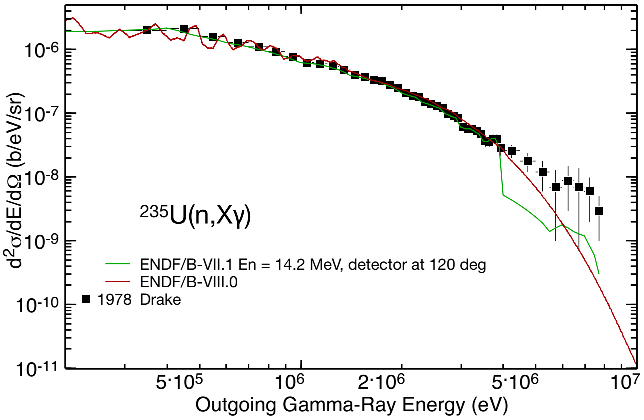

FIG. 97. (Color online) The same as in Fig. 94, but for 14.2 MeV incident neutrons.

The new evaluation for the average total gamma-ray energy released in fission is shown in Fig. 99. In the previous ENDF/B-VII.1 evaluation, the total gamma energy released in fission is a linear interpolation of the Fréhaut data [294] and was represented in ENDF File 1/MT458 from thermal to 20 MeV, despite the fact that the multiplicity was set to zero above 1.09 MeV. In the current version, the fission channel is explicitly represented from thermal to 30 MeV incident neutron energies, and the average total gamma energy produced is consistent with the PFGS and PFG multiplicity over the entire neutron energy range. Note that, while the evaluation reproduces the thermal data by construction, it is systematically higher than the Fréhaut data at higher incident energies, since the inferred data from the Los Alamos Drake measurement were chosen to match. In the future it would be useful to resolve the difference between these Los Alamos and the CEA measurements.

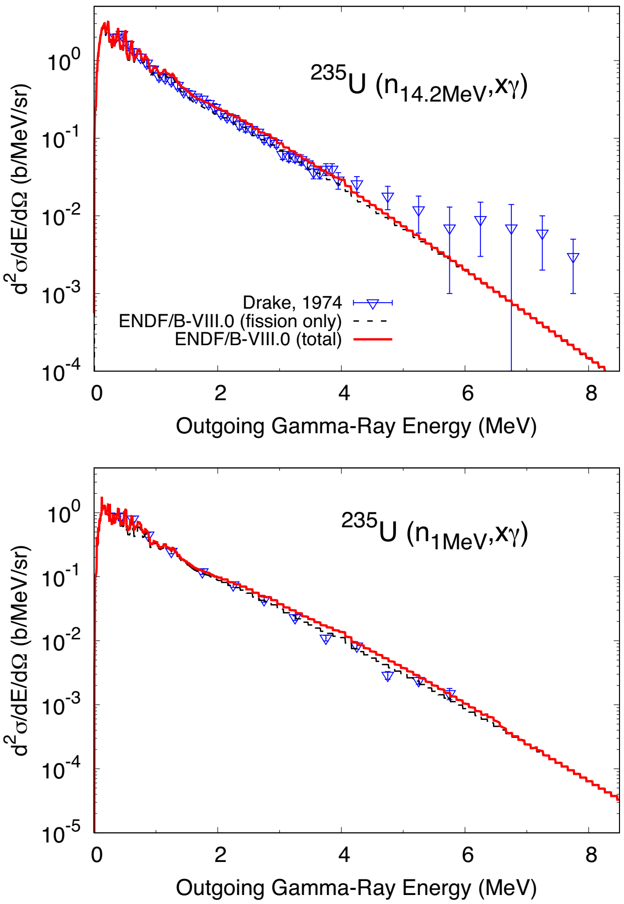

FIG. 98. (Color online) The double differential cross section of photons emitted in the bombardment of ^{235}U with 1 MeV (lower panel) and 14.2 MeV (upper panel) incident neutrons. The dashed line shows the fission contribution, which dominates at all energies.

B. ^{238}U(n,f) Prompt Fission γ-Ray Properties

The evaluation of prompt fission gamma properties for the ^{238}U(n,f) reaction is based on the assumption that the properties of PFG are similar to the ones obtained for the ^{235}U(n,f) reaction. This was found experimentally in Ref. [295], and it is motivated by the fact that the fission yields for the two reactions are reasonably similar. As a consequence, it was assumed that the average multiplicity per gamma event for ^{238}U is proportional and has the same incident neutron energy dependence as for ^{235}U. The overall proportionality factor has been calculated so that the total gamma production measured by Drake at 14.2(5) MeV and averaged over the two angles, is well reproduced. The average gamma multiplicity per fission is shown in Fig. 100, compared with a handful of available data points, digitized from presentations given at conferences. The PFGS is presented in Fig. 101. Below 1 MeV outgoing incident neutron energy, the JEFF 3.3 evaluated spectrum [272] was adopted (which was influenced by the data of Lebois), while above that energy the ^{235}U(n,f) PFGS was used, since at high outgoing gamma-ray energies, the ^{235}U evaluation was based on the latest measurement by Nishio, designed to target such energies. As in the case of other fission reactions, it was assumed that the PFGS is independent of the incident neutron energy. As a consequence, the average total gamma-ray energy is proportional to the multiplicity. Its dependence on the incident neutron energy is presented in Fig. 102, which is seen to be fairly similar to JEFF 3.3 even though the methodology adopted by the two evaluations is rather different.

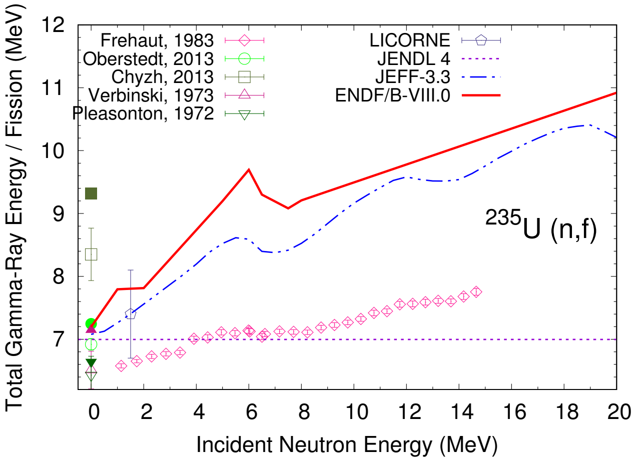

FIG. 99. (Color online) The average total gamma-ray energy as a function of incident neutron energy for the ^{235}U(n,f) reaction. Like in Fig. 92, the full symbols represent the ENDF/B-VIII.0 based extrapolation of the experimental data to include contributions from outside the energy range inherent to each experiment. ENDF/B-VIII.0 is most influenced by the Oberstedt data at thermal, and by data inferred from Drake (Los Alamos) at higher energies.

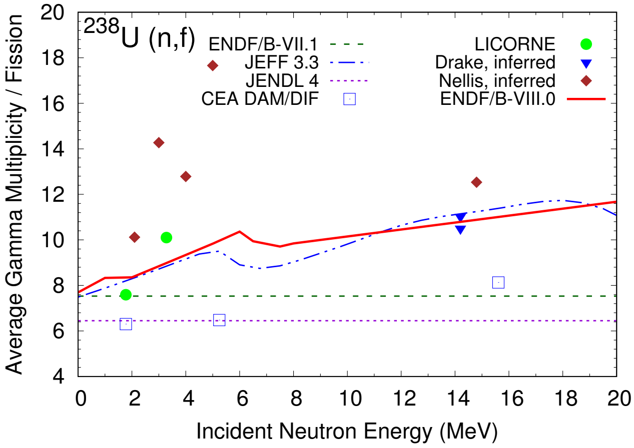

FIG. 100. (Color online) The same as in Fig. 92, but for the ^{238}U(n,f) reaction.

Both fission and capture channels were represented by file 12 in ENDF/B-VII.1, while the remainder of the gamma-ray data from other open channels were given in file 13. Hence, even though the PFG multiplicity was kept

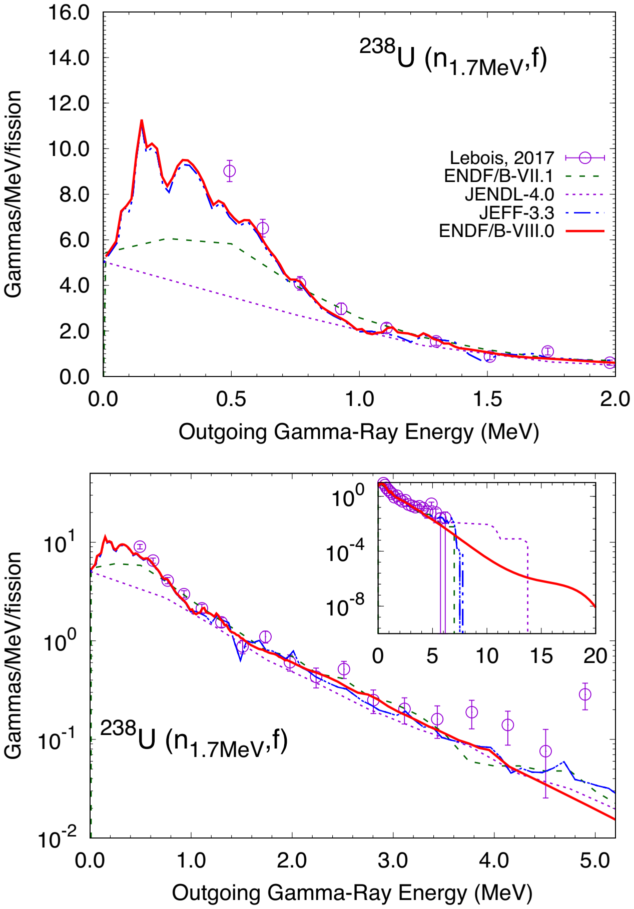

FIG. 101. (Color online) The PFGS for the ^{238}U(n$_{1.7\ \mathrm{MeV}}$,f) reaction. The new evaluation is compared against previous libraries and data. The insert to the bottom panel shows the PFGS up to 20 MeV outgoing gamma-ray energy.

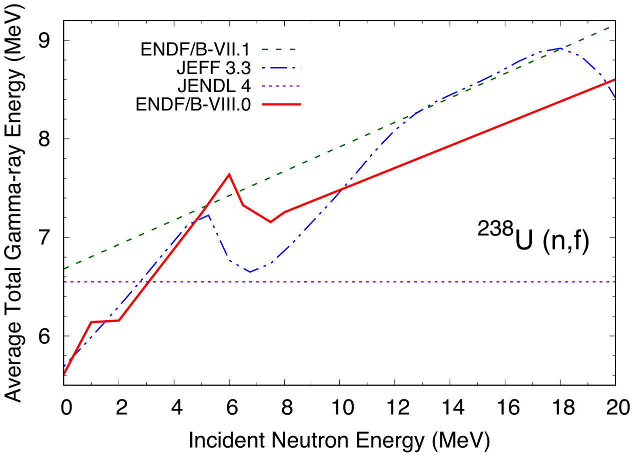

FIG. 102. (Color online) The same as in Fig. 99, but for the ^{238}U(n,f) reaction.

constant when the incident neutron energy was varied from 0 to 20 MeV, the measured total gamma production at 14.2 MeV neutron incident energy was well reproduced with the ENDF/B-VII.1 library. As shown in Fig. 103, the new evaluation follows nicely the trend of the experimental data, although it tends to underestimate available data by Nellis. However, it was found that the multiplicities extracted from Nellis data were fairly inconsistent with the Drake results for both ^{235}U(n,f) and ^{239}P(n,f) reactions (see Fig. 92 and the equivalent figure in Sec. IV C).

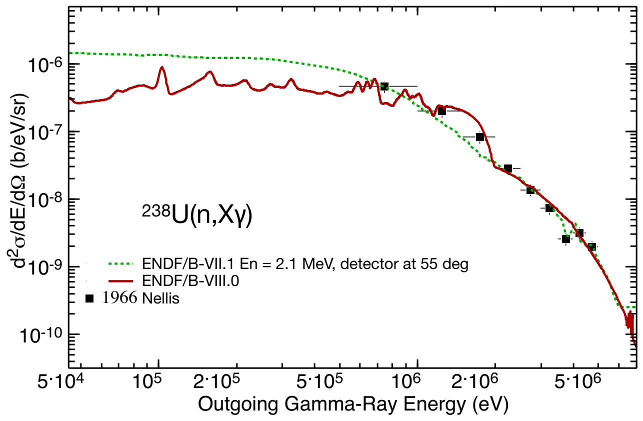

FIG. 103. (Color online) The double differential production cross section spectra of gamma-rays emitted in the bombardment of ^{238}U with 1 MeV incident neutrons.

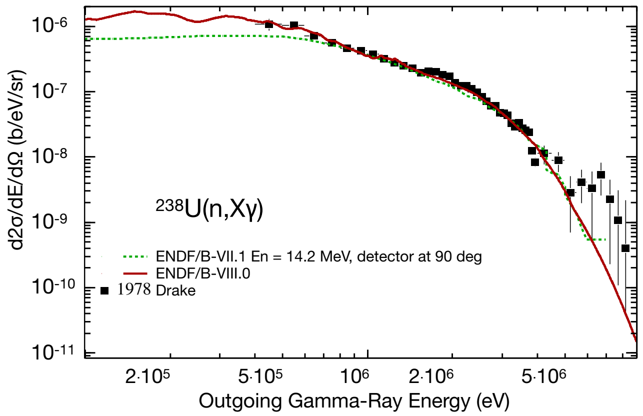

FIG. 104. (Color online) The same as in Fig. 103, but for 14.2 MeV incident neutrons.

The double differential cross section is presented in the log-log scale in Figs. 103 and 104, and in a log-lin scale in Fig. 105. Unlike for ^{235}U and ^{239}Pu neutron-induced reaction, open channels other than fission can bring significant contribution to the gamma production, even at high incident neutron energies. At 1 MeV incident neutron, the capture spectrum, which is dominant for photon energies above 1.5 MeV, is significantly harder than the experimental spectrum, as illustrated in the lower panel of Fig. 105. This feature will be corrected in a future version of the library.

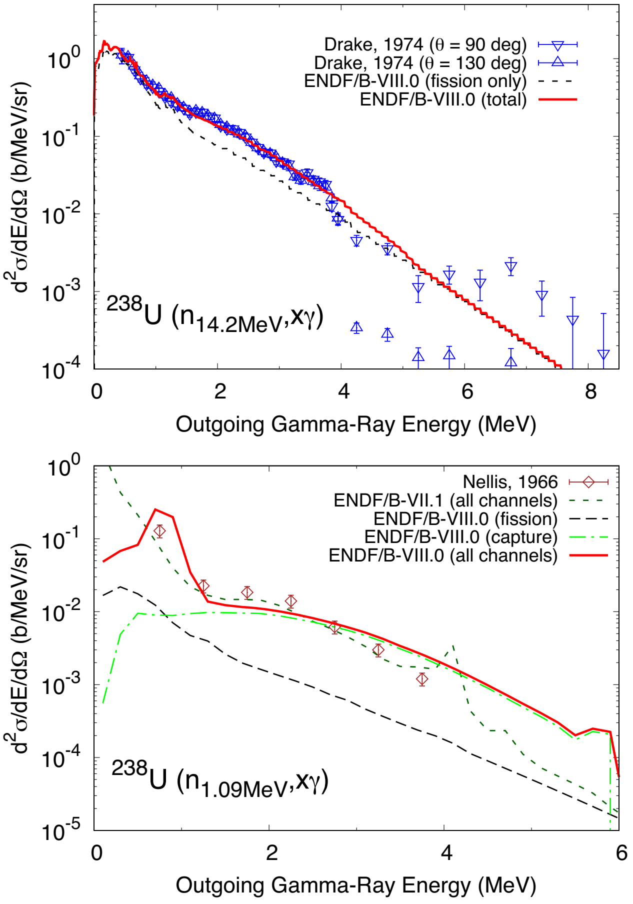

FIG. 105. (Color online) The double differential cross section of photons emitted in the bombardment of ^{238}U with 1.09 MeV (lower panel) and 14.2 MeV (upper panel) incident neutrons. The dashed line shows the fission contribution, while the capture contribution only is represented with a dash-dotted line. Unlike for the neutron induced reactions of ^{235}U and ^{239}Pu, the contribution from all open channels is significant. The ENDF/B-VII.1 is also shown with a short-dashed line.

C. ^{239}Pu(n,f) Prompt Fission γ-Ray Properties

The new evaluation of the PFGS for the ^{239}Pu(n,f) is based, like the ^{235}U(n,f) evaluation, on the latest measurements of the PFGS and CGMF simulations at thermal, and on the total production cross section data by Drake for 1 – 14 MeV incident neutron energies. Thus, the average prompt fission gamma multiplicity was adjusted so that, when an energy threshold of 100 keV is applied on the spectrum, a prompt fission gamma multiplicity of 7.33 are obtained, which is in good agreement with the mean value of the latest measurement by Gatera *et al.*, Oberstedt *et al.* [285]. The new evaluation also compares well with measurements by Verbinski [280] and the Los Alamos Ullmann *et al.* [286] measurement, when appropriate thresholds are imposed, but less so with Pleasonton *et al.* [284], who obtained a smaller value with a 90 keV threshold, and Chyzh *et al.* [281], who obtained a larger value with 150 keV threshold, even though a previous publication by the same authors have reported a 7.5 value [292] which is more in line with the current evaluation. A summary of the PFG properties at thermal neutron incident energy is presented in Table XXV, while the incident neutron energy multiplicity-dependence is depicted in Fig. 106. The multiplicity dependence is seen to be fairly similar to JEFF 3.3 even though the methodology adopted by the two evaluations is rather different. As in the case of the ^{235,238}U(n,f) reactions, all relevant open channels are given explicitly for the entire range of incident neutron energies, and, thus, the previous ENDF/B-VII.1 discontinuity in the average PFG multiplicity at 1.09 incident neutron energy is removed.

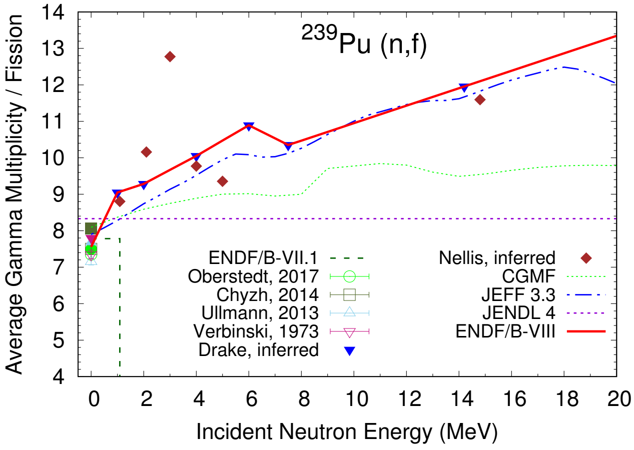

FIG. 106. (Color online) The average gamma-ray multiplicity as a function of incident neutron energy for the ^{239}Pu(n,f) reaction. Open symbols represent the reported data measured above a certain detector threshold, whereas closed symbols include our estimate including a sub-threshold corrections.

The current evaluation adopts the spectrum of Gatera *et al.* up to 2 MeV, and above that CGMF calculations are matched so an evaluation of the PFGS up to 20 MeV outgoing gamma ray energies is obtained. The evaluated PFGS is softer than the ENDF/B-VII.1 evaluation, which is based on the Verbinski *et al.* measurement [280]. At energies above 2 MeV, the PFGS measurement by Chyzh *et al.* [292] obtained by performing a singular value decomposition unfolding of the data are relatively well reproduced by the evaluation. However, the evaluation is considerably softer than the Ullmann *et al.* [286] and Chyzh *et al.* (Bayesian unfolding) data. The comparison between different experimental data sets and current and previous thermal evaluations of the PFGS is presented in Fig. 107; it is evident that the new evaluation represents a reasonable compromise between the various measured spectra above 2 MeV. The evaluation of the spectrum was also influenced by a desire to match the Drake total production spectra at higher incident energies.

For the average total gamma-ray energy per fission, the previous ENDF/B-VII.1 evaluation is a quadratic fit to an evaluated data by Fort *et al.* [296], recorded in File 1/MT458, and it extends from thermal to 20 MeV inci-

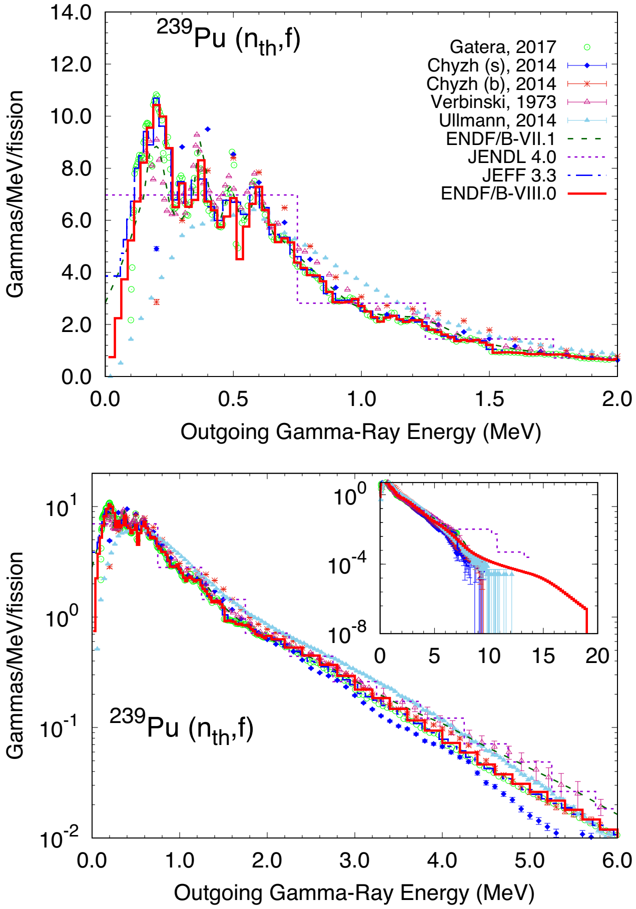

FIG. 107. (Color online) The PFGS for the ^{239}Pu(n$_{\rm th}$,f) reaction. The new evaluation is compared against previous libraries and existing data by Gatera *et al.* [285], Chyzh (b=Bayesian unfolding, s=SVD unfolding) [292], and Verbinski *et al.* [280]. The insert to the bottom panel shows the PFGS up to 20 MeV outgoing gamma-ray energy.

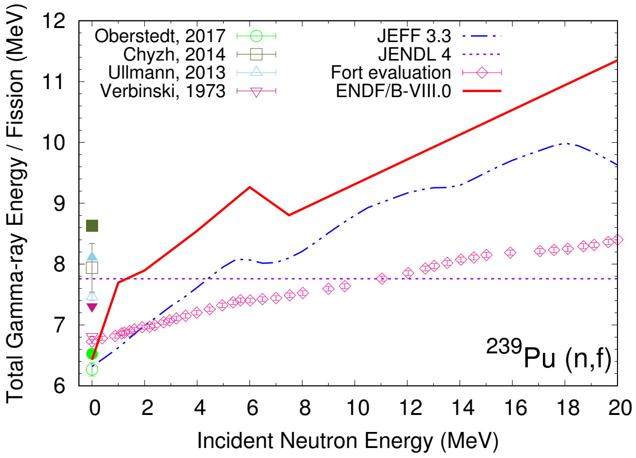

FIG. 108. (Color online) The average total gamma-ray energy as a function of incident neutron energy for the ^{239}Pu(n,f) reaction. Open symbols represent the reported data measured above a certain detector threshold, whereas closed symbols include our estimate of the sub-threshold corrections.

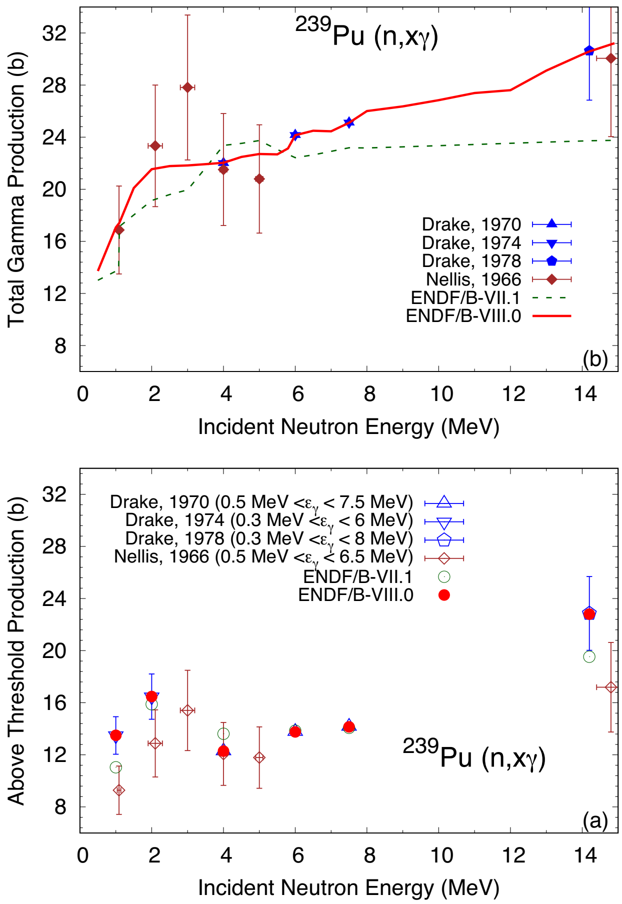

FIG. 109. (Color online) The same as in Fig. 93, but for the the ^{239}Pu(n,xγ) reaction.

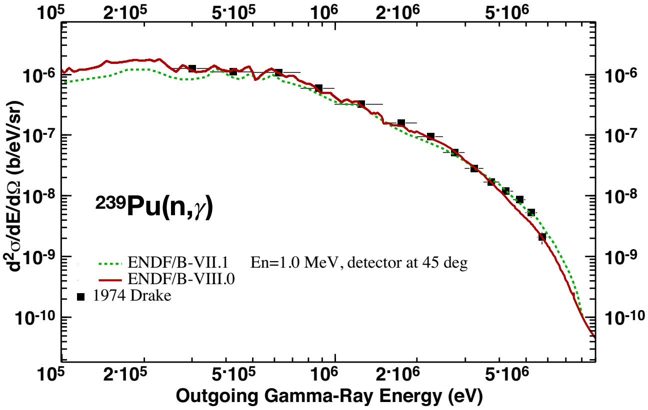

FIG. 110. (Color online) The double differential production cross section spectra of gamma-rays emitted in the bombardment of ^{239}Pu with 1 MeV incident neutrons.

dent neutron energy, although the PFG multiplicity was set to zero above 1.09 MeV. The comparison between the current evaluation and other libraries, as well as existing experimental data, is presented in Fig. 108. For thermal incident neutrons, the new evaluation for the total gamma energy released in fission is slightly lower than

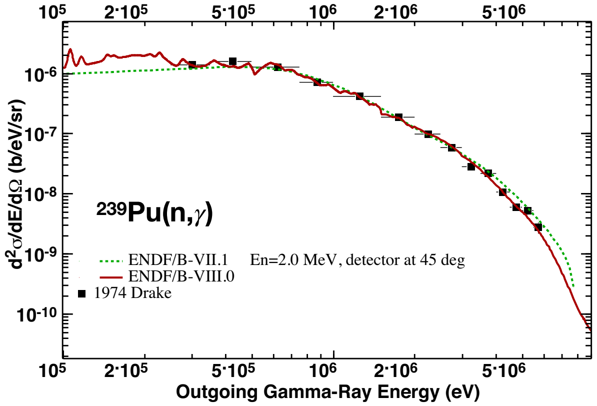

FIG. 111. (Color online) The same as in Fig. 110, but for 2 MeV incident neutrons.

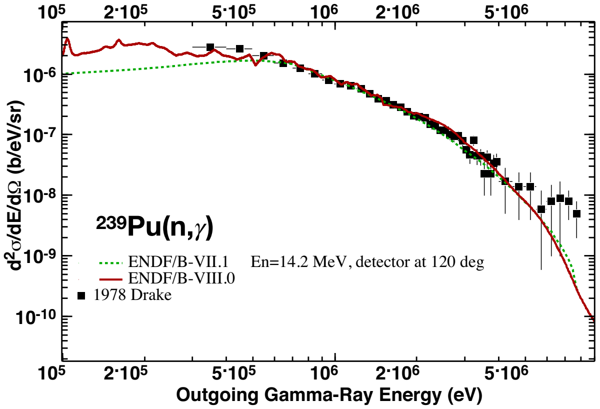

FIG. 112. (Color online) The same as in Fig. 110, but for 14.2 MeV incident neutrons.

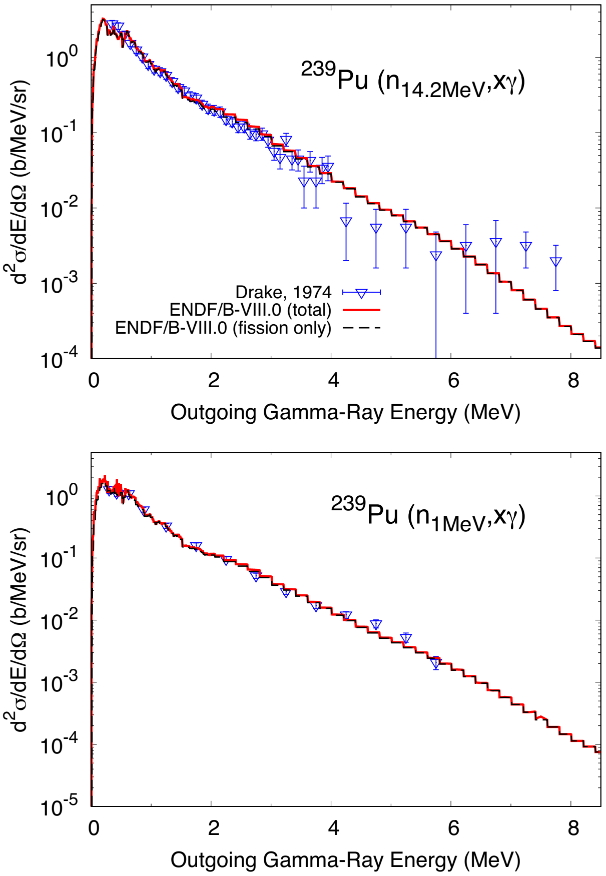

FIG. 113. (Color online) The double differential cross section of photons emitted in the bombardment of ^{239}Pu with 1 MeV (lower panel) and 14.2 MeV (upper panel) incident neutrons. The dashed line shows the fission contribution, which dominates at all energies.

in ENDF/B-VIII.1 and JEFF 3.2, and by more than 1 MeV below the JENDL 4 library (see Table XXV). However, when the appropriate energy detection threshold is taken into account, the ENDF/B-VIII.0 evaluation is in good agreement with recent measurements by Gatera *et al.*, Obserstedt *et al.* and Pleasonton *et al.*, and with CGMF simulations. In addition, the new evaluation agrees well with the recently updated JEFF 3.3 library [272]. At higher incident energies, the evaluation is well above the existing Fort evaluation, for the reason that matching information from the Los Alamos Drake data has taken priority.

The results for the total gamma production cross section are presented in Fig. 109. For application reasons and continuity with ENDF/B-VII.1 decisions, ENDF/B-VIII.0 continues to reproduce the data by Drake [287–289]. The other existing data set by Nellis *et al.* [293] are also fairly well reproduced. As in the case of ^{235}U(n,xγ) reaction, the available experimental double differential cross section are also well reproduced, at 1, 2 and 14 MeV incident neutron energy (see Figs. 110 – 112). As was the case for the ^{235}U(n,f) reaction, the fission gamma production dominates, as illustrated in Fig. 113.

V. PROMPT FISSION NEUTRON MULTIPLICITY DISTRIBUTION P(ν)

Although it is often sufficient to know the average prompt fission neutron multiplicity $\overline{\nu}$ for criticality benchmark simulations, the distribution of prompt neutron P(ν) and its first three moments are commonly used in safeguard and nuclear assay applications where neutron multiplicity counting techniques enable quantitative assessment of masses and multiplications of fissile materials [297]. Such data have not been included in past evaluations, and no ENDF format even existed for storing this information. Users in need of these data would therefore rely on a direct implementation of the neutron distribution in special-purpose transport codes [298].

ENDF/B-VIII.0 now includes evaluated data for P($\nu; E_{\text{inc}}$) for ^{235,238}U and ^{239}Pu for incident neutron energies from thermal up to 20 MeV, using a newly accepted ENDF format [299].

A. Experimental data

Accurate experimental data on P(ν) exist for many spontaneous fission reactions [300] and for only a few thermal-neutron induced reactions. Data for higher incident neutron energies are almost non-existent. A summary of the available data for the three isotopes considered here is given in Table XXVI. In addition to those data, Zucker and Holden [301] evaluated the higher moments of P(ν) using data from Soleilhac *et al.* [302] for ^{235,238}U and ^{239}Pu for incident neutron energies up to about 10 MeV. These data were deemed of poor quality and unreliable, especially above 10 MeV. Later on, Fréhaut revisited [303] the same data and derived an empirical formula as discussed below.

TABLE XXVI. Experimental data on prompt fission neutron multiplicity distribution P(ν) for neutron-induced fission reactions on ^{235}U and ^{239}Pu.

	First Author	Year	E_{inc}	EXFOR	Reference
^{235}U					
	Boldeman	1985	thermal	30772-010	[304]
	Gwin	1984	0.02-0.1 eV	12833-007	[213]
	Franklyn	1978	thermal	30544-002	[305]
	Diven	1956	80 keV	-	[306]
^{239}Pu					
	Boldeman	1985	thermal	30772-011	[304]
	Gwin	1984	0.02-0.1 eV	12833-008	[213]
	Diven	1956	80 keV	-	[306]

B. Empirical Formula

Based on the observation that all measured neutron multiplicity distributions for spontaneous and thermal neutron-induced fission reactions follow a Gaussian reasonable well, Terrell inferred [307] a formula for P(ν), which is given in cumulative form by

$$\sum_{n=0}^{\nu} P(n) = \frac{1}{\sqrt{2\pi}} \int_{-\infty}^{(\nu-\overline{\nu}+1/2+b)/\sigma} \exp(-t^2/2)dt. \quad (2)$$

In practice, Terrell ignored the parameter b which was found to be $b < 10^{-2}$ for all experimental data discussed at the time.

Fréhaut also derived [303] an empirical formula using Gaussian distributions based on his own measurements as a function of incident energy

$$P(\nu) = \frac{K}{\sigma\sqrt{2\pi}} \exp\left[-\frac{1}{2}\left(\frac{\nu-\overline{\nu}}{\sigma}\right)^2\right], \quad (3)$$

where the parameters K and σ were obtained and tabulated from a fit to Fréhaut's data up to about 10 MeV, and for ν values ranging from 0 to 7.

C. Theoretical Calculations

The Los Alamos or Madland-Nix model [228] commonly used to perform prompt fission neutron spectrum (PFNS) calculations with only a few adjustable parameters can also be used to compute $\overline{\nu}$, if enough experimental information is available on the average energy carried away by the prompt γ rays, which is in fact very limited. However, no information can be inferred from this model on the distribution P(ν). Monte Carlo codes developed in the past decade or so are now able to predict such quantities if the primary fission fragment distribution is known well enough. The `CGMF` code [308], developed at LANL, follows the individual de-excitation of all fission fragments produced in a particular fission reaction on an event-by-event basis, and can therefore infer various distributions and correlations, including P(ν). Such calculations have been performed in the case of n+^{235,238}U and n+^{239}Pu from thermal up to 20 MeV, but only for comparisons to the simplified model used in this evaluation, as explained below.

D. Evaluation

For ENDF/B-VIII.0, the empirical formula (Eq. 2) intuited by Terrell was used and scaled to match the existing evaluated $\overline{\nu}$ as a function of incident energy present in ENDF/B-VIII.0. The parameter b was set to zero, but an iterative procedure was used to correct the initial results to ensure the zeroth and first moments of the distribution are equal to 1.0 and $\overline{\nu}$ from ENDF/B-VIII.0, respectively, and that the distribution is only defined for $\nu \geq 0$. This iterative procedure converges in only a few steps and achieves all these requirements simultaneously.

Given that $\overline{\nu}(E_{\rm inc})$ has already been evaluated for ENDF/B-VIII.0, and setting b=0, the only free parameter left in Eq. 2 is σ. This parameter was fitted to reproduce the experimental ν distributions at thermal energy for all three fission reactions studied here. The results were shown to be in close agreement with the Zucker-Holden evaluation up to 10 MeV, and in reasonable agreement with `CGMF` calculations up to 20 MeV, therefore no energy dependence on σ was considered in this work.

Results for ^{235}U thermal neutron-induced fission reaction are shown in Figs. 114 and 115. In this case, relatively good agreement exists among the different experimental data sets, except for Franklyn data, and for Diven data for high-values of ν. The parameter σ appearing in Eq. 2 has been set to 1.08, as proposed by Terrell.

The incident energy dependence of the neutron multiplicity distribution is best captured by plotting the first factorial moments as a function of $E_{\rm inc}$, as shown in Fig. 116. The ENDF/B-VIII.0 evaluated data are compared to results from `CGMF` calculations, to Zucker and Holden evaluation [301] and to an evaluation by Lestone [309]. The agreement with both is quite good, even though Zucker-Holden results tend to lie above Lestone's.

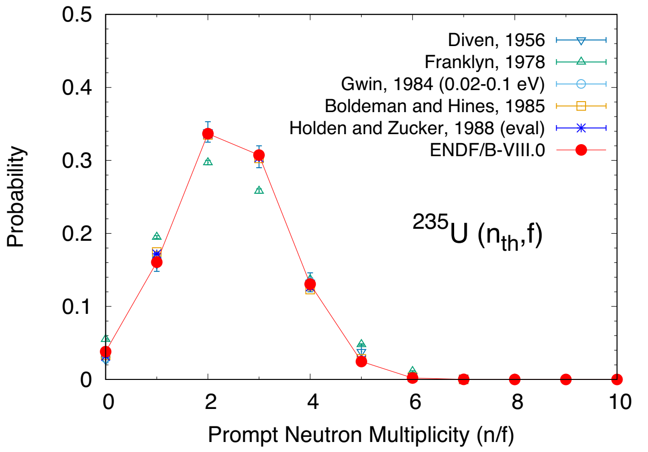

FIG. 114. (Color online) Prompt fission neutron multiplicity distribution for the thermal neutron-induced fission reaction on ^{235}U.

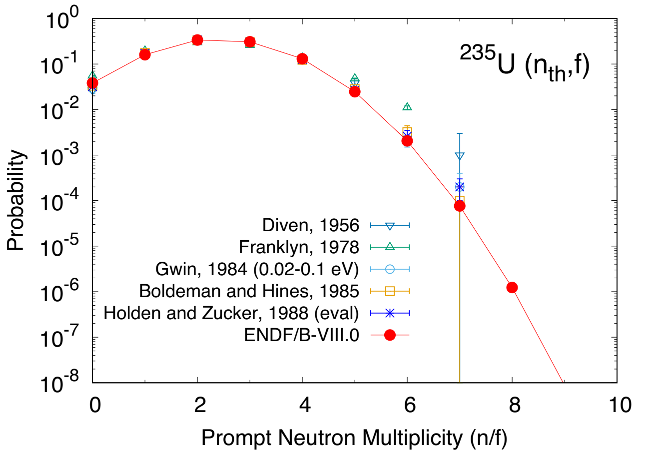

FIG. 115. (Color online) Same as Fig. 114 but in log-scale for the y-axis.

The `CGMF` results tend to underestimate the second and third factorial moments at lower incident neutron energies, mostly below the threshold for second-chance fission, and overestimate them at higher energies. A better representation of the fission fragment kinetic energies would certainly be needed to reproduce the evaluated results.

Note that Lestone results reported in Tables XXVII-XXIX correspond to the formula and parameters from Ref. [309] but tuned to reproduce $\overline{\nu}$ from ENDF/B-VIII.0. Lestone's formula present in the `MCNP`® code uses $\overline{\nu}$ as input to infer the higher moments of the distribution, as opposed to an incident neutron energy. Hence, slight differences will appear between the numbers reported here and the ones tabulated in Ref. [309].

The cross section of ^{238}U(n, f) is negligible below the fast energy range, and therefore no data exist near the thermal point. The Terrell formula was used again but with $\sigma = 1.20$ this time. As can be seen in Fig. 117, the trends of the factorial moments of P(ν) evaluated by Zucker and Holden are well reproduced up to 10 MeV, but tend to deviate below 2 MeV. This is mostly due to differences in the evaluations of $\overline{\nu}$ at low energies. Zucker and Holden report a thermal value of 2.275 compared to 2.399 for ENDF/B-VIII.0, and 2.448 for ENDF/B-VII.1. Lestone's results lie below both ENDF/B-VIII.0 and Zucker-Holden, but tend to get closer to ENDF/B-VIII.0 with increasing neutron energy.

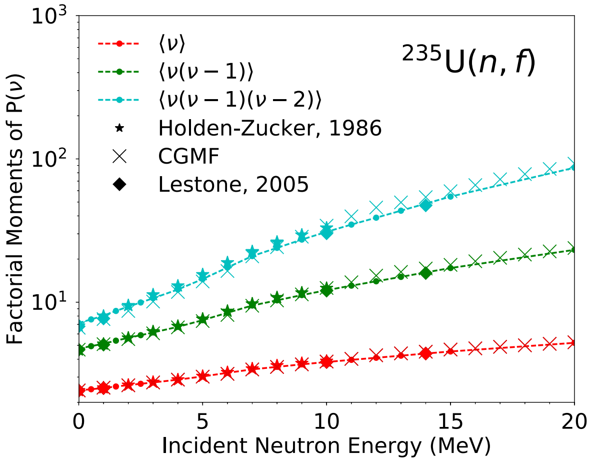

FIG. 116. (Color online) Factorial moments of the prompt neutron multiplicity distribution for the ^{235}U(n, f) reaction as a function of the incident neutron energy.

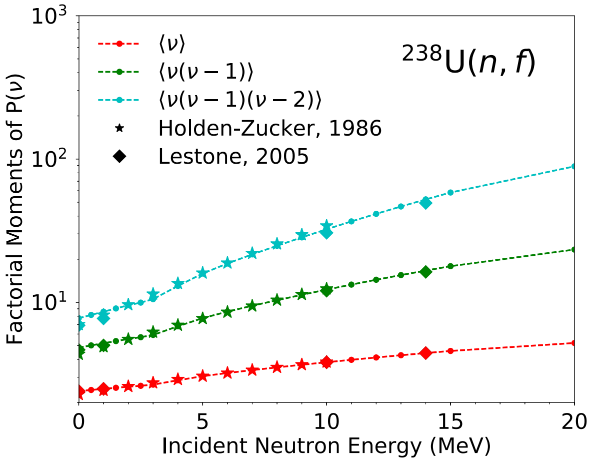

FIG. 117. (Color online) Factorial moments of the prompt neutron multiplicity distribution for the ^{238}U(n, f) reaction as a function of the incident neutron energy.

The evaluated distribution P(ν) for the thermal neutron-induced fission reaction of ^{239}Pu is shown in Figs. 118 and 119 in comparison with experimental data. The evaluation used Terrell's formula (Eq. 2) with $\sigma = 1.16$, except at the thermal energy point. Applying the Terrell equation at thermal energy would lead to values close to Lestone's result, which underestimates the probability for $\nu = 2$ by about 2%, and overestimates the experimental $P(0)$ by a factor of 2. At thermal energy, the Zucker-Holden evaluation was used instead, corrected to fit $\overline{\nu}_{\rm th}$ from ENDF/B-VIII.0.

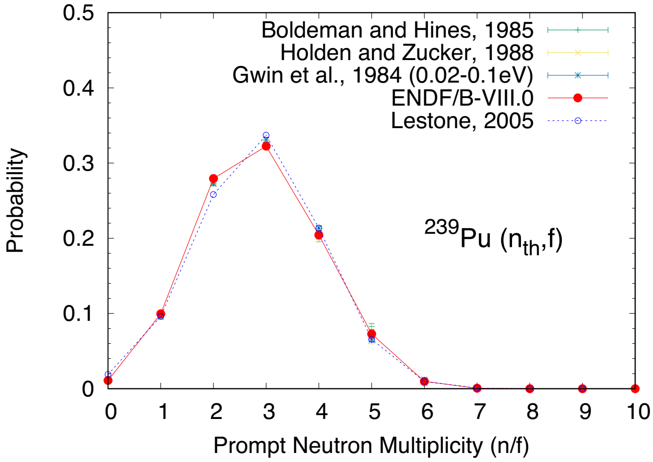

FIG. 118. (Color online) Prompt fission neutron multiplicity distribution for the thermal neutron-induced fission reaction on ^{239}Pu.

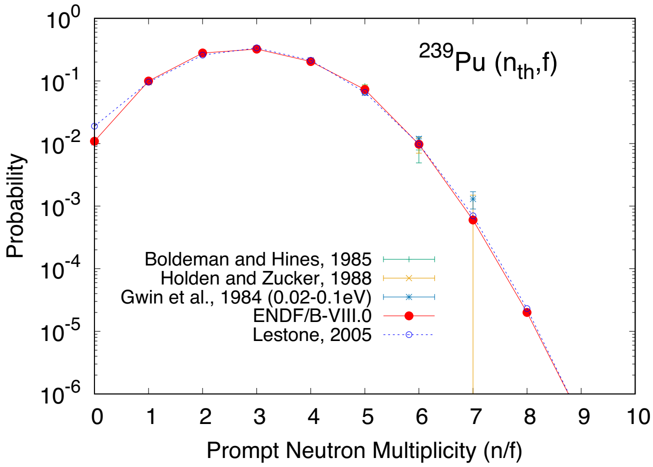

FIG. 119. (Color online) Same as Fig. 118 but in log-scale for the y-axis.

The energy dependence of the factorial moments for ^{239}Pu (n,f) is shown in Fig. 120 and is good agreement with Zucker-Holden evaluation up to 10 MeV, as well as with `CGMF` calculations all the way up to 20 MeV, except for the third factorial moment. Lestone's results are in better agreement with ENDF/B-VIII.0.

A new ENDF format was proposed and accepted to accommodate this type of data [299].

E. Delayed Neutrons from ENDF/B-VI.8

There were no changes to the delayed neutron data from ENDF/B-VI.8 in ENDF/B-VIII.0

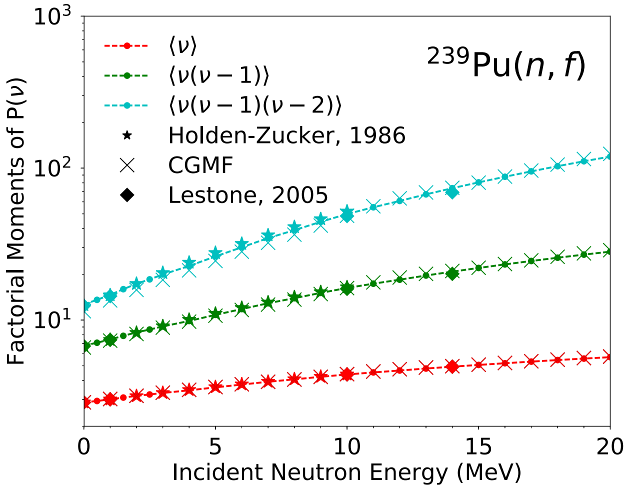

FIG. 120. (Color online) Factorial moments of the prompt neutron multiplicity distribution for ^{239}Pu(n, f) reaction as a function of the incident neutron energy.

F. Components of Energy Release Due to Fission (MT=458)

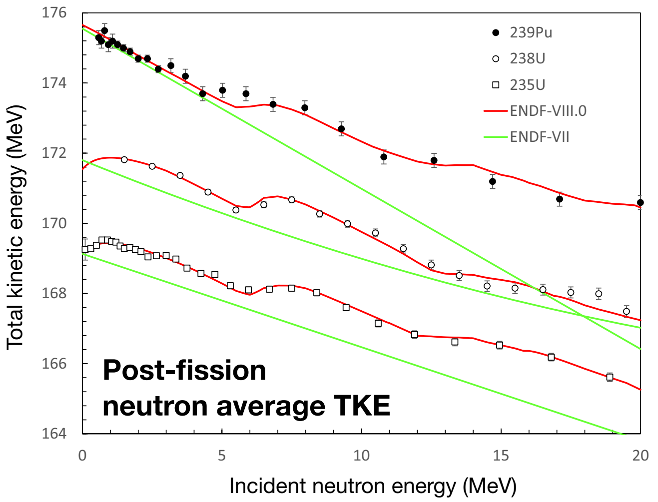

FIG. 121. (Color online) Scaled experimental data (see text) for the post-fission neutron emission average TKE as a function of incident neutron energy, E_n, for the three targets ^{239}Pu [310], ^{238}U [311], and ^{235}U [312] (symbols). The red and green curves show the ENDF-VIII.0 and VII evaluations, respectively. The ^{238}U scaled data and evaluation curve have been shifted upwards by 2 MeV, to avoid clutter.

Predictions for the incident-neutron energy dependence of the average total kinetic energy (TKE) release in the ^{239}Pu(n,f) and ^{235}U(n,f) fragment beyond the threshold of second-chance fission [313] have been confirmed by experiment [310, 312]. An evaluation of the measured energy dependence of the post-neutron emission average TKE has been performed by an adjustment of some of the model parameters described in Ref. [313] based on experimental data for the three target isotopes ^{235,238}U [311, 312] and ^{239}Pu [310]. The nominal pre-neutron emission TKEs

TABLE XXVII. Neutron multiplicity distributions and their first three factorial moments $\langle\nu\rangle$, $\langle\nu(\nu-1)\rangle$, and $\langle\nu(\nu-1)(\nu-2)\rangle$ for ^{239}Pu at thermal, 1.0, 10.0 and 14.0 MeV incident neutron energies. The ENDF/B-VIII.0 values are compared to Zucker-Holden [301] and Lestone [309] evaluations.

	^{239}**Pu**										
	Thermal			1 MeV			10 MeV			14 MeV	
n	B-VIII.0	[309]	[301]	B-VIII.0	[309]	[301]	B-VIII.0	[309]	[301]	B-VIII.0	[309]
0	0.0109	0.0189	0.0109	0.0154	0.0139	0.0085	0.0004	0.0003	0.0002	0.0001	0.0000
1	0.0995	0.0960	0.0995	0.0817	0.0793	0.0790	0.0063	0.0054	0.0038	0.0015	0.0012
2	0.2795	0.2582	0.2749	0.2342	0.2354	0.2536	0.0457	0.0434	0.0492	0.0165	0.0149
3	0.3225	0.3370	0.3269	0.3349	0.3390	0.3290	0.1709	0.1697	0.1822	0.0904	0.0870
4	0.2045	0.2137	0.2046	0.2350	0.2373	0.2328	0.3169	0.3214	0.3154	0.2462	0.2464
5	0.0727	0.0657	0.0727	0.0832	0.0806	0.0800	0.2921	0.2958	0.2687	0.3330	0.3386
6	0.0097	0.0098	0.0097	0.0145	0.0132	0.0156	0.1339	0.1323	0.1295	0.2240	0.2261
7	0.0006	0.0007	0.0006	0.0012	0.0010	0.0012	0.0304	0.0286	0.0432	0.0749	0.0733
8	0.0000	0.0000	0.0000	0.0000	0.0000	0.0003	0.0034	0.0030	0.0075	0.0124	0.0115
9	0.0000	0.0000	0.0000	0.0000	0.0000	-	0.0002	0.0002	-	0.0010	-
$\langle\nu\rangle$	2.8705	2.8705	2.876	3.0065	3.0065	3.0089	4.3837	4.3837	4.3944	4.9325	4.9325
$\langle\nu(\nu-1)\rangle$	6.7212	6.7399	6.7480	7.4508	7.4054	7.4108	16.2619	16.0483	16.4751	20.8258	20.1436
$\langle\nu(\nu-1)(\nu-2)\rangle$	12.5076	12.4148	12.5894	14.6580	14.3730	14.5928	49.86243	48.3657	51.9416	73.7387	69.2813

TABLE XXVIII. Same as Table XXVII for ^{235}U.

	^{235}**U**										
	Thermal			1 MeV			10 MeV			14 MeV	
n	B-VIII.0	[309]	[301]	B-VIII.0	[309]	[301]	B-VIII.0	[309]	[301]	B-VIII.0	[309]
0	0.0382	0.0396	0.0317	0.0312	0.0323	0.0238	0.0011	0.0011	0.0004	0.0002	0.0002
1	0.1605	0.1619	0.1717	0.1430	0.1443	0.1556	0.0148	0.0153	0.0080	0.0037	0.0039
2	0.3367	0.3315	0.3362	0.3238	0.3197	0.3217	0.0948	0.0959	0.1002	0.0371	0.0379
3	0.3073	0.3088	0.3040	0.3217	0.3222	0.3150	0.2725	0.2716	0.2779	0.1668	0.1673
4	0.1306	0.1309	0.1269	0.1475	0.1477	0.1445	0.3521	0.3497	0.3343	0.3367	0.3346
5	0.0246	0.0251	0.0267	0.0301	0.0307	0.0356	0.2048	0.2049	0.1966	0.3058	0.3045
6	0.0021	0.0022	0.0026	0.0027	0.0029	0.0034	0.0535	0.0545	0.0650	0.1250	0.1260
7	0.0001	0.0001	0.0001	0.0001	0.0001	0.0005	0.0062	0.0065	0.0175	0.0229	0.0236
8	0.0000	0.0000	-	0.0000	0.0000	-	0.0003	0.0004	-	0.0019	0.0020
9	0.0000	0.0000	-	0.0000	0.0000	-	0.0001	0.0001	-	0.0001	0.0001
$\langle\nu\rangle$	2.4140	2.4140	2.4140	2.5129	2.5129	2.5237	3.8212	3.8212	3.8750	4.3796	4.3796
$\langle\nu(\nu-1)\rangle$	4.6410	4.657	4.6382	5.0352	5.0509	5.1014	12.0300	12.0270	12.4971	16.0508	15.9567
$\langle\nu(\nu-1)(\nu-2)\rangle$	6.7163	6.779	6.8176	7.6242	7.6912	8.0012	30.2106	30.2348	32.9646	47.8910	47.3853

at low neutron energy (E_n=0 for first-chance fission, and below the thresholds discussed below for second- and third-chance fission, assuming a linear relationship between average TKE and E_n above the threshold values), were obtained by a previous analysis [313]. Similarly, model parameters which allow a downwards curve in the TKE with decreasing E_n, within a few MeV of zero (or the corresponding threshold energies for multi-chance fission) for the uranium isotopes, are also fixed at the previously assessed values [313]. A simultaneous fit to all three isotopes was obtained by an adjustment of assumed global parameters: (1) a slope in TKE versus E_n, $dTKE/dE_n = -0.337$; (2) the E_n threshold for second-chance fission TKE to start falling linearly with E_n (E_2 = 5.82 MeV); and (3) the corresponding threshold for third-chance fission (E_3 = 15.82 MeV) for the odd-mass targets (^{235}U and ^{239}Pu). The quality of the agreement with the experimental data could not be improved by allowing the first two parameters to vary with the target isotope. However, a significantly better match to the ^{238}U data was obtained by allowing for an accepted even-mass target correction to the third-chance threshold of $E_{3,\text{even}} = E_3 + \delta_{\text{even}}$, with δ_{even}=1.07 MeV. There is the possibility of a small systematic shift for each of the used data sets [310–312], which is not directly addressed here. With this in mind, the following were scaled (a) ^{235}U TKE assessment by 1.0021 to match the JENDL-4.0 and ENDF/B-VII TKE of 169.13 MeV for thermal neutrons; (b) ^{238}U assessment by 1.0038

TABLE XXIX. Same as Table XXVII for ^{238}U.

	^{238}U										
	Thermal			1 MeV			10 MeV			14 MeV	
n	B-VIII.0	[309]	[301]	B-VIII.0	[309]	[301]	B-VIII.0	[309]	[301]	B-VIII.0	[309]
0	0.0568	0.0448	0.0396	0.0489	0.0378	0.0299	0.0029	0.0015	0.0003	0.0005	0.0002
1	0.1701	0.1667	0.2530	0.1566	0.1515	0.2043	0.0240	0.0176	0.0168	0.0069	0.0042
2	0.3151	0.3263	0.2940	0.3059	0.3170	0.2996	0.1098	0.1004	0.1111	0.0472	0.0381
3	0.2786	0.3014	0.2644	0.2894	0.3128	0.2915	0.2601	0.2696	0.2892	0.1666	0.1617
4	0.1395	0.1313	0.1112	0.1525	0.1456	0.1301	0.3193	0.3415	0.3160	0.3048	0.3235
5	0.0351	0.0269	0.0312	0.0406	0.0319	0.0363	0.2038	0.2040	0.1782	0.2895	0.3052
6	0.0046	0.0026	0.0059	0.0056	0.0033	0.0074	0.0675	0.0574	0.0621	0.1427	0.1358
7	0.0003	0.0001	0.0005	0.0004	0.0002	0.0007	0.0115	0.0076	0.0166	0.0365	0.0284
8	0.0000	0.0000	0.0001	0.0000	0.0000	0.0002	0.0010	0.0005	0.0096	0.0048	0.0028
9	0.0000	0.0000	0.0000	0.0000	0.0000	0.0000	0.0000	0.0000	0.0000	0.0003	0.0002
$\langle\nu\rangle$	2.3990	2.3990	2.2754	2.4863	2.4863	2.4306	3.8144	3.8144	3.8272	4.4213	4.4213
$\langle\nu(\nu-1)\rangle$	4.8277	4.6553	4.3406	5.1763	5.0000	4.8960	12.2574	12.0374	12.4099	16.6496	16.2996
$\langle\nu(\nu-1)(\nu-2)\rangle$	7.7406	6.9035	6.9937	8.5948	7.7085	8.1396	32.3387	30.5355	34.1639	52.2602	49.3086

TABLE XXX. Fission prompt energy release values in units of MeV for $E_{\rm FR}$, $E_{\rm NP}$, $E_{\rm GP}$ and $E_{\rm P}$ for ENDF/B-VII.1 versus ENDF/B-VIII.0.

		$E_{\rm FR}(E_n)$ (Fission Fragments)		$E_{\rm NP}(E_n)$ (Prompt Neutrons)		$E_{\rm GP}(E_n)$ (Prompt Gammas)		$E_{\rm P}(E_n)$ (Total Prompt)	
Nuclide	Incident Energy E_n	VIII.0	VII.1	VIII.0	VII.1	VIII.0	VII.1	VIII.0	VII.1
^{235}U	0.0253 eV	169.130	169.130	4.829	4.838	7.281	6.600	181.240	180.568
	1.0 MeV	169.441	168.864	5.089	5.138	7.970	6.678	182.500	180.680
	14.0 MeV	166.724	165.406	8.838	9.044	10.292	7.688	185.854	182.138
^{238}U	0.0253 eV	169.542	169.800	4.631	4.558	5.610	6.680	179.783	181.038
	1.0 MeV	169.871	169.481	4.867	4.865	6.140	6.804	180.878	181.150
	14.0 MeV	166.530	166.102	9.225	8.856	7.929	8.415	183.684	183.373
^{239}Pu	0.0253 eV	175.655	175.550	6.071	6.128	6.369	6.741	188.095	188.419
	1.0 MeV	175.233	175.093	6.424	6.471	7.625	6.856	189.283	188.420
	14.0 MeV	171.660	169.158	10.644	10.927	10.034	8.039	192.338	188.124

to obtain the best match to both the JENDL-4.0 value of 169.75 MeV near threshold (∼1.3 MeV) and the ENDF/B-V TKE of 169.57 MeV for ∼3.1 MeV incident neutrons [314]; and (c) ^{239}Pu assessment by 1.00053 to match the JENDL-4.0 TKE of 175.655 MeV for thermal neutrons.

Figure 121 displays the relevant experimental data scaled by the above discussed factors, along with the present evaluation (red curves) and the previous ENDF-VII evaluation (green curves). Notice that the new evaluation captures the structure associated with multi-chance fission. A summary of the prompt fission energy release to fission fragments, neutrons, and gamma rays is given in Table XXX.

VI. NEUTRON REACTION COVARIANCES

A. Overview of ENDF/B-VIII.0 Covariances

The ENDF/B-VIII.0 neutron sublibrary is comprised of 557 distinct, mostly isotopic, materials. From the perspective of covariances, these can be grouped into several categories (new, unchanged and changed covariances) with respect to the presence or absence of covariance data. The number of these materials in each category are provided in Table XXXI. For the most part, the pre-existing covariance data were ported unchanged from ENDF/B-VII.1 [2] to ENDF/B-VIII.0 as can be seen in Table XXXI. Among the new and changed covariance data are recent results provided by the CIELO project [6, 7]. New and changed ENDF/B-VIII.0 covariances, apart from those provided by the CIELO project, are partially discussed within this paper along with their corresponding mean values.

TABLE XXXI. Summary of covariance evaluations in ENDF/B-VIII.0.

	Num. evals. with cov.	Num. evals. missing cov.	Total
New	73	95	168
Modified	34	102	136
Unchanged	75	178	253
Total	182	375	557

B. Covariance Quality Assurance

In this section, we will make some general comments on covariance quality assurance and on their intended use within respect for application calculations. It is critically important for users of covariance matrices to gain some familiarity with the sources of information used or intentionally not used in the evaluation of those matrices. Evaluated covariances are often obtained by a statistical combination of experimental data, model values and their respective covariances. Expert judgment might be applied to the resulting covariances a-posterior as was the case, for instance, for the ^{235}U(n,f) cross-section covariances. However, in general, no integral data were included in estimating evaluated uncertainties, although some limited integral data were used to "calibrate" evaluated mean values. In other words, the library may perform better in benchmark calculations than if no integral data were used, but the evaluated uncertainties and covariances do not reflect this information. When simulating specific benchmarks, it is therefore expected that the resulting propagated uncertainties could be much larger than what is known experimentally for those particular integral data.

To be acceptable for inclusion in ENDF/B-VIII.0, covariance data submitted by evaluators are required to satisfy a battery of formatting and mathematical checks that are applied as part of the quality assurance procedure associated with development of the library [315]. This includes the capacity for these data to be processed so that they can be used by various application codes. However, satisfying these tests does not guarantee that the results obtained from their use in applications will be acceptable or meaningful. That can only be ascertained by experience gained from their use. The present section discusses some general issues related to how the quality of these covariance data can be assessed, as well as how this impacts on their usage in applications.

Evaluated covariances for neutron-induced reaction cross sections in ENDF/B are intended to provide quantitative estimates of data uncertainties and correlations that are based on consideration of underlying uncertainties in the available experimental and model-calculated data, as well as on the employed evaluation procedures. Since covariances correspond to uncertainties, there are no uniquely correct covariances. Covariance data cannot be benchmarked as in the case of evaluated mean values. Covariances that are generated in an evaluation depend on the quality and specified (or assumed) uncertainties of the selected input data as well as on the evaluation methodologies used. However, covariances can be reasonable or unreasonable based on consideration of various factors that influence how these data are generated and used in applications. These judgments regarding the quality of covariance data unavoidably are subjective. Nevertheless, there is merit in assessing covariance quality in an independent and consistent way that is as unbiased as possible.

Some indication as to the basic reasonableness of a particular covariance file might be surmised, at least qualitatively, by examining it directly outside the context of particular applications through the application of a few "common sense" criteria. One of these might be the notion that the uncertainties associated with an evaluation should be consistent with the inherent quality of the input data, *e.g.*, scatter in experimental values as well as observed differences between experimental data and theoretical predictions. Another criterion could be that evaluated uncertainties for specific materials and reaction processes that are smaller in magnitude than those corresponding to similar physical processes included in the Neutron Standards (also part of ENDF/B-VIII.0 and mentioned in this paper) and are often measured as ratios to these neutron standards should be viewed as unrealistic. Also, it seems reasonable to suggest that credible correlation data ought to be provided in covariance files for specific materials and reaction process. None of these "common sense" arguments are fool-proof, however: the scatter in experimental values may be due to a normalization error that could be corrected by the evaluator; the "standards" criterion could also be criticized as it is relative to another subjective evaluation, albeit one that has received a lot more attention than most evaluations. Of course, additional or different criteria for screening individual covariance files could be imposed. As of this time, no such screening criteria, nor automated algorithms to implement them, have been established and implemented by the nuclear data evaluation community.

C. Relation to Integral Data Uncertainties

It has been evident since the early years of nuclear science that many good-quality, system-related integral data, *e.g.*, those related to criticality, tend to be significantly more accurate than the differential data that traditionally are used to produce ENDF/B evaluations. Nevertheless, these integral data have either not been included, or have been considered only indirectly, in generating ENDF/B evaluations because of the belief by the nuclear data community that this library should be a general purpose library that is based on fundamental information alone, and that it should not be overtly influenced by integral data associated with specific applications. This situation has resulted in a long-standing point of contention between many data users and ENDF/B data evaluators that is worth discussing in some detail here because of the fundamental importance of this matter from both physical and practical perspectives.

Recent applied investigations in reactor development and spent-fuel criticality safety analyses that have utilized ENDF/B covariance data to examine propagated uncertainties have led to the conclusion that the magnitudes of these derived uncertainties far exceed differences between measured integral parameters, *e.g.*, the criticality parameter k_{eff}, and corresponding values calculated using ENDF/B central values, sometimes by as much as an order of magnitude. Why are calculated criticality k_{eff} uncertainties so large, *i.e.*, often exceeding 1% (1000 pcm)? The reason is that many of the calculated integral quantities that are important for applications are extremely sensitive to certain differential data, *e.g.*, major actinide fission cross-sections, nu-bar, and fission-neutron emission spectra. Thus, even though the nuclear science community is measuring fission data to increasing accuracies, and theoretical models are improving, it still leads to large k_{eff} uncertainties calculated by simulation codes such as `MCNP`® [316]. For example, if one considers Jezebel [317] (a bare plutonium sphere) an uncertainty of 1% in the fission cross section (n,f) causes a 750 pcm uncertainty in k_{eff}; a 50 keV uncertainty in the average PFNS spectrum energy causes a 350 pcm uncertainty in k_{eff}; a 0.5% uncertainty in $\overline{\nu}$ causes a 200 pcm uncertainty in k_{eff}; and so on. These uncertainties are often given as uncorrelated as they are evaluated separately: for instance, in ENDF/B-VIII, the ^{239}Pu fission cross section, PFNS, and $\overline{\nu}$ are all evaluated independently using different physics models and uncorrelated experimental data. When one includes uncertainties owing to scattering angular distributions, inelastic scattering cross-sections and secondary neutron distributions, integral benchmark facility characterization parameters, and so on, frequently one finds that derived integral k_{eff} uncertainties of over 1000 pcm can result from using the ENDF/B covariance data. Applied nuclear data users cannot and will not accept a data library that yields C/E results that differ from unity by such large amounts. On the other hand, evaluators currently cannot produce results that meet the stringent requirements of these users based on pure, unaltered differential data alone. This is exactly why integral criticality experiments are needed, and it was the rationale for performing critical assembly measurements since the earliest days of nuclear science. One might well expect that when one computes C/E for a wide range of critical assemblies from the mean values of the ENDF data, unless some modifications are made, it will be found that rms deviations should occur that exceed 1000 pcm. But this is not the case. For example, the *rms* deviation for MCNP calculations of the 119 critical assemblies in the "Mosteller suite" [159] is about 400 pcm, *i.e.,* much smaller. To provide a more comprehensive understanding of this state of affairs we address the following questions in some detail:

- **Question 1:** Why are C/E values obtained in comparisons of measured and calculated integral results far closer to unity than might be expected from any evaluation based purely on differential data and their perceived associated uncertainties? The answer is given above, but we reiterate it here as it is an important point to make. Although many of the data in ENDF/B-VIII.0, like those in earlier versions, come from evaluations of fundamental, differential, experimental and model-calculated data, in certain cases "calibration" choices have been made to modify mean values within their uncertainty bands so as to optimize global matches to criticality (for example, the aforementioned Mosteller suite). This was done principally by making small adjustments to nu-bar. This pragmatic approach has been adopted by evaluators since most ENDF/B evaluated data users expect and demand good performance of these data in integral criticality simulations. Of course, by doing this one cannot say that ENDF/B evaluated mean values are purely based on differential information, and therefore are not influenced by any existing knowledge of integral data. In spite of this lack of purity, ENDF/B-VIII.0 cannot be considered as an "adjusted" library where integral data have been included formally in the employed evaluation procedures, *e.g.*, those that involve the least-squares method [318]. The uncertainties in ENDF/B-VIII.0, for the most part, tend to reflect available fundamental data that have been treated according to accepted evaluation procedures, and they have not been reduced, nor have any extraneous correlations been introduced, through formal inclusion of integral results.

- **Question 2:** Since many data users would like to see smaller uncertainties reflected in ENDF/B libraries, and rigorous evaluation procedures exist that would permit accurate integral data to be included, why to this day has it been considered by the ENDF/B evaluation community to be unwise to do so? The reason is that in order to incorporate integral data in a formal evaluation procedure properly would require that evaluations of all the materials and processes (or at least the most important ones) involved in the included integral benchmark facilities be carried out simultaneously. To do this would require possessing extensive knowledge of cross-reaction and cross-material covariance data for the fundamental input values that are simply not available. Of course, in spite of the absence of this much-needed information, adjusted libraries are nevertheless being generated for special applications. In these instances, ENDF/B is generally treated as a prior and integral data are introduced to adjust both cross-sections and covariances. Uncertainties are indeed reduced by these procedures. Unfortunately, special-usage libraries of this sort tend to fail when used in applications that do not closely resemble those of the benchmark suite used in the adjustment process. Therefore, such adjusted libraries should not be considered as appropriate for different applications.

- **Question 3:** What is the prognosis that the technical concerns discussed above can be resolved eventually? Several subgroups of the Nuclear Energy Agency Working Party for Evaluation Cooperation (WPEC), *e.g.*, SG-39 [15], SG-44 [319] and SG-46 [320], are attempting to address this important matter. Investigations in this area need to address several issues. First, a determination of the sensitivities of computed integral results to specific evaluated differential nuclear data needs to be made for the most important applications. This will help to focus effort in theoretical modeling, experimental measurements, and uncertainty quantification on the most important materials, with the goal of generating credible information on uncertainty magnitudes and correlations (including both cross-reaction and cross-material correlations). The subsequent focused effort on reducing uncertainties on the evaluated data can possibly reduce the need for calibration of evaluated mean values. Second, users of nuclear data for applications need to define clearly (and realistically) their quantitative needs and expectations for evaluated data accuracies. This information will aid again in focusing on reducing uncertainties in the differential experimental data and theoretical predictions of observables important for application. A productive dialogue between data users and producers is essential for this to happen. Third, evaluation methods need to be developed that include integral data selectively in ways that do not introduce excessive biases that limit their use to a few specific applications.

- **Question 4:** Should the CSEWG evaluation community that produces ENDF/B also assume responsibility for generating various adjusted libraries to satisfy the needs for specific applications? At this time it appears to be inadvisable for CSEWG to do this considering the limited resources available to this community. Its primary responsibility should be to generate needed updates to ENDF/B on a cycle of approximately 5 years. CSEWG evaluators should devote their efforts to producing the best possible general purpose library, including covariances, based on analyses that incorporate carefully vetted theoretical and experimental fundamental physics data as well as employing rigorous, contemporary evaluation methodologies. That is not to say that it is wrong for any group to produce adjusted libraries that are tailored for specific applications by proper inclusion of relevant integral benchmark data. This is simply not an appropriate task for CSEWG at this point. Furthermore, applied data users should not confuse such adjusted libraries with ENDF/B, nor should they be misused. The range of applicability of any particular adjusted library should always be clearly established and documented.

D. Outlook

In summary, while there have been improvements in the covariance content of ENDF/B-VIII.0, when compared with version VII.1, achievement of the goal of providing a library which includes comprehensive covariance data that are viewed as adequate for uncertainty propagation or data adjustment applications remains elusive. For the foreseeable future it is likely that the current incremental approach toward improving ENDF/B evaluations (including covariances) will be continued. Furthermore, one can hope that work directed toward improving the predictive accuracy of theoretical models and the quality of basic experimental data, as well as advances in evaluation methodologies that make optimal use of these data, will lessen the need for intuitive modification of evaluated mean values in order to achieve C/E consistencies for integral benchmark comparisons that will satisfy the requirements of applied data users.

VII. THERMAL NEUTRON SCATTERING SUBLIBRARY

The thermal neutron scattering sublibrary contains 33 evaluations for 24 materials. Eight materials (light water, heavy water, polyethylene, graphite, uranium dioxide, beryllium, beryllium oxide and silicon dioxide) were reevaluated, and six new materials were added (Lucite, yttrium hydride, silicon carbide, light water ice, reactor graphite, and uranium mononitride). The remaining evaluations were taken from the ENDF/B-VII.1 library (aluminum, benzene, liquid ortho- and para-hydrogen, liquid ortho- and para-deuterium, liquid and solid methane, iron, and zirconium hydride).

Three of the updated materials were separated into different evaluations: silicon dioxide is now available in alpha and beta phases, and graphite was evaluated as crystalline graphite and porous reactor grade graphite. The evaluation for liquid heavy water was separated into two evaluations, one for deuterium bound in D_2O, and one for oxygen bound in D_2O.

Previous evaluations of the ENDF/B thermal scattering sublibrary were mainly provided by two institutions: General Atomics in San Diego (ENDF/B-III to ENDF/B-V) [321] and Los Alamos National Laboratory (ENDF/B-VI to ENDF/B-VII) [322]. These evaluations were done in the Gaussian, incoherent approximation as implemented in GASKET (GA) and LEAPR (LANL), using frequency spectra obtained from inelastic neutron scattering experiments (for liquids) or simplified solid models.

In this version of the sublibrary, new and updated evaluations for ENDF/B-VIII.0 were generated by Naval Nuclear Laboratory (NNL), North Carolina State University (NCSU), and Centro Atomico Bariloche, Argentina (CAB). The efforts were coordinated by NEA/WPEC Subgroup 42. The main difference to previous evaluations is the use of computational material science methods (density functional theory, lattice dynamics, and molecular dynamics) in the calculation of the frequency spectra. The new evaluation methods vary from purely computational (NNL YH_2; NCSU Be-metal, BeO, graphite, reactor graphite, SiO_2, SiC, CH_2, $C_5O_2H_8$, UO_2, and UN), computational but adjusted to experimental data (NNL light water ice), to a mixture of computational results and experimental data (CAB H_2O and D_2O).

Details of the evaluation and validation methodologies are given below for each of the new and updated materials.

A. Yttrium Hydride (YH_2)

Yttrium hydride (YH_2) has a CaF_2 type face-centered cubic structure with Y atoms located at the vertices and faces of the unit cell and the H atoms located in the tetrahedral holes between the Y atoms. The evaluations for H and Y bound in YH_2 were generated in the incoherent approximation by Zerkle and Holmes [323] using first-principles density functional theory and lattice dynamics calculations and the LEAPR module of NJOY2012.8. The evaluations are tabulated at 293.6, 400, 500, 600, 700, 800, 1000, 1200, 1400, and 1600 K.

The calculated lattice constant for YH_2 is in excellent agreement with X-ray diffraction measurements [324]. The calculated phonon density of states (DOS) is in agreement with inelastic neutron scattering measurements [325, 326] and the heat capacity derived from the calculated phonon DOS is in agreement with high resolution heat capacity measurements [327]. Finally, the total hydrogen scattering cross section for the H-YH_2 evaluation at 293.6 K is in agreement with published measurements of $YH_{1.90}$ [328] and $YH_{1.88}$ [329] (Fig. 122).

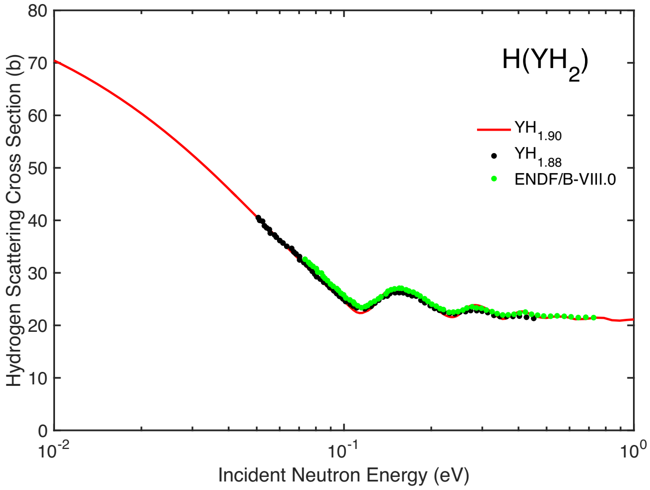

FIG. 122. (Color online) Evaluated H-YH_2 total hydrogen scattering cross section at 293.6 K compared with measurements of $YH_{1.90}$ [328] and $YH_{1.88}$ [329].

B. Water Ice (I_h)

The phase of solid H_2O encountered under common temperature and pressure conditions is ice I_h, a hexagonal crystalline structure with locally ordered but globally disordered molecular orientations. Evaluations for H and O bound in ice I_h were produced by Holmes and Zerkle [330] at NNL for the temperatures of 115, 188.15, 208.15, 228.15, 233.15, 248.15, 253.15, 268.15, and 273.15 K. The phonon spectra for H and O were calculated using first-principles density functional theory and lattice dynamics codes [330]. The modeled structure was constrained by enforcing experimentally measured lattice constants [331]. The phonon spectra were then optimized to account for global variations in molecular alignments based on experimentally measured inelastic neutron scattering energy spectra [332] and total cross sections [333]. The LEAPR module of NJOY2012.8 was used to generate the thermal scattering kernels in the incoherent approximation. Fig. 123 compares experimentally measured total cross sections [333] to ENDF/B-VIII.0 theoretical total cross sections at 115 K.

The ENDF/B-VIII.0 H(Ice-I_h) and O(Ice-I_h) thermal scattering kernels were supplied to the MC21 Monte Carlo transport code to calculate time eigenvalues for the fundamental mode flux decay in ice cylinders of different geometries and at various temperatures. Figure 124 shows a comparison of experimental data from a pulsed-neutron die-away diffusion benchmark [334], theoretical calculations using free-gas thermal scattering kernels, theoretical calculations using the ENDF/B-VII.1 liquid H(H_2O) thermal scattering kernel at a subcooled temperature, and the ENDF/B-VIII.0 H(Ice-I_h) and O(Ice-I_h) thermal scattering kernels.

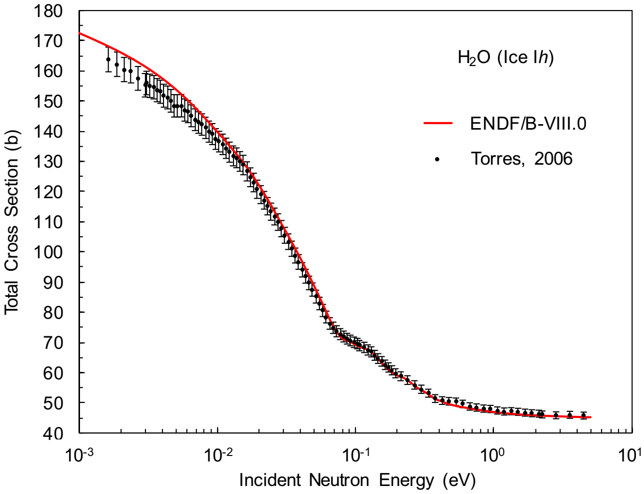

FIG. 123. (Color online) ENDF/B-VIII.0 total cross section for H_2O (ice I_h) at 115 K compared to experimental data by Torres [333].

C. Light Water (H_2O)

The evaluation for H_2O was based on the *CAB Model for Light Water* [335] and was prepared using NJOY99.396 with updates to extend the calculation grids.

Compared with the ENDF/B-VII H-H_2O evaluation by Mattes and Keinert [336], the following changes were

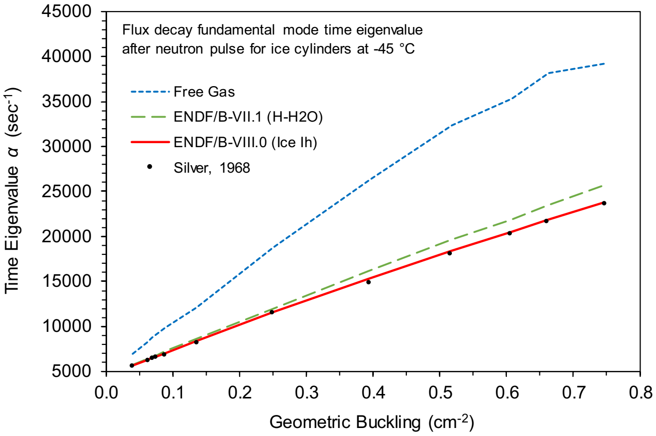

FIG. 124. (Color online) Time eigenvalues for fundamental mode flux decay for a pulsed-neutron die-away diffusion benchmark as a function of geometric buckling for various ice cylinders at 228 K. Experimental data from Silver [334] is compared to MC21 results using the ENDF/B-VIII.0 H(Ice-I_h) and O(Ice-I_h) thermal scattering kernels (bottom curve), the ENDF/B-VII.1 liquid H(H_2O) subcooled thermal scattering kernel (middle curve), and free-gas thermal scattering kernels (top curve). Experimental uncertainties are approximately the radius of the dots.

introduced:

- The low energy interaction was changed from molecular clusters represented with a free gas model, to molecular diffusion using a modified Egelstaff-Schofield diffusion model.
- A continuous spectrum derived from molecular dynamics simulations [337] replaced the continuous spectra from Haywood and Page.
- Alpha and beta grids were refined to allow a better representation of the low energy interaction.

Details of the model and its validation with experimental data can be found in Ref. [335].

The evaluation was generated at the following temperatures: 283.6, 293.6, 300.0, 323.6, 350.0, 373.6, 400.0, 423.6, 450.0, 473.6, 500.0, 523.6, 550.0, 573.6, 600.0, and 623.6 K. Scattering by oxygen atoms is not included in the tabulated scattering law data, and it must be taken into account by adding oxygen as a free gas scatterer of mass 16 to reproduce correctly measurements of the total cross section within experimental uncertainty.

The new evaluation significantly improves the agreement with experimental neutron transmission data for low incident energies (Fig. 125). This improvement is not only seen in absolute value, but also when the temperature derivative is considered (Fig. 126).

In addition to the integral benchmark results shown in Appendix B and Section XII, improvements in reactor temperature coefficients were reported by Scotta [341] and Dos Santos [342].

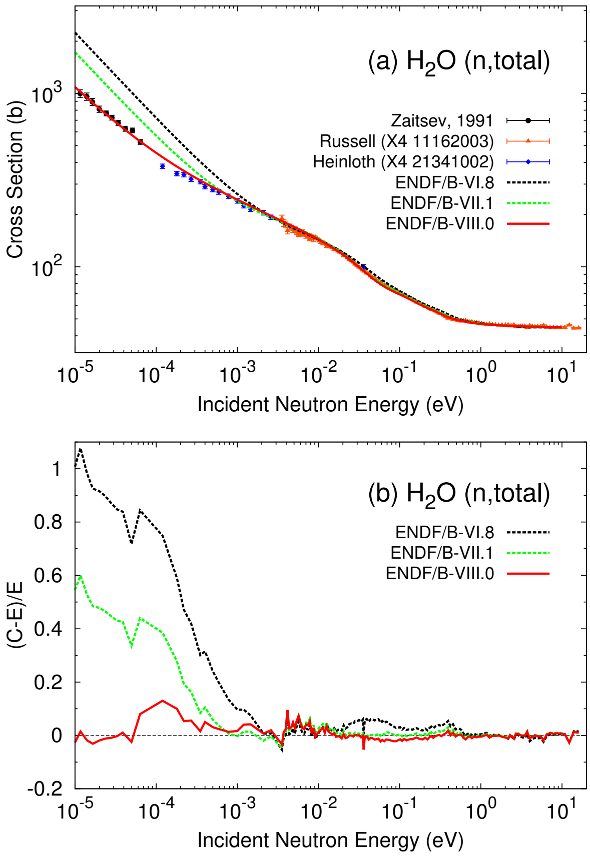

FIG. 125. (Color online) Evaluated ^1H_2O(n,tot) total cross section at 293.6 K, compared with data retrieved from EXFOR and published by Zaitsev *et al.* [338].

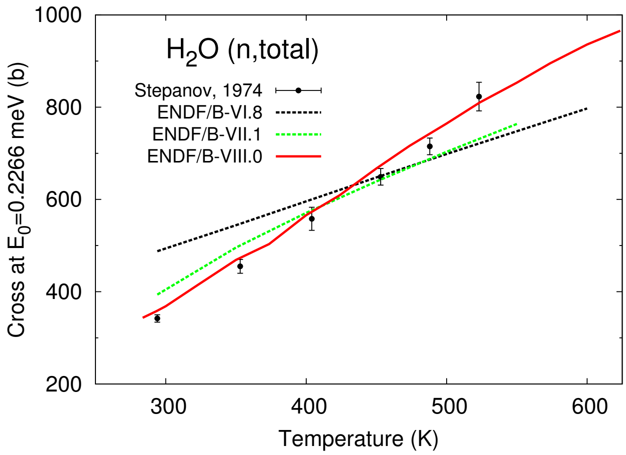

FIG. 126. (Color online) Evaluated ^1H_2O(n,tot) total cross section at different temperatures, compared with data measured by Stepanov *et al.* [339, 340] at 0.2266 meV.

D. Heavy Water (D_2O)

The evaluations for deuterium and oxygen D_2O were based on the *CAB Model for Heavy Water* [335] and were prepared using NJOY99.396 with updates to extend the calculation grids.

Compared with the ENDF/B-VII D-D_2O evaluation by Mattes and Keinert [336], the following changes were introduced:

- Low energy interaction was changed from a free gas model to molecular diffusion using the Egelstaff-Schofield diffusion model.
- The coherent inelastic component was computed in the Sköld approximation, using correction functions computed from molecular dynamics and validated with experimental data from Soper [343], instead of the analytical model used by Mattes.
- A continuous spectrum derived from molecular dynamics simulations [337] replaced the continuous spectra from Haywood and Page.
- Alpha and beta grids were refined to allow a better representation of the low energy interaction.
- Scattering by oxygen bound in heavy water is now treated explicitly in the O(D_2O) evaluation. In heavy water oxygen-16 contributes to approximately 1/3 of the total cross section and a explicit model is needed to correctly reproduce the features found in the experimental cross section, whereas in light water oxygen-16 contributes less than 8% to the total cross section and it can be modeled as a free gas.

Details of the model and its validation with experimental data can be found in Ref. [335].

The changes introduced in the evaluation allowed for a much better comparison with experimental neutron cross section data. In Fig. 127 the evaluated data are compared with measurements by Kropff and Granada retrieved from EXFOR [175]. The new evaluation represents better the reduction in the total cross section at sub-thermal energies (0.3 - 3.0 meV), which was already found in the ENDF/B-VII evaluation, but also reproduces a reduction of the experimental total cross section in the thermal range (10 - 50 meV) which was not possible with previous evaluations. This reduction in the total scattering cross section can be traced to the effects of coherent scattering in oxygen, which was not included in ENDF/B-III through ENDF/B-VII.

The new evaluation also solves an anomalous behavior of the evaluation by Mattes, which predicts a reduction of the total scattering cross section when the temperature is increased from 293 to 350 K (Fig. 128a). The new evaluation shows an increase of the total cross section with increasing temperature (Fig. 128b), and compares well with new total cross section data from transmission experiments at Indiana University [344].

The evaluation was generated at the following temperatures: 283.6, 293.6, 300.0, 323.6, 350.0, 373.6, 400.0, 423.6, 450.0, 473.6, 500.0, 523.6, 550.0, 573.6, 600.0, and 623.6 K.

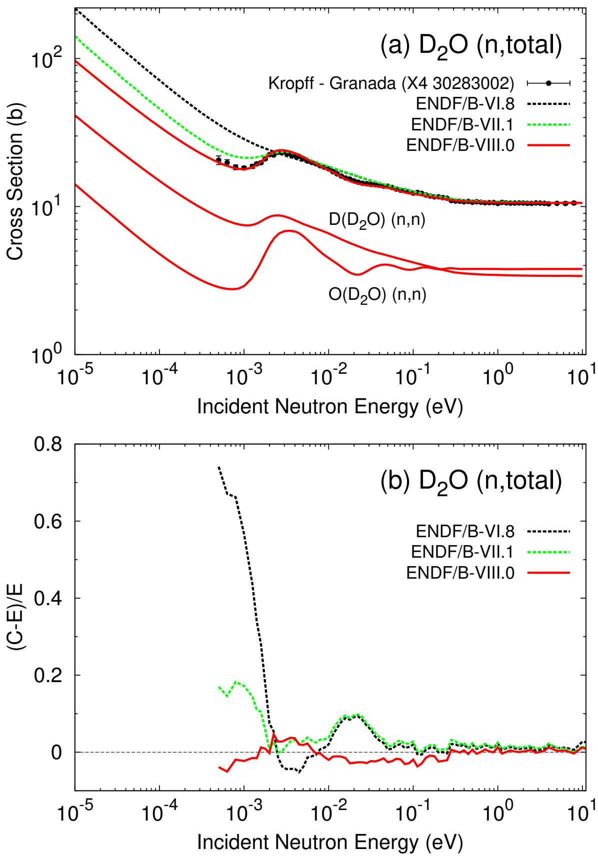

FIG. 127. (Color online) Evaluated D_2O(n,tot) total cross section at 293.6 K, compared with data retrieved from EXFOR.

The effect of the new evaluation in critical systems is significant, with changes of up to 1200 pcm in sensitive critical experiments [346]. Benchmarking with experiments in the ZED-2 reactor resulted in a reduction of 100 - 300 pcm in the multiplication factor when the new thermal scattering libraries were introduced.

E. Beryllium (Be-metal)

Beryllium-metal has been evaluated using modern ab initio lattice dynamics (AILD) techniques, whereby the phonon density of states (DOS) is calculated from ab initio simulations [347–349]. In this case electronic structure calculations were performed on the beryllium hexagonal close-packed crystal structure using the *Vienna Ab-Initio Simulation Package* (VASP)—a density functional theory (DFT) code [350, 351]—to predict Hellmann-Feynman forces. Subsequently, the phonon DOS was generated from these forces using the dynamical matrix approach in the PHONON code [352]. The phonon dispersion relations, which map phonon wave vectors to phonon energy, were also generated. These dispersion relations demonstrated reasonable agreement with measurement [349].

The phonon DOS predicted using the AILD method

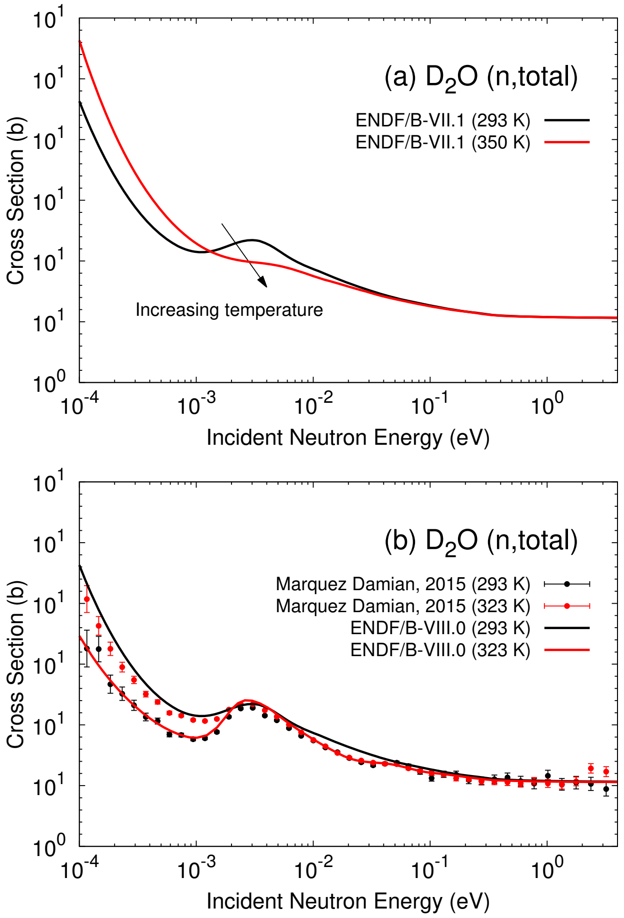

FIG. 128. (Color online) Temperature dependence of the evaluated ^2H_2O(n,tot) total cross section in the ENDF/B-VII library (a), and ENDF/B-VIII.0 library (b) compared with transmission measurements by Márquez Damián [344]. Panel (a) is taken from Fig. 1(a) of Ref. [345].

was used as the fundamental input to the generation of the TSL for Be-metal. An ENDF TSL for Be-metal (File 7, MAT26) was generated with the LEAPR module of the NJOY99.396 nuclear data processing system at the standard temperatures of 296, 400, 500, 600, 700, 800, 1000, and 1200 K within the incoherent approximation [322, 353, 354]. The symmetric TSL, $SS(\alpha,\beta)$, at 296 K tabulated in File 7, MT4 of the ENDF file is illustrated for a range of energy transfers, β, in Fig. 129. The α and β grids in this evaluation have been extended from ENDF/B-VII.1.

Coherent elastic scattering (File 7, MT2) was evaluated using a generalized routine which removes the cubic approximation conventionally applied in LEAPR through the use of a Debye-Waller matrix that explicitly treats asymmetric vibrational behavior in different crystallographic directions [355]. The Debye-Waller matrix used in this generalized routine is calculated from the PHONON code by integrating the phonon DOS.

Both the inelastic and elastic contributions of the total scattering cross section were generated as an integral of the TSL using the THERMR module of NJOY99.396 and are shown in Fig. 130. ENDF/B-VII.1 inelastic cross sections at 296 and 400 K as well as measurement are also shown. The current ENDF/B-VIII.0 evaluation demonstrates improved agreement with measured inelastic scattering cross sections when compared to ENDF/B-VII.1 [356].

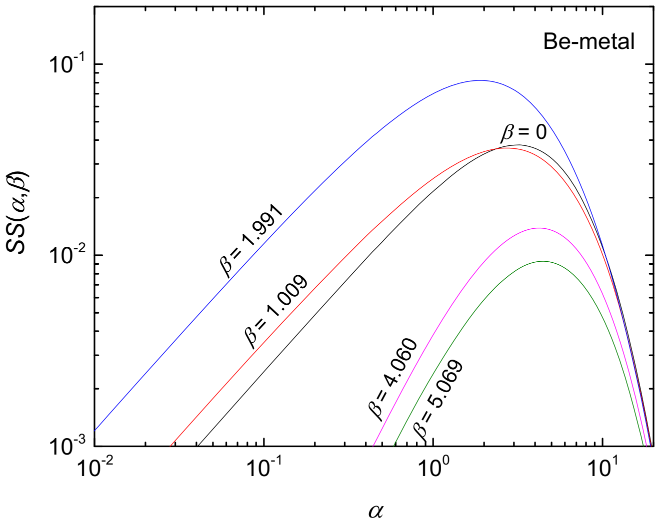

FIG. 129. (Color online) The symmetric TSL of Be-metal at 296 K as a function of momentum transfer, α, for a range of neutron energy transfers, β. $SS(\alpha,\beta)$ for each β is labeled with the corresponding line.

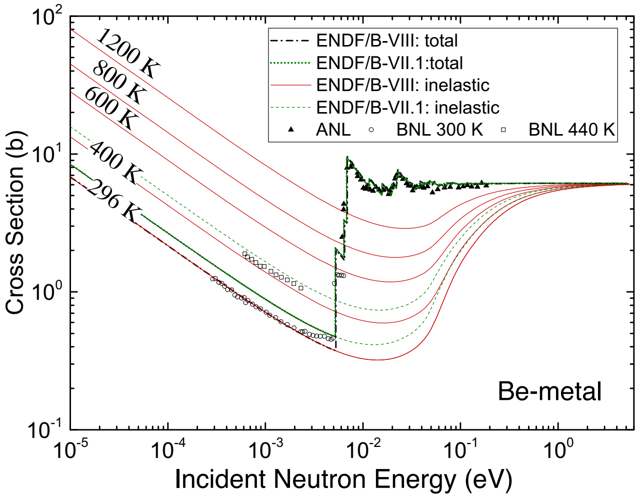

FIG. 130. (Color online) Total thermal neutron scattering cross section of Be-metal compared to measurement (BNL and ANL) [356]. Measured inelastic cross sections (BNL) correspond to 300 K and 440 K. Additionally, the ENDF/B-VIII and ENDF/B-VII.1 inelastic cross sections are shown for select temperatures.

F. Graphite (Crystalline)

Crystalline graphite was evaluated using modern AILD techniques [347, 348]. The Hellmann-Feynman forces describing atomic vibrations were calculated using the VASP DFT code [350, 351]. Graphite is a crystalline material composed of layered planar sheets of hexagonally arranged graphite atoms. While atomic vibrations within each carbon plane may be characterized by covalent bonds, the vibrational behavior between planes is dependent on Van der Waals (VDW) interactions. Furthermore, traditional DFT does not capture these VDW interactions. Therefore, DFT+VDW calculations were performed, whereby a semi-empirical VDW force field is appended to the Hellmann-Feynman forces resulting from the DFT predicted covalent electronic structure [357]. The Hellmann-Feynman forces and VDW forces were used to predict the phonon DOS using the dynamical matrix approach in the PHONON code [352]. The associated phonon dispersion relations were found to demonstrate good agreement with various scattering experiments [358–363].

Using the phonon DOS as the fundamental input, the TSL for crystalline graphite (File 7, MAT31) at 296, 400, 500, 600, 700, 800, 1000, 1200, 1600, and 2000 K were evaluated in the incoherent approximation using the LEAPR module of NJOY99.396 [322, 353, 354]. The symmetric TSL (MT4) at 296 K at various α and β values is shown in Fig. 131. The α and β grids in the present evaluation have been extended from ENDF/B-VII.1

The coherent elastic cross scattering (MT2) of crystalline graphite was evaluated using a generalized coherent elastic routine with a Debye-Waller matrix which captures the asymmetric atomic vibration resulting from the significant variation between the in-plane forces and the out-of-plane forces [355]. The integrated inelastic cross sections, processed with THERMR, are shown in Fig. 132. The evaluated total scattering cross section and the inelastic scattering cross section are compared to ENDF/B-VII.1 as well as measurement [356].

Furthermore, the coherent elastic scattering (MT2) component was also calculated using the graphite specific routine within the LEAPR module of the NJOY code. As a result, the cubic approximation is applied. Based on that, another set of TSL libraries for graphite was evaluated. These libraries have undergone benchmark testing that showed improvement in comparison to the behavior of the ENDF/B-VII.1 graphite TSL libraries [364].

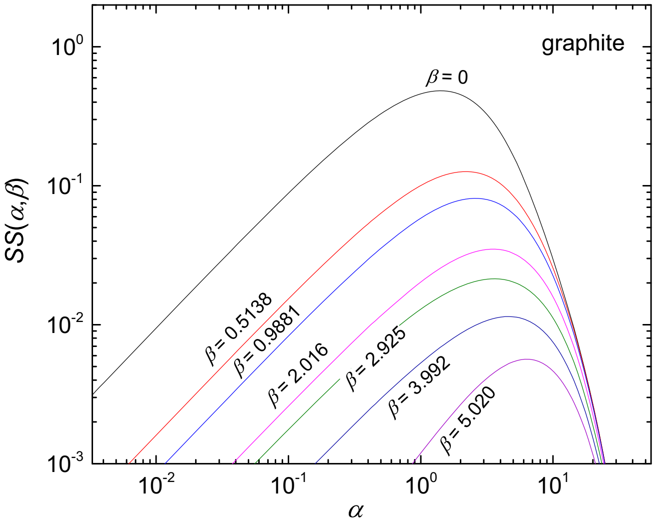

FIG. 131. (Color online) The symmetric TSL of crystalline graphite at 296 K as a function of momentum transfer, α, for a range of neutron energy transfers, β. $SS(\alpha,\beta)$ for each β is labeled above the corresponding line.

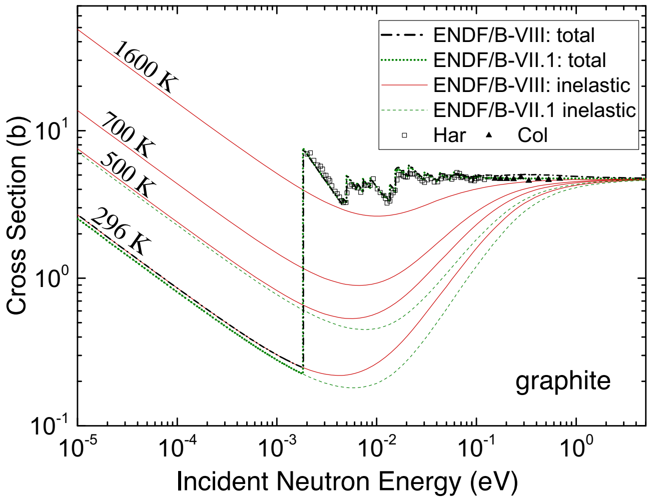

FIG. 132. (Color online) Total thermal neutron scattering cross section of graphite at 296 K for ENDF/B-VIII.0 and ENDF/B-VII.1 compared to measurement by Harwell (Har) and Columbia University (Col) [356]. The ENDF/B-VIII.0 inelastic cross sections are shown for select temperatures.

G. Nuclear/Reactor Graphite

Reactor graphite was evaluated using classical molecular dynamics (MD). Reactor graphite is multi-phase material composed of micro-crystallites connected through a carbon binder matrix; consequently, this form of graphite is highly porous and has atomic vibrational behavior that differs significantly from crystalline graphite [365]. Initially, an MD model of crystalline graphite was created and validated against measured thermodynamic properties. To capture the impact of porosity present in reactor graphite, atoms were randomly removed from the crystalline structure. Subsequently, the system was evolved to generate time dependent velocities, from which the phonon DOS was calculated as the Fourier transform of the velocity auto-correlation function [365].

The TSL for reactor graphite (File 7, MAT31) at 296, 400, 500, 600, 700, 800, 1000, 1200, 1600, and 2000 K were evaluated in the incoherent approximation using the LEAPR module of NJOY99.396 [322, 353, 354]. The symmetric TSL at 296 K for various β is shown in Fig. 133. Due to the similarities in crystalline structure, the coherent elastic scattering behavior of crystalline graphite may be assumed to be representative of reactor graphite; therefore, for the present evaluation, reactor graphite tabulates the same MT2 as ENDF/B-VIII.0 crystalline graphite.

In addition, similar to crystalline graphite, the coherent elastic scattering (MT2) component of nuclear/reactor graphite was calculated under the cubic approximation using the LEAPR module of the NJOY code. This resulted in a second set of libraries that can be implemented in nuclear applications [364].

Integrated scattering cross sections, processed with THERMR, are shown in Fig. 134. The evaluated ENDF/B-VIII.0 total cross section is compared to ENDF/B-VII.1 at 296 K. Moreover, the ENDF/B-VIII.0 inelastic cross sections are compared to cross section measurements of reactor graphite for increasing temperature [356]. The ENDF/B-VII.1 contains the traditionally available TSL library. The presented ENDF/B-VIII.0 inelastic scattering cross section for reactor graphite shows improved agreement with measurement.

Reactor graphite represents a new TSL evaluation that is included for the first time in the ENDF/B database.

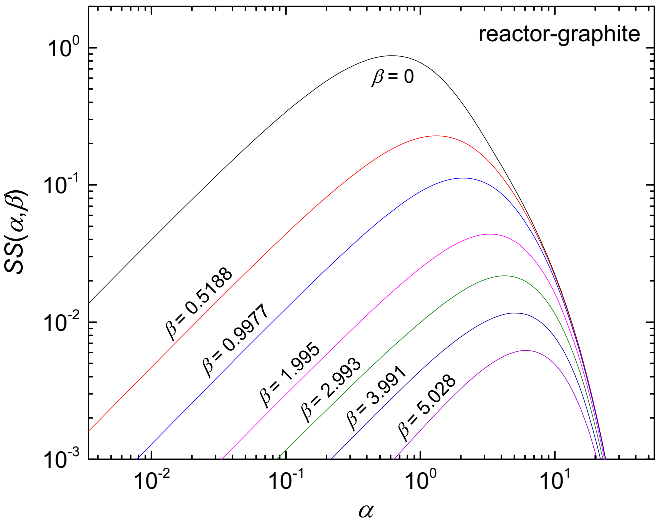

FIG. 133. (Color online) The symmetric TSL of reactor-graphite at 296 K as a function of momentum transfer, α, for a range of neutron energy transfers, β. $SS(\alpha,\beta)$ for each β is labeled above the corresponding line.

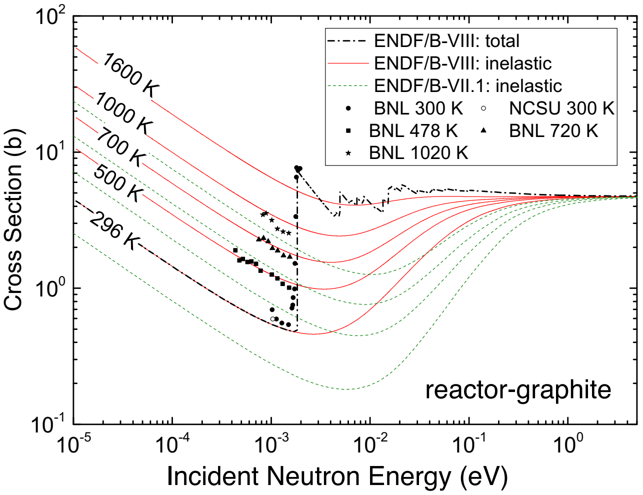

FIG. 134. (Color online) Inelastic ENDF/B-VIII.0 thermal neutron scattering cross section of reactor graphite and ENDF/B-VII.1 crystalline graphite compared to measurement [356]. The total ENDF/B-VIII.0 for reactor graphite is shown at 296 K.

H. Beryllium Oxide (BeO)

Beryllium oxide (BeO) was evaluated with the AILD method. Solid BeO has a Wurtzite crystal structure. The Hellmann-Feynman forces for this structure were generated from the VASP code and supplied to the PHONON code to determine the partial phonon density of states (DOS) for each element [347, 348]. The phonon dispersion relationships predicted by this approach were found to be in reasonable agreement with experiment [366, 367].

The TSL (File 7) was calculated from the partial phonon DOS for Be(BeO) (MAT27) and O(BeO) (MAT46) at 293.6, 400, 500, 600, 700, 800, 1000, and 1200 K using the LEAPR module of the NJOY99.393 nuclear data processing system [322, 353, 354]. The incoherent approximation was applied in the evaluation of the TSL. Figure 135 shows the symmetric TSL of Be(BeO) and O(BeO) at 293.6 K.

A generalized coherent elastic routine, which removes the cubic approximation conventionally applied in LEAPR, was used to evaluate the coherent elastic cross section [355]. The Debye-Waller matrix used in this generalized routine is calculated from the PHONON code by integrating the partial DOS. As BeO is a hexagonal material, the differences between the forces in x, y, z directions are non-negligible; therefore, the asymmetric force field would be adequately captured by using the Debye-Waller matrix method.

The ENDF/B-VIII.0 total scattering cross section of BeO is compared to ENDF/B-VII.1 in Fig. 136 and found to be in good agreement with measured total cross sections [356]. The inelastic cross sections are also compared at select temperatures. The ENDF/B-VIII.0 TSL of BeO predicts an increased contribution of inelastic scattering and decreased contribution of elastic scattering when compared to ENDF/B-VII.1.

I. Silicon Dioxide (SiO_2, α and β Phases)

Silicon dioxide (SiO_2) was evaluated using AILD techniques [347, 348, 368]. SiO_2 is a major component of rock and earth in the form of α-quartz (α-SiO_2). At tempera-

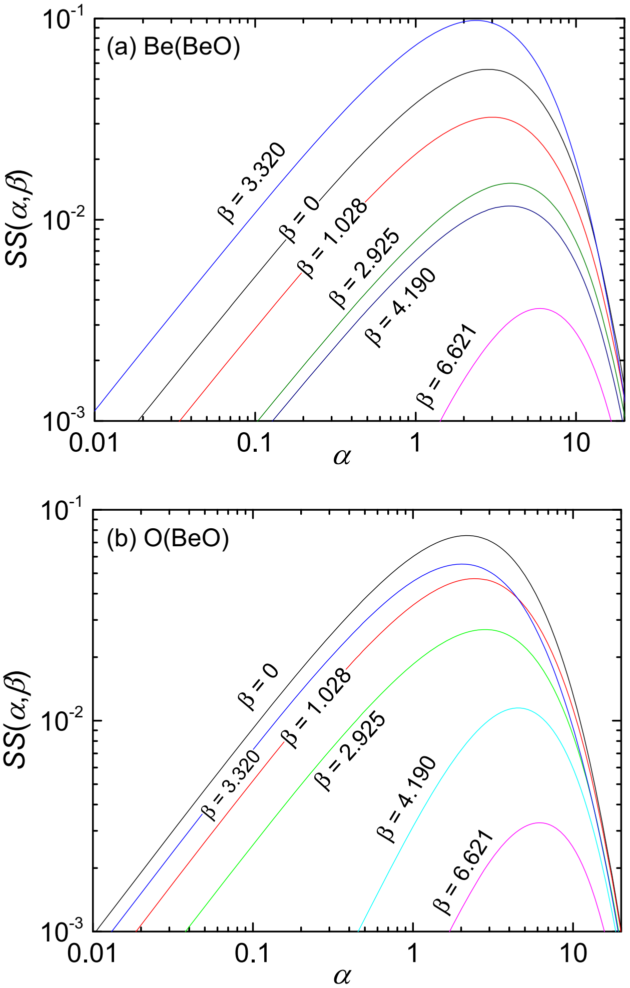

FIG. 135. (Color online) The symmetric TSL of (a) Be(BeO), and (b) O(BeO) as a function of momentum transfer, α, for various values of β at 293.6 K. $SS(\alpha,\beta)$ for each β is labeled with the corresponding line.

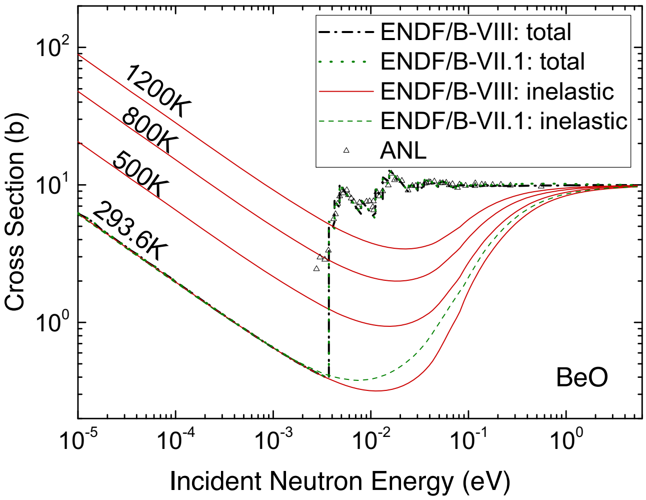

FIG. 136. (Color online) The total scattering cross section of BeO for ENDF/B-VIII and ENDF/B-VII.1 at 293.6 K, measurement at room temperature (ANL) [356]. The inelastic scattering cross section for ENDF/B-VIII.0 is also compared to ENDF/B-VII.1 at 293.6 K.

tures above 836 K the SiO_2 crystal structure undergoes a phase change to β-quartz (β-SiO_2). The unit cell atomic positions and crystalline structure of each phase were processed with the VASP code to produce optimized lattice parameters and Hellmann-Feynman forces [350, 351]. The Hellmann-Feynman forces were supplied as a fundamental input to the PHONON code which uses lattice dynamics to calculate phonon density of states [368].

The phase change in the SiO_2 crystal structure results in a change in the phonon DOS. Consequently, the inelastic and coherent elastic thermal neutron cross sections for the two phases are expected to differ. Therefore, separate ENDF TSL sets were created for each phase of SiO_2. The TSL for α-SiO_2 (File 7, MAT47) was evaluated at 293.6, 350, 400, 500, and 800 K, whereas the TSL β-SiO_2 (File 7, MAT49) was evaluated at 1000 and 1100 K. Each TSL was generated in the incoherent approximation as a mixed moderator using the LEAPR module of the NJOY99.0 nuclear data processing package and the corresponding phonon DOS [322, 353, 354]. In this case the cross sections of Si and O atoms were summed together taking into consideration the compound stoichiometry. The symmetric TSL of α-SiO_2 and β-SiO_2 are shown in Fig. 137.

The coherent elastic cross sections of both phases were evaluated separately using a modified LEAPR module which correctly accounts for the stoichiometry of Si and O in SiO_2. The total cross section and inelastic cross sections of α-SiO_2 and β-SiO_2 are illustrated in Fig. 138.

J. Silicon Carbide (SiC)

3C Silicon carbide (SiC) was evaluated with the AILD method [347, 348, 369]. Ab-initio simulations of the 3C-SiC zincblende crystal structure were performed using the VASP code. The Hellmann-Feynman forces calculated from these simulations were used in the PHONON code to determine the phonon DOS for each element in the system with the lattice dynamics method [369].

Subsequently, the partial phonon DOS for C and Si in SiC were utilized to produce the TSL (File 7) 300, 400, 500, 600, 700, 800, 1000, and 1200 K for C(3C-SiC) (MAT44) and Si(3C-SiC) (MAT43) were generated in the incoherent approximation using the NJOY99.393 code [322, 353, 354]. $SS(\alpha,\beta)$is at 300 K illustrated in Fig. 139.

The coherent elastic cross section of 3C-SiC was evaluated by the generalized Debye-Waller matrix method using a modified LEAPR routine [355]. This cross section is distributed between the C(3C-SiC) and Si(3C-SiC) File 7, MT2 using a 1/2 weighting factor. The total scattering cross section of SiC at 300 K and inelastic cross section at different temperatures are shown in Fig. 140.

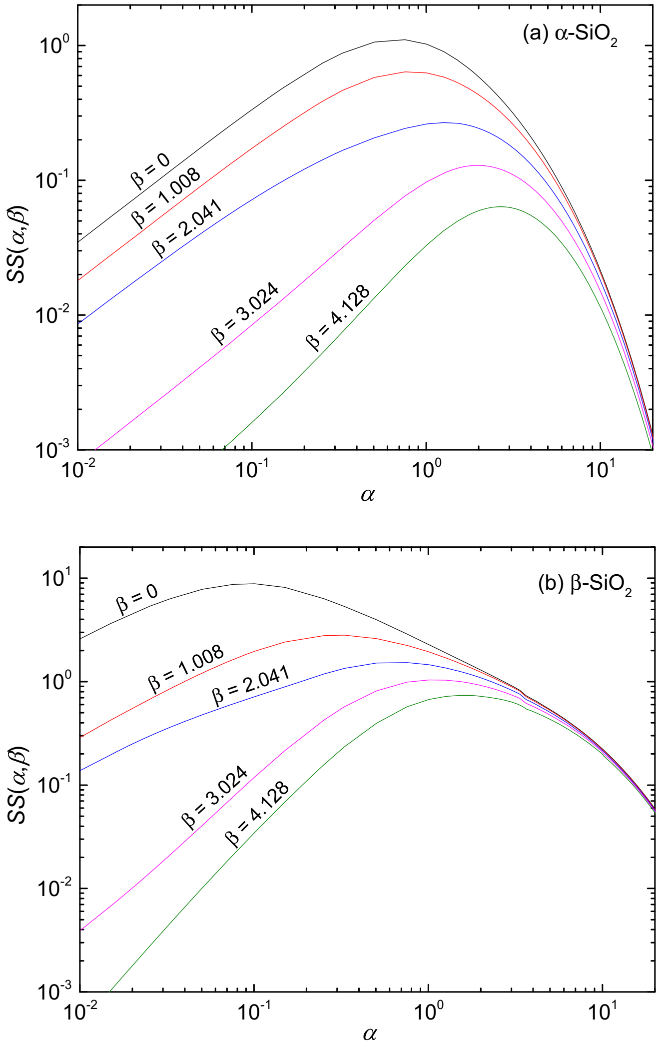

FIG. 137. (Color online) The symmetric TSL of (a) α-SiO$_2$ at 293.6 K, and (b) β-SiO$_2$ at 1000 K as a function of momentum transfer, α, for various values of β. $SS(\alpha,\beta)$ for each β is labeled above the corresponding line.

The SiC TSL evaluations, Si(3C-SiC) and C(3C-SiC), represent new evaluations in ENDF/B-VIII that are included for the first time in the ENDF/B database.

K. Polyethylene (CH$_2$)

Polyethylene is structured in long polymer chains that are composed of ethylene (CH$_2$) monomers that are attached in long molecular chains producing the polymer structure. The evaluation was based on a classical MD model composed of a supercell that contained 20 polymer chains each 200 monomers long. The model was executed using the LAMMPS code and produced the density of states (DOS) of intra and intermolecular excitations as the power spectrum of relevant atomic trajectory autocorrelation functions at a temperature of 300 K and a pressure of 1 atmosphere [347, 370, 371]. The DOS, as calculated using MD, was found to be in good agreement with the measured DOS [372].

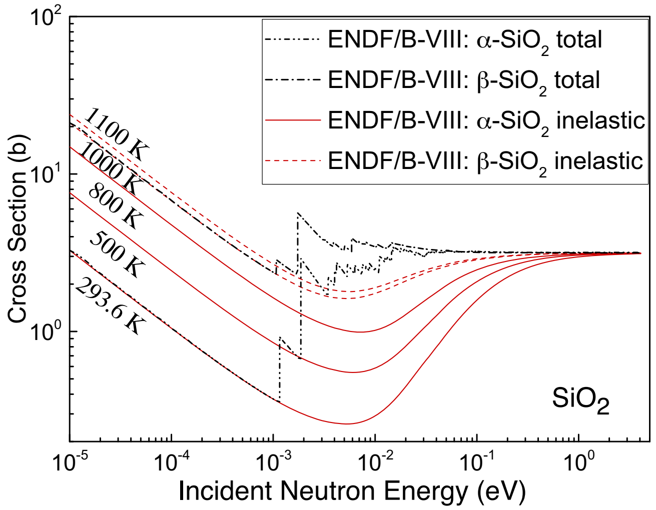

FIG. 138. (Color online) The total scattering cross section of α-SiO$_2$ at 293.6 K and β-SiO$_2$ at 1000 K. The inelastic cross section is also shown at selected temperatures.

The TSL of hydrogen in polyethylene (File 7, MAT37), H(CH$_2$), was generated using the NJOY2012.50 code system in the incoherent approximation [373]. The TSL was based on the MD calculated DOS and was generated for the temperatures 5, 77, 196, 233, 293, 300, 303, 313, 323, 333, 343, and 350 K. The TSL, $SS(\alpha,\beta)$, at various α and β values is shown in Fig. 141. The inelastic and incoherent elastic cross sections are shown in Fig. 142. The total scattering cross section, also shown in Fig. 142, demonstrates good agreement with published experimental transmission data [374].

This contribution extends the temperature range of the polyethylene TSL library from ENDF/B-VII.1. The generated data is exclusively for hydrogen bound in polyethylene. Carbon in polyethylene should be treated using the free gas approximation.

L. Polymethyl Methacrylate (C$_5$O$_2$H$_8$)

Polymethyl methacrylate (PMMA), also known as Lucite, Plexiglass, *etc.*, is structured in long polymer chains that are composed of methyl methacrylate (C$_5$O$_2$H$_8$) monomers that are attached in long molecular chains producing the polymer structure. The evaluation was based on a classical MD model composed of an amorphous supercell that contained 5 polymer chains each 370 monomers long. The model was executed using the LAMMPS code and produced the density of states (DOS) of intra and intermolecular excitations as the power spectrum of relevant atomic trajectory autocorrelation functions at a temperature of 300 K and a pressure of 1 atmosphere [347, 371, 375]. The MD model was found to reproduce

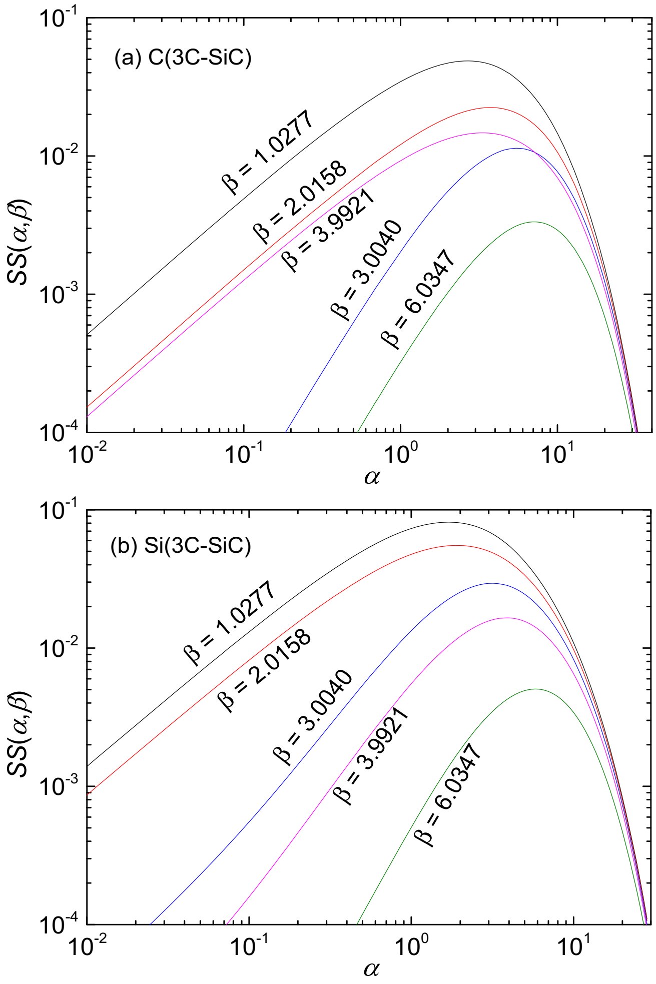

FIG. 139. (Color online) The symmetric TSL for (a) C(3C-SiC), and (b) Si(3C-SiC) at 300 K. $SS(\alpha,\beta)$ for each β is labeled above the corresponding line.

the experimental density of PMMA in the temperature range of 300 – 400 K. In addition, it reproduced the glass transition temperature to within 20 % of the measured values.

The TSL of $H(C_5O_2H_8)$ (File 7, MAT39) was generated in the incoherent approximation using the NJOY2012.50 code system [373]. The TSL was based on the MD DOS and was generated at a temperature of 300 K. Figure 143 shows the scattering law, $SS(\alpha,\beta)$, at various α and β values. Figure 144 shows the inelastic and incoherent elastic scattering cross sections, and the total scattering cross section indicating good agreement with published experimental transmission data [376].

PMMA represents a new TSL evaluation that is included for the first time in the ENDF/B database. The generated data is exclusively for hydrogen bound in PMMA. Carbon and oxygen in PMMA should be treated using the free gas approximation.

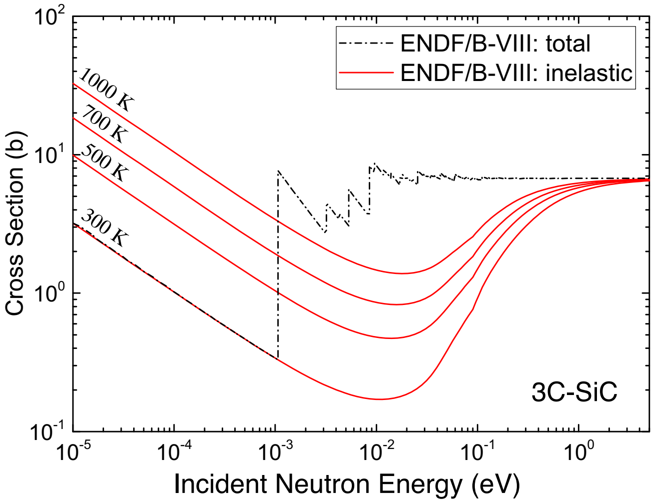

FIG. 140. (Color online) The inelastic scattering cross section of 3C-SiC shown at selected temperatures. The total scattering cross section of 3C-SiC at 300K is also shown.

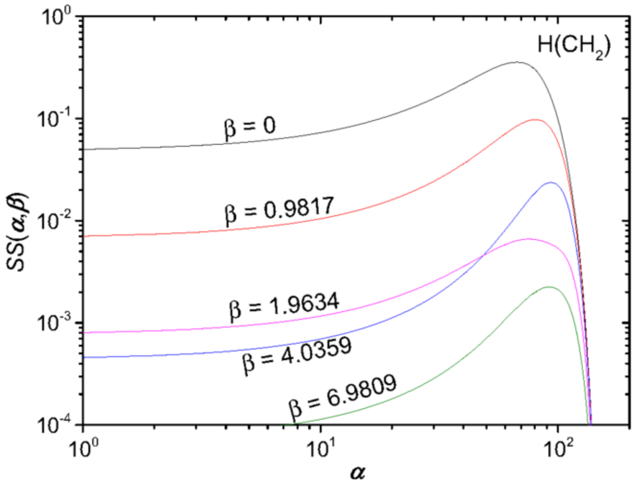

FIG. 141. (Color online) The symmetric TSL of $H(CH_2)$ as a function of momentum transfer, α, for various values of β at 300 K. $SS(\alpha,\beta)$ for each β is labeled above the corresponding line.

M. Uranium Dioxide (UO_2)

The thermal scattering law (TSL) for uranium dioxide (UO_2) has been evaluated using modern AILD techniques [347, 348, 378]. Neutron thermalization, particularly prompt effects, in UO_2 fuel may be impacted by the crystal binding effects of oxygen, the calculation of which may be facilitated with the use of TSL [379].

UO_2 crystallizes into a fluorite structure with a face-centered cubic uranium lattice and cubic oxygen sublattice. Due to the presence of uranium, the chemical binding of this material has $5f$ magnetism effects. Initially, electronic structure calculations on the anti-ferromagnetic ground-state were performed with the VASP code to pre-

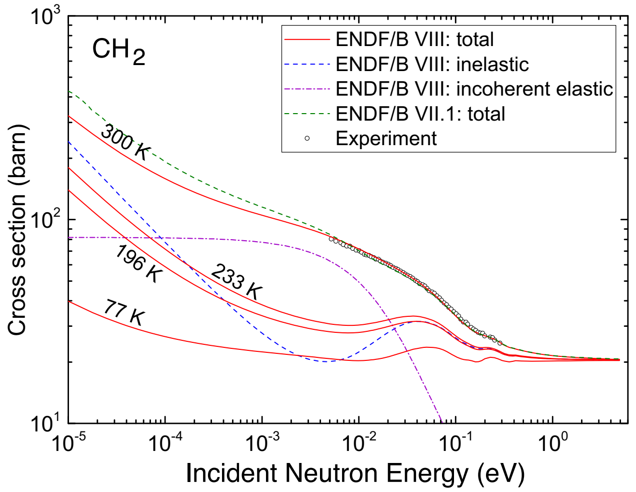

FIG. 142. (Color online) The inelastic and incoherent elastic cross sections, and total neutron scattering cross section of H(CH_2) compared to experiment [374]. The incoherent elastic and inelastic cross sections shown correspond to 300 K.

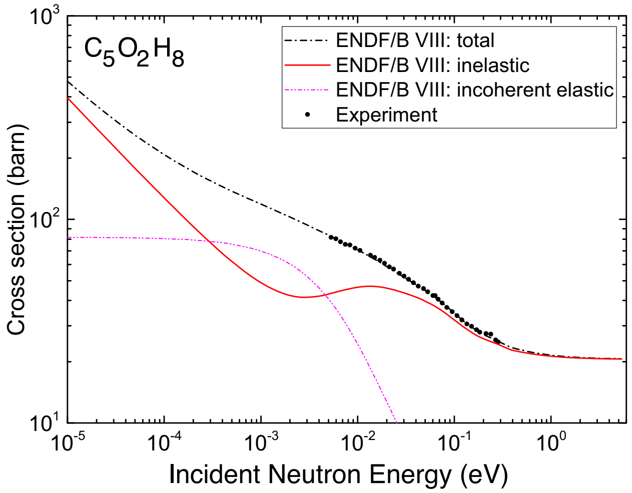

FIG. 144. (Color online) The total neutron scattering cross sections of H($C_5O_2H_8$) at 300 K compared to experiment [376]. The incoherent elastic and inelastic scattering cross sections at 300 K are also shown.

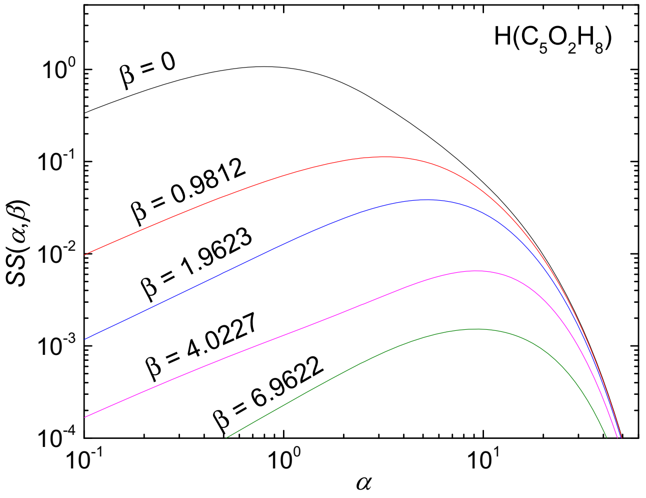

FIG. 143. (Color online) The symmetric inelastic TSL of H($C_5O_2H_8$) as a function of momentum transfer, α, for various values of β at 300 K. $SS(\alpha,\beta)$ for each β is labeled above the corresponding line.

dict the crystal structure and Hellmann-Feynman forces of UO_2 [350, 351, 378]. Subsequently, these forces were utilized within the dynamical matrix approach implemented in the PHONON code to generate the partial phonon densities of states (DOS) for uranium and oxygen in UO_2 [352]. The phonon DOS and phonon dispersion relations were found to be within reasonable agreement with neutron scattering experiments [378, 380, 381] Furthermore, the Debye-Waller factors predicted from the AILD DOS were found to have improved agreement with measurement when compared to that used in ENDF-VII.1 [321, 378, 380]. Specifically, in the present evaluation the Debye-Waller factor C/E ratio is 0.98 and 0.96 for uranium and oxygen respectively, whereas the corresponding ratios are 0.86 and 1.11 for the partial phonon DOS used in ENDF/B-VII.1.

The partial DOS were used in the LEAPR module of the NJOY99.396 nuclear data processing system to generate ENDF TSL (File 7) for U(UO_2) (MAT48) and O(UO_2) (MAT75) at the standard temperatures of 296, 400, 500, 600, 700, 800, 1000, and 1200 K [322, 353, 354]. Inelastic scattering (MT4) was evaluated in the incoherent approximation for each element using the phonon expansion [322]. Coherent elastic scattering (MT2) was evaluated using a generalized coherent elastic routine in a modified LEAPR module. The approach removes the atom site approximation traditionally used in LEAPR such that a unique Debye-Waller matrix is used for each element in the calculation of the structure factors [355]. The coherent elastic data is divided between both libraries with a 1/3 weighting fraction.

The symmetric TSL, $SS(\alpha,\beta)$, at 296 K tabulated in File 7, MT4 of the ENDF evaluations is illustrated in Fig. 145 for U(UO_2) and O(UO_2). The α and β grids for this TSL capture the resolution of the partial phonon DOS and have been extended from ENDF/B-VII.1 to ensure precise integration of $SS(\alpha,\beta)$ for incident neutrons below 5 eV. The inelastic and total scattering cross section, as shown in Fig. 146, were generated as an integral of the TSL using the THERMR module of NJOY99.396. The total thermal scattering cross section predicted at 296 K is observed to demonstrate reasonable agreement with measured total cross sections of UO_2 with natural uranium, which have been corrected for neutron absorption [377]. The ENDF/B-VIII.0 inelastic cross section of UO_2 deviates from ENDF/B-VII.1 due to improved prediction of the partial DOS for oxygen using AILD.

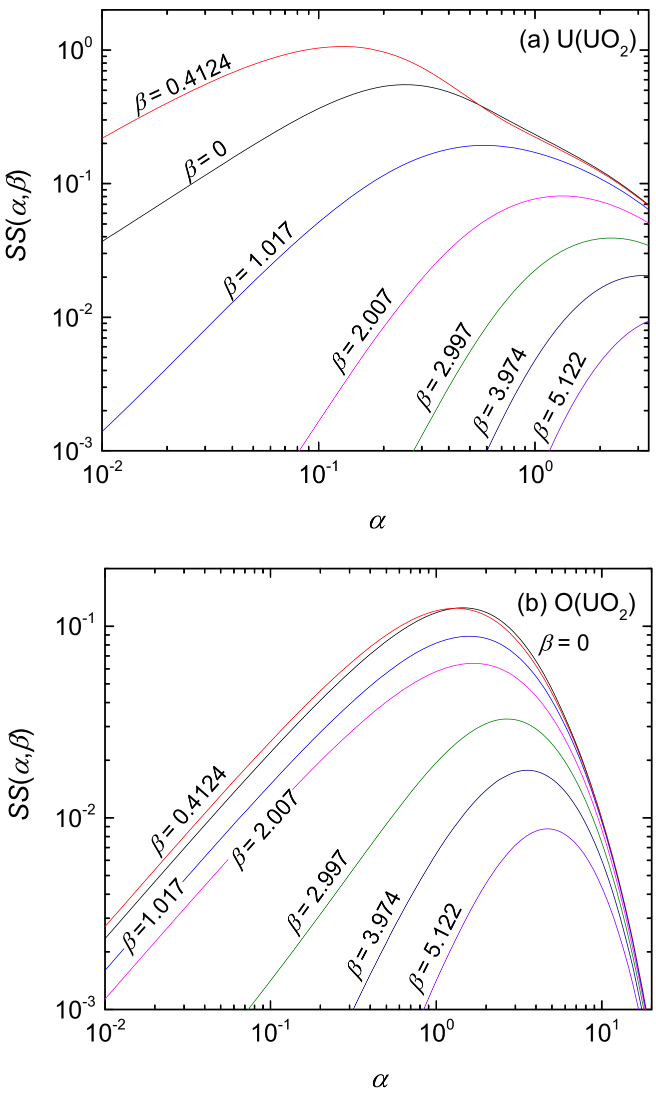

FIG. 145. (Color online) The symmetric TSL of (a) U(UO$_2$) and (b) O(UO$_2$) at 296 K as a function of momentum transfer, α, for a range of neutron energy transfers, β. $SS(\alpha,\beta)$ for each β is labeled with the corresponding line.

N. Uranium Mononitride (UN)

The thermal scattering law for uranium nitride (UN) has been evaluated using modern AILD techniques [347, 348]. UN has a rock-salt crystal structure with 5*f* electron magnetism effects contributing to chemical binding. Furthermore, as in UO$_2$ neutron thermalization in UN, particularly prompt effects, may be impacted by the crystal binding [379].

The crystal and electronic structure of UN were modeled with DFT using VASP [350, 351]. These calculations treated the 5*f* electron magnetism of UN with techniques previously applied in UO$_2$ [378, 382]. In this case the electronic density of states and ground state anti-ferromagnetism were found to demonstrate reasonable agreement with measurements [382, 383]. The Hellmann-Feynman forces predicted from the electronic structure were utilized in the PHONON code to generate the partial phonon DOS for uranium and nitrogen in UN [352]. Both the phonon DOS and phonon dispersion relations were found to be within reasonable agreement with neutron scattering experiments [384, 385].

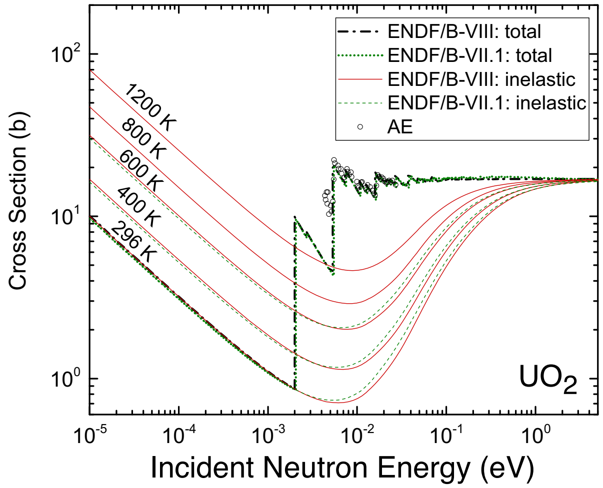

FIG. 146. (Color online) Total thermal neutron scattering cross section of UO$_2$ at 296 K compared to room temperature neutron transmission measurements by Aktiebolaget Atomenergi (AE) [377]. The inelastic cross section is shown for select temperatures. The ENDF-VII.1 total cross sections at 296 K and inelastic cross section below 600 K are shown for comparison.

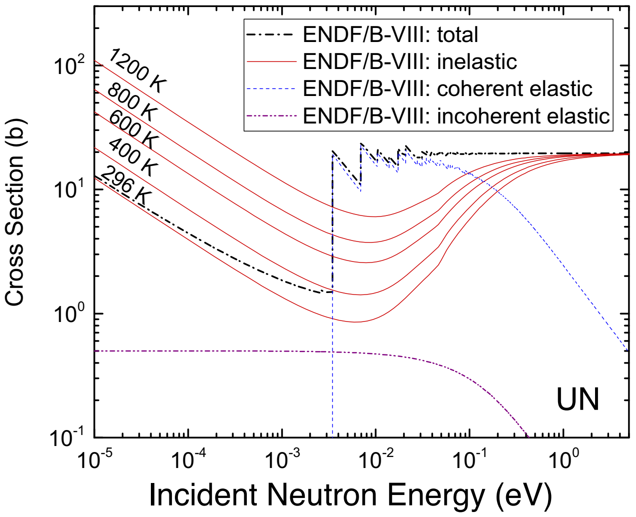

FIG. 147. (Color online) Total thermal neutron scattering cross section of UN at 296 K. The coherent and incoherent elastic contributions are shown for 296 K. The inelastic contributions to the total cross section are shown for select temperatures.

The LEAPR module of the NJOY99.396 nuclear data processing system was used to generate ENDF TSL (File 7) for U(UN) (MAT72) and N(UN) (MAT71) at the standard reactor material temperatures of 296, 400, 500, 600, 700, 800, 1000, and 1200 K [322, 353, 354]. Inelastic scattering (MT4) was evaluated in the incoherent approximation

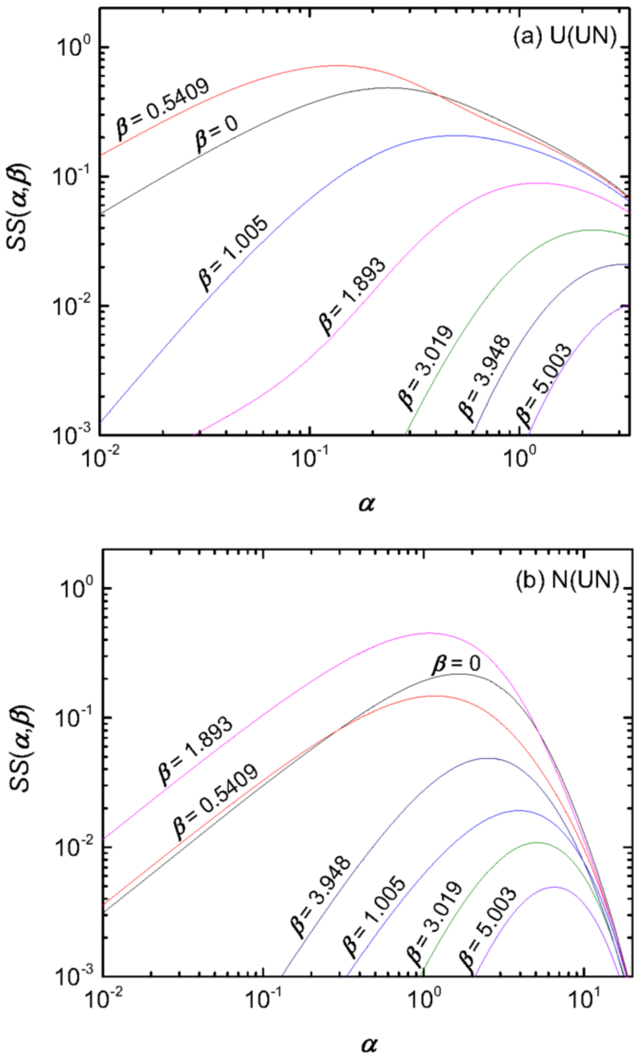

FIG. 148. (Color online) The symmetric TSL of (a) U(UN) and (b) N(UN) at 296 K as a function of momentum transfer, α, for a range of neutron energy transfers, β. $SS(\alpha,\beta)$ for each β is labeled above or below the corresponding line. An energy transfer of $\beta = 1.893$ corresponds to the maximum optical peak of 0.048 eV in the nitrogen partial phonon DOS.

for each element using the phonon expansion and the partial DOS, whereas coherent elastic scattering (MT2) was evaluated using a generalized coherent elastic routine integrated into a modified LEAPR module [322, 355]. This elastic routine removes the traditional atom site approximation, and instead uses a unique Debye-Waller matrix for each element in the calculation of the structure factors [355]. Due to the 0.5 barn incoherent nuclear cross section of N-14 [386], incoherent elastic scattering from N-14 is tabulated in MT2 of the N(UN) File 7, while the coherent elastic scattering cross section of the UN compound is tabulated entirely in the MT2 of the U(UN) File 7.

The symmetric TSL at 296 K tabulated in File 7, MT4 of the ENDF sublibraries is illustrated in Fig. 148 for U(UN) and N(UN). Oscillations observed in $SS(\alpha,\beta)$ as a function of β correspond to centering of the nitrogen partial phonon DOS around 0.048 eV optical phonons, and are consistent with neutron scattering measurements [385]. The α and β grids for this TSL evaluation capture the resolution of the partial phonon DOS and ensure precise integration of $SS(\alpha,\beta)$ for incident neutrons below 5 eV.

The inelastic, elastic, and total scattering cross sections were generated as an integral of the TSL using the THERMR module of NJOY99.396 and are shown in Fig. 147. The incoherent elastic cross section represents a significant component of the total thermal scattering cross section between 0.001 eV and 0.0253 eV, which is most evident at 296 K. The abrupt rise in the inelastic cross section near 0.05 eV is a consequence of the centering of the partial DOS of nitrogen around optical phonon peaks in the vicinity of this energy.

The UN TSL evaluations, U(UN) and N(UN), represent new evaluations that are included for the first time in the ENDF/B database.

VIII. NEUTRON CROSS SECTION STANDARDS SUBLIBRARY

The ENDF/B-VIII.0 standards evaluation [10] was adopted from an extensive international cooperative effort by the CSEWG from the United States and the IAEA responding to a need for improved neutron standards. This work was assisted by an IAEA Data Development Project “Maintenance of the Neutron Cross Section Standards” which provided a mechanism for allowing new experimental data and improvements in evaluation procedure to be used in new evaluations of the neutron standards. The neutron data standards are described in detail in the paper by Carlson *et al.* [10] in this issue of *Nuclear Data Sheets*, and only summary information is presented here.

There have been long-standing concerns about the rather small uncertainties obtained for the neutron cross section standards in previous evaluations [9]. Were previous standards affected by *unknown unknowns*?[2]. The small uncertainties’ issue led the standards committee to investigate one aspect of unknown systematic uncertainties (USU) based on the unrecognized uncertainty-estimation method [387]. The method has been used in some evaluations in the BROND library [388, 389]; it was also discussed during the Standards 2006 project (*e.g.*, see [390]).

A variation of the unrecognized uncertainty-estimation method is being used; the assumption is being made that the USU is not energy dependent [10]. We quote: “. . . unrecognized (or unknown) systematic uncertainties

---

[2] D. Rumsfeld stated: “Reports that say that something hasn’t happened are always interesting to me, because as we know, there are *known knowns*; there are things we know we know. We also know there are *known unknowns*; that is to say we know there are some things we do not know. But there are also *unknown unknowns* the ones we don’t know we don’t know. . . , it is the latter category that tend to be the difficult ones.”

are defined as a practical minimum uncertainty that can be achieved using a given measuring method (or measuring tool). No matter how many times the measurements are repeated, if we use the same method, we can not get a result with lower uncertainty. The method allows the determination of some systematic data-uncertainties usually underestimated or neglected by the measurers that allow the establishment of implicit correlations of evaluated quantities."

For neutron standards evaluation, each of the cross sections evaluated (and ^{252}Cf(sf) neutron multiplicity) had the normalization quantities for absolute measurements statistically analyzed (considering weights if needed) to obtain the standard deviation of that distribution which was regarded as the normally-distributed type B uncertainty [391] assumed to be the USU. Therefore, the larger uncertainties now obtained result from unknown systematic uncertainties based on the spread in normalization factors of absolute measurements for each cross section type and also for ^{252}Cf(sf) neutron multiplicity[3].

TABLE XXXII. Neutron Data Standards.

Reaction	Standards Energy Range
H(n,n)	1 keV to 20 MeV
^{3}He(n,p)	0.0253 eV to 50 keV
^{6}Li(n,t)	0.0253 eV to 1.0 MeV
^{10}B(n,α)	0.0253 eV to 1 MeV
^{10}B(n,$\alpha_1\gamma$)	0.0253 eV to 1 MeV
C(n,n)	10 eV to 1.8 MeV
Au(n,γ)	0.0253 eV, 0.2 to 2.5 MeV, 30 keV MACS
^{235}U(n,f)	0.0253 eV, 7.8-11 eV, 0.15 MeV to 200 MeV
^{238}U(n,f)	2 MeV to 200 MeV
^{252}Cf(sf)	Prompt fission neutron spectra

All determined unrecognized systematic uncertainties (for standard and reference quantities are listed in Table IX of Ref. [10]. Note that the determined USU for fission cross-section measurements by fission chambers amounts to 1.2%[4]. The corresponding USU for neutron capture ranges from 1.7% for ^{197}Au(n,γ) and actinides below the fission threshold (*e.g.*, ^{238}U(n,γ) below 1 MeV) to 2.4% for fissioning actinides (*e.g.*, ^{238}U(n,γ) above 1 MeV). New uncertainty estimates may be conservative as the cross-section data spread could be lower for some incident neutron energies, but the standards committee considered a new estimate to be more realistic.

The neutron cross section standards and their energy ranges are shown in Table XXXII.

The standards evaluation includes work on each of the following: the neutron cross section standards; the thermal neutron constants; the low energy gold capture cross section (MACS at 30 keV); reference cross sections for prompt gamma-ray production; very high energy fission reference cross sections; the ^{235}U thermal neutron-induced prompt fission neutron spectrum; and the ^{252}Cf spontaneous prompt fission neutron spectrum. The reference cross sections and spectra have the role of standards but they are not as well known. They have the same properties as the standards such as smooth cross sections as a function of energy. The detailed documentation [10] contains the numerical values of the mean values and associated uncertainties; full covariances for these data are available from the IAEA at `http://www-nds.iaea.org/standards`.

Since thermal data are included in the standards evaluation, the thermal constants will have an impact on the results of the evaluation. Also the thermal constants themselves will be affected by the other data in the evaluation.

Only microscopic data were used in the evaluation as input in the GMAP code due to concerns about how well the temperatures are understood for Maxwellian data and how close the thermal spectra agree with a Maxwellian. It was one exception, the Maxwellian experiment by Lounsbury *et al.* 1972 used irradiation of samples containing ^{233}U, ^{235}Uand ^{239}Pu for a year. Then the samples were analyzed by mass spectrometry to obtain α-values (α is the ratio of capture/fission cross sections). Beer *et al.* 1972 utilized Monte Carlo techniques applied to the geometry of that experiment to determine accurate thermal α-values and uncertainties for those nuclides. This Maxwellian experiment was very important in getting an accurate value of thermal capture in ^{233}U, for which no microscopic data was measured. The Westcott g-factors for fission and absorption normally given with the thermal constants were evaluated independently from the GMAP fit, see Ref. [10] for details. $\overline{\nu}_{tot}$ for ^{252}Cf(sf) from this investigation is 3.764 ±0.42%. This includes a 0.4% USU as discussed above [10]. It was 3.7692 for the previous evaluation, in excellent agreement within quoted uncertainties. The results of this work are shown in Table XXXIII. The quantities in italics are the values obtained in the previous standards evaluation [9]. The influence of the extensively used Maxwellian data on the previous evaluation was fairly strong, lowering the fission cross section and increasing the neutron multiplicity. In many cases changes in thermal constants are greater than the reported uncertainty. The ^{235}U(n,f) cross section at thermal in the ENDF/B-VII.1 library is 584.99 b. The ENDF/B-VIII evaluated files are consistent with the new standards evaluation within the quoted uncertainties, except for the ^{239}Pu fission cross section (which was carried over from Subgroup 34 unchanged, and the lower Subgroup 34 value in the file helped in the modeling of the thermal plutonium critical assemblies), and for ^{233}U (where the new standards value came too late for us to change the B-VIII.0 evaluation). Note however, that the final thermal constant for neutron capture on ^{233}U is in very good agreement with ENDF/B-VII.1 evaluation (but not with the ENDF/B-VIII.0 file).

The ^{235}U(n$_{th}$,f) thermal prompt neutron fission spec-

---

[3] The method was not applied for thermal cross section data. The 0.4% USU derived for ^{252}Cf(sf) $\bar{\nu}$ was assumed for all thermal neutron multiplicities.

[4] The fission USU almost doubles the previously quoted ENDF/B-VII.1 uncertainties [9] for ^{235}U(n,f), ^{239}Pu (n,f) and ^{238}U(n,f) from 2–5 MeV.

TABLE XXXIII. The thermal neutron constants in Standards 2017 [10]. The constants in *italics* are those obtained from the 2006 standards evaluation. Those in **bold** are the values used in ENDF/B-VIII.0 neutron sublibrary files.

Quantity	^{233}U	^{235}U	^{239}Pu	^{241}Pu
σ_{nf}(b)	533.0 (2.2) **534.1** *531.2*	587.3 (1.4) **586.7** *584.3*	752.4 (2.2) **747.4** *750.0*	1024 (11) **1012** *1014*
$\sigma_{n\gamma}$(b)	44.9 (0.9) **42.3** *45.6*	99.5 (1.3) **99.4** *99.4*	269.8 (2.5) **270.14** *271.5*	362.3 (6.1) **363.05** *361.8*
σ_{nn}(b)	12.2 (0.7) **12.2** *12.1*	14.09 (0.22) **14.11** *14.09*	7.8 (1.0) **8.1** *7.8*	11.9 (2.6) **11.3** *12.1*
$\overline{\nu_{tot}}$	2.487 (.011) **2.4852** *2.4968*	2.425 (.011) **2.4298** *2.4355*	2.878 (.013) **2.8769** *2.8836*	2.940 (.013) **2.9453** *2.9479*

trum (PFNS) is very important for reactor applications. It is also used as a reference for validating evaluated cross sections for neutron dosimeters used in many applications. Improvements in the evaluation of this spectrum were made by including measurements of the spectrum made relative to the ^{252}Cf spontaneous fission neutron spectrum and by advances in evaluation methodology [11]. The evaluation was done with least-squares `GMA` code for which both spectra together with ^{233}U(n$_{th}$,f) and ^{239}Pu(n$_{th}$,f) PFNS were evaluated simultaneously, and by considering all ratio measurements as shape data. The ^{252}Cf spontaneous fission neutron spectrum evaluation of Mannhart was used as prior for the GMA evaluation.

Due to the smaller uncertainties of the ^{252}Cf spectrum, the impact was largely on the ^{235}U spectrum. The average energy of the ^{235}U(n$_{th}$,f) PFNS was determined to be 2.00 MeV ±0.010 MeV[5], to be compared with the 2.03 MeV average energy in the previous ENDF/B-VII.1. The results of this work are documented in Refs. [11] and [10].

IX. CHARGED-PARTICLE REACTION SUBLIBRARIES

In the following subsections, each of the new evaluations added to ENDF/B-VIII.0 are detailed.

This information is also found directly in the documentation file of each evaluation. All these reactions include the elastic scattering channel, the cross section of which is unbounded at forward angles because the long-range Coulomb repulsion. Most evaluations are made by a combination of the previous ENDF/B-VII.0, ENDF/B-VII.1 evaluations, and Livermore's 'Evaluated Charged Particle Library' (ECPL) data [392]. Fig. 149 summarizes the work performed to date, where the dark blue squares indicate the reactions described in this section.

A. p + ^{7}Li

This evaluation is strongly based on the previous ENDF/B-VII.1 evaluation by P.R. Page, keeping the same angular distributions, but with the following modifications in the cross sections.

For the p + ^{7}Li → n + ^{7}Be reaction, both the ECPL and ENDF/B-VII.1 cross-sections were discarded and a new evaluation assembled based on the data matched by splines as shown in Fig. 150. The ^{7}Be ground state assembled the data of Sekharan *et al.* [401] for 0-2.35 MeV, Burke *et al.* [395] for 2.4–3.6 MeV, Abramovitch *et al.* [393] for 3.6–25 MeV, and Poppe *et al.* [397] for 25–26 MeV. The ^{7}Be excited state at 0.429 MeV assembled the

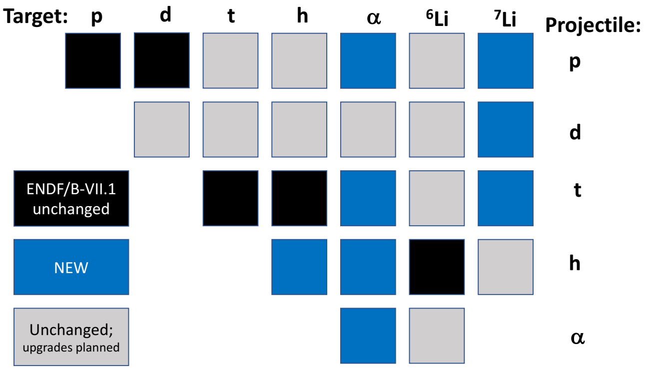

FIG. 149. (Color online) Summary of the recommendations of the best thermonuclear reaction sources for ENDF/B-VIII.0. The dark blue squares indicate the new reactions described in this section.

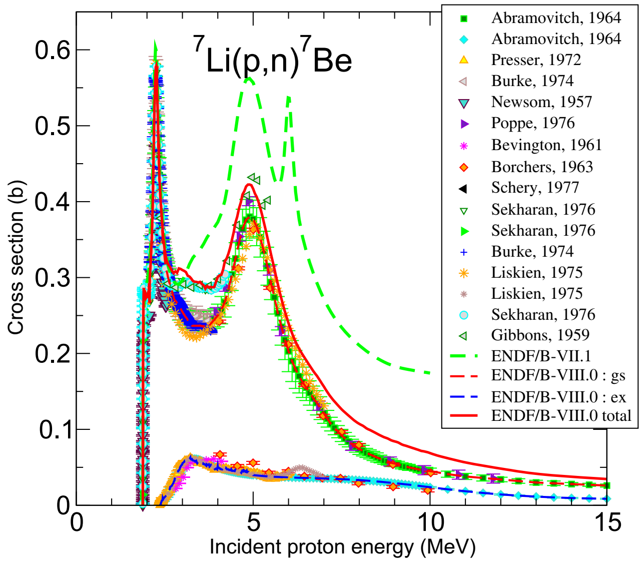

FIG. 150. (Color online) Cross section evaluation of ^{7}Li(p,n)^{7}Be (`MT` = `50`). Experimental data are from Refs. [393–403].

---

[5] Note that the `GMA` least-square fit [11] resulted in a 5 keV uncertainty of the PFNS average energy. Additional 5 keV were added from estimated unrecognized shape uncertainties [10] by re-scaling the whole covariance matrix with a 4.8 factor (*e.g.*, a minimum uncertainty around the PFNS average neutron energy increased from 0.8% to 1.8% due to the rescaling).

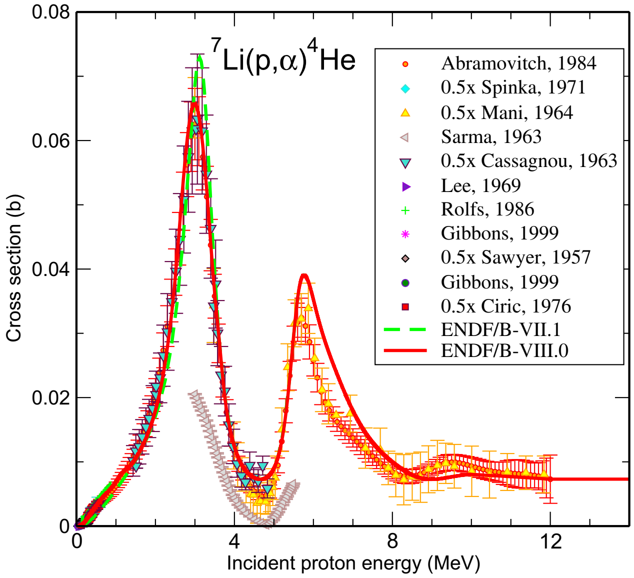

FIG. 151. (Color online) Cross section evaluation of ^{7}Li(p,α)^{4}He (`MT` = `850`). Experimental data are from Refs. [393, 403–409].

data of Presser *et al.* [394] for 2.3–5 MeV, Abramovitch *et al.* [393] for 5–25 MeV, and Poppe *et al.* [397] for 25–26 MeV.

The p + ^{7}Li → 2α evaluation used the Descouvemont *et al.* [410] S-factor up to 2.6 MeV, then used three experimental points from the Rice measurement, and from 3.15 MeV the ENDF/B-VII.1 evaluation was retained. The changes from ENDF/B-VII.1 are moderate, but still noticeable around 3 MeV, as shown in Fig. 151.

The p + ^{7}Li → d + ^{6}Li evaluation was extrapolated to 20 MeV, by lining up to the $E_p = 33.6$ MeV measurement of Kull *et al.* [411]. The remaining channels are kept unchanged from ENDF/B-VII.1.

B. d + ^{7}Li

The elastic scattering is from the ENDF/B-VII.1 evaluation. From ECPL the channels producing 2n + ^{7}Be (Fig. 152) and n + 2α are present, whereas the p + ^{8}Li cross section is based on data in two different energy ranges, up to $E_{\rm in} = 0.7$ MeV from Filippone *et al.* [412], and $0.7 < E_{\rm in} < 3.4$ MeV from Mingay *et al.* [413], with extrapolation to higher energies. The angular distributions are taken from the outgoing neutron distribution in the $n + \alpha$ channel, ignoring the mass difference between the neutron and the proton as well as the mass difference between the ^{8}Li residual and the (presumed) ^{8}Be residual in the n + α reaction.

For the d + ^{7}Li → t + ^{6}Li reaction, since the cross section data in ENDF/B-VII.1 is low, one based on the Macklin *et al.* [416] data up to $E_{\rm in} = 4$ MeV is recommended. Further, the ENDF evaluation is scaled up at higher energies, giving the evaluation of Fig. 153. The angular distributions are kept from ENDF/B-VII.1.

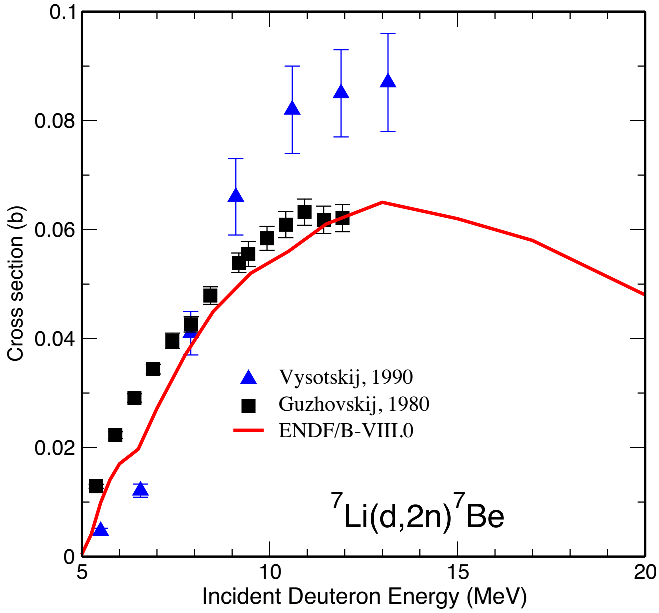

FIG. 152. (Color online) Cross section evaluation of ^{7}Li(d,2n)^{7}Be (`MT` = `16`). This channel did not exist in ENDF/B-VII.1. Experimental data are from Refs. [414, 415].

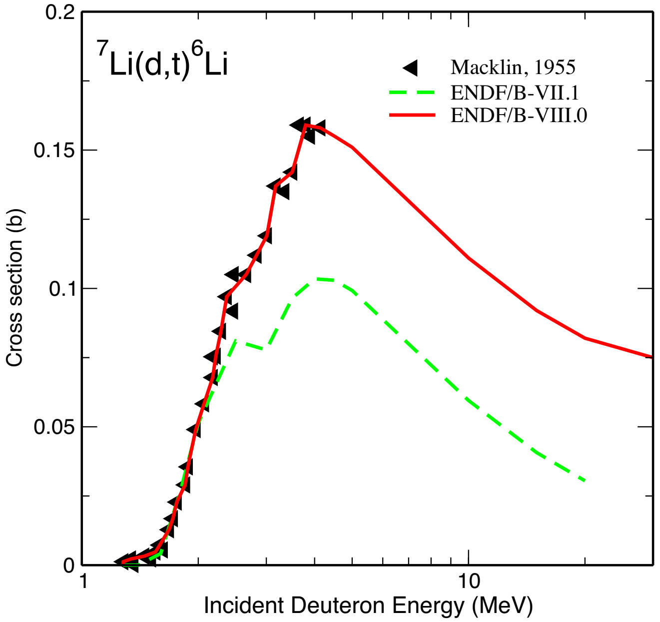

FIG. 153. (Color online) Cross section evaluation of ^{7}Li(d,t)^{6}Li (`MT` = `700`). Experimental data are from Refs. [416].

The d + ^{7}Li → p + ^{8}Li reaction of Fig. 154 is new to ENDF/B-VIII.0. It is constructed from Filippone [412] and Mingay [413] data below 0.7 MeV deuteron energy, with extrapolation to higher energies. The angular distributions are taken from the outgoing neutron distribution in data between 0.7 and 3.4 MeV, and by plausible extensions outside those ranges. The angular distributions are adopted from the neutrons in the (d,nα) channel.

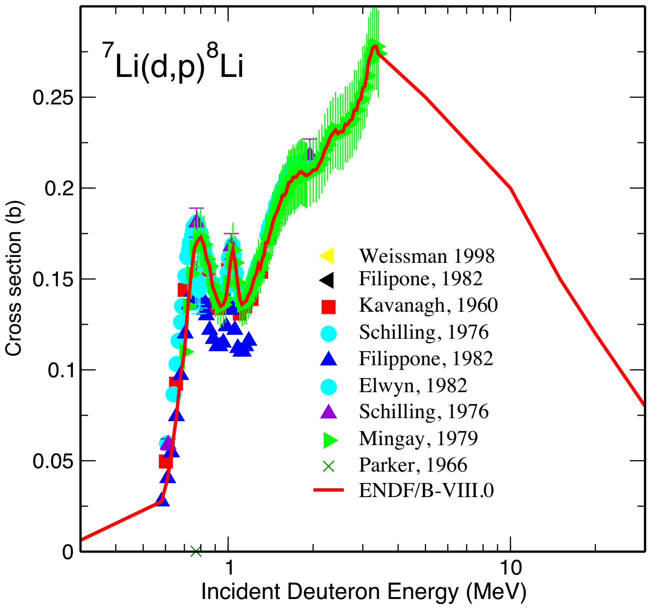

FIG. 154. (Color online) Cross section evaluation of ^{7}Li(d,p)^{8}Li (`MT` = `103`). This channel did not exist in ENDF/B-VII.1. Experimental data are from Refs. [412, 413, 417–421].

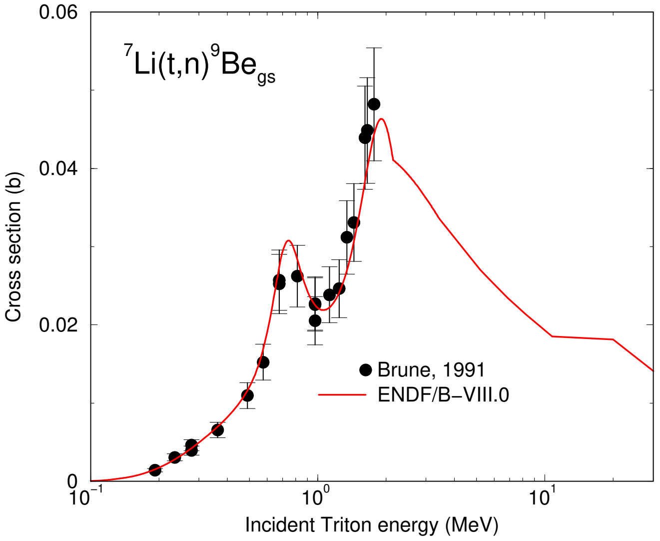

FIG. 155. (Color online) Cross section evaluation of ^{7}Li(t,n)^{9}Be (`MT` = `50`). The ^{7}Li + t reaction did not exist in ENDF/B-VII.1. Experimental data are from Ref. [422].

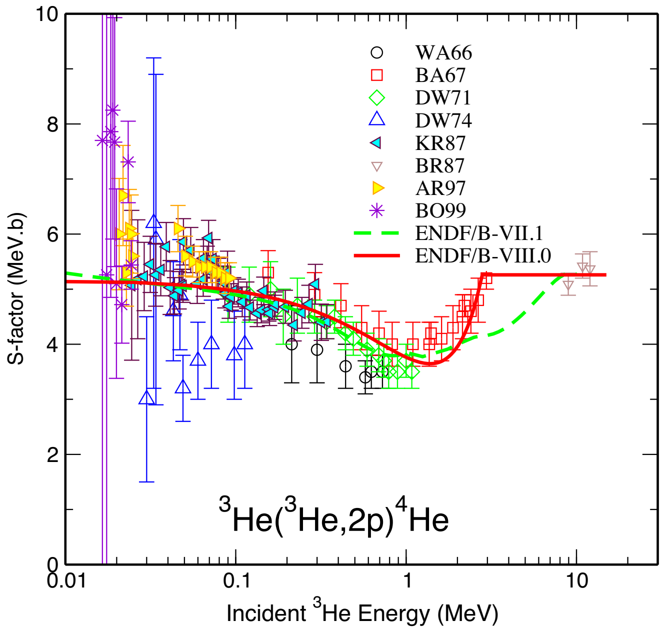

FIG. 156. (Color online) *S*-factor for ^{3}He(^{3}He,2p)^{4}He (`MT` = `111`). Experimental data are from Refs. [423–428].

C. t + ^{7}Li

This reaction did not exist in ENDF/B-VII.1. The ENDF/B-VIII.0 evaluation is based on the ECPL [392], adding the modernized (t, n) cross section shown in Fig. 155. The t + ^{7}Li → n + ^{9}Be$_{gs}$ cross sections starts with the Brune *et al.* [422] data up to 2.2 MeV (lab). The new evaluation uses 0.96 × the inclusive data in Fig. 9 in Ref. [422], since his Fig. 8 shows that this results in a good fit of the specific n + ^{9}Be$_{gs}$ measurements. Above that energy, the evaluated cross section for n + ^{9}Be → t + ^{7}Li is used, after conversion by detailed balance. The rest of the inclusive cross section of Fig. 9 of Ref. [422] is allocated to the t + ^{7}Li → 2n + ^{8}Be → 2n + 2α reaction (MT=24). The much weaker t + ^{7}Li → 3n + ^{7}Be reaction is from ECPL [392].

D. ^{3}He + ^{3}He

Most of Hale's ENDF/B-VII.1 evaluation was kept, with ^{3}He(^{3}He,^{3}He)^{3}He and ^{3}He(^{3}He,2p)α cross sections calculated from a charge-symmetric R-matrix analysis of the $T = 1$ part of the $A = 6$ system that fits t + t and ^{3}He(^{3}He, p) data of Holm *et al.* [429] at $E_{\rm in} < 2.2$ MeV, with extrapolations above that energy.

The ^{3}He + ^{3}He → 2p + α cross sections were taken from the NACRE S-factor evaluation [430]. This cross section includes the LUNA data [431], differs from the ENDF/B-VII.1 evaluation as shown in Fig. 156, but keeps its angle and energy distributions.

E. Charged-particle Elastic Scattering on ^{4}He

The Coulomb scattering cross sections for charged projectiles (p, t, ^{3}He and ^{4}He) on ^{4}He targets were calculated using the methodology developed by Perkins and Cullen [432, 433] for ECPL. None of these reactions existed in ENDF/B-VII.1. The cross sections are assumed identical to Rutherford for center-of-mass scattering angle parameter, $\mu = \cos\theta$, forward of 0.94 (20°). These elastic cross sections are represented in ENDF6 format by the LTP=12

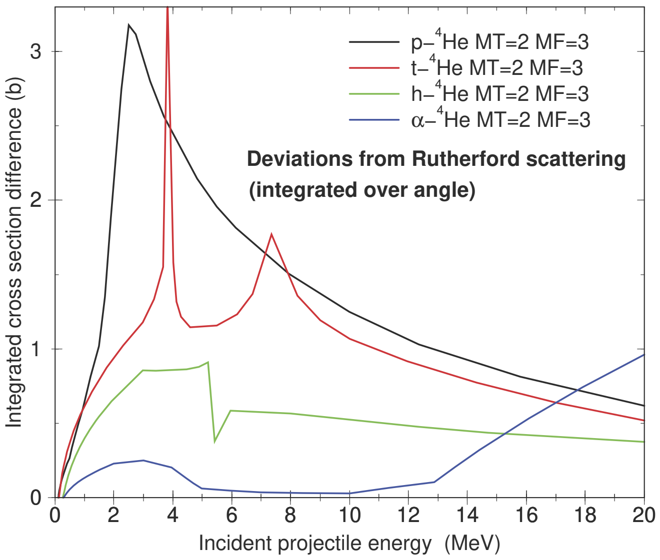

FIG. 157. (Color online) Integrated cross section differences, as stored in MF=3 for elastic scattering of p, t, ^{3}He (h) and α on ^{4}He.

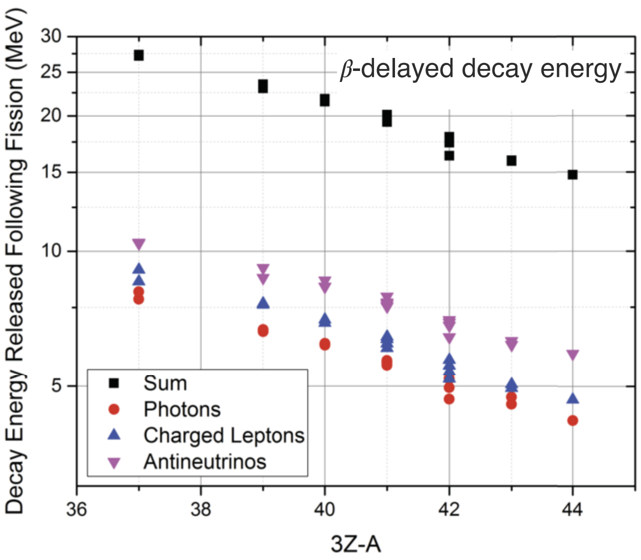

FIG. 158. (Color online) Beta-delayed decay energy, total as well as the components for the main radiation types, released following a neutron-induced fission event as function of (3Z-A).

method that stores a numerical difference with the Rutherford cross section. The angular integral of this difference is the 'effective cross section' stored in MF=3 for MT=2, and is plotted in Fig. 157 as a function of laboratory projectile energy to show positions of resonances.

X. DECAY DATA SUBLIBRARY

For the ENDF/B-VIII.0 release, the decay data sublibrary underwent a number of checks and updates, mainly on the beta intensities following beta-minus decay, X-ray energies for actinide nuclides, and some error fixes. In the previous release of the library, the mean electromagnetic (EEM) and light particle (ELP) energies values obtained from Total Absorption Gamma Spectroscopy (TAGS) experiments were used when available, as they are considered to be more precise than the ones obtained from high-resolution gamma spectroscopy, resulting in a better prediction of the decay heat following fission. In this release beta intensities from TAGS experiments [434–436] were incorporated in order to improve the electron and antineutrino spectra predictions following fission.

With an improved set of EEM, ELP values and the energy carried away by the antineutrinos, it is found that the decay energy released following fission, total as well as the main components, are a smooth function of the (3Z-A) parameter, where Z and A are the number of protons and nucleons in the compound nucleus, that is, Z=92 and A=236 for the neutron induced fission of ^{235}U. This is illustrated in Fig. 158.

Additionally, for another set of neutron-rich nuclides lacking TAGS data and yet deemed important in antineutrino spectra applications, beta intensities obtained from adjusting the electron spectra measured in Ref. [437] have been used. More details about this work can be found in Ref. [438]. In Fig. 159 the experimental electron spectra following fission for ^{235}U, ^{238}U, ^{239}Pu and ^{241}Pu [439–442] were compared with the calculations using the ENDF/B-VII.1 and the ENDF/B-VIII.0 sub-libraries showing a marked improvement with the latter.

Another update had to do with X-ray energies, which are produced following decay under two circumstances, electron capture or electron conversion. These processes create vacancies in the atomic orbitals, and as these vacancies are filled, X-rays and Auger electrons are emitted. For ENDF/B-VII.1, LLNL's EADL data, also part of the ENDF/B library, were used to calculate the energy and intensity of the transitions. The energies are calculated by a simple difference of the atomic shell binding energies listed in EADL. However, it was noticed that the Kα_1 X-ray energy for Uranium was shifted by +0.4 keV. An interim solution was implemented for ENDF/B-VIII.0, where K X-ray energies from the NIST X-ray Transition Energy Database [443] were used, for decay datasets with Z=89-96. A full implementation of this procedure will be done in the next release of the library. Finally, the datasets for the following nuclides were corrected: ^{86}As, ^{98m}Y, ^{149m}Er, ^{209}Rn, ^{220}Fr, ^{177}Ir, ^{203}Po, ^{224}Ac, ^{231}U, ^{236m}Np, ^{239}Am, and ^{253}Es.

XI. ATOMIC SUBLIBRARIES

The ENDF/B-VIII.0 library contains three atomic interaction data sublibraries that have been taken over from the ENDF/B-VI.8 library with some modest corrections made by D.E. Cullen in his EPICS2014 release

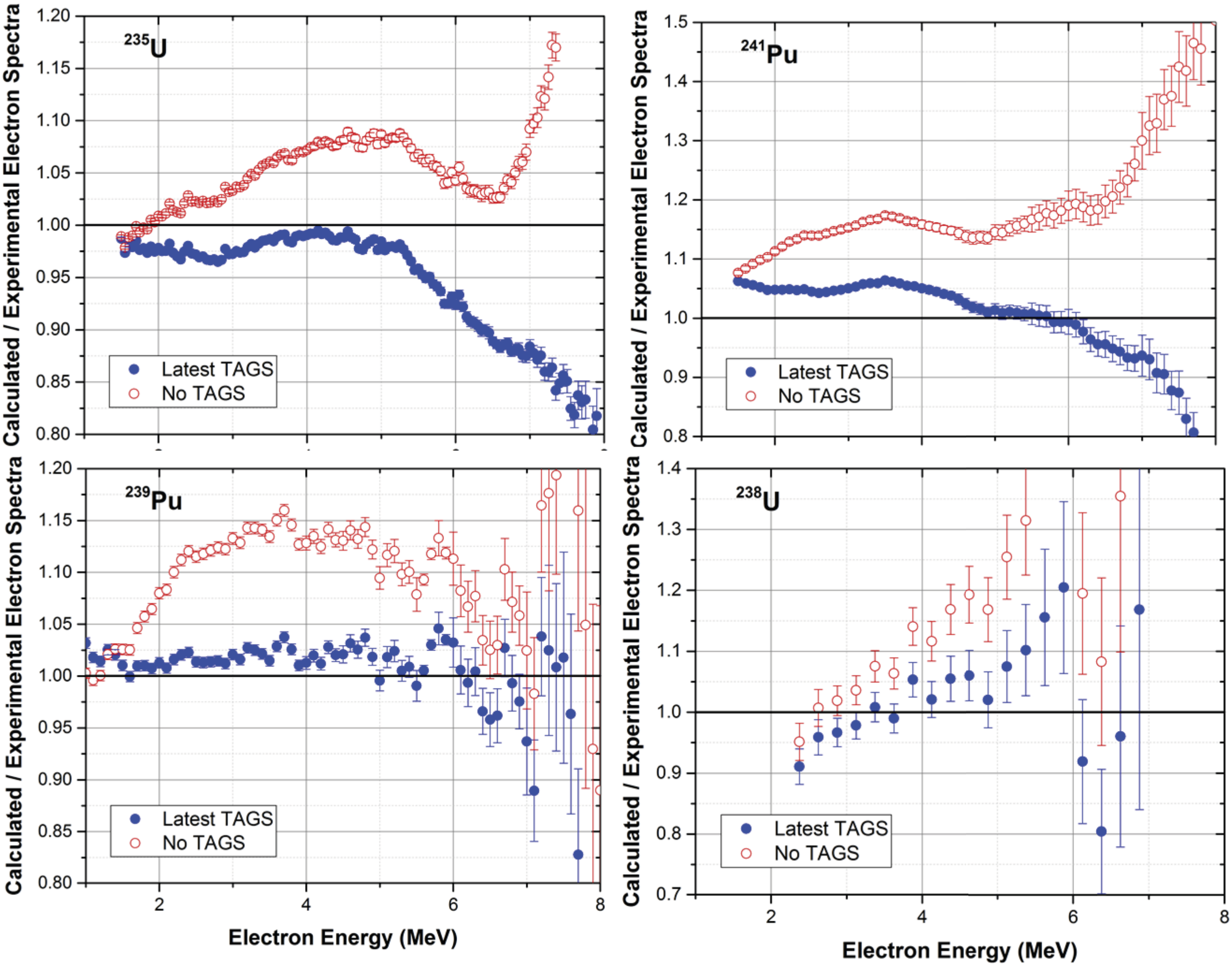

FIG. 159. (Color online) Ratio of calculated to experimental electron spectrum following the neutron induced fission of ^{235}U, ^{238}U, ^{239}Pu and ^{241}Pu. Full blue symbols correspond to the use of the ENDF/B-VIII.0 decay data sublibrary that incorporates the latest TAGS data in the beta intensities, while the red-open symbols correspond to the use of the ENDF/B-VII.1 decay data sublibrary.

[444]. These libraries are the photo-atomic, atomic relaxation and electro-atomic sublibraries and each contains elemental data for 100 materials (Z = 1 - 100) over the energy 10 eV to 100 GeV:

- **Photo-atomic sublibrary**: describes the interaction of photons with matter as well the direct production of secondary photons and electrons.
- **Atomic relaxation sublibrary**: describes the relaxation of atoms back to neutrality following an ionizing event. It describes the spectra of fluorescence photons from radiative transitions as an ionized atom returns to neutrality.
- **Electro-atomic sublibrary**: describes the interaction of electrons with matter as well as the direct production of secondary electrons and photons.

These three sublibraries are designed to be used in combination to perform detailed coupled electron-photon radiation transport calculations and are completely consistent with one another in terms of all using the same atomic parameters (e.g., subshell binding energies).

In the preparation for EPICS2014, the recent compilation of Deslattes *et al.* [445] was reviewed and several errors in the Deslattes *et al.* compilation were identified and corrected. No changes to ENDF were needed as a result of this comparison. However, it was noted that some electron interaction data was incorrectly translated from the ENDL to the ENDF format, namely MF/MT=26/527, which is defined as the average secondary electron energy after Bremsstrahlung. This was corrected.

Based on other currently available data, the EPICS2014 data showed a distinct bias in the atomic binding energies, and therefore transition energies. Recent work in Ref. [446] aims to eliminate this bias, by updating EPICS2017 to include recent atomic data that has been shown to produce better agreement to measured and theoretical results.

XII. INTEGRAL DATA TESTING SUMMARY

The integral data testing work we present in this section, to validate the ENDF/B-VIII.0 library's quality and performance, has focused mainly on criticality, with a more limited discussion on reaction rates and neutron transmission. It has also involved only a limited usage of the new sensitivity analyses tools that have been developed at organizations such as the NEA. Such tools have demonstrated their value, and will play a larger role in future ENDF efforts. They should be able to help identify where the biggest gaps and deficiencies lie, and point to possible solutions that best represent the fundamental and integral nuclear data.

A. Criticality Testing

Data testing of the ENDF/B-VIII.0 neutron and thermal scattering law files has been performed using a suite of criticality benchmarks from the International Criticality Safety Benchmark Evaluation Project, ICSBEP, [56]. The selection of benchmarks used provides a stringent test of the underlying nuclear data for the most important data files, including major actinide nuclides, structural element nuclides and common light element nuclides.

In this section, `MCNP`® criticality data testing is presented (see also the summary in Ref. [8]). Complementary testing is given in Capote *et al.* [17] in this same issue. The nomenclature E71 and E80 for the ENDF/B-VII.1 and ENDF/B-VIII.0 libraries is used in this section. Numerical calculated values are given in Appendix B, compared with measurements. Presently, though, calculated criticality uncertainties, obtained by propagating the covariance data for the various cross sections, are not provided (though examples of how this can be done are provided in the accompanying CIELO overview paper [8]). In the future we aim to provide such calculated uncertainties for all our criticality results.

ICSBEP benchmarks are identified using a three part nomenclature that defines the fuel, its molecular form and the dominant energy interval for the spectrum plus a sequential index number. The most common ICSBEP benchmark fuels are highly-enriched uranium (HEU, containing $\geq 90\%$ ^{235}U), intermediate-enriched uranium (IEU, containing $10\% \leq {}^{235}\text{U} \leq 90\%$), low-enriched uranium (LEU, containing $\leq 10\%$ ^{235}U), ^{233}U, plutonium (PU, primarily ^{239}Pu) and mixed U-Pu systems. The fuel composition is most commonly defined as one of metal (MET), compound such as UO_2 (COMP) or solution (SOL). The dominant flux spectrum is characterized as "THERMAL", "INTERMEDIATE" or "FAST" if 50% of more of the flux is below 0.625 eV, between 0.625 eV and 100 keV, or above 100 keV, respectively. Alternatively the spectrum is categorized as "MIXED" if none of these energy intervals account for at least 50% of the flux. A sample ICSBEP identifier is HEU-MET-FAST-001 corresponding to a highly-enriched uranium, metal fuel, fast spectrum benchmark. In actual practice the first letter in each part of the ICSBEP identifier is unique and so a common shorthand designation for this benchmark is HMF1.

The calculations for all k_{eff} data testing results shown here were performed using the continuous energy `MCNP`® version 6 code. The standard criticality calculation contains 50 million active neutron histories. 10,000 neutron histories per cycle with 25 warmup cycles were used to obtain a good initial source followed by an additional 5000 cycles. The `MCNP`® ACE files were created using NJOY2016. Cross section reconstruction (linearization) was done to a 0.1% tolerance followed by Doppler broadening to 293.6 K while maintaining the 0.1% reconstruction accuracy. For evaluated data files containing unresolved resonance probability tables were constructed with NJOY's PURR module using 32 bins and 64 ladders.

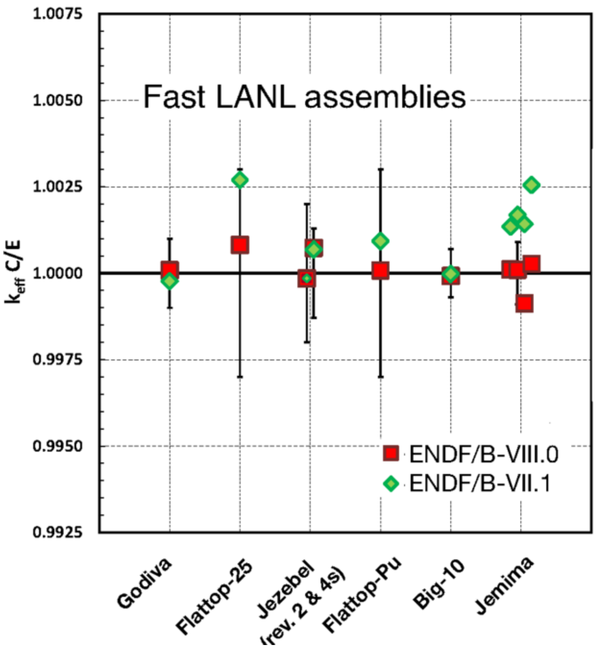

FIG. 160. (Color online) Calculated eigenvalue C/E values obtained with ENDF/B-VII.1 (E71) and ENDF/B-VIII.0 (E80) cross sections for a selection of fast LANL critical assemblies.

In the figures that follow k_{eff} C/E results are presented. Due to different modeling approximations by criticality benchmark evaluators a unity k_{eff} for every benchmark calculation is not expected. Use of C/E values allows all results to be shown in a consistent manner regardless of the specific underlying "C" and "E" values.

Figure 160 illustrates the calculated eigenvalues for a suite of fast LANL critical assemblies. These are unmoderated assemblies, either bare (HMF1 or Godiva, PMF1 or Jezebel), reflected (HMF28 or Flattop-25, PMF6 or Flattop-Pu) or a heterogeneous mix of enrichments (IMF1 or Jemima, IMF7 or Big-10). Results are shown for both ENDF/B-VII.1 (E71) and the new ENDF/B-VIII.0 (E80) files. As will be seen in many instances the E71 bare assembly results were very accurate and so it is gratifying to see these good results retained with the E80 files. The new files produce improved results for the reflected and heterogeneous assemblies. This improvement is largely due to the more accurate data present in the E80 ^{238}U evaluated file.

There are various aspects of the ICSBEP Handbook that make it a particularly valuable resource for cross section data testing. For example, there may be a suite of benchmarks with only a single attribute varied that provides test data over a wide parameter range. The HMF7 benchmark is such an example. This benchmark consists of HEU plate fuel with varying amounts of polyethylene interstitial moderator, reflector or both, yielding a suite of benchmark assemblies whose average fission energy varies by orders of magnitude. Figure 161 shows C/E calculated eigenvalues for this benchmark and the insert to this figure shows how the average C/E values have varied for the most recent ENDF/B data sets - improvements embodied in ENDF/B-VIII.0 are evident. The overall trends have not changed, with the suggestion of an increasing bias in calculated eigenvalues when the energy decreases from near 1 MeV to about 100 keV which then reverses as the average energy continues to decrease through the lower keV energy range.

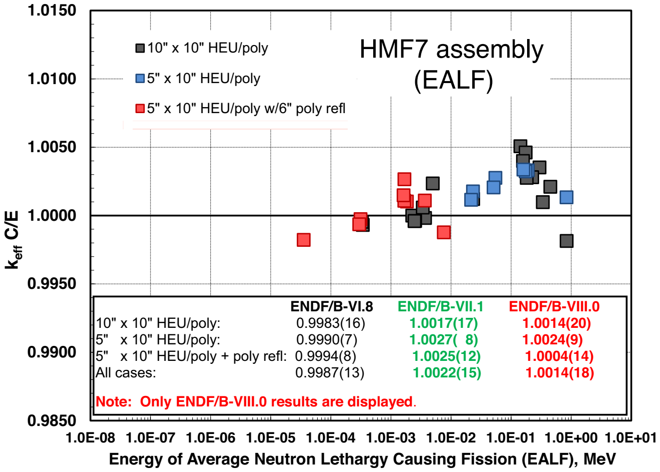

FIG. 161. (Color online) Calculated eigenvalue C/E values obtained with ENDF/B-VIII.0 cross sections for the HMF7 benchmark suite. The presence of varying amounts of polyethylene placed between and around the HEU fuel provides criticality data for a wide range of average fission energies. The figure inset shows how the average eigenvalues have varied for recent ENDF/B data sets.

Another important benchmark class is the HEU-SOL-THERM category. Many of these benchmarks are easily modeled as simple spheres or cylinders. Variation in assembly size, whether the assembly is reflected or bare and solution hydrogen-to-uranium ratio in the assembly make a correlation of calculated eigenvalue versus assembly leakage an important metric to assess the accuracy of the underlying thermal data. Results from a suite of 45 HST assemblies are shown in Fig. 162. The desired outcome from the regression analysis is a line whose intercept is unity and whose slope is zero. The dotted curves show the 95% confidence interval for the regression fit, demonstrating that the intercept is statistically equal to unity, specifically 0.9999 ± 0.0032, and the slope is statistically equal to zero, specifically -0.0008 ± 0.0085. These ± values are 95% confidence intervals on the regression coefficient. The unity intercept and zero slope goal has been attained since the work of Lubitz in the mid-1990s and has been retained with these latest data. However those earlier results were obtained by artificially shifting the thermal and low energy ^{235}U prompt ν, capture and fission nuclear data by about half a standard deviation from the evaluators preferred values. These artificial shifts have been eliminated in the E80 file.

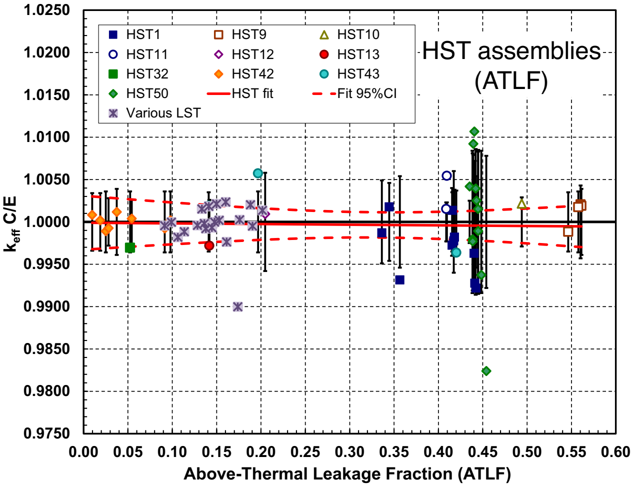

FIG. 162. (Color online) Calculated eigenvalue C/E values obtained with ENDF/B-VIII.0 cross sections for a suite of HST critical assemblies (HEU thermal solutions). The linear regression fit yields a unity intercept and zero slope, indicating no bias nor energy-dependent trend in the underlying thermal energy nuclear data. Various LST values are also displayed. Although not included in the regression fit they demonstrate that the HST regression is applicable to the LST benchmark class.

The LEU-COMP-THERM (LCT) benchmark category is of particular interest to the reactor physics community, and represents one of the larger categories for which benchmark evaluations are available in the ICSBEP Handbook. Figure 163 shows the calculated eigenvalue results for a number of LCT benchmarks. These include both water and metal reflected configurations. There is some obvious variation in a few of these benchmarks but overall the results are quite good. In total 247 LCT assemblies were modeled and an average k_{eff} C/E of 0.9992 was obtained with a population standard deviation of 0.0027 with the E80 data files. These results are virtually identical to the 0.9995 ± 0.0026 values obtained with E71.

The Pu-SOL-THERM benchmark category is important to those involved in plutonium fuel recycling. Prior to E80 calculated eigenvalues for this benchmark category were biased high, typically by about 500 pcm. As shown in Fig. 164 this bias has been eliminated with the E80 nuclear data files, as for a suite of 158 PST assemblies the

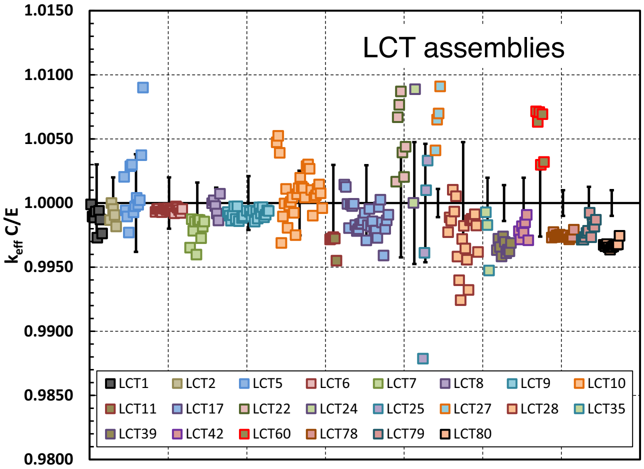

FIG. 163. (Color online) Calculated eigenvalue C/E values obtained with ENDF/B-VIII.0 cross sections for a suite of LCT critical assemblies (lattices).

average k_{eff} C/E has dropped from E71's 1.0045 ± 0.0046 to E80's 0.9998 ± 0.0047. The ± value is the standard deviation for the 158 sample population. The linear regression parameters are 0.9987 ± 0.0024 (95% confidence) for the intercept and +0.0035 ± 0.0070 (also 95% confidence). It is unfortunate that the spread in calculated eigenvalues is so large, but the uncertainties in these decades old experiments are also large, often several hundred pcm or more, and so while it is gratifying to see this improvement in the average eigenvalue there is little chance for a decrease in the spread of individual calculated eigenvalues.

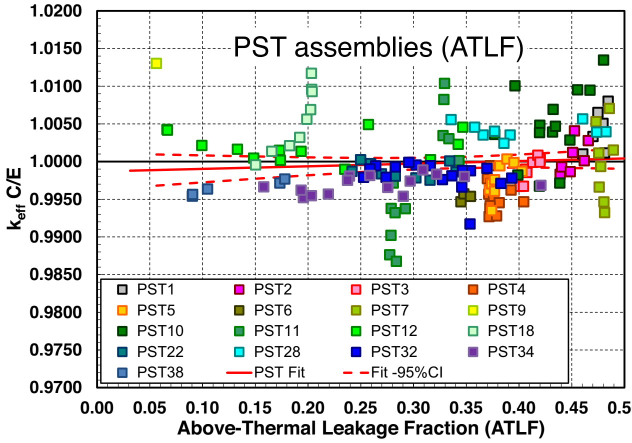

FIG. 164. (Color online) Calculated eigenvalue C/E values obtained with ENDF/B-VIII.0 cross sections for a suite of PST critical assemblies (Pu thermal solutions).

For the ^{233}U file, the relatively poor E71 performance seen in intermediate and thermal energy ^{233}U benchmarks remains in E80. This is shown in Fig. 165 for a suite of USI, UCT, and UST assemblies.

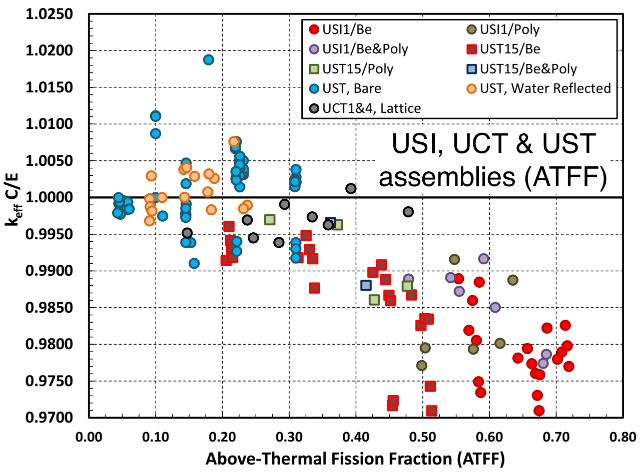

FIG. 165. (Color online) Calculated eigenvalue C/E values obtained with ENDF/B-VIII.0 cross sections for a suite of USI, UCT and UST critical assemblies (^{233}U solutions). There is an obvious trend in calculated eigenvalues versus Above-Thermal Fission Fraction. Resolution of the underlying deficiency awaits a future revision of the ^{233}U evaluated file.

A non-fissile element of considerable importance to the reactor, criticality safety and shipping communities is iron; a major constituent of steel. There are a number of ICSBEP benchmarks with iron or steel in close proximity to the fuel. The k_{eff} C/E values for a selection of these benchmarks are shown in Fig. 166. Results obtained with E71 cross sections are mostly satisfactory (with the Argonne ZPR6/10 (or PMI2) being a notable exception) but are uniformly improved with E80 data. As described earlier in this report there has been significant work to upgrade the ^{56}Fe file. The improved performance seen here serves to validate this effort.

Figure 167 displays calculated eigenvalues for a selection of benchmarks with Be or BeO. Fuels include HEU, Pu or a mix of HEU and Pu. Revisions to the ^{9}Be evaluated file were discussed previously (changes were made just to elastic angular distributions and (n,2n) neutron angular and energy distributions). The practical impact of these revisions is to lower the calculated eigenvalue by a little more than 100 pcm as the average C/E for this benchmark category is 1.0022 ± 0.0032 for E71 and 1.0010 ± 0.0033 for E80, that is, the overall previous bias was reduced by a factor of two. These ± values represent the estimated population standard deviation for the 76 assembly calculations shown here. In sharp contrast to the Fe bearing assemblies there is considerable spread in these Be assembly results. It is difficult to imagine what combination of nuclear data changes could reduce this spread and it seems more likely that new criticality experiments done to modern QA standards are needed.

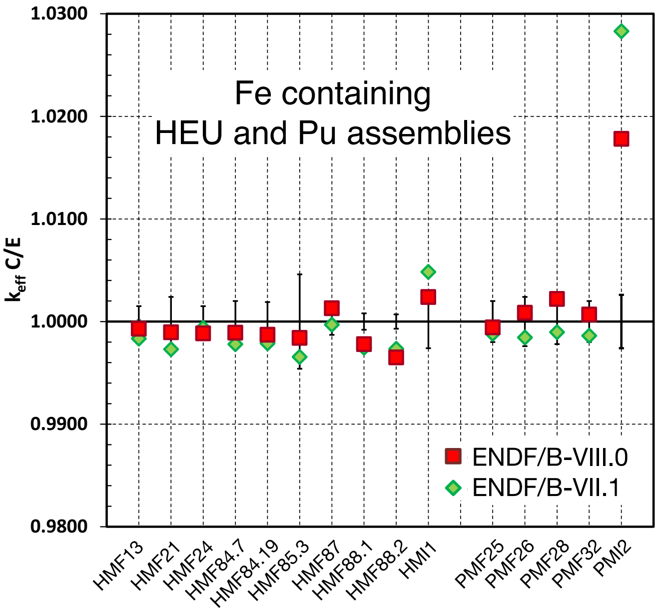

FIG. 166. (Color online) Calculated eigenvalue C/E values obtained with ENDF/B-VIII.0 cross sections for a selection of critical assemblies with iron or steel in close proximity to the fuel. The leftmost ten assemblies are HEU fueled while the rightmost five assemblies are Pu fueled.

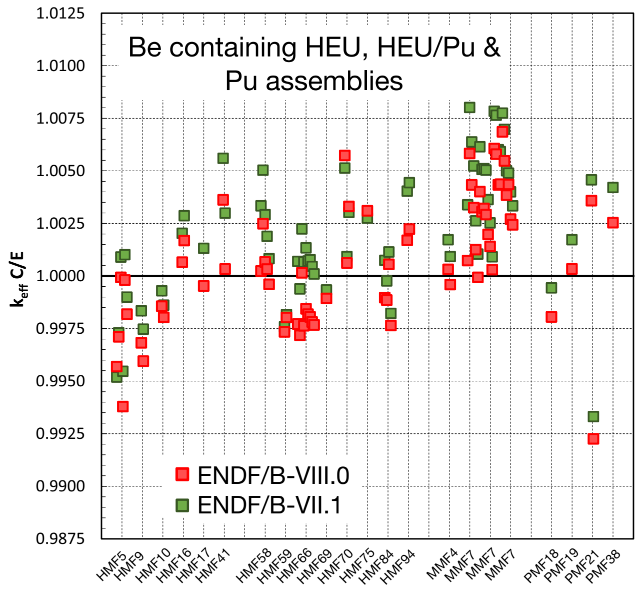

FIG. 167. (Color online) Calculated eigenvalue C/E values obtained with ENDF/B-VIII.0 cross sections for a selection of critical assemblies with Be or BeO moderators and/or reflectors. The leftmost fifteen assemblies are HEU fueled, the next two are a mix of HEU and Pu while the rightmost four assemblies are Pu fueled.

B. Delayed Neutron Testing

Although the delayed neutron data have not been changed from their ENDF/B-VII.1 values, they were tested against measurements of effective delayed neutron fraction $\beta_{\rm eff}$ in critical configurations. Unlike the situation for $k_{\rm eff}$, only a handful of measurements of $\beta_{\rm eff}$ have been reported in open literature with sufficiently detailed information. In Ref. [21] more than twenty measurements are listed, including several measurements of Rossi-α, which is closely related to $\beta_{\rm eff}$ through the prompt neutron generation life time. We avoid the term “benchmark” for these cases, because a good benchmark description, comparable to those given in the ICSBEP Handbook is not available.

These measurement data were used for testing ENDF/B-VII.0 in 2006 [1, 21] and ENDF/B-VII.1 in 2011 [2]. These comparisons were made on the basis of a non-standard version of `MCNP`®, including an approximate method to calculate $\beta_{\rm eff}$. Since then version 6 of `MCNP`®was released, in which an improved method for adjoint weighting has been implemented. This standard version of `MCNP`®produces results for both $\beta_{\rm eff}$ and Rossi-α, enabling an even better comparison between measurements and calculations. An alpha release of `MCNP`®6 was used 2012 in combination with ENDF/B-VII.1 to test the delayed neutron data in Ref. [447]. The current release of the library has been tested using a standard `MCNP`®6 release, in this case 6.1.1.

The measurement data include several cores with thermal spectrum, all of which are fueled by ^{235}U. In most of these cases the uranium is low enriched (Sheba-II, SHEcore8, Stacy cores, TCA cores, IPEN/MB01 core), with only one core with high enriched uranium (Winco slab tank). As a consequence, for thermal spectrum only the ^{235}U delayed neutron data are tested by these calculations.

For many of the fast spectrum cores, not only ^{235}U was used as fuel (Masurca, FCA, SNEAK, ZPR, Godiva), but also plutonium (FCA, ZPR, Jezebel) and a mix of the two (Masurca, FCA, SNEAK, ZPPR). Also there are cores with ^{233}U (Skidoo). Using these fast spectrum cases, the ^{233,235,238}U and ^{239}Pu data are tested. Also, one should bear in mind that the tests performed here are only sensitive to the total delayed neutron yields. The delayed neutron yields per group are not tested, nor are the values for the decay constant per group.

The results based on ENDF/B-VIII.0 are given in Tables XXXIV and XXXV and plotted in Fig. 168, as well as the results based on other libraries. As expected, the results are similar to those obtained with ENDF/VII.1. The result for Sheba-II based on ENDF/B-VII.1 is slightly different from the one in Ref. [447], because that was based on the beta4 release of the library, which contained a version of the ^{19}F data that influenced this calculation. Also, compared with Refs. [2, 447], the results for the Proteus have been omitted, because of concerns about the representativity of the model that was used.

TABLE XXXIV. The values for $C/E-1$ for the β_{eff} calculations. The uncertainty quoted for $C/E-1$ includes only the statistical uncertainty of the calculation. All the cases have a fast spectrum, except for TCA and IPEN/MB01.

	Experiment β_{eff} (pcm)	ENDF/B VIII.0 $C/E-1$ (%)	ENDF/B VII.1 $C/E-1$ (%)	JENDL 4.0 $C/E-1$ (%)	JEFF 3.1.1 $C/E-1$ (%)
TCA	771 (2.2%)	0.1±0.8	-1.0±0.8	1.3±0.8	3.9±0.7
IPEN/MB01	742 (0.9%)	0.1±0.9	1.2±0.9	0.8±0.9	4.6±1.0
Masurca/R2	721 (1.5%)	0.7±1.1	2.2±1.1	0.7±1.1	2.9±1.1
Masurca/ZONA2	349 (1.7%)	-2.9±1.5	-3.4±1.5	-3.2±1.5	1.1±1.7
FCA/XIX-1	742 (3.2%)	-2.0±1.2	0.7±1.2	2.4±1.2	3.6±1.2
FCA/XIX-2	364 (2.5%)	1.4±1.6	2.7±1.6	1.6±1.6	3.8±1.6
FCA/XIX-3	251 (1.6%)	4.4±1.9	-0.8±2.0	-3.2±2.1	-1.2±2.0
SNEAK/9C1	758 (3.2%)	-2.4±1.1	-2.6±1.1	-1.3±1.1	-0.8±1.1
SNEAK/7A	395 (5.1%)	-7.6±1.6	-5.3±1.6	-3.5±1.6	-1.0±1.5
SNEAK/7B	429 (4.9%)	-1.6±1.4	-3.0±1.4	0.2±1.4	3.7±1.3
SNEAK/9C2	426 (4.5%)	-8.7±1.5	-9.2±1.6	-9.2±1.6	-5.4±1.5
ZPR-9/34	667 (2.2%)	3.7±2.2	1.0±2.2	2.2±2.2	4.2±2.2
ZPR-U9	725 (2.3%)	-4.3±1.9	-2.1±1.8	1.5±1.9	0.8±1.9
ZPPR-21/B	381 (2.4%)	-7.9±2.3	-8.4±2.3	-11.5±2.4	-4.5±2.2
ZPR-6/10	222 (2.3%)	3.6±3.9	4.1±3.9	-1.8±4.1	3.9±0.7
Godiva	659 (1.5%)	0.3±1.1	-0.9±1.1	-2.1±1.1	-1.7±1.1
Topsy	665 (2.0%)	3.6±1.0	3.0±1.0	2.4±1.0	2.4±1.0
Jezebel	194 (5.2%)	-4.6±1.6	-2.6±1.6	-5.2±1.6	-1.0±1.6
Popsy	276 (2.5%)	2.9±1.4	1.8±1.4	1.8±1.4	4.3±1.4
Skidoo	290 (3.4%)	1.7±1.4	2.4±1.3	2.1±1.4	1.7±1.4
Flattop	360 (2.5%)	5.6±1.3	2.8±1.4	5.8±1.3	4.2±1.3

TABLE XXXV. The values for $C/E-1$ for the Rossi-α calculations. The uncertainty quoted for $C/E-1$ includes only the statistical uncertainty of the calculation. All the cases have a thermal spectrum, except for Big Ten.

	Experiment $-\alpha$ (s^{-1})	ENDF/B VIII.0 $C/E-1$ (%)	ENDF/B VII.1 $C/E-1$ (%)	JENDL 4.0 $C/E-1$ (%)	JEFF 3.1.1 $C/E-1$ (%)
SHE/core8	6.53e-3 (5.2%)	0.1±1.0	-1.2±1.2	-2.1±1.0	-3.5±1.0
Sheba-II	200.3e-6 (1.8%)	-4.0±1.4	-3.7±1.5	1.6±1.5	4.7±1.4
Stacy/run-029	122.7e-6 (3.3%)	-0.9±1.2	-0.2±1.2	0.1±1.2	3.5±1.2
Stacy/run-033	116.7e-6 (3.3%)	-0.4±1.2	-1.0±1.2	0.3±1.2	0.2±1.2
Stacy/run-046	106.2e-6 (3.5%)	-1.3±1.2	0.2±1.2	-2.3±1.2	0.7±1.1
Stacy/run-030	126.8e-6 (2.3%)	1.3±1.2	-1.3±1.2	0.1±1.2	0.9±1.2
Stacy/run-125	152.8e-6 (1.7%)	-0.6±1.2	0.9±1.2	3.3±1.2	3.2±1.2
Stacy/run-215	109.2e-6 (1.6%)	-1.1±1.2	-1.5±1.2	-1.3±1.2	0.0±1.2
Winco	1109.3e-6 (0.1%)	1.4±1.0	1.6±1.0	-1.9±1.0	0.7±1.0
Big Ten	117.0e-6 (0.9%)	-2.1±1.4	1.6±1.5	4.1±1.4	-0.3±1.5

C. Calculated Critical Masses

The calculated critical masses of actinides provide a convenient way to assess some of the changes that have been introduced in moving to ENDF/B-VIII.0 from VII.1. Two types of idealized critical masses were calculated by NRG Petten: unreflected spheres of pure actinides, having a fast neutron spectrum, and water reflected spheres of actinides dissolved in water, having a thermal neutron spectrum [448]. The former systems are especially sensitive to changes to the cross sections and the number of neutrons per fission ($\bar{\nu}$) in the fast energy region. The latter systems are sensitive to the same quantities in the thermal range. The results are shown in Tables XXXVI–XXXVIII. Compared to the same table in Ref. [2], the values for ^{239}Np have been revised: this isotope does not reach fast criticality for ENDF/B-VIII.0, VII.1 or JENDL-4.0; instead a value for k_∞ is given. Also, the value for ^{242}Pu based on ENDF/B-VII.1 has been revised.

The results for the fast critical systems for Th, Pa, U, Np, Pu and Am are mostly close to the results for ENDF/VII.1, except for ^{236}Np (-33%), ^{238}Np (-25%), ^{242}Pu (-17%), ^{244}Pu (-12%) and ^{243}Am (+23%). The results for Cm and higher Z elements almost all differ more than 10% from the ENDF/B-VII.1, with the differences going either way (positive and negative). The differences range from -50% for ^{250}Cm to +95% for ^{255}Es. These changes are related to the update of $\bar{\nu}_p$, see Sec. III G.

The results for the thermal systems, Table XXXVIII, show good consistency with values based on ENDF/B-

TABLE XXXVI. Critical masses in kg for four cross-section libraries, calculated using `MCNP`®. For nuclides without critical mass, k_∞ values are listed in Table XXXVII.

Isotope	Density (g/cm^3)	ENDF/B-VIII.0 (kg)	ENDF/B-VII.1 (kg)	JENDL-4.0 (kg)	JEFF-3.1 (kg)
Th-229	11.5751	30889.	30840.	30840.	-
Pa-229	15.2025	37.42	37.4	37.4	-
Pa-230	15.2691	36.40	36.3	36.3	-
Pa-232	15.4021	113.28	113.6	113.59	104.93
U-230	18.5209	11.25	11.2	11.2	-
U-231	18.5646	12.14	12.1	12.1	-
U-232	18.6822	6.14	6.14	6.14	3.65
U-233	18.7621	15.51	15.6	15.6	15.3
U-234	18.8431	127.39	128.0	111.6	127.4
U-235	18.9231	46.36	46.6	47.0	47.12
U-237	18.9655	226.12	225.6	237.2	75.7
Np-234	20.2171	5.40	5.40	5.40	-
Np-235	20.3035	8.06	8.06	8.06	12.03
Np-236	20.3901	7.19	10.8	10.8	15.8
Np-237	20.4762	58.59	58.7	58.7	63.8
Np-238	20.5621	14.84	19.9	19.9	12.8
Pu-236	19.3668	4.97	4.96	4.97	7.59
Pu-237	19.4491	4.99	4.97	4.97	3.18
Pu-238	19.5312	8.44	8.44	8.91	8.36
Pu-239	19.6135	10.23	10.2	10.2	10.2
Pu-240	19.6957	37.80	39.9	41.9	33.8
Pu-241	19.7780	13.13	13.1	11.8	12.2
Pu-242	19.8602	74.04	88.9	75.9	63.5
Pu-244	20.0247	101.21	115.4	115.4	250.5
Am-240	13.6033	11.05	11.1	11.1	-
Am-241	13.6601	67.19	70.2	61.3	57.2
Am-242	13.7171	10.84	10.9	12.4	13.7
Am-242m	13.7171	10.84	11.6	12.8	12.5
Am-243	13.4071	186.60	152.	191.	224.
Am-244	13.4623	18.48	-	31.8	-
Cm-240	13.2961	11.08	11.1	11.1	23.6
Cm-241	13.3517	8.04	6.99	6.99	9.82
Cm-242	13.4071	17.63	14.5	14.5	17.9
Cm-243	13.4631	5.94	5.95	5.95	6.97
Cm-244	13.5181	17.65	27.1	27.1	34.0
Cm-245	13.5731	11.81	11.8	11.8	12.6
Cm-246	13.6291	46.11	87.7	87.7	49.0
Cm-247	13.6841	8.56	7.47	7.47	7.07
Cm-248	13.7401	61.28	98.2	98.2	68.4
Cm-250	13.8501	941.63	1865.	1865.	23.6
Bk-245	14.7801	118.61	82.4	82.4	-
Bk-246	14.8406	8.86	7.77	7.79	-
Bk-247	14.9010	403.20	318	318	73.3
Bk-249	15.0219	104.65	155.	155.	211.
Bk-250	15.0824	20.58	28.2	28.2	6.01
Cf-246	14.9271	5.25	4.62	4.62	-
Cf-248	15.0486	20.39	21.9	21.9	-
Cf-249	15.1094	6.84	6.02	6.02	5.8
Cf-250	15.1702	18.17	19.1	19.2	8.88
Cf-251	15.2301	14.08	12.5	12.5	5.47
Cf-252	15.2901	3.48	3.35	3.35	5.70
Cf-253	15.3510	39.10	42.3	42.3	-
Cf-254	15.4101	8.14	7.90	7.90	4.27
Es-251	8.7730	63.60	58.0	58.0	-
Es-252	8.8080	11.13	9.56	9.56	-
Es-253	8.8430	253.19	209.	209.	182.
Es-254	8.8781	15.06	13.00	13.00	9.89
Es-255	8.9131	4936.5	2526.	2526.	11.3
Fm-255	7.2411	16.54	14.8	14.8	10.2

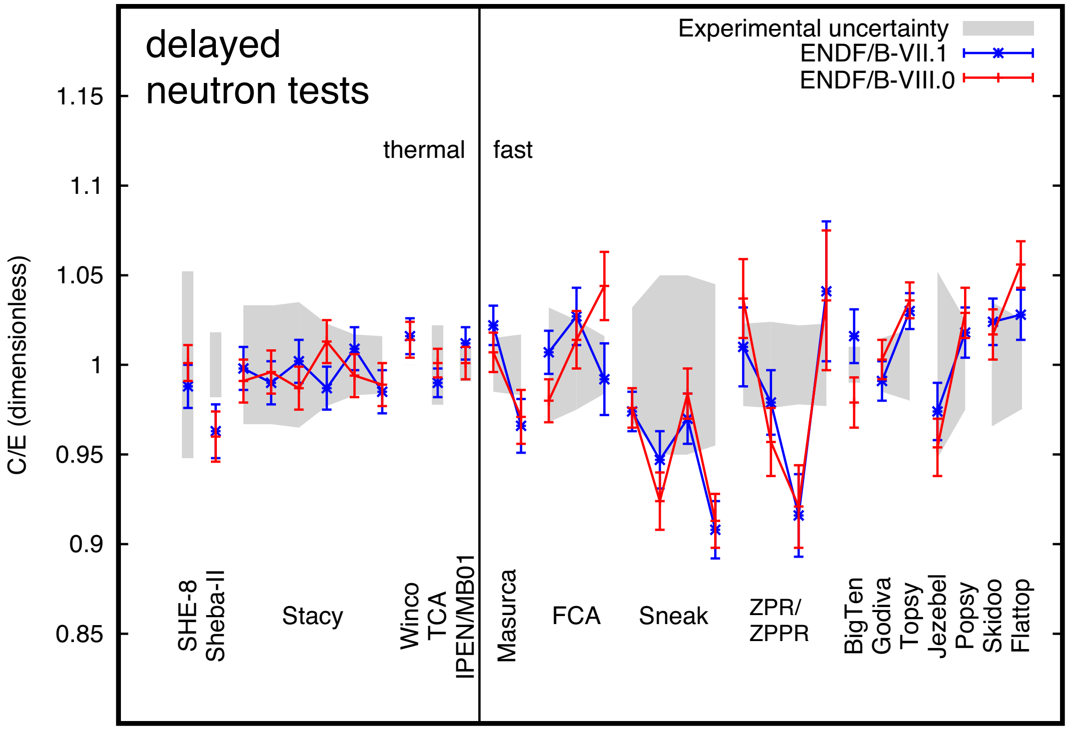

FIG. 168. The values for C/E for the delayed neutron tests. The systems are roughly ordered according to the average energy at which fission takes place, from low energy (left) to high (right).

TABLE XXXVII. Values for k_∞ for nuclides without fast critical mass, for four cross-section libraries, calculated using `MCNP`®.

Isotope	Density (g/cm^3)	ENDF/B-VIII.0 k_∞	ENDF/B-VII.1 k_∞	JENDL-4.0 k_∞	JEFF-3.1 k_∞
Th-227	11.4738	0.919	0.918	0.919	0.919
Th-228	11.5244	0.361	0.361	0.360	0.360
Th-231	11.6764	0.762	0.762	0.762	0.762
Th-232	11.7270	0.062	0.063	0.063	0.063
Th-234	11.8284	0.025	0.025	0.025	0.025
Pa-231	15.3355	0.924	0.925	0.956	0.924
Pa-233	15.4686	0.220	0.221	0.226	0.221
U-236	18.8853	0.710	0.710	0.662	0.710
U-238	19.0457	0.310	0.306	0.307	0.306
Np-239	20.6487	0.680	0.680	0.680	-
Pu-246	20.1893	0.871	0.803	0.802	0.815

TABLE XXXVIII. Minimum critical masses in grams for four cross-section libraries, calculated using `MCNP`®.

Isotope	ENDF/B-VIII.0 (g)	ENDF/B-VII.1 (g)	JENDL-4.0 (g)	JEFF-3.1.1 (g)
U-233	560.5	556.8	561.5	562.2
U-235	788.1	791.9	786.4	791.8
Pu-236	1156.4	1146.7	1135.1	1120.3
Pu-239	518.2	503.2	498.7	512.7
Pu-241	280.9	277.8	278.8	282.2
Am-242m	23.4	23.2	22.2	23.0
Cm-243	218.8	216.5	215.4	186.5
Cm-245	64.1	63.3	63.0	61.1
Cm-247	1269.2	1205.9	1200.8	2115.4
Cf-249	63.2	63.1	62.8	62.3
Cf-251	29.0	29.7	29.6	25.2

VII.1. There is a 3% increase in the minimum critical mass for ^{239}Pu related to the reduced overprediction of Pu solution criticality safety benchmarks. The minimum critical mass of ^{247}Cm has increased by 5% compared to ENDF/B-VII.1.

D. Reaction Rates in Critical Assemblies

Critical assembly reaction rate data provide a key integral validation test of ENDF (n,f), (n,2n) and (n,γ) data and `MCNP`® neutronic simulations.

For several decades the fast critical assemblies located at Los Alamos National Laboratory's TA-18 complex provided criticality and reaction rate data. These assemblies include Godiva or HMF1 (a bare HEU sphere), Jezebel or PMF1 (a bare plutonium sphere), Jezebel-23 or UMF1 (a bare ^{233}U sphere), and Flattop assemblies. Flattop-25 or HMF28 contained an HEU core surrounded by ^{238}U reflector material and Flattop-Pu or PMF6 contained a plutonium core also surrounded by ^{238}U reflector material. Criticality predictions for these assemblies have already been presented and now the discussion focuses on the available reaction rate data. All of these assemblies fall in the ICSBEP FAST category, with the predominant spectrum energy above 100 keV. However the exact spectra vary considerably from assembly-to-assembly and as a function of radius, particularly in the Flattop assemblies. Another LANL assembly that is a source of reaction rate data is the heterogeneous Big-10 assembly.

The measured reaction rate data were obtained by irradiating foils with subsequent gamma counting or using fission chambers. In most cases data were obtained at the center of the assembly, but in selected irradiations with the Flattop assemblies data were obtained at varying radial distances from the assembly center, extending well into the reflector. These radial measurements provide data over a changing average energy. As with the criticality simulations the `MCNP`® version 6 continuous energy Monte Carlo code is used. The measurement location is approximated for the center region by restricting the `MCNP`® version 6 tally to spherical 0.25 cm central region. From there the tally regions were defined by successive 0.5 cm thick shells until the core radius was reached. The same shell thickness was used through the reflector. In order to obtain adequate statistics, particularly for the smaller tally regions near the core center, the `MCNP`® version 6 simulation was run for 5025 cycles with one million neutron histories per cycle, for a total of five billion active neutron histories. The results from the first 25 cycles were not included in the final tally statistics.

The reported data, and the calculated tallies are not absolute reaction rates, but are a ratio of the reaction rate of interest to the ^{235}U(n,f) reaction. An example of how these ratios can vary within the Flattop-25 assembly is shown in Fig. 169. The central core region contains the higher average spectrum energy and so the measured and calculated ratios are highest in that location. The core in Flattop-25 has a 6.1 cm radius and so as the transition from the HEU core to the ^{238}U reflector occurs, the spectrum becomes softer. Since ^{238}U(n,f) and (n,2n) are threshold reactions their ratio to ^{235}U(n,f) quickly decreases when traversing into the reflector. It is evident that these data are modeled very well with `MCNP`® version 6.

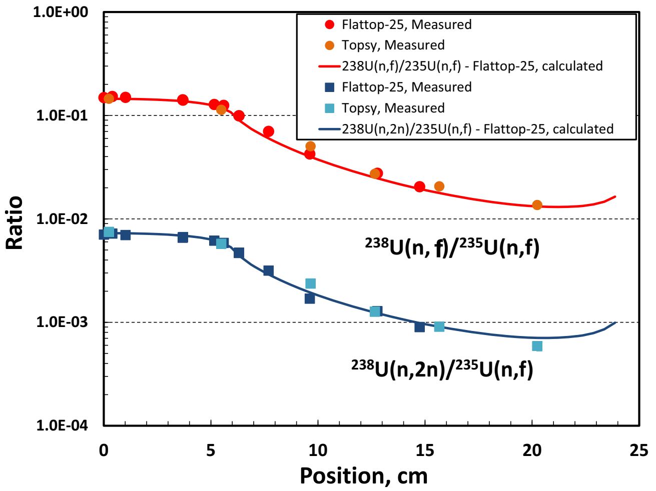

FIG. 169. (Color online) Comparison of experimental radiochemical data from Flattop-25 and Topsy, a Flattop forerunner, with calculated values for a radial traverse in the Flattop-25 assembly. The ratio of the ^{238}U(n,f) reaction rate to the ^{235}U(n,f) reaction rate and the ratio of the ^{238}U(n,2n) reaction rate to the ^{235}U(n,f) reaction rate are plotted versus radius.

Figure 170 is an alternate way to illustrate these data, namely placing the ^{238}U(n,f)/^{235}U(n,f) ratio on the abscissa and the rate of interest (in this case ^{238}U(n,2n)/^{235}U(n,f)) on the ordinate. The advantage of this representation is that data from different assemblies can be compared on a common basis. Note for example how well the Flattop-25 and Big-10, both uranium fueled assemblies, data fit together or how the Jezebel data are a small extrapolation from the Flattop-Pu assembly data. The ^{238}U(n,f)/^{235}U(n,f) ratio is commonly known as a "Spectral Index", or a measure of spectrum hardness and is used on the abscissa for many of the subsequent figures.

In Fig. 171 the ^{238}U(n,γ)/^{235}U(n,f) results are shown. Although there is much scatter in the measured data it appears that the calculations are slightly low. Figure 172 shows the results for ^{237}U(n,f)/^{235}U(n,f), while Fig. 173 shows the results for ^{236}U(n,f)/^{235}U(n,f). Results for ^{236}U(n,γ)/^{235}U(n,f) and ^{237}Np(n,γ)/^{237}Np(n,f) are shown in Figs. 174 and 175, respectively, while in Fig. 176 the results for ^{241}Am(n,γ)/^{239}Pu(n,f) are shown.

In Fig. 177, the selected reaction rate data from the HEU fueled Godiva and Flattop-25 assemblies are shown, and in Fig. 178, the selected reaction rate data from the Pu fueled Jezebel and Flattop-Pu assemblies are shown for threshold detectors. These experimental data from Los Alamos were documented in Ref. [6]. These comparisons provide an integral validation check on the quality of

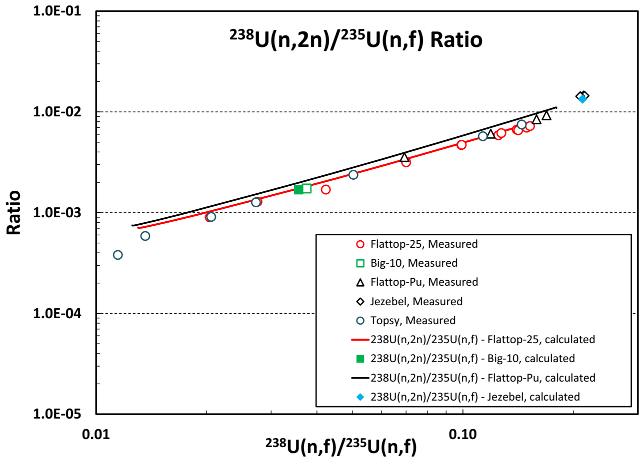

FIG. 170. (Color online) Comparison of experimental radiochemical and calculated values for radial traverses in the Flattop-25 and Topsy assemblies. The ratio of the ^{238}U(n,2n) reaction rate to the ^{235}U fission is plotted against the ratio of the ^{238}U fission rate to the ^{235}U fission rate for different positions. The abscissa is a measure of the spectrum hardness at that position, with the rightmost data close to the assembly center and the leftmost data corresponding to reflector region locations. The Big-10 and Jezebel results were measured and computed at their assembly centers.

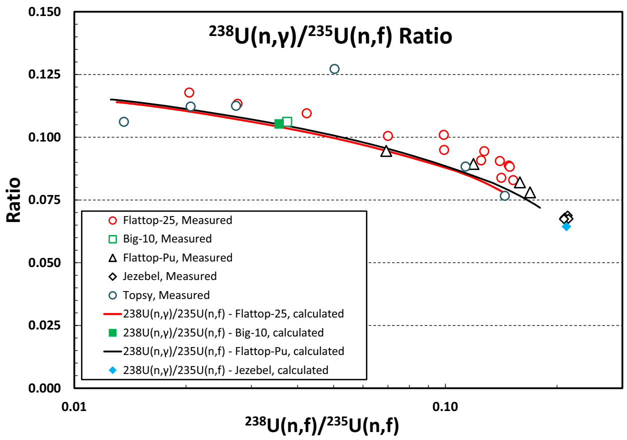

FIG. 171. (Color online) Comparison of experimental radiochemical and calculated values for radial traverses in the Flattop-25 and Topsy assemblies. The ratio of the ^{238}U(n,γ) reaction rate to the ^{235}U fission is plotted against the ratio of the ^{238}U fission rate to the ^{235}U fission rate for different positions. The abscissa is a measure of the spectrum hardness at that position, with the rightmost data close to the assembly center and the leftmost data corresponding to reflector region locations. The Big-10 and Jezebel results were measured and computed at their assembly centers.

both the threshold fission and $(n,2n)$ cross sections, and on the `MCNP`®-simulated neutron spectra in the critical assemblies. Fairly good C/E results are obtained across a wide range of incident neutron energies. Since the prompt fission neutron spectrum (PFNS) contributes importantly

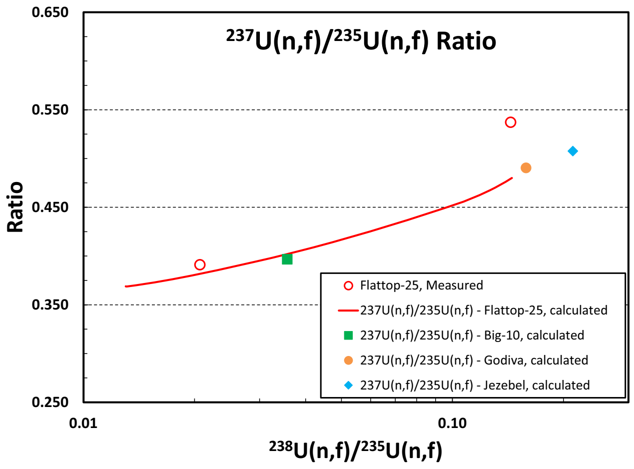

FIG. 172. (Color online) Comparison of experimental and calculated values of the ratio of the ^{237}U fission rate to the ^{235}U fission rate as a function of spectral index.

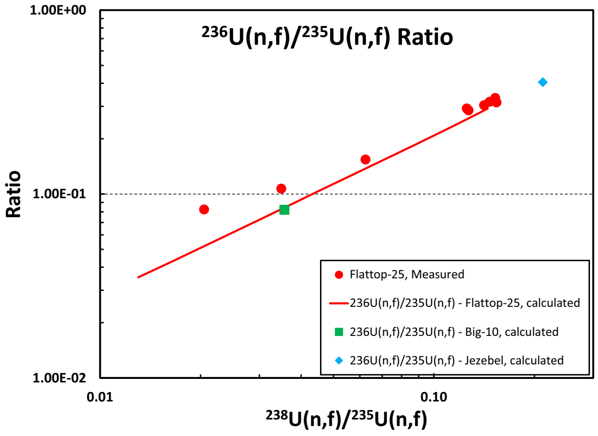

FIG. 173. (Color online) Comparison of experimental and calculated values of the ratio of the ^{236}U fission rate to the ^{235}U fission rate as a function of spectral index.

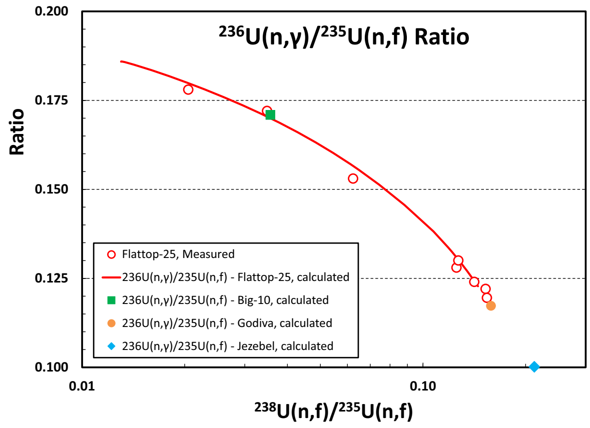

FIG. 174. (Color online) Comparison of experimental and calculated values of the ratio of the ^{236}U capture rate to the ^{235}U fission rate as a function of spectral index.

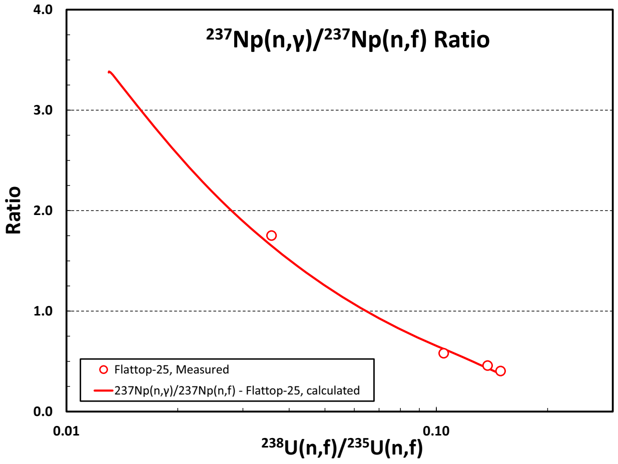

FIG. 175. (Color online) Comparison of experimental and calculated values of the ratio of the ^{237}Np capture rate to the ^{237}Np fission rate as a function of spectral index.

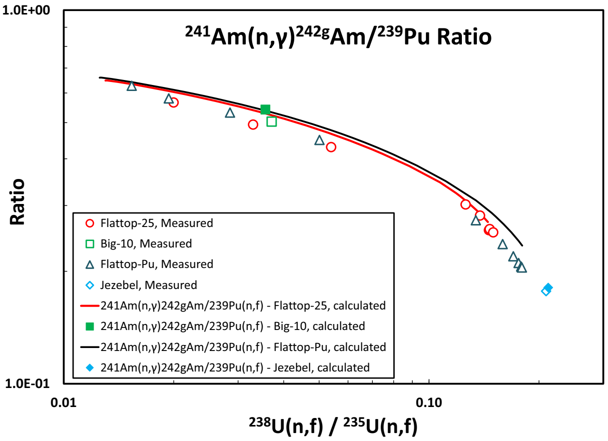

FIG. 176. (Color online) The integral ^{241}Am capture rate (divided by the ^{239}Pu fission rate) as a function of spectral index for different critical assembly locations. The measurements, which detect ^{242}Cm are divided by 0.827 to account for the fraction of ^{242g}Am that beta decays to ^{242}Cm.

to the MCNP®-calculated assembly spectrum, also shown for comparison are the Lestone NUEX PFNS data C/E values on the figures (where "E" in this case just represents the ENDF/B-VIII.0 evaluated PFNS values for 1.5 MeV incident energy neutrons).

Tables XXXIX, XL provide spectral index and reaction rate calculated values in fast critical assemblies, compared with measured data. Similar tables we have presented in the previous ENDF documentation papers [1, 2]. The change in the ^{239}Pu$(n, 2n)$, compared to VII.1, is due to the change in the evaluation as it rises from threshold.

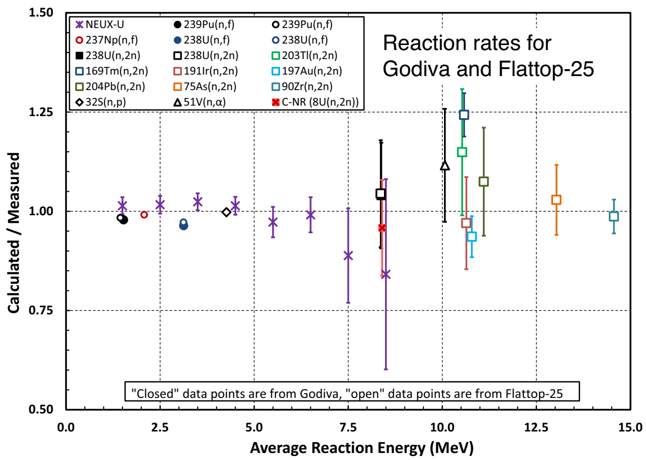

FIG. 177. (Color online) C/E value for reaction rate measurements in the HEU fueled Godiva and Flattop-25 Critical Assemblies, for threshold detectors.

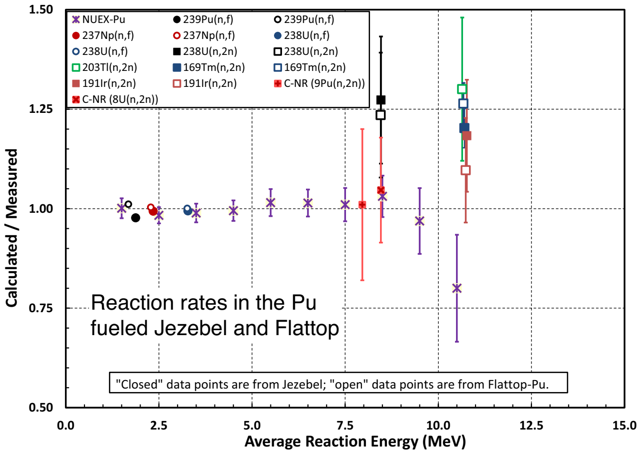

FIG. 178. (Color online) C/E value for reaction rate measurements in the Pu fueled Jezebel and Flattop-Pu Critical Assemblies, for threshold detectors.

E. Atomic Mass Spectrometry (AMS) at 25 keV and 426 keV

Table XLI compares spectrum-averaged uranium capture cross sections at 25 keV and 426 keV with the accelerator mass spectrometry measurements of Wallner [227]. The good agreement (within quoted uncertainties) reflects the priority made by the IAEA evaluators to match these data, which are thought to be accurate. Note that the uncertainty of the capture ratio is driven by the ^{235}U(n, γ) uncertainty.

TABLE XXXIX. Comparison of calculated spectra indices for ENDF/B-VIII.0 with measured values in the center of various Los Alamos critical assemblies. U238f/U235f refers to the ^{238}U fission rate divided by the ^{235}U fission rate, *etc.* Because ^{238}U and ^{237}Np are threshold fissioners, the spectral indices for these isotopes (in ratio to ^{235}U) measure the hardness of the neutron spectrum in the assembly. Exp-A refers to experimental data as documented in the CSEWG Fast Reactor Benchmark Compilation, BNL 19302 (June 1973); Exp-B refers to the same measurements, but as reanalyzed by G. Hansen, one of the lead experimentalists, and transmitted to R. MacFarlane in 1984. The C/E ratios are based on the Hansen values where available. The experimental values for Big-10 are from Selby, Ref. [449].

Assembly	Quantity	U238f/U235f	Np237f/U235f	U233f/U235f	Pu239f/U235f
Godiva	Calc	0.1583	0.8318	1.5793	1.3846
(HMF001)	Exp-B	0.1643 ±0.0018	0.8516±0.012		1.4152 ± 0.014
	Exp-A	0.1642 ±0.0018	0.837 ±0.013	1.59±0.03	1.402±0.025
	Calc/Exp	C/E=0.9636	C/E=0.9767	C/E=0.9933	C/E=0.9784
Jezebel	Calc	0.2121	0.9770	1.5560	1.4273
(PMF001)	Exp-B	0.2133 ±0.0023	0.9835 ±0.014		1.4609 ± 0.013
	Exp-A	0.2137 ±0.0023	0.962 ±0.016	1.578 ±0.027	1.448 ±0.029
	Calc/Exp	C/E=0.9943	C/E=0.9934	C/E=0.9924	C/E=0.9770
Big-10	Calc	0.0358			1.170
(IMF007)	Exp	0.0375 ±0.0009			1.198 ± 0.028
	Calc/Exp	C/E=0.954			C/E=0.977
Jezebel-23	Calc	0.2121	0.9851		
(UMF001)	Exp-B	0.2131 ±0.0026	0.9970 ±0.015		
	Exp-A	0.2131 ±0.0023	0.977 ±0.016		
	Calc/Exp	C/E=0.9951	C/E=0.988		
Flattop-25	Calc	0.1451	0.7735	1.5664	1.3622
(HMF028)	Exp-B	0.1492 ±0.0016	0.7804 ±0.01	1.608 ±0.003	1.3847 ±0.012
	Exp-A	0.149 ±0.002	0.76 ±0.01	1.60 ±0.003	1.37 ±0.02
	Calc/Exp	C/E=0.9722	C/E=0.9911	C/E=0.9741	C/E=0.9837
Flattop-Pu	Calc	0.1801	0.8593		
(PMF006)	Exp-B	0.1799 ±0.002	0.8561 ±0.012		
	Exp-A	0.180 ±0.003	0.84 ±0.01		
	Calc/Exp	C/E=1.0011	C/E=1.0037		
Flattop-23	Calc	0.1892	0.9030		
(UMF006)	Exp-B	0.1916 ±0.0021	0.9103 ±0.013		
	Exp-A	0.191 ±0.003	0.89 ±0.01		
	Calc/Exp	C/E=0.9876	C/E=0.9920		

TABLE XL. `MCNP`® calculations for ENDF/B-VIII.0 of various $(n,2n)$ and (n,γ) reaction rates in ratio to the ^{239}Pu fission rate, at the center of Jezebel and of Flattop-Pu. The only measurements available (Barr, 1971) are for the ^{241}Am capture rate creating the ground state of ^{242}Am, which then decays to curium with a branching ratio of 0.827 (this factor is included into the tabulated calculated values below). Data at other positions in Flattop-Pu are compared with calculations in Fig. 178.

Assembly	Quantity	^{239}Pu$(n,2n)$/ ^{239}Pu(n,f)	^{239}Pu(n,γ)/ ^{239}Pu(n,f)	^{241}Am$(n,2n)$/ ^{239}Pu(n,f)	^{241}Am$(n,\gamma)^{242}$Cm/ ^{239}Pu(n,f)
Jezebel	Calc	0.0023	0.035	0.0008	0.1496
	Exp				0.1486
Flattop-Pu	Calc	0.00197	0.046	0.0007	0.1937
	Exp				0.1847

TABLE XLI. AMS data for ^{235}U and ^{238}U(n,γ) from Wallner. The experimental data are compared to the spectrum-averaged cross sections calculated using the ENDF/B-VIII.0 and ENDF/B-VII.1 cross section evaluations.

Energy	^{238}U(n,γ)	ENDF/B-VIII.0	ENDF/B-VII.1	^{238}U(n,γ)/^{235}U(n,γ)	ENDF/B-VIII.0 ratio	ENDF/B-VII.1 ratio
25 keV	0.391±0.017 b	0.399±0.009 b	0.408 b	0.60±0.03	0.59±0.04	0.600
426 keV	0.108±0.004 b	0.109±0.002 b	0.109 b	0.64±0.03	0.59±0.04	0.599

F. Maxwellian-Averaged Cross Sections (MACS)

Maxwellian-averaged cross sections play an important role in power reactor developments and *s*-process nucleosynthesis calculations [450, 451]. The slow-neutron capture is mostly responsible for element formation in stars from ^{56}Fe to ^{209}Bi. The detailed analysis of Fig. 179 and Table XLII data demonstrates the nuclear astrophysics potential of ENDF libraries as a complimentary source of evaluated cross sections and reaction rates. There are noticeable differences between KADoNiS v0.3 [169] and ENDF/B-VIII.0 libraries for light and medium nuclei. ^{1,2}H and ^{3}He experience significant deviations due to differences between center of mass and lab system cross section values. Other deficiencies could be separated into three groups. ^{31}P, ^{36}S and ^{196}Hg KADoNiS values are based on a single recent measurement. Due to lack of experimental data theoretical values were adopted in KADoNiS for ^{38}Ar, ^{82}Se, ^{141}Ce. Deficiencies in the ^{18}O ENDF/B-VIII.0 evaluation arise from the lack of experimental coverage in the EXFOR database [175], while deficiencies in the ^{48}Ca ENDF/B-VIII.0 evaluation are insignificant for integral tests because of ^{48}Ca's low isotopic abundance.

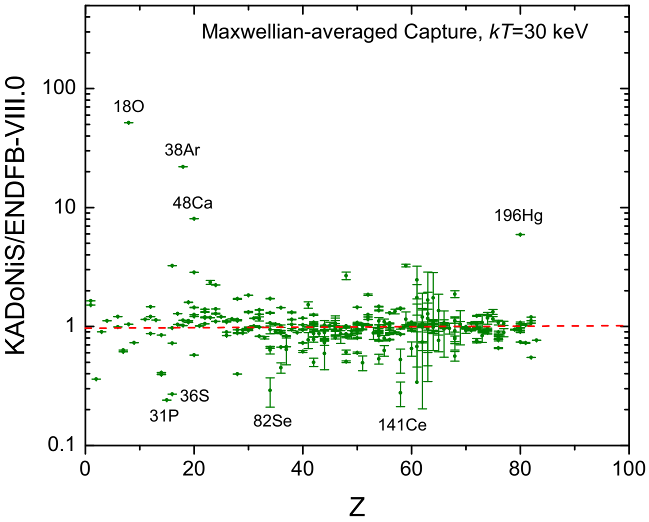

FIG. 179. (Color online) Ratio of Karlsruhe Astrophysical Database of Nucleosynthesis in Stars (KADoNiS v0.3) [169] and ENDF/B-VIII.0 Maxwellian-averaged cross sections at kT=30 keV. Potential deficiencies are highlighted.

It is commonly known that for the equilibrium *s*-process-only nuclei, the product of $\langle\sigma_{\gamma}^{\rm Maxw}(kT)\rangle$ and the solar-system abundances ($N_{(A)}$) is preserved [452]:

$$\sigma_A N_{(A)} = \sigma_{A-1} N_{(A-1)} = \text{constant}. \tag{4}$$

To verify this phenomenon, the product of Maxwellian-averaged cross sections from the ENDF/B-VIII.0 and KADoNiS libraries and the solar system abundances taken from Anders and Grevesse [453] is shown in Fig. 180.

Figure 180 shows that the ENDF/B-VIII.0 and KADoNiS v0.3 libraries closely reproduce a famous two-plateau plot [452]. Both curves are almost identical and experience deviations from the Eq. (4) predictions. These deviations can be explained by limitations of the input parameters

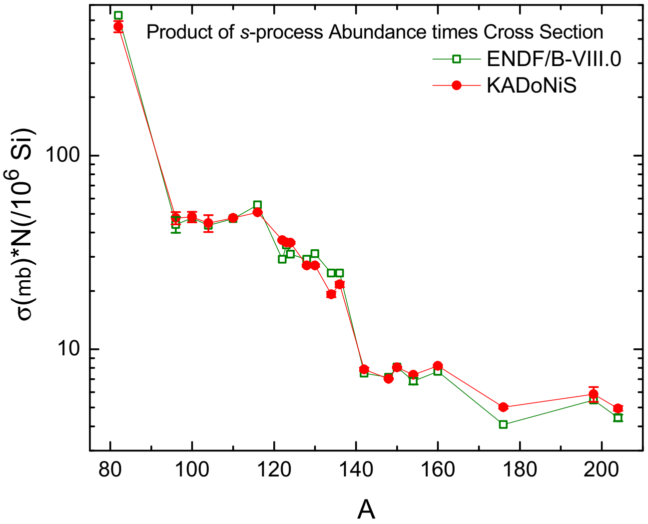

FIG. 180. (Color online) KADoNiS v0.3 [169] and ENDF/B-VIII.0 Maxwellian-averaged cross sections at kT=30 keV multiplied by solar system abundances (relative to Si = 10^6) are shown as a function of the mass number of nuclei produced in the *s*-process only.

- Ground state cross sections were used in the *s*-process temperature range of $kT = 8 - 90$ keV

- Solar system isotopic abundances are based on meteorites, planet and star surfaces data only

- New decay branches could affect the final *s*-process abundances

Simultaneously, the results in Fig. 180 show that ENDF/B-VIII.0 and KADoNiS provide comparable nuclear astrophysics results.

TABLE XLII: ENDF/B-VII.1 [2], ENDF/B-VIII.0, KADONIS v.0.3 [169] Maxwellian-averaged neutron capture cross sections and their ratios at kT=30 keV. Comments: *C*-calculated from BNL-325 data [454], *T*-theoretical data in KADONIS v.0.3 [169].

Material	**ENDF/B-VII.1** (barns)	**ENDF/B-VIII.0** (barns)	**KADONIS v.0.3** (barns)	**ENDF/B-VII.1/ENDF/B-VIII.0**	**KADONIS/ENDF/B-VIII.0**
1-H - 1	1.560E-4±5.890E-6	1.544E-4±8.865E-6	2.540E-4±2.000E-5	1.009E+0±6.873E-2	1.645E+0±9.745E-2
1-H - 2	1.980E-6±1.240E-7	1.980E-6±1.236E-7	3.000E-6±2.000E-7	1.000E+0±8.831E-2	1.515E+0±9.134E-2
1-H - 3					
2-He- 3	2.110E-5	2.109E-5	7.600E-6±6.000E-7	1.000E+0	3.603E-1±7.895E-2
2-He- 4					
3-Li- 6	3.290E-5±3.180E-6	3.290E-5		1.000E+0±9.665E-2	
3-Li- 7	4.660E-5	4.663E-5	4.200E-5±3.000E-6	1.000E+0	9.006E-1±7.143E-2
4-Be- 7					
4-Be- 9	9.320E-6±1.860E-6	9.324E-6±1.860E-6	1.040E-5±1.600E-6	1.000E+0±2.821E-1	1.115E+0±2.519E-1
5-B - 10	4.310E-4±3.450E-4	3.440E-4±2.752E-4		1.253E+0±1.131E+0	
5-B - 11	6.620E-5±2.050E-5	6.620E-5±2.047E-5		1.000E+0±4.374E-1	
6-C - 12		1.557E-5±3.112E-6	1.540E-5±1.000E-6		9.890E-1±2.101E-1
6-C - 13		1.736E-5	2.100E-5±1.000E-6		1.210E+0±4.762E-2
7-N - 14	6.700E-5	6.696E-5	4.100E-5±6.000E-5^{C}	1.000E+0	6.123E-1±1.463E+0
7-N - 15	9.180E-6±4.590E-6	9.175E-6±4.587E-6	5.800E-6±6.000E-7	1.000E+0±7.071E-1	6.322E-1±5.106E-1
8-O - 16	3.150E-5±3.160E-6	3.637E-5±3.639E-6	3.800E-5±4.000E-6	8.658E-1±1.417E-1	1.045E+0±1.452E-1
8-O - 17	4.700E-6	4.695E-6			
8-O - 18		1.716E-7	8.860E-6±8.000E-8		5.164E+1±9.029E-3
9-F - 19	4.370E-3±1.820E-4	4.372E-3±1.817E-4	3.200E-3±1.000E-4	1.000E+0±5.878E-2	7.319E-1±5.200E-2
10-Ne- 20		1.180E-4±4.125E-29	1.190E-4±1.100E-5		1.008E+0±9.244E-2
10-Ne- 21		2.261E-3±6.993E-6	1.500E-3±9.000E-4		6.634E-1±6.000E-1
10-Ne- 22		8.373E-5±6.524E-21	5.800E-5±4.000E-6		6.927E-1±6.897E-2
11-Na- 22	8.020E-3	8.019E-3		1.000E+0	
11-Na- 23	1.830E-3±1.370E-4	1.832E-3±1.371E-4	2.100E-3±2.000E-4	1.000E+0±1.058E-1	1.146E+0±1.211E-1
12-Mg- 24	3.790E-3±7.180E-4	3.789E-3±7.179E-4	3.300E-3±4.000E-4	1.000E+0±2.679E-1	8.708E-1±2.249E-1
12-Mg- 25	5.280E-3±1.310E-6	5.280E-3±1.305E-6	6.400E-3±4.000E-4	1.000E+0±3.496E-4	1.212E+0±6.250E-2
12-Mg- 26	8.610E-5±1.620E-5	8.610E-5±1.617E-5	1.260E-4±9.000E-6	1.000E+0±2.656E-1	1.463E+0±2.010E-1
13-Al- 26M		4.362E-3			
13-Al- 27	3.310E-3±5.610E-4	3.307E-3±5.612E-4	3.740E-3±3.000E-4	1.000E+0±2.400E-1	1.131E+0±1.877E-1
14-Si- 28	3.610E-3±8.000E-4	3.607E-3±8.000E-4	1.420E-3±1.300E-4	1.000E+0±3.137E-1	3.937E-1±2.399E-1
14-Si- 29	7.770E-3±8.350E-4	7.772E-3±8.349E-4	6.580E-3±6.600E-4	1.000E+0±1.519E-1	8.466E-1±1.470E-1
14-Si- 30	4.450E-3±1.520E-3	4.448E-3±1.520E-3	1.820E-3±3.300E-4	1.000E+0±4.832E-1	4.092E-1±3.868E-1
14-Si- 31		1.405E-2			
14-Si- 32		1.245E-4			
15-P - 31	7.240E-3	7.240E-3	1.740E-3±9.000E-5	1.000E+0	2.403E-1±5.172E-2
16-S - 32	5.660E-3	5.660E-3	4.100E-3±2.000E-4	1.000E+0	7.244E-1±4.878E-2
16-S - 33	2.280E-3	2.277E-3	7.400E-3±1.500E-3	1.000E+0	3.249E+0±2.027E-1
16-S - 34	2.320E-4	2.324E-4	2.260E-4±1.000E-5	1.000E+0	9.726E-1±4.425E-2
16-S - 35		6.363E-4			
16-S - 36	6.330E-4	6.331E-4	1.710E-4±1.400E-5	1.000E+0	2.701E-1±8.187E-2
17-Cl- 35	7.540E-3	7.541E-3	9.680E-3±2.100E-4	1.000E+0	1.284E+0±2.169E-2
17-Cl- 36		1.172E-2	1.200E-2±1.000E-3^{T}		1.024E+0±8.333E-2
17-Cl- 37	2.040E-3	2.043E-3	2.120E-3±7.000E-5	1.000E+0	1.038E+0±3.302E-2
18-Ar- 36	8.840E-3	8.842E-3	9.000E-3±1.500E-3^{T}	1.000E+0	1.018E+0±1.667E-1
18-Ar- 37		1.020E-2±1.191E-3			
18-Ar- 38	1.370E-4	1.365E-4	3.000E-3±3.000E-4^{T}	1.000E+0	2.197E+1±1.000E-1
18-Ar- 39		1.992E-2	8.000E-3±2.000E-3^{T}		4.017E-1±2.500E-1
18-Ar- 40	2.250E-3	2.248E-3	2.540E-3±1.000E-4	1.000E+0	1.130E+0±3.937E-2
18-Ar- 41		2.579E-2±1.241E-2			
19-K - 39	1.060E-2	1.057E-2	1.180E-2±4.000E-4	1.000E+0	1.116E+0±3.390E-2
19-K - 40	1.940E-2	1.941E-2	3.100E-2±7.000E-3^{T}	1.000E+0	1.597E+0±2.258E-1
19-K - 41	2.030E-2±1.060E-16	2.031E-2±1.057E-16	2.200E-2±7.000E-4	1.000E+0±7.356E-15	1.083E+0±3.182E-2
20-Ca- 40	5.150E-3	9.972E-3	5.730E-3±3.400E-4	5.162E-1	5.746E-1±5.934E-2
20-Ca- 41		3.854E-2	3.000E-2±7.000E-3^{T}		7.784E-1±2.333E-1
20-Ca- 42	1.240E-2	1.241E-2	1.560E-2±2.000E-3	1.000E+0	1.257E+0±1.282E-1
20-Ca- 43	3.530E-2	3.530E-2	5.100E-2±6.000E-3	1.000E+0	1.445E+0±1.176E-1
20-Ca- 44	7.740E-3	7.744E-3	9.400E-3±1.300E-3	1.000E+0	1.214E+0±1.383E-1
20-Ca- 45		2.025E-2±8.270E-3	1.750E-2±3.500E-3^{T}		8.641E-1±4.547E-1
20-Ca- 46	1.860E-3	1.860E-3	5.300E-3±5.000E-4	1.000E+0	2.850E+0±9.434E-2
20-Ca- 47		9.064E-3±3.097E-4			
20-Ca- 48	1.080E-4	1.080E-4	8.700E-4±9.000E-5	1.000E+0	8.052E+0±1.034E-1
21-Sc- 45	6.840E-2	6.840E-2	6.900E-2±5.000E-3	1.000E+0	1.009E+0±7.246E-2
22-Ti- 46	2.550E-2±1.210E-7	2.545E-2±1.209E-7	2.680E-2±3.200E-3	1.000E+0±6.715E-6	1.053E+0±1.194E-1
22-Ti- 47	4.870E-2±1.450E-3	4.868E-2±1.449E-3	6.440E-2±7.700E-3	1.000E+0±4.209E-2	1.323E+0±1.232E-1
22-Ti- 48	2.660E-2±7.040E-9	2.656E-2±7.043E-9	3.180E-2±5.100E-3	1.000E+0±3.750E-7	1.197E+0±1.604E-1
22-Ti- 49	1.580E-2±2.960E-6	1.583E-2±2.961E-6	2.210E-2±2.100E-3	1.000E+0±2.645E-4	1.396E+0±9.502E-2
22-Ti- 50	3.040E-3±8.050E-12	3.044E-3±8.050E-12	3.600E-3±4.000E-4	1.000E+0±3.740E-9	1.183E+0±1.111E-1
23-V - 49		1.475E-1			
23-V - 50	2.130E-2	2.132E-2	5.000E-2±9.000E-2^{T}	1.000E+0	2.346E+0±1.800E+0
23-V - 51	3.210E-2	3.205E-2	3.800E-2±4.000E-3	1.000E+0	1.186E+0±1.053E-1
24-Cr- 50	3.830E-2	3.828E-2	4.900E-2±1.300E-2	1.000E+0	1.280E+0±2.653E-1
24-Cr- 51		8.450E-2±2.707E-2	8.700E-2±1.600E-2^{T}		1.030E+0±3.694E-1
24-Cr- 52	7.990E-3±2.710E-4	7.992E-3±2.709E-4	8.800E-3±2.300E-3	1.000E+0±4.794E-2	1.101E+0±2.636E-1
24-Cr- 53	2.600E-2	2.598E-2	5.800E-2±1.000E-2	1.000E+0	2.233E+0±1.724E-1
24-Cr- 54	4.780E-3	4.780E-3	6.700E-3±1.600E-3	1.000E+0	1.402E+0±2.388E-1
25-Mn- 54		2.449E-1±1.387E-1			
25-Mn- 55	3.280E-2±2.670E-3	3.284E-2±2.666E-3	3.960E-2±3.000E-3	1.000E+0±1.148E-1	1.206E+0±1.110E-1
26-Fe- 54	2.160E-2±2.680E-3	2.715E-2	2.960E-2±1.300E-3	7.960E-1±1.239E-1	1.090E+0±4.392E-2
26-Fe- 55		9.097E-2±1.895E-2	7.500E-2±1.200E-2^{T}		8.245E-1±2.626E-1
26-Fe- 56	1.150E-2±1.180E-3	1.355E-2±5.309E-4	1.170E-2±5.000E-4	8.492E-1±1.098E-1	8.634E-1±5.798E-2
26-Fe- 57	2.850E-2±4.600E-3	3.601E-2	4.000E-2±4.000E-3	7.910E-1±1.616E-1	1.111E+0±1.000E-1
26-Fe- 58	1.970E-2	1.507E-2	1.350E-2±7.000E-4	1.311E+0	8.961E-1±5.185E-2
27-Co- 58	2.020E-1	2.107E-1		9.597E-1	
27-Co- 58M	6.440E-2	6.442E-2		1.000E+0	
27-Co- 59	3.440E-2	3.426E-2	3.960E-2±2.700E-3	1.005E+0	1.156E+0±6.818E-2
28-Ni- 58	3.390E-2±2.780E-3	3.387E-2±2.776E-3	3.870E-2±1.500E-3	1.000E+0±1.159E-1	1.143E+0±9.065E-2
28-Ni- 59	6.960E-2	5.102E-2	8.700E-2±1.400E-2^{T}	1.365E+0	1.705E+0±1.609E-1
28-Ni- 60	2.680E-2±1.590E-3	2.677E-2±1.594E-3	2.990E-2±7.000E-4	9.996E-1±8.417E-2	1.117E+0±6.396E-2
28-Ni- 61	9.030E-2	9.307E-2	8.200E-2±8.000E-3	9.706E-1	8.811E-1±9.756E-2
28-Ni- 62	2.380E-2	2.384E-2	2.230E-2±1.600E-3	1.000E+0	9.355E-1±7.175E-2
28-Ni- 63		5.109E-2	3.100E-2±6.000E-3^{T}		6.067E-1±1.935E-1
28-Ni- 64	2.010E-2	2.007E-2	8.000E-3±7.000E-4	1.000E+0	3.986E-1±8.750E-2
29-Cu- 63	7.150E-2	5.930E-2	5.560E-2±2.200E-3	1.206E+0	9.376E-1±3.957E-2
29-Cu- 64		1.506E-1			
29-Cu- 65	3.920E-2	3.380E-2	2.980E-2±1.300E-3	1.158E+0	8.816E-1±4.362E-2
30-Zn- 64	6.100E-2	6.102E-2	5.900E-2±5.000E-3	1.000E+0	9.669E-1±8.475E-2
30-Zn- 65	1.680E-1	1.678E-1	1.620E-1±2.700E-2^{T}	1.000E+0	9.657E-1±1.667E-1
30-Zn- 66	3.640E-2	3.643E-2	3.500E-2±3.000E-3	1.000E+0	9.607E-1±8.571E-2
30-Zn- 67	1.160E-1	1.158E-1	1.530E-1±1.500E-2	1.000E+0	1.322E+0±9.804E-2
30-Zn- 68	2.080E-2	2.076E-2	1.920E-2±2.400E-3	1.000E+0	9.250E-1±1.250E-1
30-Zn- 69		1.063E-1			
30-Zn- 70	1.170E-2	1.172E-2	2.150E-2±2.000E-3^{T}	1.000E+0	1.835E+0±9.302E-2
31-Ga- 69	1.190E-1	1.185E-1	1.390E-1±6.000E-3	1.000E+0	1.173E+0±4.317E-2
31-Ga- 70		2.101E-1			
31-Ga- 71	1.220E-1	1.223E-1	1.230E-1±8.000E-3	1.000E+0	1.005E+0±6.504E-2
32-Ge- 70	8.920E-2	8.917E-2	8.800E-2±5.000E-3	1.000E+0	9.869E-1±5.682E-2
32-Ge- 71		2.623E-1			
32-Ge- 72	5.300E-2	5.297E-2	7.300E-2±7.000E-3^{T}	1.000E+0	1.378E+0±9.589E-2
32-Ge- 73	2.100E-1	2.097E-1	2.430E-1±4.700E-2^{T}	1.000E+0	1.159E+0±1.934E-1
32-Ge- 74	4.540E-2	4.542E-2	3.760E-2±3.900E-3	1.000E+0	8.278E-1±1.037E-1
32-Ge- 75		1.418E-1			
32-Ge- 76	1.700E-2	1.700E-2	2.150E-2±1.800E-3	1.000E+0	1.265E+0±8.372E-2
33-As- 73		7.494E-1			

TABLE XLII: ENDF/B-VII.1 [2], ENDF/B-VIII.0, KADONIS v0.3 [169] Maxwellian-averaged neutron capture cross sections and their ratios at kT=30 keV. Comments: *C*-calculated from BNL-325 data [454], *T*-theoretical data in KADONIS v.0.3 [169].

Material	**ENDF/B-VII.1** (barns)	**ENDF/B-VIII.0** (barns)	**KADONIS v.0.3** (barns)	**ENDF/B-VII.1/ENDF/B-VIII.0**	**KADONIS/ENDF/B-VIII.0**
33-As- 74	1.360E+0	1.259E+0		1.082E+0	
33-As- 75	4.500E-1	4.502E-1	3.620E-1±1.900E-2	1.000E+0	8.041E-1±5.249E-2
34-Se- 74	2.080E-1	2.084E-1	2.710E-1±1.500E-2	1.000E+0	1.301E+0±5.535E-2
34-Se- 75		9.905E-1±4.047E-1			
34-Se- 76	9.580E-2	9.577E-2	1.640E-1±8.000E-3	1.000E+0	1.712E+0±4.878E-2
34-Se- 77	4.450E-1	4.449E-1	4.180E-1±7.100E-2^T	1.000E+0	9.395E-1±1.699E-1
34-Se- 78	9.070E-2	9.065E-2	6.010E-2±9.600E-3	1.000E+0	6.630E-1±1.597E-1
34-Se- 79	4.150E-1	4.147E-1	2.630E-1±4.600E-2^T	1.000E+0	6.342E-1±1.749E-1
34-Se- 80	3.930E-2	3.934E-2	4.200E-2±3.000E-3	1.000E+0	1.068E+0±7.143E-2
34-Se- 81		1.046E-1			
34-Se- 82	3.110E-2	3.110E-2	9.000E-3±8.000E-2^T	1.000E+0	2.894E-1±8.889E+0
35-Br- 79	6.870E-1	6.866E-1	6.220E-1±3.400E-2	1.000E+0	9.060E-1±5.466E-2
35-Br- 80		5.519E-1			
35-Br- 81	2.290E-1	2.287E-1	2.390E-1±7.000E-3	1.000E+0	1.045E+0±2.929E-2
36-Kr- 78	4.710E-1	3.191E-1	3.210E-1±2.600E-2	1.475E+0	1.006E+0±8.100E-2
36-Kr- 79		4.361E-1	9.590E-1±1.620E-1^T		2.199E+0±1.689E-1
36-Kr- 80	2.950E-1	2.945E-1	2.670E-1±1.400E-2	1.000E+0	9.067E-1±5.243E-2
36-Kr- 81		6.225E-1±4.051E-1	6.070E-1±1.050E-1^T		9.751E-1±6.733E-1
36-Kr- 82	1.030E-1	1.027E-1	9.000E-2±6.000E-3	1.000E+0	8.760E-1±6.667E-2
36-Kr- 83	2.670E-1	2.670E-1	2.430E-1±1.500E-2	1.000E+0	9.102E-1±6.173E-2
36-Kr- 84	2.640E-2	2.638E-2	3.800E-2±4.000E-3	1.000E+0	1.440E+0±1.053E-1
36-Kr- 85	1.220E-1	1.224E-1	5.500E-2±4.500E-2^T	1.000E+0	4.494E-1±8.182E-1
36-Kr- 86	5.070E-3	5.066E-3	3.400E-3±3.000E-4	1.000E+0	6.712E-1±8.824E-2
37-Rb- 85	2.820E-1	2.818E-1	2.340E-1±7.000E-3	1.000E+0	8.305E-1±2.991E-2
37-Rb- 86	3.170E-1	3.166E-1	2.020E-1±1.630E-1^T	1.000E+0	6.381E-1±8.069E-1
37-Rb- 87	2.330E-2	2.326E-2	1.570E-2±8.000E-4	1.000E+0	6.751E-1±5.096E-2
38-Sr- 84	3.190E-1	3.189E-1	3.000E-1±1.700E-2	1.000E+0	9.408E-1±5.667E-2
38-Sr- 85		3.318E-1			
38-Sr- 86	6.150E-2	6.147E-2	6.400E-2±3.000E-3	1.000E+0	1.041E+0±4.688E-2
38-Sr- 87	8.050E-2	8.053E-2	9.200E-2±4.000E-3	1.000E+0	1.142E+0±4.348E-2
38-Sr- 88	5.220E-3	5.369E-3	6.130E-3±1.100E-4	9.716E-1	1.142E+0±1.794E-2
38-Sr- 89	1.450E-2	1.447E-2	1.900E-2±1.400E-2^T	1.000E+0	1.313E+0±7.368E-1
38-Sr- 90	1.460E-2	1.460E-2		1.000E+0	
39-Y - 89	2.140E-2±1.850E-3	2.136E-2±1.845E-3	1.900E-2±6.000E-4	1.000E+0±1.221E-1	8.893E-1±9.195E-2
39-Y - 90	5.570E-2	5.571E-2		1.000E+0	
39-Y - 91	8.780E-2	8.780E-2		1.000E+0	
40-Zr- 90	1.890E-2±1.500E-3	1.870E-2±1.399E-3	1.930E-2±9.000E-4	1.012E+0±1.090E-1	1.032E+0±8.813E-2
40-Zr- 91	7.370E-2±2.920E-3	6.606E-2±2.490E-3	6.200E-2±3.400E-3	1.115E+0±5.472E-2	9.385E-1±6.654E-2
40-Zr- 92	4.550E-2±3.170E-3	4.142E-2±3.105E-3	3.010E-2±1.700E-3	1.097E+0±1.024E-1	7.268E-1±9.386E-2
40-Zr- 93	1.010E-1±8.920E-4	1.008E-1±8.919E-4	9.500E-2±1.000E-2	1.000E+0±1.251E-2	9.424E-1±1.056E-1
40-Zr- 94	2.900E-2±2.550E-3	2.773E-2±2.427E-3	2.600E-2±1.000E-3	1.046E+0±1.240E-1	9.377E-1±9.562E-2
40-Zr- 95	1.290E-1±1.930E-3	1.285E-1±1.933E-3	7.900E-2±1.200E-2^T	1.000E+0±2.127E-2	6.148E-1±1.526E-1
40-Zr- 96	1.030E-2±2.200E-3	9.113E-3±2.004E-3	1.070E-2±5.000E-4	1.125E+0±3.074E-1	1.174E+0±2.248E-1
41-Nb- 93	2.660E-1	2.686E-1	2.660E-1±5.000E-3	9.914E-1	9.904E-1±1.880E-2
41-Nb- 94	3.170E-1	3.174E-1	4.820E-1±9.200E-2^T	1.000E+0	1.519E+0±1.909E-1
41-Nb- 95	4.030E-1±9.780E-2	4.028E-1±9.781E-2	3.100E-1±6.500E-2^T	1.000E+0±3.434E-1	7.695E-1±3.208E-1
42-Mo- 92	6.920E-2±5.430E-3	6.917E-2±5.434E-3	7.000E-2±1.000E-2	1.000E+0±1.111E-1	1.012E+0±1.630E-1
42-Mo- 93		1.878E-1±5.483E-2			
42-Mo- 94	1.100E-1±1.170E-2	1.098E-1±1.171E-2	1.020E-1±2.000E-2	1.000E+0±1.509E-1	9.293E-1±2.232E-1
42-Mo- 95	3.760E-1±3.870E-2	3.757E-1±3.873E-2	2.920E-1±1.200E-2	1.000E+0±1.458E-1	7.771E-1±1.110E-1
42-Mo- 96	1.040E-1±9.680E-3	1.036E-1±9.683E-3	1.120E-1±8.000E-3	1.000E+0±1.322E-1	1.081E+0±1.177E-1
42-Mo- 97	3.890E-1±5.860E-2	3.888E-1±5.855E-2	3.390E-1±1.400E-2	1.000E+0±2.130E-1	8.720E-1±1.562E-1
42-Mo- 98	9.510E-2±3.750E-3	9.506E-2±3.748E-3	9.900E-2±7.000E-3	1.000E+0±5.576E-2	1.041E+0±8.096E-2
42-Mo- 99	4.800E-1	4.797E-1	2.400E-1±4.000E-2^T	1.000E+0	5.003E-1±1.667E-1
42-Mo-100	8.620E-2±4.780E-3	8.620E-2±4.776E-3	1.080E-1±1.400E-2	1.000E+0±7.835E-2	1.253E+0±1.410E-1
43-Tc- 98		1.158E+0±4.992E-1			
43-Tc- 99	1.070E+0±4.300E-3	1.070E+0±4.301E-3	9.330E-1±4.700E-2	1.000E+0±5.685E-3	8.721E-1±5.054E-2
44-Ru- 96	2.650E-1	2.654E-1	2.070E-1±8.000E-3	1.000E+0	7.800E-1±3.865E-2
44-Ru- 97		4.120E-1±3.372E-1			
44-Ru- 98	2.370E-1	2.368E-1	1.730E-1±3.600E-2^T	1.000E+0	7.307E-1±2.081E-1
44-Ru- 99	7.120E-1	7.120E-1	6.310E-1±9.900E-2^T	1.000E+0	8.862E-1±1.569E-1
44-Ru-100	2.040E-1	2.036E-1	2.060E-1±1.300E-2	1.000E+0	1.012E+0±6.311E-2
44-Ru-101	9.720E-1±8.710E-2	9.719E-1±8.708E-2	9.960E-1±4.000E-2	1.000E+0±1.267E-1	1.025E+0±9.819E-2
44-Ru-102	1.900E-1±2.650E-2	1.904E-1±2.651E-2	1.510E-1±7.000E-3	1.000E+0±1.970E-1	7.933E-1±1.468E-1
44-Ru-103	5.780E-1±1.510E-1	5.784E-1±1.511E-1	3.430E-1±5.200E-2^T	1.000E+0±3.695E-1	5.930E-1±3.021E-1
44-Ru-104	1.660E-1±1.270E-2	1.656E-1±1.270E-2	1.540E-1±6.000E-3	1.000E+0±1.085E-1	9.299E-1±8.604E-2
44-Ru-105	4.120E-1	4.123E-1		1.000E+0	
44-Ru-106	1.000E-1±2.280E-2	1.003E-1±2.279E-2		1.000E+0±3.214E-1	
45-Rh-103	8.010E-1±6.830E-2	8.007E-1±6.828E-2	8.110E-1±1.400E-2	1.000E+0±1.206E-1	1.013E+0±8.701E-2
45-Rh-104		1.229E+0			
45-Rh-105	8.280E-1	8.204E-1		1.009E+0	
46-Pd-102	4.590E-1	4.592E-1	3.690E-1±1.700E-2	1.000E+0	8.036E-1±4.607E-2
46-Pd-103		9.480E-1			
46-Pd-104	2.810E-1	2.810E-1	2.890E-1±2.900E-2	1.000E+0	1.028E+0±1.003E-1
46-Pd-105	1.190E+0±1.500E-1	1.185E+0±1.503E-1	1.200E+0±6.000E-2	1.000E+0±1.793E-1	1.013E+0±1.363E-1
46-Pd-106	2.370E-1±5.000E-2	2.370E-1±4.998E-2	2.520E-1±2.500E-2	1.000E+0±2.983E-1	1.063E+0±2.331E-1
46-Pd-107	1.300E+0±1.840E-1	1.297E+0±1.836E-1	1.340E+0±6.000E-2	1.000E+0±2.003E-1	1.033E+0±1.485E-1
46-Pd-108	2.090E-1±4.620E-2	2.090E-1±4.621E-2	2.030E-1±2.000E-2	1.000E+0±3.126E-1	9.711E-1±2.420E-1
46-Pd-109		1.094E+0			
46-Pd-110	1.570E-1	1.567E-1	1.460E-1±2.000E-2	1.000E+0	9.317E-1±1.370E-1
47-Ag-107	8.290E-1	8.294E-1	7.920E-1±3.000E-2	1.000E+0	9.549E-1±3.788E-2
47-Ag-108		1.584E+0			
47-Ag-109	9.100E-1±1.430E-1	9.100E-1±1.432E-1	7.880E-1±3.000E-2	1.000E+0±2.225E-1	8.659E-1±1.619E-1
47-Ag-110M	2.710E+0	2.710E+0		1.000E+0	
47-Ag-111	5.900E-1	5.898E-1		1.000E+0	
47-Ag-112		1.738E+0			
47-Ag-113		4.969E-1			
47-Ag-114		1.069E+0			
47-Ag-115		3.699E-1			
47-Ag-116		8.433E-1			
47-Ag-117		2.774E-1			
47-Ag-118M		7.055E-1			
48-Cd-106	4.970E-1	4.966E-1	3.020E-1±2.400E-2	1.000E+0	6.081E-1±7.947E-2
48-Cd-107		1.130E+0			
48-Cd-108	4.000E-1	3.999E-1	2.020E-1±9.000E-3	1.000E+0	5.051E-1±4.455E-2
48-Cd-109		1.204E+0±5.348E-1			
48-Cd-110	2.350E-1	2.350E-1	2.370E-1±2.000E-3	1.000E+0	1.009E+0±8.439E-3
48-Cd-111	9.240E-1	9.240E-1	7.540E-1±1.200E-2	1.000E+0	8.160E-1±1.592E-2
48-Cd-112	2.180E-1	2.179E-1	1.879E-1±1.700E-3	1.000E+0	8.621E-1±9.047E-3
48-Cd-113	6.820E-1	6.824E-1	6.670E-1±1.100E-2	1.000E+0	9.774E-1±1.649E-2
48-Cd-114	1.500E-1	1.498E-1	1.292E-1±1.300E-3	1.000E+0	8.625E-1±1.006E-2
48-Cd-115M	2.250E-1	2.249E-1	6.010E-1±2.000E-1^T	1.000E+0	2.672E+0±3.328E-1
48-Cd-116	9.080E-2	9.081E-2	7.480E-2±9.000E-4	1.000E+0	8.237E-1±1.203E-2
49-In-113	9.220E-1	9.224E-1	7.870E-1±7.000E-2	1.000E+0	8.532E-1±8.895E-2
49-In-114		1.085E+0			
49-In-115	7.720E-1	7.717E-1	7.060E-1±7.000E-2	1.000E+0	9.149E-1±9.915E-2
50-Sn-112	1.960E-1	1.956E-1	2.100E-1±1.200E-2	1.000E+0	1.073E+0±5.714E-2
50-Sn-113	6.710E-1	6.709E-1		1.000E+0	
50-Sn-114	1.530E-1	1.532E-1	1.344E-1±1.800E-3	1.000E+0	8.771E-1±1.339E-2
50-Sn-115	3.910E-1	3.913E-1	3.424E-1±8.700E-3	1.000E+0	8.750E-1±2.541E-2
50-Sn-116	1.000E-1	1.003E-1	9.160E-2±6.000E-4	1.000E+0	9.134E-1±6.550E-3
50-Sn-117	3.090E-1	3.092E-1	3.188E-1±4.800E-3	1.000E+0	1.031E+0±1.506E-2
50-Sn-118	6.530E-2	6.532E-2	6.210E-2±6.000E-4	1.000E+0	9.507E-1±9.662E-3

TABLE XLII: ENDF/B-VII.1 [2], ENDF/B-VIII.0, KADONIS v0.3 [169] Maxwellian-averaged neutron capture cross sections and their ratios at kT=30 keV. Comments: *C*-calculated from BNL-325 data [454], *T*-theoretical data in KADONIS v.0.3 [169].

Material	**ENDF/B-VII.1** (barns)	**ENDF/B-VIII.0** (barns)	**KADONIS v.0.3** (barns)	**ENDF/B-VII.1/ENDF/B-VIII.0**	**KADONIS/ENDF/B-VIII.0**
50-Sn-119	2.250E-1	2.248E-1	1.800E-1±1.000E-2	1.000E+0	8.006E-1±5.556E-2
50-Sn-120	3.800E-2	3.789E-2	3.620E-2±3.000E-4	1.003E+0	9.555E-1±8.287E-3
50-Sn-121M		3.905E-1			
50-Sn-122	1.490E-2	1.508E-2	2.190E-2±1.500E-3	9.857E-1	1.452E+0±6.849E-2
50-Sn-123	3.600E-1	3.604E-1		1.000E+0	
50-Sn-124	1.180E-2	1.152E-2	1.200E-2±1.800E-3	1.026E+0	1.041E+0±1.500E-1
50-Sn-125	9.820E-2	9.816E-2	5.900E-2±9.000E-3^T	1.000E+0	6.011E-1±1.525E-1
50-Sn-126	1.080E-2	1.081E-2	1.000E-2±4.000E-3^T	1.000E+0	9.247E-1±4.000E-1
51-Sb-121	5.110E-1	5.110E-1	5.320E-1±1.600E-2	1.000E+0	1.041E+0±3.008E-2
51-Sb-122		1.123E+0	8.940E-1±1.620E-1^T		7.963E-1±1.812E-1
51-Sb-123	3.210E-1	3.211E-1	3.030E-1±9.000E-3	1.000E+0	9.436E-1±2.970E-2
51-Sb-124	9.690E-1	9.690E-1		1.000E+0	
51-Sb-125	5.260E-1	5.259E-1	2.600E-1±7.000E-2^T	1.000E+0	4.944E-1±2.692E-1
51-Sb-126	7.350E-1	7.354E-1		1.000E+0	
52-Te-120	2.910E-1	2.913E-1	5.380E-1±2.600E-2	1.000E+0	1.847E+0±4.833E-2
52-Te-121		1.169E+0			
52-Te-121M		1.844E+0			
52-Te-122	2.350E-1	2.349E-1	2.950E-1±3.000E-3	1.000E+0	1.256E+0±1.017E-2
52-Te-123	8.070E-1	8.065E-1	8.320E-1±8.000E-3	1.000E+0	1.032E+0±9.615E-3
52-Te-124	1.350E-1	1.351E-1	1.550E-1±2.000E-3	1.000E+0	1.147E+0±1.290E-2
52-Te-125	4.170E-1	4.173E-1	4.310E-1±4.000E-3	1.000E+0	1.033E+0±9.281E-3
52-Te-126	7.960E-2	7.963E-2	8.130E-2±1.400E-3	1.000E+0	1.021E+0±1.722E-2
52-Te-127M	8.870E-1	8.868E-1		1.000E+0	
52-Te-128	3.700E-2	3.698E-2	4.440E-2±1.300E-3	1.000E+0	1.201E+0±2.928E-2
52-Te-129M	7.480E-1	7.482E-1		1.000E+0	
52-Te-130	1.430E-2	1.429E-2	1.470E-2±2.800E-3	1.000E+0	1.029E+0±1.905E-1
52-Te-131		2.849E-2			
52-Te-131M		4.319E-2			
52-Te-132	1.490E-2	1.485E-2		1.000E+0	
53-I -127	7.230E-1±9.700E-2	7.231E-1±9.699E-2	6.350E-1±3.000E-2	1.000E+0±1.897E-1	8.782E-1±1.422E-1
53-I -128		7.975E-1			
53-I -129	4.380E-1±8.500E-2	4.382E-1±8.500E-2		1.000E+0±2.743E-1	
53-I -130	6.880E-1	6.876E-1		1.000E+0	
53-I -131	2.630E-1	2.630E-1		1.000E+0	
53-I -132		1.816E-1			
53-I -132M		2.008E-1			
53-I -133		4.006E-2			
53-I -134		2.665E-2			
53-I -135	7.020E-3	7.023E-3		1.000E+0	
54-Xe-123	1.800E+0	1.796E+0		1.000E+0	
54-Xe-124	1.250E+0	7.707E-1	6.440E-1±8.300E-2	1.625E+0	8.356E-1±1.289E-1
54-Xe-125		1.638E+0			
54-Xe-126	6.720E-1	6.717E-1	3.590E-1±5.100E-2	1.000E+0	5.345E-1±1.421E-1
54-Xe-127		1.027E+0			
54-Xe-128	2.830E-1	2.827E-1	2.625E-1±3.700E-3	1.000E+0	9.286E-1±1.410E-2
54-Xe-129	4.200E-1	4.199E-1	6.170E-1±1.200E-2	1.000E+0	1.469E+0±1.945E-2
54-Xe-130	1.520E-1	1.519E-1	1.320E-1±2.100E-3	1.000E+0	8.691E-1±1.591E-2
54-Xe-131	3.060E-1±4.160E-2	3.061E-1±4.158E-2	3.400E-1±6.500E-2^T	1.000E+0±1.921E-1	1.111E+0±2.345E-1
54-Xe-132	4.730E-2±1.120E-2	4.728E-2±1.118E-2	6.460E-2±5.300E-3	1.000E+0±3.342E-1	1.366E+0±2.502E-1
54-Xe-133	1.270E-1	1.273E-1	1.270E-1±3.400E-2^T	1.000E+0	9.977E-1±2.677E-1
54-Xe-134	2.260E-2±4.970E-3	2.257E-2±4.971E-3	2.020E-2±1.700E-3	1.000E+0±3.115E-1	8.951E-1±2.358E-1
54-Xe-135	6.550E-2	6.545E-2		1.000E+0	
54-Xe-136	1.190E-3	1.186E-3	9.100E-4±8.000E-5	1.000E+0	7.675E-1±8.791E-2
55-Cs-133	4.650E-1±5.530E-2	4.647E-1±5.530E-2	5.090E-1±2.100E-2	1.000E+0±1.683E-1	1.095E+0±1.259E-1
55-Cs-134	1.160E+0	1.156E+0	7.240E-1±6.500E-2^T	1.000E+0	6.261E-1±8.978E-2
55-Cs-135	2.010E-1±3.990E-2	2.009E-1±3.985E-2	1.600E-1±1.000E-2	1.000E+0±2.804E-1	7.963E-1±2.079E-1
55-Cs-136	1.820E-1	1.821E-1		1.000E+0	
55-Cs-137	2.160E-2	2.163E-2		1.000E+0	
56-Ba-130	7.360E-1	7.361E-1	7.460E-1±3.400E-2	1.000E+0	1.013E+0±4.558E-2
56-Ba-131		8.791E-1			
56-Ba-132	4.560E-1	4.560E-1	3.970E-1±1.600E-2	1.000E+0	8.706E-1±4.030E-2
56-Ba-133	5.690E-1	5.689E-1		1.000E+0	
56-Ba-134	2.270E-1	2.270E-1	1.760E-1±5.600E-3	1.000E+0	7.752E-1±3.182E-2
56-Ba-135	4.840E-1	4.840E-1	4.550E-1±1.500E-2	1.000E+0	9.400E-1±3.297E-2
56-Ba-136	7.000E-2	7.003E-2	6.120E-2±2.000E-3	1.000E+0	8.739E-1±3.268E-2
56-Ba-137	5.870E-2	5.870E-2	7.630E-2±2.400E-3	1.000E+0	1.300E+0±3.145E-2
56-Ba-138	3.740E-3	3.740E-3	4.000E-3±2.000E-4	1.000E+0	1.070E+0±5.000E-2
56-Ba-139		4.082E-2			
56-Ba-140	1.030E-2	1.030E-2		1.000E+0	
57-La-138	3.130E-1	3.133E-1	4.190E-1±5.900E-2^T	1.000E+0	1.338E+0±1.408E-1
57-La-139	3.630E-2±5.680E-3	3.626E-2±5.680E-3	3.240E-2±3.100E-3	1.000E+0±2.215E-1	8.935E-1±1.835E-1
57-La-140	1.180E-1	1.176E-1		1.000E+0	
58-Ce-136	3.380E-1	3.381E-1	3.280E-1±2.100E-2	1.000E+0	9.702E-1±6.402E-2
58-Ce-137		7.830E-1			
58-Ce-137M		1.221E+0			
58-Ce-138	2.080E-1	2.080E-1	1.790E-1±5.000E-3	1.000E+0	8.605E-1±2.793E-2
58-Ce-139	4.080E-1	4.075E-1	2.140E-1±1.200E-1^T	1.000E+0	5.252E-1±5.607E-1
58-Ce-140	7.740E-3	7.741E-3	1.100E-2±4.000E-4	1.000E+0	1.421E+0±3.636E-2
58-Ce-141	2.750E-1±5.530E-2	2.754E-1±5.529E-2	7.600E-2±3.300E-2^T	1.000E+0±2.839E-1	2.759E-1±4.784E-1
58-Ce-142	1.990E-2	1.990E-2	2.800E-2±1.000E-3	1.000E+0	1.407E+0±3.571E-2
58-Ce-143	1.140E-1	1.143E-1		1.000E+0	
58-Ce-144	2.420E-2	2.424E-2		1.000E+0	
59-Pr-141	1.090E-1±1.070E-2	1.090E-1±1.070E-2	1.114E-1±1.400E-3	1.000E+0±1.388E-1	1.022E+0±9.896E-2
59-Pr-142	3.610E-1	3.613E-1	4.150E-1±1.780E-1^T	1.000E+0	1.149E+0±4.289E-1
59-Pr-143	1.080E-1	1.076E-1	3.500E-1±8.600E-2^T	1.000E+0	3.253E+0±2.457E-1
60-Nd-142	3.340E-2	3.344E-2	3.500E-2±7.000E-4	1.000E+0	1.047E+0±2.000E-2
60-Nd-143	2.380E-1±3.020E-2	2.384E-1±3.016E-2	2.450E-1±3.000E-3	1.000E+0±1.789E-1	1.028E+0±1.271E-1
60-Nd-144	7.490E-2	7.486E-2	8.130E-2±1.500E-3	1.000E+0	1.086E+0±1.845E-2
60-Nd-145	4.200E-1±4.630E-2	4.201E-1±4.631E-2	4.250E-1±5.000E-3	1.000E+0±1.559E-1	1.012E+0±1.108E-1
60-Nd-146	9.850E-2±1.130E-2	9.854E-2±1.132E-2	9.120E-2±1.000E-3	1.000E+0±1.624E-1	9.256E-1±1.154E-1
60-Nd-147	8.340E-1	8.339E-1	5.440E-1±9.000E-2^T	1.000E+0	6.524E-1±1.654E-1
60-Nd-148	1.400E-1±1.500E-2	1.401E-1±1.503E-2	1.470E-1±2.000E-3	1.000E+0±1.517E-1	1.049E+0±1.082E-1
60-Nd-149		7.663E-1			
60-Nd-150	1.570E-1	1.565E-1	1.590E-1±1.000E-2	1.000E+0	1.016E+0±6.289E-2
61-Pm-143		5.314E-1±3.302E-1			
61-Pm-144		1.443E+0±7.077E-1			
61-Pm-145		8.529E-1±4.656E-1			
61-Pm-146		1.578E+0			
61-Pm-147	1.050E+0±1.980E-1	1.047E+0±1.826E-1	7.090E-1±1.000E-1	1.000E+0±2.573E-1	6.771E-1±2.243E-1
61-Pm-148	1.700E+0	1.701E+0	2.970E+0±5.000E-1^T	1.000E+0	1.746E+0±1.684E-1
61-Pm-148M	7.210E+0	7.212E+0	2.453E+0±1.200E+0 ^{T}	1.000E+0	3.401E-1±4.892E-1
61-Pm-149	1.020E+0	1.021E+0	2.510E+0±7.500E-1^T	1.000E+0	2.457E+0±2.988E-1
61-Pm-150		1.939E+0			
61-Pm-151	1.020E+0	1.024E+0		1.000E+0	
62-Sm-144	8.770E-2	8.768E-2	9.200E-2±6.000E-3	1.000E+0	1.049E+0±6.522E-2
62-Sm-145		7.995E-1±2.637E-1			
62-Sm-146		3.116E-1			
62-Sm-147	9.670E-1	9.669E-1	9.730E-1±1.000E-2	1.000E+0	1.006E+0±1.028E-2
62-Sm-148	2.450E-1	2.449E-1	2.410E-1±2.000E-3	1.000E+0	9.841E-1±8.299E-3
62-Sm-149	1.780E+0±3.940E-1	1.781E+0±3.940E-1	1.820E+0±1.700E-2	1.000E+0±3.130E-1	1.022E+0±2.215E-1
62-Sm-150	4.230E-1	4.228E-1	4.220E-1±4.000E-3	1.000E+0	9.982E-1±9.479E-3
62-Sm-151	2.880E+0±8.490E-1	2.875E+0±8.489E-1	3.031E+0±6.800E-2	1.000E+0±4.176E-1	1.054E+0±2.962E-1
62-Sm-152	4.580E-1±5.650E-2	4.584E-1±5.651E-2	4.730E-1±4.000E-3	1.000E+0±1.743E-1	1.032E+0±1.236E-1

TABLE XLII: ENDF/B-VII.1 [2], ENDF/B-VIII.0, KADONIS v0.3 [169] Maxwellian-averaged neutron capture cross sections and their ratios at kT=30 keV. Comments: C-calculated from BNL-325 data [454], T-theoretical data in KADONIS v.0.3 [169].

Material	ENDF/B-VII.1 (barns)	ENDF/B-VIII.0 (barns)	KADONIS v.0.3 (barns)	ENDF/B-VII.1/ENDF/B-VIII.0	KADONIS/ENDF/B-VIII.0
62-Sm-153	9.110E-1	9.114E-1	1.095E+0±1.750E-1^T	1.000E+0	1.202E+0±1.598E-1
62-Sm-154	2.790E-1	2.794E-1	2.060E-1±9.000E-3	1.000E+0	7.372E-1±4.369E-2
63-Eu-151	3.570E+0	3.569E+0	3.478E+0±7.700E-2	1.000E+0	9.746E-1±2.214E-2
63-Eu-152	4.560E+0	4.561E+0	7.600E+0±1.200E+0^T	1.000E+0	1.666E+0±1.579E-1
63-Eu-153	2.660E+0±6.140E-1	2.664E+0±6.140E-1	2.556E+0±4.600E-2	1.000E+0±3.260E-1	9.595E-1±2.312E-1
63-Eu-154	3.470E+0	3.471E+0	4.420E+0±6.700E-1	1.000E+0	1.273E+0±1.516E-1
63-Eu-155	1.130E+0±2.170E-1	1.134E+0±2.165E-1	1.320E+0±8.400E-2	1.000E+0±2.701E-1	1.164E+0±2.013E-1
63-Eu-156	5.410E-1	5.411E-1		1.000E+0	
63-Eu-157	1.140E+0	1.141E+0		1.000E+0	
64-Gd-152	9.850E-1±3.420E-2	9.845E-1±3.415E-2	1.049E+0±1.700E-2	1.000E+0±4.905E-2	1.065E+0±3.828E-2
64-Gd-153	2.620E+0±8.580E-1	2.623E+0±8.575E-1	4.550E+0±7.000E-1^T	1.000E+0±4.624E-1	1.735E+0±3.613E-1
64-Gd-154	9.510E-1±3.770E-2	9.513E-1±3.766E-2	1.028E+0±1.200E-2	1.000E+0±5.598E-2	1.081E+0±4.127E-2
64-Gd-155	2.610E+0±1.280E-1	2.613E+0±1.281E-1	2.648E+0±3.000E-2	1.000E+0±6.934E-2	1.013E+0±5.032E-2
64-Gd-156	5.990E-1±2.570E-2	5.985E-1±2.568E-2	6.150E-1±5.000E-3	1.000E+0±6.067E-2	1.027E+0±4.366E-2
64-Gd-157	1.400E+0±4.940E-2	1.396E+0±4.941E-2	1.369E+0±1.500E-2	1.000E+0±5.005E-2	9.806E-1±3.705E-2
64-Gd-158	3.070E-1±1.300E-2	3.070E-1±1.298E-2	3.240E-1±3.000E-3	1.000E+0±5.978E-2	1.055E+0±4.327E-2
64-Gd-159		1.015E+0			
64-Gd-160	1.710E-1±1.650E-2	1.713E-1±1.649E-2	1.540E-1±2.000E-2	1.000E+0±1.362E-1	8.992E-1±1.617E-1
65-Tb-158		3.662E+0			
65-Tb-159	2.080E+0	2.075E+0	1.580E+0±1.500E-1	1.000E+0	7.614E-1±9.494E-2
65-Tb-160	2.390E+0	2.390E+0	3.240E+0±5.100E-1^T	1.000E+0	1.356E+0±1.574E-1
65-Tb-161		1.505E+0			
66-Dy-154		1.536E+0			
66-Dy-155		4.314E+0			
66-Dy-156	1.530E+0	1.533E+0	1.607E+0±9.200E-2	1.000E+0	1.048E+0±5.725E-2
66-Dy-157		3.818E+0			
66-Dy-158	1.120E+0	1.115E+0	1.060E+0±4.000E-1^T	1.000E+0	9.505E-1±3.774E-1
66-Dy-159		3.689E+0			
66-Dy-160	8.330E-1	8.329E-1	8.900E-1±1.200E-2	1.000E+0	1.069E+0±1.348E-2
66-Dy-161	1.950E+0	1.952E+0	1.964E+0±1.900E-2	1.000E+0	1.006E+0±9.674E-3
66-Dy-162	4.550E-1	4.545E-1	4.460E-1±4.000E-3	1.000E+0	9.813E-1±8.969E-3
66-Dy-163	1.090E+0	1.085E+0	1.112E+0±1.100E-2	1.000E+0	1.025E+0±9.892E-3
66-Dy-164	2.170E-1	2.168E-1	2.120E-1±3.000E-3	1.000E+0	9.777E-1±1.415E-2
67-Ho-165	1.330E+0	1.329E+0	1.280E+0±1.000E-1	1.000E+0	9.633E-1±7.813E-2
67-Ho-166M	1.180E+0	1.182E+0		1.000E+0	
68-Er-162	8.680E-1	8.680E-1	1.624E+0±1.240E-1	1.000E+0	1.871E+0±7.635E-2
68-Er-163		3.826E+0			
68-Er-164	1.920E+0	1.924E+0	1.084E+0±5.100E-2	1.000E+0	5.633E-1±4.705E-2
68-Er-165		2.791E+0			
68-Er-166	6.980E-1±7.220E-2	6.978E-1±7.216E-2	5.630E-1±5.600E-2	1.000E+0±1.462E-1	8.068E-1±1.435E-1
68-Er-167	1.550E+0±2.470E-1	1.554E+0±2.465E-1	1.425E+0±1.430E-1	1.000E+0±2.244E-1	9.170E-1±1.877E-1
68-Er-168	3.020E-1±3.430E-2	3.022E-1±3.428E-2	3.380E-1±4.400E-2	1.000E+0±1.604E-1	1.118E+0±1.727E-1
68-Er-169		7.010E-1	6.530E-1±1.140E-1^T		9.316E-1±1.746E-1
68-Er-170	2.160E-1±4.280E-2	2.156E-1±4.280E-2	1.700E-1±7.000E-3	1.000E+0±2.807E-1	7.885E-1±2.027E-1
69-Tm-168	2.060E+0	2.060E+0		1.000E+0	
69-Tm-169	1.080E+0	1.079E+0	1.129E+0±5.600E-2	1.000E+0	1.047E+0±4.960E-2
69-Tm-170	1.820E+0	1.818E+0	1.870E+0±3.300E-1^T	1.000E+0	1.029E+0±1.765E-1
69-Tm-171		9.187E-1	4.860E-1±1.440E-1^T		5.290E-1±2.963E-1
70-Yb-168		1.216E+0	1.124E+0±4.900E-2		9.247E-1±4.359E-2
70-Yb-169		2.683E+0			
70-Yb-170		7.763E-1	7.680E-1±7.000E-3		9.893E-1±9.115E-3
70-Yb-171		1.255E+0	1.210E+0±1.200E-2		9.640E-1±9.917E-3
70-Yb-172		3.544E-1	3.410E-1±3.000E-3		9.623E-1±8.798E-3
70-Yb-173		7.734E-1	7.540E-1±7.000E-3		9.750E-1±9.284E-3
70-Yb-174		1.585E-1	1.510E-1±1.700E-3		9.524E-1±1.126E-2
70-Yb-175		8.033E-1	5.580E-1pm8.300E-2^T		6.947E-1±1.487E-1
70-Yb-176		1.210E-1	1.158E-1±2.000E-3		9.568E-1±1.727E-2
71-Lu-175	1.320E+0	1.315E+0	1.219E+0±1.000E-2	1.000E+0	9.267E-1±8.203E-3
71-Lu-176	1.540E+0	1.540E+0	1.639E+0±1.400E-2	1.000E+0	1.064E+0±8.542E-3
72-Hf-174	9.500E-1	9.306E-1	9.830E-1±4.600E-2	1.021E+0	1.056E+0±4.680E-2
72-Hf-175		2.533E+0			
72-Hf-176	4.530E-1	5.093E-1	6.260E-1±1.100E-2	8.898E-1	1.229E+0±1.757E-2
72-Hf-177	1.390E+0	1.455E+0	1.544E+0±1.200E-2	9.536E-1	1.061E+0±7.772E-3
72-Hf-178	2.960E-1	3.034E-1	3.190E-1±3.000E-3	9.757E-1	1.051E+0±9.404E-3
72-Hf-179	9.790E-1	9.587E-1	9.220E-1±8.000E-3	1.021E+0	9.617E-1±8.677E-3
72-Hf-180	2.320E-1	2.105E-1	1.570E-1±2.000E-3	1.103E+0	7.459E-1±1.274E-2
72-Hf-181		2.554E-1	1.940E-1±3.100E-2^T		7.596E-1±1.598E-1
72-Hf-182		1.441E-1	1.410E-1±8.000E-3		9.782E-1±5.674E-2
73-Ta-180	1.750E+0	1.753E+0	1.465E+0±1.000E-1	1.000E+0	8.358E-1±6.826E-2
73-Ta-181	8.500E-1	8.502E-1	7.660E-1±1.500E-2	1.000E+0	9.009E-1±1.958E-2
73-Ta-182	1.040E+0	1.036E+0	1.120E+0±1.800E-1^T	1.000E+0	1.081E+0±1.607E-1
74-W -180	5.600E-1±1.220E-1	5.599E-1±1.221E-1	6.600E-1±5.300E-2	1.000E+0±3.084E-1	1.179E+0±2.324E-1
74-W -181		2.974E+0			
74-W -182	2.920E-1±1.130E-2	2.865E-1±9.974E-3	2.740E-1±8.000E-3	1.019E+0±5.194E-2	9.564E-1±4.544E-2
74-W -183	5.750E-1±2.550E-2	5.768E-1±2.541E-2	5.150E-1±1.500E-2	9.966E-1±6.253E-2	8.928E-1±5.282E-2
74-W -184	2.520E-1±1.680E-2	2.520E-1±1.576E-2	2.230E-1±5.000E-3	1.001E+0±9.145E-2	8.848E-1±6.645E-2
74-W -185		1.131E+0	5.840E-1±5.300E-2		5.163E-1±9.075E-2
74-W -186	1.920E-1±4.860E-3	1.889E-1±4.726E-3	2.350E-1±9.000E-3	1.017E+0±3.559E-2	1.244E+0±4.574E-2
75-Re-185	1.170E+0	1.157E+0	1.535E+0±6.200E-2	1.009E+0	1.326E+0±4.039E-2
75-Re-186M		2.683E+0			
75-Re-187	1.020E+0	1.006E+0	1.160E+0±5.700E-2	1.009E+0	1.153E+0±4.914E-2
76-Os-184		7.234E-1	5.900E-1±3.900E-2		8.156E-1±6.610E-2
76-Os-185		2.590E+0			
76-Os-186		4.567E-1	4.100E-1±1.700E-2		8.978E-1±4.146E-2
76-Os-187		1.187E+0	9.660E-1±3.100E-2		8.137E-1±3.209E-2
76-Os-188		3.625E-1	2.930E-1±1.400E-2		8.082E-1±4.778E-2
76-Os-189		1.083E+0	1.168E+0±4.700E-2		1.078E+0±4.024E-2
76-Os-190		3.569E-1	2.740E-1±1.200E-2		7.678E-1±4.380E-2
76-Os-191		1.223E+0±6.413E-1	1.280E+0±2.800E-1^T		1.047E+0±5.684E-1
76-Os-192		2.358E-1	1.550E-1±7.000E-3		6.574E-1±4.516E-2
77-Ir-191	1.170E+0	1.271E+0±9.922E-5	1.350E+0±4.300E-2	9.189E-1±7.805E-5	1.062E+0±3.185E-2
77-Ir-192		2.383E+0±6.611E-1	2.080E+0±4.500E-1^T		8.729E-1±3.518E-1
77-Ir-193	1.020E+0	1.118E+0±1.264E-4	9.940E-1±7.000E-2	9.076E-1±1.130E-4	8.888E-1±7.042E-2
77-Ir-194M		1.697E+0			
78-Pt-190		9.307E-1±3.938E-1	5.080E-1±4.400E-2		5.459E-1±4.319E-1
78-Pt-191		1.769E+0±1.724E+0			
78-Pt-192		4.060E-1±1.048E-1	5.900E-1±1.200E-1^T		1.453E+0±3.287E-1
78-Pt-193		8.171E-1±2.905E-1	1.123E+0±2.400E-1^T		1.374E+0±4.148E-1
78-Pt-194		3.186E-1±4.355E-2	3.650E-1±8.500E-2^T		1.146E+0±2.700E-1
78-Pt-195		8.014E-1±2.211E-1	8.600E-1±2.000E-1^T		1.073E+0±3.609E-1
78-Pt-196		2.008E-1±3.136E-2	1.830E-1±1.600E-2		9.114E-1±1.790E-1
78-Pt-197		3.443E-1±3.055E-1			
78-Pt-198		1.336E-1±1.119E-2	9.220E-2±4.600E-3		6.900E-1±9.749E-2
79-Au-197	6.130E-1±7.720E-3	6.183E-1±1.059E-6	5.820E-1±9.000E-3	9.911E-1±1.260E-2	9.413E-1±1.546E-2
80-Hg-196	3.440E-2	3.442E-2	2.040E-1±8.000E-3	1.000E+0	5.928E+0±3.922E-2
80-Hg-197		1.277E+0			
80-Hg-197M		1.910E+0			
80-Hg-198	1.610E-1	1.613E-1	1.730E-1±1.500E-2	1.000E+0	1.073E+0±8.671E-2
80-Hg-199	3.910E-1	3.912E-1	3.740E-1±2.300E-2	1.000E+0	9.561E-1±6.150E-2
80-Hg-200	1.280E-1	1.277E-1	1.150E-1±1.200E-2	1.000E+0	9.005E-1±1.043E-1
80-Hg-201	2.560E-1	2.556E-1	2.640E-1±1.400E-2	1.000E+0	1.033E+0±5.303E-2
80-Hg-202	8.530E-2	8.532E-2	6.320E-2±1.900E-3	1.000E+0	7.408E-1±3.006E-2

TABLE XLII: ENDF/B-VII.1 [2], ENDF/B-VIII.0, KADONIS v0.3 [169] Maxwellian-averaged neutron capture cross sections and their ratios at kT=30 keV. Comments: *C*-calculated from BNL-325 data [454], *T*-theoretical data in KADONIS v.0.3 [169].

Material	ENDF/B-VII.1 (barns)	ENDF/B-VIII.0 (barns)	KADONIS v.0.3 (barns)	ENDF/B-VII.1/ENDF/B-VIII.0	KADONIS/ENDF/B-VIII.0
80-Hg-203		3.952E-1±1.517E-1	9.800E-2±1.700E-2^T		2.480E-1±4.212E-1
80-Hg-204	4.330E-2	4.326E-2	4.200E-2±4.000E-3	1.000E+0	9.710E-1±9.524E-2
81-Tl-203	1.710E-1	1.705E-1	1.240E-1±8.000E-3	1.000E+0	7.274E-1±6.452E-2
81-Tl-204		4.989E-1±2.335E-1	2.150E-1±3.800E-2^T		4.310E-1±5.003E-1
81-Tl-205	5.260E-2	5.257E-2	5.400E-2±4.000E-3	1.000E+0	1.027E+0±7.407E-2
82-Pb-204	7.240E-2±2.870E-3	7.244E-2±2.872E-3	8.100E-2±2.300E-3	1.000E+0±5.606E-2	1.118E+0±4.876E-2
82-Pb-205		2.115E-1±6.312E-2	1.250E-1±2.200E-2		5.910E-1±3.465E-1
82-Pb-206	1.360E-2±4.220E-4	1.359E-2±4.221E-4	1.450E-2±3.000E-4	1.000E+0±4.392E-2	1.067E+0±3.732E-2
82-Pb-207	8.260E-3±8.270E-4	8.260E-3±8.274E-4	9.900E-3±5.000E-4	1.000E+0±1.417E-1	1.199E+0±1.122E-1
82-Pb-208	6.550E-4±3.280E-4	6.551E-4±3.276E-4	3.600E-4±3.000E-5	1.000E+0±7.071E-1	5.495E-1±5.069E-1
83-Bi-209	3.350E-3±4.400E-4	3.345E-3±4.402E-4	2.560E-3±3.000E-4	1.000E+0±1.861E-1	7.654E-1±1.762E-1
83-Bi-210M		1.742E-2			
84-Po-208		9.603E-2±3.388E-2			
84-Po-209		3.441E-2			
84-Po-210		1.792E-3±2.129E-6	3.300E-3±3.000E-3^T		1.841E+0±9.091E-1
88-Ra-223	5.990E-1	5.989E-1		1.000E+0	
88-Ra-224	2.260E-1	2.259E-1		1.000E+0	
88-Ra-225	6.500E-1	6.504E-1		1.000E+0	
88-Ra-226	4.460E-1	4.460E-1		1.000E+0	
89-Ac-225	1.880E+0±5.660E-1	1.879E+0±5.663E-1		1.000E+0±4.262E-1	
89-Ac-226	2.220E+0±6.740E-1	2.224E+0±6.740E-1		1.000E+0±4.285E-1	
89-Ac-227	1.360E+0±3.680E-1	1.361E+0±3.679E-1		1.000E+0±3.823E-1	
90-Th-227	1.170E+0±6.410E-1	1.173E+0±6.413E-1		1.000E+0±7.732E-1	
90-Th-228	7.480E-1±1.910E-1	7.477E-1±1.913E-1		1.000E+0±3.619E-1	
90-Th-229	1.710E+0±4.090E-1	1.708E+0±4.091E-1		1.000E+0±3.387E-1	
90-Th-230	6.990E-1±1.680E-1	6.990E-1±1.680E-1		1.000E+0±3.400E-1	
90-Th-231	1.540E+0±6.060E-1	1.539E+0±6.056E-1		1.000E+0±5.565E-1	
90-Th-232	4.870E-1±5.120E-3	4.868E-1±5.117E-3		1.000E+0±1.487E-2	
90-Th-233	5.990E-1±2.880E-1	5.988E-1±2.876E-1		1.000E+0±6.793E-1	
90-Th-234	1.770E-1±5.960E-2	1.770E-1±5.964E-2		1.000E+0±4.766E-1	
91-Pa-229	1.760E+0±2.160E+0	1.764E+0±2.162E+0		1.000E+0±1.733E+0	
91-Pa-230	6.930E-1±6.050E-1	6.926E-1±6.047E-1		1.000E+0±1.235E+0	
91-Pa-231	2.090E+0	2.087E+0		1.000E+0	
91-Pa-232	4.310E-1±2.670E-1	4.310E-1±2.669E-1		1.000E+0±8.757E-1	
91-Pa-233	2.250E+0	2.245E+0		1.000E+0	
92-U -230	4.150E-1±3.530E-1	4.149E-1±3.532E-1		1.000E+0±1.204E+0	
92-U -231	4.900E-1±4.680E-1	4.899E-1±4.684E-1		1.000E+0±1.352E+0	
92-U -232	6.350E-1±1.950E-1	6.346E-1±1.948E-1		1.000E+0±4.341E-1	
92-U -233	4.240E-1±6.100E-2	3.439E-1±4.140E-2		1.233E+0±1.876E-1	
92-U -234	5.640E-1±9.630E-2	5.641E-1±9.625E-2		1.000E+0±2.413E-1	
92-U -235	6.930E-1±2.240E-1	7.168E-1		9.664E-1±3.238E-1	
92-U -236	5.510E-1±2.670E-2	5.506E-1±2.674E-2		1.000E+0±6.867E-2	
92-U -237	4.580E-1	4.581E-1		1.000E+0	
92-U -238	4.000E-1±6.180E-3	3.950E-1		1.014E+0±1.544E-2	
92-U -239	9.210E-1	1.234E+0		7.458E-1	
92-U -240	3.170E-1	3.171E-1		1.000E+0	
92-U -241	8.840E-1	8.842E-1		9.998E-1	
93-Np-234	2.010E-1±1.840E-1	2.013E-1±1.843E-1		1.000E+0±1.295E+0	
93-Np-235	2.000E+0±1.490E+0	2.002E+0±1.486E+0		1.000E+0±1.050E+0	
93-Np-236	4.180E-1±3.960E-1	4.184E-1±3.964E-1		1.000E+0±1.340E+0	
93-Np-236M		2.444E-1			
93-Np-237	2.120E+0±1.820E-1	2.115E+0±1.822E-1		1.000E+0±1.219E-1	
93-Np-238	5.220E-1±2.350E-1	5.218E-1±2.348E-1		1.000E+0±6.363E-1	
93-Np-239	1.640E+0±4.680E-1	1.644E+0±4.675E-1		1.000E+0±4.022E-1	
94-Pu-236	2.490E-1±1.120E-1	2.492E-1±1.118E-1		1.000E+0±6.345E-1	
94-Pu-237	3.740E-1±3.780E-1	3.741E-1±3.782E-1		1.000E+0±1.430E+0	
94-Pu-238	7.690E-1±7.810E-2	7.688E-1±7.812E-2		1.000E+0±1.437E-1	
94-Pu-239	5.280E-1±5.500E-2	5.434E-1		9.716E-1±1.042E-1	
94-Pu-240	6.910E-1±5.220E-4	6.747E-1±6.851E-4		1.025E+0±1.266E-3	
94-Pu-241	5.520E-1±9.170E-2	5.519E-1±9.166E-2		1.000E+0±2.349E-1	
94-Pu-242	5.320E-1±1.660E-2	5.321E-1±1.658E-2		1.000E+0±4.407E-2	
94-Pu-243	4.570E-1	4.498E-1		1.017E+0	
94-Pu-244	3.270E-1±8.970E-2	3.270E-1±8.974E-2		1.000E+0±3.881E-1	
94-Pu-245		1.408E+0			
94-Pu-246	2.040E-1±7.820E-2	2.042E-1±7.818E-2		1.000E+0±5.415E-1	
95-Am-240	5.790E-1±4.880E-1	5.794E-1±4.878E-1		1.000E+0±1.191E+0	
95-Am-241	2.550E+0±7.640E-2	2.467E+0±7.395E-2		1.032E+0±4.240E-2	
95-Am-242	5.470E-1	5.469E-1		1.000E+0	
95-Am-242M	6.530E-1±3.260E-1	6.527E-1±3.258E-1		1.000E+0±7.060E-1	
95-Am-243	2.430E+0±2.220E-1	2.430E+0±2.215E-1		1.000E+0±1.289E-1	
95-Am-244	8.810E-1	8.809E-1		1.000E+0	
95-Am-244M	8.530E-1	8.533E-1		1.000E+0	
96-Cm-240	1.040E+0±8.150E-1	1.043E+0±8.152E-1		1.000E+0±1.105E+0	
96-Cm-241	2.290E-1±2.590E-1	2.292E-1±2.586E-1		1.000E+0±1.595E+0	
96-Cm-242	1.030E+0±2.470E-1	1.028E+0±2.474E-1		1.000E+0±3.403E-1	
96-Cm-243	4.560E-1±3.100E-1	4.561E-1±3.104E-1		1.000E+0±9.626E-1	
96-Cm-244	7.740E-1±2.030E-1	7.736E-1±2.027E-1		1.000E+0±3.706E-1	
96-Cm-245	5.970E-1±3.180E-1	5.968E-1±3.178E-1		1.000E+0±7.530E-1	
96-Cm-246	4.630E-1±1.180E-1	4.632E-1±1.176E-1		1.000E+0±3.590E-1	
96-Cm-247	4.300E-1±2.550E-1	4.296E-1±2.548E-1		1.000E+0±8.389E-1	
96-Cm-248	2.870E-1±7.280E-2	2.866E-1±7.281E-2		1.000E+0±3.593E-1	
96-Cm-249	1.900E-1±2.150E-1	1.897E-1±2.151E-1		1.000E+0±1.604E+0	
96-Cm-250	1.990E-1±6.830E-2	1.990E-1±6.832E-2		1.000E+0±4.856E-1	
97-Bk-245	2.610E+0±1.150E+0	2.614E+0±1.146E+0		1.000E+0±6.199E-1	
97-Bk-246	1.080E+0±1.020E+0	1.076E+0±1.016E+0		1.000E+0±1.335E+0	
97-Bk-247	1.920E+0±7.760E-1	1.921E+0±7.762E-1		1.000E+0±5.714E-1	
97-Bk-248	1.200E+0±1.170E+0	1.198E+0±1.166E+0		1.000E+0±1.377E+0	
97-Bk-249	1.570E+0±3.010E-1	1.572E+0±3.006E-1		1.000E+0±2.704E-1	
97-Bk-250	1.170E+0±1.300E+0	1.168E+0±1.299E+0		1.000E+0±1.573E+0	
98-Cf-246	8.630E-1±4.530E-1	8.633E-1±4.527E-1		1.000E+0±7.416E-1	
98-Cf-247		7.975E-1			
98-Cf-248	5.800E-1±1.870E-1	5.802E-1±1.871E-1		1.000E+0±4.560E-1	
98-Cf-249	7.450E-1±3.290E-1	7.449E-1±3.293E-1		1.000E+0±6.252E-1	
98-Cf-250	4.340E-1±9.770E-2	4.343E-1±9.770E-2		1.000E+0±3.181E-1	
98-Cf-251	5.570E-1±4.020E-1	5.565E-1±4.024E-1		1.000E+0±1.023E+0	
98-Cf-252	1.490E-1±4.950E-2	1.489E-1±4.947E-2		1.000E+0±4.697E-1	
98-Cf-253	8.890E-1±4.400E-1	8.887E-1±4.397E-1		1.000E+0±6.997E-1	
98-Cf-254	1.570E-1±9.140E-2	1.568E-1±9.139E-2		1.000E+0±8.241E-1	
99-Es-251	1.570E+0±6.070E-1	1.574E+0±6.069E-1		1.000E+0±5.452E-1	
99-Es-252	4.540E-1±4.520E-1	4.542E-1±4.523E-1		1.000E+0±1.408E+0	
99-Es-253	2.030E+0±1.120E+0	2.025E+0±1.115E+0		1.000E+0±7.788E-1	
99-Es-254	1.010E+0±5.980E-1	1.012E+0±5.979E-1		1.000E+0±8.351E-1	
99-Es-254M	5.370E-1±5.260E-1	5.371E-1±5.255E-1		1.000E+0±1.384E+0	
99-Es-255	2.160E+0±1.360E+0	2.163E+0±1.358E+0		1.000E+0±8.881E-1	
100-Fm-255	3.130E-1±3.920E-1	3.130E-1±3.923E-1		1.000E+0±1.773E+0	

G. Thermal Integral Quantities in ENDF/B-VIII.0

A summary of the thermal fission and neutron capture cross sections is provided in Table XLIII.

TABLE XLIII: Thermal neutron fission and capture cross sections of actinide nuclides from Atlas of Neutron Resonances [132], ENDF/B-VIII.0, ENDF/B-VII.1 [2] and JENDL-4.0u+ [4] libraries (^{a} No resonance parameters measured).

	Fission				Capture			
Material	**Atlas** (barns)	**ENDFB-VIII.0** (barns)	**ENDFB-VII.1** (barns)	**JENDL-4.0u+** (barns)	**Atlas** (barns)	**ENDFB-VIII.0** (barns)	**ENDFB-VII.1** (barns)	**JENDL-4.0u+** (barns)
$^{227}\mathrm{Th}^{a}$	2.020E+2±1.300E+1	2.021E+2	2.021E+2	2.021E+2		4.052E+2	4.052E+2	4.052E+2
$^{228}\mathrm{Th}$	<0.3	1.501E-1	1.501E-1	1.501E-1	1.230E+2±1.500E+1	1.229E+2	1.229E+2	1.229E+2
$^{229}\mathrm{Th}$	3.080E+1±1.500E+0	3.092E+1	3.092E+1	3.092E+1	6.280E+1±6.000E+0	7.056E+1	7.056E+1	7.056E+1
$^{230}\mathrm{Th}$		9.494E-3	9.494E-3	9.494E-3	2.290E+1±3.000E-1	2.341E+1	2.341E+1	2.341E+1
$^{231}\mathrm{Th}^{a}$		4.001E+1	4.001E+1	4.001E+1		1.631E+3	1.631E+3	1.631E+3
$^{232}\mathrm{Th}$	5.200E-5±4.000E-5			5.371E-5	7.350E+0±3.000E-2	7.338E+0	7.338E+0	7.338E+0
$^{233}\mathrm{Th}$	1.500E+1±2.000E+0	1.501E+1	1.501E+1	1.501E+1	1.330E+3±5.000E+1	1.291E+3	1.291E+3	1.291E+3
$^{234}\mathrm{Th}^{a}$	<0.01	5.002E-3	5.002E-3	5.002E-3	1.800E+0±5.000E-1	1.801E+0	1.801E+0	1.801E+0
$^{229}\mathrm{Pa}^{a}$		1.000E+0	1.000E+0	1.000E+0		3.999E+2	3.999E+2	3.999E+2
$^{230}\mathrm{Pa}^{a}$	1.500E+3±2.500E+2	1.500E+3	1.500E+3	1.500E+3		3.801E+2	3.801E+2	3.801E+2
$^{231}\mathrm{Pa}$	2.000E-2±1.000E-3	2.087E-2	2.087E-2	2.365E-2	2.006E+2±2.300E+0	2.007E+2	2.007E+2	2.017E+2
$^{232}\mathrm{Pa}$	1.502E+3±2.800E+1	1.487E+3	1.487E+3	1.487E+3	2.460E+2±3.000E+1	5.890E+2	5.890E+2	5.890E+2
$^{233}\mathrm{Pa}$	<0.1			2.502E-6	3.950E+1±1.200E+0	4.252E+1	4.252E+1	3.942E+1
$^{230}\mathrm{U}^{a}$	2.500E+1±1.000E+1	2.501E+1	2.501E+1	2.501E+1		2.001E+2	2.001E+2	2.001E+2
$^{231}\mathrm{U}^{a}$	4.000E+2±3.000E+2	2.501E+2	2.501E+2	2.501E+2		2.001E+1	2.001E+1	2.001E+1
$^{232}\mathrm{U}$	7.680E+1±4.800E+0	7.652E+1	7.652E+1	7.652E+1	7.490E+1±1.600E+0	7.539E+1	7.539E+1	7.539E+1
$^{233}\mathrm{U}$	5.291E+2±1.200E+0	5.341E+2	5.313E+2	5.314E+2	4.550E+1±7.000E-1	4.233E+1	4.526E+1	4.526E+1
$^{234}\mathrm{U}$	6.700E-2±1.400E-2	6.710E-2	6.702E-2	6.702E-2	9.980E+1±1.300E+0	1.009E+2	1.003E+2	1.003E+2
$^{235}\mathrm{U}$	5.826E+2±1.100E+0	5.867E+2	5.851E+2	5.850E+2	9.880E+1±8.000E-1	9.938E+1	9.869E+1	9.869E+1
$^{236}\mathrm{U}$	6.600E-2±1.300E-2	4.711E-2	4.711E-2	2.594E-4	5.090E+0±1.000E-1	5.134E+0	5.134E+0	5.123E+0
$^{237}\mathrm{U}$	<0.35	1.702E+0	1.702E+0	1.702E+0	4.430E+2±1.670E+2	4.523E+2	4.523E+2	4.523E+2
$^{238}\mathrm{U}$	3.00E-06	1.852E-5	1.680E-5	1.680E-5	2.680E+0±1.900E-2	2.684E+0	2.683E+0	2.683E+0
$^{239}\mathrm{U}^{a}$	1.400E+1±3.000E+0	1.423E+1	1.425E+1		2.200E+1±5.000E+0	2.253E+1	2.233E+1	
$^{240}\mathrm{U}^{a}$		1.079E-3	1.079E-3			1.917E+1	1.917E+1	
$^{241}\mathrm{U}^{a}$		4.265E-1	4.165E-1			4.771E+2	4.761E+2	
$^{234}\mathrm{Np}^{a}$	9.000E+2±3.000E+2	2.001E+3	2.001E+3	2.001E+3		1.101E+2	1.101E+2	1.101E+2
$^{235}\mathrm{Np}^{a}$		5.302E+1	5.302E+1	5.302E+1	1.500E+2±2.000E+0	1.551E+2	1.551E+2	1.551E+2
$^{236}\mathrm{Np}$	3.007E+3±9.000E+1	2.808E+3	2.808E+3	2.808E+3	1.42E+02	1.213E+2	1.213E+2	1.213E+2
$^{236m}\mathrm{Np}$		2.442E+3				1.427E+2		
$^{237}\mathrm{Np}$	2.000E-2±1.000E-3	2.037E-2	2.037E-2	2.019E-2	1.759E+2±2.900E+0	1.754E+2	1.754E+2	1.781E+2
$^{238}\mathrm{Np}$	2.088E+3±3.000E+1	2.202E+3	2.202E+3	2.202E+3		4.795E+2	4.795E+2	4.795E+2
$^{239}\mathrm{Np}^{a}$		2.801E-2	2.801E-2	2.801E-2	6.800E+1±1.000E+1	4.501E+1	4.501E+1	4.501E+1
$^{236}\mathrm{Pu}$	1.700E+2±3.500E+1	1.400E+2	1.400E+2	1.400E+2	1.59E+01	2.756E+1	2.756E+1	2.756E+1
$^{237}\mathrm{Pu}^{a}$	2.455E+3±2.950E+2	2.296E+3	2.296E+3	2.296E+3		2.001E+2	2.001E+2	2.001E+2
$^{238}\mathrm{Pu}$	1.790E+1±4.000E-1	1.777E+1	1.777E+1	1.777E+1	5.400E+2±7.000E+0	4.129E+2	4.129E+2	4.129E+2
$^{239}\mathrm{Pu}$	7.481E+2±2.000E+0	7.474E+2	7.479E+2	7.474E+2	2.693E+2±2.900E+0	2.701E+2	2.707E+2	2.715E+2
$^{240}\mathrm{Pu}$	5.600E-2±3.000E-2	5.632E-2	6.405E-2	3.620E-2	2.895E+2±1.400E+0	2.895E+2	2.876E+2	2.893E+2
$^{241}\mathrm{Pu}$	1.011E+3±6.200E+0	1.012E+3	1.012E+3	1.012E+3	3.621E+2±5.100E+0	3.630E+2	3.630E+2	3.630E+2
$^{242}\mathrm{Pu}$	<0.2	1.382E-2	1.382E-2	2.436E-3	1.850E+1±5.000E-1	2.127E+1	2.127E+1	1.988E+1
$^{243}\mathrm{Pu}$	1.960E+2±1.600E+1	2.041E+2	1.814E+2		8.700E+1±1.000E+1	9.915E+1	8.813E+1	
$^{244}\mathrm{Pu}$		1.715E-3	1.715E-3	1.715E-3	1.700E+0±1.000E-1	1.710E+0	1.710E+0	1.710E+0
$^{245}\mathrm{Pu}$		1.167E-1			1.500E+2±3.000E+1	1.167E+1		
$^{246}\mathrm{Pu}$		3.201E-3	3.201E-3	3.201E-3		8.003E+1	8.003E+1	8.003E+1
$^{240}\mathrm{Am}^{a}$		1.500E+3	1.500E+3	1.500E+3		2.801E+2	2.801E+2	2.801E+2
$^{241}\mathrm{Am}$	3.200E+0±9.000E-2	3.122E+0	3.122E+0	3.122E+0	5.870E+2±1.200E+1	6.843E+2	6.843E+2	6.843E+2
$^{242}\mathrm{Am}$	2.100E+3±2.000E+2	2.095E+3	2.095E+3	2.420E+3	3.300E+2±5.000E+1	2.190E+2	2.190E+2	3.302E+2
$^{242m}\mathrm{Am}$	6.200E+3±2.000E+2	6.400E+3	6.400E+3	6.401E+3	1.290E+3±3.000E+2	1.231E+3	1.231E+3	1.141E+3
$^{243}\mathrm{Am}$	1.983E-1±4.300E-3	8.134E-2	8.134E-2	8.158E-2	7.510E+1±1.800E+0	8.042E+1	8.042E+1	7.926E+1
$^{244}\mathrm{Am}^{a}$	2.300E+3±3.000E+2	2.301E+3	2.301E+3	2.301E+3		6.002E+2	6.002E+2	1.000E+3
$^{244m}\mathrm{Am}^{a}$	1.600E+3±3.000E+2	1.601E+3	1.601E+3	1.601E+3		4.001E+2	4.001E+2	6.002E+2
$^{240}\mathrm{Cm}^{a}$		3.001E+1	3.001E+1	3.001E+1		5.001E+1	5.001E+1	5.001E+1
$^{241}\mathrm{Cm}^{a}$		1.000E+3	1.000E+3	1.000E+3		2.000E+2	2.000E+2	2.000E+2
$^{242}\mathrm{Cm}$	<5	4.665E+0	4.665E+0	4.665E+0	1.600E+1±5.000E+0	1.913E+1	1.913E+1	1.913E+1
$^{243}\mathrm{Cm}$	6.170E+2±2.000E+1	5.873E+2	5.874E+2	5.873E+2	1.300E+2±1.000E+1	1.314E+2	1.314E+2	1.314E+2
$^{244}\mathrm{Cm}$	1.040E+0±2.000E-1	1.022E+0	1.022E+0	1.022E+0	1.520E+1±1.200E+0	1.524E+1	1.524E+1	1.524E+1
$^{245}\mathrm{Cm}$	2.144E+3±5.800E+1	2.054E+3	2.054E+3	2.054E+3	3.690E+2±1.700E+1	3.470E+2	3.470E+2	3.470E+2
$^{246}\mathrm{Cm}$	1.400E-1±5.000E-2	4.401E-2	4.401E-2	4.401E-2	1.220E+0±1.600E-1	1.179E+0	1.179E+0	1.179E+0
$^{247}\mathrm{Cm}$	8.190E+1±4.400E+0	9.474E+1	9.474E+1	9.474E+1	5.700E+1±1.000E+1	5.993E+1	5.993E+1	5.993E+1
$^{248}\mathrm{Cm}$	3.700E-1±5.000E-2	3.366E-1	3.366E-1	3.366E-1	2.630E+0±2.600E-1	2.872E+0	2.872E+0	2.872E+0
$^{249}\mathrm{Cm}^{a}$		1.000E+1	1.000E+1	1.000E+1	1.600E+0±8.000E-1	1.601E+0	1.601E+0	1.601E+0
$^{250}\mathrm{Cm}^{a}$		2.137E-2	2.137E-2	2.137E-2		8.133E+1	8.133E+1	8.133E+1
$^{245}\mathrm{Bk}^{a}$		2.902E+0	2.902E+0	2.902E+0	7.460E+2±4.000E+1	1.000E+3	1.000E+3	1.000E+3
$^{246}\mathrm{Bk}^{a}$		1.801E+3	1.801E+3	1.801E+3		7.001E+2	7.001E+2	7.001E+2
$^{247}\mathrm{Bk}^{a}$		3.702E+0	3.702E+0	3.702E+0		1.000E+3	1.000E+3	1.000E+3
$^{248}\mathrm{Bk}^{a}$		2.001E+3	2.001E+3	2.001E+3		8.601E+2	8.601E+2	8.601E+2
$^{249}\mathrm{Bk}$		3.970E+0	3.970E+0	3.970E+0		7.110E+2	7.110E+2	7.110E+2
$^{250}\mathrm{Bk}^{a}$	9.600E+2±1.500E+2	9.805E+2	9.805E+2	9.805E+2	3.50E+02	7.805E+2	7.805E+2	7.805E+2
$^{246}\mathrm{Cf}^{a}$		1.401E+3	1.401E+3	1.401E+3		1.701E+3	1.701E+3	1.701E+3
$^{247}\mathrm{Cf}$		5.922E-1				5.922E+1		
$^{248}\mathrm{Cf}^{a}$		7.002E+2	7.002E+2	7.002E+2		1.700E+3	1.700E+3	1.700E+3
$^{249}\mathrm{Cf}$	1.642E+3±3.300E+1	1.673E+3	1.673E+3	1.673E+3	4.970E+2±2.100E+1	5.065E+2	5.065E+2	5.065E+2
$^{250}\mathrm{Cf}$		1.120E+2	1.120E+2	1.120E+2	2.034E+3±2.000E+2	2.018E+3	2.018E+3	2.018E+3
$^{251}\mathrm{Cf}$	4.895E+3±2.500E+2	4.939E+3	4.939E+3	4.939E+3	2.850E+3±1.500E+2	2.864E+3	2.864E+3	2.864E+3
$^{252}\mathrm{Cf}$	3.200E+1±4.000E+0	3.303E+1	3.303E+1	3.303E+1	2.040E+1±1.500E+0	2.071E+1	2.071E+1	2.071E+1
$^{253}\mathrm{Cf}$	1.300E+3±2.400E+2	1.301E+3	1.301E+3	1.301E+3	1.760E+1±1.800E+0	2.000E+1	2.000E+1	2.000E+1
$^{254}\mathrm{Cf}^{a}$		2.001E+0	2.001E+0	2.001E+0	4.500E+0±1.500E+0	4.502E+0	4.502E+0	4.502E+0
$^{251}\mathrm{Es}^{a}$		4.303E+1	4.303E+1	4.303E+1	1.840E+2±1.500E+1	2.001E+2	2.001E+2	2.001E+2
$^{252}\mathrm{Es}^{a}$		2.001E+3	2.001E+3	2.001E+3		2.001E+2	2.001E+2	2.001E+2
$^{253}\mathrm{Es}$		2.502E+0	2.502E+0	2.502E+0		1.839E+2	1.839E+2	1.839E+2
$^{254}\mathrm{Es}^{a}$	1.970E+3±2.000E+2	2.129E+3	2.129E+3	2.129E+3	2.830E+1±2.500E+0	2.831E+1	2.831E+1	2.831E+1
$^{254m}\mathrm{Es}$	1.826E+3±8.000E+1	2.001E+3	2.001E+3	2.001E+3		2.501E+2	2.501E+2	2.501E+2
$^{255}\mathrm{Es}^{a}$		5.004E-1	5.004E-1	5.004E-1	5.500E+1±1.000E+1	5.500E+1	5.500E+1	5.500E+1
$^{255}\mathrm{Fm}^{a}$		3.362E+3	3.362E+3	3.362E+3		2.701E+2	2.701E+2	2.701E+2

H. Quasi-differential Benchmarks for $n + \mathrm{Be}$

The RPI quasi-differential experiment was previously described in Ref. [455] and Ref. [456], more recently beryllium results were analyzed in Ref. [457]. These experimental data and similar analysis methods were used to compare the new ENDF/B-VIII.0 evaluation with the previous ENDF/B-VII.1 evaluation. In this experiment 8 EJ-301 liquid scintillators surrounded a cylindrical Be sample of 7.62 cm in diameter and 4 or 8 cm thick. The distance between the neutron source and sample was 30 m and the sample-to-detector distance was 0.5 m. A pulsed neutron beam ($\approx$ 8 ns wide) from the RPI 60 MeV electron LINAC scattered from the sample to the detectors. The geometry of this setup was designed to minimize cross talk between the detectors, and pulse shape analysis was used to remove gamma background. The measured data are useful in the energy range from 0.5 to 20 MeV and cover scattering angles from 26 to 154.2 degrees. These quasi-differential data were compared to detailed simulations of the experimental setup. Due to the low room return background, the entire room was omitted from the simulation; the simulation included the beam path, sample, another flight path pipe that was on an adjacent beamline, and the sample holder table [456]. The detectors were represented by `MCNP`® 6.1 [458] point detectors (F5 tally) that are used in conjunction with the energy dependent efficiency to tally the time of flight detector response. A procedure to experimentally determine the shape of the energy dependent neutron detection efficiency was used [456]. The simulations were first compared and normalized to scattering from carbon, and the same normalization factor was used for Be data.

The results are shown for angles of 51 and 154 degrees in Fig. 181. The plotted experimental uncertainty includes about 5% normalization systematic uncertainty. In general the new evaluation did not change much from ENDF/B-VII.1 and both agree with the experimental data in most of the energy region. At 51 degrees the two evaluations are within the uncertainty of the experimental data. Between 1-2 MeV and 3 MeV the new evaluation is slightly closer to the experiment. At the back scattering angle of 154.3 degrees the new evaluation agrees with the experimental data better between 3-4 MeV but is lower and in worse agreement than ENDF/B-VII.1 between 1 to 1.5 MeV.

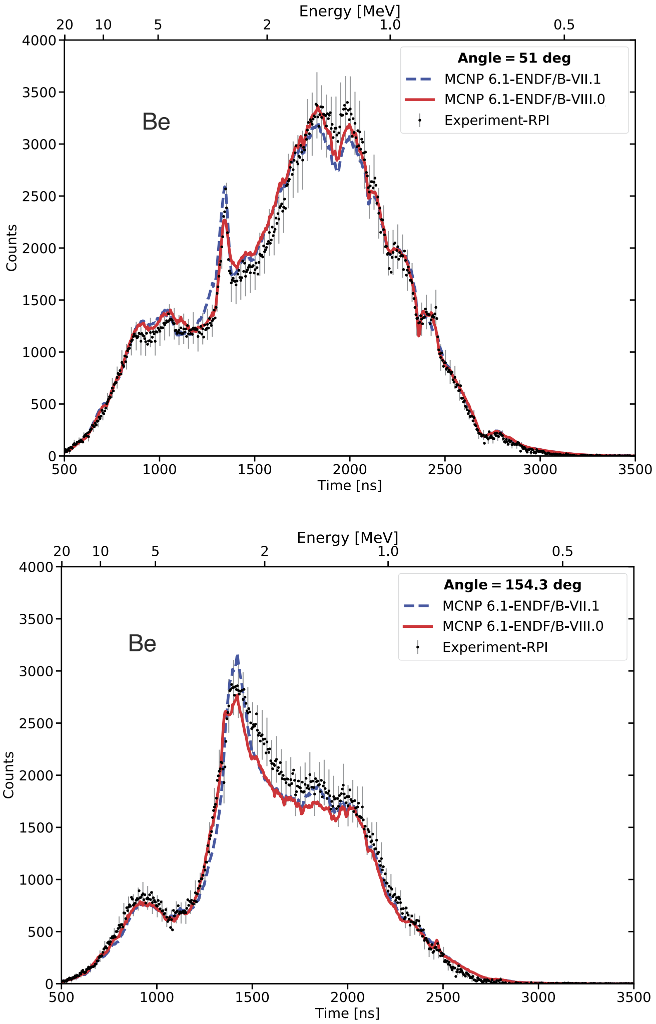

FIG. 181. (Color online) Measured neutron counts per 5 ns time bin as a function time of flight for an angle of 51 degrees (upper panel) and 154.3 degrees (lower panel) relative to the incident neutron beam. The upper x-axis is approximately the incident neutron energy, see Ref. [456] for more details.

I. 14 MeV Neutron Transmission

The ENDF/B-VIII.0 library can be tested against experimental data from several groups employing a 14 MeV neutron source. As for previous releases, the data from LLNL, FNS, and Oktavian were used (more information can be found in Ref. [447]). The same set of cases was simulated as in Ref. [447], but in most cases the differences are small, hardly to be noticed in plots. Therefore only selected results are presented here and the focus is on cases where differences appear between ENDF/B-VIII.0 and ENDF/B-VII.1.

The pulsed sphere measurements, carried out at LLNL from the 1960s to 1985 [459, 460], measured neutron leakage spectra from spherical target materials induced by a 14-MeV neutron beam brought to the center of these spheres. Various target sphere materials (from H_2O to ^{239}Pu) of different sphere thicknesses were investigated with five neutron detectors (Pilot B, Stilbene, NE-213A, NE-213B, NE-213C). These measurements were designed with the aim that the simple geometry of the measurements could be easily simulated to validate Monte Carlo transport codes and nuclear data libraries. These pulsed sphere benchmarks were extensively used for validating ENDF/B-VI data [461], but only results for ^{235,238}U, ^{239}Pu, ^{6}Li and ^{9}Be were shown in the ENDF/VII.0 and ENDF/B-VII.1 papers [1, 2].

For validating ENDF/B-VIII.0 data, these measurements and literature on them were revisited [462–465]: In 2005, Frankle [462, 463] recommended that the measured data should be only compared to the cutoff of the detector response function, otherwise the validation might be unreliable. It was also shown that a collimator in the beamline has overall negligible impact on the ^{239}Pu measurement except for the lowest energies (below 1.6 MeV). A recent study by Kaiba *et al.* [465] highlighted that the concrete surrounding the beamline has a significant impact on the measured spectrum, while the accuracy of the path length and detector angle had negligible impact on the final results. Also, the question was raised whether the missing D-D peak at 2.8 MeV of the neutron source in the `MCNP`® model could adversely impact simulation results below 4 MeV outgoing neutron energies. This question is currently under investigation.

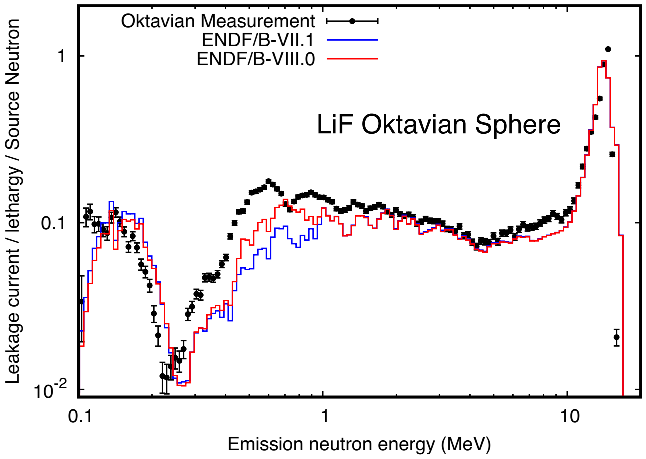

FIG. 182. (Color online) Simulation of 14 MeV neutron transmission through LiF. ENDF/B-VII.1 results are from Ref. [447].

For neutron transmission through LiF, the data show an improvement in the calculated spectrum below 1 MeV (Fig. 182). The calculated spectrum of transmission through cobalt has improved above 1 MeV, but deteriorated somewhat below 1 MeV (Fig. 183). For copper, the calculated spectrum has improved slightly between 1 and 3 MeV, but above 3 MeV it is further away from the measured data (Fig. 184). The results for beryllium are mixed (Fig. 185), while the results for oxygen hardly differ from the results based on ENDF/B-VII.1 (Fig. 186).

The results for iron are particularly relevant, as the iron data have been revised for this release. Some results for the LLNL Pulsed Spheres and the FNS experiments are shown in Fig. 187. The results show improvements for the leakage spectrum after 5 cm of Fe, at a large angle (66.8°). On the other hand, in the spectrum after 20 cm, at an angle of 24.9°, no such improvements are visible. The results for the LLNL Pulsed Sphere experiments are inconclusive, showing an improvement at short time intervals, but lesser results at longer time intervals.

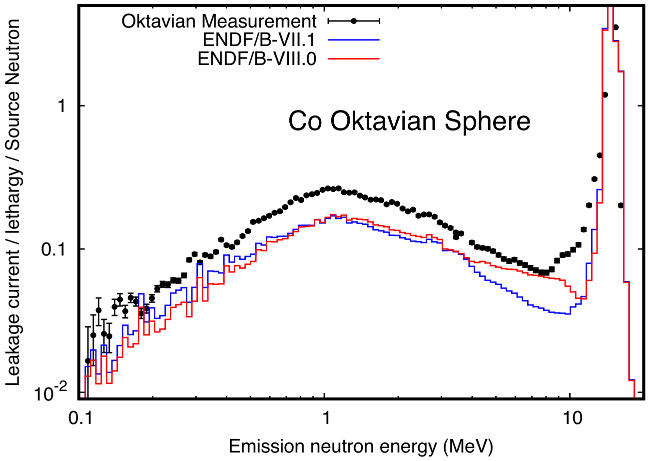

FIG. 183. (Color online) Simulation of 14 MeV neutron transmission through Co. ENDF/B-VII.1 results are from Ref. [447].

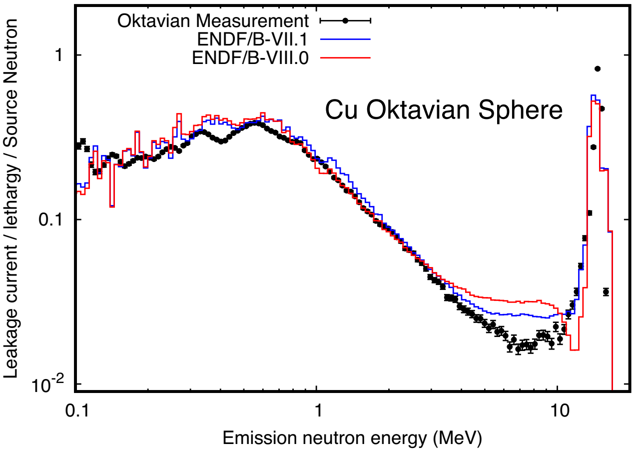

FIG. 184. (Color online) Simulation of 14 MeV neutron transmission through Cu. ENDF/B-VII.1 results are from Ref. [447].

In Fig. 188, MCNP-6.1.1 simulation results using ENDF/B-VII.1 and ENDF/B-VIII.0 are compared to the ^{235,238}U and ^{239}Pu experimental data recommended to be used for validation in Ref. [464]. The simulated results using ENDF/B-VII.1 and ENDF/B-VIII.0 are very similar for ^{239}Pu while improvements can be seen for 200–270 ns for ^{235}U and 150–220 ns for ^{238}U which can be partially attributed to the changes in the respective PFNS.

More comprehensive benchmarking against the larger set of the pulsed sphere measurements will be undertaken in the future.

XIII. ENDF-6 AND GNDS FORMAT OPTIONS

The ENDF/B-VIII library is available in two formats: in addition to the well-known ENDF-6 format that

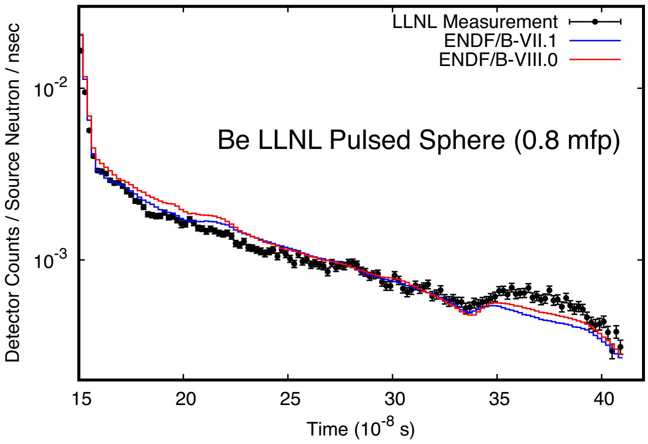

FIG. 185. (Color online) Simulation of 14 MeV neutron transmission through 0.8 mean free path (mfp) Be. ENDF/B-VII.1 results are from Ref. [447].

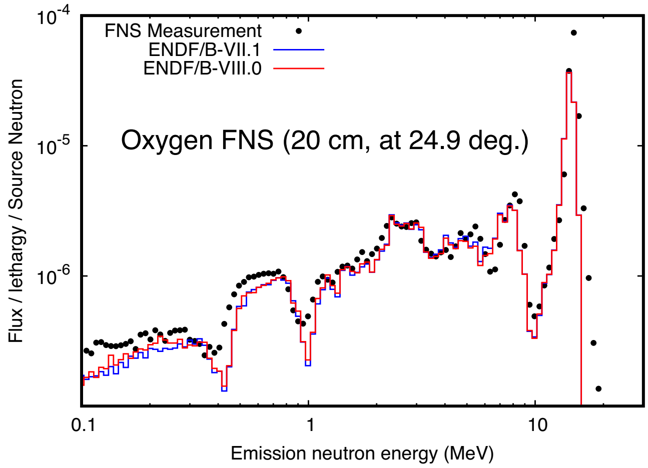

FIG. 186. (Color online) Simulation of 14 MeV neutron transmission through 20 cm O at 24.9°. ENDF/B-VII.1 results are from Ref. [447].

has been used to store previous versions of the library, the library is also available in the Generalized Nuclear Database Structure (GNDS) (GNDS/XML format version 2.1).

A. ENDF-6 Format Changes

With each major release of the ENDF library, CSEWG publishes a new version of the ENDF-6 format manual. The ENDF/B-VIII.0 release is no exception. In addition to the usual formatting improvements and minor corrections, there were a series of major format and/or manual revisions:

- Simplified equations for charged-particle interpolation rule INT=6 (Chapter 0.5.2.1)

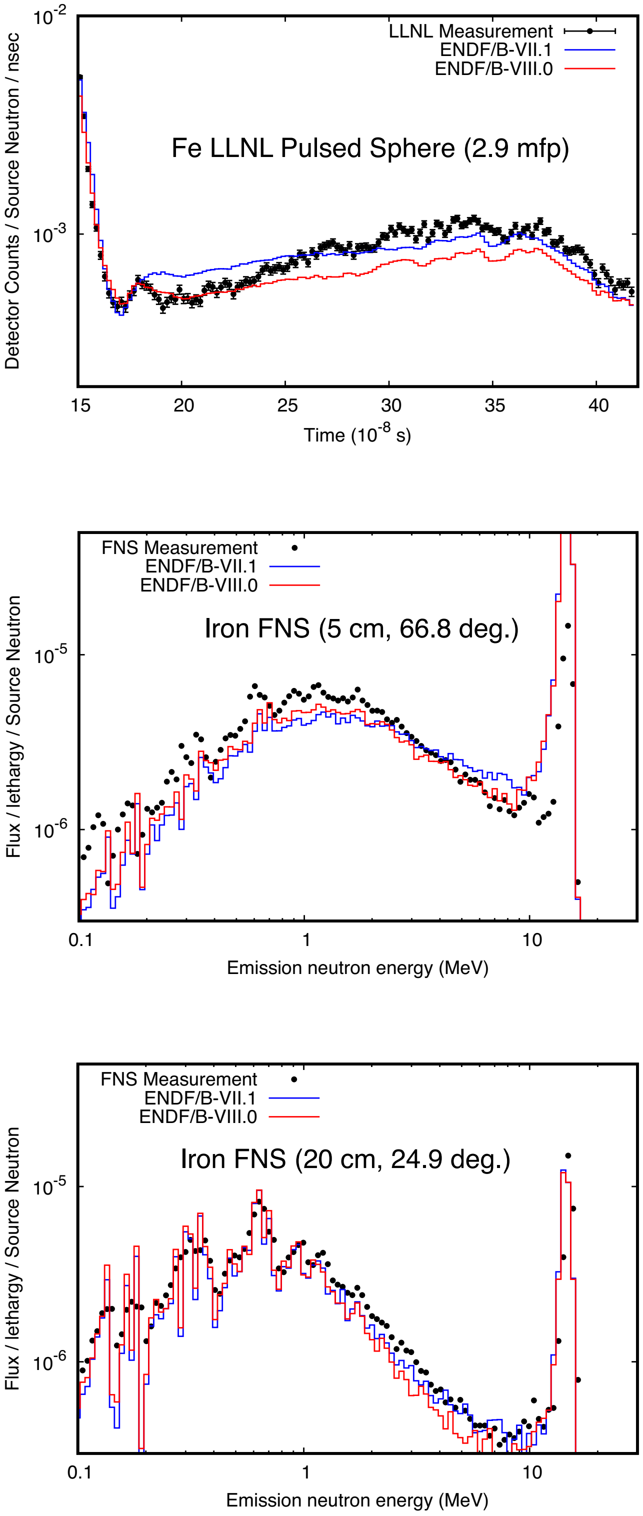

FIG. 187. (Color online) Simulation of 14 MeV neutron transmission through 2.9 mean free path (mfp) Fe (top), 5 cm Fe at 66.8° (middle) and 20 cm Fe at 24.9° (bottom) [447].

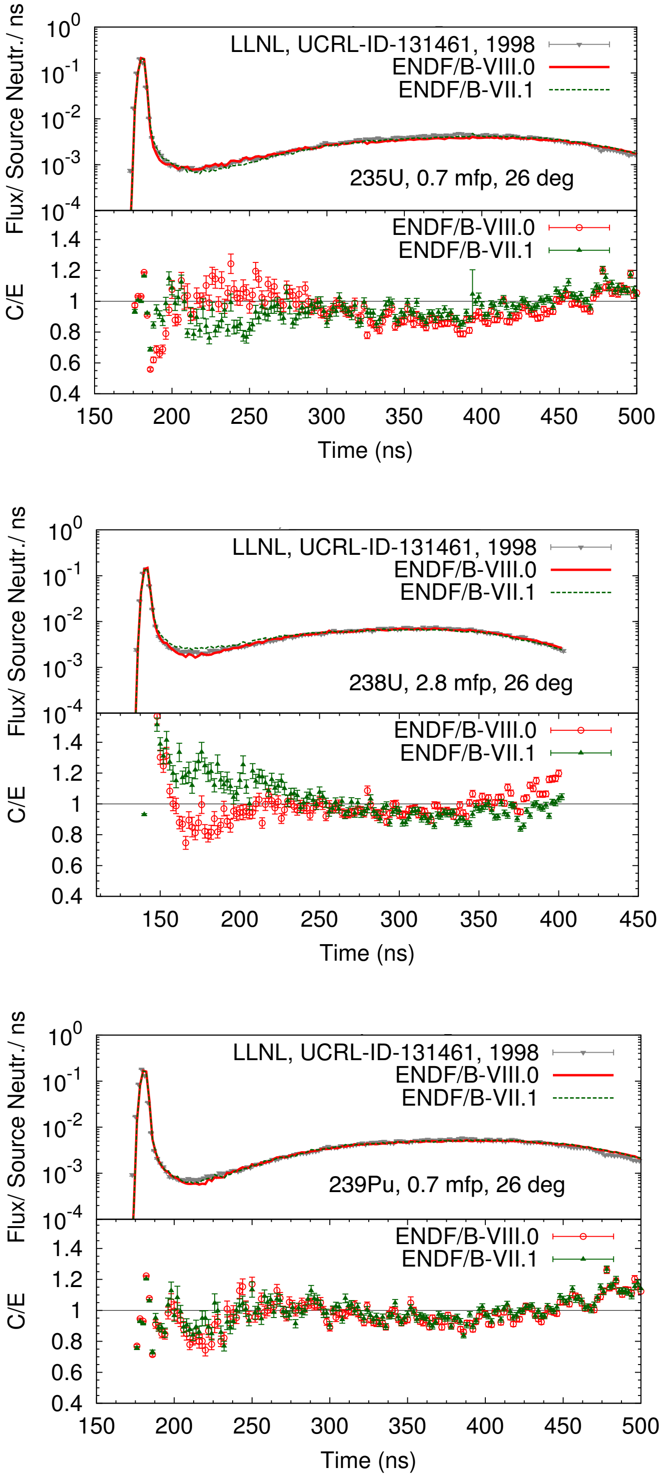

FIG. 188. (Color online) MCNP-6 simulated results of the LLNL ^{235,238}U and ^{239}Pu pulsed sphere benchmarks using ENDF/B-VII.1 and ENDF/B-VIII.0 are compared to experimental data. For ^{235}U and ^{239}Pu, spheres of 0.7 mean free path length were measured at an angle of 26 degree with the NE-213B detector, while for ^{238}U, a 2.8 mean free path thick sphere was measured at the same angle with the same detector.

- Line numbering optional (Chapter 0.6)
- Explain notation for ENDF formats and relation to punch-card history (Chapter 0.6)
- Clarify allowed number formats (Chapter 0.6.2)
- Define allowed ASCII characters (Chapter 0.6.4.1)
- Tabular form of F.E.R. (Chapter 1)
- Q values now computed using atomic masses (Chapter 3.3.2)
- $P(\nu|E)$ for fission neutrons (Chapter 6)
- Kalbach interpolation fix (Chapter 6)
- Provision for subactnide fission (Chapter 10, 40)
- Rewritten chapter on atomic form factors or scattering functions (Chapter 27)
- Clarified MAT numbers for TSL data (Appendix C)
- New kinematics discussion (Appendix E)
- CODATA2010 constants (Appendix I)

The ENDF-6 format was frozen in May 2017 in preparation for both the ENDF/B-VIII.0 release and the release of GNDS.

B. GNDS Format

The GNDS structure was designed by Subgroup #38 of the Working Party for Evaluation Cooperation (WPEC SG38), and will eventually replace the punch-card based ENDF-6 format. GNDS defines a physics-based, hierarchical structure for representing nuclear data that can be expressed in a file using XML, JSON, HDF5 or any ‘format’ that supports a hierarchical structure. In addition to storing evaluated nuclear data, GNDS can also store processed data needed by Monte Carlo and deterministic transport codes (e.g. grouped cross sections and transfer matrices).

The GNDS/XML version of the ENDF-VIII.0 library was created by translating the ENDF-6 files into GNDS using the code FUDGE (For Updating Data and Generating Evaluations) developed by Lawrence Livermore National Laboratory. FUDGE is capable of translating evaluations back and forth between ENDF-6 and GNDS formats. FUDGE also provides a framework for creating, modifying and processing nuclear data. In addition to the processing discussed in Section XIV, FUDGE is also capable of generating ACE files to support `MCNP`® [458].

Simultaneously releasing the library in two different formats helps address two important goals. The first goal is to provide continuity so users can immediately use the ENDF-VIII.0 library through familiar tools that depend on the ENDF-6 format. The second goal is to encourage users to begin adopting the new GNDS standard.

The authors recognize that adopting a new data standard requires substantial effort from the nuclear data community. To facilitate the transition, WPEC has organized a new subgroup (WPEC SG43) to focus on designing an Application Program Interface (API) for reading and writing GNDS files (subgroup website: `https://www.oecd-nea.org/science/wpec/sg43/`).

Since the two formats contain the same underlying data, nuclear data users will be able to test GNDS capabilities by comparing results with similar tools that use data from ENDF-6. Cross-validating results between the two libraries are expected to help discover errors and build confidence that GNDS data access is performing as expected.

To this end, the GNDS access library called GIDI (or 'General Interaction Data Interface') [466] was implemented in LLNL's Monte Carlo and deterministic particle transport codes, Mercury [467, 468] and Ardra [469]. Integral testing of the ENDF/B-VIII.0 neutron sublibrary in GNDS format was performed for a set of ICSBEP fast critical assembly evaluations. Monte Carlo simulations were run with point-wise continuous energy cross sections and deterministic simulations with a 230 group cross-section set. k_{eff} simulated with Mercury and Ardra are compared to benchmark values and `MCNP`® results in Table XLIV. The current implementations of the GNDS format and GIDI do not include URR, neutron thermal scattering laws, up-scatter and angular biasing yet. Nevertheless, agreement with `MCNP`® version 6 is seen to be good, providing some verification of the implementation methods of the processed data in various transport codes.

XIV. DATA PROCESSING WITH NJOY, AMPX, FUDGE AND PREPRO

A. NJOY

The NJOY Nuclear Data Processing System has been used to create ACE formatted files for all neutron evaluations of the ENDF/B-VIII.0 library. Some validation checks have been performed on all the ACE files that have been produced using the checkACE [470] suite of tools and no major problems have been found.

NJOY is a modular program with a variety of subprograms each performing an unique task in a multi-step sequence that starts from the original ENDF-formatted file and ends with an ACE file suitable for use in an MCNP calculation. The ENDF/B-VIII.0 files processed here used NJOY2016.8 [471] and employed NJOY's RECONR, BROADR, UNRESR, HEATR, PURR, GASPR, and ACER modules. RECONR is used to create a unionized energy grid for all cross sections of a given evaluated file. If resolved resonance parameters are present, they are expanded into the appropriate pointwise cross sections, typically scattering, capture and possibly fission. Also, with the Limited Reich-Moore (LRF-7) format, there may be resonant charged particle and/or inelastic scattering cross sections. Linear interpolation is used for intervening energy points, and the density of energy points is sufficient to assure that this interpolation is accurate to within a user specified tolerance. For the files generated herein, that tolerance is 0.1%. The output from RECONR is passed to BROADR.

In BROADR, the cross sections are Doppler broadened to 293.6 K. NJOY allows the user to specify a different linear interpolation tolerance as part of its BROADR input, but in most instances (including here) the same linear interpolation tolerance as used in RECONR was maintainted. The Doppler broadening of the cross sections for ENDF/B-VIII.0 uses a new feature introduced in NJOY2012.75 (and included in NJOY2016). This feature will Doppler broaden all non-threshold cross sections up to the top of the resolved resonance range. Older versions of NJOY would not broaden above the lowest threshold reaction regardless of the limits of the resolved resonance range. This new feature was added because many of the ENDF/B-VIII.0 evaluations have resolved resonances above the lowest threshold reaction and would not have been properly Doppler broadened with the older versions of NJOY. With the new feature, all of the resolved resonances are properly broadened as expected.

To ensure that all the resolved resonances are properly broadened, simply accept the default values for the `thnmax` parameter on card 3 of the BROADR input.

Here is an example of BROADR input for ^{238}U at room temperature:

```
broadr
 -21 -22 -30  / Card1
 9237         / Card2
 0.001        / Card3
 293.6        / Card4
 0            / Card5--Stop
```

Using the default values for BROADR in this way will ensure that all the resolved resonances are properly Doppler broadened.

The UNRESR and HEATR modules are usually run following the use of RECONR and BROADR. While they are not necessarily needed for the MCNP transport calculations performed herein, they are important and necessary steps to create a complete processed file. Therefore these steps were included in the generic NJOY processing. The PURR module is used to create unresolved resonance probability tables and 16 probability bins with 64 ladders were used. The GASPR module is used to accumulate the various cross sections that produce charged particles (p, d, t, ^{3}He, and α) into a single cross section. It is not necessary for transport calculations, but is often used for calculating production of the particle of interest. Finally, ACER is used to accumulate the various quantities into `MCNP`®'s ACE format.

TABLE XLIV. Comparison of calculated k_{eff} for evaluated criticality experiments described in the ICSBEP Handbook. Eigenvalues were calculated with the ENDF/B-VIII.0 cross section library in ENDF format (MCNP®) and in GNDS format (Mercury [467, 468] and Ardra [469]).

Assembly	**Benchmark**	**MCNP®version6**	**Mercury**	**Ardra**
HEU_MET_FAST_001	1.0000± 0.0010	1.00009±0.00008	1.00010±9.82E-05	1.00018
HEU_MET_FAST_028	1.0000± 0.0030	1.00082±0.00009	1.00088±9.94E-05	1.00027
MIX_MET_FAST_001	1.0000± 0.0016	0.99928±0.00008	0.99946±9.93E-05	0.99943
PU_MET_FAST_001-rev2	1.0000± 0.0020	0.99985±0.00008	0.99984±9.89E-05	1.00006
PU_MET_FAST_006	1.0000± 0.0030	1.00008±0.00010	1.00022±9.91E-05	0.99832
U233_MET_FAST_001	1.0000± 0.0010	1.00049±0.00008	0.99986±9.80E-05	1.00069
U233_MET_FAST_006	1.0000± 0.0014	1.00002±0.00010	0.99944±9.84E-05	0.99859

B. AMPX

The AMPX code system [472] has been continuously developed since the early 1970s and is used to produce cross section libraries for the SCALE code system [473]. AMPX is available as part of the SCALE package. Dedicated funding from the US Nuclear Criticality Safety Program (NCSP) for AMPX modernization has facilitated modernization of the AMPX code package. Key processing capabilities of AMPX include:

- generation of temperature-dependent continuous-energy cross section data;
- resonance self-shielding for resolved and unresolved resonance ranges (URR);
- generation of probability tables for the URR;
- generation of energy and angle distributions for secondary particles;
- processing of thermal scattering law data, S(α,β), for thermal moderators;
- processing of particle-yield and decay data;
- production of cross-section covariance data files for sensitivity/uncertainty analyses;
- performance of multi-group averaging operations; and
- generation of continuous-energy weighting spectra.

The original Bondarenko methodology used for multigroup libraries, was recently enhanced including: (a) using continuous-energy flux spectra from CENTRM to precalculate shielding factors for homogeneous and heterogeneous lattices, (b) improving unresolved self-shielding by using the same probability tables as used for the continuous-energy libraries, (c) developing a new method for elastic removal corrections, and (d) generating lambda factors for use with the intermediate resonance approximation [474]. These improvements were made possible by the tighter integration between SCALE and AMPX, as the SCALE CENTRM module is used in the generation of the data.

In order to simplify the generation of the input files for the computational modules, AMPX comes with a Graphical User Interface program (ExSite), which allows to select desired ENDF formatted files and extract abbreviated information from the files. This information is used to generate input files based on user input such as group structure, flux, and desired temperatures.

The ENDF/B-VIII.0 library was processed into multigroup as well as continuous energy libraries and tested with the VALID suite [475]. In addition, the covariance information was processed and combined with an existing SCALE covariance library to account for covariance matrices not given in ENDF/B-VIII.0.

C. FUDGE

Nuclear data processing at Lawrence Livermore National Laboratory is handled by the code FUDGE. FUDGE (For Updating Data and Generating Evaluations) is written primarily in Python, with some performance-critical sections written in C. The code is driven by Python scripts rather than input decks, and can also be used interactively from the Python command prompt.

In addition to translating data from ENDF-6 into GNDS and vice-versa (as described in Section XIII), FUDGE processing capabilities also include

- reconstructing cross sections and angular distributions from resonance parameters,
- Doppler-broadening neutron-induced cross sections to account for thermal motion in a target,
- converting parameterized reaction product distributions (e.g., Kalbach-Mann) into point-wise data for visualization,
- generating multi-group data (e.g., cross sections and transfer matrices), used primarily in deterministic transport codes, and
- calculating cumulative density functions (CDFs) from probability density functions (PDFs) to facilitate Monte Carlo sampling.

While testing the ENDF-VIII.0 library, LLNL used FUDGE to process the neutron, charged-particle, photonuclear and photo-atomic sub-libraries for use in deterministic and Monte Carlo transport applications. Processed libraries were generated at three temperatures: 0.02585 eV/k, 1 eV/k and 100 eV/k (or 300 K, 11.6 kK and 1.16 MK). Multi-group libraries were produced including 230-group cross sections and transfer matrices up to Legendre order 9 (the 230-group set is commonly used at LLNL, and spans energies from 1.3 meV to 20 MeV).

D. PREPRO

1. *Overview*

The codes in the PREPRO code system are designed to pre-process ENDF formatted data, for later, further processing for use in applications. Each code in this modular set of computer codes reads and writes evaluated nuclear data in the ENDF format. Each code performs one or more independent operations on the data. The codes are available on CD-ROM from the IAEA Nuclear Data Section, free of charge upon request or can be downloaded from `http://www-nds.iaea.org/ndspub/endf/prepro/`.

2. *Features of 2017 Version*

Compared to earlier versions of these codes the 2017 version has the following features,

- **PREPRO uses 9 or 10 digit precision for all ENDF output.** For example consider: 9 digits: 12324.56789, versus 7 digits: 1.234567+3. The 9 digit output is a hundred times more precise compared to the 7 digit output. This is very important for narrow milli-eV wide resonances in the keV or today even in the MeV energy range.
- **BEST INPUTs and testing inputs are provided separately for all codes.** As distributed, PREPRO includes a series of test cases to quickly run each code to insure it is operating correctly. The input for these test runs is designed to allow adequate testing in a reasonable amount of time; as such this input may not correspond to what is recommended for production work. The recommended inputs are provided in a separate directory from the test inputs.
- **LINKING and TRACKING sequences of codes,** have now been simplified by having each code identify itself when it starts and when it finishes correctly in its output report (.LST files), and if it does not finish correctly each code will identify the problem that caused it to terminate and print an ERROR message rather than the code name. This allows the user to automate and run long sequences of codes and still easily monitor performance.
- **MORE COMPLETE packages are included for each type of computer;** in particular the graphics codes EVALPLOT and COMPLOT are now included so that users can quickly view nuclear data on their computer screen and/or produce Postscript files for later use, i.e., as in reports. Interactive graphics are a powerful tool that allows one to quickly check the enormous amount of data currently included in modern nuclear data libraries.
- **ENDF/B Tested:** All of ENDF/B-VII, version 0 and 1, as well as all ENDF/B-VIII beta releases, have been processed to high precision at many temperatures to create POINT2009 (VII.0) and POINT2012 (VII.1) data, and the results are now available on-line at `http://www-nds.iaea.org/point2009/pt2009.htm` and `http://www.nndc.bnl.gov/endf/b7.1/POINT2012/POINT2012.htm`.

3. *Specific Code Improvements*

- **LINEAR has improved BEST input parameters,** based on extensive use of the earlier versions of the PREPRO codes. Of particular note is decreasing the minimum cross section from 10^{-10} to 10^{-30} barns to be linearized (tabulated data below the minimum are copied, ignoring the ENDF interpolation code). This has a rather dramatic effect, particularly on neutron and charged particle reactions, which often have long, slowly decreasing tails toward the reaction threshold. Here the cross section can be quite small, but extends over a large energy range, so there might be an integral effect. Since this extension has only a minor effect on the overall size of the pre-processed ENDF data it is now accurately included.
- **ENDF2C is a new code for PREPRO 2017,** to insure that ALL PREPRO output in the ENDF format are completely FORTRAN, C and C++ compatible.
- **SPECTRA was a new code for PREPRO 2010,** which starting from models and tabulated data, linearizes and tabulates neutron emission spectra (MF=5); it is similar to and is an extension of the LINEAR code that performs a similar function for cross sections (MF=3). It has been extended for 2017.
- **RECENT for 2017 is extended** to handle multiple resolved resonance energy ranges for the general Reich-Moore (LRF=7) resolved resonance formalism. The other resolved formalisms calculate and

output total, elastic, capture and fission cross sections. The general Reich-Moore allows many more output R-matrix channels; RECENT 2017 has been further extended and allows up to 10 output channels. The extension to multiple LRF=7 resonance regions makes PREPRO capable of handling all current and planned evaluations.

- **SIGMA1 for 2017 has been updated for improved low energy treatment,** as well as improved accuracy and consistency throughout. For 2017 Doppler broadening is now restricted to an upper limit of 10 MeV, i.e., all tabulated cross sections at energies higher than this are assumed to be temperature independent and are copied exactly as read from the ENDF input to the ENDF output.
- **Doppler Broadening High Energy Cutoff:** Today many modern evaluations extend to very high energies well above the traditional ENDF 20 MeV end for evaluations. In these cases the theoretical models used for the evaluations change at or near 20 MeV, which can cause an abrupt change (a non-physical discontinuity) in cross sections. To compensate for the "intent" of the evaluators, PREPRO Doppler broadening now only extends up to 10 MeV. This has the effect of making the "discontinuities" in the cross section at or near 20 MeV, temperature independent.
- **SIXPAK and ACTIVATE have been extended** to handle newer data that can now be coded using MF=3, 6, 9, and 10 formats.

XV. FUTURE WORK

In the coming years the CSEWG community will continue to advance the quality of the ENDF database. In the course of the present work, the many improvements still needed have become apparent, despite the progress we have made. We anticipate that the next release, ENDF/B-VIII.1, will occur in about five years time.

We highlight one main area where we anticipate an upgrade in the next release: fission product yields (FPYs). These were not updated for the current release. Our current FPY data date back to England and Rider's seminal work from around 1990, with some modest updates made for plutonium fast neutron FPYs for ENDF/B-VII.1. The availability of improved experimental data, and theory and modeling techniques, makes such a focus timely, as well as the continued importance of FPYs and related data (delayed neutrons, gammas, heating) for a variety of applications.

Additionally, particular attention will be paid to improve the treatment of uncertainties and covariances in the evaluated nuclear data, and to address some of the general questions mentioned in Section VI. Closer communication between covariance evaluators and end-users is certainly required to improve the currently unsatisfying situation.

The current ENDF/B-VIII.0 library significantly benefited from the advances made by the CIELO project. The pilot phase of this project has now been completed [8], but its success has led to a desire to continue, and evolve the collaboration. This will be done by the IAEA for the neutron cross sections, and by the NEA, for integral validation feedback of CIELO. A tabulation of some of the main findings of the CIELO collaboration, together with priorities for future work, is given towards the end of the CIELO overview paper [8].

ACKNOWLEDGMENTS

We thank Dr. P. Obložinský for valuable feedback on this paper. We are most grateful for the substantial contributions to the work made by retirees. Work at Brookhaven National Laboratory was sponsored by the Office of Nuclear Physics, Office of Science of the U.S. Department of Energy under Contract No. DE-AC02-98CH10886 with Brookhaven Science Associates, LLC. Work at Los Alamos National Laboratory was carried out under the auspices of the National Nuclear Security Agency of the U.S. Department of Energy under Contract No. DE-AC52-06NA25396. Work at ORNL was supported by the US Department of Energy (DOE), Nuclear Criticality Safety Program (NCSP) funded and managed by the National Nuclear Security Administration for DOE under contract DE-AC05-00OR22725. Work at Lawrence Livermore National Laboratory was performed under Contract DE-AC52-07NA27344. Work at Oak Ridge National Laboratory was authored by UT-Battelle, LLC under Contract No. DE-AC05-00OR22725 with the U.S. Department of Energy.

[1] M. B. Chadwick, P. Obložinský, M. Herman *et al.*, "ENDF/B-VII.0: Next generation evaluated nuclear data library for nuclear science and technology," Nucl. Data Sheets **107**, 2931 (2006).

[2] M. B. Chadwick, M. W. Herman, P. Obložinský *et al.*, "ENDF/B-VII.1 nuclear data for science and technology: Cross sections, covariances, fission product yields and decay data," Nucl. Data Sheets **112**, 2887 (2011).

[3] A. J. Koning *et al.*, "Status of the JEFF nuclear data library," J. Korean Phys. Soc. **59**, 1057 (2011).

[4] K. Shibata, O. Iwamoto, T. Nakagawa *et al.*, "JENDL-4.0: A new library for nuclear science and engineering," J. Nucl. Sci. Technol. **48**, 1 (2011).

[5] G. Chiba, K. Okumura, K. Sugino, Y. Nagaya, K. Yokoyama, T. Kugo, M. Ishikawa, and S. Okajima, "JENDL-4.0 benchmarking for fission reactor applications," J. Nucl. Sci. Technol. **48**, 172 (2011).

[6] M. B. Chadwick, E. Dupont, E. Bauge *et al.*, "The CIELO collaboration: Neutron reactions on ^{1}H, ^{16}O, ^{56}Fe, ^{235}U, ^{238}U and ^{239}Pu," Nucl. Data Sheets **118**, 1 (2014).

[7] M. B. Chadwick, R. Capote, A. Trkov *et al.*, "The CIELO collaboration: Progress in international evaluations of neutron reactions on Oxygen, Iron, Uranium and Plutonium," Eur. Phys. J. Web Conf. **146**, 02001 (2017). ND2016: International Conference on Nuclear Data for Science and Technology, September 11-15, 2016 (Bruges, Belgium).

[8] M. B. Chadwick, R. Capote, A. Trkov *et al.*, "CIELO collaboration summary results: International evaluations of neutron reactions on uranium, plutonium, iron, oxygen and hydrogen," Nucl. Data Sheets **148**, 189 (2018).

[9] A. D. Carlson, V. G. Pronyaev, D. L. Smith *et al.*, "International evaluation of neutron cross section standards," Nucl. Data Sheets **110**, 3215 (2009).

[10] A. D. Carlson, V. G. Pronyaev, R. Capote *et al.*, "Evaluation of the neutron data standards," Nucl. Data Sheets **148**, 143 (2018).

[11] R. Capote, Y. Chen, F. Hambsch *et al.*, "Prompt fission neutron spectra of actinides," Nucl. Data Sheets **131**, 1 (2016).

[12] E. M. Zsolnay, R. Capote, H. Nolthenius, and A. Trkov, "Summary description of the new international reactor dosimetry and fusion file (IRDFF release 1.0)," Tech. Rep. INDC(NDS)-0616, IAEA, Vienna, Austria (2012).

[13] R. Capote, K. I. Zolotarev, V. G. Pronyaev, and A. Trkov, "Updating and extending the IRDF-2002 dosimetry library," J. ASTM Int. **9**, JAI104119 (2012).

[14] C. D. S. Jean *et al.*, "Coordinated evaluation of ^{239}Pu in the resonance region," Tech. Rep. NEA/WPEC-34, OECD Nuclear Energy Agency, Paris, France (2014).

[15] G. Palmiotti, M. Salvatores *et al.*, "Methods and approaches to provide feedback from nuclear and covariance data adjustment for improvement of nuclear data files," Tech. Rep. NEA/WPEC-39, NEA, Paris, France. in preparation.

[16] G. Noguere *et al.*, "Thermal scattering kernel $S(\alpha, \beta)$: Measurement, evaluation and application," Tech. Rep. NEA/WPEC-42, NEA, Paris, France. in preparation.

[17] R. Capote, A. Trkov *et al.*, "IAEA CIELO evaluation of neutron-induced reactions on ^{235}U and ^{238}U targets for incident energies up to 30 MeV," Nucl. Data Sheets **148**, 254 (2018).

[18] S. Mosby *et al.*, "^{235}Pu(n,γ) from 10 eV to 1.3 MeV," Nucl. Data Sheets **148**, 312 (2018).

[19] M. Herman, A. Trkov, R. Capote *et al.*, "Evaluation of neutron reactions on iron isotopes for CIELO and ENDF/B-VIII.0," Nucl. Data Sheets **148**, 214 (2018).

[20] D. Neudecker *et al.*, "Evaluations of energy spectra of neutrons emitted promptly in neutron-induced fission of ^{235}U and ^{239}Pu," Nucl. Data Sheets **148**, 293 (2018).

[21] S. C. van der Marck, "Benchmarking ENDF/B-VII.0," Nucl. Data Sheets **107**, 3061 (2006).

[22] A. Kahler, R. E. MacFarlane, R. D. Mosteller *et al.*, "ENDF/B-VII.1 neutron cross section data testing with critical assembly benchmarks and reactor experiments," Nucl. Data Sheets **112**, 2997 (2011).

[23] S. V. Zabrodskaya, A. V. Ignatyuk, V. N. Koscheev *et al.*, "ROSFOND - Rossiyskaya natsionalnaya biblioteka nejtronnykh dannykh," VANT, Nucl. Constants **1-2**, 3 (2007).

[24] *ROSFOND Manual.* Obninsk, Russia Federation (2006). in Russian.

[25] R. Arcilla, D. Brown, and M. Herman, "Continuous integration and deployment software to automate nuclear data verification and validation," Nucl. Data Sheets **118**, 422 (2014).

[26] C. R. Howell, Q. Chen, T. S. Carman *et al.*, "Toward a resolution of the neutron-neutron scattering-length issue," Phys. Lett. B **444**, 252 (1998).

[27] D. Cokinos and E. Melkonian, "Measurement of the 2200 m/sec neutron-proton capture cross section," Phys. Rev. C **15**, 1636 (1977).

[28] W. Dilg, "Measurement of the neutron-proton total cross section at 132 eV," Phys. Rev. C **11**, 103 (1975).

[29] Y. Fujita, K. Kobayashi, T. Oosaki, and R. C. Block, "Measurement of the Neutron-Proton Total Cross Section Using 24 keV Iron Filtered Neutrons," Nucl. Phys. **A258**, 1 (1976).

[30] W. Allen and A. Ferguson, "The n-p Cross Section in the Range 60-550 keV," Proc. Phys. Soc. Sect. A **68**, 1077 (1955).

[31] B. H. Daub, V. Henzl, M. A. Kovash, J. L. Matthews, Z. W. Miller, K. Shoniyozov, and H. Yang, "Measurements of the neutron-proton and neutron-carbon total cross section from 150 to 800 keV," Phys. Rev. C **87**, 014005 (2013).

[32] J. C. Davis and H. H. Barschall, "Fast-Neutron Total Cross Section of Deuterium," Phys. Rev. C **3**, 1798 (1971).

[33] J. C. Davis, K. A. Weaver, D. Hilscher, H. H. Barschall, and A. B. Smith, "Total Cross Section of Protons for 2.5-MeV Neutrons," Phys. Rev. C **4**, 1061 (1971).

[34] W. P. Abfalterer, F. B. Bateman, F. S. Dietrich, R. W. Finlay, R. C. Haight, and G. L. Morgan, "Measurement of Neutron Total Cross Sections up to 560 MeV," Phys. Rev. C **63**, 044608 (2001).

[35] P. W. Lisowski, R. E. Shamu, G. F. Auchampaugh, N. S. P. King, M. S. Moore, G. L. Morgan, and T. S. Singleton, "Search for Resonance Structure in the n-p Total Cross Section Below 800 MeV," PHYS. REV. LETT. **49**, 255 (1982).

[36] N. Boukharouba, F. B. Bateman, C. E. Brient, A. D. Carlson, S. M. Grimes, R. C. Haight, T. N. Massey, and O. A. Wasson, "Measurement of the n-p Elastic Scattering Angular Distribution at $E_n = 10$ MeV," PHYS. REV. C **65**, 014004 (2001).

[37] J. D. Seagrave, "Recoil Deuterons and Disintegration Protons from the n-d Interaction,and n-p Scattering at $E_n = 14.1$ MeV," PHYS. REV. **97**, 757 (1955).

[38] T. Nakamura, "Angular Distribution of n-p Scattering at 14.1 MeV," J. PHYS. SOC. JPN. **15**, 1359 (1960).

[39] W. Buerkle and G. Mertens, "Measurement of the neutron-proton differential cross section at 14.1 MeV," FEW BODY SYST. **22**, 11 (1997).

[40] E. Greiner and H. Karge, "Investigation of n-p-scattering at 14.1 MeV," ANNALEN DER PHYSIK **16**, 354 (1965).

[41] A. Suhami and R. Fox, "Neutron-proton small angle scattering," PHYS. LETT. B **24**, 173 (1967).

[42] S. Shirato and K. Saito, "On the Differential Cross Section for Neutron-Proton Scattering at 14.1 MeV," J. PHYS. SOC. JPN. **36**, 331 (1974).

[43] M. Drosg and D. M. Drake, "180° n-p Cross Sections for Fast Neutron Measurements with Counter Telescopes," NUCL. INSTRUM. METH. PHYS. RES. **160**, 143 (1979).

[44] E. R. Flynn and P. J. Bendt, "n-p Differential Scattering Cross Section At 22.5 MeV," PHYS. REV. **128**, 1268 (1962).

[45] J. P. Scanlon, G. H. Stafford, J. J. Thresher, P. H. Bowen, and A. Langsford, "Angular Distributions for n-p Scattering In The Energy Range 22.5 To 110 MeV," NUCL. PHYS. **41**, 401 (1963).

[46] G. Fink, P. Doll, T. D. Ford, R. Garrett, W. Heeringa, K. Hofmann, H. O. Klages, and H. Krupp, "Backward Angle n-p Differential Cross Sections from 22 to 50 MeV," NUCL. PHYSICS, SECT. A **518**, 561 (1990).

[47] J. L. Romero, J. A. Jungerman, F. P. Brady, W. J. Knox, and Y. Ishizaki, "Elastic Scattering of 36.0- and 46.3-MeV Neutrons from Deuterium," PHYS. REV. C **2**, 2134 (1970).

[48] T. C. Montgomery, B. E. Bonner, F. P. Brady, W. B. Broste, and M. W. McNaughton, "Neutron-Proton Differential Cross Section Measurements at 25.8 and 50.0 MeV," PHYS. REV. C **16**, 499 (1977).

[49] D. Holslin, J. McAninch, P. A. Quin, and W. Haeberli, "New test of nucleon-nucleon potential models," PHYS. REV. LETT. **61**, 1561 (1988).

[50] J. Brock, A. Chisholm, J. Duder, R. Garrett, and J. Poletti, "Analysing power for neutron-proton scattering at 14.1 MeV," NUCL. PHYS. A **361**, 368 (1981).

[51] G. J. Weisel, W. Tornow, C. R. Howell, P. D. Felsher, M. Al Ohali, Z. P. Chen, R. L. Walter, J. M. Lambert, P. A. Treado, and I. Slaus, "Neutron-Proton Analyzing Power Data between 7.6 and 18.5 MeV," PHYS. REV. C **46**, 1599 (1992).

[52] W. Tornow, C. R. Howell, M. L. Roberts, P. D. Felsher, Z. M. Chen, R. L. Walter, G. Mertens, and I. Slaus, "Low-Energy Neutron-Proton Analyzing Power and the New Bonn Potential and Paris Potential Predictions," PHYS. REV. C **37**, 2326 (1988).

[53] J. Wilczynski, J. Hansmeyer, F. P. Brady, P. Doll, W. Heeringa, J. C. Hiebert, H. O. Klages, and P. Plischke, "Measurements of the Neutron-Proton Analyzing Power in the Energy Range from 17 to 50 MeV," NUCL. PHYSICS, SECT. A **425**, 458 (1984).

[54] A. D. Carlson, V. Pronyaev, G. M. Hale *et al.*, "A new evaluation of the neutron data standards," EUR. PHYS. J. WEB CONF. **146**, 02025 (2017). ND2016: International Conference on Nuclear Data for Science and Technology, September 11-15, 2016 (Bruges, Belgium).

[55] R. Mosteller, J. Campbell, and R. Little TRANS. AM. NUCL. SOC. **92**, 669 (2005).

[56] J. Briggs, ed., *International Handbook of Evaluated Criticality Safety Benchmark Experiments (ICSBEP)*. Paris: Organization for Economic Co-operation and Development-Nuclear Energy Agency (OECD-NEA) (2016). NEA/NSC/DOC(95)03.

[57] M. Chadwick, P. Young, R. MacFarlane *et al.*, "LA150 documentation of cross sections, heating, and damage: part A (incident neutrons) and part B (incident protons)," Report LA-UR-99-1222, Los Alamos National Laboratory, USA (1999).

[58] K. Kozier, D. Roubtsov, R. Rao, J. Svenne, L. Canton, A. Plompen, M. Stanoiu, M. Nankov, and C. Rouki, "Status of deuterium nuclear data for simulation of heavy water reactors," in *Proceedings of International Conference on Future of Heavy Water Reactors, Ottawa, Ontario, Canada, October 02-05* (2011).

[59] J. Svenne, L. Canton, K. Kozier, and L. Townsend, "Reevaluating low-energy neutron-deuteron elastic scattering using three-nucleon theory," in *Proceedings of International Conference on Nuclear Data for Science and Technology 2007, Nice, France, April 22-27, 2007*, EDP Sciences (2007). DOI: 10.1051/ndata:07208.

[60] J. Svenne, L. Canton, and K. Kozier, "Neutron-deuteron scattering calculation for evaluated neutron data libraries," FEW-BODY SYST. **44**, 31 (2008).

[61] N. Nankov, A. Plompen, S. Kopecky *et al.*, "The Angular Distribution of Neutrons Scattered from Deuterium below 2 MeV," NUCL. DATA SHEETS **119**, 98 (2014).

[62] K. S. Kozier, "Energy and spatial dependence of MCNP simulations for ZED-2 critical experiments," in *Proceedings of CNS 23rd Nuclear Simulation Symposium, Ottawa, Nov. 2-4, Ontario, Canada*, Canadian Nuclear Society, Canada (2008).

[63] J. Márquez Damián, J. Granada, and D. Roubtsov, "Improvement on the calculation of D_2O moderated critical systems with new thermal neutron scattering libraries," ANNALS NUCL. ENERGY **71**, 206 (2014).

[64] E. Pirovano, R. Beyer, A. Junghans, N. Nankov, R. Nolte, M. Nyman, and A. Plompen, "Backward-forward reaction asymmetry of neutron elastic scattering on deuterium," PHYS. REV. C **95**, 024601 (2017).

[65] L. Faddeev and S. Merkuriev, *Quantum Scattering Theory for Several Particle Systems*. Springer (1993).

[66] E. Alt, P. Grassberger, and W. Sandhas, "Reduction of the three-particle collision problem to multi-channel two-particle Lippmann-Schwinger equations," NUCL. PHYS. B **2**, 167 (1967).

[67] H. Witała, A. Nogga, H. Kamada, W. Glöckle, J. Golak, and R. Skibinski, "Modern nuclear force predictions for the neutron-deuteron scattering lengths," PHYS. REV. C **68**, 034002 (2003).

[68] P. Doleschall, I. Borbély, Z. Papp, and W. Plessas, "Nonlocality in the nucleon-nucleon interaction and three-nucleon bound states," Phys. Rev. C **67**, 064005 (2003).

[69] B. Morillon, R. Lazauskas, and J. Carbonell, "Influence of the *ab initio* n–d cross sections in the critical heavy-water benchmarks," Annals Nucl. Energy **54**, 167 (2013).

[70] D. Roubtsov, K. S. Kozier, J. C. Chow, A. J. M. Plompen, S. Kopecky, J. P. Svenne, and L. Canton, "Reactivity impact of ^{2}H and ^{16}O elastic scattering nuclear data on critical systems with heavy water," Nucl. Data Sheets **118**, 414 (2014).

[71] G. Vedrenne, "Neutron interactions on deuterium," J. de Physique - Colloque **27**, C1 (1966). EXFOR Entry 21148.

[72] R. B. Firestone and Z. Revay, "Thermal neutron capture cross sections for ^{16,17,18}O and ^{2}H," Phys. Rev. C **93**, 044311 (2016).

[73] M. Sowerby, B. Patrick, C. Uttley, and K. Diment, "The ratio of the ^{6}Li(n,α) to ^{10}B(n,α) cross-sections from 10 eV TO 80 keV and recommended values of the ^{10}B(n,α) cross-section," J. Nucl. Energy **24**, 323 (1970).

[74] R. A. Schrack, G. P. Lamaze, and O. A. Wasson, "A Measurement of the ^{10}B(n,$\alpha\gamma$)^{7}Li Cross Section in the keV Energy Region," Nucl. Sci. Eng. **68**, 189 (1978).

[75] G. P. Lamaze, R. A. Schrack, and O. A. Wasson, "A New Measurement of the ^{6}Li(n,α)T Cross Section," Nucl. Sci. Eng. **68**, 183 (1978).

[76] W. P. Poenitz, "Measurements of the ^{6}Li(n,α)T Cross Section in the keV Energy Range," Z. für Physik **268**, 359 (1974).

[77] R. L. Macklin, R. W. Ingle, and J. Halperin, "6Li(n,α)T Cross Section from 70 to 3000 keV from the ^{235}U(n,f) Calibration of a Thin Glass Scintillator," Nucl. Sci. Eng. **71**, 205 (1979).

[78] G. Giorginis. Private communication from G. Giorginis to A. Carlson (2014).

[79] M. Drosg, D. M. Drake, and J. Masarik, "Calibration of a Li-Glass Detector for Neutron Energies Above 50 keV by the ^{1}H(t,n)^{3}He Reaction," Nucl. Inst. Meth. Phys. Res. **B94**, 319 (1994).

[80] C. M. Bartle, "Total Cross Sections for the ^{6}Li(n,α)^{3}H Reaction between 2 and 10 MeV," Nucl.Phys. **A330**, 1 (1979).

[81] M. Devlin, T. N. Taddeucci, G. M. Hale, R. C. Haight, and J. M. O'Donnell, "Differential Cross Section Measurements for the ^{6}Li(n,t)α Reaction in the Few MeV Region," in *American Institute of Physics Conference Series* (J. Jolie, A. Zilges, N. Warr, and A. Blazhev, eds.), **1090** of *American Institute of Physics Conference Series*, 215 (2009).

[82] H. H. Knitter, C. Budtz-Jorgensen, M. Mailly and R. Vogt Tech. Rep. CBMN Report EUR 5726e, CBNM Euratom Laboratory (1977).

[83] A. B. Smith, P. Guenther, D. Havel and J. F. Whalen, "Note on the 250 keV resonance in the total neutron cross section of ^{6}Li," Nuclear Data and Measurement Series ANL/NDM-29, Argonne National Laboratory (1977).

[84] R. Lane, A. Langsdorf, J. Monahan, and A. Elwyn, "The angular distributions of neutrons scattered from various nuclei," Annals Phys. **12**, 135 (1961).

[85] H. H. Hogue, P. L. Von Behren, D. H. Epperson *et al.*, "Differential Elastic and Inelastic Scattering of 7- to 15-MeV Neutrons from Beryllium," Nucl. Sci. Eng. **68**, 38 (1978).

[86] G. J. Fischer, "Cross section for the (n,2n) production in Be^9," Phys. Rev. **108**, 99 (1957).

[87] H. C. Catron, M. D. Goldberg, R. W. Hill, J. M. Le Blanc, J. P. Stoering, C. J. Taylor, and M. A. Williamson, "Deuterium and Beryllium (n,2n) Cross Sections Between 6 and 10 MeV," Phys. Rev. **123**, 218 (1961).

[88] D. M. Drake, G. F. Auchampaugh, E. D. Arthur, C. E. Ragan, and P. G. Young, "Double-Differential Beryllium Neutron Cross Sections at Incident Neutron Energies of 5.9, 10.1, and 14.2 MeV," Nucl. Sci. Eng. **63**, 401 (1977).

[89] Y. S. A. Takahashi, E. Ichimura and H. Sugimoto, "Measurement of double differential neutron emission cross sections for incident neutrons of 14 MeV," J. Nucl. Sci. Technol. **25**, 215 (1988).

[90] I. Murata, S. Takaki, K. Shiken, K. Kondo, H. Miyamaru, K. Ochiai, T. Nishitani, and C. Konno, "Measurement of the angle-correlated neutron spectrum for the ^{9}Be(n,2n) reaction with a pencil-beam DT neutron source," in *Proceedings of the International Conference of Nuclear Data for Science and Technology (ND2007)*, (Nice, France) (2008). 22-27 April 2007.

[91] C. T. Hibdon and C. O. Muehlhause, "Neutron Cross Sections at 115 eV and 300 eV," Phys. Rev. **76**, 100 (1949).

[92] R. A. S. R. B. Schwartz and H. T. Heaton, "Total Neutron Cross Sections of Silicon and Beryllium," Bull. Am. Phys. Soc. **16**, 495 (1971).

[93] G. F. Auchampaugh, S. Plattard, and N. W. Hill, "Neutron Total Cross-Section Measurements of ^{9}Be, ^{10,11}B, and ^{12,13}C from 1.0 to 14 MeV Using the ^{9}Be(d,n)^{10}B Reaction as a 'White' Neutron Source," Nucl. Sci. Eng. **69**, 30 (1979).

[94] J. A. Harvey, H. A. Mook, N. W. Hill, and O. Shahal, "Solid State Effects on Thermal Neutron Cross Sections and on Low Energy Resonances," in *Proceedings of the International Conference of Nuclear Data for Science and Technology* (K. Böckhoff, ed.), (Antwerp, Netherlands), 961, Springer, Dordrecht (1983). 6-10 September, 1982.

[95] R. W. Finlay, W. P. Abfalterer, G. Fink, E. Montei, T. Adami, P. W. Lisowski, G. L. Morgan, and R. C. Haight, "Neutron Total Cross Sections at Intermediate Energies," Phys. Rev. **C47**, 237 (1993).

[96] Y. Danon, R. C. Block, M. Rapp, F. Saglime, D. P. Barry, N. J. Drindak, J. Hoole, and G. Leinweber, "High-accuracy filtered neutron beam and high-energy transmission measurements at the Gaerttner Laboratory," in *Proceedings of the International Conference of Nuclear Data for Science and Technology (ND2007)*, (Nice, France), 401 (2008). 22-27 April 2007.

[97] M. J. Rapp, Y. Danon, F. J. Saglime, R. M. Bahran, D. G. Williams, G. Leinweber, D. P. Barry, and R. C. Block, "Beryllium and Graphite Neutron Total Cross-Section Measurements from 0.4 to 20 MeV," Nucl. Sci. Eng. **172**, 268 (2012).

[98] R. A. Schrack, O. A. Wasson, D. C. Larson, J. K. Dickens, and J. H. Todd, "A Relative Measurement of the ^{10}B(n,$\alpha_1\gamma$)^{7}Li Cross Section Between 0.2 and 4.0 MeV," Nucl. Sci. Eng. **114**, 352 (1993).

[99] P. Martin *et al.* Private communication of H. Wiegmann to A. Carlson (1981).

[100] R. M. Sealock and J. C. Overley, "^{10}B(n,α)^{7}Li,^{7}Li* Differential Cross Section Measurements between 0.2 and 1.25 MeV," PHYS. REV. C **13**, 2149 (1976).

[101] G. Giorginis and V. Khryachkov, "The cross-section of the ^{10}B(n,α)^{7}Li reaction measured in the MeV energy range," NUCL. INST. METH. PHYS. RES. A **562**, 737 (2006).

[102] W. P. Abfalterer, F. B. Bateman, F. S. Dietrich, R. W. Finlay, R. C. Haight, and G. L. Morgan, "Measurement of Neutron Total Cross Sections up to 560 MeV," PHYS. REV. C **63**, 044608 (2001).

[103] O.A. Wasson, A.D. Carlson and R.A. Schrack, "Total Neutron Cross Section Measurements of ^{10}B and ^{11}B," in *Proc. of the International Conference on Nuclear Data for Science and Technology, Gatlinburg, TN* (1994).

[104] K. M. Diment and C. A. Uttley, "The neutron total cross-section of carbon between 100 eV and 10 MeV," U.K. report to EANDC No.94AL, Atomic Energy Research Establishment (AERE), Harwell, United Kingdom (1968).

[105] Y. Danon, R. C. Block, M. J. Rapp, F. J. Saglime, G. Leinweber, D. P. Barry, N. J. Drindak, and J. G. Hoole, "Beryllium and Graphite High-Accuracy Total Cross-Section Measurements in the Energy Range from 24 to 900 keV," NUCL. SCI. ENG. **161**, 321 (2009).

[106] B. H. Daub, V. Henzl, M. A. Kovash, J. L. Matthews, Z. W. Miller, K. Shoniyozov, and H. Yang, "Measurements of the neutron-proton and neutron-carbon total cross section from 150 to 800 keV," PHYS. REV. C **87**, 014005 (2013).

[107] S. Cierjacks, F. Hinterberger, G. Schmalz, D. Erbe, P. v. Rossen, and B. Leugers, "High Precision Time-of-Flight Measurements of Neutron Resonance Energies in Carbon and Oxygen between 3 and 30 MeV," NUCL. INST. METH. **169**, 185 (1980).

[108] F.G. Perey, T.A. Love, and W.E. Kinney, "A test of neutron total cross-section evaluations from 0.2 MeV to 20 MeV for C, O, Al, Is, Ca, Fe, and SiO2," Tech. Rep. ORNL-4823, Oak Ridge National Laboratory (1972).

[109] G. M. Hale and M. W. Paris, "Neutron cross sections for carbon and oxygen from new R-matrix analyses of the ^{13,14}C and ^{17}O systems," EUR. PHYS. J. WEB CONF. **146**, 02027 (2017). ND2016: International Conference on Nuclear Data for Science and Technology, September 11-15, 2016 (Bruges, Belgium).

[110] A. Negret *et al.*, "The Limits of the GAINS Spectrometer," NUCL. DATA SHEETS **119**, 179 (2014). Private communication from A. Negret (2013).

[111] V. C. Rogers, V. J. Orphan, C. G. Hoot, and V. V. Verbinski, "Gamma-Ray Production Cross Sections for Carbon and Nitrogen from Threshold to 20.7 MeV," NUCL. SCI. ENG. **58**, 298 (1975).

[112] S.A. Wender, S.J. Seestrom-Morris, and R.O. Nelson, "A white neutron source from 1 to 400 MeV," J. PHYS. G: NUCL. PHYS. SUPPL. **14**, 417 (1988).

[113] W. Galati *et al.*, "Scattering of neutrons by carbon from 3 to 7 MeV," PHYS. REV. C **5**, 1508 (1972).

[114] H. O. Cohn, J. K. Bair, and H. B. Willard, "Carbon-13 Neutron Total Cross Section," PHYS. REV. **122**, 534 (1961).

[115] C. S. Schneider, "Coherent nuclear scattering amplitudes of germanium, copper and oxygen for thermal neutrons," ACTA CRYSTALLOGR. A **32**, 375 (1976).

[116] M. Ohkubo, "Neutron total cross section measruements on oxygen, aluminum and carbon below 930 keV," Tech. Rep. JAERI-M-86-193, Japan Atomic Energy Research Institute (1987). Data corrected for hydrogen content by A. Plompen (2013).

[117] C. H. Johnson, J. L. Fowler, N. W. Hill, and J. M. Ortolf in *Proceedings of the International Conference on Nuclear Cross Sections for Technology*, (Knoxville, TN, USA), 807 (1979). NBS Special Publication **594**, 1980.

[118] J. L. Fowler, C. H. Johnson, and R. M. Feezel, "Level structure of ^{17}O from neutron total cross sections," PHYS. REV. C **8**, 545 (1973).

[119] S. Ciejracks, F. Hinterberger, G. Schmalz, D. Erbe, P. v Rossen, and B. Leugers, "High precision time-of-flight measurements of neutron resonance energies in carbon and oxygen between 3 and 30 MeV," NUCL. INST. METH. **169**, 185 (1980).

[120] J. K. Bair and F. X. Haas, "Total neutron yield from the reactions ^{13}C$(\alpha, n)^{16}$O and ^{17,18}O$(\alpha, n)^{20,21}$Ne," PHYS. REV. C **7**, 1356 (1973).

[121] G. Giorginis, "IRMM measurement in 2007 of the ^{16}O$(n, \alpha)^{13}$C cross section." Personal communication to G. Hale (2016).

[122] Y. Danon, E. Blain, A. Daskalakis *et al.*, "Measurement of total cross section of water and ^{16}O in the MeV energy range," in *Proceedings of AccApp '15*, (Washington, DC, USA), 345 (2015).

[123] S. Kopecky and A. Plompen, "Low-energy scattering data for oxygen," in *NEMEA-7/CIELO Workshop Proceedings*, OECD (2014).

[124] W. Dilg, L. Koester, and W. Nistler, "The Neutron-Deuteron Scattering Lengths," PHYS. LETT. B **36**, 208 (1971).

[125] L. Koester, W. Waschkowski, J. Meier, G. Rau, and M. Salehi, "Experimental Study on p-Wave Neutron Strength Functions for Light Nuclei," Z. FÜR PHYSIK **A330**, 387 (1988).

[126] R. Block, Y. Fujita, K. Kobayashi, and T. Oosaki, "Precision neutron total cross section measurements near 24 keV," J. NUCL. SCI. TECHNOL. **12**, 1 (1975).

[127] M. Ohkubo Tech. Rep. JAERI-M 86, Japan Atomic Energy Research Institute (1987).

[128] J. L. Fowler, C. H. Johnson, and R. M. Feezel, "Level structure of ^{17}O from neutron total cross sections," PHYS. REV. C **8**, 545 (1973).

[129] R. J. Holt, H. E. Jackson, R. M. Laszewski, J. E. Monahan, and J. R. Specht, "Effects of channel and potential radiative transitions in the ^{17}O$(\gamma, n_0)^{16}$O effects of channel and potential radiative transitions in the ^{17}O$(\gamma, n_0)^{16}$O reaction," PHYS. REV. C **18**, 1962 (1978).

[130] M. Igashira, Y. Nagai, K. Masuda, T. Ohsaki, and H. Kitazawa, "Measurement of the ^{16}O$(n, \gamma)^{17}$O reaction cross section at stellar energy and the critical role of nonresonant p-wave neutron capture," ASTROPHYS. J. **441**, L89 (1995).

[131] Y. Nagai Tech. Rep. JAERI 97M03065, Japan Atomic Energy Research Institute (1999).

[132] S. F. Mughabghab, *Atlas of Neutron Resonances: Thermal Cross Sections and Resonance Parameters.* Amsterdam: Elsevier (2006).

[133] K. Shibata, T. Kawano, T. Nakagawa *et al.*, "Japanese Evaluated Nuclear Data Library Version 3 Revision-3: JENDL-3.3," J. NUCL. SCI. TECHNOL. **39**, 1125 (2002).

[134] S. MacMullin, M. Boswell, M. Devlin *et al.*, "Partial γ-ray production cross sections for $(n,xn\gamma)$ reactions in natural argon at 1–30 MeV," PHYS. REV. C **85**, 064614 (2012).

[135] T. Kawano, P. Talou, M. B. Chadwick, and T. Watanabe, "Monte Carlo simulation for particle and γ-ray emissions in statistical Hauser-Feshbach model," J. NUCL. SCI. TECHNOL. **47**, 462 (2010).

[136] K. H. Guber, S. Kopecky, P. Schillebeeckx, K. Kauwenberghs, and P. Siegler, "Neutron-induced cross section measurements of calcium," NUCL. DATA SHEETS **119**, 113 (2014).

[137] S. Cierjacks *et al.*, "High resolution total neutron cross-sections between 0.5–30 MeV," Tech. Rep. KFK-1000, Karlsruhe Institute of Technology (1968).

[138] F. G. Perey *et al.*, "A test of neutron total cross-section evaluations from 0.2 to 20 MeV for C, O, Al, Si, Ca, Fe, and SiO_2," Tech. Rep. ORNL-4823, Oak Ridge National Laboratory (1972).

[139] C. H. Johnson *et al.*, "Total cross section of calcium," Tech. Rep. ORNL-4844, Oak Ridge National Laboratory (1973).

[140] U. N. Singh, H. I. Liou, J. Rainwater, G. Hacken, W. Makofske, and J. B. Garg, "Neutron resonance spectroscopy: Calcium," PHYS. REV. C **10**, 2143 (1974).

[141] G. Audi, F. Kondev, M. Wang, B. Pfeiffer, X. Sun, J. Blachot, and M. MacCormick, "The Nubase2012 evaluation of nuclear properties," CHIN. PHYS. C **36**, 1157 (2012).

[142] N. M. Larson, "Updated users' guide for SAMMY: Multilevel R-Matrix fits to neutron data using Bayes' equations," Tech. Rep. ORNL/TM-9179/R8, Oak Ridge National Laboratory (2008).

[143] M. T. Pigni, I. C. Gauld, and S. Croft, "Early applications of the R-matrix SAMMY code for charged-particle induced reactions and related covariances," EUR. PHYS. J. WEB CONF. **146**, 02019 (2017). ND2016: International Conference on Nuclear Data for Science and Technology, September 11-15, 2016 (Bruges, Belgium).

[144] F. Münnich, "Untersuchung der Energietönung und des Wirkungsquerschnittes einiger durch thermische Neutronen ausgelöster (n,α)-Prozesse," Z. FÜR PHYSIK **153**, 106 (1958). in German.

[145] A. M. Lane, R. G. Thomas, and E. P. Wigner, "Giant resonance interpretation of the nucleon-nucleus interaction," PHYICAL REV. **98**, 693 (1955).

[146] F. H. Froehner, "Evaluation of resonance data for Cr Fe Ni below 300 keV," in *Neutron Data of Structural Materials for Fast Reactors* (K. Böckhoff, ed.), (Oxford), 138, OECD, Pergamon Press (1977). Proceedings of a Specialists' Meeting held at the Central Bureau for Nuclear Measurements, (Geel, Belgium), 5-8 December, 1977.

[147] "The JEF-2.2 nuclear data library," Tech. Rep. JEFF Report 17, NEA Data Bank (2000).

[148] B. McDermott, E. Blain, N. Thompson *et al.*, "^{56}Fe capture cross section experiments at the RPI LINAC Center," EUR. PHYS. J. WEB CONF. **146**, 11038 (2017). ND2016: International Conference on Nuclear Data for Science and Technology, September 11-15, 2016 (Bruges, Belgium).

[149] C. M. Perey, F. G. Perey, J. A. Harvey, N. W. Hill, and N. M. Larson, "^{56}Fe and ^{60}Ni resonance parameters," in *Conference on Nuclear Data for Science and Technology*, (Juelich, West Germany), 41 (1991).

[150] W. E. Kinney and J. W. Mcconnell, "High resolution neutron scattering experiments at ORELA," in *International Conference on the Interaction of Neutrons with Nuclei*, (Lowell, MA, USA), 1319 (1976).

[151] "JEFF-3.2 evaluated data library," OECD NEA, Paris, France (2014), [Online] Available at https://www.oecd-nea.org/dbforms/data/eva/evatapes/jeff_32/.

[152] E. Dupont, P. Ribon, H. Weigmann, and G. Vanpraet, "High resolution measurement of the neutron inelastic scattering crosssection of ^{56}Fe," in *Conference on Nuclear Data for Science and Technology*, (Trieste, Italy), 529 (1997).

[153] A. Negret, C. Borcea, P. Dessagne, M. Kerveno, A. Olacel, A. J. M. Plompen, and M. Stanoiu, "Cross-section measurements for the ^{56}Fe(n,xnγ) reactions," PHYS. REV. C **90**, 034602 (2014).

[154] H. Vonach, S. Tagesen, M. Wagner, and V. Pronyaev, "Evaluation of the fast neutron cross sections of ^{56}Fe including complete covariance information," Tech. Rep. Physical Data 13-7, Fachinformationszentrum, Karlsruhe, W. Germany (1992).

[155] K. Berthold, C. Nazareth, G. Rohr, and H. Weigman, "Total cross section of natural Fe." Private communication (1994).

[156] A. Smith and P. Guenther, "Scattering of MeV neutrons from elemental iron," NUCL. SCI. ENG. **73**, 186 (1980).

[157] M. Herman, R. Capote, B. V. Carlson, P. Obložinský, M. Sin, A. Trkov, H. Wienke, and V. Zerkin, "EMPIRE: Nuclear reaction model code system for data evaluation," NUCL. DATA SHEETS **108**, 2655 (2007).

[158] S. Kunieda, R. C. Haight, T. Kawano *et al.*, "Measurement and model analysis of $(n,x\alpha)$ cross sections for Cr, Fe, ^{59}Co, and ^{58,60}Ni from threshold energy to 150 MeV," PHYS. REV. C **85**, 054602 (2012).

[159] R. D. Mosteller, "MCNP results for ENDF/B-VII.1 beta4," Tech. Rep. LA-UR-11-06327, Los Alamos National Laboratory (2011).

[160] V. Sobes and L. C. Leal, "Results for the intermediate-spectrum Zeus benchmark obtained with new ^{63,65}Cu cross-section evaluations," TRANS. AM. NUCL. SOC. **110** (2014).

[161] S. F. Mughabghab, M. Divadeenam, and N. E. Holden, *Neutron Cross Sections, Vol. 1, Neutron Resonance Parameters and Thermal Cross Sections, Part A, Z=1-60*. Academic Press (1981).

[162] M. S. Pandey, J. B. Garg, and J. A. Harvey, "Neutron total cross-sections and resonance parameters of ^{63}Cu and ^{65}Cu. I," PHYS. REV. C **15**, 600 (1977).

[163] F. Perey, "Computer code GENOA," (1967). unpublished.

[164] V. Sobes and L. Leal, "Application of the SAMINT methodology to the new cross section evaluations of ^{63}Cu and ^{65}Cu*," EUR. PHYS. J. WEB CONF. **146**, 02016 (2017). ND2016: International Conference on Nuclear Data for Science and Technology, September 11-15, 2016 (Bruges, Belgium).

[165] K. Guber Private communication cited in Ref. [164] (2011).

[166] V. Sobes, R. MacDonald, L. C. Leal *et al.*, "Thermal total cross section measurement for ^{63}Cu and ^{65}Cu at

the MIT Reactor," Trans. Am. Nucl. Soc. **105** (2011).

[167] J. M. Blatt and L. C. Biedenharn, "The angular distribution of scattering and reaction cross sections," Rev. Mod. Phys. **24**, 258 (1952).

[168] M. Weigand, C. Beinrucker, A. Couture *et al.*, "The ^{63}Cu(n,γ) cross section measured via 25 keV activation and time-of-flight," Phys. Rev. C **95**, 015808 (2017).

[169] I. Dillmann, M. Heil, F. Käppeler, R. Plag, T. Rauscher, and F. Thielemann, "KADoNiS – the Karlsruhe Astrophysical Database of Nucleosynthesis in Stars, v.0.3," AIP Conf. Proc. **819**, 123 (2006).

[170] "KADoNiS – the Karlsruhe Astrophysical Database of Nucleosynthesis in Stars, v.1.0," Göthe Universität (2017), [Online] Available at `http://exp-astro.physik.uni-frankfurt.de/kadonis1.0/`.

[171] A. J. Koning and J. P. Delaroche, "Local and global nucleon optical models from 1 keV to 200 MeV," Nucl. Phys. A **713**, 231 (2003).

[172] M. Avrigeanu, A. C. Obreja, F. L. Roman, V. Avrigeanu, and W. von Oertzen, "Complementary optical-potential analysis of α-particle elastic scattering and induced reactions at low energies," At. Data Nucl. Data Tables **95**, 501 (2009).

[173] S. Kunieda, S. Chiba, K. Shibata, A. Ichihara, and E. S. Sukhovitskii, "Coupled-channels optical model analyses of nucleon-induced reactions for medium and heavy nuclei in the energy region from 1 keV to 200 MeV," J. Nucl. Sci. Technol. **44**, 838 (2007).

[174] B. Champine, M. E. Gooden, Krishichayan, E. B. Norman, N. D. Scielzo, M. A. Stoyer, K. J. Thomas, A. P. Tonchev, W. Tornow, and B. S. Wang, "Measurement of the ^{169}Tm$(n, 3n)^{167}$Tm cross section and the associated branching ratios in the decay of ^{167}Tm," Phys. Rev. C **93**, 014611 (2016).

[175] N. Otuka, E. Dupont, V. Semkova, B. Pritychenko, and otherss, "Towards a more complete and accurate experimental nuclear reaction data library (EXFOR): International collaboration between nuclear reaction data centres (NRDC)," Nucl. Data Sheets **120**, 272 (2014).

[176] I. Sirakov, B. Becker, R. Capote, E. Dupont, S. Kopecky, C. Massimi, and P. Schillebeeckx, "Results of total cross section measurements for ^{197}Au in the neutron energy region from 4 to 108 keV at GELINA," Eur. Phys. J. A **49**, 144 (2013).

[177] I. Sirakov, B. Becker, R. Capote, S. Kopecky, C. Massimi, V. G. Pronyaev, P. Schillebeeckx, A. Trkov, and G. Žerovnik, "Evaluation of neutron induced reaction cross sections on gold," JRC 78690, EUR 25803 EN, Luxembourg: Publ. Off. Eur. Union (2013).

[178] C. Massimi, B. Becker, E. Dupont *et al.*, "Neutron capture cross section measurements for ^{197}Au from 3.5 to 84 keV at GELINA," Eur. Phys. J. A **50**, 124 (2014).

[179] A. Trkov, R. Capote, I. Kodeli, and L. Leal, "Evaluation of tungsten nuclear reaction data with covariances," Nucl. Data Sheets **109**, 2905 (2008).

[180] A. Trkov, R. Capote, E. Soukhovitskii, L. Leal, M. Sin, I. Kodeli, and D. Muir, "Covariances of evaluated nuclear cross section data for ^{232}Th, ^{180,182,183,184,186}W and ^{55}Mn," Nucl. Data Sheets **112**, 3098 (2011).

[181] M. T. Pigni *et al.* in *Proceedings of PHYSOR 2012: Advances in Reactor Physics, Knoxville, TN, April 15-20, 2012*, American Nuclear Society (2012).

[182] M. Pigni, L. Leal, M. Dunn *et al.*, "Evaluation of tungsten neutron cross sections in the resolved resonance region," Nucl. Data Sheets **118**, 147 (2014).

[183] M. T. Pigni *et al.* in *International Conference on Nuclear Criticality Safety (ICNC 2015), Charlotte, NC, September 13-17, 2015*, American Nuclear Society (2015).

[184] C. Lampoudis, S. Kopecky, P. Schillebeeckx, P. Siegler, and K. Guber, "Neutron total and capture cross section of tungsten isotopes," J. Korean Phys. Soc. **59**, 1860 (2011).

[185] J. A. Harvey, "EXFOR entry 13770." Private Communication (1980).

[186] M. Goldberg and S. Mughabghab, "Neutron cross sections," Tech. Rep. BNL-325 Report Supplement 2, Brookhaven National Laboratory, Upton, NY, USA (1966).

[187] Z. M. Bartolome *et al.*, "Neutron radiative capture and transmission measurements of W and Zr isotopes in the kev region," Nucl. Sci. Eng. **37**, 137 (1969).

[188] H. S. Camarda *et al.*, "Neutron resonance spectroscopy. XII. The separated isotopes of W," Phys. Rev. C **8**, 1813 (1973).

[189] M. Ohkubo, "Neutron transmission and scattering measurements on tungsten resonances," Tech. Rep. JAERI-M 5624, Japan Atomic Energy Research Institute (1974).

[190] R. L. Macklin *et al.*, "Neutron-capture cross sections of the tungsten isotopes ^{182}W, ^{183}W, ^{184}W, and ^{186}W from 2.6 to 2000 keV," Tech. Rep. LA-9200-MS, Los Alamos National Laboratory, Los Alamos, NM, USA (1982).

[191] S. F. Mughabghab, *Neutron Cross Sections, Vol. 1, Part B.* Academic Press (1984).

[192] Y. A. Alexandrov *et al.* Yad. Fiz. **10**, 328 (1969).

[193] K. Knopf and W. Waschkowsky, "Wechselwirkung von Neutronen mit Wolfram und seinen Isotopen," Z. für Naturforschung **42**, 909 (1987). in German.

[194] S. J. Friesenhahn, E. Haddad, F. H. Fröhner, and W. M. Lopez, "The neutron capture cross section of the tungsten isotopes from 0.01 to 10 electron volts," Nucl. Sci. Eng. **26**, 487 (1966).

[195] A. M. Hurst, R. B. Firestone, B. W. Sleaford, N. C. Summers, Z. Révay, L. Szentmiklósi, M. S. Basunia, T. Belgya, J. E. Escher, and M. Krtička, "Investigation of the tungsten isotopes via thermal neutron capture," Phys. Rev. C **89**, 14606 (2014).

[196] A. J. Koning and D. Rochman, "Modern nuclear data evaluation with the TALYS code system," Nucl. Data Sheets **113**, 2841 (2012).

[197] A. J. Koning, "Bayesian Monte Carlo method for nuclear data evaluation," Eur. Phys. J. A **51**, 1 (2015).

[198] V. G. Pronyaev, R. Capote, A. Trkov, G. Noguere, and A. Wallner, "New fit of thermal neutron constants (TNC) for ^{233,235}U, ^{239,241}Pu and ^{252}Cf(sf): Microscopic vs. Maxwellian data," Eur. Phys. J. Web Conf. **146**, 02045 (2017). ND2016: International Conference on Nuclear Data for Science and Technology, September 11-15, 2016 (Bruges, Belgium).

[199] "IAEA CIELO data development project within the international pilot project of the OECD/NEA," International Atomic Energy Agency, Vienna, Austria (2017), R. Capote and A. Trkov (coordinators), [Online] Available at `https://www-nds.iaea.org/CIELO/`.

[200] P. G. Young, M. B. Chadwick, R. E. MacFarlane, P. Talou, T. Kawano, D. G. Madland, and W. B. Wil-

son, "Evaluation of neutron reactions for ENDF/B-VII: $^{232-241}$U and ^{239}Pu," NUCL. DATA SHEETS **108**, 2589 (2007).

[201] A. Trkov, R. Capote, and V. G. Pronyaev, "Current issues in nuclear data evaluation methodology: ^{235}U prompt fission neutron spectra and multiplicity for thermal neutrons," NUCL. DATA SHEETS **123**, 8 (2015).

[202] A. Trkov and R. Capote, "Evaluation of the prompt fission neutron spectrum of thermal-neutron induced fission in ^{235}U," PHYS. PROC. **64**, 48 (2015).

[203] M. T. Pigni, R. Capote, A. Trkov, and V. G. Pronyaev, "n+^{235}U resonance parameters and neutron multiplicities in the energy region below 100 eV," EUR. PHYS. J. WEB CONF. **146**, 02011 (2017). ND2016: International Conference on Nuclear Data for Science and Technology, September 11-15, 2016 (Bruges, Belgium).

[204] L. Leal, International Atomic Energy Agency, Vienna, Austria, see IAEA CIELO webpage, IRSN.v2 resonance parameter in u235ib02i2g6cnu3f2 file, [Online] Available at `https://www-nds.iaea.org/CIELO/`.

[205] M. Jandel, T. A. Bredeweg, E. M. Bond *et al.*, "New precision measurements of the ^{238}U(n,γ) cross section," PHYS. REV. LETT. **109**, 202506 (2012). EXFOR Entry 14149.

[206] Y. Danon, D. Williams, R. Bahran, E. Blain, B. McDermott, D. Barry, G. Leinweber, R. Block, and M. Rapp, "Simultaneous measurement of ^{238}U fission and capture cross sections from 0.01 eV to 3 keV using a gamma multiplicity detector," NUCL. SCI. ENG. **187**, 291 (2017).

[207] M. Ishikawa, "Recommendation from ADJ2010 adjustment," OECD NEA, Paris, France (2013), Kick-off Meeting of WPEC Subgroup 39, [Online] Available at `https://www.oecd-nea.org/science/wpec/sg39/Meeting2_Nov2013/01_ADJ2010_Recom_Ishikawa.pdf`.

[208] M. Fukushima, K. Yokoyama, O. Iwamoto, and Y. Nagaya, "Benchmark tests for ENDF/B-VIII.0 beta1 using sodium-void reactivity worth of FCA-XXVII-1," OECD NEA, Paris, France (2016), SG39 Meeting, [Online] Available at `https://www.oecd-nea.org/science/wpec/sg39/Meeting_December2016/SG39_4_KYokoyama_1.pdf`.

[209] A. Trkov, R. Capote, M. T. Pigni, V. G. Pronyaev, M. Sin, and E. S. Soukhovitskii, "Evaluation of the neutron induced reactions on ^{235}U from 2.25 keV up to 30 MeV," EUR. PHYS. J. WEB CONF. **146**, 02029 (2017). ND2016: International Conference on Nuclear Data for Science and Technology, September 11-15, 2016 (Bruges, Belgium).

[210] R. L. Reed, R. W. Hockenbury, and R. C. Block, "Prompt neutron multiplicity measurements for neutron-induced fission of ^{233}U and ^{235}U," Tech. Rep. COO-3058-39, Rensselaer Polytechnic Institute, Troy, NY, USA (1973).

[211] R. L. Reed, *Neutron Multiplicity Measurements for Neutron-Induced Fission of ^{233}U and ^{235}U.* PhD thesis, Rensselaer Polytechnic Institute (1973).

[212] R. E. Howe, T. W. Phillips, and C. D. Bowman, "Prompt fission neutrons from eV resonances in ^{235}U: Measurement and correlation with other fission properties," PHYS. REV. C **13**, 195 (1976).

[213] R. Gwin, R. R. Spencer, and R. W. Ingle, "Measurements of the energy dependence of prompt neutron emission from ^{233}U, ^{235}U, ^{239}Pu, and ^{241}Pu for $E_n = 0.005$ to 10 eV relative to emission from spontaneous fission of ^{252}Cf," NUCL. SCI. ENG. **87**, 381 (1984).

[214] A. J. Plompen, T. Kawano, and R. Capote Noy, "Inelastic scattering and capture cross-section data of major actinides in the fast neutron region," Tech. Rep. INDC(NDS)-0597, International Atomic Energy Agency, Vienna, Austria (2012).

[215] E. Bauge, G. Bélier, J. Cartier *et al.*, "Coherent investigation of nuclear data at CEA DAM: Theoretical models, experiments and evaluated data," EUR. PHYS. J. A **48**, 113 (2012).

[216] G. D. Saussure, L. W. Weston, R. Gwin, R. W. Ingle, J. H. Todd, R. W. Hockenbury, R. R. Fullwood, and A. Lottin, "Measurement of the neutron capture and fission cross sections and of their ratio, α, for ^{233}U, ^{235}U, and ^{239}Pu," in *Proceedings of the Nuclear Data For Reactors Conference, Paris 1966, Vol.2*, no. STI/PUB/140, 233 (1967). IAEA, Vienna, 1967.

[217] J. Balibrea-Correa, E. Mendoza, D. Cano-Ott *et al.* (n_TOF Collaboration), "Measurement of the neutron capture cross section of the fissile isotope ^{235}U with the CERN n_TOF total absorption calorimeter and a fission tagging based on micromegas detectors," EUR. PHYS. J. WEB CONF. **146**, 11021 (2017). ND2016: International Conference on Nuclear Data for Science and Technology, September 11-15, 2016 (Bruges, Belgium).

[218] E. S. Soukhovitskiı, R. Capote, J. M. Quesada *et al.*, "Nucleon scattering on actinides using a dispersive optical model with extended couplings," PHYS. REV. C **94**, 064605 (2016).

[219] R. Capote, E. S. Soukhovitskiı, J. M. Quesada *et al.*, "Is a global coupled-channel dispersive optical model potential for actinides feasible?," PHYS. REV. C **C72**, 064610 (2005).

[220] R. Capote, S. Chiba, E. S. Soukhovitskiı *et al.*, "A global dispersive coupled-channel optical model potential for actinides," J. NUCL. SCI. TECHNOL. **45**, 333 (2008).

[221] R. Capote, M. Herman, P. Obložinský *et al.*, "RIPL-3: Reference Input Parameter Library for calculation of nuclear reactions and nuclear data evaluations," NUCL. DATA SHEETS **110**, 3107 (2009). ISSN 0090-3752.

[222] R. Capote, V. Osorio, R. López, E. Herrera, and M. Piris, "Analysis of experimental data on neutron-induced reactions and development of code PCROSS for the calculation of differential pre-equilibrium emission spectra with modelling of the level density function," Tech. Rep. IAEA(CUB)-004, International Atomic Energy Agency, Vienna, Austria (1991). Final report on research contract 5472/RB.

[223] W. Hauser and H. Feshbach, "The inelastic scattering of neutrons," PHYS. REV. **87**, 366 (1952).

[224] M. Sin, R. Capote, M. Herman, and A. Trkov, "Modelling neutron-induced reactions on $^{232-237}$U from 10 keV up to 30 MeV," NUCL. DATA SHEETS **139**, 138 (2017).

[225] M. Sin and R. Capote, "Transmission through multi-humped fission barriers with absorption: A recursive approach," PHYS. REV. C **77**, 054601 (2008).

[226] M. Sin, R. Capote, M. Herman, and A. Trkov, "Extended optical model for fission," PHYS. REV. C **93**, 034605 (2016).

[227] A. Wallner, T. Belgya, M. Bichler *et al.*, "Novel method to study neutron capture of ^{235}U and ^{238}U simultaneously at keV energies," PHYS. REV. LETT. **112**, 192501 (2014). EXFOR entry 23170.

[228] D. G. Madland and J. R. Nix, "New calculation of prompt fission neutron spectra and average prompt neu-

tron multiplicities," Nucl. Sci. Eng. **81**, 213 (1982).

[229] D. Neudecker, P. Talou, D. L. Smith, R. Capote, M. E. Rising, and A. C. Kahler, "Evaluation of the ^{239}Pu prompt fission neutron spectrum induced by neutrons of 500 keV and associated covariances," Nucl. Inst. Meth. Phys. Res. A **80**, 791 (2015).

[230] J. P. Lestone and E. F. Shores, "Uranium and plutonium average prompt-fission neutron energy spectra (PFNS) from the analysis of NTS NUEX data," Nucl. Data Sheets **119**, 213 (2014).

[231] D. Neudecker *et al.*, "The need for precise and well-documented experimental data on prompt fission neutron spectra from neutron-induced fission of ^{239}Pu," Nucl. Data Sheets **289**, 1 (2016).

[232] T. N. Taddeucci *et al.*, "Multiple-scattering corrections to measurements of the prompt fission neutron spectrum," Nucl. Data Sheets **123**, 135 (2015).

[233] M. Devlin *et al.*, "The prompt fission neutron spectrum of ^{235}U(n,f) below 2.5 MeV for incident neutrons from 0.7 to 20 MeV," Nucl. Data Sheets **148**, 322 (2018).

[234] M. Sugimoto, A. B. Smith, and P. Guenther, "Ratio of the prompt fission neutron spectra of ^{239}Pu to that of ^{235}U," Nucl. Sci. Eng. **97**, 235 (1987).

[235] G. S. Boikov *et al.*, "Spectrum of neutrons accompanying fission of ^{232}Th, ^{235}U, and ^{238}U by 2.9 MeV and 14.7 MeV neutrons (below and above the threshold of emission fission," Sov. J. Nucl. Phys. **53**, 392 (1991). EXFOR subentry 41110.009.

[236] M. E. Rising, P. Talou, T. Kawano, and A. K. Prinja, "Evaluation and uncertainty quantification of prompt fission neutron spectra of uranium and plutonium isotopes," Nucl. Sci. Eng. **175**, 81 (2013).

[237] H. I. Kim, C. Paradela, I. Sirakov *et al.*, "Neutron capture cross section measurements for ^{238}U in the resonance region at GELINA," Eur. Phys. J. A **52**, 170 (2016).

[238] F. Mingrone, C. Massimi, G. Vannini *et al.* (n_TOF collaboration), "Neutron capture cross section measurement of ^{238}U at the CERN n_TOF facility in the energy region from 1 eV to 700 keV," Phys. Rev. C **95**, 034604 (2017).

[239] J. L. Ullmann, T. Kawano, T. A. Bredeweg *et al.*, "Cross section and γ-ray spectra for ^{238}U(n,γ) measured with the DANCE detector array at the Los Alamos Neutron Science Center," Phys. Rev. C **89**, 034603 (2014).

[240] H. Derrien, L. C. Leal, N. M. Larson, and A. Courcelle, "Neutron resonance parameters and calculated cross sections from Reich-Moore analysis of experimental data in the neutron energy range from 0 to 20 keV," Tech. Rep. ORNL/TM-2005/241, Oak Ridge National Laboratory (2005).

[241] D. K. Olsen, G. de Saussure, R. B. Perez, E. G. Silver, F. C. Difilippo, R. W. Ingle, and H. Weaver, "Precise measurement and analysis of neutron transmission through Uranium-238," Nucl. Sci. Eng. **62**, 479 (1977).

[242] D. K. Olsen, G. de Saussure, R. B. Perez, F. C. Difilippo, and R. W. Ingle, "Note on ^{238}U + n resolved resonance energies," Nucl. Sci. Eng. **66**, 141 (1978).

[243] A. Trkov, G. L. Molnár, Z. Révay, S. F. Mughabghab, R. B. Firestone, V. G. Pronyaev, A. L. Nichols, and M. C. Moxon, "Revisiting the ^{238}U thermal capture cross section and gamma-ray emission probabilities from ^{239}Np decay," Nucl. Sci. Eng. **150**, 336 (2005).

[244] W. P. Poenitz, "Data interpretation, objective, evaluation procedures and mathematical technique for the evaluation of energy-dependent ratio, shape and cross section data," in *Proceedings of the Conference on Nuclear Data Evaluation Methods and Procedures*, no. BNL-NCS-51363, 249 (1981).

[245] W. P. Poenitz, J. F. Whalen, and A. B. Smith, "Total neutron cross sections of heavy nuclei," Nucl. Sci. Eng. **78**, 333 (1981).

[246] W. P. Poenitz and J. F. Whalen, "Neutron total cross section measurements in the energy region from 47 keV to 20 MeV," Tech. Rep. ANL/NDM-80, Argonne National Laboratory (1983).

[247] I. Tsubone, Y. Nakajima, Y. Furuta, and Y. Kanda, "Neutron total cross sections of ^{181}Ta and ^{238}U from 24.3 keV to 1 MeV and average resonance parameters," Nucl. Sci. Eng. **88**, 579 (1984).

[248] L. L. Litvinskii, V. P. Vertebnyi, V. A. Libman, and A. V. Murzin, "Neutron cross sections and average resonance parameters of ^{238}U for 55- and 144-keV neutrons," Sov. At. Energy **62**, 241 (1987).

[249] J. A. Harvey, N. W. Hill, F. G. Perey, G. L. Tweed, and L. C. Leal, "High-resolution neutron transmission measurements on ^{235}U, ^{239}Pu and ^{238}U," in *Proceedings of the International Conference On Nuclear Data for Science and Technology,*, (Mito, Japan), 115 (1988).

[250] P. Z. Hien, V. H. Tan, and N. P. Xuan, "Total neutron cross-section of U-238 as measured with filtered neutrons for 55 and 144 keV," Tech. Rep. INDC(NDS)-265, International Atomic Energy Agency (1992).

[251] E. S. Sukhovitskii, S. Chiba, O. Iwamoto, K. Shibata, T. Fukahori, and G. Mororovskij, "Programs OPTMAN and SHEMMAN version 8 (2004)," Tech. Rep. JAERI-Data/Code 2005-002, Japan Atomic Energy Agency (2005).

[252] E. S. Soukhovitski, S. Chiba, R. Capote, J. M. Quesada, S. Kunieda, and G. Mororovskij, "Supplement to OPTMAN code, manual version 10 (2008)," Tech. Rep. JAERI-Data/Code 2008-025, Japan Atomic Energy Agency (2008).

[253] J. M. Quesada, R. Capote, E. S. Soukhovitskii, and S. Chiba, "Rotational-vibrational description of nucleon scattering on actinide nuclei using a dispersive coupled-channel optical model," Nucl. Data Sheets **118**, 270 (2014).

[254] R. Capote, A. Trkov, M. Sin, M. Herman, A. Daskalakis, and Y. Danon, "Physics of neutron interactions with ^{238}U: New developments and challenges," Nucl. Data Sheets **118**, 26 (2014).

[255] P. Romano and C. Lubitz, "PFNS & other adjustments for 239Pu," Brookhaven National Laboratory, Upton, NY, USA (2014), CSEWG Meeting, Brookhaven National Laboratory, Nov. 3-5, 2014, [Online] Available at https://indico.bnl.gov/getFile.py/access?contribId=52&sessionId=7&resId=0&materialId=slides&confId=868.

[256] F. Hambsch, A. Tudora, G. Vladuca, and S. Oberstedt, "Prompt fission neutron spectrum evaluation for ^{252}Cf(sf) in the frame of the multi-modal fission model," Annals Nucl. Eng. **32**, 1032 (2005).

[257] T. Ohsawa, T. Horiguchi, and M. Mitsuhashi, "Multimodal analysis of prompt neutron spectra for ^{238}Pu(sf), ^{240}Pu(sf), ^{242}Pu(sf) and ^{239}Pu(n$_{\rm th}$,f)," Nucl. Phys. A **665**, 3 (2000).

[258] A. Chatillon *et al.*, "Measurement of prompt neutron spectra from the ^{239}Pu(n,f) fission reaction for incident neutron energies from 1 to 200 MeV," Phys. Rev. C **89**, 014611 (2014). EXFOR entry 14379.

[259] T. Granier, "Reanalysis of ^{239}Pu prompt fission neutron spectra," Phys. Procedia **64**, 183 (2015).

[260] D. McNabb, J. D. Anderson, R. W. Bauer, J. A. Becker, F. S. Dietrich, P. Navratil, M. B. Chadwick, and P. G. Young, "Evaluation of the ^{239}Pu(n,2n) integrated cross section," Tech. Rep. UCRL-ID-143328, Lawerence Livermore National Laboratory (2001).

[261] R. W. Lougheed, W. Webster, M. N. Namboodiri *et al.*, "^{239}Pu and ^{241}Am(n, 2n) cross-section measurements near E_n= 14 MeV," Radiochimica Acta **90**, 833 (2002).

[262] O. Bouland, H. Derrien, N. M. Larson, and L. C. Leal, "R-matrix analysis of the ^{240}Pu neutron cross sections in the thermal to 5700-eV energy range," Nucl. Sci. Eng. **127**, 2 (1997).

[263] D. Rochman, A. J. Koning, and J. C. Sublet, "Proposal of 51 isotopes for ENDF/B-VIII," Los Alamos National Laboratory, Los Alamos, NM, USA (2017), Mini CSWEG meeting, May 4-5, 2017, presented by R. Capote, [Online] Available at `https://indico.bnl.gov/getFile.py/access?resId=0&materialId=slides&contribId=41&sessionId=8&subContId=5&confId=2967`.

[264] J. Tuli, "Nuclear Wallet Cards," Brookhaven National Laboratory, Upton, NY (2011).

[265] H. Choi, R. Firestone, R. Lindstrom, G. Molnar, S. Mughabghab, R. Paviotti-Corcuera, Z. Revay, A. Trkov, V. Zerkin, and C. Zhou, "Database of prompt gamma rays from slow neutron capture for elemental analysis," Tech. Rep. STI/PUB/1263, International Atomic Energy Agency, Vienna, Austria (2007).

[266] D. E. Cullen, "PREPRO 2017 home page," International Atomic Energy Agency, Vienna, Austria (2017), [Online] Available at `https://www-nds.iaea.org/public/endf/prepro/`.

[267] R. E. MacFarlane and A. C. Kahler, "Methods for Processing ENDF/B-VII with NJOY," Nucl. Data Sheets **111**, 2739 (2010).

[268] B. R. Beck, "FUDGE: A program for performing nuclear data testing and sensitivity studies," in *AIP Conference Proceedings*, **769**, 503 (2004).

[269] R. Q. Wright, "Prompt-nubar calculations for 53 actinides," Tech. Rep. ORNL/TM-2015/30, Oak Ridge National Laboratory (2005).

[270] M. C. Brady, R. Q. Wright, and T. R. England, "Actinide nuclear data for reactor physics calculations," Tech. Rep. ORNL/CSD/TM-266, Oak Ridge National Laboratory (1991).

[271] R. Q. Wright, M. C. Brady-Rapp, and R. M. Westfall, "Prompt-nubar calculations for 27 actinides," Trans. Am. Nucl. Soc. (2014).

[272] O. Serot, "Prompt fission gamma spectra and multiplicities for JEFF-3.3," Tech. Rep. JEFF/DOC-1828, OECD NEA (2017).

[273] B. Becker, P. Talou, T. Kawano, Y. Danon, and I. Stetcu, "Monte carlo Hauser-Feshbach predictions of prompt fission γ rays: Application to $n_{\rm th}$+^{235}U, $n_{\rm th}$+^{239}Pu, and ^{252}Cf (sf)," Phys. Rev. C **87**, 014617 (2013).

[274] I. Stetcu, P. Talou, T. Kawano, and M. Jandel, "Properties of prompt-fission γ rays," Phys. Rev. C **90**, 024617 (2014).

[275] P. Talou, T. Kawano, I. Stetcu, J. P. Lestone, E. McKigney, and M. B. Chadwick, "Late-time emission of prompt fission γ rays," Phys. Rev. C **94**, 064613 (2016).

[276] E. Kwan, C. Wu, R. Haight *et al.*, "Prompt energy distribution of ^{235}U(n,f) at bombarding energies of 1–20 mev," Nucl. Inst. Meth. Phys. Res. Sect. A: Accel. Spectrometers, Detect. Assoc. Equip. **688**, 55 (2012).

[277] K. Nishio Private communication (2016).

[278] F. Pleasonton, R. L. Ferguson, and H. W. Schmitt, "Prompt gamma rays emitted in the thermal-neutron-induced fission of ^{235}U," Phys. Rev. C **6**, 1023 (1972).

[279] A. Oberstedt, T. Belgya, R. Billnert *et al.*, "Improved values for the characteristics of prompt-fission γ-ray spectra from the reaction ^{235}U($n_{\rm th}$,f)," Phys. Rev. C **87**, 051602 (2013).

[280] V. V. Verbinski, H. Weber, and R. E. Sund, "Prompt gamma rays from ^{235}U(n,f), ^{239}Pu(n,f), and spontaneous fission of ^{252}Cf," Phys. Rev. C **7**, 1173 (1973).

[281] A. Chyzh, C. Y. Wu, E. Kwan, R. A. Henderson, T. A. Bredeweg, R. C. Haight, A. C. Hayes-Sterbenz, H. Y. Lee, J. M. O'Donnell, and J. L. Ullmann, "Total prompt γ-ray emission in fission of ^{235}U, ^{239,241}Pu, and ^{252}Cf," Phys. Rev. C **90**, 014602 (2014).

[282] R. W. Peelle and F. C. Maienschein, "Spectrum of photons emitted in coincidence with fission of ^{235}U by thermal neutrons," Phys. Rev. C **3**, 373 (1971).

[283] M. Jandel, T. A. Bredeweg, E. M. Bond *et al.*, "Prompt γ-ray emission in neutron induced fission of ^{235}U," Tech. Rep. LA-UR-12-24975, Los Alamos National Laboratory (2013). To be published.

[284] F. Pleasonton, "Prompt γ-rays emitted in the thermal-neutron induced fission of ^{233}U and ^{239}Pu," Nucl. Phys. A **213**, 413 (1973).

[285] A. Gatera, T. Belgya, W. Geerts *et al.*, "Prompt-fission γ-ray spectral characteristics from ^{239}Pu($n_{\rm th}, f$)," Phys. Rev. C **95**, 064609 (2017).

[286] J. L. Ullmann, E. M. Bond, T. A. Bredeweg *et al.*, "Prompt γ-ray production in neutron-induced fission of ^{239}Pu," Phys. Rev. C **87**, 044607 (2013).

[287] D. M. Drake, J. C. Hopkins, C. S. Young, and H. Condé, "Gamma-ray-production cross sections for fast neutron interactions with several elements," Nucl. Sci. Eng. **40**, 294 (1970).

[288] D. M. Drake, "Cross sections of Uranium-235 and Plutonium-239 for neutrons producing gamma rays," Nucl. Sci. Eng. **55**, 427 (1974).

[289] D. M. Drake, E. D. Arthur, and M. G. Silbert, "Cross sections for gamma-ray production by 14-MeV neutrons," Nucl. Sci. Eng. **65**, 49 (1978).

[290] S. Oberstedt Private communication (2017).

[291] L. Steward and R. E. Hunter, "Evaluated neutron-induced gamma-ray production cross sections for ^{235}U and ^{238}U," Tech. Rep. LA-4918, Los Alamos National Laboratory (1972).

[292] A. Chyzh, C. Y. Wu, E. Kwan *et al.*, "Systematics of prompt γ-ray emission in fission," Phys. Rev. C **87**, 034620 (2013).

[293] D. O. Nellis and I. L. Morgan, "Gamma ray production cross sections for U235, U238, and Pu239," Tech. Rep. 2791, Oak Ridge National Laboratory (1966).

[294] J. Fréhaut, A. Bertin, and R. Bois, "Mesure de $\bar{\nu}_p$ pour la fission de ^{232}Th, ^{235}U et ^{237}Np induite par des neutrons d'energie comprise entre 1 et 15 meV," in *International Conference on Nuclear Data for Science and Technology, Antwerp, Belgium*, (Reidel, Dordrech, Holland) (1983).

[295] M. Lebois, J. N. Wilson, P. Halipré *et al.*, "Comparative measurement of prompt fission γ-ray emission from fast-neutron-induced fission of ^{235}U and ^{238}U," Phys. Rev. C **92**, 034618 (2015).

[296] E. Fort, J. Frehaut, and P. Long, "Prompt gammas emitted in fission," Tech. Rep. JEF/DOC-219, OECD NEA (1999).

[297] J. M. Verbeke, "Neutron multiplicity counting: Credible regions for reconstruction parameters," Nucl. Sci. Eng. **182**, 481 (2016).

[298] D. E. Cullen, "Sampling the number of neutrons emitted per fission," Tech. Rep. UCRL-TR-222526, Lawrence Livermore National Laboratory (2006).

[299] (Cross Section Evaluation Working Group (CSEWG)), "ENDF-6 formats manual," Tech. Rep. unassigned, Brookhaven National Laboratory (2018).

[300] P. Santi and M. Miller, "Reevaluation of prompt neutron emission multiplicity distributions for spontaneous fission," Nucl. Sci. Eng. **160**, 190 (2008).

[301] M. S. Zucker and N. E. Holden, "Energy dependence of the neutron multiplicity P_ν in fast neutron induced fission of ^{235,238}U and ^{239}Pu," Tech. Rep. BNL-38491, Brookhaven National Laboratory (1986).

[302] M. Soleilhac, J. Fréhaut, and J. Gauriau, "Energy dependence of p_ν for neutron-induced fission of ^{235}U, ^{238}U and ^{239}Pu from 1.3 to 15 MeV," J. Nucl. Energy **23**, 257 (1969).

[303] J. Fréhaut, "Proceedings of a consultants' meeting on physics of neutron emission in fission, Mito, Japan, 24-27 May 1988," Tech. Rep. IAEA INDC(NDS)-220, International Atomic Energy Agency (1989).

[304] J. W. Boldeman and M. G. Hines, "Prompt neutron emission probabilities following spontaneous and thermal neutron fission," Nucl. Sci. Eng. **91**, 114 (1985).

[305] C. B. Franklyn, C. Hofmeyer, and D. W. Mingay, "Angular correlation of neutrons from thermal-neutron fission of ^{235}U," Phys. Lett. B **78**, 564 (1978).

[306] B. C. Diven, H. C. Martin, R. F. Taschek, and J. Terrell, "Multiplicities of fission neutrons," Phys. Rev. **101**, 1012 (1956).

[307] J. Terrell, "Distributions of fission neutron numbers," Phys. Rev. **108**, 783 (1957).

[308] P. Talou, B. Becker, T. Kawano, M. B. Chadwick, and Y. Danon, "Advanced Monte Carlo modeling of prompt fission neutrons for thermal and fast neutron-induced fission reactions on Pu239," Phys. Rev. C **83**, 064612 (2011).

[309] J. P. Lestone, "Energy and isotope dependence of neutron energy and isotope dependence of neutron multiplicity distributions," Tech. Rep. LA-UR-05-0288, Los Alamos National Laboratory (2005).

[310] K. Meierbachtol *et al.*, "Total kinetic energy release in ^{239}Pu(n,f) post-neutron emission from 0.5 to 50 MeV incident neutron energy," Phys. Rev. C **94**, 34611 (2016).

[311] C. M. Zöller, *Investigation of Neutron-Induced Fission of ^{238}U in the Energy Range from 1 MeV to 500 MeV*. PhD thesis, Technische Hochschule Darmstadt, Germany (1995).

[312] D. L. Duke *et al.*, "Fission-fragment properties in ^{238}U(n,f) between 1 and 30 MeV," Phys. Rev. C **94**, 54604 (2016).

[313] J. P. Lestone and T. T. Strother, "Energy dependence of plutonium and uranium average fragment total kinetic energies," Nucl. Data Sheets **118**, 208 (2014).

[314] R. Sher and C. Beck, "Fission energy release for 16 fissioning nuclides," Tech. Rep. EPRI-NP-1771, Electric Power Research Institute, Stanford University (1981).

[315] CSEWG Covariance Committee, "Guidance on generating neutron reaction data covariances for the ENDF/B library." Brookhaven National Laboratory, Upton, NY, USA, [Online] Available at `http://www.nndc.bnl.gov/csewg/covdocs.jsp`.

[316] (X-5 Monte Carlo Team), "MCNP–a general Monte Carlo N-Particle transport code, version 5, volume 1: Overview and theory," Tech. Rep. LA-UR-03-1987, Los Alamos National Laboratory (1987).

[317] J. Favorite and R. Brewer, "PU-MET-FAST-001 bare sphere of plutonium-239 metal (4.5 at.% 240Pu, 1.02 wt.% Ga)," in *International Handbook of Evaluated Criticality Safety Benchmark Experiments (ICSBEP)* (J. Briggs, ed.), Paris: Organization for Economic Cooperation and Development-Nuclear Energy Agency (OECD-NEA) (2016). NEA/NSC/DOC(95)03.

[318] M. Salvatores and G. Palmiotti, "Methods and issues for the combined use of integral experiments and covariance data," Tech. Rep. NEA/WPEC-33, OECD NEA (2013).

[319] V. Sobes and C. S. Jean, "Investigation of covariance data in general purpose nuclear data libraries," Tech. Rep. NEA/WPEC-44, OECD NEA (2017).

[320] M. Salvatores and G. Palmiotti, "Efficient and effective use of integral experiments of nuclear data validation," Tech. Rep. NEA/WPEC-46, OECD NEA (2017).

[321] J. Koppel and D. Houston, "Reference manual for ENDF thermal neutron scattering data," Tech. Rep. GA-8774, General Atomics (1978). ENDF-269.

[322] R. MacFarlane, "New thermal neutron scattering files for ENDF/B-VI release 2," Tech. Rep. LA-12639-MS, Los Alamos National Laboratory (1994).

[323] M. Zerkle and J. Holmes, "A thermal neutron scattering law for yttrium hydride," Eur. Phys. J. Web Conf. **146**, 13005 (2017). ND2016: International Conference on Nuclear Data for Science and Technology, September 11-15, 2016 (Bruges, Belgium).

[324] J. Daou and P. Vajda, "Hydrogen ordering and metal-semiconductor transitions in the system YH_{2+x}," Phys. Rev. B **45**, 10907 (1992).

[325] J. J. Rush, H. E. Flotow, D. W. Conner, and C. L. Thaper, "Vibration spectra of yttrium and uranium hydride by inelastic scattering of cold neutrons," J. Chem. Phys. **45**, 3817 (1966).

[326] T. J. Udovic, J. J. Rush, and I. S. Anderson, "Local-mode dynamics in YH_2 and YD_2 by isotope-dilution neutron spectroscopy," Phys. Rev. B **50**, 15739 (1994).

[327] H. E. Flotow, D. R. Osborn, and K. Otto, "Heat capacity and thermodynamic functions of YH_2 and YD_2 from 5 to 350 K and the hydrogen vibration frequencies," J. Chem. Phys. **36**, 866 (1962).

[328] P. Voderwisch and K. Waßerroth, "Total neutron-photon scattering cross section of yttrium hydride," Atomkernenergie **14**, 370 (1969).

[329] K. Brand, "Total neutron cross sections of chemical bound protons and deuterons in some metal hydrides

and deuterides," Atomkernenergie **17**, 113 (1971).

[330] J. Holmes, M. Zerkle, and D. Heinrichs, "Benchmarking a first-principles thermal neutron scattering law for water ice with a diffusion experiment," Eur. Phys. J. Web Conf. **146**, 13004 (2017). ND2016: International Conference on Nuclear Data for Science and Technology, September 11-15, 2016 (Bruges, Belgium).

[331] K. Röttger *et al.*, "Lattice constants and thermal expansion of H_2O and D_2O ice Ih between 10 and 265 K," Acta Crystallogr. **B50**, 644 (1994).

[332] J. Li *et al.*, "Neutron spectroscopic investigation of dynamics of water ice," J. Mol. Liq. **100/1**, 1 (2002).

[333] L. Torres *et al.*, "Total cross section of benzene at 90 K and light water ice at 115 K," Nucl. Inst. Meth. Phys. Res. B **251**, 304 (2006).

[334] E. G. Silver, "A pulsed neutron investigation of the effect of temperature on the decay of a thermal-neutron population in H_2O ice," Nucl. Sci. Eng. **34**, 275 (1968).

[335] J. I. Marquez Damian, D. Malaspina, and J. R. Granada, "CAB models for water: A new evaluation of the thermal neutron scattering laws for light and heavy water in ENDF-6 format," Annals Nucl. Energy **65**, 280 (2014).

[336] M. Mattes and J. Keinert, "Thermal neutron scattering data for the moderator materials H_2O, D_2O and ZrH_x in ENDF-6 format," Tech. Rep. INDC (NDS)-0470, International Atomic Energy Agency (2005).

[337] J. I. Marquez Damian, D. Malaspina, and J. R. Granada, "Vibrational spectra of light and heavy water with application to neutron cross section calculations," The J. Chem. Phys. **139**, 024504 (2013).

[338] K. Zaitsev *et al.*, "The total cross sections of the interaction of ultracold neutrons with H_2O and D_2O," At. Energy **70**, 238 (1991).

[339] S. B. Stepanov, V. E. Zhitarev, F. M. Zelenyuk, and V. Y. Krasilnikov, "Temperature dependence of total cold neutron cross section in light water and benzene," At. Energy **37**, 1094 (1974).

[340] S. B. Stepanov and V. E. Zhitarev, "Total cross section for the interaction of cold neutrons with water," At. Energy **41**, 743 (1976).

[341] J. P. Scotta, G. Noguere, D. Bernard, J. I. Marquez Damian, and A. Santamarina, "Impact of the thermal scattering law of H in H_2O on the isothermal temperature reactivity coefficients for UOX and MOX fuel lattices in cold operating conditions," Eur. Phys. J. Nucl. Sci. Technol. **2**, 28 (2016).

[342] A. D. Santos in *Proceedings of the International Conference on Mathematics and Computational Methods Applied to Nuclear Science and Engineering (M& C 2017)*, (Jeju, Korea) (2017).

[343] A. Soper and C. Benmore, "Quantum differences between heavy and light water," Phys. Rev. Lett. **101**, 065502 (2008).

[344] J. I. Marquez Damian, J. R. Granada, D. V. Baxter, S. R. Parnell, and D. C. Evans, "Measurement of the total cross section of heavy water in the 0.1 meV–1 eV energy range at 20 and 50 °c," Il Nuovo Cimento **38C**, 178 (2015).

[345] J. I. Marquez Damian, J. R. Granada, F. Cantargi, and D. Roubtsov, "New evaluation of thermal neutron scattering libraries for light and heavy water," Eur. Phys. J. Web Conf. **146**, 13001 (2017). ND2016: International Conference on Nuclear Data for Science and Technology, September 11-15, 2016 (Bruges, Belgium).

[346] J. I. Marquez Damian, J. R. Granada, and D. Roubtsov, "Improvement on the calculation of D_2O moderated critical systems with new thermal neutron scattering libraries," Annals Nucl. Energy **71**, 206 (2014).

[347] A. I. Hawari, "Modern techniques for inelastic thermal neutron scattering analysis," Nucl. Data Sheets **188**, 172 (2014).

[348] A. I. Hawari *et al.*, "Ab initio generation of thermal neutron scattering cross sections," in *Physor-2004: The Physics of Fuel Cycles and Advanced Nuclear Systems-Global Developments*, (Chicago, Illinois, USA) (2004).

[349] J. L. Wormald and A. I. Hawari, "Generation of phonon density of states and thermal scattering law using ab initio molecular dynamics," Prog. Nucl. Energy **110**, 461 (2017).

[350] G. Kresse and J. Furthermüller, "Efficient iterative schemes for ab initio total-energy calculations using a plane-wave basis set," Phys. Rev. B **54**, 11169 (1996).

[351] G. Kresse and J. Furthermüller, "Efficiency of ab initio total energy calculations for metals and semiconductors using a plane-wave basis set," Comput. Mater. Sci. **6**, 1 (1996).

[352] K. Parlinski *et al.*, "First-principle determination of the soft mode in cubic ZrO_2," Phys. Rev. Lett. **78**, 4063 (1997).

[353] R. E. Macfarlane and D. W. Muir, "The NJOY nuclear data processing system, version 91," Tech. Rep. LA-12740-MS, Los Alamos National Laboratory (1994).

[354] (Cross Section Evaluation Working Group (CSEWG)), "ENDF-6 formats manual," Tech. Rep. BNL-90365-2009 Rev. 2, Brookhaven National Laboratory (2012).

[355] Y. Zhu and A. I. Hawari, "Implementation of a generalized coherent elastic scattering formulation for thermal neutron scattering analysis," in *ICNC-2015: International Conference on Nuclear Criticality Safety*, (Charlotte, North Carolina, USA) (2015).

[356] D. J. Hughes and R. B. Schwartz, "Neutron cross sections," Tech. Rep. BNL-325, Brookhaven National Laboratory, Upton, NY, USA (1958). Second Edition.

[357] S. Grimme, "Semiempirical GGA-type density functional constructed with a long-range dispersion corrections," J. Comput. Chem. **27**, 1787 (2006).

[358] R. Niklow *et al.*, "Lattice dynamics of pyrolytic graphite," Phys. Rev. B **5**, 4951 (1972).

[359] C. Oshima *et al.*, "Surface phonon dispersion curves of graphite (0001) over the entire energy region," Solid State Commun. **65**, 1601 (1988).

[360] G. Benedek *et al.*, "Surface phonons in layered crystals: theoretical apsects," Surf. Sci. **20**, 1 (1994).

[361] J. L. Wilkes, "Phonons in graphite studied by EELS," J. Electron Spectrosc. Relat. Phenom. **44**, 355 (1987).

[362] S. Siebentritt *et al.*, "Surface phonon dispersion in graphite and in a lanthanum graphite intercalation compound," Phys. Rev. B **55**, 7927 (1997).

[363] J. Maultzsh *et al.*, "Phonon dispersion in graphite," Phys. Rev. Lett. **92**, 075501 (2004).

[364] A. Hawari, S. van der Marck, A. Kahler *et al.*, in preparation.

[365] A. I. Hawari and V. H. Gillette, "Inelastic thermal neutron scattering cross sections for reactor-grade graphite,"

NUCL. DATA SHEETS **188**, 176 (2014).

[366] A. Bosak, K. Schmalzl, M. Krisch, W. van Beek, and V. Kolobanov, "Lattice dynamics of beryllium oxide: inelastic x-ray scattering and ab initio calculations," PHYS. REV. B **77**, 224303 (2008).

[367] G. L. Ostheller, R. E. Schmunk, R. M. Brugger, and R. J. Kearney, "Phonon dispersion relation of beryllium oxide," in *Neutron Inelastic Scattering Vol. I. Proceedings of a Symposium on Neutron Inelastic Scattering*, (Copenhagen, Denmark) (1968).

[368] J. C. Holmes *et al.*, "Development of an ENDF thermal library for SiO_2 and testing of criticality effects," TRANS. AM. NUCL. SOC. **104** (2011).

[369] Y. Zhu *et al.*, "Thermal neutron scattering cross sections for silicon carbide," TRANS. AM. NUCL. SOC. **108** (2013).

[370] A. I. Hawari *et al.*, "Development of a thermal neutron scattering law for polyethylene using molecular dynamics simulations," TRANS. AM. NUCL. SOC. **115**, 1126 (2016).

[371] S. Plimpton, "Fast parallel algorithms for short-range molecular dynamics," J. COMPUT. PHYS. **117**, 1 (1995).

[372] C. M. Lavelle *et al.*, "Toward a new polyethylene scattering law determined using inelastic neutron scattering," NUCL. INST. METH. PHYS. RES. A **711**, 166 (2013).

[373] R. E. Macfarlane *et al.*, "The NJOY nuclear data processing system, version 2012," Tech. Rep. LA-UR-12-27079, Los Alamos National Laboratory (2012).

[374] J. R. Granada, J. Dawidowski, R. Mayer, and V. Gillette, "Thermal neutron cross section and transport properties of polyethylene," NUCL. INST. METH. PHYS. RES. A **261**, 573 (1987).

[375] A. I. Hawari *et al.*, "Analysis of thermal neutron scattering in polymethyl methacrylate (lucite)," TRANS. AM. NUCL. SOC. **113** (2015).

[376] G. Sibona *et al.*, "Thermal neutron cross sections and diffusion parameters of plexiglass," ANNALS NUCL. ENERGY **18**, 689 (1991).

[377] S. F. Beshai, "Total cross-sections of U, UO_2 and ThO_2 for thermal and subthermal neutrons," Tech. Rep. AE-222, Aktiebolaget Atomenergi (1966).

[378] J. L. Wormald and A. I. Hawari, "Ab initio generation of thermal neutron scattering law for uranium dioxide," TRANS. AM. NUCL. SOC. **114** (2016).

[379] J. R. Beyster *et al.*, "Integral neutron thermalization," Tech. Rep. GA-8280, General Atomics (1967).

[380] G. Dolling *et al.*, "The crystal dynamics of uranium dioxide," CAN. J. PHYS. **43**, 8 (1965).

[381] J. W. L. Pang *et al.*, "Phonon density of states and anharmonicity of UO_2," PHYS. REV. B **89**, 115132 (2014).

[382] N. A. Curry, "An investigation of the magnetic structure of uranium nitride by neutron diffraction," PROC. PHYS. SOC. **86**, 1193 (1965).

[383] P. R. Norton *et al.*, "Nature of the $5f$ electrons in uranium nitride: A photoelectron spectroscopic study of UN, U, UO_2, ThN, and Th," PHYS. REV. B **21**, 6 (1980).

[384] G. Dolling *et al.*, "Phonon dispersion relation of uranium nitride above and below the Neel temperature," in *International Conference on Lattice Dynamics*, (Paris, France) (1977).

[385] A. A. Aczel, G. Granroth, G. MacDougall, W. Buyers, D. Abernathy, G. Samolyuk, G. Stocks, and S. Nagler, "Quantum oscillations of nitrogen atoms in uranium nitride," NAT. COMMUN. **3**, 1124 (2012).

[386] V. F. Sears, "Neutron scattering lengths and cross sections," NEUTRON NEWS **3**, 26 (1992).

[387] E. Gai, "Some Algorithms for the Nuclear Data Evaluation and Construction of the Uncertainty Covariance Matrices," VOPR. ATOM. NAUKI I TECH., SER. NUCLEAR CONSTANTS **Issue 1–2**, 56 (2007).

[388] E. Gai and A. Ignatyuk, "Uncertainties and Covariances of the Fission Cross Sections and the Fission Neutron Multiplicities for Actinides," NUCL. DATA SHEETS **109**, 2890 (2008).

[389] A. Blokhin, E. Gai, A. Ignatyuk, I. Koba, V. Manokhin, and V. Pronyaev, "New Version of Neutron Evaluated Data Library BROND-3," VOPR. ATOM. NAUKI I TECH., SER. NUCLEAR CONSTANTS **Issue 2**, 62 (2016).

[390] S. Badikov and E. Gai, "Some sources of the underestimation of evaluated cross-section uncertainties," Tech. Rep. INDC(NDS)-0438, IAEA, Vienna, Austria (2003).

[391] Working Group 1 of the Joint Committee for Guides in Metrology (JCGM/WG 1), ed., *JCGM 100:2008, Evaluation of measurement data: Guide to the expression of uncertainty in measurement* (2008).

[392] R. M. White, D. A. Resler, and S. I. Warshaw, "Evaluation of charged-particle reactions for fusion applications," in *Nuclear Data for Science and Technology* (S. M. Qaim, ed.), (Juelich, Federal Republic of Germany), 13 (1991).

[393] S. Abramovich, B. J. Guzhovskij, V. Zherebcov, and A. Zvenigorodskij, "Estimated values of total and differential cross sections of proton interactions with nuclei Li-6 and Li-7," VOP AT NAUKI I TEKHN SER YAD KONSTANTY **114**, 17 (1984).

[394] G. Presser and R. Bass, "Reactions ^{7}Li+n, ^{7}Li+p and excited states of the A = 8 system," NUCL. PHYS. A **182**, 321 (1972).

[395] C. Burke, M. Lunnon, and H. Lefevre, "Li7(p,n0)Be7 angular distributions to Ep= 3.8 MeV," PHYS. REV. C **10**, 1299 (1974).

[396] H. Newson, R. Williamson, K. Jones, J. Gibbons, and H. Marshak, "Li7(p,n), (p,p$'\gamma$), and (p,γ) reactions near neutron threshold," PHYS. REV. **108**, 1294 (1957).

[397] C. Poppe, J. Anderson, J. Davis, S. Grimes, and C. Wong, "Cross sections for the Li7(p,n)Be7 reaction between 4.2 and 26 MeV," PHYS. REV. C **14**, 438 (1976).

[398] P. Bevington, W. Rolland, and H. Lewis, "Relative yields of neutron groups from the Li7(p,n)Be7, Be7* reactions," PHYS. REV. **121**, 871 (1961).

[399] R. Borchers and C. Poppe, "Neutrons from proton bombardment of lithium," PHYS. REV. **129**, 2679 (1963).

[400] S. Schery, L. Young, R. Doering, S. M. Austin, and R. Bhowmik, "Activation and angular distribution measurements of ^{7}Li(p,n)^{7}Be(0.0+ 0.49 MeV) for Ep= 25–45 MeV: A technique for absolute neutron yield determination," NUCL. INST. METH. **147**, 399 (1977).

[401] K. Sekharan, H. Laumer, B. Kern, and F. Gabbard, "A neutron detector for measurement of total neutron production cross sections," NUCL. INST. METH. **133**, 253 (1976).

[402] H. Liskien and A. Paulsen, "Neutron production cross sections and energies for the reactions ^{7}Li(p,n)^{7}Be and

^{7}Li(p,n)^{7}Be," At. Data Nucl. Data Tables **15**, 57 (1975).

[403] J. Gibbons and R. Macklin, "Total neutron yields from light elements under proton and alpha bombardment," Phys. Rev. **114**, 571 (1959).

[404] H. Spinka, T. Tombrello, and H. Winkler, "Low-energy cross sections for ^{7}Li(p,α)4He and ^{6}Li(p,α)^{3}He," Nucl. Phys. A **164**, 1 (1971).

[405] G. S. Mani, R. Freeman, F. Picard, A. Sadeghi, and D. Redon, "Study of the reaction Li7(p,α)α up to 12 MeV proton energy," Nucl. Phys. **60**, 588 (1964).

[406] N. Sarma, K. Jayaraman, and C. Kumar, "Mechanism of the Li7(p,α)He4 reaction," Nucl. Phys. **44**, 205 (1963).

[407] Y. Cassagnou, J. Jeronymo, G. Mani, A. Sadeghi, and P. Forsyth, "The Li7(p,α)He4 reaction (erratum)," Nucl. Phys **41**, 176 (1963).

[408] C. Rolfs and R. Kavanagh, "The ^{7}Li(p,α)^{4}He cross section at low energies," Nucl. Phys. A **455**, 179 (1986).

[409] D. M. Ciric, R. V. Popic, R. B. Zakula, B. Z. Stepancic, M. R. Aleksic, and J. P. Setrajcic, "The interaction of ^{7}Li isotope with low energy proton and triton beams," Rev. Sci. Res. **6**, 115 (1976). EXFOR subentry F0033.001.

[410] P. Descouvemont, A. Adahchour, C. Angulo, A. Coc, and E. Vangioni-Flam, "Compilation and R-matrix analysis of Big Bang nuclear reaction rates," At. Data Nucl. Data Tables **88**, 203 (2004).

[411] L. Kull, "(p, d) reactions with Li6, Li7, and Be9," Phys. Rev. **163**, 1066 (1967).

[412] B. Filippone, A. Elwyn, W. Ray Jr, and D. Koetke, "Absolute cross section for Li7(d,p)Li8 and solar neutrino capture rates," Phys. Rev. C **25**, 2174 (1982).

[413] D. Mingay, "Measurement of the absolute total cross section for the reaction ^{7}Li(d,p)^{8}Li at low energies," South Afr. J. Phys. **2**, 107 (1979).

[414] O. Vysotskij, O. Gorpinich, V. Zaritskij, S. Kondratyev, V. Prokopenko, S. Rakitin, V. Sklyarenko, V. Stepanenko, and V. Tokarevskij, "Excitation functions of ^{6}Li(d,n)^{7}Be and ^{7}Li(d,2n)^{7}Be," in *Conference on nuclear spectroscopy and nuclear structure*, (Leningrad, USSR) (1990).

[415] B. Y. Guzhovskij, S. Abramovich, A. Zvenigorodski, V. Protopopov, G. Sleptsov, and S. Trusillo, "Total cross sections of the ^{6}Li(d,n)^{7}Be, ^{7}Li(d,2n)^{7}Be, ^{6}Li(t,2n)^{7}Be reactions," Izvestiya Akademii Nauk SSSR, Seriya Fizicheskaya **44**, 1983 (1980).

[416] R. Macklin and H. Banta, "Tritium production from lithium by deuteron bombardment," Phys. Rev. **97**, 753 (1955).

[417] L. Weissman, C. Broude, G. Goldring, R. Hadar, M. Hass, F. Schwamm, and M. Shaanan, "A new measurement of the ^{7}Li(d,p)^{8}Li cross section and consequences for ^{7}Be(p,γ)8B," Nucl. Phys. A **630**, 678 (1998).

[418] R. W. Kavanagh, "Proton capture in ^{7}Be," Nucl. Phys. **15**, 411 (1960).

[419] A. Schilling, N. Mangelson, K. Nielson, D. Dixon, M. Hill, G. Jensen, and V. Rogers, "An accurate measurement of the ^{7}Li(d,p)^{8}Li excitation function from E_d= 0.6 MeV to 2.0 MeV," Nucl. Phys. A **263**, 389 (1976).

[420] A. Elwyn, R. Holland, C. Davids, and W. Ray Jr, "Li7(d,p)Li8 reaction cross section near 0.78 MeV," Phys. Rev. C **25**, 2168 (1982).

[421] P. D. Parker, "Be$^7(p,\gamma)$B^8," Phys. Rev. **150**, 851 (1966).

[422] C. Brune, R. Kavanagh, S. Kellogg, and T. Wang, "Cross sections for ^{3}H(^{7}Li,n)^{9}Be and ^{3}H(^{7}Li,n-tot)," Phys. Rev. C **43**, 875 (1991).

[423] N. M. Wang, V. M. Novatskii, G. M. Osetinskii, N. K. Chien, and I. A. Chepurchenko, "Investigation of ^{3}He + ^{3}He reactions," Sov. J. Nucl. Phys. **3**, 777 (1976). EXFOR subentry A1060.001.

[424] M. R. Dwarakanath and H. Winkler, "^{3}He(^{3}He, $2p$)^{4}He," Phys. Rev. C **4**, 1532 (1971).

[425] M. R. Dwarakanath, "^{3}He(^{3}He, $2p$)^{4}He," Phys. Rev. C **9**, 805 (1974).

[426] A. Krauss, H. Becker, H. Trautvetter, and C. Rolfs, "Astrophysical S(E) factor of ^{3}He(^{3}He,2p)4He at solar energies," Nucl. Phys. A **467**, 273 (1987).

[427] R. E. Brown, F. D. Correll, P. M. Hegland, J. A. Koepke, and C. H. Poppe, "^{3}He + ^{3}He reaction cross sections for 17.9, 21.7 and 24.0 MeV," Phys. Rev. C **35**, 383 (1987).

[428] R. Bonetti, C. Broggini, L. Campajola *et al.* (LUNA Collaboration), "First measurement of the ^{3}He(^{3}He, $2p$)^{4}He cross section down to the lower edge of the solar Gamow peak," Phys. Rev. Lett. **82**, 5205 (1999).

[429] D. M. Holm and H. V. Argo, "$t-t$ elastic scattering from 1.6 to 2.0 MeV," Phys. Rev. **101**, 1772 (1956).

[430] C. Angulo, M. Arnould, M. Rayet *et al.* (NACRE Collaboration), "A compilation of charged-particle induced thermonuclear reaction rates," Nucl. Phys. A **656**, 3 (1999).

[431] M. Junker, C. Arpesella, E. Bellotti *et al.* (LUNA Collaboration), "The cross section of ^{3}He(^{3}He,$2p$)^{4}He measured at solar energies," Nucl. Phys. B (Proceedings Suppl. **70**, 382 (1999).

[432] J. J. Devaney and M. L. Stein, "Plasma energy deposition from nuclear elastic scattering," Nucl. Sci. Eng. **46**, 323 (1971).

[433] S. T. Perkins and D. E. Cullen, "Elastic nuclear plus interference cross sections for light-charge particles," Nucl. Sci. Eng. **77**, 20 (1981).

[434] R. C. Greenwood, R. G. Helmer, M. H. Putnam, and K. D. Watts, "Measurement of β^--decay intensity distributions of several fission-product isotopes using a total absorption γ-ray spectrometer," Nucl. Inst. Meth. Phys. Res. A **390**, 95 (1997).

[435] A. Algora, D. Jordan, J. L. Taín *et al.*, "Reactor decay heat in ^{239}Pu: Solving the γ discrepancy in the 4–3000-s cooling period," Phys. Rev. Lett. **105**, 202501 (2010).

[436] B. C. Rasco, M. Wolińska-Cichocka, A. Fijałkowska *et al.*, "Decays of the three top contributors to the reactor $\overline{\nu}_e$ high-energy spectrum, ^{92}Rb, ^{96gs}Y, and ^{142}Cs, studied with total absorption spectroscopy," Phys. Rev. Lett. **117**, 092501 (2016).

[437] G. Rudstam, P. Johansson, O. Tengblad, P. Aagaard, and J. Eriksen, "Beta and gamma spectra of short-lived fission products," At. Data Nucl. Data Tables **45**, 239 (1990).

[438] A. A. Sonzogni, T. D. Johnson, and E. A. McCutchan, "Nuclear structure insights into reactor antineutrino spectra," Phys. Rev. C **91**, 011301(R) (2015).

[439] F. von Feilitzsch, A. A. Hahn, and K. Schreckenbach, "Experimental beta-spectra from ^{239}Pu and ^{235}U thermal neutron fission products and their correlated antineu-

trino spectra," Phys. Lett. B **118**, 162 (1982).

[440] K. Schreckenbach, G. Colvin, W. Gelletly, and F. von Feilitzsch, "Determination of the antineutrino spectrum from ^{235}U thermal neutron fission products up to 9.5 MeV," Phys. Lett. B **160**, 325 (1985).

[441] A. A. Hahn, K. Schreckenbach, W. Gelletly, F. von Feilitzsch, G. Colvin, and B. Krusche, "Antineutrino spectra from ^{241}Pu and ^{239}Pu thermal neutron fission products," Phys. Lett. B **218**, 365 (1989).

[442] N. Haag, A. Gütlein, M. Hofmann, L. Oberauer, W. Potzel, K. Schreckenbach, and F. M. Wagner, "Experimental determination of the antineutrino spectrum of the fission products of ^{238}U," Phys. Rev. Lett. **112**, 122501 (2014).

[443] "NIST X-Ray transition energy database." National Institute of Standards and Technology, Gaithersburg, MD, US, [Online] Available at `https://www.nist.gov/pml/x-ray-transition-energies-database`.

[444] D. E. Cullen, "EPICS2014: Electron Photon Interaction Cross Sections (version 2014)," Tech. Rep. IAEA-NDS-218, International Atomic Energy Agency, Vienna, Austria (2014).

[445] R. D. Deslattes, E. G. Kessler, P. Indelicato, L. de Billy, E. Lindroth, and J. Anton, "X-ray transition energies: new approach to a comprehensive evaluation," Rev. Mod. Phys. **75**, 35 (2003).

[446] D. E. Cullen, "A survey of atomic binding energies for use in EPICS2017," Tech. Rep. IAEA-NDS-224, International Atomic Energy Agency, Vienna, Austria (2017).

[447] S. C. van der Marck, "Benchmarking ENDF/B-VII.1, JENDL-4.0 and JEFF-3.1.1 with MCNP6," Nucl. Data Sheets **113**, 2935 (2012).

[448] S. C. van der Marck, "Minimum critical masses and their uncertainties for several fissile nuclides and reflectors," in *ICNC-2015: International Conference on Nuclear Criticality Safety*, (Charlotte, North Carolina, USA) (2015).

[449] H. D. Selby, M. R. M. Innes, D. W. Barr, A. L. Keksis, R. A. Meade, C. J. Burns, M. B. Chadwick, and T. C. Williams, "Fission product data measured at los alamos for fission spectrum and thermal neutrons on ^{239}Pu, ^{235}U, and ^{238}U," Nucl. Data Sheets **111**, 2891 (2010).

[450] Z. Y. Bao, H. Beer, F. Käppeler, F. Voss, K. Wisshak, and T. Rauscher, "Neutron cross sections for nucleosynthesis studies," At. Data Nucl. Data Tables **76**, 70 (2000).

[451] B. Pritychenko and S. F. Mughabghab, "Neutron thermal cross sections, Westcott factors, resonance integrals, Maxwellian averaged cross sections and astrophysical reaction rates calculated from the ENDF/B-VII.1, JEFF-3.1.2, JENDL-4.0, ROSFOND-2010, CENDL-3.1 and EAF-2010 evaluated data libraries," Nucl. Data Sheets **113**, 3120 (2012).

[452] C. E. Rolfs and W. S. Rodney, *Cauldrons in the Cosmos*. The University of Chicago Press (1988).

[453] E. Anders and N. Grevesse, "Abundances of the elements - meteoritic and solar," Geochimica et Cosmochimica Acta **53**, 197 (1989).

[454] S. F. Mughabghab, M. Divadeenam, and N. E. Holden, *Neutron Cross Sections, Vol.1, Neutron Resonance Parameters and Thermal Cross Sections, Part A, Z = 1-60*. Academic Press, New York (1981).

[455] F. Saglime, Y. Danon, R. Block, M. Rapp, R. Bahran, G. Leinweber, D. Barry, and N. Drindak, "A system for differential neutron scattering experiments in the energy range from 0.5 to 20 MeV," Nucl. Inst. Meth. Phys. Res. A **620**, 401 (2010).

[456] A. Daskalakis, R. Bahran, E. Blain *et al.*, "Quasi-differential neutron scattering from ^{238}U from 0.5 to 20 MeV," Annals Nucl. Energy **73**, 455 (2014).

[457] A. Daskalakis, E. Blain, G. Leinweber, M. Rapp, D. Barry, R. Block, and Y. Danon, "Assessment of beryllium and molybdenum nuclear data files with the RPI neutron scattering system in the energy region from 0.5 to 20 MeV," Eur. Phys. J. Web Conf. **146**, 11037 (2017). ND2016: International Conference on Nuclear Data for Science and Technology, September 11-15, 2016 (Bruges, Belgium).

[458] T. Goorley, M. James, T. Booth *et al.*, "Initial MCNP6 release overview," Nucl. Technol. **180**, 298 (2012).

[459] C. Wong, J. D. Anderson, and P. Brown, "Livermore pulsed sphere program: Program summary through july 1971," Tech. Rep. UCRL-ID-51144, Lawrence Livermore Laboratory (1972).

[460] A. A. Marchetti and G. W. Hedstrom, "New Monte Carlo simulation of the LLNL pulsed-sphere experiments," Tech. Rep. UCRL-ID-131461, Lawrence Livermore Laboratory (1998).

[461] R. D. Mosteller, S. C. Frankle, and P. G. Young, "Data testing of ENDF/B-VI with MCNP: Critical experiments, thermal-reactor lattices, and time-of-flight measurements," Tech. Rep. LA-UR-96-2143, Los Alamos National Laboratory (1996).

[462] S. C. Frankle, "Possible impact of additional collimators on the LLNL pulsed sphere experiments (U)," Tech. Rep. LA-UR-05-5877, Los Alamos National Laboratory (2005).

[463] S. C. Frankle, "LLNL pulsed sphere measurements and detector response functions (U)," Tech. Rep. LA-UR-05-5878, Los Alamos National Laboratory (2005).

[464] S. C. Frankle, "README file for running a LLNL pulsed-sphere benchmark," Tech. Rep. LA-UR-05-5879, Los Alamos National Laboratory (2005).

[465] T. Kaiba, A. Trkov, and R. Capote Noy, "Analysis of ^{238}U Livermore pulsed sphere experiments benchmark evaluations," Tech. Rep. INDC(NDS)-0742, International Atomic Energy Agency (2017).

[466] M. McKinley and B. Beck, "Implementation of the Generalized Interaction Data Interface (GIDI) in the Mercury Monte Carlo code," in *ANS M&C/SNA/MC 2015*, (Nashville, TN, US) (2015).

[467] P. Brantley, S. Dawson *et al.*, "Mercury user guide: Version d.16," Tech. Rep. LLNL-SM-560687 Mod #6, Lawrence Livermore National Laboratory (2014).

[468] P. Brantley, R. Bleile, S. Dawson *et al.*, "Mercury user guide: Version 5.6.," Tech. Rep. LLNL-SM-560687 (Modification #12), Lawrence Livermore National Laboratory (2017).

[469] U. Hanebutte and P. Brown, "Ardra, scalable parallel code system to perform neutron and radiation transport calculations," Tech. Rep. UCRL-TB-132078, Lawrence Livermore National Laboratory, Livermore, CA, USA (1999).

[470] D. K. Parsons, "The rules of CHECKACE – a suite of checking codes for MCNP ACE cross section files," Tech. Rep. XCP-5:15-032, Los Alamos National Laboratory (2015).

[471] A. Kahler, J. L. Conlin, and A. P. McCartney, "NJOY2016." Los Alamos National Laboratory, Los

Alamos, NM, USA, [Online] Available at https://njoy.github.io/NJOY2016.

[472] D. Wiarda, M. L. Williams, C. Celik, and M. E. Dunn, "AMPX-2000: A cross-section processing system for generating nuclear data for criticality safety applications," in *International Conference on Nuclear Criticality Safety (ICNC 2015)* (2015).

[473] "SCALE code system, version 6.2.1," Tech. Rep. ORNL/TM-2005/39, Oak Ridge National Laboratory, Oak Ridge, TN, USA (2016). Available from Radiation Safety Information Computational Center as CCC-834.

[474] M. L. Williams, D. Wiarda, K. S. Kim, and M. A. Jessee, "Multigroup data processing for the embedded self-shielding method in SCALE," in *PHYSOR 2016*, (Sun Valley, ID, USA) (2016).

[475] W. J. Marshall and B. T. Rearden, "The SCALE verified archived library of inputs and data – VALID," in *Proceedings of NCSD 2013: Criticality Safety in the Modern Era – Raising the Bar*, (Wilmington, NC, USA) (2013).

Appendix A: Summary of Changes Between ENDF/B-VII.1 and ENDF/B-VIII.0

TABLE XLV: Summary of the origins of and recent changes to the neutron (`neutrons`) sublibrary. Evaluations modified for ENDF/B-VIII.0 are given in bold.

		Last	RRR		URR		Smooth Region		High-energy		
File name	Main source	mod.	Lab.	Year	Lab.	Year	Lab.	Year	Lab.	Year	Note
n-000_n_001.endf	**ENDF/B-VIII.0**	**2016**					**LANL**	**2016**			
n-001_H_001.endf	**ENDF/B-VIII.0; CIELO 2017; Standards 2017**	**2017**					**LANL**	**2017**			**R-matrix analysis; COMMARA-2.0 covariances added in 2011**
n-001_H_002.endf	**ENDF/B-VIII.0**	**2017**					**LANL**	**1994**	**LANL**	**1997**	**JEFF-3.2 ang dists, otw. B-VI below 50MeV; COMMARA-2.0 covariances added in 2011**
n-001_H_003.endf	ENDF/B-VII.0	2006					LANL	2001			R-matrix analysis
n-002_He_003.endf	**ENDF/B-VIII.0; Standards 2017**	**2011**					**LANL**	**2011**			**Originally from ENDF/B-III; capture replaced in 2011, (n,p) in 1990.**
n-002_He_004.endf	**ENDF/B-VII.1**	**2017**					**LANL**	**2010**			**R-matrix analysis**
n-003_Li_006.endf	**ENDF/B-VIII.0; Standards 2017**	**2017**					**LANL**	**2017**			**R-matrix analysis; EGAF primary gammas; COMMARA-2.0 covariances added in 2011**
n-003_Li_007.endf	**ENDF/B-VI**	**2016**					**LANL**	**1988**			**EGAF primary gammas**
n-004_Be_007.endf	**ENDF/B-VIII.0**	**2016**					**LANL/ LLNL**	**2017**			**ENDF/B-VII.1 R-matrix analysis up to 8.1MeV; TALYS calc. above; EGAF primary gammas; Low-fidelity covariances added in 2011**
n-004_Be_009.endf	**ENDF/B-VIII.0**	**2017**					**LANL/ JAEA**	**2011**			**Capture updated for VII.1; JENDL-4 energy and angular dists.**
n-005_B_010.endf	**ENDF/B-VIII.0; Standards 2017**	**2017**					**LANL**	**2017**			**R-matrix analysis**
n-005_B_011.endf	**ENDF/B-VIII.0**	**2016**					**LANL**	**2015**			**Angular dist. recalculated; EGAF primary gammas**
n-006_C_012.endf	**ENDF/B-VIII.0; Standards 2017**	**2016**					**LANL**	**2016**	**LANL**	**2006**	**R-matrix analysis**
n-006_C_013.endf	**ENDF/B-VIII.0; Standards 2017**	**2017**					**LANL**	**2017**	**LANL**	**2006**	**R-matrix analysis**
n-007_N_014.endf	ENDF/B-VI	2006					LANL	1994	LANL	1997	
n-007_N_015.endf	**ENDF/B-VI**	**2016**					**LANL**	**1983**			
n-008_O_016.endf	**ENDF/B-VIII.0; CIELO 2017**	**2017**					**LANL**	**2017**	**LANL**	**2006**	**R-matrix analysis below 7 MeV; elastic and (n,α) changed**
n-008_O_017.endf	ENDF/B-V	2006	BNL	1978			BNL	1978			
n-008_O_018.endf	**ROSFOND**	**2017**	**BNL**	**2005**			**IPPE**	**2006**			
n-009_F_019.endf	**ENDF/B-VII.0**	**2016**	**ORNL**	**2003**			**ORNL**	**1990**			**EGAF primary gammas**
n-010_Ne_020.endf	**TENDL-2015**	**2017**	**TENDL**	**2015**			**TENDL**	**2015**	**TENDL**	**2015**	**TENDL+EMPIRE**
n-010_Ne_021.endf	**TENDL-2015**	**2017**	**TENDL**	**2015**			**TENDL**	**2015**	**TENDL**	**2015**	**TENDL+EMPIRE**
n-010_Ne_022.endf	**TENDL-2015**	**2017**	**TENDL**	**2015**			**TENDL**	**2015**	**TENDL**	**2015**	**TENDL+EMPIRE**
n-011_Na_022.endf	JEF-2.2	2006	BNL	1981	BNL	1982	ECN	1982			
n-011_Na_023.endf	**ENDF/B-V**	**2016**	**ORNL**	**1977**			**ORNL**	**1977**			**EGAF primary gammas**
n-012_Mg_024.endf	**JENDL-3**	**2017**	**JNDC**	**1987**			**JNDC**	**1987**			**COMMARA-2.0 covariances added in 2011**

TABLE XLV: Summary of the origins of and recent changes to the neutron (`neutrons`) sublibrary. Evaluations modified for ENDF/B-VIII.0 are given in bold.

File name	Main source	Last mod.	RRR Lab.	RRR Year	URR Lab.	URR Year	Smooth Region Lab.	Smooth Region Year	High-energy Lab.	High-energy Year	Note
n-012_Mg_025.endf	JENDL-3	2006	JNDC	1987			JNDC	1987			Low-fidelity covariances added in 2011
n-012_Mg_026.endf	JENDL-3	2006	JNDC	1987			JNDC	1987			Low-fidelity covariances added in 2011
n-013_Al_026m1.endf	**ENDF/B-VIII.0**	**2017**	**BNL**	**2017**			**BNL**	**2017**			**TENDL+EMPIRE**
n-013_Al_027.endf	**ENDF/B-VI**	**2016**	**ORNL**	**2001**			**LANL**	**1994**	**LANL**	**1997**	**EGAF primary gammas**
n-014_Si_028.endf	**ENDF/B-VI**	**2016**	**ORNL**	**1996**			**ORNL**	**1996**	**LANL**	**1999**	**EGAF primary gammas**
n-014_Si_029.endf	ENDF/B-V	2006	ORNL	1999			ORNL	1996	LANL	1997	
n-014_Si_030.endf	ENDF/B-VI	2006	ORNL	1996			ORNL	1996	LANL	1996	
n-014_Si_031.endf	**ENDF/B-VIII.0**	**2017**	**BNL**	**2017**			**BNL**	**2017**			**TENDL+EMPIRE**
n-014_Si_032.endf	**ENDF/B-VIII.0**	**2017**	**TENDL**	**2015**			**BNL**	**2017**			**TENDL+EMPIRE**
n-015_P_031.endf	ENDF/B-V	2006					LLNL	1977	LANL	1997	No RRR parameters given
n-016_S_032.endf	JENDL-3.2	2006	JNDC	1987			JNDC	1994			
n-016_S_033.endf	JENDL-3.2	2006	JNDC	1987			JNDC	1994			
n-016_S_034.endf	JENDL-3.2	2006	JNDC	1987			JNDC	1994			
n-016_S_035.endf	**ENDF/B-VIII.0**	**2017**	**TENDL**	**2015**			**BNL**	**2017**			**TENDL+EMPIRE**
n-016_S_036.endf	JENDL-3.2	2006					JNDC	1994			No RRR parameters given
n-017_Cl_035.endf	**ENDF/B-VIII.0**	**2017**	**ORNL**	**2017**			**LANL**	**2000**			**EGAF primary gammas**
n-017_Cl_036.endf	**ENDF/B-VIII.0**	**2017**	**TENDL**	**2015**			**BNL**	**2017**			**TENDL+EMPIRE**
n-017_Cl_037.endf	**ENDF/B-VIII.0**	**2017**	**ORNL**	**2007**			**LANL**	**2016**			**EGAF primary gammas**
n-018_Ar_036.endf	JEF-2.2	2006	ECN	1982	ECN	1982	ECN	1982			
n-018_Ar_037.endf	**TENDL-2015**	**2017**	**TENDL**	**2015**			**TENDL**	**2015**	**TENDL**	**2015**	**TENDL+EMPIRE**
n-018_Ar_038.endf	JEF-2.2	2006	ECN	1982	ECN	1982	ECN	1982			
n-018_Ar_039.endf	**ENDF/B-VIII.0**	**2017**	**BNL**	**2017**			**BNL**	**2017**			**TENDL+EMPIRE**
n-018_Ar_040.endf	**ENDF/B-VIII.0**	**2017**	**JNDC**	**1994**			**LANL**	**2011**			
n-018_Ar_041.endf	**TENDL-2015**	**2017**	**TENDL**	**2015**			**TENDL**	**2015**	**TENDL**	**2015**	**TENDL+EMPIRE**
n-019_K_039.endf	JENDL-3.2	2008	ORNL	2007			JNDC	1994			
n-019_K_040.endf	JENDL-3.2	2006					JNDC	1994			No RRR parameters given
n-019_K_041.endf	JENDL-3.2	2008	ORNL	2007			JNDC	1994			
n-020_Ca_040.endf	**ENDF/B-VIII.0**	**2016**	**ORNL**	**2016**			**NRG**	**2004**	**NRG**	**2004**	
n-020_Ca_041.endf	**ENDF/B-VIII.0**	**2017**	**BNL**	**2017**			**BNL**	**2017**			**TENDL+EMPIRE**
n-020_Ca_042.endf	JEFF-3.1	2006	JNDC	1987			NRG	2004	NRG	2004	
n-020_Ca_043.endf	JEFF-3.1	2006	JNDC	1987			NRG	2004	NRG	2004	
n-020_Ca_044.endf	JEFF-3.1	2006	JNDC	1987			NRG	2004	NRG	2004	
n-020_Ca_045.endf	**TENDL-2015**	**2017**	**TENDL**	**2015**			**TENDL**	**2015**	**TENDL**	**2015**	**TENDL+EMPIRE**
n-020_Ca_046.endf	JEFF-3.1	2006					NRG	2004	NRG	2004	No RRR parameters given
n-020_Ca_047.endf	**TENDL-2015**	**2017**	**TENDL**	**2015**			**TENDL**	**2015**	**TENDL**	**2015**	**TENDL+EMPIRE**
n-020_Ca_048.endf	JEFF-3.1	2006	JNDC	1987			NRG	2004	NRG	2004	
n-021_Sc_045.endf	**ENDF/B-VI**	**2016**	**BNL**	**1981**			**ANL/ LLNL**	**1992**			**LANL corrections in 2000, 2016**
n-022_Ti_046.endf	ENDF/B-VII.1	2010	ORNL	2009			LANL	2008			
n-022_Ti_047.endf	ENDF/B-VII.1	2010	ORNL	2009			LANL	2008			
n-022_Ti_048.endf	**ENDF/B-VII.1**	**2017**	**ORNL**	**2009**			**LANL**	**2008**			
n-022_Ti_049.endf	ENDF/B-VII.1	2010	ORNL	2009			LANL	2008			
n-022_Ti_050.endf	ENDF/B-VII.1	2010	ORNL	2009			LANL	2008			
n-023_V_049.endf	**ENDF/B-VIII.0**	**2017**	**TENDL**	**2015**			**BNL**	**2017**			**TENDL+EMPIRE**
n-023_V_050.endf	JENDL-4.0	2011	JNDC	2010			JNDC	2010			
n-023_V_051.endf	ENDF/B-VII.1	2011	JNDC	2010			LANL	2010			
n-024_Cr_050.endf	ENDF/B-VII.1	2006	ORNL	2010			LANL/ JAEA	1989	LANL/ JAEA	1997	Modifications in 2000, 2011 in fast region; COMMARA-2.0 covariances added in 2011
n-024_Cr_051.endf	**TENDL-2015**	**2017**	**TENDL**	**2015**			**TENDL**	**2015**	**TENDL**	**2015**	**TENDL+EMPIRE**
n-024_Cr_052.endf	ENDF/B-VII.1	2006	ORNL	2010			LANL/ JAEA	1989	LANL/ JAEA	1997	Modifications in 2000, 2011 in fast region; COMMARA-2.0 covariances added in 2011
n-024_Cr_053.endf	ENDF/B-VII.1	2006	ORNL	2010			LANL/ JAEA	1989	LANL/ JAEA	1997	Modifications in 2000, 2011 in fast region; COMMARA-2.0 covariances added in 2011
n-024_Cr_054.endf	ENDF/B-VII.1	2006	ORNL	2010			LANL/ JAEA	1989	LANL/ JAEA	1997	Modifications in 2000, 2011 in fast region
n-025_Mn_054.endf	**TENDL-2015**	**2017**	**TENDL**	**2015**			**TENDL**	**2015**	**TENDL**	**2015**	**TENDL+EMPIRE**
n-025_Mn_055.endf	IAEA	2011	ORNL	2008	ORNL	2008	IAEA	2011	IAEA	2011	Max energy 60 MeV
n-026_Fe_054.endf	**ENDF/B-VIII.0; CIELO 2017**	**2017**	**BNL/ IRSN**	**2016**			**BNL/ IAEA**	**2017**	**BNL/ IAEA**	**2017**	
n-026_Fe_055.endf	**TENDL-2015**	**2017**	**TENDL**	**2015**			**TENDL**	**2015**	**TENDL**	**2015**	**TENDL+EMPIRE**
n-026_Fe_056.endf	**ENDF/B-VIII.0; CIELO 2017**	**2017**	**JAEA**	**2011**			**IAEA/ BNL**	**2017**	**IAEA/ BNL**	**2017**	
n-026_Fe_057.endf	**ENDF/B-VIII.0; CIELO 2017**	**2017**	**BNL**	**2016**			**BNL/ IAEA**	**2017**	**BNL/ IAEA**	**2017**	
n-026_Fe_058.endf	**ENDF/B-VIII.0; CIELO 2017**	**2017**	**IAEA**	**2005**	**IAEA**	**2005**	**BNL/ IAEA**	**2017**	**BNL/ IAEA**	**2017**	
n-027_Co_058.endf	**ENDF/B-VIII.0**	**2016**	**BNL**	**2011**	**BNL**	**2011**	**BNL**	**2011**			
n-027_Co_058m1.endf	JEF-2.2	2006	ECN	1982			ECN	1982			Evaluation year unknown, mods. In 1984, 1985, 1987
n-027_Co_059.endf	**ENDF/B-VIII.0**	**2017**	**ORNL**	**1992**			**LANL**	**2016**			

TABLE XLV: Summary of the origins of and recent changes to the neutron (`neutrons`) sublibrary. Evaluations modified for ENDF/B-VIII.0 are given in bold.

File name	Main source	Last mod.	RRR Lab.	RRR Year	URR Lab.	URR Year	Smooth Region Lab.	Smooth Region Year	High-energy Lab.	High-energy Year	Note
n-028_Ni_058.endf	**ENDF/B-VIII.0**	**2017**	**ORNL**	**2009**			**LANL**	**2012**	**LANL**	**1997**	**COMMARA-2.0 covariances added in 2011**
n-028_Ni_059.endf	**ENDF/B-VIII.0**	**2016**	**JAEA**	**2009**	**JAEA**	**2009**	**LANL**	**2012**	**LANL**	**1997**	**JENDL-4.0 RRR & URR**
n-028_Ni_060.endf	**ENDF/B-VIII.0**	**2017**	**ORNL**	**2009**			**LANL**	**2012**	**LANL**	**1997**	**COMMARA-2.0 covariances added in 2011**
n-028_Ni_061.endf	**ENDF/B-VIII.0**	**2017**	**JAERI**	**1992**			**LANL**	**2012**	**LANL**	**1997**	**JENDL-3.2 RRR**
n-028_Ni_062.endf	**ENDF/B-VIII.0**	**2017**	**BNL/ JSI**	**2011**	**BNL/ JSI**	**2011**	**LANL**	**2012**	**LANL**	**1997**	**Resonance re-evaluation year between 2009-2011**
n-028_Ni_063.endf	**ENDF/B-VIII.0**	**2017**	**TENDL**	**2015**			**BNL**	**2017**			**TENDL+EMPIRE**
n-028_Ni_064.endf	**ENDF/B-VIII.0**	**2017**	**JNDC**	**1987**			**LANL**	**2012**	**LANL**	**1997**	**RRR from JENDL-4.0 which is JENDL-2**
n-029_Cu_063.endf	**ENDF/B-VIII.0**	**2017**	**ORNL**	**2016**			**LANL**	**2016**	**LANL**	**1998**	
n-029_Cu_064.endf	**ENDF/B-VIII.0**	**2017**	**BNL**	**2017**			**BNL**	**2017**			**TENDL+EMPIRE**
n-029_Cu_065.endf	**ENDF/B-VIII.0**	**2017**	**ORNL**	**2016**			**LANL**	**2016**	**LANL**	**1998**	
n-030_Zn_064.endf	JENDL-4.0	2010	JAEA	2009	JAEA	2009	JAEA	2009			
n-030_Zn_065.endf	JENDL-4.0	2010			JAEA	2009	JAEA	2009			No RRR parameters given, only URR parameters
n-030_Zn_066.endf	JENDL-4.0	2010	JAEA	2009	JAEA	2009	JAEA	2009			
n-030_Zn_067.endf	JENDL-4.0	2010	JAEA	2009	JAEA	2009	JAEA	2009			
n-030_Zn_068.endf	**JENDL-4.0**	**2016**	**JAEA**	**2009**	**JAEA**	**2009**	**JAEA**	**2009**			
n-030_Zn_069.endf	**ENDF/B-VIII.0**	**2017**	**BNL**	**2017**			**BNL**	**2017**			**TENDL+EMPIRE**
n-030_Zn_070.endf	JENDL-4.0	2010	JAEA	2009	JAEA	2009	JAEA	2009			
n-031_Ga_069.endf	JENDL-3.3; WPEC/SG-23	2006	BNL	2006			JNDC	1994			
n-031_Ga_070.endf	**ENDF/B-VIII.0**	**2017**	**BNL**	**2017**			**BNL**	**2017**			**TENDL+EMPIRE**
n-031_Ga_071.endf	CENDL-3; WPEC/SG-23	2006	JNDC	1994			CNDC	2001			
n-032_Ge_070.endf	ENDF/B-VII.0; WPEC/SG-23	2006	BNL	2004	BNL	2004	BNL/ JAERI	2004			
n-032_Ge_071.endf	**ENDF/B-VIII.0**	**2017**	**TENDL**	**2015**			**BNL**	**2017**			**TENDL+EMPIRE**
n-032_Ge_072.endf	ENDF/B-VII.0; WPEC/SG-23	2006	BNL	2004	BNL	2004	BNL/ JAERI	2004			
n-032_Ge_073.endf	ENDF/B-VII.0; WPEC/SG-23	2006	BNL	2004	BNL	2004	BNL/ JAERI	2004			
n-032_Ge_074.endf	ENDF/B-VII.0; WPEC/SG-23	2006	BNL	2004	BNL	2004	BNL/ JAERI	2004			
n-032_Ge_075.endf	**ENDF/B-VIII.0**	**2017**	**BNL**	**2017**			**BNL**	**2017**			**TENDL+EMPIRE**
n-032_Ge_076.endf	ENDF/B-VII.0; WPEC/SG-23	2006	BNL	2004	BNL	2004	BNL/ JAERI	2004			
n-033_As_073.endf	**ENDF/B-VIII.0**	**2017**	**LANL**	**2010**			**LANL**	**2010**			**RRR is simple picket fence**
n-033_As_074.endf	**ENDF/B-VIII.0**	**2017**	**BNL**	**2006**	**BNL**	**2006**	**LANL/ LLNL/ KAERI**	**2016**			
n-033_As_075.endf	**ENDF/B-VIII.0**	**2017**	**JNDC**	**1990**	**JNDC**	**1990**	**LANL**	**2010**			
n-034_Se_074.endf	JENDL-3; WPEC/SG-23	2006	JNDC	1990	JNDC	1990	JNDC	1990			Newer JENDL-4.0 (2009) evaluation available
n-034_Se_075.endf	**TENDL-2015**	**2017**	**TENDL**	**2015**			**TENDL**	**2015**	**TENDL**	**2015**	**TENDL+EMPIRE**
n-034_Se_076.endf	JENDL-3; WPEC/SG-23	2006	JNDC	1990	JNDC	1990	JNDC	1990			Newer JENDL-4.0 (2009) evaluation available
n-034_Se_077.endf	JENDL-3; WPEC/SG-23	2006	JNDC	1990	JNDC	1990	JNDC	1990			Newer JENDL-4.0 (2009) evaluation available
n-034_Se_078.endf	JENDL-3; WPEC/SG-23	2006	JNDC	1990	JNDC	1990	JNDC	1990			Newer JENDL-4.0 (2009) evaluation available
n-034_Se_079.endf	JENDL-3; WPEC/SG-23	2006	JNDC	1990	JNDC	1990	JNDC	1990			Newer JENDL-4.0 (2009) evaluation available
n-034_Se_080.endf	JENDL-3; WPEC/SG-23	2006	JNDC	1990	JNDC	1990	JNDC	1990			Newer JENDL-4.0 (2009) evaluation available
n-034_Se_081.endf	**ENDF/B-VIII.0**	**2017**	**BNL**	**2017**			**BNL**	**2017**			**TENDL+EMPIRE**
n-034_Se_082.endf	JENDL-3; WPEC/SG-23	2006	BNL	2006	BNL	1990	JNDC	1990			Newer JENDL-4.0 (2009) evaluation available
n-035_Br_079.endf	JENDL-3.2; WPEC/SG-23	2006	JNDC	1990	JNDC	1993	JNDC	1990			Newer JENDL-4.0 (2009) evaluation available
n-035_Br_080.endf	**ENDF/B-VIII.0**	**2017**	**BNL**	**2017**			**BNL**	**2017**			**TENDL+EMPIRE**
n-035_Br_081.endf	JENDL-3.2; WPEC/SG-23	2006	BNL	2006	BNL	1993	JNDC	1990			Newer JENDL-4.0 (2009) evaluation available
n-036_Kr_078.endf	**ENDF/B-VIII.0**	**2016**	**JAEA**	**2009**	**JAEA**	**2009**	**LANL**	**2016**			**Resonances from JENDL-4.0**
n-036_Kr_079.endf	**ENDF/B-VIII.0**	**2017**	**BNL**	**2017**			**BNL**	**2017**			**TENDL+EMPIRE**
n-036_Kr_080.endf	JENDL-3; WPEC/SG-23	2006	JNDC	1990	JNDC	1990	JNDC	1990			
n-036_Kr_081.endf	**TENDL-2015**	**2017**	**TENDL**	**2015**			**TENDL**	**2015**	**TENDL**	**2015**	**TENDL+EMPIRE**

TABLE XLV: Summary of the origins of and recent changes to the neutron (`neutrons`) sublibrary. Evaluations modified for ENDF/B-VIII.0 are given in bold.

		Last	RRR		URR		Smooth Region		High-energy		
File name	Main source	mod.	Lab.	Year	Lab.	Year	Lab.	Year	Lab.	Year	Note
n-036_Kr_082.endf	JENDL-3; WPEC/SG-23	2006	BNL	2006	BNL	1990	JNDC	1990			
n-036_Kr_083.endf	CENDL-3; WPEC/SG-23	2006	CNDC	2001	CNDC	2001	CNDC	2001			
n-036_Kr_084.endf	JENDL-3; WPEC/SG-23	2006	BNL	2006	BNL	1990	JNDC	1990			
n-036_Kr_085.endf	ENDF/B-VII.0; WPEC/SG-23	2006	BNL	2006	BNL	2006	BNL	2006			
n-036_Kr_086.endf	JENDL-3; WPEC/SG-23	2006	BNL	2006			JNDC	1990			
n-037_Rb_085.endf	JENDL-3; WPEC/SG-23	2006	BNL	2006	BNL	1990	JNDC	1990			
n-037_Rb_086.endf	ENDF/B-VII.0; WPEC/SG-23	2006	BNL	2006	BNL	2006	BNL	2006			
n-037_Rb_087.endf	JENDL-3; WPEC/SG-23	2006	JNDC	1990	JNDC	1990	JNDC	1990			
n-038_Sr_084.endf	ENDF/B-VII.0; WPEC/SG-23	2006	BNL	2006	BNL	2006	BNL	2006			
n-038_Sr_085.endf	**ENDF/B-VIII.0**	**2017**	**BNL**	**2017**			**BNL**	**2017**			**TENDL+EMPIRE**
n-038_Sr_086.endf	JENDL-3; WPEC/SG-23	2006	BNL	2006	JNDC	1990	JNDC	1990			
n-038_Sr_087.endf	JENDL-3; WPEC/SG-23	2006	JNDC	1990	JNDC	1990	JNDC	1990			
n-038_Sr_088.endf	**CENDL-3; WPEC/SG-23**	**2016**	**BNL**	**2006**			**CNDC**	**2001**			**Corrected RRR typos in 2015, 2016**
n-038_Sr_089.endf	CENDL-3; WPEC/SG-23	2006			JNDC	1990	CNDC	2001			No RRR parameters given, only URR parameters
n-038_Sr_090.endf	JENDL-3.2; WPEC/SG-23	2006			JNDC	1990	JNDC	1993			No RRR parameters given, only URR parameters
n-039_Y_089.endf	**ENDF/B-VII.1**	**2016**	**BNL**	**2006**			**LANL**	**2009**			**Minor bug fixes 2013, 2016**
n-039_Y_090.endf	ENDF/B-VII.0; WPEC/SG-23	2006	BNL	2006	BNL	2006	BNL	2006			
n-039_Y_091.endf	JENDL-3; WPEC/SG-23	2006			JNDC	1990	JNDC	1990			No RRR parameters given, only URR parameters
n-040_Zr_090.endf	**ENDF/B-VII.1**	**2016**	**BNL**	**2011**	**BNL**	**2011**	**BNL/KAERI**	**2011**			**COMMARA-2.0 covariances added in 2011; RRR revised 2013**
n-040_Zr_091.endf	**ENDF/B-VII.1**	**2016**	**BNL**	**2011**	**BNL**	**2011**	**BNL/KAERI**	**2011**			**COMMARA-2.0 covariances added in 2011; RRR revised 2013**
n-040_Zr_092.endf	**ENDF/B-VII.1**	**2016**	**BNL**	**2011**	**BNL**	**2011**	**BNL/KAERI**	**2011**			**COMMARA-2.0 covariances added in 2011; RRR revised 2013**
n-040_Zr_093.endf	ENDF/B-VII.1	2011	BNL	2011	BNL	2011	BNL/KAERI	2011			COMMARA-2.0 covariances added in 2011
n-040_Zr_094.endf	**ENDF/B-VII.1**	**2017**	**BNL**	**2011**	**BNL**	**2011**	**BNL/KAERI**	**2011**			**COMMARA-2.0 covariances added in 2011; RRR revised 2013; RRR & URR matching fixed 2016**
n-040_Zr_095.endf	ENDF/B-VII.1	2011	BNL	2011	BNL	2011	BNL/KAERI	2011			COMMARA-2.0 covariances added in 2011
n-040_Zr_096.endf	**ENDF/B-VII.1**	**2016**	**BNL**	**2011**	**BNL**	**2011**	**BNL/KAERI**	**2011**			**COMMARA-2.0 covariances added in 2011; RRR revised 2013; RRR & URR matching fixed 2016**
n-041_Nb_093.endf	**ENDF/B-VI**	**2017**	**JAEA**	**2009**	**JAEA**	**2009**	**LANL**	**1997**	**LANL**	**1997**	**RRR & URR from JENDL-4.0**
n-041_Nb_094.endf	JENDL-3; WPEC/SG-23	2006	JNDC	1990	JNDC	1990	JNDC	1990			
n-041_Nb_095.endf	JENDL-3; WPEC/SG-23	2006			JNDC	1990	JNDC	1990			No RRR parameters given, only URR parameters; COMMARA-2.0 covariances added in 2011
n-042_Mo_092.endf	JENDL-3.2; WPEC/SG-23	2006	JNDC	1993	JNDC	1993	JNDC	1993			
n-042_Mo_093.endf	**TENDL-2015**	**2017**	**TENDL**	**2015**			**TENDL**	**2015**	**TENDL**	**2015**	**TENDL+EMPIRE**
n-042_Mo_094.endf	JENDL-3.2; WPEC/SG-23	2006	BNL	2006	BNL	1993	JNDC	1993			COMMARA-2.0 covariances added in 2011
n-042_Mo_095.endf	**ENDF/B-VII.1**	**2017**	**BNL**	**2010**	**BNL**	**2010**	**BNL/KAERI**	**2010**			**COMMARA-2.0 covariances added in 2011**
n-042_Mo_096.endf	JENDL-3.2; WPEC/SG-23	2006	JNDC	1993	JNDC	1993	JNDC	1993			COMMARA-2.0 covariances added in 2011
n-042_Mo_097.endf	JENDL-3.3; WPEC/SG-23	2006	BNL	2006	JNDC	2001	JNDC	2001			COMMARA-2.0 covariances added in 2011

TABLE XLV: Summary of the origins of and recent changes to the neutron (`neutrons`) sublibrary. Evaluations modified for ENDF/B-VIII.0 are given in bold.

		Last	RRR		URR		Smooth Region		High-energy		
File name	Main source	mod.	Lab.	Year	Lab.	Year	Lab.	Year	Lab.	Year	Note
n-042_Mo_098.endf	JENDL-3.3; WPEC/SG-23	2006	JNDC	1993	JNDC	1993	JNDC	2001			COMMARA-2.0 covariances added in 2011
n-042_Mo_099.endf	JENDL-3; WPEC/SG-23	2006			JNDC	1990	JNDC	1990			No RRR parameters given, only URR parameters
n-042_Mo_100.endf	CENDL-3; WPEC/SG-23	2006	JNDC	1989	JNDC	1989	CNDC	2001			RRR & URR from JENDL-3; COMMARA-2.0 covariances added in 2011
n-043_Tc_098.endf	**TENDL-2015**	**2017**	**TENDL**	**2015**			**TENDL**	**2015**	**TENDL**	**2015**	**TENDL+EMPIRE**
n-043_Tc_099.endf	**ENDF/B-VII.1**	**2017**	**BNL**	**2010**	**BNL**	**2010**	**BNL**	**2006**			**Covariances from BNL-LANL collaboration 2006**
n-044_Ru_096.endf	JENDL-3; WPEC/SG-23	2006			JNDC	1990	JNDC	1990			No RRR parameters given, only URR parameters
n-044_Ru_097.endf	**TENDL-2015**	**2017**	**TENDL**	**2015**			**TENDL**	**2015**	**TENDL**	**2015**	**TENDL+EMPIRE**
n-044_Ru_098.endf	JENDL-3; WPEC/SG-23	2006			JNDC	1990	JNDC	1990			No RRR parameters given, only URR parameters
n-044_Ru_099.endf	JENDL-3.2; WPEC/SG-23	2006	JNDC	2001	JNDC	1993	JNDC	1993			
n-044_Ru_100.endf	JENDL-3; WPEC/SG-23	2006	BNL	2006	JNDC	1990	JNDC	1990			
n-044_Ru_101.endf	ENDF/B-VII.0; WPEC/SG-23	2006	BNL/ KAERI	1999	BNL/ KAERI	1999	BNL/ KAERI	2006			COMMARA-2.0 covariances added in 2011
n-044_Ru_102.endf	CENDL-3; WPEC/SG-23	2006	BNL	2006	CNDC	2001	CNDC	2001			COMMARA-2.0 covariances added in 2011
n-044_Ru_103.endf	CENDL-3; WPEC/SG-23	2006	BNL	2006	CNDC	2001	CNDC	2001			COMMARA-2.0 covariances added in 2011
n-044_Ru_104.endf	CENDL-3; WPEC/SG-23	2006	JNDC	1990	JNDC	2001	CNDC	2001			RRR & URR from JENDL-3; COMMARA-2.0 covariances added in 2011
n-044_Ru_105.endf	CENDL-3; WPEC/SG-23	2006					CNDC	2001			No RRR parameters given
n-044_Ru_106.endf	JENDL-3; WPEC/SG-23	2006			JNDC	1990	JNDC	1990			No RRR parameters given, only URR parameters; COMMARA-2.0 covariances added in 2011
n-045_Rh_103.endf	ENDF/B-VII.1	2006	BNL	2010	BNL	2010	BNL/ KAERI	2006			COMMARA-2.0 covariances added in 2011
n-045_Rh_104.endf	**ENDF/B-VIII.0**	**2017**	**BNL**	**2017**			**BNL**	**2017**			**TENDL+EMPIRE**
n-045_Rh_105.endf	**ENDF/B-VIII.0**	**2016**	**JAEA**	**2016**	**JNDC**	**1990**	**JNDC**	**1990**			**RRR now MLBW**
n-046_Pd_102.endf	ENDF/B-VI; WPEC/SG-23	2006	BNL	2006			LANL	1996			
n-046_Pd_103.endf	**ENDF/B-VIII.0**	**2017**	**TENDL**	**2015**			**BNL**	**2017**			**TENDL+EMPIRE**
n-046_Pd_104.endf	ENDF/B-VI; WPEC/SG-23	2006	BNL	2006			LANL	1996			
n-046_Pd_105.endf	ENDF/B-VII.0; WPEC/SG-23	2006	BNL/ KAERI	1999	BNL/ KAERI	1999	BNL/ KAERI	2006			COMMARA-2.0 covariances added in 2011
n-046_Pd_106.endf	ENDF/B-VI; WPEC/SG-23	2006	BNL	2006			LANL	1996			COMMARA-2.0 covariances added in 2011
n-046_Pd_107.endf	JENDL-3.2; WPEC/SG-23	2006	JNDC	1993	JNDC	1993	JNDC	1993			COMMARA-2.0 covariances added in 2011
n-046_Pd_108.endf	ENDF/B-VI; WPEC/SG-23	2006	BNL	2006			LANL	1996			COMMARA-2.0 covariances added in 2011
n-046_Pd_109.endf	**ENDF/B-VIII.0**	**2017**	**BNL**	**2017**			**BNL**	**2017**			**TENDL+EMPIRE**
n-046_Pd_110.endf	ENDF/B-VI; WPEC/SG-23	2006	BNL	2006			LANL	1996			
n-047_Ag_107.endf	JENDL-3.2; WPEC/SG-23	2006	BNL	2006	JNDC	1993	JNDC	1993			
n-047_Ag_108.endf	**ENDF/B-VIII.0**	**2017**	**BNL**	**2017**			**BNL**	**2017**			**TENDL+EMPIRE**
n-047_Ag_109.endf	ENDF/B-VII.1; WPEC/SG-23	2006	BNL	2010	BNL	2010	BNL/ KAERI	2006			Low-fidelity covariances added in 2011
n-047_Ag_110m1.endf	**JENDL-3.3;** **WPEC/SG-23**	**2017**	**BNL**	**2006**	**JNDC**	**1990**	**JNDC**	**1990**			
n-047_Ag_111.endf	ENDF/B-VII.0; WPEC/SG-23	2006	BNL	2006	BNL	2006	BNL	2006			
n-047_Ag_112.endf	**ENDF/B-VIII.0**	**2017**	**BNL**	**2017**			**BNL**	**2017**			**TENDL+EMPIRE**
n-047_Ag_113.endf	**ENDF/B-VIII.0**	**2017**	**BNL**	**2017**			**BNL**	**2017**			**TENDL+EMPIRE**
n-047_Ag_114.endf	**ENDF/B-VIII.0**	**2017**	**BNL**	**2017**			**BNL**	**2017**			**TENDL+EMPIRE**
n-047_Ag_115.endf	**ENDF/B-VIII.0**	**2017**	**BNL**	**2017**			**BNL**	**2017**			**TENDL+EMPIRE**
n-047_Ag_116.endf	**ENDF/B-VIII.0**	**2017**	**BNL**	**2017**			**BNL**	**2017**			**TENDL+EMPIRE**
n-047_Ag_117.endf	**ENDF/B-VIII.0**	**2017**	**BNL**	**2017**			**BNL**	**2017**			**TENDL+EMPIRE**
n-047_Ag_118m1.endf	**ENDF/B-VIII.0**	**2017**	**BNL**	**2017**			**BNL**	**2017**			**TENDL+EMPIRE**
n-048_Cd_106.endf	JENDL-3.3; WPEC/SG-23	2011	IRRM	2010	JNDC	2001	JNDC	2001			
n-048_Cd_107.endf	**ENDF/B-VIII.0**	**2017**	**BNL**	**2017**			**BNL**	**2017**			**TENDL+EMPIRE**
n-048_Cd_108.endf	ENDF/B-VI; WPEC/SG-23	2011	IRRM	2010	ORNL	1991	ANL	1994			
n-048_Cd_109.endf	**TENDL-2015**	**2017**	**TENDL**	**2015**			**TENDL**	**2015**	**TENDL**	**2015**	**TENDL+EMPIRE**
n-048_Cd_110.endf	ENDF/B-VI; WPEC/SG-23	2011	IRRM	2010	ORNL	1991	ANL	1994			
n-048_Cd_111.endf	JENDL-3.3; WPEC/SG-23	2011	IRRM	2010	JNDC	1994	JNDC	1994			

TABLE XLV: Summary of the origins of and recent changes to the neutron (`neutrons`) sublibrary. Evaluations modified for ENDF/B-VIII.0 are given in bold.

			RRR		URR		Smooth Region		High-energy		
File name	Main source	Last mod.	Lab.	Year	Lab.	Year	Lab.	Year	Lab.	Year	Note
n-048_Cd_112.endf	ENDF/B-VI; WPEC/SG-23	2011	IRRM	2010	ORNL	1991	ANL	1994			
n-048_Cd_113.endf	CENDL-3	2011	BNL	2010	BNL	2010	CNDC	2001			
n-048_Cd_114.endf	ENDF/B-VI; WPEC/SG-23	2011	IRRM	2010	ORNL	1991	ANL	1994			
n-048_Cd_115m1.endf	ENDF/B-VII.0; WPEC/SG-23	2006	BNL	2006	BNL	2006	BNL	2006			
n-048_Cd_116.endf	ENDF/B-VI; WPEC/SG-23	2011	IRRM	2010	ORNL	1991	ANL	1994			
n-049_In_113.endf	JENDL-3; WPEC/SG-23	2006	BNL	2006	JNDC	1990	JNDC	1990			
n-049_In_114.endf	**ENDF/B-VIII.0**	**2017**	**BNL**	**2017**			**BNL**	**2017**			**TENDL+EMPIRE**
n-049_In_115.endf	JENDL-3.2; WPEC/SG-23	2006	BNL	2006	JNDC	1982	JNDC	1993			
n-050_Sn_112.endf	JENDL-3; WPEC/SG-23	2006	BNL	2006	JNDC	1990	JNDC	1990			
n-050_Sn_113.endf	ENDF/B-VII.0; WPEC/SG-23	2006	BNL	2006	BNL	2006	BNL	2006			
n-050_Sn_114.endf	JENDL-3; WPEC/SG-23	2006	BNL	2006	JNDC	1990	JNDC	1990			
n-050_Sn_115.endf	JENDL-3; WPEC/SG-23	2006	BNL	2006	JNDC	1990	JNDC	1990			
n-050_Sn_116.endf	JENDL-3; WPEC/SG-23	2006	BNL	2006	JNDC	1990	JNDC	1990			
n-050_Sn_117.endf	JENDL-3.2; WPEC/SG-23	2006	BNL	2006	JNDC	1993	JNDC	1993			
n-050_Sn_118.endf	JENDL-3; WPEC/SG-23	2006	BNL	2006	JNDC	1990	JNDC	1990			
n-050_Sn_119.endf	JENDL-3; WPEC/SG-23	2006	BNL	2006	JNDC	1990	JNDC	1990			
n-050_Sn_120.endf	**JENDL-3; WPEC/SG-23**	**2016**	**BNL**	**2006**	**JNDC**	**1990**	**LANL**	**2015**			
n-050_Sn_121m1.endf	**ENDF/B-VIII.0**	**2017**	**BNL**	**2017**			**BNL**	**2017**			**TENDL+EMPIRE**
n-050_Sn_122.endf	**JENDL-3; WPEC/SG-23**	**2017**	**BNL**	**2006**			**JNDC**	**1990**			**Fix typo in RRR formatting**
n-050_Sn_123.endf	JENDL-3; WPEC/SG-23	2006			JNDC	1990	JNDC	1990			No RRR parameters given, only URR parameters
n-050_Sn_124.endf	**JENDL-3.2; WPEC/SG-23**	**2017**	**BNL**	**2006**			**JNDC**	**1993**			**Fix typo in RRR formatting**
n-050_Sn_125.endf	ENDF/B-VII.0; WPEC/SG-23	2006	BNL	2006	BNL	2006	BNL	2006			
n-050_Sn_126.endf	JENDL-3; WPEC/SG-23	2006			JNDC	1990	JNDC	1990			No RRR parameters given, only URR parameters
n-051_Sb_121.endf	CENDL-3; WPEC/SG-23	2006	BNL	2006	JNDC	1994	CNDC	2001			CENDL eval year uncertain
n-051_Sb_122.endf	**ENDF/B-VIII.0**	**2017**	**BNL**	**2017**			**BNL**	**2017**			**TENDL+EMPIRE**
n-051_Sb_123.endf	CENDL-3; WPEC/SG-23	2006	BNL	2006	JNDC	1994	CNDC	2001			CENDL eval year uncertain
n-051_Sb_124.endf	**JENDL-3; WPEC/SG-23**	**2016**			**JNDC**	**1990**	**JNDC**	**1990**			**No RRR parameters given, only URR parameters; Correct outgoing spectra in 2015**
n-051_Sb_125.endf	JENDL-3; WPEC/SG-23	2006			JNDC	1990	JNDC	1990			
n-051_Sb_126.endf	ENDF/B-VII.0; WPEC/SG-23	2006	BNL	2006	BNL	2006	BNL	2006			
n-052_Te_120.endf	JENDL-3; WPEC/SG-23	2006			JNDC	1990	JNDC	1990			No RRR parameters given, only URR parameters
n-052_Te_121.endf	**ENDF/B-VIII.0**	**2017**	**BNL**	**2017**			**BNL**	**2017**			**TENDL+EMPIRE**
n-052_Te_121m1.endf	**ENDF/B-VIII.0**	**2017**	**BNL**	**2017**			**BNL**	**2017**			**TENDL+EMPIRE**
n-052_Te_122.endf	JENDL-3.2; WPEC/SG-23	2006	BNL	2006	JNDC	1993	JNDC	1993			
n-052_Te_123.endf	JENDL-3.2; WPEC/SG-23	2006	BNL	2006	JNDC	1993	JNDC	1993			
n-052_Te_124.endf	JENDL-3.2; WPEC/SG-23	2006	BNL	2006	JNDC	1993	JNDC	1993			
n-052_Te_125.endf	JENDL-3; WPEC/SG-23	2006	BNL	2006	JNDC	1990	JNDC	1990			
n-052_Te_126.endf	JENDL-3.2; WPEC/SG-23	2006	BNL	2006	JNDC	1993	JNDC	1993			
n-052_Te_127m1.endf	JENDL-3; WPEC/SG-23	2006			JNDC	1990	JNDC	1990			No RRR parameters given, only URR parameters
n-052_Te_128.endf	JENDL-3; WPEC/SG-23	2006	BNL	2006	JNDC	1990	JNDC	1990			
n-052_Te_129m1.endf	JENDL-3; WPEC/SG-23	2006			JNDC	1990	JNDC	1990			No RRR parameters given, only URR parameters
n-052_Te_130.endf	CENDL-3; WPEC/SG-23	2006	BNL	2006	JNDC	1994	CNDC	2001			
n-052_Te_131.endf	**ENDF/B-VIII.0**	**2017**	**BNL**	**2017**			**BNL**	**2017**			**TENDL+EMPIRE**
n-052_Te_131m1.endf	**ENDF/B-VIII.0**	**2017**	**BNL**	**2017**			**BNL**	**2017**			**TENDL+EMPIRE**

TABLE XLV: Summary of the origins of and recent changes to the neutron (`neutrons`) sublibrary. Evaluations modified for ENDF/B-VIII.0 are given in bold.

		Last	RRR		URR		Smooth Region		High-energy		
File name	Main source	mod.	Lab.	Year	Lab.	Year	Lab.	Year	Lab.	Year	Note
n-052_Te_132.endf	**ENDF/B-VIII.0; WPEC/SG-23**	**2017**	**BNL**	**2006**	**BNL**	**2006**	**LANL**	**2016**			
n-053_I_127.endf	**ENDF/B-VI; WPEC/SG-23**	**2016**	**BNL**	**2006**			**LANL**	**2005**			**COMMARA-2.0 covariances added in 2011**
n-053_I_128.endf	**ENDF/B-VIII.0**	**2017**	**BNL**	**2017**			**BNL**	**2017**			**TENDL+EMPIRE**
n-053_I_129.endf	JENDL-3; WPEC/SG-23	2006	BNL	2006	JNDC	1990	JNDC	1990			COMMARA-2.0 covariances added in 2011
n-053_I_130.endf	ENDF/B-VII.0; WPEC/SG-23	2006	BNL	2006	BNL	2006	BNL	2006			
n-053_I_131.endf	JENDL-3; WPEC/SG-23	2006			JNDC	1990	JNDC	1990			No RRR parameters given, only URR parameters
n-053_I_132.endf	**ENDF/B-VIII.0**	**2017**	**BNL**	**2017**			**BNL**	**2017**			**TENDL+EMPIRE**
n-053_I_132m1.endf	**ENDF/B-VIII.0**	**2017**	**BNL**	**2017**			**BNL**	**2017**			**TENDL+EMPIRE**
n-053_I_133.endf	**ENDF/B-VIII.0**	**2017**	**BNL**	**2017**			**BNL**	**2017**			**TENDL+EMPIRE**
n-053_I_134.endf	**ENDF/B-VIII.0**	**2017**	**BNL**	**2017**			**BNL**	**2017**			**TENDL+EMPIRE**
n-053_I_135.endf	CENDL-3; WPEC/SG-23	2006					CNDC	2001			No RRR parameters given
n-054_Xe_123.endf	**ENDF/B-VII.1**	**2016**					**LLNL**	**2011**			**No RRR parameters given**
n-054_Xe_124.endf	**ENDF/B-VIII.0**	**2016**	**JAEA**	**2009**	**JAEA**	**2009**	**LANL**	**2016**			
n-054_Xe_125.endf	**ENDF/B-VIII.0**	**2017**	**BNL**	**2017**			**BNL**	**2017**			**TENDL+EMPIRE**
n-054_Xe_126.endf	JENDL-3; WPEC/SG-23	2006	BNL	2006	JNDC	1990	JNDC	1990			
n-054_Xe_127.endf	**ENDF/B-VIII.0**	**2017**	**BNL**	**2017**			**BNL**	**2017**			**TENDL+EMPIRE**
n-054_Xe_128.endf	JENDL-3; WPEC/SG-23	2006	BNL	2006	JNDC	1990	JNDC	1990			
n-054_Xe_129.endf	JENDL-3; WPEC/SG-23	2006	BNL	2006	JNDC	1990	JNDC	1990			
n-054_Xe_130.endf	ENDF/B-V; WPEC/SG-23	2006	BNL	2006			BNL	1978			
n-054_Xe_131.endf	ENDF/B-VII.0; WPEC/SG-23	2006	BNL/ KAERI	1999	BNL/ KAERI	1999	BNL/ KAERI	2006			COMMARA-2.0 covariances added in 2011
n-054_Xe_132.endf	CENDL-3; WPEC/SG-23	2006	BNL	2006	JNDC	1990	CNDC	2001			COMMARA-2.0 covariances added in 2011
n-054_Xe_133.endf	JENDL-3; WPEC/SG-23	2006			JNDC	1990	JNDC	1990			No RRR parameters given, only URR parameters
n-054_Xe_134.endf	CENDL-3; WPEC/SG-23	2006	BNL	2006	JNDC	1990	CNDC	2001			COMMARA-2.0 covariances added in 2011
n-054_Xe_135.endf	**JENDL-3; WPEC/SG-23**	**2016**	**JNDC**	**1990**	**JNDC**	**1990**	**JNDC**	**1990**			**Convert RRR from SLBW to MLBW in 2016**
n-054_Xe_136.endf	CENDL-3; WPEC/SG-23	2006	BNL	2006			CNDC	2000			
n-055_Cs_133.endf	ENDF/B-VII.1	2006	BNL	2010	BNL	2010	BNL	2006			COMMARA-2.0 covariances added in 2011
n-055_Cs_134.endf	JENDL-3; WPEC/SG-23	2006	BNL	2006	JNDC	1990	JNDC	1990			
n-055_Cs_135.endf	JENDL-3; WPEC/SG-23	2006	BNL	2006	JNDC	1990	JNDC	1990			COMMARA-2.0 covariances added in 2011
n-055_Cs_136.endf	JENDL-3; WPEC/SG-23	2006			JNDC	1990	JNDC	1990			No RRR parameters given, only URR parameters
n-055_Cs_137.endf	JENDL-3; WPEC/SG-23	2006			JNDC	1990	JNDC	1990			No RRR parameters given, only URR parameters
n-056_Ba_130.endf	JENDL-3; WPEC/SG-23	2006	BNL	2006	JNDC	1990	JNDC	1990			
n-056_Ba_131.endf	**ENDF/B-VIII.0**	**2017**	**BNL**	**2017**			**BNL**	**2017**			**TENDL+EMPIRE**
n-056_Ba_132.endf	JENDL-3; WPEC/SG-23	2006	BNL	2006	JNDC	1990	JNDC	1990			
n-056_Ba_133.endf	ENDF/B-VII.0; WPEC/SG-23	2006	BNL	2006	BNL	2006	BNL	2006			
n-056_Ba_134.endf	JENDL-3; WPEC/SG-23	2006	BNL	2006	JNDC	1990	JNDC	1990			
n-056_Ba_135.endf	JENDL-3; WPEC/SG-23	2006	BNL	2006	JNDC	1990	JNDC	1990			
n-056_Ba_136.endf	JENDL-3; WPEC/SG-23	2006	BNL	2006	JNDC	1990	JNDC	1990			
n-056_Ba_137.endf	JENDL-3; WPEC/SG-23	2006	BNL	2006	JNDC	1990	JNDC	1990			
n-056_Ba_138.endf	CENDL-3; WPEC/SG-23	2006	BNL	2006			CNDC	2001			
n-056_Ba_139.endf	**ENDF/B-VIII.0**	**2017**	**BNL**	**2017**			**BNL**	**2017**			**TENDL+EMPIRE**
n-056_Ba_140.endf	JEF-2; WPEC/SG-23	2006	ENEA	1977	ENEA	1977	ENEA	1989			RRR randomly generated
n-057_La_138.endf	JENDL-3; WPEC/SG-23	2006	JNDC	1990	JNDC	1990	JNDC	1990			
n-057_La_139.endf	CENDL-3; WPEC/SG-23	2006	BNL	2006	JNDC	1993	CNDC	2001			COMMARA-2.0 covariances added in 2011
n-057_La_140.endf	ENDF/B-VII.0; WPEC/SG-23	2006	BNL	2006	BNL	2006	BNL	2006			
n-058_Ce_136.endf	ENDF/B-VII.0; WPEC/SG-23	2006	BNL	2006	BNL	2006	BNL	2006			

TABLE XLV: Summary of the origins of and recent changes to the neutron (`neutrons`) sublibrary. Evaluations modified for ENDF/B-VIII.0 are given in bold.

File name	Main source	Last mod.	RRR Lab.	RRR Year	URR Lab.	URR Year	Smooth Region Lab.	Smooth Region Year	High-energy Lab.	High-energy Year	Note
n-058_Ce_137.endf	**ENDF/B-VIII.0**	**2017**	**BNL**	**2017**			**BNL**	**2017**			**TENDL+EMPIRE**
n-058_Ce_137m1.endf	**ENDF/B-VIII.0**	**2017**	**BNL**	**2017**			**BNL**	**2017**			**TENDL+EMPIRE**
n-058_Ce_138.endf	ENDF/B-VII.0; WPEC/SG-23	2006	BNL	2006	BNL	2006	BNL	2006			
n-058_Ce_139.endf	ENDF/B-VII.0	2006	BNL	2006	BNL	2006	BNL	2006			
n-058_Ce_140.endf	JENDL-3; WPEC/SG-23	2006	BNL	2006			JNDC	1990			
n-058_Ce_141.endf	CENDL-3; WPEC/SG-23	2006	BNL	2006	JNDC	1990	CNDC	2000			
n-058_Ce_142.endf	JENDL-3.2; WPEC/SG-23	2006	BNL	2006	JNDC	1993	JNDC	1993			
n-058_Ce_143.endf	ENDF/B-VII.0; WPEC/SG-23	2006	BNL	2006	BNL	2006	BNL	2006			
n-058_Ce_144.endf	JENDL-3; WPEC/SG-23	2006			JNDC	1990	JNDC	1990			No RRR parameters given, only URR parameters
n-059_Pr_141.endf	ENDF/B-VII.0; WPEC/SG-23	2006	BNL	2006	BNL	2006	BNL/ KAERI	2006			COMMARA-2.0 covariances added in 2011
n-059_Pr_142.endf	ENDF/B-VII.0; WPEC/SG-23	2006	BNL	2006	BNL	2006	BNL	2006			
n-059_Pr_143.endf	JENDL-3; WPEC/SG-23	2006	BNL	2006	JNDC	1990	JNDC	1990			
n-060_Nd_142.endf	ENDF/B-VII.0; WPEC/SG-23	2006	BNL	2006	BNL	2006	BNL/ KAERI	2006			
n-060_Nd_143.endf	ENDF/B-VII.0; WPEC/SG-23	2006	BNL/ KAERI	1999	BNL/ KAERI	1999	BNL/ KAERI	2006			COMMARA-2.0 covariances added in 2011
n-060_Nd_144.endf	ENDF/B-VII.0; WPEC/SG-23	2006	BNL	2006	BNL	2006	BNL/ KAERI	2006			
n-060_Nd_145.endf	ENDF/B-VII.0	2006	BNL	2010	BNL	2010	BNL/ KAERI	2006			COMMARA-2.0 covariances added in 2011
n-060_Nd_146.endf	ENDF/B-VII.0; WPEC/SG-23	2006	BNL	2006	BNL	2006	BNL/ KAERI	2006			COMMARA-2.0 covariances added in 2011
n-060_Nd_147.endf	ENDF/B-VII.0; WPEC/SG-23	2006	BNL	2006	BNL	2006	BNL/ KAERI	2006			
n-060_Nd_148.endf	ENDF/B-VII.0; WPEC/SG-23	2006	BNL	2006	BNL	2006	BNL/ KAERI	2006			COMMARA-2.0 covariances added in 2011
n-060_Nd_149.endf	**ENDF/B-VIII.0**	**2017**	**BNL**	**2017**			**BNL**	**2017**			**TENDL+EMPIRE**
n-060_Nd_150.endf	ENDF/B-VII.0; WPEC/SG-23	2006	BNL	2006	BNL	2006	BNL/ KAERI	2006			
n-061_Pm_143.endf	**TENDL-2015**	**2017**	**TENDL**	**2015**			**TENDL**	**2015**	**TENDL**	**2015**	**TENDL+EMPIRE**
n-061_Pm_144.endf	**TENDL-2015**	**2017**	**TENDL**	**2015**			**TENDL**	**2015**	**TENDL**	**2015**	**TENDL+EMPIRE**
n-061_Pm_145.endf	**TENDL-2015**	**2017**	**TENDL**	**2015**			**TENDL**	**2015**	**TENDL**	**2015**	**TENDL+EMPIRE**
n-061_Pm_146.endf	**ENDF/B-VIII.0**	**2017**	**TENDL**	**2015**			**BNL**	**2017**			**TENDL+EMPIRE**
n-061_Pm_147.endf	JENDL-3; WPEC/SG-23	2006	JNDC	1990	JNDC	1990	JNDC	1990			COMMARA-2.0 covariances added in 2011
n-061_Pm_148.endf	JENDL-3; WPEC/SG-23	2006			JNDC	1990	JNDC	1990			No RRR parameters given, only URR parameters
n-061_Pm_148m1.endf	**CENDL-3; WPEC/SG-23**	**2016**	**BNL**	**1973**			**CNDC**	**2001**			**Lone resonance converted from SLBW to MLBW**
n-061_Pm_149.endf	JENDL-3; WPEC/SG-23	2006			JNDC	1990	JNDC	1990			No RRR parameters given, only URR parameters
n-061_Pm_150.endf	**ENDF/B-VIII.0**	**2017**	**BNL**	**2017**			**BNL**	**2017**			**TENDL+EMPIRE**
n-061_Pm_151.endf	ENDF/B-VII.0; WPEC/SG-23	2006	BNL	2006	BNL	2006	BNL	2006			
n-062_Sm_144.endf	**ENDF/B-VII.0; WPEC/SG-23**	**2016**	**BNL**	**2006**	**BNL**	**2006**	**BNL/ KAERI**	**2006**			**Fix URR grid in 2016**
n-062_Sm_145.endf	**TENDL-2015**	**2017**	**TENDL**	**2015**			**TENDL**	**2015**	**TENDL**	**2015**	**TENDL+EMPIRE**
n-062_Sm_146.endf	**ENDF/B-VIII.0**	**2017**	**BNL**	**2017**			**BNL**	**2017**			**TENDL+EMPIRE**
n-062_Sm_147.endf	ENDF/B-VII.0; WPEC/SG-23	2006	BNL	2006	BNL	2006	BNL/ KAERI	2006			
n-062_Sm_148.endf	ENDF/B-VII.0; WPEC/SG-23	2006	BNL	2006	BNL	2006	BNL/ KAERI	2006			
n-062_Sm_149.endf	ENDF/B-VII.0; WPEC/SG-23	2006	BNL	2006	BNL	2006	BNL/ KAERI	2006			COMMARA-2.0 covariances added in 2011
n-062_Sm_150.endf	ENDF/B-VII.0; WPEC/SG-23	2006	BNL	2006	BNL	2006	BNL/ KAERI	2006			
n-062_Sm_151.endf	**ENDF/B-VII.0; WPEC/SG-23**	**2016**	**BNL**	**2006**	**BNL**	**2006**	**BNL/ KAERI**	**2006**			**COMMARA-2.0 covariances added in 2011**
n-062_Sm_152.endf	ENDF/B-VII.0; WPEC/SG-23	2006	BNL	2006	BNL	2006	BNL/ KAERI	2006			COMMARA-2.0 covariances added in 2011; Fix spectra in 2015
n-062_Sm_153.endf	ENDF/B-VII.0; WPEC/SG-23	2006	BNL	2006	BNL	2006	BNL/ KAERI	2006			
n-062_Sm_154.endf	ENDF/B-VII.0; WPEC/SG-23	2006	BNL	2006	BNL	2006	BNL/ KAERI	2006			
n-063_Eu_151.endf	CENDL-3; WPEC/SG-23	2006	BNL	2006	JNDC	1989	CNDC	2001			
n-063_Eu_152.endf	JENDL-3; WPEC/SG-23	2006	ORNL	1988	JNDC	1990	JNDC	1990			

TABLE XLV: Summary of the origins of and recent changes to the neutron (`neutrons`) sublibrary. Evaluations modified for ENDF/B-VIII.0 are given in bold.

		Last	RRR		URR		Smooth Region		High-energy		
File name	Main source	mod.	Lab.	Year	Lab.	Year	Lab.	Year	Lab.	Year	Note
n-063_Eu_153.endf	**ENDF/B-VII.0**	**2017**	**BNL**	**2011**	**BNL**	**2011**	**BNL/ KAERI**	**2006**			**COMMARA-2.0 covariances added in 2011; Double differential spectra fixed 2015**
n-063_Eu_154.endf	**CENDL-3; WPEC/SG-23**	**2017**	**BNL**	**2006**	**JNDC**	**1990**	**CNDC**	**2001**			
n-063_Eu_155.endf	CENDL-3; WPEC/SG-23	2006	JNDC	1990	JNDC	1990	CNDC	2001			COMMARA-2.0 covariances added in 2011
n-063_Eu_156.endf	JENDL-3; WPEC/SG-23	2006			JNDC	1990	JNDC	1990			No RRR parameters given, only URR parameters
n-063_Eu_157.endf	ENDF/B-VII.0; WPEC/SG-23	2006	BNL	2006	BNL	2006	BNL	2006			
n-064_Gd_152.endf	ENDF/B-VII.0; WPEC/SG-23	2006	BNL	2006	BNL	2006	BNL	2006			Covariances from ORNL (RR) and LANL (Fast)
n-064_Gd_153.endf	ENDF/B-VII.0; WPEC/SG-23	2006	BNL	2006	BNL	2006	BNL	2006			Covariances from ORNL (RR) and LANL (Fast)
n-064_Gd_154.endf	ENDF/B-VII.0; WPEC/SG-23	2006	BNL	2006	BNL	2006	BNL	2006			Covariances from ORNL (RR) and LANL (Fast)
n-064_Gd_155.endf	ENDF/B-VII.0; WPEC/SG-23	2006	BNL	2006	BNL	2006	BNL	2006			Covariances from ORNL (RR) and LANL (Fast)
n-064_Gd_156.endf	ENDF/B-VII.0; WPEC/SG-23	2006	BNL	2006	BNL	2006	BNL	2006			COMMARA-2.0 covariances added in 2011
n-064_Gd_157.endf	ENDF/B-VII.0; WPEC/SG-23	2006	BNL	2006	BNL	2006	BNL	2006			COMMARA-2.0 covariances added in 2011
n-064_Gd_158.endf	ENDF/B-VII.0; WPEC/SG-23	2006	BNL	2006	BNL	2006	BNL	2006			COMMARA-2.0 covariances added in 2011
n-064_Gd_159.endf	**ENDF/B-VIII.0**	**2017**	**BNL**	**2017**			**BNL**	**2017**			**TENDL+EMPIRE**
n-064_Gd_160.endf	ENDF/B-VII.0; WPEC/SG-23	2006	BNL	2006	BNL	2006	BNL	2006			COMMARA-2.0 covariances added in 2011
n-065_Tb_158.endf	**ENDF/B-VIII.0**	**2017**	**TENDL**	**2015**			**BNL**	**2017**			**TENDL+EMPIRE**
n-065_Tb_159.endf	JENDL-3; WPEC/SG-23	2006	BNL	2006	JNDC	1990	JNDC	1990			
n-065_Tb_160.endf	ENDF/B-VII.0; WPEC/SG-23	2006	BNL	2006	BNL	2006	BNL	2006			
n-065_Tb_161.endf	**ENDF/B-VIII.0**	**2017**	**TENDL**	**2015**			**BNL**	**2017**			**TENDL+EMPIRE**
n-066_Dy_154.endf	**JENDL-4.0**	**2016**			**JAEA**	**2009**	**JAEA**	**2009**			**No RRR parameters given, only URR parameters**
n-066_Dy_155.endf	**ENDF/B-VIII.0**	**2017**	**BNL**	**2017**			**BNL**	**2017**			**TENDL+EMPIRE**
n-066_Dy_156.endf	ENDF/B-VII.0; WPEC/SG-23	2006	BNL	2006	BNL	2006	BNL/ KAERI	2006			
n-066_Dy_157.endf	**ENDF/B-VIII.0**	**2017**	**BNL**	**2017**			**BNL**	**2017**			**TENDL+EMPIRE**
n-066_Dy_158.endf	ENDF/B-VII.0; WPEC/SG-23	2006	BNL	2006	BNL	2006	BNL/ KAERI	2006			
n-066_Dy_159.endf	**JENDL-4.0**	**2016**			**JAEA**	**2009**	**JAEA**	**2009**			**No RRR parameters given, only URR parameters**
n-066_Dy_160.endf	**ENDF/B-VII.0; WPEC/SG-23**	**2017**	**KAERI**	**2001**	**KAERI**	**2001**	**BNL/ KAERI**	**2006**			
n-066_Dy_161.endf	ENDF/B-VII.0; WPEC/SG-23	2006	KAERI	2001	KAERI	2001	BNL/ KAERI	2006			
n-066_Dy_162.endf	ENDF/B-VII.0; WPEC/SG-23	2006	KAERI	2001	KAERI	2001	BNL/ KAERI	2006			
n-066_Dy_163.endf	ENDF/B-VII.0; WPEC/SG-23	2006	KAERI	2001	KAERI	2001	BNL/ KAERI	2006			
n-066_Dy_164.endf	ENDF/B-VII.0; WPEC/SG-23	2006	KAERI	2001	KAERI	2001	BNL/ KAERI	2006			
n-067_Ho_165.endf	ENDF/B-VI; WPEC/SG-23	2006	BNL	2006			LANL	1988			
n-067_Ho_166m1.endf	**ENDF/B-VII.0; WPEC/SG-23**	**2017**	**BNL**	**2006**	**BNL**	**2006**	**BNL**	**2006**			
n-068_Er_162.endf	**JENDL-3.3; WPEC/SG-23**	**2017**	**TIT/ JAERI**	**2001**			**TIT/ JAERI**	**2001**			
n-068_Er_163.endf	**ENDF/B-VIII.0**	**2017**	**BNL**	**2017**			**BNL**	**2017**			**TENDL+EMPIRE**
n-068_Er_164.endf	**JENDL-3.3; WPEC/SG-23**	**2017**	**TIT/ JAERI**	**2001**			**TIT/ JAERI**	**2001**			
n-068_Er_165.endf	**ENDF/B-VIII.0**	**2017**	**BNL**	**2017**			**BNL**	**2017**			**TENDL+EMPIRE**
n-068_Er_166.endf	**JENDL-3.3; WPEC/SG-23**	**2017**	**BNL**	**2006**			**TIT/ JAERI**	**2001**			**COMMARA-2.0 covariances added in 2011**
n-068_Er_167.endf	**JENDL-3.3; WPEC/SG-23**	**2017**	**BNL**	**2006**	**TIT/ JAERI**	**2001**	**TIT/ JAERI**	**2001**			**COMMARA-2.0 covariances added in 2011**
n-068_Er_168.endf	**JENDL-3.3; WPEC/SG-23**	**2017**	**BNL**	**2006**			**TIT/ JAERI**	**2001**			**COMMARA-2.0 covariances added in 2011**
n-068_Er_169.endf	**ENDF/B-VIII.0**	**2017**	**TENDL**	**2015**			**BNL**	**2017**			**TENDL+EMPIRE**

TABLE XLV: Summary of the origins of and recent changes to the neutron (`neutrons`) sublibrary. Evaluations modified for ENDF/B-VIII.0 are given in bold.

		Last	RRR		URR		Smooth Region		High-energy		
File name	Main source	mod.	Lab.	Year	Lab.	Year	Lab.	Year	Lab.	Year	Note
n-068_Er_170.endf	**JENDL-3.3; WPEC/SG-23**	**2017**	**BNL**	**2006**	**IPPE**	**2006**	**TIT/ JAERI**	**2001**			**COMMARA-2.0 covariances added in 2011**
n-069_Tm_168.endf	**ENDF/B-VII.1**	**2017**	**BNL**	**2011**			**BNL**	**2011**			**Fix capture gamma spectrum**
n-069_Tm_169.endf	**ENDF/B-VII.1**	**2017**	**BNL**	**2011**	**BNL**	**2011**	**BNL**	**2011**			
n-069_Tm_170.endf	**ENDF/B-VII.1**	**2017**	**BNL**	**2011**	**BNL**	**2011**	**BNL**	**2011**			
n-069_Tm_171.endf	**ENDF/B-VIII.0**	**2017**	**TENDL**	**2015**			**BNL**	**2017**			**TENDL+EMPIRE**
n-070_Yb_168.endf	**JENDL-4.0**	**2016**	**JAEA**	**2010**	**JAEA**	**2010**	**JAEA**	**2010**			
n-070_Yb_169.endf	**ENDF/B-VIII.0**	**2017**	**BNL**	**2017**			**BNL**	**2017**			**TENDL+EMPIRE**
n-070_Yb_170.endf	**JENDL-4.0**	**2016**	**JAEA**	**2010**	**JAEA**	**2010**	**JAEA**	**2010**			
n-070_Yb_171.endf	**JENDL-4.0**	**2016**	**JAEA**	**2010**	**JAEA**	**2010**	**JAEA**	**2010**			
n-070_Yb_172.endf	**JENDL-4.0**	**2016**	**JAEA**	**2010**	**JAEA**	**2010**	**JAEA**	**2010**			
n-070_Yb_173.endf	**JENDL-4.0**	**2016**	**JAEA**	**2010**	**JAEA**	**2010**	**JAEA**	**2010**			
n-070_Yb_174.endf	**JENDL-4.0**	**2016**	**JAEA**	**2010**	**JAEA**	**2010**	**JAEA**	**2010**			
n-070_Yb_175.endf	**ENDF/B-VIII.0**	**2017**	**TENDL**	**2015**			**BNL**	**2017**			**TENDL+EMPIRE**
n-070_Yb_176.endf	**JENDL-4.0**	**2016**	**JAEA**	**2010**	**JAEA**	**2010**	**JAEA**	**2010**			
n-071_Lu_175.endf	ENDF/B-VI	2006	BNL	1984	BNL	1998	ORNL	1998			
n-071_Lu_176.endf	ENDF/B-VI	2006	BNL	1984	BNL	1998	ORNL	1998			
n-072_Hf_174.endf	**ENDF/B-VIII.0**	**2017**	**ORNL**	**2009**	**ORNL**	**2009**	**LANL**	**2016**			**RR source is JEFF-3.1 and ENDF/B-VI**
n-072_Hf_175.endf	**ENDF/B-VIII.0**	**2017**	**BNL**	**2017**			**BNL**	**2017**			**TENDL+EMPIRE**
n-072_Hf_176.endf	**ENDF/B-VIII.0**	**2017**	**ORNL**	**2009**	**ORNL**	**2009**	**LANL**	**2016**			**RR source is JEFF-3.1 and ENDF/B-VI**
n-072_Hf_177.endf	**ENDF/B-VIII.0**	**2017**	**ORNL**	**2009**	**ORNL**	**2009**	**LANL**	**2016**			**RR source is JENDL-3.3 and ENDF/B-VI**
n-072_Hf_178.endf	**ENDF/B-VIII.0**	**2017**	**ORNL**	**2009**	**ORNL**	**2009**	**LANL**	**2016**			**RR source is JEFF-3.1 and ENDF/B-VI**
n-072_Hf_179.endf	**ENDF/B-VIII.0**	**2017**	**ORNL**	**2009**	**ORNL**	**2009**	**LANL**	**2016**			**RR source is JENDL-3.3 and ENDF/B-VI**
n-072_Hf_180.endf	**ENDF/B-VIII.0**	**2017**	**ORNL**	**2009**	**ORNL**	**2009**	**LANL**	**2016**			**RR source is JEFF-3.1 and ENDF/B-VI**
n-072_Hf_181.endf	**JENDL-4.0**	**2016**			**JAEA**	**2010**	**JAEA**	**2010**			**No RRR parameters given, only URR parameters**
n-072_Hf_182.endf	**JENDL-4.0**	**2016**			**JAEA**	**2010**	**JAEA**	**2010**			**No RRR parameters given, only URR parameters**
n-073_Ta_180.endf	**ENDF/B-VII.1**	**2017**					**LLNL**	**2011**			**No RRR parameters given; Grids fixed in 2016**
n-073_Ta_181.endf	**ENDF/B-VII.1**	**2017**	**BNL**	**1973**	**BNL**	**1973**	**LLNL**	**2011**			**RR generated by TALYS from Atlas parameters tabulated in JEFF-3.1.1; Cross section energy range fix in 2015**
n-073_Ta_182.endf	ENDF/B-IV	2006	BNL	1971	BNL	1971	BNL	1971			
n-074_W_180.endf	**IAEA W CRP**	**2017**	**BNL**	**2006**			**IAEA**	**2011**			
n-074_W_181.endf	**ENDF/B-VIII.0**	**2017**	**TENDL**	**2015**			**BNL**	**2017**			**TENDL+EMPIRE**
n-074_W_182.endf	**ENDF/B-VIII.0**	**2017**	**ORNL**	**2014**			**IAEA**	**2011**			
n-074_W_183.endf	**IAEA W CRP**	**2017**	**ORNL**	**2014**			**IAEA**	**2011**			
n-074_W_184.endf	**IAEA W CRP**	**2016**	**ORNL**	**2014**	**ORNL**		**IAEA**	**2011**			
n-074_W_185.endf	**ENDF/B-VIII.0**	**2017**	**BNL**	**2017**			**BNL**	**2017**			**TENDL+EMPIRE**
n-074_W_186.endf	**IAEA W CRP**	**2017**	**ORNL**	**2014**	**ORNL**		**IAEA**	**2011**			
n-075_Re_185.endf	**ENDF/B-VII.1**	**2017**	**BNL**	**1984**	**BNL**	**1984**	**LLNL**	**2011**			**R' in RRR corrected in 2015**
n-075_Re_186m1.endf	**ENDF/B-VIII.0**	**2017**	**BNL**	**2017**			**BNL**	**2017**			**TENDL+EMPIRE**
n-075_Re_187.endf	**ENDF/B-VII.1**	**2017**	**BNL**	**1984**	**BNL**	**1984**	**LLNL**	**2011**			**R' in RRR corrected in 2015**
n-076_Os_184.endf	**ENDF/B-VIII.0**	**2016**			**JAEA**	**2010**	**JAEA**	**2010**			**No RRR parameters given, only URR parameters**
n-076_Os_185.endf	**ENDF/B-VIII.0**	**2017**	**TENDL**	**2015**			**BNL**	**2017**			**TENDL+EMPIRE**
n-076_Os_186.endf	**JENDL-4.0**	**2016**	**JAEA**	**2010**	**JAEA**	**2010**	**JAEA**	**2010**			
n-076_Os_187.endf	**JENDL-4.0**	**2016**	**JAEA**	**2010**	**JAEA**	**2010**	**JAEA**	**2010**			
n-076_Os_188.endf	**JENDL-4.0**	**2016**	**JAEA**	**2010**	**JAEA**	**2010**	**JAEA**	**2010**			
n-076_Os_189.endf	**JENDL-4.0**	**2016**	**JAEA**	**2010**	**JAEA**	**2010**	**JAEA**	**2010**			
n-076_Os_190.endf	**JENDL-4.0**	**2016**	**JAEA**	**2010**	**JAEA**	**2010**	**JAEA**	**2010**			
n-076_Os_191.endf	**TENDL-2015**	**2017**	**TENDL**	**2015**			**TENDL**	**2015**	**TENDL**	**2015**	**TENDL+EMPIRE**
n-076_Os_192.endf	**ENDF/B-VIII.0**	**2016**	**JAEA**	**2010**	**JAEA**	**2010**	**JAEA**	**2010**			
n-077_Ir_191.endf	ENDF/B-VII.0	2006	BNL	2006			LANL/BNL	2006			
n-077_Ir_192.endf	**TENDL-2015**	**2017**	**TENDL**	**2015**			**TENDL**	**2015**	**TENDL**	**2015**	**TENDL+EMPIRE**
n-077_Ir_193.endf	ENDF/B-VII.0	2006	BNL	2006	BNL	2006	LANL	2006			
n-077_Ir_194m1.endf	**ENDF/B-VIII.0**	**2017**	**BNL**	**2017**			**BNL**	**2017**			**TENDL+EMPIRE**
n-078_Pt_190.endf	**TENDL-2015**	**2017**	**TENDL**	**2015**			**TENDL**	**2015**	**TENDL**	**2015**	**TENDL+EMPIRE**
n-078_Pt_191.endf	**TENDL-2015**	**2017**	**TENDL**	**2015**			**TENDL**	**2015**	**TENDL**	**2015**	**TENDL+EMPIRE**
n-078_Pt_192.endf	**TENDL-2015**	**2017**	**TENDL**	**2015**			**TENDL**	**2015**	**TENDL**	**2015**	**TENDL+EMPIRE**
n-078_Pt_193.endf	**TENDL-2015**	**2017**	**TENDL**	**2015**			**TENDL**	**2015**	**TENDL**	**2015**	**TENDL+EMPIRE**
n-078_Pt_194.endf	**TENDL-2015**	**2017**	**TENDL**	**2015**			**TENDL**	**2015**	**TENDL**	**2015**	**TENDL+EMPIRE**
n-078_Pt_195.endf	**TENDL-2015**	**2017**	**TENDL**	**2015**			**TENDL**	**2015**	**TENDL**	**2015**	**TENDL+EMPIRE**
n-078_Pt_196.endf	**TENDL-2015**	**2017**	**TENDL**	**2015**			**TENDL**	**2015**	**TENDL**	**2015**	**TENDL+EMPIRE**
n-078_Pt_197.endf	**TENDL-2015**	**2017**	**TENDL**	**2015**			**TENDL**	**2015**	**TENDL**	**2015**	**TENDL+EMPIRE**
n-078_Pt_198.endf	**TENDL-2015**	**2017**	**TENDL**	**2015**			**TENDL**	**2015**	**TENDL**	**2015**	**TENDL+EMPIRE**
n-079_Au_197.endf	**ENDF/B-VII.0; Standards 2017**	**2017**	**IRMM**	**2017**	**IRMM**	**2017**	**LANL**	**1984**			**TENDL+EMPIRE**
n-080_Hg_196.endf	JENDL-3.3	2006	JNDC	1997			JNDC	1997	LANL	1998	
n-080_Hg_197.endf	**ENDF/B-VIII.0**	**2017**	**BNL**	**2017**			**BNL**	**2017**			**TENDL+EMPIRE**
n-080_Hg_197m1.endf	**ENDF/B-VIII.0**	**2017**	**BNL**	**2017**			**BNL**	**2017**			**TENDL+EMPIRE**
n-080_Hg_198.endf	JENDL-3.3	2006	JNDC	1997			JNDC	1997	LANL	1998	
n-080_Hg_199.endf	JENDL-3.3	2006	JNDC	1997			JNDC	1997	LANL	1998	

TABLE XLV: Summary of the origins of and recent changes to the neutron (`neutrons`) sublibrary. Evaluations modified for ENDF/B-VIII.0 are given in bold.

		Last	RRR		URR		Smooth Region		High-energy		
File name	Main source	mod.	Lab.	Year	Lab.	Year	Lab.	Year	Lab.	Year	Note
n-080_Hg_200.endf	JENDL-3.3	2006	JNDC	1997			JNDC	1997	LANL	1998	
n-080_Hg_201.endf	JENDL-3.3	2006	JNDC	1997			JNDC	1997	LANL	1998	
n-080_Hg_202.endf	JENDL-3.3	2006	JNDC	1997			JNDC	1997	LANL	1998	
n-080_Hg_203.endf	**TENDL-2015**	**2017**	**TENDL**	**2015**			**TENDL**	**2015**	**TENDL**	**2015**	**TENDL+EMPIRE**
n-080_Hg_204.endf	JENDL-3.3	2006					JNDC	1997	LANL	1998	No RRR parameters given
n-081_Tl_203.endf	ENDF/B-VII.1	2011	BNL	2011	BNL	2011	BNL	2011			
n-081_Tl_204.endf	**TENDL-2015**	**2017**	**TENDL**	**2015**			**TENDL**	**2015**	**TENDL**	**2015**	**TENDL+EMPIRE**
n-081_Tl_205.endf	ENDF/B-VII.1	2011	BNL	2011	BNL	2011	BNL	2011			
n-082_Pb_204.endf	JEFF-3.1	2006	JNDC	1987			NRG	2004	NRG	2004	COMMARA-2.0 covariances added in 2011
n-082_Pb_205.endf	**TENDL-2015**	**2017**	**TENDL**	**2015**			**TENDL**	**2015**	**TENDL**	**2015**	**TENDL+EMPIRE**
n-082_Pb_206.endf	JEFF-3.1	2006	ORNL	1989			NRG	2004	NRG	2004	COMMARA-2.0 covariances added in 2011
n-082_Pb_207.endf	JEFF-3.1	2006	ORNL	1989			NRG	2004	NRG	2004	COMMARA-2.0 covariances added in 2011
n-082_Pb_208.endf	**ENDF/B-VII.0**	**2017**	**ORNL/LANL**	**2006**			**LANL**	**1996**	**LANL**	**2006**	**RRR updated in 2006 by LANL; COMMARA-2.0 covariances added in 2011**
n-083_Bi_209.endf	ENDF/B-VI	2006	BNL	1984			ANL	1989	LANL	1999	COMMARA-2.0 covariances added in 2011
n-083_Bi_210m1.endf	**ENDF/B-VIII.0**	**2017**	**BNL**	**2017**			**BNL**	**2017**			**TENDL+EMPIRE**
n-084_Po_208.endf	**TENDL-2015**	**2017**	**TENDL**	**2015**			**TENDL**	**2015**	**TENDL**	**2015**	**TENDL+EMPIRE**
n-084_Po_209.endf	**ENDF/B-VIII.0**	**2017**	**TENDL**	**2015**			**BNL**	**2017**			**TENDL+EMPIRE**
n-084_Po_210.endf	**TENDL-2015**	**2017**	**TENDL**	**2015**			**TENDL**	**2015**	**TENDL**	**2015**	**TENDL+EMPIRE**
n-088_Ra_223.endf	JENDL-3	2006					TIT/JAERI	1988			No RRR parameters given
n-088_Ra_224.endf	JENDL-3	2006					TIT/JAERI	1988			No RRR parameters given
n-088_Ra_225.endf	JENDL-3	2006					TIT/JAERI	1988			No RRR parameters given
n-088_Ra_226.endf	JENDL-3	2006	TIT/JAERI	1988			TIT/JAERI	1988			
n-089_Ac_225.endf	**JENDL-4.0**	**2016**					**JAEA**	**2010**			**No RRR parameters given**
n-089_Ac_226.endf	**JENDL-4.0**	**2016**					**JAEA**	**2010**			**No RRR parameters given**
n-089_Ac_227.endf	**JENDL-4.0**	**2016**					**JAEA**	**2010**			**No RRR parameters given**
n-090_Th_227.endf	JENDL-4.0	2010					JAEA	2010			
n-090_Th_228.endf	**JENDL-4.0**	**2016**	**JAEA**	**2010**	**JAEA**	**2010**	**JAEA**	**2010**			
n-090_Th_229.endf	JENDL-4.0	2010	JAEA	2010	JAEA	2010	JAEA	2010			
n-090_Th_230.endf	**JENDL-4.0**	**2016**	**JAEA**	**2010**	**JAEA**	**2010**	**JAEA**	**2010**			
n-090_Th_231.endf	**JENDL-4.0**	**2016**					**JAEA**	**2010**			
n-090_Th_232.endf	**IAEA Th-U CRP**	**2016**	**ORNL**	**2005**	**IRMM**	**2005**	**IAEA**	**2006**	**IAEA**	**2006**	
n-090_Th_233.endf	**JENDL-4.0**	**2016**					**JAEA**	**2010**			
n-090_Th_234.endf	**JENDL-4.0**	**2016**					**JAEA**	**2010**			
n-091_Pa_229.endf	**JENDL-4.0**	**2016**					**JAEA**	**2010**			**No RRR parameters given**
n-091_Pa_230.endf	**JENDL-4.0**	**2016**					**JAEA**	**2010**			**No RRR parameters given**
n-091_Pa_231.endf	**IAEA Th-U CRP**	**2016**	**ORNL/BNL**	**2006**	**ORNL**	**2006**	**IAEA**	**2006**	**IAEA**	**2006**	
n-091_Pa_232.endf	**JENDL-4.0**	**2016**	**JAEA**	**2010**	**JAEA**	**2010**	**JAEA**	**2010**			
n-091_Pa_233.endf	**IAEA Th-U CRP**	**2016**	**ORNL**	**2006**	**IAEA**	**2003**	**IAEA**	**2006**	**IAEA**	**2006**	
n-092_U_230.endf	**JENDL-4.0**	**2016**					**JAEA**	**2010**			**No RRR parameters given**
n-092_U_231.endf	**JENDL-4.0**	**2016**					**JAEA**	**2010**			**No RRR parameters given**
n-092_U_232.endf	JENDL-4.0	2010	JAEA	2010	JAEA	2010	JAEA	2010			
n-092_U_233.endf	**ENDF/B-VII.0**	**2017**	**IAEA**	**2017**	**JAEA**	**2010**	**JAEA**	**2010**			**Bound level changed from JENDL-4.0 RRR**
n-092_U_234.endf	ENDF/B-VII.0	2006	LANL	2006	LANL	2006	LANL/IAEA	2010			COMMARA-2.0 covariances added in 2011
n-092_U_235.endf	**ENDF/B-VIII.0; Standards 2017; CIELO 2017**	**2017**	**ORNL/IAEA**	**2017**	**ORNL**	**1997**	**IAEA/LANL**	**2017**			**Largely new evaluation; URR cross section rescaled to match Standards 2017 but URR parameters not updated.**
n-092_U_236.endf	ENDF/B-VII.0	2006	BNL	1989	BNL	1978	LANL	2010			COMMARA-2.0 covariances added in 2011
n-092_U_237.endf	**ENDF/B-VII.0**	**2017**	**JNDC**	**1993**	**JNDC**	**1993**	**LANL**	**2010**			
n-092_U_238.endf	**ENDF/B-VIII.0; Standards 2017; CIELO 2017**	**2017**	**JRC-Geel/ORNL**	**2017**	**JRC-Geel/ORNL**	**2017**	**IAEA/LANL**	**2006**			**Largely new evaluation**
n-092_U_239.endf	**ENDF/B-VII.1**	**2016**	**LLNL**	**2016**	**LLNL**	**2011**	**LLNL**	**2011**			
n-092_U_240.endf	**ENDF/B-VII.0**	**2017**	**LANL**	**2003**	**LANL**	**2003**	**LANL**	**2003**			**Resonances from ENDF/B-VI 242Pu evaluation**
n-092_U_241.endf	**ENDF/B-VII.0**	**2017**	**LANL/BNL**	**2016**	**LANL**	**2000**	**LANL**	**2000**			
n-093_Np_234.endf	**JENDL-4.0**	**2016**					**JAEA**	**2010**			**No RRR parameters given**
n-093_Np_235.endf	**JENDL-4.0**	**2016**					**JAEA**	**2010**			**No RRR parameters given**

TABLE XLV: Summary of the origins of and recent changes to the neutron (`neutrons`) sublibrary. Evaluations modified for ENDF/B-VIII.0 are given in bold.

			RRR		URR		Smooth Region		High-energy		
File name	Main source	Last mod.	Lab.	Year	Lab.	Year	Lab.	Year	Lab.	Year	Note
n-093_Np_236.endf	**JENDL-4.0**	**2016**	**JAEA**	**2010**	**JAEA**	**2010**	**JAEA**	**2010**			**RQ Wright nubars added in 2016**
n-093_Np_236m1.endf	**ENDF/B-VIII.0**	**2016**	**JAEA**	**2010**			**LANL**	**2012**			
n-093_Np_237.endf	ENDF/B-VII.0	2006	LANL	2010	LANL	2006	LANL	2010			COMMARA-2.0 covariances added in 2011
n-093_Np_238.endf	**JENDL-4.0**	**2016**	**JAEA**	**2010**	**JAEA**	**2010**	**JAEA**	**2010**			**RQ Wright nubars added in 2016**
n-093_Np_239.endf	**JENDL-4.0**	**2016**					**JAEA**	**2010**			**No RRR parameters given**
n-094_Pu_236.endf	**JENDL-4.0**	**2016**	**JAEA**	**2010**	**JAEA**	**2010**	**JAEA**	**2010**			
n-094_Pu_237.endf	**JENDL-4.0**	**2016**					**JAEA**	**2010**			**No RRR parameters given**
n-094_Pu_238.endf	**ENDF/B-VII.1**	**2016**	**JAEA**	**2010**	**JAEA**	**2010**	**LANL**	**2010**			
n-094_Pu_239.endf	**ENDF/B-VIII.0; Standards 2017; CIELO 2017**	**2017**	**ORNL/ CEA**	**2012**	**ORNL**	**1993**	**LANL/ IAEA**	**2017**			**WPEC/SG-34 RRR and RRR covariance; New fission data**
n-094_Pu_240.endf	**ENDF/B-VIII.0**	**2017**	**ORNL**	**2017**	**ORNL**	**1986**	**LANL**	**2009**			**Unclear when URR evaluated**
n-094_Pu_241.endf	ENDF/B-VI	2010	ORNL	2003	ORNL	1988	ORNL	1988			Fission cross section covariance added in 2010 by LANL
n-094_Pu_242.endf	JENDL-4.0	2011	BNL	2011	BNL	2011	JAEA	2010			COMMARA-2.0 covariances added in 2011
n-094_Pu_243.endf	**ENDF/B-V**	**2016**	**LLNL**	**1976**	**LLNL**	**1976**	**LLNL**	**1976**			**RQ Wright nubars added in 2016**
n-094_Pu_244.endf	**JENDL-4.0**	**2016**	**JAEA**	**2010**	**JAEA**	**2010**	**JAEA**	**2010**			**RQ Wright nubars added in 2016**
n-094_Pu_245.endf	**ENDF/B-VIII.0**	**2017**	**BNL**	**2017**			**BNL**	**2017**			**TENDL+EMPIRE**
n-094_Pu_246.endf	**JENDL-4.0**	**2016**					**JAEA**	**2010**			**No RRR parameters given; RQ Wright nubars added in 2016**
n-095_Am_240.endf	**JENDL-4.0**	**2016**					**JAEA**	**2010**			**No RRR parameters given**
n-095_Am_241.endf	**ENDF/B-VII.0**	**2017**	**JAEA**	**2010**	**JAEA**	**2010**	**LANL**	**2017**			**(n,2n) and capture changed**
n-095_Am_242.endf	**ENDF/B-VII.0**	**2016**	**JAEA**	**2000**	**JAEA**	**2000**	**LANL**	**2004**			
n-095_Am_242m1.endf	**ENDF/B-VII.0**	**2017**	**JAEA**	**2000**	**JAEA**	**2000**	**LANL**	**2005**			**COMMARA-2.0 covariances added in 2011**
n-095_Am_243.endf	**ENDF/B-VII.0**	**2017**	**BNL**	**2011**	**BNL**	**2011**	**LANL**	**2006**			**COMMARA-2.0 covariances added in 2011**
n-095_Am_244.endf	JENDL-3	2006					JAEA	1988			No RRR parameters given
n-095_Am_244m1.endf	JENDL-3	2006					JAEA	1988			No RRR parameters given
n-096_Cm_240.endf	**JENDL-4.0**	**2016**					**JAEA**	**2010**			**No RRR parameters given**
n-096_Cm_241.endf	**JENDL-4.0**	**2016**					**JAEA**	**2010**			**No RRR parameters given; RQ Wright nubars added in 2016**
n-096_Cm_242.endf	**JENDL-4.0**	**2016**	**JAEA**	**2010**	**JAEA**	**2010**	**JAEA**	**2010**			**RQ Wright nubars added in 2016**
n-096_Cm_243.endf	**JENDL-4.0**	**2017**	**JAEA**	**2010**	**JAEA**	**2010**	**JAEA**	**2010**			
n-096_Cm_244.endf	**JENDL-4.0**	**2016**	**JAEA**	**2010**	**JAEA**	**2010**	**JAEA**	**2010**			**RQ Wright nubars added in 2016**
n-096_Cm_245.endf	JENDL-4.0	2010	JAEA	2010	JAEA	2010	JAEA	2010			
n-096_Cm_246.endf	**JENDL-4.0**	**2016**	**JAEA**	**2010**	**JAEA**	**2010**	**JAEA**	**2010**			**RQ Wright nubars added in 2016**
n-096_Cm_247.endf	**JENDL-4.0**	**2016**	**JAEA**	**2010**	**JAEA**	**2010**	**JAEA**	**2010**			**RQ Wright nubars added in 2016**
n-096_Cm_248.endf	**JENDL-4.0**	**2017**	**JAEA**	**2010**	**JAEA**	**2010**	**JAEA**	**2010**			**RQ Wright nubars added in 2016**
n-096_Cm_249.endf	**JENDL-4.0**	**2016**					**JAEA**	**2010**			**No RRR parameters given; RQ Wright nubars added in 2016**
n-096_Cm_250.endf	**JENDL-4.0**	**2016**	**JAEA**	**2010**	**JAEA**	**2010**	**JAEA**	**2010**			**RQ Wright nubars added in 2016**
n-097_Bk_245.endf	**JENDL-4.0**	**2016**					**JAEA**	**2010**			**No RRR parameters given; RQ Wright nubars added in 2016**
n-097_Bk_246.endf	**JENDL-4.0**	**2016**					**JAEA**	**2010**			**No RRR parameters given; RQ Wright nubars added in 2016**
n-097_Bk_247.endf	**JENDL-4.0**	**2016**					**JAEA**	**2010**			**No RRR parameters given; RQ Wright nubars added in 2016**
n-097_Bk_248.endf	**JENDL-4.0**	**2016**					**JAEA**	**2010**			**No RRR parameters given; RQ Wright nubars added in 2016**
n-097_Bk_249.endf	**JENDL-4.0**	**2016**	**JAEA**	**2010**	**JAEA**	**2010**	**JAEA**	**2010**			**RQ Wright nubars added in 2016**
n-097_Bk_250.endf	**JENDL-4.0**	**2016**					**JAEA**	**2010**			**No RRR parameters given; RQ Wright nubars added in 2016**
n-098_Cf_246.endf	**JENDL-4.0**	**2016**					**JAEA**	**2010**			**No RRR parameters given; RQ Wright nubars added in 2016**

TABLE XLV: Summary of the origins of and recent changes to the neutron (`neutrons`) sublibrary. Evaluations modified for ENDF/B-VIII.0 are given in bold.

		Last	RRR		URR		Smooth Region		High-energy		
File name	Main source	mod.	Lab.	Year	Lab.	Year	Lab.	Year	Lab.	Year	Note
n-098_Cf_247.endf	**ENDF/B-VIII.0**	**2017**	**BNL**	**2017**			**BNL**	**2017**			**TENDL+EMPIRE**
n-098_Cf_248.endf	**JENDL-4.0**	**2016**					**JAEA**	**2010**			**No RRR parameters given; RQ Wright nubars added in 2016**
n-098_Cf_249.endf	**JENDL-4.0**	**2017**	**JAEA**	**2010**	**JAEA**	**2010**	**JAEA**	**2010**			**RQ Wright nubars added in 2016**
n-098_Cf_250.endf	**JENDL-4.0**	**2016**	**JAEA**	**2010**	**JAEA**	**2010**	**JAEA**	**2010**			**RQ Wright nubars added in 2016**
n-098_Cf_251.endf	**JENDL-4.0**	**2016**	**JAEA**	**2010**	**JAEA**	**2010**	**JAEA**	**2010**			**RQ Wright nubars added in 2016**
n-098_Cf_252.endf	**JENDL-4.0**	**2016**	**JAEA**	**2010**	**JAEA**	**2010**	**JAEA**	**2010**			**RQ Wright nubars added in 2016**
n-098_Cf_253.endf	**JENDL-4.0**	**2016**					**JAEA**	**2010**			**No RRR parameters given; RQ Wright nubars added in 2016**
n-098_Cf_254.endf	**JENDL-4.0**	**2016**					**JAEA**	**2010**			**No RRR parameters given; RQ Wright nubars added in 2016**
n-099_Es_251.endf	**JENDL-4.0**	**2016**					**JAEA**	**2010**			**No RRR parameters given; RQ Wright nubars added in 2016**
n-099_Es_252.endf	**JENDL-4.0**	**2016**					**JAEA**	**2010**			**No RRR parameters given; RQ Wright nubars added in 2016**
n-099_Es_253.endf	**JENDL-4.0**	**2016**	**JAEA**	**2010**			**JAEA**	**2010**			**Artificial resonance added to match capture RI; RQ Wright nubars added in 2016**
n-099_Es_254.endf	**JENDL-4.0**	**2016**					**JAEA**	**2010**			**No RRR parameters given; RQ Wright nubars added in 2016**
n-099_Es_254m1.endf	**JENDL-4.0**	**2016**					**JAEA**	**2010**			**No RRR parameters given**
n-099_Es_255.endf	**JENDL-4.0**	**2016**					**JAEA**	**2010**			**No RRR parameters given; RQ Wright nubars added in 2016**
n-100_Fm_255.endf	**JENDL-4.0**	**2016**					**JAEA**	**2010**			**No RRR parameters given; RQ Wright nubars added in 2016**

TABLE XLVI: Summary of the origins of and recent changes to the light charged particle sublibraries. Evaluations modified for ENDF/B-VIII.0 are given in bold.

File name	Main source	Last mod.	Lab.	Year	Note
p (`protons`) sublibrary					
p-001_H_001.endf	ENDF/B-VI.6	2006	LANL	1998	R-matrix analysis
p-001_H_002.endf	ENDF/B-VI.6	2006	LANL/ECN	1997	R-matrix analysis, primary gamma fix
p-001_H_003.endf	ENDF/B-VII.0	2006	LANL	2001	R-matrix analysis
p-002_He_003.endf	ENDF/B-VII.0	2006	LANL	1983	R-matrix analysis
p-002_He_004.endf	**ECPL**	**2016**	**LLNL**	**1999**	
p-003_Li_006.endf	ENDF/B-VII.0	2006	LANL	2001	R-matrix analysis
p-003_Li_007.endf	**ENDF/B-VII.0**	**2016**	**LANL/LLNL**	**2010**	**R-matrix analysis, modifications from ENDL2009**
p-004_Be_009.endf	ENDF/B-VI.0	2006	LANL	1988	LA-11753-MS
p-005_B_010.endf	ENDF/B-VII.0	2006	LANL	2005	R-matrix analysis
p-006_C_012.endf	ENDF/B-VI.6	2006	LANL/ECN	1996	LA150
p-006_C_013.endf	**ENDF/B-VII.0**	**2016**	**LANL**	**2004**	**R-matrix analysis**
p-007_N_014.endf	ENDF/B-VI.6	2006	LANL/ECN	1997	LA150
p-008_O_016.endf	ENDF/B-VI.6	2006	LANL/ECN	1996	LA150
p-013_Al_027.endf	ENDF/B-VII.0	2006	LANL/ECN	1997	LA150, MF6/MT5 correction
p-014_Si_028.endf	**ENDF/B-VII.0**	**2016**	**LANL/ECN**	**1997**	**LA150, MF6/MT5 correction**
p-014_Si_029.endf	ENDF/B-VII.0	2006	LANL/ECN	1997	LA150, MF6/MT5 correction
p-014_Si_030.endf	ENDF/B-VII.0	2006	LANL/ECN	1997	LA150, MF6/MT5 correction
p-015_P_031.endf	ENDF/B-VII.0	2006	LANL/ECN	1997	LA150, MF6/MT5 correction
p-020_Ca_040.endf	ENDF/B-VII.0	2006	LANL/ECN	1997	LA150, MF6/MT5 correction
p-024_Cr_050.endf	ENDF/B-VII.0	2006	LANL/ECN	1997	LA150, MF6/MT5 correction
p-024_Cr_052.endf	ENDF/B-VII.0	2006	LANL	1997	LA150, MF6/MT5 correction
p-024_Cr_053.endf	ENDF/B-VII.0	2006	LANL/ECN	1997	LA150, MF6/MT5 correction
p-024_Cr_054.endf	ENDF/B-VII.0	2006	LANL/ECN	1997	LA150, MF6/MT5 correction
p-026_Fe_054.endf	ENDF/B-VII.0	2006	LANL/ECN	1996	LA150, MF6/MT5 correction
p-026_Fe_056.endf	ENDF/B-VII.0	2006	LANL/ECN	1996	LA150, MF6/MT5 correction
p-026_Fe_057.endf	ENDF/B-VII.0	2006	LANL/ECN	1996	LA150, MF6/MT5 correction
p-028_Ni_058.endf	ENDF/B-VII.0	2006	LANL/ECN	1997	LA150, MF6/MT5 correction
p-028_Ni_060.endf	ENDF/B-VII.0	2006	LANL/ECN	1997	LA150, MF6/MT5 correction
p-028_Ni_061.endf	ENDF/B-VII.0	2006	LANL/ECN	1997	LA150, MF6/MT5 correction
p-028_Ni_062.endf	ENDF/B-VII.0	2006	LANL/ECN	1997	LA150, MF6/MT5 correction
p-028_Ni_064.endf	ENDF/B-VII.0	2006	LANL/ECN	1997	LA150, MF6/MT5 correction

TABLE XLVI: Summary of the origins of and recent changes to the light charged particle sublibraries. Evaluations modified for ENDF/B-VIII.0 are given in bold.

File name	Main source	Last mod.	Lab.	Year	Note
p-029_Cu_063.endf	ENDF/B-VII.0	2006	LANL/ECN	1998	LA150, MF6/MT5 correction
p-029_Cu_065.endf	ENDF/B-VII.0	2006	LANL/ECN	1998	LA150, MF6/MT5 correction
p-041_Nb_093.endf	ENDF/B-VII.0	2006	LANL	1997	LA150, MF6/MT5 correction
p-074_W_182.endf	ENDF/B-VI.6	2006	LANL	1996	LA150
p-074_W_183.endf	ENDF/B-VII.0	2006	LANL	1996	LA150, MF6/MT5 correction
p-074_W_184.endf	ENDF/B-VII.0	2006	LANL	1996	LA150, MF6/MT5 correction
p-074_W_186.endf	ENDF/B-VI.6	2006	LANL	1996	LA150
p-080_Hg_196.endf	ENDF/B-VII.0	2006	LANL/JAERI	1998	LA150, MF6/MT5 correction
p-080_Hg_198.endf	ENDF/B-VII.0	2006	LANL/JAERI	1998	LA150, MF6/MT5 correction
p-080_Hg_199.endf	ENDF/B-VII.0	2006	LANL/JAERI	1998	LA150, MF6/MT5 correction
p-080_Hg_200.endf	ENDF/B-VII.0	2006	LANL/JAERI	1998	LA150, MF6/MT5 correction
p-080_Hg_201.endf	ENDF/B-VII.0	2006	LANL/JAERI	1998	LA150, MF6/MT5 correction
p-080_Hg_202.endf	ENDF/B-VII.0	2006	LANL/JAERI	1998	LA150, MF6/MT5 correction
p-080_Hg_204.endf	ENDF/B-VII.0	2006	LANL/JAERI	1998	LA150, MF6/MT5 correction
p-082_Pb_206.endf	ENDF/B-VI.6	2006	LANL/ECN	1996	LA150
p-082_Pb_207.endf	ENDF/B-VII.0	2006	LANL/ECN	1996	LA150, MF6/MT5 correction
p-082_Pb_208.endf	ENDF/B-VII.0	2006	LANL/ECN	1996	LA150, MF6/MT5 correction
p-083_Bi_209.endf	ENDF/B-VI.7	2006	LANL	1998	LA150
d (`deuterons`) sublibrary					
d-001_H_002.endf	**ENDF/B-VII.0**	**2016**	**LANL**	**2001**	**R-matrix analysis**
d-001_H_003.endf	**ENDF/B-VII.0**	**2016**	**LANL**	**1995**	**R-matrix analysis**
d-002_He_003.endf	ENDF/B-VII.0	2001	LANL	2001	R-matrix analysis
d-003_Li_006.endf	**ENDF/B-VII.0**	**2016**	**LANL**	**2004**	**R-matrix analysis**
d-003_Li_007.endf	**ENDL2010**	**2016**	**LLNL**	**2010**	**Updated ECPL**
t (`tritons`) sublibrary					
t-001_H_003.endf	ENDF/B-VII.0	2006	LANL	2001	R-matrix analysis
t-002_He_003.endf	ENDF/B-VII.0	2006	LANL	2001	R-matrix analysis
t-002_He_004.endf	**ECPL**	**2016**	**LLNL**	**1999**	
t-003_Li_006.endf	ENDF/B-VII.0	2006	LANL	2001	R-matrix analysis
t-003_Li_007.endf	**ENDL2011**	**2016**	**LLNL**	**2016**	**Updated ECPL**
^{3}He (`helium3s`) sublibrary					
h-002_He_003.endf	**ENDL2011**	**2016**	**LLNL**	**2010**	**Updated ENDF/B-VII.0**
h-002_He_004.endf	**ECPL**	**2016**	**LLNL**	**1999**	
h-003_Li_006.endf	ENDF/B-VII.0	2006	LANL	2002	R-matrix analysis
α (`alphas`) sublibrary					
a-002_He_004.endf	**ECPL**	**2016**	**LLNL**	**1999**	

TABLE XLVII: Summary of the origins of and recent changes to the thermal neutron scattering (`thermal_scatt`) sublibrary. Evaluations modified for ENDF/B-VIII.0 are given in bold. Note all files were modified to correct the MAT numbering of the sublibrary.

File name	Main source	Last mod.	Lab.	Year	Note
tsl-ortho-D.endf	ENDF/B-VII.0	2016	LANL	1993	
tsl-para-D.endf	ENDF/B-VII.0	2016	LANL	1993	
tsl-ortho-H.endf	ENDF/B-VII.0	2016	LANL	1993	
tsl-para-H.endf	ENDF/B-VII.0	2016	LANL	1993	
tsl-013_Al_027.endf	ENDF/B-VII.0	2016	LANL	2005	
tsl-026_Fe_056.endf	ENDF/B-VII.0	2016	LANL	2005	
tsl-Be-metal.endf	**ENDF/B-VIII.0**	**2016**	**NCSU**	**2016**	
tsl-BeinBeO.endf	**ENDF/B-VIII.0**	**2016**	**NCSU**	**2016**	
tsl-OinBeO.endf	**ENDF/B-VIII.0**	**2016**	**NCSU**	**2016**	
tsl-HinH2O.endf	**ENDF/B-VIII.0**	**2016**	**CAB (Argentina)**	**2016**	
tsl-HinIceIh.endf	**ENDF/B-VIII.0**	**2016**	**BAPL**	**2016**	
tsl-OinIceIh.endf	**ENDF/B-VIII.0**	**2016**	**BAPL**	**2016**	
tsl-DinD2O.endf	**ENDF/B-VIII.0**	**2016**	**CAB (Argentina)**	**2016**	
tsl-OinD2O.endf	**ENDF/B-VIII.0**	**2016**	**CAB (Argentina)**	**2016**	
tsl-benzene.endf	**ENDF-269**	**2017**	**GA**	**1969**	**Corrected spelling; No LEAPR inputs available**
tsl-HinC5O2H8.endf	**ENDF/B-VIII.0**	**2016**	**NCSU**	**2015**	
tsl-HinCH2.endf	**ENDF/B-VIII.0**	**2016**	**NCSU**	**2015**	
tsl-l-CH4.endf	ENDF/B-VII.0	2016	LANL	1993	
tsl-s-CH4.endf	ENDF/B-VII.0	2016	LANL	1993	
tsl-graphite.endf	**ENDF/B-VIII.0**	**2016**	**NCSU**	**2016**	
tsl-reactor-graphite.endf	**ENDF/B-VIII.0**	**2016**	**NCSU**	**2016**	
tsl-CinSiC.endf	**ENDF/B-VIII.0**	**2016**	**NCSU**	**2014**	
tsl-SiinSiC.endf	**ENDF/B-VIII.0**	**2016**	**NCSU**	**2014**	
tsl-SiO2-alpha.endf	**ENDF/B-VIII.0**	**2016**	**NCSU**	**2011**	
tsl-SiO2-beta.endf	**ENDF/B-VIII.0**	**2016**	**NCSU**	**2011**	

TABLE XLVII: Summary of the origins of and recent changes to the thermal neutron scattering (`thermal_scatt`) sublibrary. Evaluations modified for ENDF/B-VIII.0 are given in bold. Note all files were modified to correct the MAT numbering of the sublibrary.

File name	Main source	Last mod.	Lab.	Year	Note
tsl-HinYH2.endf	**ENDF/B-VIII.0**	**2016**	**BAPL**	**2016**	
tsl-YinYH2.endf	**ENDF/B-VIII.0**	**2016**	**BAPL**	**2016**	
tsl-HinZrH.endf	ENDF/B-VII.0	2016	LANL	1993	
tsl-ZrinZrH.endf	ENDF/B-VII.0	2016	LANL	1993	
tsl-OinUO2.endf	**ENDF/B-VIII.0**	**2016**	**NCSU**	**2016**	
tsl-UinUO2.endf	**ENDF/B-VIII.0**	**2016**	**NCSU**	**2016**	
tsl-NinUN.endf	**ENDF/B-VIII.0**	**2017**	**NCSU**	**2017**	
tsl-UinUN.endf	**ENDF/B-VIII.0**	**2017**	**NCSU**	**2017**	

Appendix B: Summary of Criticality k_{eff} C/E Changes Between ENDF/B-VII.1 and ENDF/B-VIII.0

Tabulated below are the k_{eff} C/E results for a large collection of ICSBEP benchmarks [56]. For ENDF/B-VII.1 we use the .80c and .20t continuous energy and thermal scattering kernel files, respectively, that are distributed with the `MCNP`®6 code. The ENDF/B-VIII.0 results were obtained using the "beta5" files released in the Fall 2017 which are substantially equivalent to the final ENDF/B-VIII.0 files.

The ENDF/B-VIII.0 results include use of new scattering kernels for light and heavy water, polyethylene, beryllium, beryllium-oxide and reactor graphite. The latter representing a significant change over the legacy, crystalline graphite, scattering kernel used in the past. Other scattering kernels rarely appear in these ICSBEP benchmarks, and if they do we have continued to use the ENDF/B-VII.1 .20t files. Another change is in the MCNP input decks, as for ENDF/B-VIII.0 we no longer provide elemental carbon. The natural carbon file is one of the ENDF Standards but is no longer a complete transport capable file. Hence all ICSBEP MCNP input decks have been upgraded by replacing the 6000.xxc material with the corresponding isotope identifiers, 6012.xxc and 6013.xxc.

One final observation. We provide two results for the legacy LANL Jezebel benchmark (PMF1). The ICSBEP model has been revised in recent years. The "rev2" model was recommended through the release of ENDF/B-VII.1 whereas the "rev4" model is a recent upgrade.

TABLE XLVIII: Summary of criticality k_{eff} C/E changes between ENDF/B-VII.1 (E71) and ENDF/B-VIII.0 (E80).

Name	E71 k_{eff} C/E	E80 k_{eff} C/E
HEU-MET-FAST		
HMF1	0.99977	0.99994
HMF2.2	1.00228	1.00020
HMF2.3	1.00038	0.99835
HMF2.4	0.99955	0.99757
HMF2.5	0.99989	0.99784
HMF2.6	1.00125	0.99929
HMF3.1	0.99502	0.99290
HMF3.2	0.99445	0.99195
HMF3.3	0.99897	0.99673
HMF3.4	0.99727	0.99495
HMF3.5	1.00144	0.99949
HMF3.6	1.00155	0.99960
HMF3.7	1.00200	1.00039
HMF3.8	1.00211	1.00054

TABLE XLVIII: Summary of criticality k_{eff} C/E changes between ENDF/B-VII.1 (E71) and ENDF/B-VIII.0 (E80).

Name	E71 k_{eff} C/E	E80 k_{eff} C/E
HMF3.9	1.00223	1.00067
HMF3.10	1.00505	1.00395
HMF3.11	1.00881	1.00859
HMF3.12	1.00862	0.99956
HMF4	1.00093	1.00047
HMF5.1	0.99519	0.99574
HMF5.2	0.99729	0.99690
HMF5.3	1.00090	0.99974
HMF5.4	0.99547	0.99398
HMF5.5	1.00101	1.00003
HMF5.6	0.99899	0.99826
HMF7.1	0.99804	0.99831
HMF7.2	1.00228	1.00232
HMF7.3	1.00106	1.00113
HMF7.4	1.00351	1.00373
HMF7.5	1.00245	1.00322
HMF7.6	1.00510	1.00518
HMF7.7	1.00416	1.00464
HMF7.8	1.00217	1.00315
HMF7.9	1.00389	1.00424
HMF7.10	1.00112	1.00141
HMF7.11	1.00188	1.00262
HMF7.12	0.99971	1.00028
HMF7.13	1.00113	1.00007
HMF7.14	1.00052	1.00092
HMF7.15	1.00064	0.99978
HMF7.16	1.00058	0.99963
HMF7.17	1.00069	0.99962
HMF7.18	1.00109	0.99982
HMF7.19	1.00121	1.00120
HMF7.20	1.00326	1.00336
HMF7.21	1.00338	1.00337
HMF7.22	1.00323	1.00352
HMF7.23	1.00311	1.00273
HMF7.24	1.00266	1.00230
HMF7.25	1.00264	1.00189
HMF7.26	1.00212	1.00128
HMF7.35	1.00199	0.99911
HMF7.36	1.00343	1.00127
HMF7.37	1.00279	1.00117
HMF7.38	1.00267	1.00137
HMF7.39	1.00309	1.00204
HMF7.40	1.00474	1.00296
HMF7.41	1.00147	0.99991
HMF7.42	1.00134	0.99976
HMF7.43	1.00065	0.99831
HMF8	0.99695	0.99666
HMF9.1	0.99834	0.99700
HMF9.2	0.99747	0.99602
HMF10.1	0.99929	0.99852
HMF10.2	0.99861	0.99814
HMF11	1.00001	0.99786
HMF12	0.99900	0.99879
HMF13	0.99834	0.99995
HMF14	0.99871	0.99628
HMF15	0.99491	0.99516
HMF16.1	1.00203	1.00085
HMF16.2	1.00286	1.00177
HMF17	1.00131	0.99960
HMF18	1.00003	1.00042
HMF19	1.00698	1.00590

TABLE XLVIII: Summary of criticality k_{eff} C/E changes between ENDF/B-VII.1 (E71) and ENDF/B-VIII.0 (E80).

TABLE XLVIII: Summary of criticality k_{eff} C/E changes between ENDF/B-VII.1 (E71) and ENDF/B-VIII.0 (E80).

Name	E71 k_{eff} C/E	E80 k_{eff} C/E
HMF20	1.00084	1.00023
HMF21	0.99730	0.99985
HMF22	0.99759	0.99736
HMF24	0.99939	0.99879
HMF25.1	1.00020	1.00039
HMF25.2	1.00215	1.00215
HMF25.3	1.00475	1.00477
HMF25.4	1.00585	1.00593
HMF25.5	1.00631	1.00658
HMF27	1.00087	1.00045
HMF28	1.00270	1.00069
HMF29	1.00574	1.00335
HMF30	1.00208	1.00089
HMF31	1.00479	1.00215
HMF32.1	1.00422	1.00170
HMF32.2	1.00462	1.00226
HMF32.3	1.00011	0.99812
HMF32.4	1.00083	0.99994
HMF33.1	0.99983	1.00168
HMF33.2	0.99834	0.99809
HMF34.1	0.99813	0.99715
HMF34.2	0.99966	0.99861
HMF34.3	0.99836	0.99886
HMF36.1	0.99978	0.99747
HMF36.2	0.99899	0.99700
HMF37.1	1.00268	0.99877
HMF37.2	0.99817	0.99565
HMF38.1	1.00336	1.00140
HMF38.2	1.00206	1.00154
HMF40	1.00543	1.00553
HMF41.1	1.00559	1.00352
HMF41.2	1.00298	1.00019
HMF41.3	1.00178	1.00027
HMF41.4	1.00655	1.00505
HMF41.5	1.00237	1.00056
HMF41.6	1.00367	1.00195
HMF43.1	0.99954	1.00016
HMF43.2	0.99868	0.99985
HMF43.3	0.99918	1.00055
HMF43.4	0.99796	0.99965
HMF43.5	0.99887	1.00058
HMF44.1	1.00044	1.00067
HMF44.2	1.00006	1.00005
HMF44.3	1.00017	1.00043
HMF44.4	0.99981	1.00015
HMF44.5	1.00061	1.00073
HMF49.1	0.99899	0.99912
HMF49.2	1.00034	1.00021
HMF49.3	0.99929	0.99935
HMF50	0.99910	0.99959
HMF51.1	0.99804	0.99813
HMF51.2	0.99859	0.99880
HMF51.3	0.99761	0.99790
HMF51.4	0.99812	0.99852
HMF51.9	0.99664	0.99679
HMF51.14	0.99920	0.99936
HMF51.15	0.99816	0.99847
HMF51.16	0.99829	0.99849
HMF51.17	0.99856	0.99867
HMF51.18	0.99560	0.99573
HMF52	1.00566	1.00379
HMF55	1.00272	1.00179
HMF57.1	0.98963	0.98932
HMF57.2	0.99819	0.99797
HMF57.3	1.01720	1.01694
HMF57.4	0.98797	0.98747
HMF57.5	1.02191	1.02149
HMF57.6	0.99675	0.99642
HMF58.1	1.00333	1.00010
HMF58.2	1.00503	1.00253
HMF58.3	1.00291	1.00072
HMF58.4	1.00188	1.00018
HMF58.5	1.00082	0.99941
HMF59.1	0.99758	0.99720
HMF59.2	0.99816	0.99784
HMF60	1.00674	1.00656
HMF61	1.00460	1.00367
HMF63.1	1.00115	1.00380
HMF63.2	1.00194	1.00481
HMF64.1	0.99581	0.99547
HMF64.2	0.99609	0.99588
HMF64.3	0.99422	0.99380
HMF65	0.99853	0.99895
HMF66.1	1.00069	0.99799
HMF66.2	0.99938	0.99730
HMF66.3	1.00223	1.00004
HMF66.4	1.00067	0.99767
HMF66.5	1.00134	0.99855
HMF66.6	1.00071	0.99821
HMF66.7	1.00077	0.99820
HMF66.8	1.00045	0.99774
HMF66.9	1.00009	0.99770
HMF67.1	1.00510	1.00545
HMF67.2	1.00230	1.00163
HMF69	0.99933	0.99899
HMF70.1	1.00513	1.00585
HMF70.2	1.00092	1.00085
HMF70.3	1.00302	1.00345
HMF72.1	1.00844	1.00400
HMF72.3	1.00939	1.00920
HMF73	1.00775	0.99935
HMF75	1.00274	1.00326
HMF78.1	0.99503	0.99450
HMF78.3	0.99657	0.99600
HMF78.5	0.99709	0.99597
HMF78.7	0.99858	0.99609
HMF78.9	0.99593	0.99441
HMF78.11	0.99626	0.99462
HMF78.13	0.99724	0.99583
HMF78.15	0.99736	0.99578
HMF78.17	0.99704	0.99563
HMF78.23	0.99900	0.99861
HMF78.25	0.99821	0.99769
HMF78.27	0.99671	0.99614
HMF78.29	1.00219	1.00055
HMF78.31	0.99584	0.99516
HMF78.33	0.99625	0.99492
HMF78.35	0.99536	0.99485
HMF78.37	0.99764	0.99707
HMF78.39	0.99789	0.99725
HMF78.41	0.99754	0.99783
HMF78.43	0.99762	0.99699
HMF79.1	1.00005	1.00027
HMF79.2	0.99963	0.99945
HMF79.3	1.00047	1.00045
HMF79.4	1.00140	1.00110
HMF79.5	1.00022	1.00013
HMF82pre.1	0.99721	0.99680
HMF82pre.2	0.99719	0.99624
HMF82pre.3	0.99942	0.99854
HMF84.1	0.99965	0.99948
HMF84.2	1.00000	0.99955
HMF84.3	1.00074	0.99908
HMF84.4	0.99934	0.99843
HMF84.5	1.00585	1.00685
HMF84.6	0.99923	0.99542
HMF84.7	0.99780	0.99941
HMF84.8	1.00905	1.00896
HMF84.9	1.00348	1.00289
HMF84.10	1.00191	0.99683
HMF84.11	1.00190	1.00108
HMF84.12	0.99809	0.99751
HMF84.13	0.99978	0.99828
HMF84.14	1.00051	0.99899
HMF84.15	0.99867	0.99827
HMF84.16	0.99976	0.99899
HMF84.17	1.00073	1.00159
HMF84.18	0.99807	0.99557
HMF84.19	0.99787	0.99866
HMF84.20	1.00356	1.00369
HMF84.21	1.00084	1.00074
HMF84.22	0.99880	0.99563
HMF84.23	1.00017	0.99989
HMF84.24	0.99920	0.99844
HMF84.25	0.99864	0.99802
HMF84.26	1.00114	1.00062
HMF84.27	0.99822	0.99768
HMF85.1	1.00028	0.99468
HMF85.2	1.00455	0.99708
HMF85.3	0.99655	0.99888
HMF85.4	1.00023	0.99563
HMF85.5	1.00094	1.00085

TABLE XLVIII: Summary of criticality k_{eff} C/E changes between ENDF/B-VII.1 (E71) and ENDF/B-VIII.0 (E80).

TABLE XLVIII: Summary of criticality k_{eff} C/E changes between ENDF/B-VII.1 (E71) and ENDF/B-VIII.0 (E80).

Name	E71 k_{eff} C/E	E80 k_{eff} C/E
HMF85.6	1.00633	1.00374
HMF87	0.99970	1.00152
HMF88.1	0.99745	0.99755
HMF88.2	0.99734	0.99637
HMF89	1.00100	1.00090
HMF90.1	1.00627	1.00360
HMF90.2	1.00291	0.99974
HMF91	1.00002	0.99716
HMF92.1	1.00267	1.00269
HMF92.2	1.00381	1.00411
HMF92.3	1.00461	1.00498
HMF92.4	1.00406	1.00450
HMF93	1.00556	1.00613
HMF94.1	1.00403	1.00174
HMF94.2	1.00443	1.00273
HMF100.1	1.00181	1.00152
HMF100.2	1.00223	1.00178
HEU-MET-INTER		
HMI1	1.00484	1.00201
HMI6.1	0.99524	0.99793
HMI6.2	0.99678	1.00016
HMI6.3	0.99931	1.00201
HMI6.4	1.00547	1.00390
HEU-COMP-INTER		
HCI3.1	1.00638	1.00806
HCI3.2	1.00585	1.00851
HCI3.3	1.00552	1.00807
HCI3.4	1.00402	1.00823
HCI3.5	1.00574	1.00909
HCI3.6	0.99612	0.99869
HCI3.7	0.99587	0.99875
HCI5.1	1.00840	1.01578
HCI5.2	1.04545	1.03308
HCI5.3	1.02048	1.01268
HCI5.4	1.10618	1.11289
HCI5.5	0.93583	0.96991
HEU-MET-MIXED		
HMM1	1.00251	1.00054
HMM2	1.00667	1.00259
HMM3	1.00756	1.00369
HMM4	1.00246	0.99828
HMM12	0.99628	1.00504
HMM15	0.99737	0.99420
HMM16.1	1.00223	0.99915
HMM16.2	1.00318	0.99971
HMM17	0.99540	0.99288
HMM20.1	1.00489	1.00155
HMM20.2	1.00357	0.99966
IEU-MET-FAST		
IMF1.1	1.00134	1.00013
IMF1.2	1.00169	1.00029
IMF1.3	1.00142	0.99911
IMF1.4	1.00255	1.00016
IMF2	0.99881	0.99607
IMF3	1.00228	0.99951
IMF4	1.00737	1.00477
IMF5	1.00178	1.00088
IMF6	0.99615	0.99390
IMF7d	0.99998	0.99981
IMF8	1.00533	1.00399
IMF9	1.01052	1.00696
IMF10	1.00087	1.00101
IMF12	1.00230	1.00068
IMF13	1.00275	1.00232
IMF14.1	1.00106	1.00087
IMF14.2	1.00091	1.00135
IMF15	1.00347	1.00181
IMF16	0.99902	0.99773
IEU-COMP-FAST		
ICF1	0.99892	0.99791
ICF4	1.00225	1.00011
PU-MET-FAST		
PMF1, rev2	0.99992	0.99985
PMF1, rev4	1.00069	1.00068
PMF2	1.00003	1.00132
PMF5	1.00112	0.99914
PMF6	1.00093	0.99985
PMF8	0.99759	0.99753
PMF9	1.00515	1.00499
PMF10	0.99956	0.99772
PMF11	1.00005	1.00052
PMF12	1.00225	1.00116
PMF13	0.99992	0.99454
PMF14	0.99394	0.98665
PMF15	0.99598	0.99976
PMF16.1	1.02031	1.02307
PMF16.2	1.00709	1.01009
PMF16.3	1.00537	1.00812
PMF16.4	1.00473	1.00787
PMF16.5	1.00446	1.00782
PMF16.6	1.00686	1.01031
PMF18	0.99943	0.99802
PMF19	1.00172	1.00058
PMF20	0.99886	0.99707
PMF21.1	1.00457	1.00355
PMF21.2	0.99331	0.99234
PMF22	0.99844	0.99794
PMF23	0.99990	0.99833
PMF24	1.00175	1.00096
PMF25	0.99880	0.99985
PMF26	0.99845	1.00152
PMF27	1.00301	1.00274
PMF28	0.99896	1.00311
PMF29	0.99564	0.99599
PMF30	1.00281	1.00208
PMF31	1.00438	1.00449
PMF32	0.99862	1.00129
PMF33	0.99942	0.99841
PMF35	0.99780	0.99699
PMF36	1.00649	1.00608
PMF38d	1.00180	1.00039
PMF39	0.99225	0.99175
PMF40	0.99680	0.99409
PMF41	1.00573	1.00490
PMF44.1	1.00288	1.00269
PMF44.2	1.00198	1.00358
PMF44.3	1.00158	1.00112
PMF44.4	1.00222	1.00216
PMF44.5	1.00157	1.00060
PMF45.1	1.00125	0.99601
PMF45.2	1.00755	1.00285
PMF45.3	1.00637	1.00290
PMF45.4	1.00680	1.00301
PMF45.5	1.00695	1.00203
PMF45.6	1.00590	1.00858
PMF45.7	1.00526	1.00699
PU-MET-INTER		
PMI2	1.02830	1.01723
PMI3	1.00364	1.00167
PMI4	1.00273	0.99923
MIX-MET-FAST		
MMF1	0.99951	0.99918
MMF2.1	1.00536	1.00369
MMF2.2	1.00526	1.00360
MMF2.3	1.00539	1.00427
MMF3	1.00129	1.00120
MMF4.1	1.00102	1.00043
MMF4.2	1.00022	0.99937
MMF5	1.00484	1.00483
MMF7.1	1.00338	1.00100
MMF7.2	1.00801	1.00578
MMF7.3	1.00637	1.00436
MMF7.4	1.00523	1.00329
MMF7.5	1.00262	1.00116
MMF7.6	1.00104	1.00035
MMF7.7	1.00614	1.00427
MMF7.8	1.00506	1.00286
MMF7.9	1.00510	1.00290
MMF7.10	1.00503	1.00302
MMF7.11	1.00363	1.00195
MMF7.12	1.00252	1.00138
MMF7.13	1.00091	1.00043
MMF7.14	1.00783	1.00607
MMF7.15	1.00764	1.00580
MMF7.16	1.00600	1.00437
MMF7.17	1.00591	1.00444
MMF7.18	1.00774	1.00710
MMF7.19	1.00697	1.00546
MMF7.20	1.00500	1.00393

TABLE XLVIII: Summary of criticality k_{eff} C/E changes between ENDF/B-VII.1 (E71) and ENDF/B-VIII.0 (E80).

TABLE XLVIII: Summary of criticality k_{eff} C/E changes between ENDF/B-VII.1 (E71) and ENDF/B-VIII.0 (E80).

Name	E71 k_{eff} C/E	E80 k_{eff} C/E
MMF7.21	1.00489	1.00446
MMF7.22	1.00400	1.00266
MMF7.23	1.00333	1.00255
MMF9	1.00023	0.99969
MMF10	0.99983	0.99911
MMF11.1	1.00107	1.00023
MMF11.2	0.99710	0.99610
MMF11.3	0.99951	0.99903
MMF11.4	1.00191	1.00113
MIX-COMP-FAST		
MCF1	1.00067	0.99751
MCF2	0.99822	0.99500
MCF3.1	0.99959	0.99935
MCF3.2	0.99984	0.99985
MCF4	1.00388	0.99774
MCF5	0.99584	0.99586
MCF6	1.00247	0.99938
MIX-MET-INTER		
MMI3	1.00961	1.00682
MMI4	1.00652	1.00426
MIX-MET-MIXED		
MMM1	1.00062	1.00093
U233-MET-FAST		
UMF1	0.99986	1.00044
UMF2.1	0.99898	1.00016
UMF2.2	1.00031	1.00162
UMF3.1	0.99930	0.99967
UMF3.2	0.99981	1.00000
UMF4.1	0.99866	0.99957
UMF4.2	0.99559	0.99646
UMF5.1	0.99603	0.99766
UMF5.2	0.99534	0.99739
UMF6	0.99887	0.99995
HEU-SOL-THERM		
HST1.1	0.99760	0.99769
HST1.2	0.99363	0.99307
HST1.3	1.00158	1.00155
HST1.4	0.99749	0.99647
HST1.5	0.99847	0.99858
HST1.6	1.00185	1.00196
HST1.7	0.99705	0.99715
HST1.8	0.99838	0.99842
HST1.9	0.99353	0.99251
HST1.10	0.99310	0.99318
HST4.1	0.98593	0.98140
HST4.2	0.98136	0.97573
HST4.3	0.98843	0.98218
HST4.4	0.99080	0.98416
HST4.5	0.98950	0.98341
HST4.6	0.98609	0.98026
HST6.1	0.98481	0.98397
HST6.2	0.98791	0.98865
HST6.3	0.99836	0.99958
HST6.4	1.00063	1.00191
HST6.5	1.00785	1.00899
HST6.6	0.99910	1.00049
HST6.7	1.00077	1.00238
HST6.8	0.98426	0.98411
HST6.9	0.98759	0.98794
HST6.10	0.99814	0.99936
HST6.11	1.00080	1.00232
HST6.12	0.98378	0.98256
HST6.13	0.98588	0.98626
HST6.14	0.99917	1.00053
HST6.15	1.00678	1.00781
HST6.16	0.99872	1.00014
HST6.17	1.00052	1.00210
HST6.18	1.00011	1.00153
HST6.19	1.00725	1.00845
HST6.20	0.99913	1.00066
HST6.21	1.00095	1.00232
HST6.22	0.99845	0.99922
HST6.23	1.00050	1.00203
HST6.24	1.00770	1.00920
HST6.25	0.99941	1.00072
HST6.26	1.00118	1.00252
HST6.27	0.98553	0.98487
HST6.28	0.98682	0.98751
HST6.29	1.00139	1.00275
HST9.1	1.00297	1.00213
HST9.2	1.00239	1.00167
HST9.3	1.00212	1.00198
HST9.4	0.99786	0.99857
HST10.1	1.00129	1.00224
HST11.1	1.00478	1.00548
HST11.2	1.00083	1.00146
HST12.1	1.00107	1.00096
HST13.1	0.99738	0.99703
HST19.1	0.99746	0.99680
HST19.2	0.99918	0.99957
HST19.3	0.99475	0.99556
HST20.1	0.99395	0.98822
HST20.2	1.00068	0.99431
HST20.3	1.00942	1.00351
HST20.4	1.00932	1.00344
HST20.5	1.01857	1.01078
HST25.1	1.00067	1.00143
HST25.2	0.99963	1.00031
HST25.3	0.99512	0.99583
HST25.4	1.00050	1.00107
HST25.5	1.00186	1.00245
HST25.6	1.00821	1.00888
HST25.7	1.01177	1.01234
HST25.8	1.00992	1.01075
HST25.9	1.00361	1.00465
HST25.10	1.00785	1.00902
HST25.11	1.00694	1.00829
HST25.12	1.00568	1.00697
HST25.13	1.01294	1.01434
HST25.14	1.00424	1.00552
HST25.15	0.99879	0.99993
HST25.16	1.00909	1.01048
HST25.17	1.00112	1.00233
HST25.18	0.99885	0.99996
HST27.1	0.99591	0.99637
HST27.2	0.99683	0.99663
HST27.3	0.99769	0.99774
HST27.4	0.99850	0.99822
HST27.5	0.99647	0.99595
HST27.6	0.99142	0.99186
HST27.7	0.99785	0.99808
HST27.8	1.00045	1.00031
HST27.9	0.99797	0.99767
HST28.1	0.99653	0.99734
HST28.2	0.99714	0.99743
HST28.3	0.99827	0.99911
HST28.4	0.99893	0.99933
HST28.5	0.99369	0.99452
HST28.6	0.99746	0.99774
HST28.7	0.99767	0.99857
HST28.8	0.99788	0.99825
HST28.9	0.99545	0.99627
HST28.10	0.99390	0.99405
HST28.11	0.99695	0.99775
HST28.12	0.99435	0.99458
HST28.13	0.99601	0.99649
HST28.14	0.99618	0.99612
HST28.15	1.00418	1.00477
HST28.16	1.00046	1.00051
HST28.17	0.99576	0.99623
HST28.18	0.99661	0.99685
HST32.1	0.99780	0.99692
HST38.1	0.99507	0.99469
HST38.2	0.99722	0.99648
HST38.3	0.99759	0.99748
HST38.4	0.99523	0.99532
HST38.5	0.99514	0.99491
HST38.6	0.99672	0.99602
HST38.7	0.99761	0.99748
HST38.8	0.99835	0.99760
HST38.9	0.99862	0.99739
HST38.10	0.99722	0.99663
HST38.11	0.99621	0.99624
HST38.12	0.99594	0.99601
HST38.13	1.00081	1.00046
HST38.14	1.00154	1.00093
HST38.15	1.00079	1.00001
HST38.16	1.00008	0.99928
HST38.17	0.99683	0.99581
HST38.18	0.99515	0.99453
HST38.19	0.99720	0.99674
HST38.20	0.99734	0.99674
HST38.21	0.99716	0.99714

TABLE XLVIII: Summary of criticality k_{eff} C/E changes between ENDF/B-VII.1 (E71) and ENDF/B-VIII.0 (E80).

TABLE XLVIII: Summary of criticality k_{eff} C/E changes between ENDF/B-VII.1 (E71) and ENDF/B-VIII.0 (E80).

Name	E71 k_{eff} C/E	E80 k_{eff} C/E
HST38.22	0.99758	0.99689
HST38.23	0.99694	0.99638
HST38.24	0.99709	0.99617
HST38.25	0.99726	0.99657
HST38.26	0.99794	0.99728
HST38.27	0.99735	0.99677
HST38.28	0.99746	0.99683
HST42.1	1.00097	1.00040
HST42.2	0.99992	0.99947
HST42.3	1.00140	1.00033
HST42.4	1.00224	1.00139
HST42.5	1.00021	0.99915
HST42.6	1.00049	0.99932
HST42.7	1.00136	1.00019
HST42.8	1.00205	1.00081
HST43.1	0.99608	0.99634
HST43.2	1.00585	1.00583
HST43.3	1.00198	1.00145
HST49.1	0.99765	0.99724
HST49.2	0.98935	0.98776
HST49.3	0.99676	0.99700
HST49.4	0.99794	0.99890
HST49.5	1.00028	1.00173
HST49.6	1.00398	1.00546
HST49.7	1.00431	1.00578
HST49.8	1.00296	1.00426
HST49.9	0.99703	0.99653
HST49.10	0.98765	0.98647
HST49.11	0.99176	0.99140
HST49.12	0.99454	0.99490
HST49.13	0.99551	0.99620
HST49.14	0.99669	0.99765
HST49.15	0.99867	0.99999
HST49.16	0.99735	0.99837
HST49.17	0.99705	0.99820
HST49.18	0.99879	1.00046
HST49.19	0.99960	1.00173
HST49.20	0.99800	1.00011
HST50.1	1.01211	1.01049
HST50.2	1.00412	1.00256
HST50.3	1.00630	1.00391
HST50.4	1.00569	1.00448
HST50.5	1.00222	1.00177
HST50.6	1.01073	1.00916
HST50.7	1.00051	0.99831
HST50.8	1.00035	0.99887
HST50.9	1.00048	0.99809
HST50.10	0.98397	0.98254
HST50.11	0.99496	0.99364
LEU-SOL-THERM		
LST4.1	1.00096	1.00141
LST4.2	1.00175	1.00195
LST4.3	0.98970	0.99976
LST4.4	1.00205	1.00207
LST4.5	1.00206	1.00200
LST4.6	1.00166	1.00168
LST4.7	1.00184	1.00159
LST7.1	0.99886	0.99937
LST7.2	0.99992	1.00023
LST7.3	0.99755	0.99798
LST7.4	0.99984	0.99997
LST7.5	0.99921	0.99914
LST20.1	1.00039	1.00026
LST20.2	0.99993	0.99991
LST20.3	0.99916	0.99901
LST20.4	1.00024	1.00012
LST21.1	0.99957	0.99941
LST21.2	0.99978	0.99952
LST21.3	0.99868	0.99848
LST21.4	1.00018	1.00003
HEU-MET-THERM		
HMT10.2	1.00256	1.00140
HMT12	1.01224	1.01008
HMT14	1.01406	1.01123
HMT31	1.00493	1.00419
LEU-MET-THERM		
LMT7.1	1.00146	0.99970
LMT7.2	1.00092	1.00011
LMT7.3	0.99936	0.99921
LMT7.4	0.99833	0.99829
LMT7.5	0.99697	0.99722
LMT7.6	0.99370	0.99424
LEU-COMP-THERM		
LCT1.1	0.99975	0.99983
LCT1.2	0.99926	0.99915
LCT1.3	0.99870	0.99870
LCT1.4	0.99928	0.99941
LCT1.5	0.99715	0.99723
LCT1.6	0.99910	0.99907
LCT1.7	0.99849	0.99855
LCT1.8	0.99752	0.99770
LCT2.1	0.99875	0.99873
LCT2.2	1.00008	1.00015
LCT2.3	0.99944	0.99976
LCT2.4	0.99900	0.99920
LCT2.5	0.99802	0.99798
LCT5.1	1.00254	1.00220
LCT5.2	0.99975	0.99930
LCT5.3	0.99898	0.99917
LCT5.4	0.99755	0.99771
LCT5.5	1.00499	1.00278
LCT5.6	1.00548	1.00318
LCT5.7	1.00139	0.99958
LCT5.8	1.00141	0.99995
LCT5.9	1.00196	1.00043
LCT5.10	1.00118	0.99983
LCT5.11	1.00182	1.00048
LCT5.12	1.00646	1.00462
LCT5.13	1.01205	1.00919
LCT6.1	1.00005	0.99949
LCT6.2	1.00048	0.99972
LCT6.3	1.00025	0.99967
LCT6.4	1.00005	0.99971
LCT6.5	0.99979	0.99950
LCT6.6	1.00021	0.99958
LCT6.7	1.00000	0.99969
LCT6.8	0.99984	0.99950
LCT6.9	0.99986	0.99966
LCT6.10	0.99987	0.99958
LCT6.11	0.99985	0.99936
LCT6.12	0.99965	0.99931
LCT6.13	0.99933	0.99903
LCT6.14	0.99975	0.99973
LCT6.15	0.99974	0.99934
LCT6.16	0.99978	0.99968
LCT6.17	0.99950	0.99934
LCT6.18	0.99941	0.99942
LCT7.1	0.99750	0.99677
LCT7.2	0.99867	0.99893
LCT7.3	0.99763	0.99802
LCT7.4	0.99800	0.99850
LCT7.5	0.99703	0.99617
LCT7.6	0.99896	0.99881
LCT7.7	0.99845	0.99866
LCT7.8	0.99833	0.99716
LCT7.9	0.99822	0.99809
LCT7.10	0.99846	0.99873
LCT8.1	0.99990	1.00005
LCT8.2	1.00017	1.00032
LCT8.5	0.99972	0.99970
LCT8.7	0.99947	0.99927
LCT8.8	0.99911	0.99867
LCT8.11	1.00065	1.00078
LCT9.1	0.99911	0.99908
LCT9.2	0.99905	0.99884
LCT9.3	0.99857	0.99859
LCT9.4	0.99905	0.99931
LCT9.5	0.99975	0.99979
LCT9.6	0.99887	0.99879
LCT9.7	0.99982	0.99967
LCT9.8	0.99902	0.99881
LCT9.10	0.99883	0.99881
LCT9.11	0.99893	0.99894
LCT9.13	0.99926	0.99936
LCT9.15	0.99954	0.99960
LCT9.16	0.99902	0.99892
LCT9.17	0.99966	0.99971
LCT9.18	0.99853	0.99856
LCT9.19	0.99968	0.99956
LCT9.20	0.99892	0.99876
LCT9.21	0.99960	0.99948
LCT9.22	0.99927	0.99890
LCT9.23	0.99997	0.99980

TABLE XLVIII: Summary of criticality k_{eff} C/E changes between ENDF/B-VII.1 (E71) and ENDF/B-VIII.0 (E80).

Name	E71 k_{eff} C/E	E80 k_{eff} C/E
LCT9.24	0.99880	0.99863
LCT9.25	0.99916	0.99908
LCT9.26	0.99917	0.99932
LCT9.27	0.99937	0.99954
LCT10.1	1.00496	1.00481
LCT10.2	1.00522	1.00514
LCT10.3	1.00415	1.00419
LCT10.4	0.99681	0.99651
LCT10.5	0.99950	0.99881
LCT10.6	1.00008	0.99979
LCT10.7	1.00122	1.00125
LCT10.8	0.99788	0.99786
LCT10.9	0.99994	0.99984
LCT10.10	1.00024	1.00019
LCT10.11	1.00062	1.00036
LCT10.12	0.99975	0.99956
LCT10.13	0.99758	0.99740
LCT10.14	1.00203	1.00090
LCT10.15	1.00258	1.00158
LCT10.16	1.00309	1.00209
LCT10.17	1.00247	1.00133
LCT10.18	1.00239	1.00105
LCT10.19	1.00173	1.00058
LCT10.20	1.00401	1.00311
LCT10.21	1.00410	1.00320
LCT10.22	1.00367	1.00237
LCT10.23	1.00213	1.00103
LCT10.24	1.00020	0.99886
LCT10.25	1.00171	1.00045
LCT10.26	1.00217	1.00063
LCT10.27	1.00233	1.00118
LCT10.28	1.00267	1.00131
LCT10.29	1.00207	1.00071
LCT10.30	1.00067	0.99994
LCT11.2	0.99747	0.99729
LCT11.3	0.99723	0.99723
LCT11.7	0.99729	0.99734
LCT11.9	0.99726	0.99746
LCT11.15	0.99533	0.99544
LCT17.1	1.00143	1.00150
LCT17.2	1.00100	1.00114
LCT17.3	0.99964	0.99982
LCT17.4	0.99803	0.99797
LCT17.5	0.99989	0.99958
LCT17.6	1.00002	0.99979
LCT17.7	0.99986	0.99990
LCT17.8	0.99822	0.99830
LCT17.9	0.99770	0.99778
LCT17.10	0.99809	0.99812
LCT17.11	0.99842	0.99842
LCT17.12	0.99860	0.99834
LCT17.13	0.99881	0.99875
LCT17.14	0.99915	0.99913
LCT17.15	0.99742	0.99726
LCT17.16	0.99864	0.99850
LCT17.17	1.00010	0.99954
LCT17.18	0.99867	0.99819
LCT17.19	0.99923	0.99892
LCT17.20	0.99829	0.99792
LCT17.21	0.99842	0.99769
LCT17.22	0.99781	0.99728
LCT17.23	0.99973	0.99957
LCT17.24	1.00051	1.00055
LCT17.25	0.99849	0.99834
LCT17.26	0.99650	0.99596
LCT17.27	0.99841	0.99801
LCT17.28	0.99915	0.99867
LCT17.29	0.99950	0.99897
LCT22.1	1.00278	1.00172
LCT22.2	1.00703	1.00674
LCT22.3	1.00769	1.00766
LCT22.4	1.00806	1.00860
LCT22.5	1.00344	1.00385
LCT22.6	1.00160	1.00213
LCT22.7	1.00395	1.00436
LCT24.1	1.00113	0.99998
LCT24.2	1.00892	1.00906
LCT25.1	0.98833	0.98784
LCT25.2	0.99584	0.99604
LCT25.3	1.00064	1.00121
LCT25.4	1.00256	1.00325
LCT27.1	1.00278	1.00265

TABLE XLVIII: Summary of criticality k_{eff} C/E changes between ENDF/B-VII.1 (E71) and ENDF/B-VIII.0 (E80).

Name	E71 k_{eff} C/E	E80 k_{eff} C/E
LCT27.2	1.00522	1.00514
LCT27.3	1.00562	1.00572
LCT27.4	1.00782	1.00755
LCT28.1	0.99824	0.99798
LCT28.2	0.99918	0.99887
LCT28.3	0.99899	0.99849
LCT28.4	1.00122	1.00094
LCT28.5	0.99954	0.99947
LCT28.6	1.00089	1.00058
LCT28.7	0.99638	0.99581
LCT28.8	0.99449	0.99423
LCT28.9	0.99282	0.99263
LCT28.10	0.99703	0.99732
LCT28.11	0.99784	0.99795
LCT28.12	0.99633	0.99658
LCT28.13	0.99524	0.99560
LCT28.14	0.99279	0.99324
LCT28.15	0.99805	0.99828
LCT28.16	0.99821	0.99873
LCT28.17	0.99833	0.99852
LCT28.18	0.99887	0.99926
LCT28.19	0.99787	0.99816
LCT28.20	0.99580	0.99624
LCT35.1	0.99997	0.99937
LCT35.2	0.99891	0.99871
LCT35.3	0.99524	0.99482
LCT39.1	0.99712	0.99632
LCT39.2	0.99807	0.99709
LCT39.3	0.99713	0.99643
LCT39.4	0.99639	0.99590
LCT39.5	0.99760	0.99729
LCT39.6	0.99719	0.99694
LCT39.7	0.99716	0.99640
LCT39.8	0.99710	0.99609
LCT39.9	0.99687	0.99652
LCT39.10	0.99752	0.99680
LCT42.1	0.99816	0.99816
LCT42.2	0.99804	0.99740
LCT42.3	0.99897	0.99797
LCT42.4	0.99838	0.99782
LCT42.5	0.99930	0.99878
LCT42.6	0.99937	0.99913
LCT42.7	0.99776	0.99720
LCT60.1	0.99999	1.00374
LCT60.2	0.99986	1.00466
LCT60.3	0.99983	1.00353
LCT60.4	0.99768	1.00186
LCT60.5	0.99974	1.00318
LCT60.6	0.99842	1.00203
LCT78.1	0.99850	0.99728
LCT78.2	0.99856	0.99748
LCT78.3	0.99848	0.99731
LCT78.4	0.99857	0.99740
LCT78.5	0.99888	0.99762
LCT78.6	0.99868	0.99770
LCT78.7	0.99848	0.99754
LCT78.8	0.99849	0.99734
LCT78.9	0.99869	0.99744
LCT78.10	0.99834	0.99705
LCT78.11	0.99860	0.99750
LCT78.12	0.99852	0.99764
LCT78.13	0.99847	0.99743
LCT78.14	0.99859	0.99726
LCT78.15	0.99906	0.99801
LCT79.1	0.99831	0.99682
LCT79.2	0.99841	0.99707
LCT79.3	0.99856	0.99738
LCT79.4	0.99896	0.99766
LCT79.5	0.99907	0.99773
LCT79.6	0.99906	0.99930
LCT79.7	0.99761	0.99760
LCT79.8	0.99801	0.99827
LCT79.9	0.99826	0.99849
LCT79.10	0.99869	0.99867
LCT80.1	0.99821	0.99693
LCT80.2	0.99821	0.99680
LCT80.3	0.99823	0.99653
LCT80.4	0.99823	0.99656
LCT80.5	0.99836	0.99664
LCT80.6	0.99809	0.99678
LCT80.7	0.99836	0.99681
LCT80.8	0.99843	0.99677

TABLE XLVIII: Summary of criticality k_{eff} C/E changes between ENDF/B-VII.1 (E71) and ENDF/B-VIII.0 (E80).

TABLE XLVIII: Summary of criticality k_{eff} C/E changes between ENDF/B-VII.1 (E71) and ENDF/B-VIII.0 (E80).

Name	E71 k_{eff} C/E	E80 k_{eff} C/E
LCT80.9	0.99828	0.99667
LCT80.10	0.99864	0.99683
LCT80.11	0.99889	0.99755
PU-SOL-THERM		
PST1.1	1.00604	1.00106
PST1.2	1.00752	1.00314
PST1.3	1.01035	1.00660
PST1.4	1.00457	1.00123
PST1.5	1.00869	1.00505
PST1.6	1.00969	1.00790
PST2.1	1.00384	0.99828
PST2.2	1.00490	0.99934
PST2.3	1.00375	0.99828
PST2.4	1.00653	1.00145
PST2.5	1.00926	1.00424
PST2.6	1.00500	1.00043
PST2.7	1.00769	1.00247
PST3.1	1.00281	0.99673
PST3.2	1.00233	0.99633
PST3.3	1.00516	0.99908
PST3.4	1.00427	0.99868
PST3.5	1.00562	0.99965
PST3.6	1.00572	0.99991
PST3.7	1.00680	1.00098
PST3.8	1.00558	0.99968
PST4.1	1.00383	0.99752
PST4.2	0.99875	0.99248
PST4.3	1.00079	0.99466
PST4.4	0.99887	0.99264
PST4.5	0.99977	0.99365
PST4.6	1.00170	0.99557
PST4.7	1.00553	0.99979
PST4.8	1.00114	0.99516
PST4.9	1.00057	0.99450
PST4.10	1.00222	0.99646
PST4.11	1.00051	0.99469
PST4.12	1.00295	0.99716
PST4.13	1.00030	0.99434
PST5.1	1.00235	0.99610
PST5.2	1.00297	0.99697
PST5.3	1.00340	0.99750
PST5.4	1.00516	0.99932
PST5.5	1.00636	1.00034
PST5.6	1.00575	1.00013
PST5.7	1.00416	0.99855
PST5.8	0.99938	0.99349
PST5.9	1.00218	0.99624
PST6.1	1.00083	0.99439
PST6.2	1.00189	0.99608
PST6.3	1.00152	0.99544
PST7.2	1.00928	1.00713
PST7.3	1.00357	1.00148
PST7.5	1.00915	1.00521
PST7.6	1.00322	0.99913
PST7.7	1.00529	1.00124
PST7.8	0.99879	0.99471
PST7.9	0.99717	0.99321
PST7.10	1.00099	0.99667
PST9.3a	1.01902	1.01277
PST10.1	1.01818	1.01372
PST10.2	1.01465	1.00960
PST10.3	1.00830	1.00286
PST10.4	1.01255	1.00731
PST10.5	1.01025	1.00454
PST10.6	1.00932	1.00395
PST10.7	1.00243	0.99691
PST10.8	1.00379	0.99790
PST10.9	1.01485	1.00949
PST10.10	1.00282	0.99725
PST10.11	1.00985	1.00429
PST10.12	1.00968	1.00430
PST10.13	1.01588	1.00996
PST10.14	1.00969	1.00377
PST11.16.1	1.00991	1.00349
PST11.16.2	1.01480	1.00809
PST11.16.3	1.01679	1.01030
PST11.16.4	1.00928	1.00285
PST11.16.5	1.00608	1.00007
PST11.18.1	0.99437	0.98770
PST11.18.2	1.00015	0.99407
PST11.18.3	0.99743	0.99035
PST11.18.4	0.99348	0.98700
PST11.18.5	1.00379	0.99673
PST11.18.6	1.00036	0.99363
PST11.18.7	0.99979	0.99327
PST12.1	1.00560	1.00028
PST12.2	1.00605	1.00066
PST12.3	1.00717	1.00202
PST12.4	1.00766	1.00213
PST12.5	1.00966	1.00423
PST12.6	1.00669	1.00420
PST12.7	1.00539	1.00262
PST12.8	1.00428	1.00025
PST12.9	1.00981	1.00484
PST12.10	1.00403	0.99896
PST12.11	1.00671	1.00135
PST12.12	1.00691	1.00149
PST12.13	1.00960	1.00411
PST18.1	1.00850	1.00950
PST18.2	1.01159	1.01260
PST18.3	1.00928	1.00914
PST18.4	1.00752	1.00680
PST18.5	1.00644	1.00556
PST18.6	1.00467	1.00331
PST18.7	1.00388	1.00213
PST18.8	1.00368	1.00145
PST18.9	1.00193	0.99935
PST22.1	0.99973	0.99887
PST22.2	1.00205	1.00020
PST22.3	1.00093	0.99759
PST22.4	1.00133	0.99765
PST22.5	1.00216	0.99785
PST22.6	1.00280	0.99871
PST22.7	1.00423	0.99974
PST22.8	1.00491	1.00041
PST22.9	1.00366	0.99882
PST28.1	1.00777	1.00349
PST28.2	1.00729	1.00262
PST28.3	1.00893	1.00418
PST28.4	1.00866	1.00356
PST28.5	1.00985	1.00472
PST28.6	1.01105	1.00528
PST28.7	1.00814	1.00405
PST28.8	1.00803	1.00406
PST28.9	1.01004	1.00547
PST32.1	0.99590	0.99150
PST32.2	1.00142	0.99693
PST32.3	1.00281	0.99802
PST32.4	1.00247	0.99750
PST32.5	1.00455	0.99921
PST32.6	1.00455	0.99946
PST32.7	1.00524	0.99979
PST32.8	1.00452	0.99908
PST32.9	1.00317	0.99754
PST32.10	1.00518	0.99934
PST32.11	1.00458	0.99892
PST32.12	1.00367	0.99781
PST32.13	1.00236	0.99767
PST32.14	1.00196	0.99703
PST32.15	1.00403	0.99910
PST32.16	1.00380	0.99880
PST32.17	1.00390	0.99893
PST34.1	1.00006	0.99701
PST34.2	1.00165	0.99805
PST34.3	0.99953	0.99578
PST34.4	1.00259	0.99808
PST34.5	0.99995	0.99533
PST34.6	1.00124	0.99629
PST34.7	0.99861	0.99851
PST34.8	0.99911	0.99859
PST34.9	0.99774	0.99737
PST34.10	0.99732	0.99637
PST34.11	0.99877	0.99807
PST34.12	0.99853	0.99760
PST34.13	0.99704	0.99562
PST34.14	0.99689	0.99549
PST34.15	0.99729	0.99594
PST38.1	1.00262	0.99702
PST38.2	1.00307	0.99744
PST38.3	1.00196	0.99634
PST38.4	1.00105	0.99528
PST38.5	1.00131	0.99584
U233-SOL-INTER		
USI1.1	0.98547	0.98221

TABLE XLVIII: Summary of criticality k_{eff} C/E changes between ENDF/B-VII.1 (E71) and ENDF/B-VIII.0 (E80).

Name	E71 k_{eff} C/E	E80 k_{eff} C/E
USI1.2	0.98100	0.97796
USI1.3	0.98186	0.97895
USI1.4	0.99348	0.99164
USI1.5	0.98497	0.98257
USI1.6	0.98643	0.98502
USI1.7	0.98238	0.97978
USI1.8	0.98203	0.98012
USI1.9	0.97950	0.97739
USI1.10	0.97902	0.97697
USI1.11	0.98064	0.97863
USI1.12	0.98171	0.97812
USI1.13	0.98243	0.97941
USI1.14	0.99140	0.98908
USI1.15	0.98047	0.97734
USI1.16	0.98164	0.97950
USI1.17	0.98951	0.98720
USI1.18	0.97889	0.97602
USI1.19	0.97566	0.97304
USI1.20	0.98082	0.97933
USI1.21	0.97352	0.97095
USI1.22	0.97873	0.97585
USI1.23	0.99051	0.98874
USI1.24	0.99289	0.98892
USI1.25	0.98546	0.98189
USI1.26	0.98950	0.98595
USI1.27	0.99132	0.98887
USI1.28	0.98366	0.98052
USI1.29	0.97794	0.97489
USI1.30	0.97902	0.97710
USI1.31	0.99139	0.98846
USI1.32	0.97630	0.97342
USI1.33	0.99440	0.99155
U233-COMP-THERM		
UCT1.1	0.99892	0.99606
UCT1.2	1.00050	0.99772
UCT1.3	1.00218	1.00051
UCT1.4	0.99973	0.99718
UCT1.5	0.99878	0.99622
UCT1.6	0.99726	0.99545
UCT1.7	1.00255	0.99882
UCT1.8	0.99939	0.99542
UCT4	0.99639	0.99660
U233-SOL-THERM		
UST1.1	1.00085	0.99902
UST1.2	1.00016	0.99846
UST1.3	0.99972	0.99787
UST1.4	1.00048	0.99884
UST1.5	0.99980	0.99790
UST5.1	1.00179	0.99997
UST5.2	1.00500	1.00293
UST8	1.00096	0.99914
UST9.1	0.99949	0.99770
UST9.2	1.00103	0.99939
UST9.3	1.00164	0.99996
UST9.4	0.99953	0.99787
UST12.1	1.00078	0.99893
UST12.2	1.00012	0.99846
UST12.3	1.00964	1.00758
UST12.4	1.00287	1.00073
UST12.5	1.00503	1.00286
UST12.6	1.00582	1.00381
UST12.7	1.00188	0.99981
UST12.8	0.99912	0.99680
UST13.1	1.00614	1.00307
UST13.2	1.00616	1.00329
UST13.3	1.00656	1.00341
UST13.4	1.00717	1.00385
UST13.5	1.00795	1.00501
UST13.6	1.00706	1.00393
UST13.7	1.00734	1.00388
UST13.8	1.00793	1.00504
UST13.9	1.00820	1.00475
UST13.10	1.00878	1.00561
UST13.11	1.00593	1.00293
UST13.12	1.00699	1.00410
UST13.13	1.00438	1.00142
UST13.14	1.00750	1.00447
UST13.15	1.02164	1.01874
UST13.16	0.99401	0.99101
UST13.17	0.99691	0.99383
UST13.18	1.00056	0.99783
UST13.19	0.99696	0.99387

TABLE XLVIII: Summary of criticality k_{eff} C/E changes between ENDF/B-VII.1 (E71) and ENDF/B-VIII.0 (E80).

Name	E71 k_{eff} C/E	E80 k_{eff} C/E
UST13.20	1.00026	0.99746
UST13.21	1.00292	0.99997
UST15.1	0.99044	0.98671
UST15.2	0.98584	0.98256
UST15.3	0.98684	0.98348
UST15.4	0.99032	0.98802
UST15.5	0.98658	0.98342
UST15.6	0.97707	0.97427
UST15.7	0.98804	0.98604
UST15.8	0.97351	0.97094
UST15.9	0.96913	0.96599
UST15.10	0.99011	0.98791
UST15.11	0.99339	0.98979
UST15.12	0.99410	0.99080
UST15.13	0.99208	0.98880
UST15.14	0.99865	0.99654
UST15.15	0.99008	0.98667
UST15.16	0.98883	0.98593
UST15.17	0.99812	0.99625
UST15.18	0.97494	0.97164
UST15.19	0.97518	0.97232
UST15.20	0.99532	0.99178
UST15.21	0.99835	0.99479
UST15.22	0.99642	0.99287
UST15.23	0.99445	0.99164
UST15.24	0.99096	0.98765
UST15.25	0.99824	0.99695
UST15.26	0.99432	0.99140
UST15.27	0.99905	0.99606
UST15.28	0.99698	0.99413
UST15.29	0.99563	0.99294
UST15.30	0.99488	0.99194
UST15.31	0.99412	0.99180
UST16.1	1.00520	1.00276
UST16.2	1.00660	1.00379
UST16.3	1.00533	1.00209
UST16.6	0.99696	0.99384
UST16.7	0.99579	0.99300
UST16.8	0.99532	0.99174
UST16.10	1.00485	1.00146
UST16.11	1.00533	1.00238
UST16.12	1.00555	1.00214
UST16.13	1.00572	1.00261
UST16.14	1.00560	1.00237
UST16.15	1.00647	1.00351
UST16.16	1.01043	1.00758
UST16.17	0.99554	0.99266
UST16.18	0.99702	0.99400
UST16.21	1.00972	1.00664
UST16.22	1.00966	1.00663
UST16.23	1.01001	1.00686
UST16.25	1.00205	0.99910
UST16.26	1.00791	1.00467
UST16.27	1.00508	1.00185
UST16.28	1.00082	0.99761
UST16.29	1.00137	0.99849
UST16.30	1.00034	0.99727
UST16.31	1.01158	1.00869
UST16.32	1.01420	1.01113
UST16.33	1.01396	1.01104
UST17.1	1.00466	1.00258
UST17.2	1.00044	0.99831
UST17.3	1.00513	1.00318
UST17.4	1.00608	1.00405
UST17.5	1.00196	1.00001
UST17.6	1.00084	0.99872
UST17.7	1.00037	0.99813